

Redox Ambi-valence of Phenylcyanamide Ligands in Ruthenium Complexes

by

Mohammad Mahbubur Rahman Choudhuri, M.Sc.

A Thesis submitted to the Faculty of Graduate Studies
in partial fulfillment of the requirements for the degree of
Doctor of Philosophy

Carleton University

Ottawa, Canada

December 2013

Copyright © 2013, Mohammad Mahbubur Rahman Choudhuri

The undersigned hereby recommend to
the Faculty of Graduate Studies and Research
acceptance of the thesis

Redox Ambi-valence of Phenylcyanamide Ligands in Ruthenium Complexes

Submitted by

Mohammad Mahbubur Rahman Choudhuri, M.Sc.

in partial fulfillment of the requirements
for the degree of Doctor of Philosophy

Chair, Department of Chemistry

Thesis Supervisor

External Examiner

Carleton University

Abstract

Four dinuclear ruthenium (II)-terpyridine-bipyridine complexes of bridging substituted (dimethyl-, unsubstituted dichloro- and tetrachloro-) 1,4-dicyanamidebenzene dianion ligands have been synthesized. The singly oxidized complexes were characterized by vis-NIR, IR and EPR spectroscopies which confirm a valence configuration with the oxidized bridging ligand.

Six dinuclear ruthenium (II)-terpyridine-bipyridine complexes of bridging substituted (tetramethyl-, dimethyl-, unsubstituted, dichloro-, tetrachloro-) azodi(phenylcyanamide) ligands have been synthesized. The EPR spectroscopy, supported by IR and vis-NIR spectroelectrochemistry of singly oxidized complexes showed a transition in non-innocent behaviour of the bridging ligand and established the ligand-centred radical descriptions for tetramethyl-/dimethyl-, a delocalized metal-ligand mixed-valence description for unsubstituted, and a localized metal-centred mixed-valence descriptions for dichloro-/tetrachloro- azodi(phenylcyanamide) complexes.

Six mononuclear ruthenium (II)-(dmsO-S)-bipyridine complexes of substituted (pentachloro-, tetrachloro-, trichloro-, dichloro-, monochloro- and unsubstituted) phenylcyanamide monoanion ligands were synthesized and characterized. The complexes exhibited photo-induced Ru-S to Ru-O and thermal Ru-O to Ru-S linkage isomerism in solutions and solid polymer films. The quantum yields (0.43-0.06) of photo-induced Ru-S to Ru-O linkage isomerism are shown to decrease with increasing donor properties of the phenylcyanamide ligand. The thermal Ru-O to Ru-S back reaction ($k = 4.52 - 2.61 \times 10^{-3} \text{ s}^{-1}$) showed a modest decrease with decrease in the donor properties of the phenylcyanamide ligand. The scan rate dependent cyclic voltammograms demonstrated

redox-induced Ru-S to Ru-O and Ru-O to Ru-S linkage isomerism and provided estimates of ground state isomerism rates. DFT calculations established the non-innocent behaviour of phenylcyanamide ligands.

Five mononuclear neutral ruthenium (III)-terpyridine-chloride complexes of substituted (pentachloro-, tetrachloro-, trichloro-, dichloro-, monochloro-) phenylcyanamide monoanion ligands were synthesized. The paramagnetic NMR spectroscopy of complexes in dimethylsulfoxide provided estimates of pi-carbon spin density distributions of phenylcyanamide ligands (0.7-3.0 %) and suggested a Ru (III)-centred spin in disagreement with the gas-phase DFT spin density calculations which gave mostly ligand-centred spin. It is suggested that specific solvent-solute interactions stabilize the Ru (III) oxidation state.

Acknowledgements

I would like to express my deepest sense of gratitude to my research supervisor, Dr. R. J. Crutchley, for his knowledgeable guidance, continuous assistance, encouragement and constructive criticism in making this research work a success.

Special thanks go to Dr. Wolfgang Kaim and Dr. Biprajit Sarkar of University of Stuttgart, Germany, for performing EPR experiments on complexes. I would also like to thank Dr. Glen Yap of the University of Delaware who performed X-ray crystallography and Dr. Serge Gorelsky of the University of Ottawa for DFT calculations in solutions. Thanks to Jim Logan for keeping our computers and instruments running smoothly, and especially for setting-up the instrument for photochemical measurements. Thanks to Tony O'Neil and Keith Bourque for their technical assistance with IR and NMR experiments. Thanks are due for everyone at Stores (Susa, Peter, Tanya) for their prompt actions in placing the orders for chemicals and glassware. I would also like to thank my fellow Labmates Dr. Arezoo Habibagahi, Carmen Harb, Pavel Kravstov, Diane Jodoin, Fatemeh Habibagahi, and Alex Daniel for their cooperation throughout this research work and for keeping the lab entertaining. Thanks to Shah Shakib for drawing an excellent piece of SolidWorks diagram for photochemical measurements and Sayeed Mirza Kareem for editing figures. Special thanks to Tanwin for showing patience in proof-reading few chapters of this thesis.

None of this would have been possible without the unending love and support of my parents, brothers and relatives. Thanks to my fellow friends in Ottawa Palash, Zulhasnine, Abeer, Salehin, Zakir, Tabrez, Rabbi, Nafish, Aad-yeen, Nur, Rafiq and many others who distracted me from the lab long enough to ensure that I stayed sane.

Dedication

This thesis is dedicated to my parents Mohammad Ali Akbar

and Kamrun Nahar Begum

Table of Contents

Title Page	i
Acceptance Form	ii
Abstract	iii
Acknowledgements	v
Dedication	vi
Table of Contents	vii
List of Tables	xii
List of Figures	xxv
List of Schemes	xxviii
List of Abbreviations	xxx

Chapter 1: General Introduction

1.1	Scope of Thesis Research	1
1.2	Non-Innocent Ligand Behaviour	5
1.2.1	Non-innocent Ligand Behaviour in Mononuclear Complexes	8
1.2.2	Non-innocent Behavior of Bridging Ligands in Dinuclear Complexes	11
1.2.3	Experimental Determination of Non-Innocent Behaviour	14
1.3	Aromatic Cyanamide Ligands	34
1.3.1	The Structure of Phenylcyanamide Ligand	35
1.4	Research Strategies and Goals	42
1.5	References	46

Chapter 2: Non-Innocence of 1,4-Dicyanamidebenzene Ligands in Dinuclear Ruthenium Complexes

2.1	Introduction	53
2.1.1	Research Objectives	53
2.2	Experimentals	56
2.2.1	Starting Materials	56

2.2.2	Synthesis	58
2.2.3	Physical Measurements	63
2.2.4	Theoretical Calculations	65
2.3	Results and Discussion	67
2.3.1	Synthesis	67
2.3.2	Molecular Structure	68
2.3.3	Electronic Structure	70
2.3.4	IR Spectroscopy	74
2.3.5	¹ H NMR Spectroscopy	77
2.3.6	Electronic Absorption Spectroscopy	89
2.3.7	Cyclic Voltammetry	91
2.3.8	EPR Spectroscopy	94
2.3.9	Paramagnetic ¹ H NMR Study on Singly Oxidized Complexes	97
2.3.10	Vis-NIR Spectroelectrochemistry	98
2.3.11	IR Spectroelectrochemistry	105
2.4	Conclusion	113
2.5	References	114

Chapter 3: Redox Ambi-valence of 4,4'-Azodi(phenylcyanamide) Ligands in Dinuclear Ruthenium Complexes

3.1	Introduction	118
3.1.1	Research Objectives	118
3.2	Synthesis of Substituted Azodicyd (R_2R_2' adpcH ₂) Ligands	122
3.2.1	Reviews on the Synthesis of Azobenzene Derivatives	123
3.2.2	Reviews on the Synthesis of Aromatic Cyanamide Ligands	130
3.2.3	Synthetic Strategy	138
3.2.4	Synthesis of Precursor Compounds for Substituted Azodianilines	143
3.2.5	Synthesis of Substituted Azodianilines	147
3.2.6	Synthesis of Substituted Azodicyd (R_2R_2' adpcH ₂) Ligands	150
3.2.7	Concluding Remarks	153
3.3	Experimental	156
3.3.1	Starting Materials.	156
3.3.2	Metal Complex Precursor Synthesis	158

3.3.3	Synthesis of R_2R_2' adpcH ₂ Ligands and Tl ₂ [R ₂ R _{2'} adpc] Salts	159
3.3.4	Synthesis of [{Ru(tpy)(bpy)} ₂ (μ-R ₂ R _{2'} adpc)][PF ₆] ₂ Complexes	161
3.3.5	Physical Measurements	165
3.3.6	Theoretical Calculations	168
3.4	Results	170
3.4.1	Synthesis of Complexes	170
3.4.2	X-ray Crystallography	171
3.4.3	IR Spectroscopy	174
3.4.4	¹ H NMR Spectroscopy	177
3.4.5	Electronic Absorption Spectroscopy	196
3.4.6	Cyclic Voltammetry	200
3.4.7	EPR Spectroscopy	203
3.4.8	IR Spectroelectrochemistry	205
3.4.9	Vis-NIR Spectroelectrochemistry	216
3.4.10	Theoretical Calculations	226
3.5	Discussion	236
3.5.1	Synthesis	236
3.5.2	Spectroscopic Analysis, Cyclic Voltammetry and Theory	237
2.4	Conclusion	240
2.4	References	241

Chapter 4: Phenylcyanamide Ligand Control of Linkage Isomerism in Ruthenium-Sulfoxide Complexes

4.1	Introduction	249
4.1.1	Scope of Research	249
4.1.2	Transition Metal Sulfoxide Complexes	251
4.1.3	Linkage Isomerism in Ruthenium-Sulfoxide Complexes	253
4.1.4	Initial Studies on Sulfoxide Isomerism	255
4.1.5	Recent Studies on Sulfoxide Isomerism	257
4.1.6	Characterization of Linkage Isomerism	264
4.1.7	Research Objectives	271
4.2	Experimental	273
4.2.1	Starting Materials	273
4.2.2	Synthesis of Precursor Ligands and Complexes	275
4.2.3	Synthesis of <i>cis</i> -[Ru(bpy) ₂ (R-pcyd)(dmsO-S)][PF ₆]	278

	Complexes	
4.2.4	Physical Measurements	282
4.2.5	Theoretical Calculations	294
4.3	Results	295
4.3.1	Synthesis	295
4.3.2	Molecular Structure	296
4.3.3	Electronic Structure	298
4.3.4	IR Spectroscopy	302
4.3.5	NMR Spectroscopy	307
4.3.6	Electronic Absorption Spectroscopy and Photo-induced Linkage Isomerism	326
4.3.7	Cyclic Voltammetry and Redox-induced Linkage Isomerism	335
4.4	Discussion	343
4.4.1	Synthesis.	343
4.4.2	Linkage Isomerism in <i>cis</i> -[Ru(bpy) ₂ (R-pcyd)(dmsos)] [PF ₆] Complexes	344
4.5	Conclusions and Future Work	348
4.6	References	349

Chapter 5: Redox-Ambiguity of Phenylcyanamide Ligands in Neutral Ruthenium Complexes

5.1	Introduction	355
5.1.1	Research Scope and Design Criteria	355
5.1.2	Research Objectives	360
5.2	Experimentals	363
5.2.1	Starting Materials	363
5.2.2	Synthesis	364
5.2.3	Physical Measurements	368
5.2.4	Oscillator Strength Calculation	370
5.2.5	Theoretical Calculations	370
5.3	Results and Discussion	372
5.3.1	Synthesis	372
5.3.2	X-ray Crystallography	373
5.3.3	IR Spectroscopy	382
5.3.4	Electronic Structure	384
5.3.5	Electronic Absorption Spectroscopy	391
5.3.6	Cyclic Voltammetry	399
5.3.7	Paramagnetic ¹ H NMR Spectroscopy	403

5.4	Conclusions and Future Work	417
5.5	References	419
Chapter 6: Conclusion and Future Work		
6.1	Research Summary	423
6.2	Concluding Remarks	430
6.3	Future Studies	432
Chapter 7: Appendices		
7.1	Appendix-A Supporting Tables and Figures for Chapter 1	435
7.2	Appendix-B Supporting Tables and Figures for Chapter 2	437
7.3	Appendix-C Supporting Tables and Figures for Chapter 3	447
7.4	Appendix-D Supporting Tables and Figures for Chapter 4	469
7.5	Appendix-E Supporting Tables and Figures for Chapter 5	488

List of Tables

Table 2.3.1: Infrared Data of $\nu(\text{NCN})$ Bands in Free $\text{R}_2\text{R}_2'\text{dicydH}_2$, $\text{Tl}_2[\text{R}_2\text{R}_2'\text{dicyd}]$ and $[\{\text{Ru}(\text{tpy})(\text{bpy})\}_2(\mu\text{-R}_2\text{R}_2'\text{dicyd})]^{2+}$ Complexes (1-4)	75
Table 2.3.2: 300 MHz ^1H NMR Data of $[\{\text{Ru}(\text{tpy})(\text{bpy})\}_2(\mu\text{-R}_2\text{R}_2'\text{dicyd})][\text{PF}_6]_2$ Complexes (1-4) in $\text{DMSO-}d_6$.	78
Table 2.3.3: Quantitative Electronic Absorption Data ^a of $[\{\text{Ru}(\text{tpy})(\text{bpy})\}_2(\mu\text{-R}_2\text{R}_2'\text{dicyd})][\text{PF}_6]_2$ Complexes (1-4) and Their Oxidized Forms (1⁺-4⁺ , 1²⁺-4²⁺) in DMF	90
Table 2.3.4: Cyclic Voltammetry Data ^a of $[\text{Ru}(\text{tpy})(\text{bpy})\text{Cl}][\text{PF}_6]$ and $[\{\text{Ru}(\text{tpy})(\text{bpy})\}_2(\mu\text{-R}_2\text{R}_2'\text{dicyd})][\text{PF}_6]_2$ Complexes (1-4) and $[\text{AsPh}_4]_2[\text{R}_2\text{R}_2'\text{dicyd}]$ Salts	92
Table 3.4.1: Crystal Data and Structure Refinement for $[\text{AsPh}_4]_2[\text{Me}_2\text{adpc}](\mathbf{5g})$	172
Table 3.4.2: Selected Crystal Structure Data for $[\text{AsPh}_4]_2[\text{Me}_2\text{adpc}](\mathbf{5g})$	173
Table 3.4.3: Infrared Data for $\nu(\text{NCN})$ Bands of Free Ligands (4a-4f , 5a-5e) and $[\{\text{Ru}(\text{tpy})(\text{bpy})\}_2(\mu\text{-R}_2\text{R}_2'\text{adpc})]^{2+}$ Complexes (7a-7f).	175
Table 3.4.4: 300 MHz ^1H NMR Data of $\text{R}_2\text{R}_2'\text{adpcH}_2$ (4a-4f) in $\text{DMSO-}d_6$	178
Table 3.4.5: 300 MHz ^1H NMR Data of $\text{Tl}_2[\text{R}_2\text{R}_2'\text{adpc}]$ (5a-5e) in $\text{DMSO-}d_6$.	181
Table 3.4.6: 300 MHz ^1H NMR data for $[\{\text{Ru}(\text{tpy})(\text{bpy})\}_2(\mu\text{-R}_2\text{R}_2'\text{adpc})](\text{PF}_6)_2$ Complexes (7a-7f) in $\text{DMSO-}d_6$.	183
Table 3.4.7: Quantitative Electronic Absorption Data ^a of $\text{Tl}_2[\text{R}_2\text{R}_2'\text{adpc}]$ Salts (5a-5c , 5e) and $[\{\text{Ru}(\text{tpy})(\text{bpy})\}_2(\mu\text{-R}_2\text{R}_2'\text{adpc})][\text{PF}_6]_2$ (7a-7f) Complexes and their Oxidized Forms (5a⁺-5c⁺ , 5e⁺ , 7a⁺-7f⁺ and 7a²⁺-7f²⁺) ^b in DMF	198
Table 3.4.8: Cyclic Voltammetry Data of $\text{Tl}_2[\text{R}_2\text{R}_2'\text{adpc}]$ and $[\{\text{Ru}(\text{tpy})(\text{bpy})\}_2(\mu\text{-R}_2\text{R}_2'\text{adpc})][\text{PF}_6]_2$ (7a-7e)	201
Table 3.4.9: Low Energy NIR Band Properties of $\{\text{Ru}(\text{tpy})(\text{bpy})\}_2(\mu\text{-R}_2\text{R}_2'\text{adpc})]^{3+}$ Complexes (7a⁺-7e⁺)	224
Table 4.3.1: IR Data of <i>cis</i> - $[\text{Ru}(\text{bpy})_2(\text{R-pcyd})(\text{dmsO})][\text{PF}_6]$ Complexes.	303
Table 4.3.2: ^1H NMR Data of <i>cis</i> - $[\text{Ru}(\text{bpy})_2(\text{R-pcyd})(\text{dmsO-S})]$ Complexes (4a-4f) in $\text{dmsO-}d_6$.	310
Table 4.3.3: Electronic Absorption Data of <i>cis</i> - $[\text{Ru}(\text{bpy})_2(\text{R-pcyd})(\text{dmsO-S/O})][\text{PF}_6]$ Complexes in dmsO . R- <i>pcyd</i> is a Phenylcyanamide Ligand	328
Table 4.3.4: Photochemical Data of <i>cis</i> - $[\text{Ru}(\text{bpy})_2(\text{R-pcyd})(\text{dmsO})][\text{PF}_6]$ Complexes (4a-4f) in dmsO .	333

Table 4.3.5: Cyclic Voltammetry Data of <i>cis</i> -[Ru(bpy) ₂ (R-pcyd)(dmsu)][PF ₆] Complexes (4a-4f) in dmsu	337
Table 4.3.6: Cyclic Voltammetry Data of <i>cis</i> -[Ru(bpy) ₂ (R-pcyd)(dmsu)] Complexes (4a-4f) in Acetonitrile.	339
Table 5.3.1: Crystal Data and Structure Refinement for [Ru(tpy)Cl ₃]-2DMSO Complex.	375
Table 5.3.2: Selected Crystal Structure Data for [Ru(tpy)Cl ₃]-2DMSO Complex.	376
Table 5.3.3: Crystal Data and Structure Refinement for <i>trans</i> -[Ru(tpy)(Cl ₃ pcyd)Cl ₂]-2CH ₃ CN Complex (3).	380
Table 5.3.4: Selected Crystal Structure Data for <i>trans</i> -[Ru(tpy)(Cl ₃ pcyd)Cl ₂]-2CH ₃ CN Complex (3).	381
Table 5.3.5: IR Data of ν(NCN) Bands in Free Protonated R-pcydH Ligands, in Thallium Salts and in <i>trans</i> -[Ru(tpy) ₂ (R-pcyd)Cl ₂] Complexes (1-5).	383
Table 5.3.6: Quantitative Electronic Absorption Data of Ru(tpy)Cl ₃ and <i>trans</i> -[Ru(tpy)(R-pcyd)Cl ₂] Complexes (1-5) in DMF and CH ₂ Cl ₂ .	393
Table 5.3.7: Cyclic Voltammetry and Vis-NIR LMCT Energy Data of Ru(tpy)Cl ₃ and <i>trans</i> -[Ru(tpy)(R-pcyd)Cl ₂] Complexes (1-5) in DMF and CH ₂ Cl ₂ at 25 °C.	400
Table 5.3.8: ¹ H NMR Spectral Data of <i>trans</i> -[Ru(tpy)(R-pcyd)Cl ₂] Complexes (1-5) and Free R-pcydH Ligands in dmsu- <i>d</i> ₆	406
Table 5.3.9: Isotropic Shifts of R-pcyd Protons and R-pcyd Phenyl Carbon π-Spin Densities of <i>trans</i> -[Ru(tpy)(R-pcyd)Cl ₂] Complexes (1-5).	415
Table A.1: Atomic Coordinates of Phenylcyanamide Monoanion (pcyd ⁻).	435
Table A.2: Atomic Coordinates of 1,4-Dicyanamide Benzene Dianion (dicyd ²⁻)	435
Table A.3: Atomic Coordinates of 4,4'-Azodi(phenylcyanamide) (adpc ²⁻).	436
Table B.1: Atomic Coordinates of [{Ru(tpy)(bpy)} ₂ (μ-dicyd)] ²⁺ Complex.	437
Table B.2: Atomic Coordinates of [{Ru(tpy)(bpy)} ₂ (μ-dicyd)] ³⁺ Complex.	440
Table B.3: Atomic Coordinates of [{Ru(tpy)(bpy)} ₂ (μ-dicyd)] ⁴⁺ Complex.	442
Table C.1: X-ray Crystallography Data of [AsPh] ₂ [Me ₂ adpc] (5g).	447
Table C.2: Atomic Coordinates of the Geometry Optimized Structure of [{Ru(tpy)(bpy)} ₂ (μ-Me ₄ adpc)] ³⁺ Complex (7a ⁺).	449
Table C.3: Atomic Coordinates of the Geometry Optimized structure of [{Ru(tpy)(bpy)} ₂ (μ-adpc)] ³⁺ Complex (7c ⁺).	453

Table C.4: Atomic Coordinates of the Geometry Optimized Structure of $[\{\text{Ru}(\text{tpy})(\text{bpy})\}_2(\mu\text{-Cl}_4\text{adpc})]^{3+}$ Complex (7e⁺).	456
Table C.5: Atomic Coordinates of the Geometry Optimized Structure of $[\{\text{Ru}(\text{tpy})(\text{bpy})\}_2(\mu\text{-meta-adpc})]^{3+}$ Complex (7f⁺).	459
Table C.6: Atomic Coordinates of the Geometry Optimized Structure of <i>meta-adpc</i> ²⁻ (5e).	462
Table D.1: Atomic Coordinates of <i>cis</i> - $[\text{Ru}(\text{bpy})_2(\text{pcyd})(\text{dmsO-S})]^+$ Complex (4a).	469
Table D.2: Atomic Coordinates of <i>cis</i> - $[\text{Ru}(\text{bpy})_2(\text{pcyd})(\text{dmsO-O})]^+$ Complex.	470
Table D.3: Atomic Coordinates of <i>cis</i> - $[\text{Ru}(\text{bpy})_2(\text{pcyd})(\text{dmsO-S})]^{2+}$ Complex (4a⁺).	472
Table D.4: Atomic Coordinates of <i>cis</i> - $[\text{Ru}(\text{bpy})_2(\text{pcyd})(\text{dmsO-O})]^{2+}$ Complex.	474
Table D.5: Atomic Coordinates of <i>cis</i> - $[\text{Ru}(\text{bpy})_2(\text{Cl}_5\text{pcyd})(\text{dmsO-S})]^+$ Complex (4a).	475
Table D.6: Raw and Derived Data for the Determination of Quantum Yield of S→O isomerization of <i>cis</i> - $[\text{Ru}(\text{bpy})_2(\text{Cl}_5\text{pcyd})(\text{dmsO-S})][\text{PF}_6]$ Complex (4f) in dmsO.	484
Table D.7: Raw and Derived Data for the Determination of Thermal O→S Isomerization Rate (<i>k</i> _{OS1}) of <i>cis</i> - $[\text{Ru}(\text{bpy})_2(\text{Cl}_5\text{pcyd})(\text{dmsO-O})][\text{PF}_6]$ Complex (4f) in dmsO.	485
Table E.1: X-ray Crystallography Data of $\text{Ru}(\text{ttpy})\text{Cl}_3 \cdot 2\text{DMSO}$ Complex.	488
Table E.2: X-ray Crystallography Data of <i>trans</i> - $[\text{Ru}(\text{ttpy})(\text{Cl}_3\text{pcyd})\text{Cl}_2] \cdot 2\text{CH}_3\text{CN}$ Complex.	491
Table E.3: Atomic Coordinates of $\text{Ru}(\text{tpy})\text{Cl}_3$ Complex.	496
Table E.4: Atomic Coordinates of <i>trans</i> - $[\text{Ru}(\text{tpy})(\text{Clpcyd})\text{Cl}_2]$ Complex.	497
Table E.5: Atomic Coordinates of <i>trans</i> - $[\text{Ru}(\text{tpy})(\text{Cl}_2\text{pcyd})\text{Cl}_2]$ Complex.	498
Table E.6: Atomic Coordinates of <i>trans</i> - $[\text{Ru}(\text{tpy})(\text{Cl}_3\text{pcyd})\text{Cl}_2]$ Complex.	499
Table E.7: Atomic Coordinates of <i>trans</i> - $[\text{Ru}(\text{tpy})(\text{Cl}_4\text{pcyd})\text{Cl}_2]$ Complex.	501

List of Figures

- Figure 1.1:** Hole-(a) and electron-(b) transfer superexchange metal-metal coupling in the dinuclear mixed-valence Ru(II)- μ -BL²⁻-Ru(III) complex. 11
- Figure 1.2:** EPR spectra of (a) [$\{\text{Ru}(\text{NH}_3)_5\}_2(\mu\text{-dicyd})\}^{3+}$] experiment (blue lines) and simulated (red lines), (b) [$\{\text{Ru}(\text{NH}_3)_5\}_2(\mu\text{-dicyd})\}^{5+}$] experiment (green lines) and simulated (black lines) in DMF at 4 K and (c) [$\{\text{Ru}(\text{tpy})(\text{thd})_5(\mu\text{-dicyd})\}^+$] experiment (top) and simulated (bottom) in frozen CH₂Cl₂ at 100 K. 19
- Figure 1.3:** ¹H NMR spectrum of [$\text{Ru}(\text{NH}_3)_5(2,3\text{-Cl}_2\text{pcyd})\}^+$] in DMSO-*d*₆ showing phenyl proton (*ortho*, *meta*, *para*) resonances ligand in the region between 20 and -25 ppm. The insert shows the *cis* and *trans* ammine region from 50 to 320 ppm. The four strong peaks from 4 to 0 ppm are assigned to water, DMSO, acetone and TMS, respectively. The arrows show the alignment of Ru(III) spin with that of an external magnetic field (H₀) and the resultant phenyl hydrogen atom spin moments. 24
- Figure 1.4:** IR spectra showing the reduction of Ru(III) complexes, (a) *mer*-[$\text{Ru}(\text{NH}_3)_3(\text{bpy})(2,3\text{-Cl}_2\text{pcyd})\}^{2+}$] and (b) [$\text{Ru}(\text{NH}_3)_5(2,3,5,6\text{-Cl}_4\text{pcyd})\}^{2+}$] in nitromethane, to the fully reduced Ru(II) complexes. 27
- Figure 1.5:** Optically transparent thin-layer electrode cell (OTTLE) electronic absorption spectra of (a) [$\text{Ru}(\text{tpy})(\text{bpy})(2,3,4,5\text{-Cl}_4\text{pcyd})\}^+$] forming [$\text{Ru}(\text{tpy})(\text{bpy})(2,3,4,5\text{-Cl}_4\text{pcyd})\}^{2+}$] and (b) *mer,mer*-[$\{\text{Ru}(\text{NH}_3)_3(\text{bpy})\}_2(\mu\text{-Cl}_2\text{dicyd})\}^{4+}$] forming mixed-valence Ru^{III} - Ru^{II} complex *mer,mer*-[$\{\text{Ru}(\text{NH}_3)_3(\text{bpy})\}_2(\mu\text{-Cl}_2\text{dicyd})\}^{3+}$] under anodic and cathodic potentials respectively. 29
- Figure 1.6:** DFT calculated spin density distribution of (A) [$\text{Ru}(\text{NH}_3)_5(\text{pcyd})\}^{2+}$] ion (i) in gas-phase, (ii) in dielectric continuum (PCM) calculations and (B) [$\{\text{Ru}(\text{NH}_3)_5\}_2(\mu\text{-dicyd})\}^{3+}$] in (i) vacuum, (ii) in dielectric continuum (PCM), and (iii) with explicit electrostatic interactions. 33
- Figure 1.7:** Structures of aromatic phenylcyanamide anion ligands. (i) phenylcyanamide monoanion (R-pcyd⁻), (ii) *anti*- and *syn*- (iii) 1,4-dicyanamide benzene dianions (R₂R₂'dicyd²⁻), (iv) 4,4'-azodi(phenylcyanamide) dianions (R₂R₂'adpc²⁻), (v) 3,3'-azodi(phenylcyanamide) dianions (*meta*-adpc²⁻). 35
- Figure 1.8:** Selected frontier molecular orbitals of (a) phenylcyanamide monoanion (b) 1,4-dicyanamidebenzene dianion and (c) 4,4'-azodi(phenylcyanamide) as calculated by gas-phase DFT calculation using B3LYP/6-31G* model 55
- Figure 2.1.1:** The bridging R₂R₂'dicyd²⁻ and ancillary ttpy and bpy ligands used in the synthesis of [$\{\text{Ru}(\text{ttpy})(\text{bpy})\}_2(\mu\text{-R}_2\text{R}_2'\text{dicyd})\}^{2+}$] complexes (1-4). 68
- Figure 2.3.1:** Geometry optimized structure of [$\{\text{Ru}(\text{ttpy})(\text{bpy})\}_2(\mu\text{-dicyd})\}[\text{PF}_6]_2$] complex. (a) horizontal and (b) vertical views. 71

Figure 2.3.2: Gas-phase semi-empirical calculation (PM3) of the orbital energies and wavefunctions of [$\{\text{Ru}(\text{tpy})(\text{bpy})\}_2(\mu\text{-dicyd})\]^{2+}$ (2).	71
Figure 2.3.3: Gas phase semi-empirical calculation (PM3) of the orbital energies and β -wavefunctions of [$\{\text{Ru}(\text{tpy})(\text{bpy})\}_2(\mu\text{-dicyd})\]^{3+}$ (2 ⁺).	72
Figure 2.3.4: Gas phase semi-empirical calculation (PM3) of the orbital energies and LUMO and HOMO wavefunctions of [$\{\text{Ru}(\text{tpy})(\text{bpy})\}_2(\mu\text{-dicyd})\]^{4+}$ (2 ²⁺).	73
Figure 2.3.5: IR spectrum of Cl ₂ dicydH ₂ ligand on KBr Disc.	75
Figure 2.3.6: IR spectrum of Tl ₂ [Cl ₂ dicyd ₂] salt on KBr Disc.	76
Figure 2.3.7: IR spectrum of [$\{\text{Ru}(\text{ttpy})(\text{bpy})\}_2(\mu\text{-Cl}_2\text{dicyd})$] [PF ₆] ₂ Complex (3) on KBr Disc.	76
Figure 2.3.8: ¹ H NMR spectrum of [Ru(ttpy)(bpy)Cl] [PF ₆] complex in DMSO- <i>d</i> ₆ .	80
Figure 2.3.9: ¹ H- ¹ H COSY spectrum of [Ru(ttpy)(bpy)Cl] [PF ₆] complex in DMSO- <i>d</i> ₆ .	80
Figure 2.3.10: ¹ H NMR spectrum of [$\{\text{Ru}(\text{ttpy})(\text{bpy})\}_2(\mu\text{-Me}_2\text{dicyd})$] [PF ₆] ₂ Complex (1) in DMSO- <i>d</i> ₆ .	81
Figure 2.3.11: ¹ H NMR spectrum of [$\{\text{Ru}(\text{ttpy})(\text{bpy})\}_2(\mu\text{-dicyd})$] [PF ₆] ₂ Complex (2) in DMSO- <i>d</i> ₆ .	81
Figure 2.3.12: ¹ H NMR spectrum of [$\{\text{Ru}(\text{ttpy})(\text{bpy})\}_2(\mu\text{-Cl}_2\text{dicyd})$] [PF ₆] ₂ Complex (3) in DMSO- <i>d</i> ₆ .	82
Figure 2.3.13: ¹ H NMR spectrum of [$\{\text{Ru}(\text{ttpy})(\text{bpy})\}_2(\mu\text{-Cl}_4\text{dicyd})$] [PF ₆] ₂ complex (4) in DMSO- <i>d</i> ₆ .	82
Figure 2.3.14: ¹ H- ¹ H COSY spectrum of [$\{\text{Ru}(\text{ttpy})(\text{bpy})\}_2(\mu\text{-Me}_2\text{dicyd})$] [PF ₆] ₂ complex (1) in DMSO- <i>d</i> ₆ .	83
Figure 2.3.15: ¹ H- ¹ H COSY spectrum of [$\{\text{Ru}(\text{ttpy})(\text{bpy})\}_2(\mu\text{-dicyd})$] [PF ₆] ₂ complex (2) in DMSO- <i>d</i> ₆ .	84
Figure 2.3.16: ¹ H- ¹ H COSY spectrum of [$\{\text{Ru}(\text{ttpy})(\text{bpy})\}_2(\mu\text{-Cl}_2\text{dicyd})$] [PF ₆] ₂ complex (3) in DMSO- <i>d</i> ₆ .	85
Figure 2.3.17: ¹ H- ¹ H COSY spectrum of [$\{\text{Ru}(\text{ttpy})(\text{bpy})\}_2(\mu\text{-Cl}_4\text{dicyd})$] [PF ₆] ₂ complex (4) in DMSO- <i>d</i> ₆ .	86
Figure 2.3.18: Numbering scheme used to assign ttpy and bpy proton resonances in [Ru(ttpy)(bpy)Cl] [PF ₆] and [$\{\text{Ru}(\text{ttpy})(\text{bpy})\}_2(\mu\text{-R}_2\text{R}_2'\text{dicyd})$] [PF ₆] ₂ complexes (1-4) in DMSO- <i>d</i> ₆ .	87
Figure 2.3.19: Quantitative electronic absorption spectra of [$\{\text{Ru}(\text{ttpy})(\text{bpy})\}_2(\mu\text{-R}_2\text{R}_2'\text{dicyd})$] [PF ₆] ₂ complexes in DMF. R ₂ R ₂ 'dicyd = Me ₂ - (a); unsubstituted, H ₄ - (b); Cl ₂ - (c); Cl ₄ -dicyd (d).	89

- Figure 2.3.20:** Cyclic Voltammograms of [$\{\text{Ru}(\text{tpp})\}_2(\mu\text{-R}_2\text{R}_2'\text{dicyd})$][PF_6]₂ Complexes (1-4) in DMF. Electrolyte 0.1 M TBAH, Scan Rate 0.1 V / s. $\text{R}_2\text{R}_2'\text{dicyd} = \text{Cl}_4\text{-}$ (a); $\text{Cl}_2\text{-}$ (b); unsubstituted, $\text{H}_4\text{-}$ (c); $\text{Me}_2\text{-dicyd}$ (d). 93
- Figure 2.3.21:** EPR spectrum of oxidized [$\text{Ru}(\text{tpy})(\text{bpy})(2,4\text{-Cl}_2\text{pcyd})$][PF_6] in DMF at 110K. 94
- Figure 2.3.22:** EPR spectra of [$\{\text{Ru}(\text{tpp})\}_2(\mu\text{-dicyd})$]³⁺ (**2**⁺) in DMF solution at a) room temperature and b) 110K, a weak signal from an organic impurity is observed at $g = 2.003$. 95
- Figure 2.3.23:** EPR spectra of [$\{\text{Ru}(\text{tpp})\}_2(\mu\text{-Cl}_4\text{dicyd})$]³⁺ in DMF solution at 110K. A weak signal from an organic impurity is observed at $g = 2.003$. 96
- Figure 2.3.24:** Vis-NIR spectroelectrochemical oxidation of [$\{\text{Ru}(\text{tpp})\}_2(\mu\text{-Me}_2\text{dicyd})$]²⁺ to form a) [$\{\text{Ru}(\text{tpp})\}_2(\mu\text{-Me}_2\text{dicyd})$]³⁺ and b) [$\{\text{Ru}(\text{tpp})\}_2(\mu\text{-Me}_2\text{dicyd})$]⁴⁺ in DMF, 0.1 M TBAH. a) 0 – 0.44 V, b) 0.68 – 0.80 V vs. Ag / AgCl. 99
- Figure 2.3.25:** Vis-NIR spectroelectrochemical oxidation of [$\{\text{Ru}(\text{tpp})\}_2(\mu\text{-dicyd})$]²⁺ to form a) [$\{\text{Ru}(\text{tpp})\}_2(\mu\text{-dicyd})$]³⁺ and b) [$\{\text{Ru}(\text{tpp})\}_2(\mu\text{-dicyd})$]⁴⁺ in DMF, 0.1 M TBAH. a) 0 – 0.66 V, b) 0.85 – 0.98 V vs. Ag / AgCl. 100
- Figure 2.3.26:** Vis-NIR spectroelectrochemical oxidation of [$\{\text{Ru}(\text{tpp})\}_2(\mu\text{-Cl}_2\text{dicyd})$]²⁺ to form a) [$\{\text{Ru}(\text{tpp})\}_2(\mu\text{-Cl}_2\text{dicyd})$]³⁺ and b) [$\{\text{Ru}(\text{tpp})\}_2(\mu\text{-Cl}_2\text{dicyd})$]⁴⁺ in DMF, 0.1 M TBAH. a) 0 – 0.76 V, b) 0.90 – 1.03 V vs. Ag / AgCl. 102
- Figure 2.3.27:** Vis-NIR Spectroelectrochemical Oxidation of [$\{\text{Ru}(\text{tpp})\}_2(\mu\text{-Cl}_4\text{dicyd})$]²⁺ to form a) [$\{\text{Ru}(\text{tpp})\}_2(\mu\text{-Cl}_4\text{dicyd})$]³⁺ and b) [$\{\text{Ru}(\text{tpp})\}_2(\mu\text{-Cl}_4\text{dicyd})$]⁴⁺ in DMF, 0.1 M TBAH. a) 0 – 0.86 V, b) 0.97 – 1.0 V vs. Ag / AgCl. 103
- Figure 2.3.28:** IR spectroelectrochemical oxidation of $\text{Me}_2\text{dicyd}^{2-}$ a) to form $\text{Me}_2\text{-adpc}^-$ radical anion and b) to form $\text{Me}_2\text{-adpc}^0$ (Bottom) in DMF, 0.1 M TBAH in DMF, 0.1M TBAH. a) 0 – 0.10 V, b) 0.10 – 0.80 V vs. Ag/ AgCl 106
- Figure 2.3.29:** IR spectroelectrochemical oxidation of [$\text{Ru}(\text{tpy})(\text{bpy})(2,4\text{-Cl}_2\text{pcyd})$]⁺ to form [$\text{Ru}(\text{tpy})(\text{bpy})(2,4\text{-Cl}_2\text{pcyd})$]²⁺ in DMF, 0.1 M TBAH. 0 - 0.74 V vs. Ag / AgCl. 107
- Figure 2.3.30:** IR spectroelectrochemical oxidation of [$\{\text{Ru}(\text{tpp})\}_2(\mu\text{-Me}_2\text{dicyd})$]²⁺ to form a) [$\{\text{Ru}(\text{tpp})\}_2(\mu\text{-Me}_2\text{dicyd})$]³⁺ and b) [$\{\text{Ru}(\text{tpp})\}_2(\mu\text{-Me}_2\text{dicyd})$]⁴⁺, in DMF, 0.1 M TBAH. a) 0 – 0.25 V, b) 0.25 – 0.87 V vs Ag / AgCl. 108
- Figure 2.3.31:** IR spectroelectrochemical oxidation of [$\{\text{Ru}(\text{tpp})\}_2(\mu\text{-dicyd})$]²⁺ to form a) [$\{\text{Ru}(\text{tpp})\}_2(\mu\text{-dicyd})$]³⁺ and b) [$\{\text{Ru}(\text{tpp})\}_2(\mu\text{-dicyd})$]⁴⁺, in DMF, 0.1 M TBAH. a) 0 – 0.50 V, b) 0.50 – 0.80 V vs Ag / AgCl. 109

Figure 2.3.32: IR spectroelectrochemical oxidation of [$\{\text{Ru}(\text{tpp})\}_2(\mu\text{-Cl}_2\text{dicyd})\}^{2+}$ to form a) [$\{\text{Ru}(\text{tpp})(\text{bpy})\}_2(\mu\text{-Cl}_2\text{dicyd})\}^{3+}$ and b) [$\{\text{Ru}(\text{tpp})(\text{bpy})\}_2(\mu\text{-Cl}_2\text{dicyd})\}^{4+}$, in DMF, 0.1 M TBAH. a) 0 – 0.78 V, b) 0.78 – 0.92 V vs Ag / AgCl.	110
Figure 2.3.33: IR spectroelectrochemical oxidation of [$\{\text{Ru}(\text{tpp})(\text{bpy})\}_2(\mu\text{-Cl}_4\text{dicyd})\}^{2+}$ to form [$\{\text{Ru}(\text{tpp})(\text{bpy})\}_2(\mu\text{-Cl}_4\text{dicyd})\}^{3+}$ in DMF, 0.1 M TBAH. 0 – 0.90 V vs Ag / AgCl.	112
Figure 3.1.1: Substituted 4,4'-azodi(phenylcyanamide) dianion ($\text{R}_2\text{R}_2'\text{adpc}^{2-}$).	118
Figure 3.1.2: The bridging $\text{R}_2\text{R}_2'\text{adpc}^{2-}$ and ancillary tpy and bpy ligands used in the synthesis of [$\{\text{Ru}(\text{tpy})(\text{bpy})\}_2(\mu\text{-R}_2\text{R}_2'\text{adpc})\}^{2+}$ complexes.	121
Figure 3.3.1: The low energy NIR band of [$\{\text{Ru}(\text{tpy})(\text{bpy})\}_2(\mu\text{-Me}_2\text{adpc})\}^{3+}$ (7b ⁺) in DMF showing the best fit of the three Gaussian curves (dashed lines) used for the calculation of oscillator strength.	167
Figure 3.4.1: ORTEP drawing of anionic $\text{Me}_2\text{adpc}^{2-}$ ligand (5g). The solvent of crystallization and hydrogen atoms have been omitted for clarity. Ellipsoids are depicted at 30 % probability.	171
Figure 3.4.3: IR spectrum of $\text{Me}_2\text{adpcH}_2$ ligand (4b) on KBr.	175
Figure 3.4.4: IR spectrum of $\text{Tl}_2[\text{Me}_2\text{adpc}]$ salt (5a) on KBr.	176
Figure 3.4.5: IR spectrum of [$\{\text{Ru}(\text{tpy})(\text{bpy})\}_2(\mu\text{-Me}_2\text{adpc})\} [\text{PF}_6]_2$ (7b) on KBr.	176
Figure 3.4.7: ^1H NMR spectrum of $\text{Me}_4\text{adpcH}_2$ ligand (4a) in $\text{DMSO-}d_6$	179
Figure 3.4.8: ^1H NMR spectrum of $\text{Me}_2\text{adpcH}_2$ ligand (4b) in $\text{DMSO-}d_6$	179
Figure 3.4.9: ^1H NMR spectrum of $\text{Cl}_2\text{adpcH}_2$ ligand (4e) in $\text{DMSO-}d_6$	180
Figure 3.4.10: ^1H NMR spectrum of <i>meta</i> - adpcH_2 ligand (4f) in $\text{DMSO-}d_6$	180
Figure 3.4.11: ^1H NMR spectrum of $\text{Tl}_2[\text{Me}_2\text{adpc}]$ (5a) in $\text{DMSO-}d_6$	181
Figure 3.4.12: ^1H NMR spectrum of $\text{Tl}_2[\text{Cl}_2\text{adpc}]$ (5c) in $\text{DMSO-}d_6$	182
Figure 3.4.13: ^1H NMR spectrum of $\text{Tl}_2[\textit{meta}\text{-adpc}]$ (5e) in $\text{DMSO-}d_6$.	182
Figure 3.4.14: ^1H NMR spectrum of [$\{\text{Ru}(\text{tpy})(\text{bpy})\}_2(\mu\text{-Me}_4\text{adpc})\} [\text{PF}_6]_2$ complex (7a) in $\text{DMSO-}d_6$.	186
Figure 3.4.15: ^1H NMR spectrum of [$\{\text{Ru}(\text{tpy})(\text{bpy})\}_2(\mu\text{-Me}_2\text{adpc})\} [\text{PF}_6]_2$ complex (7b) in $\text{DMSO-}d_6$.	186
Figure 3.4.16: ^1H NMR spectrum of [$\{\text{Ru}(\text{tpy})(\text{bpy})\}_2(\mu\text{-Cl}_2\text{adpc})\} [\text{PF}_6]_2$ complex (7d) in $\text{DMSO-}d_6$.	187

Figure 3.4.17: ^1H NMR spectrum of $[\{\text{Ru}(\text{tpy})(\text{bpy})\}_2(\mu\text{-Cl}_4\text{adpc})] [\text{PF}_6]_2$ complex (7e) in $\text{DMSO-}d_6$.	187
Figure 3.4.18: ^1H NMR spectrum of $[\{\text{Ru}(\text{tpy})(\text{bpy})\}_2(\mu\text{-meta-adpc})] [\text{PF}_6]_2$ complex (7f) in $\text{DMSO-}d_6$.	188
Figure 3.4.19: $^1\text{H-}^1\text{H}$ COSY spectrum of $[\{\text{Ru}(\text{tpy})(\text{bpy})\}_2(\mu\text{-Me}_4\text{adpc})] [\text{PF}_6]_2$ complex (7a) in $\text{DMSO-}d_6$.	189
Figure 3.4.20: $^1\text{H-}^1\text{H}$ COSY spectrum of $[\{\text{Ru}(\text{tpy})(\text{bpy})\}_2(\mu\text{-Me}_2\text{adpc})] [\text{PF}_6]_2$ complex (7b) in $\text{DMSO-}d_6$.	190
Figure 3.4.21: $^1\text{H-}^1\text{H}$ COSY spectrum of $[\{\text{Ru}(\text{tpy})(\text{bpy})\}_2(\mu\text{-Cl}_2\text{adpc})] [\text{PF}_6]_2$ complex (7d) in $\text{DMSO-}d_6$.	191
Figure 3.4.22: $^1\text{H-}^1\text{H}$ COSY spectrum of $[\{\text{Ru}(\text{tpy})(\text{bpy})\}_2(\mu\text{-Cl}_4\text{adpc})] [\text{PF}_6]_2$ complex (7e) in $\text{DMSO-}d_6$.	192
Figure 3.4.23: Numbering scheme used to assign tpy and bpy proton resonances in $[\{\text{Ru}(\text{tpy})(\text{bpy})\}_2(\mu\text{-R}_2\text{R}_2'\text{adpc})] [\text{PF}_6]_2$ complex (7a-7f) in $\text{DMSO-}d_6$.	193
Figure 3.4.24: Quantitative electronic absorption spectra of $\text{Ti}_2[\text{R}_2\text{R}_2'\text{adpc}]$ (5a-5c) in DMF. $\text{R}_2\text{R}_2'\text{adpc} = \text{Me}_2\text{-}$ (5a); unsubstituted, $\text{H}_4\text{-}$ (5b) and Cl_2adpc (5c).	196
Figure 3.4.25: Quantitative electronic absorption spectra of $[\{\text{Ru}(\text{tpy})(\text{bpy})\}_2(\mu\text{-R}_2\text{R}_2'\text{adpc})] [\text{PF}_6]_2$ complexes (7a-7f) in DMF. $\text{R}_2\text{R}_2'\text{adpc} = \text{Me}_4\text{-}$ (7a); $\text{Me}_2\text{-}$ (7b); unsubstituted, $\text{H}_4\text{-}$ (7c); $\text{Cl}_2\text{-}$ (7d); $\text{Cl}_4\text{-}$ (7e) and <i>meta-adpc</i> (7f).	197
Figure 3.4.26: Cyclic voltammograms of $[\{\text{Ru}(\text{tpy})(\text{bpy})\}_2(\mu\text{-R}_2\text{R}_2'\text{adpc})] [\text{PF}_6]_2$ complexes in 0.1 M TBAH in acetonitrile at scan rate 0.1 V / s. $\text{R}_2\text{R}_2'\text{adpc} = \text{Me}_4\text{-}$ (a); $\text{Me}_2\text{-}$ (b); unsubstituted, $\text{H}_4\text{-}$ (c); $\text{Cl}_2\text{-}$ (d); $\text{Cl}_4\text{-}$ (e) and <i>meta-adpc</i> (f).	202
Figure 3.4.27: EPR spectra of $[\{\text{Ru}(\text{tpy})(\text{bpy})\}_2(\mu\text{-R}_2\text{R}_2'\text{adpc})]^{3+}$ in acetonitrile. $\text{R}_2\text{R}_2' = \text{Me}_4\text{-}$ at 295 K (a); $\text{Cl}_2\text{-}$ at 10 K (b); $\text{Cl}_4\text{-}$ at 110 K (c).	204
Figure 3.4.28: IR spectroelectrochemical oxidation of A) $[\text{Ru}(\text{tpy})(\text{bpy})(2,4\text{-Cl}_2\text{pcyd})]^+$ to form $[\text{Ru}(\text{tpy})(\text{bpy})(2,4\text{-Cl}_2\text{pcyd})]^{2+}$ and B) adpc^{2-} anion (5b) to form $\text{adpc}^{\bullet-}$ radical anion (5b⁺) in DMF, 0.1 M TBAH. A) 0 - 0.74 V, B) 0 - 0.20 V vs. Ag / AgCl).	206
Figure 3.4.29: IR spectroelectrochemical oxidation of $[\{\text{Ru}(\text{tpy})(\text{bpy})\}_2(\mu\text{-Me}_4\text{adpc})]^{2+}$ (7a) to form A) $[\{\text{Ru}(\text{tpy})(\text{bpy})\}_2(\mu\text{-Me}_4\text{adpc})]^{3+}$ (7a⁺) and B) $[\{\text{Ru}(\text{tpy})(\text{bpy})\}_2(\mu\text{-Me}_4\text{adpc})]^{4+}$ (7a²⁺) in DMF, 0.1 M TBAH. A) 0 - 0.58 V, B) 0.58 - 0.70 V vs. Ag / AgCl.	207
Figure 3.4.30: IR spectroelectrochemical oxidation of $[\{\text{Ru}(\text{tpy})(\text{bpy})\}_2(\mu\text{-Me}_2\text{adpc})]^{2+}$ (7b) to form A) $[\{\text{Ru}(\text{tpy})(\text{bpy})\}_2(\mu\text{-Me}_2\text{adpc})]^{3+}$ (7b⁺) and B) $[\{\text{Ru}(\text{tpy})(\text{bpy})\}_2(\mu\text{-Me}_2\text{adpc})]^{4+}$ (7b²⁺) in DMF, 0.1 M TBAH. A) 0 - 0.64 V, B) 0.64 - 0.72 V vs. Ag / AgCl.	208

Figure 3.4.31: IR spectroelectrochemical oxidation of $[\{\text{Ru}(\text{tpy})(\text{bpy})\}_2(\mu\text{-adpc})]^{2+}$ (**7c**) to form A) $[\{\text{Ru}(\text{tpy})(\text{bpy})\}_2(\mu\text{-adpc})]^{3+}$ (**7c⁺**) and B) $[\{\text{Ru}(\text{tpy})(\text{bpy})\}_2(\mu\text{-adpc})]^{4+}$ (**7c²⁺**) in DMF, 0.1 M TBAH. A) 0-0.66 V, B) 0.66 - 0.80 V vs. Ag / AgCl 209

Figure 3.4.32: IR spectroelectrochemical oxidation of $[\{\text{Ru}(\text{tpy})(\text{bpy})\}_2(\mu\text{-Cl}_2\text{adpc})]^{2+}$ (**7d**) to form A) $[\{\text{Ru}(\text{tpy})(\text{bpy})\}_2(\mu\text{-Cl}_2\text{adpc})]^{3+}$ (**7d⁺**) and B) $[\{\text{Ru}(\text{tpy})(\text{bpy})\}_2(\mu\text{-Cl}_2\text{adpc})]^{4+}$ (**7d²⁺**) in DMF, 0.1 M TBAH. A) 0 - 0.66 V, B) 0.66 - 0.82 V vs. Ag / AgCl. 210

Figure 3.4.33: IR spectroelectrochemical oxidation of $[\{\text{Ru}(\text{tpy})(\text{bpy})\}_2(\mu\text{-Cl}_4\text{adpc})]^{2+}$ (**7e**) to form A) $[\{\text{Ru}(\text{tpy})(\text{bpy})\}_2(\mu\text{-Cl}_4\text{adpc})]^{3+}$ (**7e⁺**) and B) $[\{\text{Ru}(\text{tpy})(\text{bpy})\}_2(\mu\text{-Cl}_4\text{adpc})]^{4+}$ (**7e²⁺**) in DMF, 0.1 M TBAH. A) 0 - 0.80 V, B) 0.80 - 0.90 V vs. Ag / AgCl. 211

Figure 3.4.34: IR spectroelectrochemical oxidation of $[\{\text{Ru}(\text{tpy})(\text{bpy})\}_2(\mu\text{-meta-adpc})]^{2+}$ (**7f**) to form A) $[\{\text{Ru}(\text{tpy})(\text{bpy})\}_2(\mu\text{-meta-adpc})]^{3+}$ (**7f⁺**) and B) $[\{\text{Ru}(\text{tpy})(\text{bpy})\}_2(\mu\text{-meta-adpc})]^{4+}$ (**7f²⁺**) in DMF, 0.1 M TBAH. A) 0 - 0.50 V, B) 0.50 - 0.65 V vs. Ag / AgCl. 212

Figure 3.4.35: Vis-NIR spectroelectrochemical oxidation of $\text{Cl}_2\text{adpc}^{2-}$ (**5c**) forming $\text{Cl}_2\text{adpc}^{\bullet-}$ radical anion (**5c⁺**) (top) and $\text{Me}_2\text{adpc}^{2-}$ (**5a**) forming $\text{Me}_2\text{adpc}^{\bullet-}$ radical anion (**5a⁺**) (bottom) in DMF, 0.1 M TBAH. (Top) 0 - 0.80 V and (Bottom) 0 - 0.18 V vs. Ag / AgCl. 217

Figure 3.4.36: Vis-NIR spectroelectrochemical oxidation of $[\{\text{Ru}(\text{tpy})(\text{bpy})\}_2(\mu\text{-Me}_4\text{adpc})]^{2+}$ (**7a**) forming A) $[\{\text{Ru}(\text{tpy})(\text{bpy})\}_2(\mu\text{-Me}_4\text{adpc})]^{3+}$ (**7a⁺**) and B) $[\{\text{Ru}(\text{tpy})(\text{bpy})\}_2(\mu\text{-Me}_4\text{adpc})]^{4+}$ (**7a²⁺**) in DMF, 0.1 M TBAH. A) 0 - 0.48V, B) 0.50 - 0.58 V vs. Ag / AgCl. 218

Figure 3.4.37: Vis- NIR spectroelectrochemical oxidation of $[\{\text{Ru}(\text{tpy})(\text{bpy})\}_2(\mu\text{-Me}_2\text{adpc})]^{2+}$ (**7b**) forming A) $[\{\text{Ru}(\text{tpy})(\text{bpy})\}_2(\mu\text{-Me}_2\text{adpc})]^{3+}$ (**7b⁺**) and (B) $[\{\text{Ru}(\text{tpy})(\text{bpy})\}_2(\mu\text{-Me}_2\text{adpc})]^{4+}$ (**7b²⁺**) in DMF, 0.1 M TBAH. A) 0 - 0.56 V, B) 0.56 - 0.66 V vs. Ag / AgCl. 219

Figure 3.4.38: Vis- NIR spectroelectrochemical oxidation of $[\{\text{Ru}(\text{tpy})(\text{bpy})\}_2(\mu\text{-adpc})]^{2+}$ (**7c**) forming A) $[\{\text{Ru}(\text{tpy})(\text{bpy})\}_2(\mu\text{-adpc})]^{3+}$ (**7c⁺**) and B) $[\{\text{Ru}(\text{tpy})(\text{bpy})\}_2(\mu\text{-adpc})]^{4+}$ (**7c²⁺**) in DMF, 0.1 M TBAH. A) 0 - 0.75 V, B) 0.80 - 1.00 V vs. Ag / AgCl. 220

Figure 3.4.39: Vis-NIR spectroelectrochemical oxidation of $[\{\text{Ru}(\text{tpy})(\text{bpy})\}_2(\mu\text{-Cl}_2\text{adpc})]^{2+}$ (**7d**) forming A) $[\{\text{Ru}(\text{tpy})(\text{bpy})\}_2(\mu\text{-Cl}_2\text{adpc})]^{3+}$ (**7d⁺**) and B) $[\{\text{Ru}(\text{tpy})(\text{bpy})\}_2(\mu\text{-Cl}_2\text{adpc})]^{4+}$ (**7d²⁺**) in DMF, 0.1 M TBAH. A) 0 - 0.78 V, B) 0.81 - 0.98 V vs. Ag / AgCl. 221

Figure 3.4.40: Vis-NIR spectroelectrochemical oxidation of $[\{\text{Ru}(\text{tpy})(\text{bpy})\}_2(\mu\text{-Cl}_4\text{adpc})]^{2+}$ (**7e**) forming A) $[\{\text{Ru}(\text{tpy})(\text{bpy})\}_2(\mu\text{-Cl}_4\text{adpc})]^{3+}$ (**7e⁺**) and B) $[\{\text{Ru}(\text{tpy})(\text{bpy})\}_2(\mu\text{-Cl}_4\text{adpc})]^{4+}$ (**7e²⁺**) in DMF, 0.1 M TBAH. A) 0 - 0.78 V; B) 0.81 - 0.98 V vs. Ag / AgCl. 222

- Figure 3.4.41:** Vis-NIR spectroelectrochemical oxidation of $[\{\text{Ru}(\text{tpy})(\text{bpy})\}_2(\mu\text{-meta-adpc})]^{2+}$ (**7f**) forming $[\{\text{Ru}(\text{tpy})(\text{bpy})\}_2(\mu\text{-meta-adpc})]^{3+}$ (**7f⁺**) in DMF, 0.1 M TBAH. 0 - 1.27 V vs Ag / AgCl. 223
- Figure 3.4.42:** Low energy NIR bands of $[\{\text{Ru}(\text{tpy})(\text{bpy})\}_2(\mu\text{-R}_2\text{R}_2'\text{adpc})]^{3+}$ complexes (**7a⁺**-**7a⁺**). $\text{R}_2\text{R}_2'\text{adpc} = \text{Me}_4\text{-}$ (**7a⁺**); $\text{Me}_2\text{-}$ (**7b⁺**); Unsubstituted, $\text{H}_4\text{-}$ (**7c⁺**); $\text{Cl}_2\text{-}$ (**7d⁺**); $\text{Cl}_4\text{-adpc}$ (**7e⁺**). 223
- Figure 3.4.43:** DFT calculation of orbital energies and selected molecular orbitals of $[\{\text{Ru}(\text{tpy})(\text{bpy})\}_2(\mu\text{-adpc})]^{2+}$ (**7c**). 227
- Figure 3.4.44:** DFT calculation of orbital energies and selected β -molecular orbitals of $[\{\text{Ru}(\text{tpy})(\text{bpy})\}_2(\mu\text{-Me}_4\text{adpc})]^{3+}$ (**7a⁺**). 228
- Figure 3.4.45:** DFT calculation of orbital energies and selected β -molecular orbitals of $[\{\text{Ru}(\text{tpy})(\text{bpy})\}_2(\mu\text{-adpc})]^{3+}$ (**7c⁺**). 229
- Figure 3.4.46:** DFT calculation of orbital energies and selected β -molecular orbitals of $[\{\text{Ru}(\text{tpy})(\text{bpy})\}_2(\mu\text{-Cl}_4\text{adpc})]^{3+}$ (**7e⁺**). 230
- Figure 3.4.47:** DFT calculation of spin density distribution of $[\{\text{Ru}(\text{tpy})(\text{bpy})\}_2(\mu\text{-R}_2\text{R}_2'\text{adpc})]^{3+}$ complexes (**7a⁺**, **7c⁺** and **7e⁺**). $\text{R}_2\text{R}_2'\text{adpc} = \text{Me}_4\text{-}$ (**7a⁺**), unsubstituted (**7c⁺**) and Cl_4adpc (**7e⁺**). 231
- Figure 3.4.48:** Spin density distribution in the lowest energy triplet state of the $[\{\text{Ru}(\text{tpy})(\text{bpy})\}_2(\mu\text{-adpc})]^{4+}$ cation (**7c²⁺**). H atoms are not shown for clarity. Isosurface contour value for the spin density is 0.004 a.u. 233
- Figure 3.4.49:** TD-DFT calculated spectra of $[\{\text{Ru}(\text{tpy})(\text{bpy})\}_2(\mu\text{-adpc})]^{4+}$ (**7c²⁺**) and $[\{\text{Ru}(\text{tpy})(\text{bpy})\}_2(\mu\text{-Cl}_2\text{adpc})]^{4+}$ (**7d²⁺**) in both singlet and triplet ground states 234
- Figure 4.1.1:** Binding modes of sulfoxide ligand in metal-sulfoxide complexes: (a) $\eta^1\text{-S}$ -binding, (b) $\eta^1\text{-O}$ -binding, (c) Side-on ($\eta^2\text{-S,O}$)-symmetric or asymmetric binding, (d) $\mu\text{-O}$ -bridging type, (e) $\mu\text{-S,O}$ -bridging type. 252
- Figure 4.1.2:** Electrochemically induced linkage isomerism in Ruthenium-sulfoxide complexes (ECEC square-scheme mechanism). 254
- Figure 4.1.3:** Photo-induced linkage isomerism in ruthenium-sulfoxide complexes 254
- Figure 4.1.4:** Photo-induced S \rightarrow O and thermal O \rightarrow S linkage isomerism of dimethyl sulfoxide (dmsO) ligand in $[\text{Ru}(\text{tpy})(\text{L}2)(\text{dmsO})]$ complexes. L2 = bidentate ligand. 257
- Figure 4.1.5:** Qualitative MO scheme showing possible electronic transition in octahedral Ru-polypyridyl complexes.. 259
- Figure 4.1.6:** Electronic state diagram of (A) $[\text{Ru}(\text{tpy})(\text{bpy})(\text{dmsO})]^{2+}$ and (B) $[\text{Ru}(\text{bpy})_2(\text{OSOR})]^{2+}$ where OSOR is 2-methylsulfinyl benzoate.. 263
- Figure 4.1.7:** (a) MLCT excitation of $S\text{-}[\text{Ru}(\text{bpy})_2(\text{OSOR})]^+$ (blue traces) forming its linkage isomer $O\text{-}[\text{Ru}(\text{bpy})_2(\text{OSOR})]^+$ (red traces), (b) thermal 265

reversion of O -[Ru(bpy) ₂ (OSOR)] ⁺ to initial S -[Ru(bpy) ₂ (OSOR)] ⁺ (blue traces) in methanol. Insert shows the decay profile of O -bound isomer.	
Figure 4.1.8: The R-pcyd ⁻ and ancillary ligands bpy and dmsO ligands used in the synthesis of cis -[Ru(bpy) ₂ (R-pcyd)(dmsO(- S))] ⁺ complexes (4a-4f).	272
Figure 4.2.1: Instrumental arrangement for quantum yield measurement: (A) LED light, (B) Tristar Coolbase, (C) Heat-Sink, (D) DC Power Supply, © Buck Puck DC Driver, (F) Dimmable Potentiometer, (G) Neutral Density Filter, (H) Quartz Cell Holder, (I) Quartz Cell, (J) Light source in the Spectrophotometer, (K) Detector in the Spectrophotometer.	285
Figure 4.2.2: Photo generation of Fe(II) from Fe(III) used in ferrioxalate actinometry	287
Figure 4.3.1: Geometry optimized structures of (a) cis -[Ru(bpy) ₂ (pcyd)(dmsO- S)] ⁺ (4a) and (b) cis -[Ru(bpy) ₂ (pcyd)(dmsO- O)] ⁺ complexes.	296
Figure 4.3.2: DFT calculation of orbital energies and selected molecular orbitals of [Ru(bpy) ₂ (pcyd)(dmsO- S)] ⁺ .	299
Figure 4.3.3: DFT calculation of orbital energies and selected molecular orbitals of [Ru(bpy) ₂ (pcyd)(dmsO- O)] ⁺ .	300
Figure 4.3.4: Spin density distribution of (a) cis -[Ru(bpy) ₂ (pcyd)(dmsO- S)] ²⁺ and (b) cis -[Ru(bpy) ₂ (pcyd)(dmsO- O)] ²⁺ .	301
Figure 4.3.5: IR spectrum of cis -[Ru(bpy) ₂ (Cl ₅ -pcyd) (dmsO- S)] [PF ₆] complex (4f) on KBr.	304
Figure 4.3.6: Calculated IR spectrum of [Ru(bpy) ₂ (pcyd) (dmsO- S)] [PF ₆] complex (4a) showing (A) ν (NCN) (top) and (B) ν (SO, Ru- S) (bottom) bands.	305
Figure 4.3.7: Calculated IR spectrum of [Ru(bpy) ₂ (pcyd) (dmsO- O)] [PF ₆] complex (4a) showing (A) ν (NCN) (top) and (B) ν (SO, Ru- O) (bottom) bands.	306
Figure 4.3.8: ¹ H NMR spectrum of cis -[Ru(bpy) ₂ (Cl ₄ pcyd) ₂] in dmsO- d_6 .	308
Figure 4.3.9: ¹ H- ¹ H COSY spectrum of cis -[Ru(bpy) ₂ (Cl ₄ pcyd) ₂] in dmsO- d_6 .	309
Figure 4.3.10: ¹ H NMR spectrum of cis -[Ru(bpy) ₂ (Cl ₅ pcyd) (dmsO- S)] [PF ₆] complex (4f) in DMSO- d_6 .	313
Figure 4.3.11: ¹ H NMR spectrum of cis -[Ru(bpy) ₂ (Cl ₄ pcyd) (dmsO- S)] [PF ₆] complex (4e) in dmsO- d_6 .	313
Figure 4.3.12: ¹ H NMR spectrum of cis -[Ru(bpy) ₂ (Cl ₃ pcyd) (dmsO- S)] [PF ₆] complex (4d) in dmsO- d_6 .	314
Figure 4.3.13: ¹ H NMR spectrum of cis -[Ru(bpy) ₂ (Cl ₂ pcyd) (dmsO- S)] [PF ₆] complex (4c) in dmsO- d_6 .	314
Figure 4.3.14: ¹ H NMR spectrum of cis -[Ru(bpy) ₂ (Clpcyd) (dmsO- S)] [PF ₆] complex (4b) in dmsO- d_6 .	315

Figure 4.3.15: ^1H NMR spectrum of <i>cis</i> -[Ru(bpy) ₂ (dmsO)(pcyd)][PF ₆] complex (4a) in dmsO- <i>d</i> ₆ .	315
Figure 4.3.16: ^1H - ^1H COSY spectrum of <i>cis</i> -[Ru(bpy) ₂ (Cl ₅ pcyd)(dmsO-S)][PF ₆] complex (4f) in dmsO- <i>d</i> ₆ .	316
Figure 4.3.17: ^1H - ^1H COSY spectrum of <i>cis</i> -[Ru(bpy) ₂ (Cl ₄ pcyd)(dmsO-S)][PF ₆] complex (4e) in dmsO- <i>d</i> ₆ .	317
Figure 4.3.18: ^1H - ^1H COSY spectrum of <i>cis</i> -[Ru(bpy) ₂ (Cl ₃ pcyd)(dmsO-S)][PF ₆] complex (4d) in dmsO- <i>d</i> ₆ .	318
Figure 4.3.19: ^1H - ^1H COSY spectrum of <i>cis</i> -[Ru(bpy) ₂ (Cl ₂ pcyd)(dmsO-S)][PF ₆] complex (4c) in dmsO- <i>d</i> ₆ .	319
Figure 4.3.20: ^1H - ^1H COSY spectrum of <i>cis</i> -[Ru(bpy) ₂ (Clpcyd)(dmsO-S)][PF ₆] complex (4b) in dmsO- <i>d</i> ₆ .	320
Figure 4.3.21: ^1H - ^1H COSY spectrum of <i>cis</i> -[Ru(bpy) ₂ (pcyd)(dmsO-S)][PF ₆] complex (4a) in dmsO- <i>d</i> ₆ .	321
Figure 4.3.22: ^1H NMR spectra of [Ru(bpy) ₂ (Cl ₄ pcyd)(dmsO)][PF ₆] complex (4e) in dmsO- <i>d</i> ₆ (A) initial S-isomer (blue), (B) partially photolyzed (red).	322
Figure 4.3.23: Numbering schemes used for the assignment of bpy and dmsO proton resonances in (i) precursor <i>cis</i> -[Ru(bpy) ₂ (R-pcyd) ₂] and (ii) [Ru(bpy) ₂ (R-pcyd)(dmsO-S)] ⁺ complexes (4a-4f).	323
Figure 4.3.24: Photo-induced S→O and thermal O→S linkage isomerism of <i>cis</i> -[Ru(bpy) ₂ (R-pcyd)(dmsO-S)] ⁺ complexes (4a-4f).	326
Figure 4.3.25: Quantitative electronic absorption spectra of <i>cis</i> -[Ru(bpy) ₂ (Cl ₅ pcyd)(dmsO-S)][PF ₆] (blue) and [Ru(bpy) ₂ (Cl ₅ pcyd)(dmsO-O)][PF ₆] (red) in dmsO.	327
Figure 4.3.26: Photo-induced S→O isomerization of <i>cis</i> -[Ru(bpy) ₂ (Cl ₅ pcyd)(dmsO-S)][PF ₆] complex (4f) in dmsO showing gradual depletion of the 405 nm band of the S-bonded isomer with concomitant development of a band at 512 nm for the O-bonded isomer. Irradiation time: 0-120 s.	330
Figure 4.3.27: Thermal O→S isomerization of photogenerated <i>cis</i> -[Ru(bpy) ₂ (Cl ₅ pcyd)(dmsO-O)][PF ₆] complex in dmsO with gradual depletion of the 512 nm band of the O-bonded isomer with concomitant development of the 405 nm band of the S-bonded isomer. Reaction time: 0-1498 s.	330
Figure 4.3.28: Photo-induced S→O isomerization of <i>cis</i> -[Ru(bpy) ₂ (Cl ₅ pcyd)(dmsO-S)] ⁺ (4f) in propylene carbonate: time = 0, <i>cis</i> -[Ru(bpy) ₂ (Cl ₅ pcyd)(dmsO-S)] ⁺ (blue line) and after 120 s irradiation, <i>cis</i> -[Ru(bpy) ₂ (Cl ₅ pcyd)(dmsO-O)] ⁺ (red line).	331
Figure 4.3.29: Thermal O→S isomerization of photogenerated <i>cis</i> -[Ru(bpy) ₂ (Cl ₅ pcyd)(dmsO-O)][PF ₆] complex in propylene carbonate showing gradual depletion of the 488 nm band of the O-bonded isomer with concomitant development of the 405 nm band of the S-bonded isomer.	331

Reaction time: 0-11700 s.

Figure 4.3.30: Photo-induced S→O isomerization of *cis*-[Ru(bpy)₂(Cl₅pcyd)(dmsO-S)]⁺ (**4f**) in PMMA polymer film: time = 0, *cis*-[Ru(bpy)₂(Cl₅pcyd)(dmsO-S)]⁺ (blue line) and after 120 s irradiation, *cis*-[Ru(bpy)₂(Cl₅pcyd)(dmsO-O)]⁺ (red line). 332

Figure 4.3.31: Thermal O→S isomerization of photogenerated *cis*-[Ru(bpy)₂(Cl₅pcyd)(dmsO-O)][PF₆] complex in PMMA polymer film showing gradual depletion of the 508 nm band of the O-bonded isomer with concomitant development of the 412 nm band of the S-bonded isomer. Reaction time: 0- 600 s. 332

Figure 4.3.32: Cyclic voltammograms of *cis*-[Ru(bpy)₂(Cl₅pcyd)(dmsO-S)][PF₆] complex (**4f**) (a, blue) and after partial photolysis (b, red), in dmsO, 0.1 M TBAH, Scan rate 1.0 V/s. 336

Figure 4.3.33: Cyclic voltammograms of *cis*-[Ru(bpy)₂(dmsO)(Cl₅pcyd)][PF₆] (**4f**) (a) scan range (0-1.80 V) (b) scan range (0-2.40 V), first redox cycle, (c) scan range (0.2.40 V), second redox cycle, in acetonitrile, 0.1 M TBAH, scan rate 1.0 V/s, arrows show scan direction, numbers show consecutive oxidative and reductive scans. 338

Figure 4.3.34: Cyclic voltammograms of *cis*-[Ru(bpy)₂(Cl₅pcyd)(dmsO-S)][PF₆] complex (**4f**) in acetonitrile, 0.1 M TBAH, at scan rates from 0.05 to 20 V/s. 340

Figure 4.4.2: Qualitative electronic state diagram (a) for photochromic *cis*-[Ru(bpy)₂(R-pcyd)(dmsO)][PF₆] complexes showing excited state. (b) enlarged view of the excited state reaction coordinate. 346

Figure 5.1.1: Ruthenium dinuclear system involving extended π conjugation, where L is a conjugated organic spacer. 357

Figure 5.1.2: Poling of a neutral complex (a) random orientation of polar domains prior to poling, (b) introduction of electric field (poling), (c) electric field removed, dipole locked in a non-random manner. Zigzag line represents the polymer matrix. 358

Figure 5.1.3: (i) *trans*-[Ru(tpy)(R-pcyd)Cl₂], (ii) proposed mixed-valence complex [$\{\text{Ru}^{\text{III}}(\text{tpy})\text{Cl}_2\}(\mu\text{-dicyd}^{2-})\{\text{Ru}^{\text{II}}(\text{N}3)(\text{P}2)\}$] where [Ru^{III}(tpy)Cl₂]⁺ is the acceptor Ru(III) and [Ru^{II}(N3)(P2)]⁺ is the donor Ru(II) unit. P2 and N3 are P and N based bidentate and tridentate ligands that stabilize Ru(II) state. 359

Figure 5.1.4: The R-pcyd⁻ and ancillary tpy ligands used in the synthesis of *trans*-[Ru(tpy)(R-pcyd)Cl₂] complexes (**1-5**). 362

Figure 5.2.1: Electronic spectrum of *trans*-[Ru(tpy)(Cl₅pcyd)Cl₂] (**5**) in CH₂Cl₂ showing the best fit of the three Gaussian curves (dashed lines) used for the calculation of oscillator strength. 370

Figure 5.3.1: ORTEP drawing of Ru(tpy)Cl₃·2DMSO complex. The solvent 374

molecules of crystallization have been omitted.

- Figure 5.3.2:** ORTEP drawing of *trans*-[Ru(tpy)(Cl₃pcyd)Cl₂] \cdot 2CH₃CN complex. The solvent molecules of crystallization have been omitted. 378
- Figure 5.3.3:** IR spectrum of *trans*-[Ru(tpy)(Cl₂pcyd)Cl₂] complex on KBr. 383
- Figure 5.3.4:** DFT calculated IR spectrum of *trans*-[Ru(tpy)(Cl₂pcyd)Cl₂] complex in vacuum. 384
- Figure 5.3.5:** DFT calculation of orbital energies and selected molecular orbitals of Ru(tpy)Cl₃ complex. 385
- Figure 5.3.6:** DFT calculation of orbital energies and selected molecular orbitals of *trans*-[Ru(tpy)(Clpcyd)Cl₂] complex. 387
- Figure 5.3.7:** DFT calculation of orbital energies and selected molecular orbitals of *trans*-[Ru(tpy)(Cl₄pcyd)Cl₂] complex. 388
- Figure 5.3.8:** Spin density distributions of (a) Ru(tpy)Cl₃ and (b-f) *trans*-[Ru(tpy)(R-pcyd)Cl₂] complexes. R = H- (b), Cl- (c), Cl₂- (d), Cl₃- (e), Cl₄- (f). 390
- Figure 5.3.9:** Quantitative electronic absorption spectra of Ru(tpy)Cl₃ complex in DMF and in CH₂Cl₂. 392
- Figure 5.3.10:** Calculated electronic absorption spectrum of Ru(tpy)Cl₃ complex in vacuum. 392
- Figure 5.3.11:** Quantitative electronic absorption spectra of *trans*-[Ru(tpy)(R-pcyd)Cl₂] complexes (1-5) in DMF. (R = Cl₅-, Cl₄-, Cl₃-, Cl₂-, Cl-). 395
- Figure 5.3.12:** Quantitative electronic absorption spectra of *trans*-[Ru(tpy)(R-pcyd)Cl₂] complexes in CH₂Cl₂. (R = Cl₅-, Cl₄-, Cl₃-, Cl₂-, Cl-). 395
- Figure 5.3.13:** Calculated electronic absorption spectra (a-c) of *trans*-[Ru(tpy)(R-pcyd)Cl₂] complexes in vacuum. R = Cl₄-(a), Cl₃-(b), Cl₂-(c). 396
- Figure 5.3.14:** Distribution of LMCT Oscillator Strength (f) relative to LMCT energy (eV) for *trans*-[Ru(bpy)₂(R-pcyd)Cl₂] complexes in CH₂Cl₂ (blue triangle) and in DMF (red squares). (R = Cl₅-, Cl₄-, Cl₃-, Cl₂-, Cl-). 398
- Figure 5.3.15:** CV's of Ru(tpy)Cl₃ complex in CH₂Cl₂ (blue) and in DMF (red). Scan rate 0.1 V/s and supporting electrolyte, 0.1 M TBAH. 399
- Figure 5.3.16:** Cyclic voltammograms of *trans*-[Ru(tpy)(R-pcyd)Cl₂] complexes in 0.1 M TBAH CH₂Cl₂ at scan rate 0.1 V/s. R = (a) 5, (b) 4, (c) 3, (d) 2, (e) 1. 401
- Figure 5.3.17:** Cyclic voltammograms of *trans*-[Ru(tpy)(R-pcyd)Cl₂] complexes in 0.1 M TBAH DMF at scan rate 0.1 V/s. R = (a) 5, (b) 4, (c) 3, (d) 2, (e) 1. 402
- Figure 5.3.18:** ¹H NMR spectrum of Ru(tpy)Cl₃ complex in dms-*d*₆. 407

Figure 5.3.19: ^1H - ^1H COSY spectrum of $\text{Ru}(\text{ttpy})\text{Cl}_3$ complex in $\text{dms}\text{-}d_6$	407
Figure 5.3.20: ^1H NMR spectrum of <i>trans</i> - $[\text{Ru}(\text{ttpy})(\text{Cl}_5\text{pcyd})\text{Cl}_2]$ complex (5) in $\text{dms}\text{-}d_6$.	408
Figure 5.3.21: ^1H - ^1H COSY spectrum of <i>trans</i> - $[\text{Ru}(\text{ttpy})(\text{Cl}_5\text{pcyd})\text{Cl}_2]$ complex (5) in $\text{dms}\text{-}d_6$	408
Figure 5.3.22: ^1H NMR spectrum of <i>trans</i> - $[\text{Ru}(\text{ttpy})(\text{Cl}_4\text{pcyd})\text{Cl}_2]$ complex (4) in $\text{dms}\text{-}d_6$.	409
Figure 5.3.23: ^1H - ^1H COSY spectrum of <i>trans</i> - $[\text{Ru}(\text{ttpy})(\text{Cl}_4\text{pcyd})\text{Cl}_2]$ complex (4) in $\text{dms}\text{-}d_6$	409
Figure 5.3.24: ^1H NMR spectrum of <i>trans</i> - $[\text{Ru}(\text{ttpy})(\text{Cl}_3\text{pcyd})\text{Cl}_2]$ complex (3) in $\text{dms}\text{-}d_6$.	410
Figure 5.3.25: ^1H - ^1H COSY spectrum of <i>trans</i> - $[\text{Ru}(\text{ttpy})(\text{Cl}_3\text{pcyd})\text{Cl}_2]$ complex (3) in $\text{dms}\text{-}d_6$	410
Figure 5.3.26: ^1H NMR spectrum of <i>trans</i> - $[\text{Ru}(\text{ttpy})(\text{Cl}_2\text{pcyd})\text{Cl}_2]$ complex (2) in $\text{dms}\text{-}d_6$.	411
Figure 5.3.27: ^1H - ^1H COSY spectrum of <i>trans</i> - $[\text{Ru}(\text{ttpy})(\text{Cl}_2\text{pcyd})\text{Cl}_2]$ complex (2) in $\text{dms}\text{-}d_6$	411
Figure 5.3.28: ^1H NMR spectrum of <i>trans</i> - $[\text{Ru}(\text{ttpy})(\text{Clpcyd})\text{Cl}_2]$ complex (1) in $\text{dms}\text{-}d_6$	412
Figure 5.3.29: Numbering scheme used to assign the proton resonances from ttpy and R-pcyd ligands in $\text{Ru}(\text{ttpy})\text{Cl}_3$ and <i>trans</i> - $[\text{Ru}(\text{ttpy})(\text{R-pcyd})\text{Cl}_2]$ complexes (1-5).	412
Figure 5.3.30: The alignment of Ru(III) spin with that of an external magnetic field (H_0) and the resultant phenyl hydrogen atom spin moments.	414
Figure B.1: ^1H NMR spectrum of 4-(<i>tert</i> -butylphenyl)-2,2':6',2''-terpyridine (ttpy) ligand in $\text{dms}\text{-}d_6$	446
Figure B.2: ^1H - ^1H COSY spectrum of 4-(<i>tert</i> -butylphenyl)-2,2':6',2''-terpyridine (ttpy) ligand in $\text{dms}\text{-}d_6$.	446
Figure C.1: DFT calculation of orbital energies and selected frontier molecular orbitals of free <i>meta</i> -adpc ²⁻ dianion.	463
Figure C.2: DFT calculation of (a) spin density distribution and (b) orbital energies and selected β -molecular orbitals of $[\{\text{Ru}(\text{tpy})(\text{bpy})\}_2(\mu\text{-meta-adpc})]^{3+}$ (7a ⁺).	464
Figure C.3: DFT calculation of orbital energies and selected α -molecular orbitals of $[\{\text{Ru}(\text{tpy})(\text{bpy})\}_2(\mu\text{-Me}_4\text{adpc})]^{2+}$ (7a ⁺)	465
Figure C.4: DFT calculation of orbital energies and selected α -molecular	466

orbitals of $[\{\text{Ru}(\text{tpy})(\text{bpy})\}_2(\mu\text{-adpc})]^{2+}$ (**7c**⁺).

Figure C.5: DFT calculation of orbital energies and selected α -molecular orbitals of $[\{\text{Ru}(\text{tpy})(\text{bpy})\}_2(\mu\text{-Cl}_4\text{adpc})]^{2+}$ (**7e**⁺). 467

Figure C.6: Cyclic voltammograms of $\text{Tl}_2[\text{R}_2\text{R}_2'\text{adpc}]$ in DMF. 0.1M TBAH, scan rate 0.1 V/s. $\text{R}_2\text{R}_2'\text{adpc}^{2-} = \text{Cl}_2\text{adpc}^{2-}$ (a), adpc^{2-} (b), $\text{Me}_2\text{adpc}^{2-}$ (c). 467

Figure C.7: Quantitative electronic absorption spectrum of $\text{Tl}_2[\text{meta-adpc}]$ (**5e**) in DMF. 468

Figure C.8: Vis-NIR spectroelectrochemical oxidation of meta-adpc^{2-} (**5e**) forming $\text{meta-adpc}^{\bullet-}$ radical anion (**5e**⁺) 468

Figure D.1: DFT calculation of orbital energies and selected molecular orbitals of $[\text{Ru}(\text{bpy})_2(\text{Cl}_5\text{pcyd})(\text{dmsO-S})]^+$ (**4f**). 477

Figure D.2: IR spectra of $\text{cis-}[\text{Ru}(\text{bpy})_2(\text{Cl}_5\text{-pcyd})(\text{dmsO})][\text{PF}_6]$ complex (**4f**) on KBr pellet: (a) S-bonded (blue) and (b) partially photolyzed (red). 478

Figure D.3: Cyclic voltammograms of $\text{cis-}[\text{Ru}(\text{bpy})(\text{R-pcyd})(\text{dmsO-S})][\text{PF}_6]$ complexes (**4a-4f**) in dmsO. R-pcyd is (a) unsubstituted, (b) Cl-, (c) Cl₂-, (d) Cl₃-, (e) Cl₄-, (f) Cl₅-phenylcyanamide Scan rate 1.0 V/s, 0.1 M TBAH. 479

Figure D.4: Cyclic voltammograms of $\text{cis-}[\text{Ru}(\text{bpy})(\text{R-pcyd})(\text{dmsO-S})][\text{PF}_6]$ complexes (**4a-4f**) in acetonitrile. R-pcyd is (a) unsubstituted, (b) Cl-, (c) Cl₂-, (d) Cl₃-, (e) Cl₄-, (f) Cl₅-phenylcyanamide Scan rate 1.0 V/s, 0.1 M TBAH. 480

Figure D.5: Cyclic voltammograms of $\text{cis-}[\text{Ru}(\text{bpy})_2(\text{Cl}_3\text{pcyd})(\text{dmsO-S})][\text{PF}_6]$ complex (**4d**) in acetonitrile, 0.1 M TBAH, at scan rates from 0.05 to 15 V/s. 481

Figure D.6: Cyclic voltammograms of $\text{cis-}[\text{Ru}(\text{bpy})_2(\text{Cl}_2\text{pcyd})(\text{dmsO-S})][\text{PF}_6]$ complex (**4c**) in acetonitrile, 0.1 M TBAH, at scan rates from 0.05 to 15 V/s. 482

Figure D.7: Plot of $[\ln(C_T) - \ln(C_T - C_p)]$ versus irradiation time (t) to determine the overall quantum yield $\Phi_{\text{S} \rightarrow \text{O}}$ for $\text{cis-}[\text{Ru}(\text{bpy})_2(\text{Cl}_5\text{-pcyd})(\text{dmsO-S})][\text{PF}_6]$ complex (**4f**) in dmsO. The equations for the line is $y = 0.24x$, with $R^2 = 0.995$. Data taken from Table D.6. 484

Figure D.8: First order plot for thermal O→S linkage isomerism of dmsO in $\text{cis-}[\text{Ru}(\text{bpy})_2(\text{Cl}_5\text{-pcyd})(\text{dmsO-O})][\text{PF}_6]$ complex (**4f**) in dmsO. The equation for the line is $y = -0.0026x - 0.894$, with $R^2 = 0.999$. 486

Figure D.9: First order plot for thermal O→S linkage isomerism of dmsO in $\text{cis-}[\text{Ru}(\text{bpy})_2(\text{Cl}_5\text{-pcyd})(\text{dmsO-O})][\text{PF}_6]$ complex (**4f**) in propylene carbonate. The equation for the line is $y = -0.011x - 1.65$, with $R^2 = 0.999$. 486

Figure D.10: First order plot for thermal O→S linkage isomerism of dmsO in $\text{cis-}[\text{Ru}(\text{bpy})_2(\text{Cl}_5\text{-pcyd})(\text{dmsO-O})][\text{PF}_6]$ complex (**4f**) on PMMA polymer film. The equation for the line is $y = -0.0024x - 2.27$, with $R^2 = 0.993$. 487

Figure E.1: DFT calculation of orbital energies and selected molecular orbitals of $\text{trans-}[\text{Ru}(\text{tpy})(\text{Cl}_2\text{pcyd})\text{Cl}_2]$ complex. 502

Figure E.2: DFT calculation of orbital energies and selected molecular orbitals of *trans*-[Ru(tpy)(Cl₃pcyd)Cl₂] complex. 503

List of Schemes

Scheme 1.1: Structural Change associated with Redox Transformations of Non-innocently behaving Ligands. (i) Nitrosyls; (ii) Dioxygen, Azo-compounds; (iii) α -Diimine, α -Dithiolene, α -Dioxolene; (iv) Quinone/Semiquinone/Catecholates; (v) Tetracyanoethylene (TCNE) and analogues; (vi) 1,2,4,5-Tetrazine derivatives; (vii) Unsaturated C _n Chains.	6
Scheme 1.2: Valence Tautomer Equilibria of Cu ^m /Q ⁿ System (Q = <i>o</i> -Quinone, Q ^{•-} = Semi-quinone) and Q ²⁻ = Catecholate).	9
Scheme 1.3: Delocalized Resonance Structures of (i) L _k Mn ^x /R _n E ^y (L _k = (C ₅ R' ₅)(CO) ₂ , E ⁻ and E ^{•-} = deprotonated <i>p</i> -phenylenediamine anion and radical and (ii) Ru ^x /Q ^y (Q ^{•-} = semi-quinone) and Q ²⁻ = catecholate) systems	10
Scheme 2.3.1: Synthetic Scheme for Dinuclear [Ru(tpy)(bpy)] ₂ (μ -R ₂ R ₂ 'dicyd)][PF ₆] ₂ Complexes (1-4)	67
Scheme 3.2.1: Cyanation of Aromatic Amine forming Aromatic Cyanamide.	122
Scheme 3.2.2: Two major steps in the Syntheses of substituted Azodi(phenylcyanamide) (R ₂ R ₂ 'adpcH ₂) Ligands from Azodianilines: (i) Preparation of R ₂ R ₂ '-azodianilines from Phenylamine, (ii) Cyanation of Azodianilines to form Azodi(phenylcyanamide) (R ₂ R ₂ 'adpcH ₂)	123
Scheme 3.2.3: Synthesis of Azobenzenes via Azo Coupling Reaction. R = H, -NO ₂ ; R' = NR ₃ -, -NH ₂ -, -OH.	124
Scheme 3.2.4: Synthesis of Azobenzenes via Mills Reaction.	125
Scheme 3.2.5: Oxidation of Phenylamine forming Nitrosobenzene: two major side reactions forming Azoxy- and Nitrobenzene.	126
Scheme 3.2.6: Synthesis of Nitrosobenzene from Phenylamines using Oxone in CH ₂ Cl ₂ /H ₂ O Biphasic system. R = -CF ₃ , -NO ₂ , -H, -Br.	127
Scheme 3.2.7: Synthesis of Azobenzene from Azoxybenzene via Wallach Reaction. R = -H, -NO ₂ , -COCH ₃ , -COOH.	127
Scheme 3.2.8: Synthesis of Azobenzenes via Perborate/Acetic acid Oxidation method.	128
Scheme 3.2.9: Synthesis of Azobenzenes by Reductive coupling of Nitrobenzene. R = -H, -Me, -Cl, -Br, -CN, MeCO-, MeCO ₂ -.	129
Scheme 3.2.10: Synthesis of Azobenzene by Reduction of Azoxybenzene. R,R' = -H, -Me, -OMe, -OEt, -Cl.	130

Scheme 3.2.11: Synthesis of Phenylcyanamide from Phenylamine using Cyanogen Halide Method	131
Scheme 3.2.12: Synthesis of Phenylcyanamide from Phenylamine using Thiourea Method	133
Scheme 3.2.13: Synthesis of Phenylcyanamide from Phenylamine using Thiocarbamate Method.	134
Scheme 3.2.14: Proposed Mechanism for the Synthesis of Phenylcyanamide from the Dithiocarbamate salt using DIB and Concentrated NH ₃ .	135
Scheme 3.2.15: Synthesis of Phenylcyanamide from Phenylamine using Isocyanate Method	136
Scheme 3.2.16: Proposed mechanism for the synthesis of Phenylcyanamide from Isocyanate using NaN(SiMe ₃) ₂ .	137
Scheme 3.2.17: Synthesis of R ₂ R ₂ '-azodianilines. R ₂ R ₂ ' = H ₂ -, Me ₂ - ; H ₄ - ; <i>meta</i> -H ₄	139
Scheme 3.2.18: Synthesis of R ₂ R ₂ '-azodianilines. R ₂ R ₂ ' = Cl ₂ -, H ₂ - ; Cl ₄ -	140
Scheme 3.2.19: Synthesis of R ₂ R ₂ '-azodianilines. R ₂ R ₂ ' = Me ₄ -	140
Scheme 3.2.20: Synthesis of R ₂ R ₂ '-adpcH ₂ . R ₂ R ₂ ' = H ₂ -, Me ₂ -; H ₄ -; Me ₄ -; Cl ₂ -, H ₂ -; Cl ₄ -.	142
Scheme 3.2.21: Synthesis of R ₂ R ₂ '-adpcH ₂ . R ₂ R ₂ ' = H ₄ -; H ₂ -, Me ₂ - , <i>meta</i> -H ₄ -.	142
Scheme 3.2.22: Synthesis of R ₂ R ₂ '-adpcH ₂ . R ₂ R ₂ ' = H ₄ -; H ₂ -, Me ₂ - .	142
Scheme 3.5.1: Synthetic Scheme used to prepare [{Ru(tpy)(bpy)} ₂ (μ-R ₂ R ₂ 'adpc)][PF ₆] ₂ Complexes (7b-7f). R ₂ R ₂ 'adpc = Me ₂ -, unsubstituted, Cl ₂ -, Cl ₄ -, and <i>meta</i> -adpc	236
Scheme 3.5.2: Synthetic Scheme used to prepare [{Ru(tpy)(bpy)} ₂ (μ-Me ₄ adpc)][PF ₆] ₂ Complex.	236
Scheme 4.1.1: Deactivation Pathways for Photo-excited Singlet Species with Rates (<i>k_i</i> 's): Photochemical Reaction (<i>k_r</i>), Singlet-Triplet Intersystem Crossing (<i>k_{isc}</i>), Internal Conversion (<i>k_{ic}</i>), Luminescence (<i>k_f</i>)	269
Scheme 4.3.1: Assignment of the Redox Couples and Rates of Linkage Isomerism.	341
Scheme 4.4.1: Synthetic Scheme for <i>cis</i> -[Ru(bpy) ₂ (R-pcyd)(dmsO-S)][PF ₆] Complexes (4a-4f).	343
Scheme 5.3.1: Reaction Scheme for the Synthesis of <i>trans</i> -[Ru(tpy)(R-pcyd)Cl ₂] Complexes. (1-5)	372

List of Abbreviations

ΔG_c	Free energy of comproportionation
$\Phi_{S \rightarrow O}$	Quantum yield of photo-induced S \rightarrow O isomerism
acac	Acetylacetonate
adpc ²⁻	4,4'-azodi(phenylcyanamide)
azodicyd	4,4'-azodi(phenylcyanamide)
B3LYP	Beck three parameter hybrid exchange and Lee-Yang-Parr correlation functionals
bpy	2,2'-bipyridine
BuLi	<i>n</i> -butyllithium
COSY	Correlated spectroscopy
Cl ₂ adpc ²⁻	3,3'-dichloro-4,4'-azodi(phenylcyanamide)
Cl ₄ adpc ²⁻	2,2':5,5'-tetrachloro-4,4'-azodi(phenylcyanamide)
Cl ₂ dicyd ²⁻	2,5-dichloro-1,4-dicyanamide benzene
Cl ₄ dicyd ²⁻	2,3,4,5-tetrachloro-1,4-dicyanamide benzene
Clpcyd ⁻	4-chlorophenylcyanamide
Cl ₂ pcyd ⁻	2,4-dichlorophenylcyanamide
Cl ₃ pcyd ⁻	2,4,5-trichlorophenylcyanamide
Cl ₄ pcyd ⁻	2,3,5,6-tetrachlorophenylcyanamide
Cl ₅ pcyd ⁻	2,3,4,5,6-pentachlorophenylcyanamide
CNS	Creutz, Newton and Sutin
CV	Cyclic voltammetry
DCNQI	<i>N,N'</i> -dicyanoquinonediimine
dicyd ²⁻	1,4-dicyanamide benzene dianion
DFT	Density functional theory
DMF	<i>N,N'</i> -dimethylformamide
DMSO	Dimethylsulfoxide
dppe	ethylenebis(diphenylphosphine)
EPR	Electron Paramagnetic Resonance

E_{op}	LMCT band energy
E_{IT} (or λ)	Energy of the intervalence transition
f	Oscillator strength
Fc	Ferrocene
$H_{\text{MM}'}$	Metal-metal coupling element
$H_{\text{LM}'}$	Metal-ligand coupling element
H_{ad}	Acceptor-donor coupling element (Hush model)
$H_{\text{MM}'}$	Metal-metal coupling element (CNS model)
HOMO	Highest occupied molecular orbital
ICT	Optical information and communication technology
IR	Infra-red
IT	Intervalence transition
IVCT	Intervalence charge transfer
K_{c}	Comproportionation constant
k_{SO}	Redox-induced S \rightarrow O isomerization rate
k_{OS1}	Thermal O \rightarrow S back reaction rate
k_{OS2}	Redox-induced O \rightarrow S back reaction rate
LF	Ligand-field
LMCT	Ligand-to-metal charge transfer
LUMO	Lowest unoccupied molecular orbital
$\text{Me}_2\text{adpc}^{2-}$	2,2'-dimethyl-4,4'-azodi(phenylcyanamide)
$\text{Me}_4\text{adpc}^{2-}$	2,2':5,5'-tetramethyl- 4,4'-azodi(phenylcyanamide)
mal	Malonate
Me_2DCNQI	2,5-dimethyl- <i>N,N'</i> -dicyanoquinonediimine
$\text{Me}_2\text{dicyd}^{2-}$	2,5-dimethyl-1,4-dicyanamidobenzene
Me-pic	4-methyl-2- pyridinecarboxylate
MLCT	Metal-to-ligand charge transfer
<i>meta</i> -adpc ²⁻	3,3'-azodi(phenylcyanamide)
metazodicyd	3,3'-azodi(phenylcyanamide)
MMCT	Metal-to-metal charge transfer

NHE.	Normal hydrogen electrode
NIL	Non-innocent ligand
NIR	Near-infrared
NLO	Non-linear optical
NMR	Nuclear magnetic resonance
Ox	Oxalate ligand
OSOR	2-methylsulfinyl benzoate
OSSO	Dimethylbis (methylsulfinylmethyl) silane
OTTLE	Optically transparent thin layer electrode
pcyd ⁻	Phenylcyanamide
PCM	Polarizable Continuum Model
phen	1,10-phenanthroline
pic	2-pyridinecarboxylate
PMMA	Poly(methylmethacrylate)
Py	Pyridine
PySO	2-(isopropylsulfinylmethyl) pyridine
Pz	Pyrazine
SOMO	Singly occupied molecular orbital
thd	2,2,6,6-tetramethyl-3,5-heptanedione
TBAH	Tetrabutylammonium hexafluorophosphate
TCNQ	7,7,8,8-tetracyano- <i>p</i> -quinodimethane
tdpc ²⁻	3,6-bis-(4-phenylcyanamide)-1,2,4,5-tetrazine
TOCSY	Total correlated spectroscopy
tmen	<i>N,N'</i> -tetramethyl ethylene diamine
Tp ⁻	hydrotris(pyrazol-1-yl)borate
tpy	2,2':6',2''-terpyridine
ttpy	4-(<i>tert</i> -butylphenyl)-2,2':6',2''-terpyridine
vis-NIR	Visible-Near-infrared
λ_{outer}	Outer-sphere reorganizational energy

Chapter 1: General Introduction

Scope of Thesis Research

The study of complexes with redox-active ligands, frequently called ‘non-innocently’ behaving ligands, has received special attention in recent years due to their fundamental importance in bio-inorganic chemistry¹, potential applications in catalysis² as well as in designing modern electro-optic and magnetic materials.³⁻⁶

The computing and information technology industries have grown drastically over the past years as the search for “smaller” and “faster” high capacity computing and data storage as well as telecommunication and information processing devices continue to drive today’s society. This has revolutionized research in the field of material science with much of the focus being centred on the development of novel electro-optic and magnetic materials. Many of these novel materials are based on redox-active metal-ligand donor-acceptor ($D^+ - A^-$) complexes or mixed-valence complexes ($M-L-M^+$) with redox-active bridging ligands, where the sought-after physical properties are often expressed via non-innocently behaving ligand functionalities, in conjugation with the redox-active metal. Prime examples include: (i) molecular conductivity and switching properties of $Cu^{n+} - TCNQ^{n-}$ with partially reduced $TCNQ^{n-}$ ligands^{7a} or high temperature superconductivity of $YBa_2Cu_3O_{7-x}$ with partially oxidized oxide bridges,^{7b} (ii) molecular magnetism with redox-active ligands such as monoatomic $O^{2-/•-}$, diatomic cyanide, or polyatomic $TCNQ^{n-}$ as spin carriers or superexchange mediators^{7c-e}, and (iii) attainment of the metal-to-ligand, ligand-to-metal, or ligand-to-ligand charge transfer excited states

by readily oxidized and reduced ligands in photoactive components such as sensitizers or emitters.^{7f}

In the construction of novel molecular materials, a mixed-valence complex (M-L-M⁺) can be considered as a molecular unit building block. Polymerization and retention of electronic delocalization between unit building blocks could lead to potentially conducting long-chain molecular wires. Dinuclear mixed-valence complexes with polarizable bridging ligands, particularly those of ruthenium, have demonstrated important viability to the construction of molecular electronic devices for signal processing. Many of these complexes show intense NIR charge transfer absorptions, intensity and energy of which can be tuned by the variation of metal-metal coupling¹⁶⁻¹⁹. These properties are well-suited for applications in variable optical attenuators (electro-optic switching) in NIR telecommunication devices as well as in smart windows to filter-out the radiant heat whilst transmitting visible light. Neutral dinuclear mixed-valence (M-L-M⁺) complexes (donor-acceptor molecules) when incorporated in a polymer matrix may exhibit non-linear optical (NLO) effects. The properties (electrochemistry, dipole moment, NIR absorption) of these donor-acceptor molecular units, pertinent to optoelectronic material applications, are determined by the degree of non-innocence of bridging ligands. Purposeful design of donor-acceptor systems and materials require that the expression and recognition of these properties be understood.

Redox-active ligands may occur in several different formal oxidation states when bound to a transition metal. The possible change of oxidation states *i.e.* redox *ambivalence* of such “suspect” ligands gives rise to an uncertainty in the assignment of oxidation-state distribution in redox-active metal-ligand combinations and, thereby, leads

to an ambiguity in the interpretation of complexes' electrochemical and spectroscopic properties. However, "innocence" or "non-innocence" is not the permanent attribute of redox-active ligands; molecules can behave as "innocent" or "non-innocent" ligands towards redox-active metals under specific circumstances and in certain coordination situations.^{4d} Recently, the redox *ambi-valence* of phenylcyanamide ligands has been addressed in dinuclear and mononuclear ruthenium complexes.^{5,6,8,9,21}

The bridging 1,4-dicyanamidebenzene dianion (dicyd^{2-}) is an efficient mediator of antiferromagnetic and resonance exchange in dinuclear $[\{\text{Ru}(\text{NH}_3)_5(\mu\text{-R}_2\text{R}_2'\text{dicyd})\}^{3+/4+}]$ complexes.¹⁵⁻¹⁹ The reason for this efficiency is the close match in energy between $\text{Ru(III)}d\pi$ and the π -HOMO of the bridging ligand, which permits hole-transfer superexchange metal-metal coupling. Combined EPR spectroscopy and DFT calculations have unambiguously established Ru(III) -centred spin in $[\{\text{Ru}(\text{NH}_3)_5\}_2(\mu\text{-R}_2\text{R}_2'\text{dicyd})]^{3+}$ and supported a mixed-valence description $\text{Ru(II)-R}_2\text{R}_2'\text{dicyd}^{2-}\text{-Ru(III)}$ of the complex, in which the natural dianionic form of the bridging dicyd^{2-} anion is retained.⁵ On the other hand, Bonvoisin⁶ *et al* reported a structurally characterized dinuclear complex $[\{\text{Ru}(\text{tpy})(\text{thd})\}_2(\mu\text{-dicyd})]^+$ where tpy is 2,2';6',2"-terpyridine and thd⁻ is 2,2,6,6-tetramethyl-3,5-heptanedione, whose EPR spectrum has unambiguously established a radical-centered description, $\text{Ru(II)-dicyd}^{\bullet-}\text{-Ru(II)}$, of the complex reflecting the bridging ligand's non-innocent behavior. Such a transition in redox behavior of dicyd^{2-} anion must be a consequence of the replacement of σ -donor amine by the π -acceptor terpyridine ligand that stabilizes $\text{Ru(III)} d\pi$ orbital relative to the π -HOMO of the bridging dicyd^{2-} ligand, leading to a configuration with Ru(II) ions and an oxidized radical anion $\text{dicyd}^{\bullet-}$.

Non-innocence of phenylcyanamide ligands has also been addressed in mononuclear ruthenium-phenylcyanamide complexes. While EPR and NMR spectroscopy unambiguously established Ru(III)-centred spin in $[\text{Ru}(\text{NH}_3)_5(\text{R-pcyd})]^+$ complexes⁸ where R-pcyd is substituted phenylcyanamide, and confirms the valence configuration of Ru(III)-(R-pcyd⁻) for these complexes, DFT calculations of the spin density distribution of $[\text{Ru}(\text{Tp})(\text{dppe})(\text{R-pcyd})]^+$ complexes, where dppe is ethylenebis(diphenylphosphine), Tp⁻ is hydrotris(pyrazol-1-yl)borate and R-pcyd⁻ is 3-chlorophenyl-cyanamide (3-Clpcyd⁻) and Cl₅pcyd⁻, revealed a transition from substantial Ru(II)-(3-Clpcyd^{•0}) character for the 3-Clpcyd species to a more localized Ru(III)-Cl₅pcyd⁻ description for the Cl₅pcyd species.⁹

The degree of non-innocence of redox-active phenylcyanamide ligands is therefore determined by the relative energy of the Ru(III)dπ and the π-HOMO of the phenylcyanamide ligand which in turn, depends on the electronic nature of ancillary ligand as well as substituents on the phenylcyanamide ligand. Such redox-ambivalence of phenylcyanamide ligands may lead to an uncertainty in the assignment of proper oxidation state distributions in newly developed ruthenium-phenylcyanamide complexes. In general, the proper description of oxidation states is fundamental to an understanding of electronic (electrochemical and spectroscopic) properties of complexes that have potential for applications in opto-electronic (molecular wire, NIR opto-electronic switches filter, attenuator, modulator) and magnetic materials.

The aim of the present thesis research is to design and characterize novel mononuclear and dinuclear ruthenium complexes of redox-active phenylcyanamide ligands and investigate their viability as molecular building units in NIR

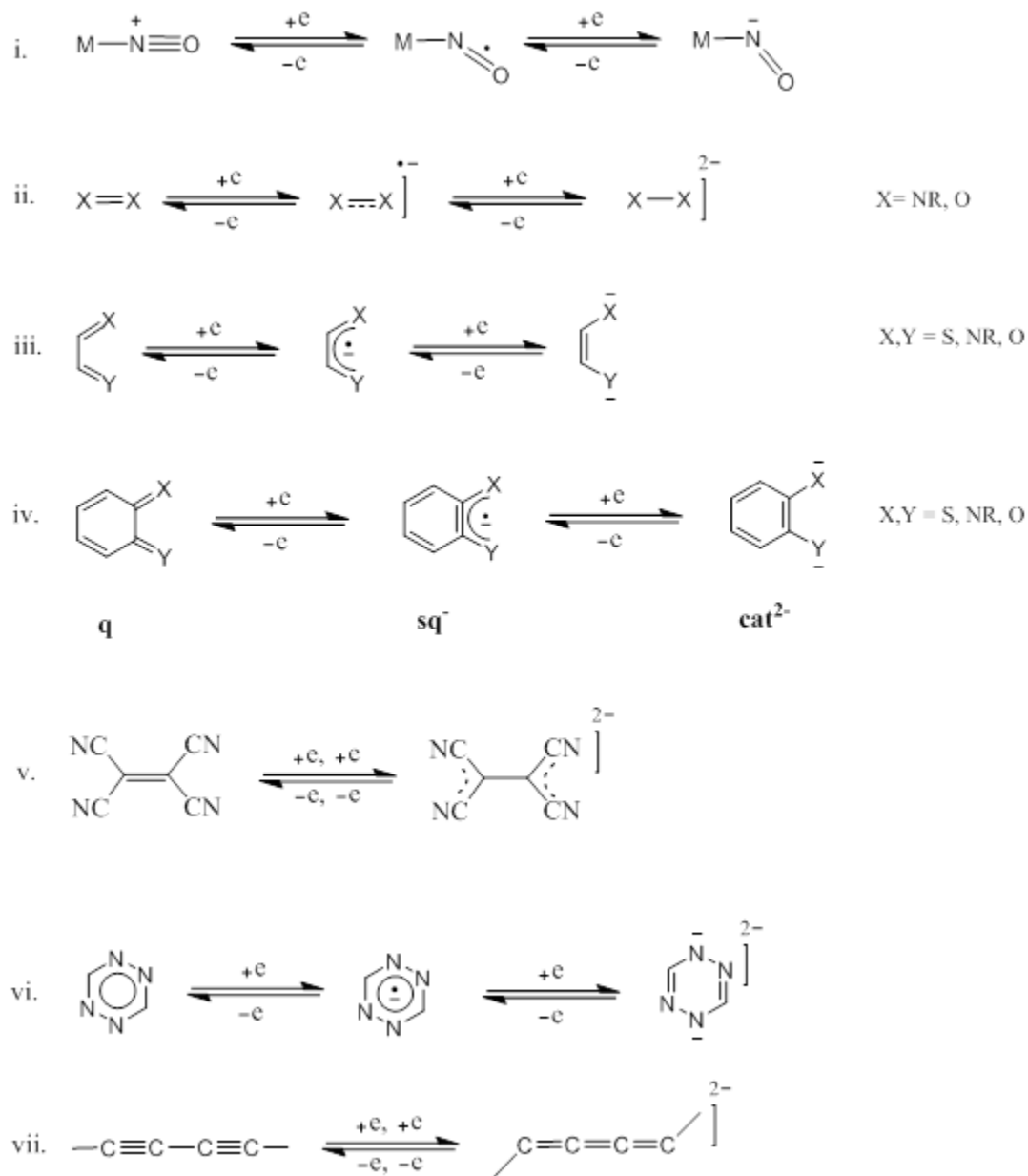
telecommunication and non-linear optical (NLO) devices. The focus of the research is mainly centered on the identification and recognition of the non-innocent behavior or redox *ambi-valence* of redox-active phenylcyanamide ligands under various coordination environments (ancillary ligand and substituents on the redox-active ligand) and external conditions (solvent, light) and their role on the electrochemical and spectroscopic properties of the mononuclear and dinuclear ruthenium complexes.

Prior to considering the mononuclear and dinuclear ruthenium complexes of redox-active phenylcyanamide ligands that form the subject of this thesis, a detailed discussion regarding non-innocent ligand behavior, characterization of complexes with non-innocently behaving ligands will be given. Of course, throughout the introduction, a focus will be placed on ruthenium phenylcyanamide complexes.

1.2 Non-Innocent Ligand Behaviour

In general, the term “redox-active” refers to the oxidizable or reducible nature of a metal or a ligand in their coordination complexes. According to Jorgensen²², ligands are “innocent” when they allow oxidation states of the central atoms (metal) to be defined. The expression “non-innocent”, in contrast, conveys an uncertainty, and literally, an *ambi-valence* of oxidation-state assignments of certain redox-active ligands. Originally, the expression “non-innocent” was coined to describe the oxidation state ambiguity of redox active ligands such as $O_2/O_2^{\bullet-}/O_2^{2-}$ or $NO^+/NO^{\bullet}/NO^-$ in their transition metal complexes, in contrast to “innocent”, unequivocally charge-defined ligands such as H_2O , NH_3 , or Cl^- . The redox *ambi-valence* of such “suspect” ligands makes it difficult to assign unambiguous “physical” oxidation number to the metal center. The simplest case of a redox *ambi-valent* ligand is NO. Combined electron paramagnetic resonance (EPR)

Scheme 1.1: Structural Change associated with Redox Transformations of Non-innocently behaving Ligands. (i) Nitrosyls; (ii) Dioxygen, Azo-compounds; (iii) α -Diimine, α -Dithiolene, α -Dioxolene; (iv) Quinone/Semiquinone/Catecholates; (v) Tetracyanoethylene (TCNE) and analogues; (vi) 1,2,4,5-Tetrazine derivatives; (vii) Unsaturated C_n Chains.



and Mossbauer spectroscopy showed that the brown ring ion $[\text{Fe}(\text{NO})(\text{H}_2\text{O})_5]^{2+}$, alternatively formulated as $\text{Fe}(\text{I})\text{-NO}^+$, $\text{Fe}(\text{II})\text{-NO}^\bullet$ (NO is neutral in this case), or a $\text{Fe}(\text{III})\text{-NO}^-$ complex, is best described by the latter formulation.²³ Many reviews have appeared in the literature that cover the broader aspects of non-innocent ligands, their occurrence and role in bioinorganic chemistry, catalysis and electro-optic and magnetic materials.¹⁻⁴ Scheme 1.1 shows some frequently occurring non-innocent ligand functionalities and their structural changes associated with redox-transformations.

The term “non-innocent” is often (inaccurately) taken to mean simply that the ligands in a complex are redox-active, such that “non-innocence” is a function of redox-active ligand alone. This is not applicable when metal-centred and ligand-centred frontier orbitals are at very different energies, such that their redox potentials are widely separated. For example, $[\text{Ru}(\text{bpy})_3]^{2+}$ where bpy is 2,2'-bipyridine, undergoes metal-centred oxidation at 1.26 V vs NHE and a series of ligand centred reduction starting at -1.35 V.²⁴ These redox events can be described quite unambiguously as metal-centred or ligand-centred due to wide separation of the $\text{Ru}(\text{II})d\pi$ HOMO and the π^* LUMO of the bpy ligand, where the redox processes of the metal and the ligand take place. On the other hand, when the ligand and metal-centred redox orbitals are close in energy (increased covalency), the metal or ligand-centred redox processes cannot be assigned unambiguously, and so described the ligand “non-innocent”. For example, while the first reduction in $[\text{Cr}(\text{bpy})_3]^{3+}$ is metal centred to give a species, $[\text{Cr}(\text{II})(\text{bpy})_3]^{2+}$, the next reduction results in transfer of two electrons (approximately) to the ligand π^* levels to give a species best described as $[\text{Cr}(\text{III})(\text{bpy})(\text{bpy}^\bullet)_2]$ and further reduction also results in delocalized behaviour. The bpy ligand is redox-active in both complexes but the term

“non-innocent” applies far more to the chromium complex than to the ruthenium complex.²⁵ McCleverty and Ward, therefore, emphasized the necessity of particular coordination situation and referring to “non-innocent behavior” rather than “non-innocent ligands” (NILs).^{4d}

Recently, the term “non-innocent” has also been applied to non-redox-active ligands in order to indicate the perturbation of metal coordination by the unexpected reactivity of ligands in response to external stimuli.²⁶

1.2.1 Non-innocent Ligand Behaviour in Mononuclear Complexes

As mentioned before, the degree of non-innocence of a redox-active ligand is largely determined by the relative energy of the frontier (redox) orbitals on the metal and the ligand. A close energy match between metal and ligand-centred orbitals results in a significant covalency in the metal-ligand bond, such that the redox-states based on the metal and the ligand become very similar in energy, leading to an ambiguity in the assignment of the oxidation state distribution of the complex.⁴

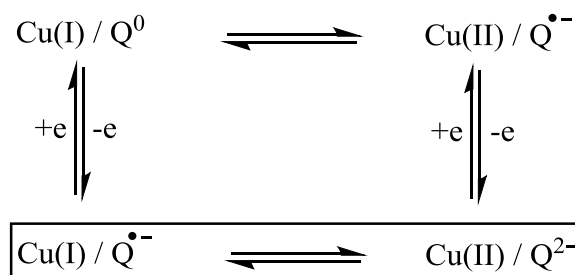
Depending on the extent of mixing between metal and ligand based frontier orbitals, mononuclear transition metal complexes with redox-active ligands may exhibit barrier separated localized two (or more) valence tautomeric forms or a barrierless delocalized electronic state having equilibrated contributions from multiple resonance forms.

The valence tautomers or (redox-isomers), involving two (or more) different species in equilibrium and separated by an activation barrier, is shown below.



The occurrence of a barrier between two or more valence or redox isomeric forms has been observed for several species, including iron, manganese, cobalt and copper complexes of *o*-quinonoid (1,2-dioxolene) ligands.^{4e,27} In general, large structural and chemical difference gives rise to a barrier between valence tautomeric forms that may exist in temperature dependent equilibrium. In the case of copper complexes (Scheme 1.2), the two valence tautomeric forms Cu(I)/Q^{•-} and Cu(II)/Q²⁻ were identified and distinguished by EPR spectroscopy with characteristic $g = 2.005$ for the radical centred (semiquinone) spin on the former and $g = 2.12$ for the copper(II) centred spin on the latter.^{27a,b} The Cu(II)/Q^{•-} and Cu(I)/Q⁰ forms have also been identified for selected cases.^{27c}

Scheme 1.2: Valence Tautomer Equilibria of Cu^m/Qⁿ System (Q = *o*-Quinone, Q^{•-} = Semi-quinone) and Q²⁻ = Catecholate).

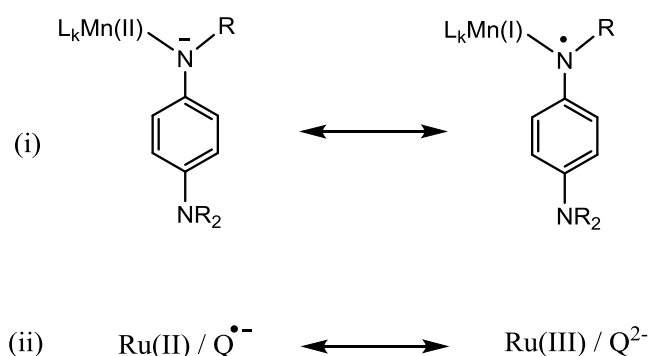


On the other hand, when there is a significant mixing between metal and ligand based orbitals, there can be a barrierless delocalized state of two or more resonance structures, describing only one species with one potential energy minimum, as shown below.



This gives rise to ambiguous or non-integer oxidation state assignment of the metal and non-innocent ligand fragments. The extent of delocalization is determined by the relative energies of frontier orbitals of the metal and the redox-active non-innocent ligand. Such delocalized electron distributions are prevalent in Ru-non-innocent ligand chemistry. This resonance situation was observed in many organometallic manganese complexes containing redox active anilido ligands, for example in $\text{Mn}(\text{CO})_2(\text{C}_5\text{R}'_5(\text{ER}_n))$ complexes²⁸ where ER_n = redox-active deprotonated phenylenediamine ligand, (Scheme 1.3 a) as well as in ruthenium-quinone complexes²⁹ (Scheme 1.3 b).

Scheme 1.3: Delocalized Resonance Structures of (i) $\text{L}_k\text{Mn}^x/\text{R}_n\text{E}^y$ ($\text{L}_k = (\text{C}_5\text{R}'_5)(\text{CO})_2$, E^- and $\text{E}^{\bullet-}$ = deprotonated *p*-phenylenediamine anion and radical and (ii) Ru^x/Q^y ($\text{Q}^{\bullet-}$ = semi-quinone) and Q^{2-} = catecholates) systems



The ambiguous oxidation state for both families of complexes was established by EPR spectroscopy and computational methods. In the case of ruthenium quinone complexes, the modification of quinones as well as ancillary ligands (L) resulted in more localized metal-centred or ligand-centred spins.²⁹

1.2.2 Non-innocent Behavior of Bridging Ligands in Dinuclear Complexes

Superexchange is the term given to electron exchange or charge transfer between two metal centers which is mediated by the orbitals of a bridging ligand. A simple schematic energy level diagram for superexchange in a dinuclear mixed-valence ruthenium complex $\text{Ru(II)}-\mu\text{-BL-Ru(III)}$ with bridging ligand BL is shown in Figure 1.1.

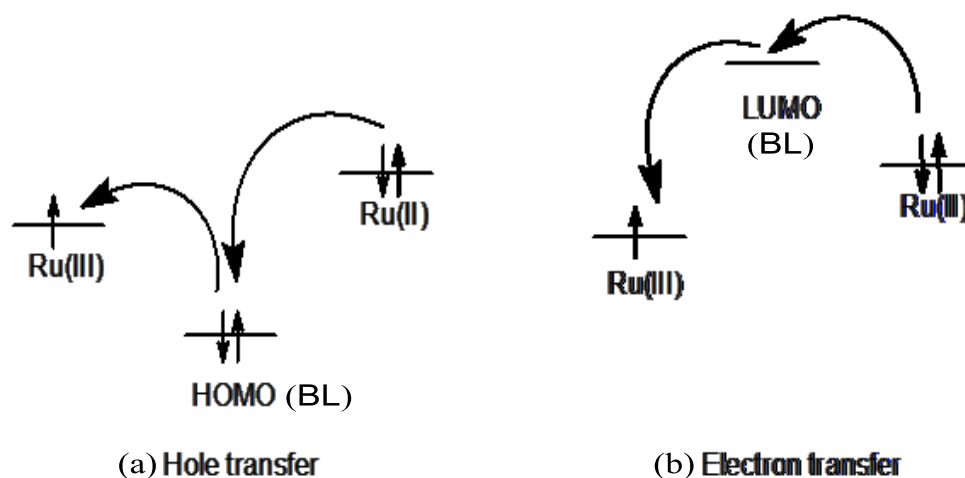


Figure 1.1: Hole-(a) and electron-(b) transfer superexchange metal-metal coupling in the dinuclear mixed-valence $\text{Ru(II)}-\mu\text{-BL}^{2-}\text{-Ru(III)}$ complex.

The mechanism of the concerted hole-transfer superexchange (Figure 1.1 a) can be viewed as an initial transfer of an electron from the bridging ligand's π -HOMO to the Ru(III) (π -acceptor) orbitals and subsequent transfer of the electron from the Ru(II) (π -donor) orbitals to the π -HOMO of the bridging ligand. Because the concerted event effectively represents an electron-hole moving across the system from the acceptor to the donor end, the mechanism portrayed "hole-transfer" superexchange. "Electron-transfer" superexchange occurs when the bridging ligand's π -LUMO provides the pathway, and the mechanistic sequence of steps is reversed relative to the hole-transfer mechanism. In

this case, the concerted event is that of an electron moving from the donor metal Ru(II) end of the system to the acceptor metal Ru(III) end. The vast majority of mixed-valence systems, typically [Ru(III), Ru(II)] dimer, incorporated π -acceptor bridging ligands such pyrazine and other polypyridyl ligands, in which metal-metal coupling was dominated by electron-transfer pathway. Examples of multidentate ligands which do mediate metal-metal coupling via hole-transfer superexchange include the malononitrile anion(MN⁻), the triazole anion, bibenzimidazolate dianion, tetrapyridyl diphenyl dianion and all of their respective derivatives.^{30a-d} However, these ligands all act as both π -donors and π -acceptors, and the information they provide involves contribution from both hole- and electron transfer pathways. Only few families of π -donor ligands, for example azodicarbonyl dianion (adc-R²⁻),^{30e-h} 1,4-dicyanamide benzene dianion (dicyd²⁻)¹⁵⁻¹⁹ are reported that exhibit purely hole-transfer superexchange. The dicyd²⁻ anion, one of the π -donor bridging ligands studied in the present research work, has shown excellent efficiency as a hole-transfer superexchange mediator for metal-metal coupling in dinuclear pentaammine, tetraammine and triammineruthenium complexes.

Provided the orbitals are symmetry-matched, optimal superexchange (both hole and electron-transfer) requires that metal and bridging ligand frontier orbitals have similar energies, and therefore that the bonding be significantly covalent. The hole-transfer superexchange requires that the bridging ligand be oxidizable (*i.e.* non-innocent) at similar potential as the metal ions, such that the following two states, metal-centred mixed-valence (a) and the radical-centred state (b), are almost similar in energies.



(a)



(b)

For a weakly coupled system, the localized mixed-valence structure (a) is more stabilized than the radical-centred complex (b). As the energy gap between Ru(II) $d\pi$ and the π -HOMO of the bridging ligand decreases, *i.e.*, when the system becomes strongly coupled, significant covalency leads to a delocalized state as shown in the following resonance forms and

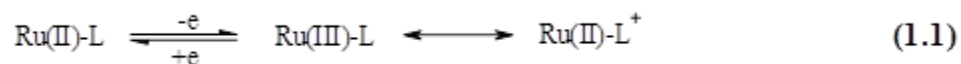


the question of formal oxidation state is blurred. The non-innocence of the redox-active bridging ligand, therefore, leads to an ambiguity in the oxidation state distribution in the complex. In the extreme case, when the π -HOMO of the bridging ligand is significantly above the Ru(III) $d\pi$ -orbitals, the ligand is completely oxidized to give the localized radical-centred complex (b). Kaim's EPR studies^{30e-h} of dinuclear $[\{\text{Ru}(\text{bpy})\}_2(\mu\text{-adc-R})]^{3+}$ complexes, where bridging adc-R^{2-} is substituted azodicarbonyl dianion, have shown strongly coupled delocalized states of complexes in which the spin density distribution between the mixed-valence $\text{Ru(III)}-(\mu\text{-adc}^{2-})\text{-Ru(II)}$ and the radical-centred alternatives $\text{Ru(II)}-(\mu\text{-adc-R}^{\bullet})\text{-Ru(II)}$ varied as a function of the electron donating/withdrawing properties of R. Similarly, the electron-transfer superexchange also requires partially reducible (non-innocent) bridging ligand which in the strongly coupled case may lead to redox ambi-valence and in the extreme case, to the ligand-centred (reduced) radical species. For example, the redox-active tetracyanoquinone (TCNQ) remains in its natural neutral form in *tetra*-nuclear $\{[\mu_4;(\eta^1)_4\text{-TCNQ}][\text{Re}(\text{bpy})(\text{CO})_3]_4\}^{4+}$,^{31a-b} while it is partially or fully reduced species in $\{[\mu_4;(\eta^1)_4\text{-TCNQ}][\text{Ru}(\text{NH}_3)_5]_4\}^{8+}$ complexes.^{31c-d}

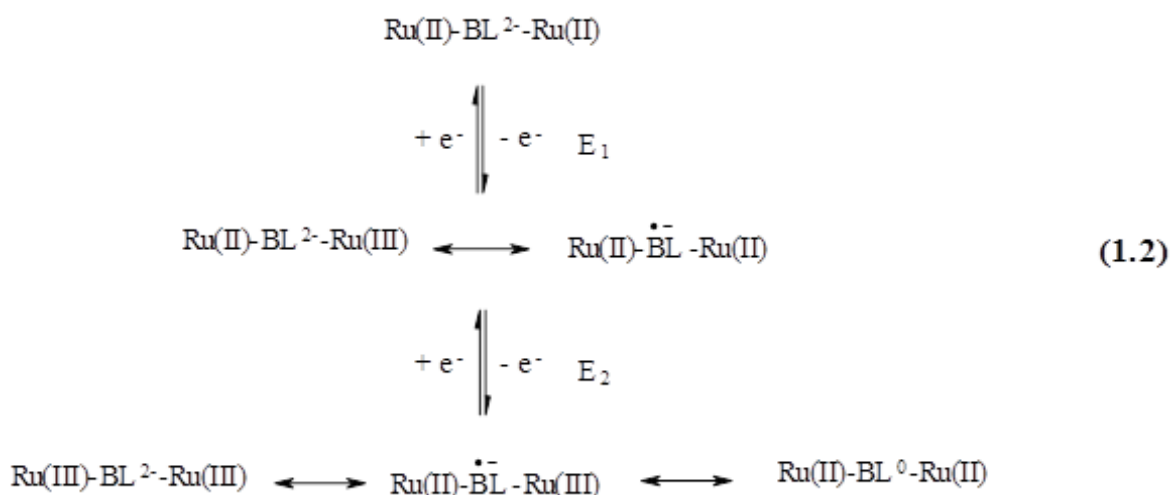
In summary, metal-metal coupling in dinuclear complexes requires that the metal-ligand bonding be significantly covalent and the bridging ligand reducible/oxidizable (non-innocently behaving) at similar potentials to metal-centered redox events. In addition, the non-innocent behavior of the bridging ligand is an essential prerequisite for highly delocalized Class III mixed-valence system.

1.2.3 Experimental Determination of Non-Innocent Behaviour

As discussed in the previous sections, an occasional consequence from the presence of unrecognized non-innocently behaving ligand is the erroneous assignment of the oxidation state distribution of the complex. In the mononuclear ruthenium complexes with oxidizable anionic ligand L, the uncertainty of the redox events can be shown by the following Eq. 1.1.



In dinuclear complexes, the presence of oxidizable dianionic bridging ligands leads to more complicated situations, as shown in the Eq. 1.2

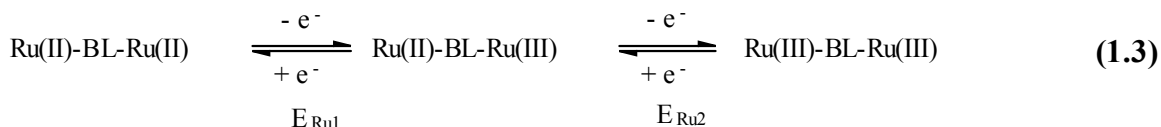


Several physical methods are available to establish the most appropriate oxidation state assignment in transition metal complexes. These can include EPR, NMR, UV-Vis-NIR, infrared and X-ray absorption spectroscopies and X-ray crystallography. In open-shell cases, EPR and paramagnetic NMR spectroscopies can provide the most unambiguous and appropriate oxidation state distribution in complexes containing non-innocent ligands. UV-vis-NIR and IR spectroscopies may provide supporting evidence to such assignments. Quantum mechanical calculations (semi-empirical, density functional) may provide further insight into the valence configurations and often confirms the assignments by reproducing experimental data. Electrochemical information on redox couples is only useful when supported by spectroscopic characterization (spectroelectrochemistry). Here we describe a brief account of various physical methods that are popularly used to investigate non-innocent behavior or redox ambi-valence of redox-active ligands in their mononuclear and dinuclear complexes with special attention given to the ruthenium complexes of phenylcyanamide ligands.

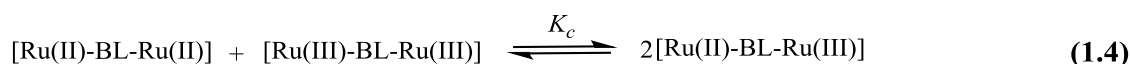
Electrochemistry

Electrochemical techniques such as polarography, cyclic voltammetry, and differential pulse voltammetry are frequently used for the characterization of redox-active complexes. Voltammetric measurements provide information on the stability of complexes upon redox transformation and provide insight into the mechanism of reactions associated with electron transfer processes. The reversibility of a redox wave often gives a first indication for the possibility of chemically isolating the electrochemically formed species.

For a dinuclear mixed-valence complex, where the bridging ligand BL is not redox-active, the metal-centred redox events can be shown by the following Eq. 1.3.



The stability of the mixed-valence state is quantified by the comproportionation constant, K_c , which is defined for the equilibrium shown in Eq. 1.4.



The Eq. 1.4 may be viewed as the sum of the redox events described in Eq.1.3, K_c is thus available experimentally from the difference between the two metal-centred redox couples, $\Delta E = E_{\text{Ru2}} - E_{\text{Ru1}}$. via the Eq. 1.5

$$\ln K_c = \frac{\Delta G_c}{RT} = \frac{nF\Delta E}{RT} \quad (1.5)$$

However, voltammetric data alone cannot provide any information on redox-active sites (metal or ligand) in complexes containing both redox-active metal and ligands. The information on redox potentials is only helpful when supported by other spectroscopic techniques (EPR, UV-vis-NIR, IR spectroelectrochemistry), reflecting the energy and reactivity associated with the electronic structures of complexes in various oxidation states.

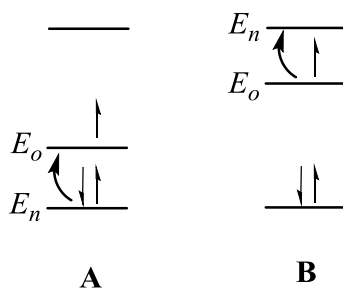
EPR Spectroscopy

The most compelling and unambiguous assignment of redox active site in an open-shell structure, especially the paramagnetic species with $S = \frac{1}{2}$ spin, can be obtained from electron paramagnetic resonance spectroscopy (EPR). The g -value of a EPR signal provides information as to whether the singly occupied molecular orbital (SOMO) is of mostly metal or organic character.

The g -value for free electron is $g_e = 2.0023$ and deviation of the g -value from g_e may be attributed to the admixture of higher excited states to the ground state and spin-orbit coupling effects as shown in the following Eq. 1.6.^{32a}

$$g = g_e - \frac{2}{3} \sum_i \sum_n \sum_{kj} \frac{\langle \Psi_0 | \xi_k \mathbf{L}_{ik} \delta_k | \Psi_n \rangle \langle \Psi_n | \xi_k \mathbf{L}_{ij} \delta_j | \Psi_0 \rangle}{E_n - E_0} = g_e + \Delta g \dots \quad (1.6)$$

where ξ_k is spin-orbit coupling constant of participating atoms, \mathbf{L} is the angular momentum operator, and $E_n - E_0$ is the difference between the energy of the singly occupied molecular orbital (E_0) and the other completely occupied or unoccupied molecular orbitals (E_n). Since the energy differences are in the denominator in the equation, only neighbouring levels need to be considered as contributing significantly to Δg . However, there are two alternatives regarding the sign of $E_n - E_0$ as shown below



For dominating $E_n < E_o$ (case **A**), g becomes larger than $g_e = 2.0023$, while for dominating $E_n > E_o$ (case **B**), g decreases relative to g_e . Ligand centered radical species typically exhibit very sharp and narrow EPR lines (natural line width < 0.04 mT), well resolved spectra, a signal at room temperature and a relatively small g factor anisotropy ($\Delta g \leq \pm 0.02$) due to very small spin-orbit coupling constants for light atoms (C, N, H, O etc.).^{32a} On the other hand, the participation of metal center in singly molecular orbital (SOMO) can be approximately measured by the observation of a broad EPR signal, a characteristic g value (> 2) and an especially large g anisotropy $\Delta g = g_1 - g_3$.^{32b,c} The anisotropy in g value arises from large spin-orbit coupling constants (ξ) for heavy transition metals like Ru or Os. The large spin-orbit coupling results in rapid relaxation of paramagnetic heavy metal ion, such as Ru(III) ($\tau_s = 10^{-12} - 10^{-11}$ s) and often causes significant line broadening of the metal centered EPR signal so that EPR signal can be only detected at very low temperature (~ 4 K).

An illustration of the metal-centred and radical-centred spins in dinuclear ruthenium complexes is shown in the Figure 1.2. The EPR spectra of $[\{\text{Ru}(\text{NH}_3)_5\}_2(\mu\text{-dicyd})]^{3+}$ and $[\{\text{Ru}(\text{NH}_3)_5\}_2(\mu\text{-dicyd})]^{5+}$ in DMF solution (Figure 1.2 a-b) are characterized by broad axial signals for Ru(III) ions, with $g_{\perp}, g_{\parallel} = 2.421, 2.003$ and $g_{\perp}, g_{\parallel} = 2.291, 1.770$, respectively, confirming the metal-centred mixed-valence configurations, $\text{Ru(II)-R}_2\text{R}_2'\text{dicyd}^{2-}\text{-Ru(III)}$ and $\text{Ru(III)-R}_2\text{R}_2'\text{dicyd}^{2-}\text{-Ru(IV)}$, respectively.⁵ On the other hand, the EPR spectrum of $[\{\text{Ru}(\text{tpy})(\text{thd})\}_2(\mu\text{-dicyd})]^+$ (Figure 1.2 c, top) is characterized by a sharp isotropic signal with $g = 2.02$, confirming the valence configuration, $\text{Ru(II)-dicyd}^{\bullet-}\text{-Ru(II)}$, for this radical complex.⁶

Like dinuclear pentaammineruthenium complexes, EPR spectroscopy also confirmed Ru(III)-centred spin density distribution in mononuclear $[\text{Ru}(\text{NH}_3)_5(\text{R-pcyd})]^{2+}$ complexes.⁸ The EPR spectra of these mononuclear complexes were also characterized by broad and axial signals for Ru(III) ions, with anisotropic g values

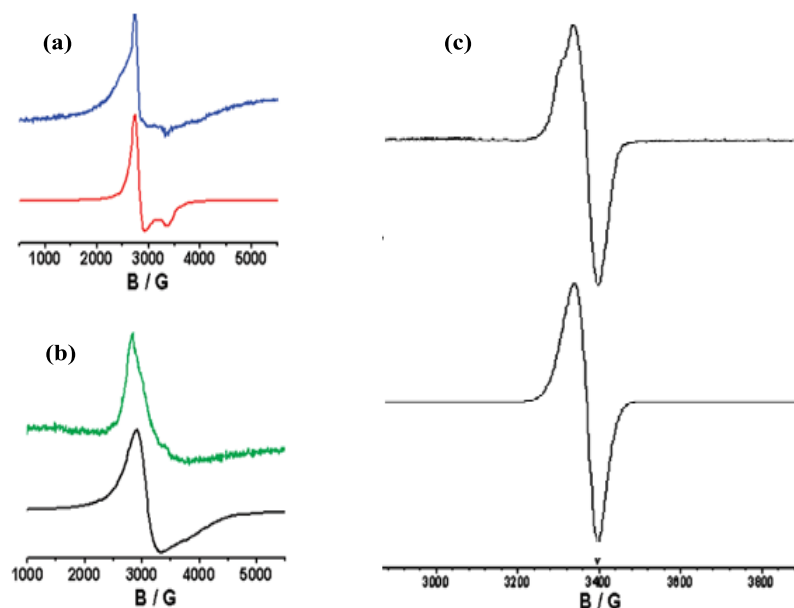


Figure 1.2: EPR spectra of (a) $[\{\text{Ru}(\text{NH}_3)_5\}_2(\mu\text{-dicyd})]^{3+}$ experiment (blue lines) and simulated (red lines), (b) $[\{\text{Ru}(\text{NH}_3)_5\}_2(\mu\text{-dicyd})]^{5+}$ experiment (green lines) and simulated (black lines) in DMF at 4 K and (c) $[\{\text{Ru}(\text{tpy})(\text{thd})_5(\mu\text{-dicyd})\}]^+$ experiment (top) and simulated (bottom) in frozen CH_2Cl_2 at 100 K. Adapted from ref. (5,6).

(g_{\perp} , $g_{\parallel} = 2.291\text{-}2.421$, $1.770\text{-}2.003$) that unambiguously established the valence configuration, Ru(III)-(R- $\text{pcyd}^{\cdot-}$), for these complexes.

EPR spectroscopy has been a powerful tool to unambiguously assign the oxidation state distributions in paramagnetic complexes containing non-innocent redox active ligands. However, cost and availability of EPR instrumentation to researchers are

significant disadvantages and some radical complexes can be EPR silent even at very low temperatures. Some delocalized radical complexes are EPR silent due to extensive mixing of metal and ligand based frontier orbitals that results in significant line broadening even at liquid helium temperature.^{32d} In addition, EPR spectroscopy is not useful for the assignment of closed-shell valence structures (all paired electrons, diamagnetic) as well as open-shell triplet structures with antiferromagnetically coupled odd electrons.^{32e}

Paramagnetic ¹H NMR Spectroscopy

Paramagnetic ¹H NMR spectroscopy can provide an estimate of spin density distribution in transition metal complexes of redox active ligands and thereby provide insight into the orbital parentage of a SOMO.^{5,8}

In a paramagnetic molecule, the interaction or coupling of magnetic nuclei with unpaired electrons gives rise to a chemical shift contribution in the ¹H NMR spectrum, the magnitude of the shift may be anisotropic depending on the molecule's orientation with respect to the external magnetic field. In solution, rapid molecular rotation results in an average value of the shift anisotropy, consequently, giving rise to an isotropic shift. This isotropic shift (δ_{iso}) can be determined experimentally by measuring the difference in shift of a given atom in a paramagnetic compound (δ_{obs}) and that of the same atom in an analogous diamagnetic compound (δ_{dia}), as in Eq. 1.7.

$$\delta_{\text{iso}} = \delta_{\text{obs}} - \delta_{\text{dia}} \quad (1.7)$$

The interaction between magnetic nuclei and unpaired electrons giving rise to molecular paramagnetism can be formally divided into two contributions³³: i) through-bond contact shift and ii) through-space pseudocontact or dipolar shift.

$$\delta_{\text{iso}} = \delta_{\text{con}} - \delta_{\text{dip}} \quad (1.8)$$

The contact shift results from the presence of spin density at the resonating nucleus, and as such, the magnitude of the shift is proportional to the amount of spin density at the nucleus. For paramagnetic transition metal complexes, unpaired spin density originating in metal orbitals can be transferred onto the ligand by ‘direct delocalization’ mechanism via both σ and π bonding interactions (either empty or full π ligand molecular orbitals can be involved in the latter). A nucleus can also feel the spin density indirectly via ‘spin polarization mechanism’ *i.e.*, unpaired electron density is induced on the resonating nucleus via spin polarization of unpaired electron on the doubly occupied molecular orbital. For example, unpaired electron density on $p\pi$ orbital on carbon atom of phenyl ring can spin polarize C-H σ -bonding electrons and thereby induce spin density on both carbon and H nuclei. The contact shift is scalar in nature as it is independent of molecular rotation. The spin-only expression commonly used to obtain the contact shift term from the isotropic NMR shift is given by Eq. 1.9 in SI units.^{33a,b}

$$\delta_{\text{con}} = A_c \frac{g\mu_B S(S+1)}{g_N \mu_N 3kT} \quad (1.9)$$

where A_c is the contact hyperfine coupling constant (in Joules, J), g is the average g value in solution, g_N is the nuclear g -factor, μ_B and μ_N are electron and nuclear Bohr magneton respectively. By convention, a positive δ_{con} value and hence a *downfield* shift in the

resonance of the nucleus in question favors dominant direct delocalization mechanism. Conversely, a negative δ_{con} value and hence an *upfield* shift in the resonance of the nucleus in question favors a dominant spin polarization mechanism, whereby spin density is induced in the resonating nucleus.

The pseudocontact shift (or dipolar shift) is the result of a through-space non-exchange coupling interaction between the nuclear magnetic moment and the electron magnetic moments, that result from spin density at points all over the molecule (except that at the resonating nucleus). It is customary to further divide the pseudocontact interaction into metal-centered and ligand-centered terms. The former considers the unpaired electrons to be localized on the metal center while the latter considers the unpaired electron density to be delocalized on the ligand. Based on the metal-centered term, where unpaired electrons are assumed to be localized only on the metal ion, a point dipole model leads to an expression for evaluating the pseudocontact contribution to the isotropic shift. For an axially symmetric system, the spin-only expression for the pseudocontact shift term is given by Eq. 1.10.^{33a,b}

$$\delta_{\text{dip}} = \frac{\mu_{\text{B}}^2 S(S+1)}{9kT} \times \frac{(3\cos^2\theta - 1)}{r^3} \times (g_{\parallel}^2 - g_{\perp}^2) \quad (1.10)$$

where θ is the angle between the principal symmetry axis of the complex and the vector between the metal ion center and nucleus whose NMR is being observed, r is the distance between the metal ion and the nucleus, g_{\parallel} and g_{\perp} represent the g anisotropy (determined by EPR spectroscopy) of the system in the direction parallel and perpendicular, respectively, to the principle symmetry axis of the complex, and the remaining terms have been previously defined. Eq. 1.10 suggests that the magnitude of a pseudocontact

shift depends upon the magnitudes of the geometric factor (θ), the g anisotropy term and the distance of the nucleus in question from the metal (express as $1/r^3$).

If the contact contribution (δ_{con}) dominates the isotropic shift or if the pseudocontact shift (δ_{dip}) has been factored out, the contact hyperfine coupling constant A_c can be obtained via Eq. 1.9. As previously mentioned, the presence of spin density at the resonating nucleus arises from a direct delocalization and spin polarization mechanisms, contributions from which can be calculated through a molecular orbital treatment. The direct delocalization contribution to hyperfine coupling, (A_d) can be obtained by the Eq. 1.11. ^{33a,b}

$$\frac{A_d}{h} = \frac{K\rho}{2S} \quad (1.11)$$

where K is the isotropic hyperfine coupling due to a full electron on the atom (estimated as 1420 MHz), and $\rho/2S$ is the spin density at the nucleus in question normalized to one electron. The spin polarization contribution to hyperfine coupling (A_p), that is, when an unpaired electron on the $p\pi$ orbital on the carbon atom induces spin density on the same atom as well as on other atoms σ -bonded to the carbon nucleus in question, the Eq. 1.11 takes the form: ^{33a,b}

$$\frac{A_p}{h} = \frac{Q\rho_c^\pi}{2S} \quad (1.12)$$

where Q is the proportionality constant (estimated as -70 MHz)^{33b} and ρ_c^π is the π -spin density on the carbon atom.

Alternatively, the π -spin density on the carbon atom can be obtained, from the contact shift contribution to the observed isotropic shifts of protons that experience induced spin density via spin polarization of unpaired electron in $p\pi$ orbital of the carbon atom on the σ (C-H) bond, by using Eq. 1.13, through Eq. 1.9 and 1.12:

$$\rho_c^\pi = \frac{\delta_{con}}{Q \times h} \times \frac{g_N \mu_N 3kT}{g \mu_B S(S+1)} \quad (1.13)$$

The induced spin density on the σ -bonded H atom is equal in magnitude but of opposite sign to ρ_c^π .

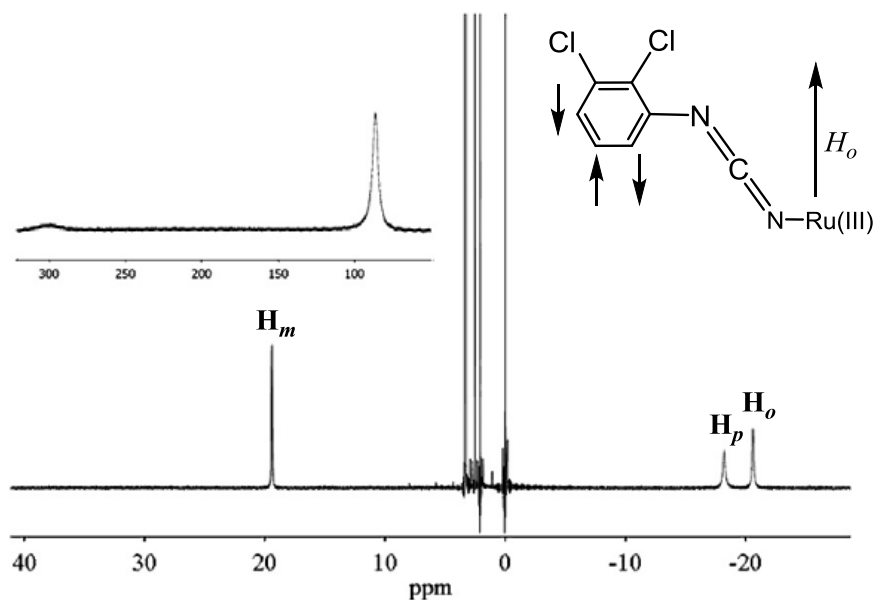


Figure 1.3: ^1H NMR spectrum of $[\text{Ru}(\text{NH}_3)_5(2,3\text{-Cl}_2\text{pcyd})]^+$ in $\text{DMSO-}d_6$ showing phenyl proton (*ortho*, *meta*, *para*) resonances ligand in the region between 20 and -25 ppm. The insert shows the *cis* and *trans* ammine region from 50 to 320 ppm. The four strong peaks from 4 to 0 ppm are assigned to water, DMSO, acetone and TMS, respectively. The arrows show the alignment of Ru(III) spin with that of an external magnetic field (H_o) and the resultant phenyl hydrogen atom spin moments. Adapted from ref. (8).

Spin distributions in mononuclear Fe(III) and Ru(III)arylacetylide complexes have been characterized by ^1H NMR spectroscopy to derive spin densities on carbon atoms.⁴ Recently, seven mononuclear $[\text{Ru}(\text{NH}_3)_5(\text{R-pcyd})]^{2+}$ and four dinuclear $[\{\text{Ru}(\text{NH}_3)_5\}_2(\text{R}_2\text{R}_2'\text{dicyd})]^{4+}$ where R-pcyd^- = substituted phenylcyanamide monoanion and $\text{R}_2\text{R}_2'\text{dicyd}^{2-}$ = substituted 1,4-dicyanamidebenzene dianion, were characterized by paramagnetic ^1H NMR spectroscopy and spin density distributions were determined.^{5,8} In these complexes, the spin density on the Ru(III) ion is π -delocalized into the phenyl ring carbon on the phenylcyanamide ligands and its sign alternate as a consequence of the spin polarization effect of unpaired electron on the doubly occupied σ (C-H) bonding electrons, which resulted in an *upfield* shifts for *ortho* and *para* protons and *downfield* shifts for *meta* protons, as shown in the Figure 1.3 for mononuclear $[\text{Ru}(\text{NH}_3)_5(\text{R-pcyd})]^{2+}$ complexes. Dipolar contributions of isotropic chemical shifts were estimated from the EPR data, using Eq. 1.10 and factored out using Eq. 1.8 to obtain the contact shift contribution to the isotropic shift, which gave estimates of π -spin densities on phenyl ring carbons by the Eq. 1.13. Calculated spin densities on phenyl ring carbons were only 0.55% -1.03 %, which were in good agreement with the EPR data and established the Ru(III)-centred spin in $[\text{Ru}(\text{NH}_3)_5(\text{R-pcyd})]^{2+}$ complexes. Similar calculations on dinuclear $[\{\text{Ru}(\text{NH}_3)_5\}_2(\text{R}_2\text{R}_2'\text{dicyd})]^{4+}$ complexes gave about 1.9 % π -spin density on the phenyl carbons of $\text{R}_2\text{R}_2'\text{dicyd}^{2-}$ ligands, confirming the valence configuration, Ru(III)- $\text{R}_2\text{R}_2'\text{dicyd}^{2-}$ -Ru(III), of these complexes.

Although paramagnetic ^1H NMR is a powerful physical method for estimating spin density distribution in complexes with redox-active ligands, quantitative estimates of spin densities are only possible if EPR data are available so that the dipolar contributions

can be factored out from the observed isotropic shifts. Only in specific cases, it is possible to factor out or ignore the dipolar contributions. In addition, due to large spin moment of unpaired electron leading to a rapid nuclear relaxation, paramagnetic NMR spectra are characterized by very broad and weak signals distributed unusually in a wide chemical shift range, often outside the normal (0-15 ppm) range of proton shifts for most organic compounds, limiting their use for the characterization purpose.^{33a,b}

Vibrational Spectroscopy

Vibrational spectroscopy (IR, Raman) has been very successful in identifying and characterizing species $O_2^{0/\bullet-/2-}$, $TCNE^{0/\bullet-/2-}$ as well as bpy and quinones in various oxidation states in their transition metal complexes.^{1,4} Typically, the formation of anion radicals results in lengthening of multiple bonds in some reducible ligands, O_2 (O=O), TCNE (C=C, C=N) or in quinones (C=C, C=O), and thereby reducing corresponding stretching frequencies with respect to those in the neutral forms. On the other hand, some single bonds such as the one connecting the pyridine rings on bipyridine are shortened upon reduction and exhibit a high frequency shift in the corresponding vibrations. A very useful experimental extension of this correlation is Time-Resolved-Resonance-Raman spectroscopy, which has allowed the anion radical ligand formed in MLCT excited states to be characterized.^{32a}

IR spectroelectrochemical studies have been successfully used to assign the oxidation state of ruthenium in Ru-phenylcyanamide complexes.^{18,34-36} In a previous study, IR spectroelectrochemical reduction of mononuclear *mer*- $[Ru(NH_3)_3(bpy)(2,3-Cl_2pcyd)]^{2+}$ and $[Ru(NH_3)_5(2,3,5,6-Cl_4pcyd)]^{2+}$ complexes (Figure 1.4), resulted in a high frequency shift of the $\nu(NCN)$ band of the coordinated phenylcyanamide ligand upon

change in oxidation state of ruthenium from Ru(III) to Ru(II).¹⁸ Similar high frequency shift in $\nu(\text{NCN})$ band was observed upon single electron reduction of dinuclear $[\{\text{Ru}(\text{NH}_3)_5\}_2(\mu\text{-R}_2\text{R}_2'\text{dicyd})]^{4+}$ complexes (where $\text{R}_2\text{R}_2'\text{dicyd}$ = substituted 1,4-dicyanamide benzene dianion), forming the mixed-valence species Ru(II)-dicyd²⁻-Ru(III). The observed high frequency shift in $\nu(\text{NCN})$ band has been attributed to a shift in the

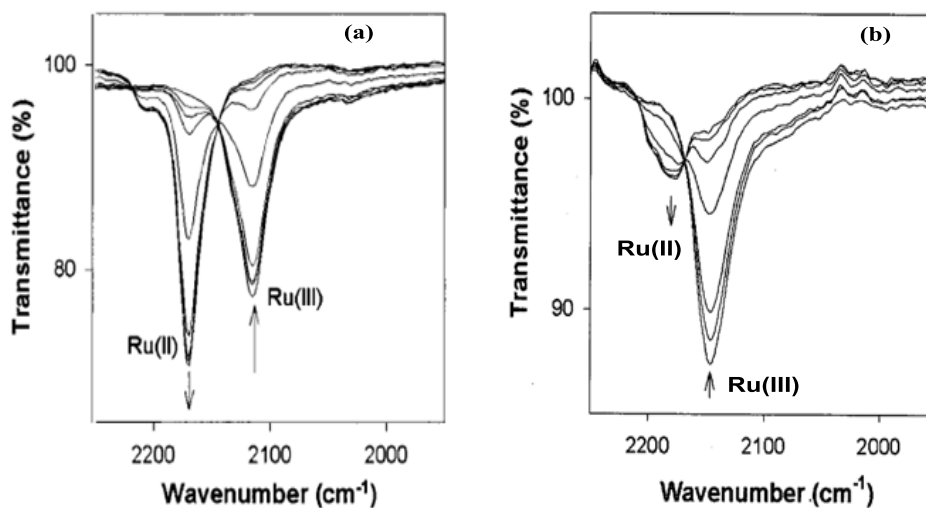
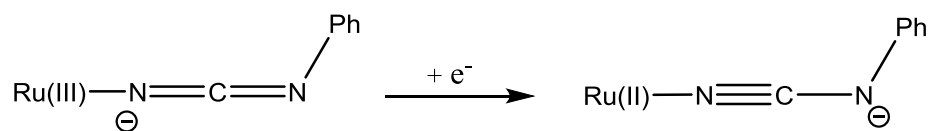


Figure 1.4: IR spectra showing the reduction of Ru(III) complexes, (a) *mer*- $[\text{Ru}(\text{NH}_3)_3(\text{bpy})(2,3\text{-Cl}_2\text{pcyd})]^{2+}$ and (b) $[\text{Ru}(\text{NH}_3)_5(2,3,5,6\text{-Cl}_4\text{pcyd})]^{2+}$ in nitromethane, to the fully reduced Ru(II) complexes. Adapted from ref. (18).

resonance form of the cyanamide group with the oxidation state of ruthenium, as shown below.



Combined EPR, ¹H NMR spectroscopies supported by DFT calculations of these complexes unambiguously established the mixed-valence state, Ru(II)-dicyd²⁻-Ru(III), of these complexes.⁵ These results provided strong support for using IR

spectroelectrochemistry as a powerful diagnostic tool for the assignment of redox-active sites in dinuclear $[\{\text{Ru}(\text{tpy})(\text{bpy})\}_2(\mu\text{-R}_2\text{R}_2'\text{adpc})]^{3+}$ and $[\{\text{Ru}(\text{tpy})(\text{bpy})\}_2(\mu\text{-R}_2\text{R}_2'\text{dicyd})]^{3+}$ complexes studied in the present research work.³⁶ In addition to assignment of Ru(III)/Ru(II) states, IR spectroscopic techniques can also be used to test the localized/delocalized character of the mixed-valence complexes, as its time scale (10^{-13} s) gives an instantaneous view of the state of a fluxional molecule.

UV-vis-NIR Spectroscopy

UV-visible-NIR spectroelectrochemical techniques have been traditionally used to characterize the mixed-valence properties of dinuclear complexes with redox-active ligands. A conventional metal-centred mixed-valence system is characterized by the appearance of a low energy NIR band. On the basis of band position, intensity and shape, this low energy NIR band is traditionally assigned to the metal-to-metal intervalence charge transfer (MMCT) transitions. For example, the electrochemical reduction of $[\{\text{Ru}(\text{NH}_3)_5\}_2(\mu\text{-R}_2\text{R}_2'\text{dicyd})]^{4+}$ in acetonitrile, forming the mixed-valence state $[\{\text{Ru}(\text{NH}_3)_5\}_2(\mu\text{-R}_2\text{R}_2'\text{dicyd})]^{3+}$, resulted in a gradual decrease in intensity of the cyanamide-to-Ru(III) LMCT band at 1100 nm with the development of an MMCT (or IT band in literature) band at 1200-1500 nm (Figure 1.5 (b)). The appearance of a NIR band is frequently taken as a sufficient and convincing evidence for a metal-centred mixed-valence situation. However, care should be taken before making such an assignment for complexes with non-innocent bridging ligand because many radical complexes exhibit absorption features of variable intensity in the near-infrared (NIR) region, owing to low-lying intra-ligand or charge-transfer transitions, and such absorptions can be easily mistaken for intervalence charge transfer bands.^{32a,37} An unambiguous assignment

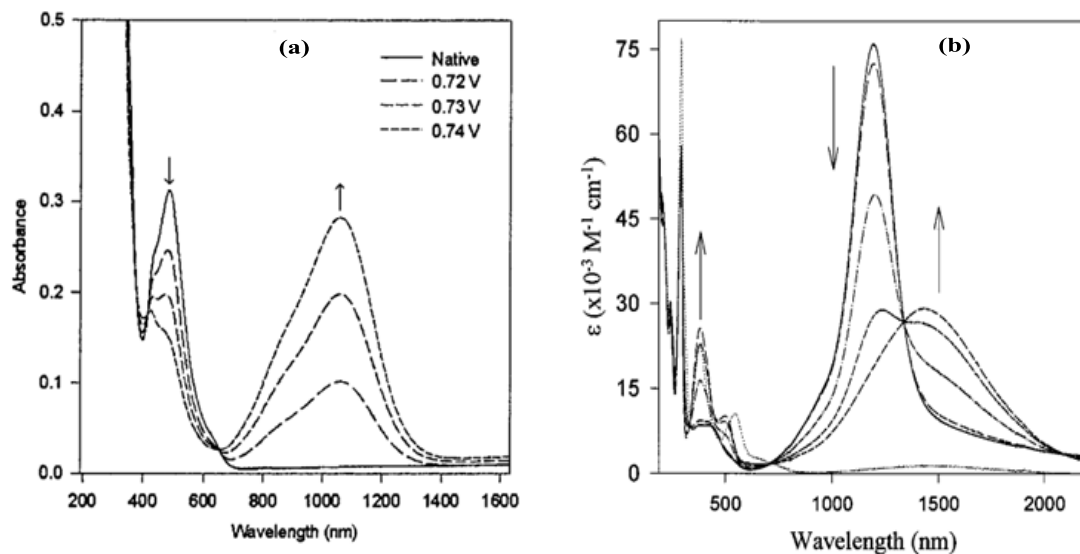


Figure 1.5: Optically transparent thin-layer electrode (OTTLE) cell electronic absorption spectra of (a) $[\text{Ru}(\text{tpy})(\text{bpy})(2,3,4,5\text{-Cl}_4\text{pcyd})]^+$ forming $[\text{Ru}(\text{tpy})(\text{bpy})(2,3,4,5\text{-Cl}_4\text{pcyd})]^{2+}$ and (b) $\text{mer,mer-}[\{\text{Ru}(\text{NH}_3)_3(\text{bpy})\}_2(\mu\text{-Cl}_2\text{dicyd})]^{4+}$ forming mixed-valence $\text{Ru}^{\text{III}} - \text{Ru}^{\text{II}}$ complex $\text{mer,mer-}[\{\text{Ru}(\text{NH}_3)_3(\text{bpy})\}_2(\mu\text{-Cl}_2\text{dicyd})]^{3+}$ under anodic and cathodic potentials respectively. Adapted from ref. (14,19).

of the NIR band is only possible if data from other spectroscopic techniques such as EPR spectroscopy are available. For example, the anionic complex $[\{\text{Ru}(\text{acac})_2\}_2(\mu\text{-L})]^-$ where $\text{L} = 3,3',4,4'\text{-tetramino-}3,3'\text{-}4,4'\text{-tetrahydrobiphenyl}$, is a radical species, $\text{Ru}(\text{II})\text{-L}^{\bullet}\text{-Ru}(\text{II})$, with the reduced bridging ligand, whereas, the cationic form of the complex, $[\{\text{Ru}(\text{acac})_2\}_2(\mu\text{-L})]^+$, is a mixed-valent species, $\{\text{Ru}(\text{III})\text{-L-Ru}(\text{II}) \leftrightarrow \text{Ru}(\text{IV})\text{-BL}^{2-}\text{-Ru}(\text{III})\}$.³⁷ Both intermediates exhibit NIR absorption bands (2160 and 1570 nm, respectively), however, EPR spectroscopy clearly shows the difference with isotropic $g = 2.003$ for the anion complex and $g_{\perp} = 2.197$ and $g_{\parallel} = 1.922$ for the cation complex.

Provided the mixed-valence description of dinuclear complexes are established by other physical methods, the MMCT band properties may provide more insight into the extent of metal-metal coupling (H_{MM}). According Hush model for weakly coupled (Class

I) mixed-valence system, the IT band properties can be related to the magnitude of the metal-metal coupling $H_{MM'}$ by the Eq. 1.14.^{38a}

$$H_{MM'} = \frac{303(E_{MMCT} \times f)^{1/2}}{r} \quad (1.14)$$

where r is the transition dipole moment length in Å, E_{MMCT} is the MMCT band energy in cm^{-1} at ϵ_{max} and f is the oscillator strength of the MMCT band. The oscillator strength, f , of the MMCT band can be calculated from experimental data, assuming Gaussian band shape, by the Eq.1.15 a.^{38a}

$$f = 4.61 \times 10^{-9} \epsilon_{\text{max}} \Delta\nu_{1/2} \quad (1.15 \text{ a})$$

where ϵ_{max} represents the maximum extinction coefficient in $\text{M}^{-1}\text{cm}^{-1}$ and $\Delta\nu_{1/2}$ represents the bandwidth at half-peak height in cm^{-1} .

The Hush model can be used to predict the MMCT band width according to the Eq. 1.16.^{38a}

$$\Delta\nu_{1/2} = (2310\nu_{\text{max}}) \quad (1.16)$$

where ν_{max} is the MMCT energy in cm^{-1} . Given success at predicting bandwidths for weakly coupled systems, the Hush model was widely accepted. Creutz, Newton and Sutin (CNS) revisited the Eq.1.14 and showed that it can be used to calculate metal-ligand coupling elements (H_{LM}) for any donor-acceptor system, provided overlap may be neglected, and the charge transfer dipole moment lies along the donor-acceptor bonding axis.^{38b} In practice, metal-ligand coupling elements (H_{LM}) could then be determined from Eq. 1.15 by replacing MMCT spectral data with the corresponding metal-to-ligand or

ligand-to-metal charge transfer spectral data. According to the CNS model, the metal-ligand coupling element for Ru(III)-cyanamide chromophore can be then expressed by Eq. 1.17.¹⁷

$$H_{LM} = \frac{303(E_{LMCT} \times f)^{1/2}}{r} \quad (1.17)$$

where, H_{LM} is Ru(III)-cyanamide coupling element expressed in cm^{-1} , E_{LMCT} is the energy of the LMCT transition in cm^{-1} , r is the transition dipole moment length in \AA and f is the oscillator strength of cyanamide-to-Ru(III) LMCT band. The oscillator strength (f) of the cyanamide-to Ru(III) LMCT band is therefore a measure of the extent of π -coupling between Ru(III)d π and the π -HOMO of the cyanamide ligand. While Hush model is successful in predicting the spectral behaviour of weakly coupled system, the CNS model has had success with more strongly coupled Class II systems.¹⁷

X-ray Crystallography

X-ray crystallography often assists in elucidating oxidation state distribution within a redox-active metal-ligand system by the observation of the variation in specific M-L, C-C and C-E bond distances and metal-ligand bond angles. For example, the redox-transformations NIL^{Ox} -to- NIL^{\bullet} -to- NIL^{Red} for dioxolene-type ligands (NIL) are accompanied by a decrease in the average C-C bond lengths from 1.48 \AA to 1.42 \AA and increase in the C-O bond lengths from 1.22 \AA to 1.34 \AA .^{2a} It has been observed that, in mononuclear and dinuclear ruthenium-phenylcyanamide complexes, the redox transformation Ru(II)→ Ru(III) is accompanied by a decrease in Ru-N(cyanamide) bond lengths from 2.04-2.09 \AA to 1.94-1.98 \AA and the attainment of approximate linearity of

Ru-NCN bond (171-175°) from the bent structure (164-169°).¹⁰⁻²⁰ However, X-ray crystallography data should not be used as a sole method for characterizing the oxidation states Ru(III) or Ru(II), it can only provide supporting evidence to an assignment based on other physical techniques.

Theoretical Calculations

Quantum mechanical calculations may provide insight into oxidation state distribution in complexes containing redox-active ligands, often as supporting evidence of experimental results, or indirectly about electronic structure when other experimental methods have not provided unambiguous assignment of oxidation states.

In open-shell cases, EPR and ¹H NMR spectroscopy has often been used to estimate the spin density distribution from the experimental data and to subsequently assign the most appropriate valence description in complexes containing redox-active ligands. Quantum chemical calculations provide independent access to EPR and NMR parameters, and to charge and spin density distributions. As spin polarization and spin delocalization tend to be pronounced in transition metal system, density functional calculations (DFT) have provided valuable insights into the electronic structure and oxidation states.^{32e,39} The DFT method is designed to deal with the total charge density and is well-suited for spin density analysis of transition metal complexes in comparison to other post-Hartree-Fock spin density calculations.

In a recent study, DFT calculations on [Ru(Tp)(dppe)(R-pcyd)]⁺, where dppe = ethylenebis(diphenylphosphine), Tp⁻ = hydrotris(pyrazol-1-yl)borate, R-pcyd = substituted phenylcyanamide ligands, demonstrated a variation in the non-innocent behaviour of phenylcyanamide ligands, as a function of their donor strengths.⁹

dinuclear $[\{\text{Ru}(\text{NH}_3)_5\}(\mu\text{-dicyd})]^{3+}$ unambiguously established Ru(III)-centred spin density,^{5,8} gas-phase DFT calculations showed spin density mostly located on the pcyd and dicyd ligand (> 90%) (Figure 1.6 A (i) and 1.6 B (i)). Implicit solvent calculations at the PCM (Polarizable Continuum Model) level shifted the spin density towards Ru ion from 8% to 48 % in the mononuclear complex $[\text{Ru}(\text{NH}_3)_5(\text{pcyd})]^{2+}$ (Figure 1.6 A (ii)). On the other hand, implicit solvent calculations only slightly perturbed the spin distribution in the dinuclear complex (Figure 1.6 B (ii)). A much greater effect (45 % spin density on Ru) was obtained using an explicit electrostatic model in which 10 negative and 4 positive point charges were placed in the hydrogen bonding proximity (2.0 Å) to ammine ligands and the cyanamide groups, respectively, to mimic the solvent-solute interactions of the complex with polar solvents (Figure 1.6 B (iii)).

1.3 Aromatic Cyanamide Ligands

Research on aromatic cyanamide ligands or in general, phenylcyanamide ligands can be dated back to early 1970's, however, it was not late 1980's that the coordination chemistry of phenylcyanamide ligands and its substituted derivatives received much attention in scientific community. The Crutchley group has been exploring the coordination chemistry of aromatic mono and dicyanamide ligands in families of mononuclear and dinuclear complexes of Ru, Fe, Cu, Pt, Pd for the last 30 years. By purposeful tuning of the electronic nature of both metal and phenylcyanamide ligands via inner-sphere (σ and π donor/acceptor properties of ancillary ligands) and outer-sphere coordination (donor-acceptor or dielectric properties of solvent) manipulation, the Crutchley group has demonstrated fascinating electro-optic and magnetic properties of mononuclear and dinuclear phenylcyanamide complexes that have potential for

applications in molecular conducting and switching devices, NIR telecommunications, non-linear optical (NLO) materials as well as in magnetic materials.^{8-20,40,41}

1.3.1 The Structure of Phenylcyanamide Ligands

The physical and electronic structures of aromatic mono- and dicyanamide ligands are well-known.⁴¹ Here we provide a brief account of structures of free anionic and coordinated phenylcyanamide ligands used in the present research work (Figure 1.7), in conjugation with their calculated electronic structures.

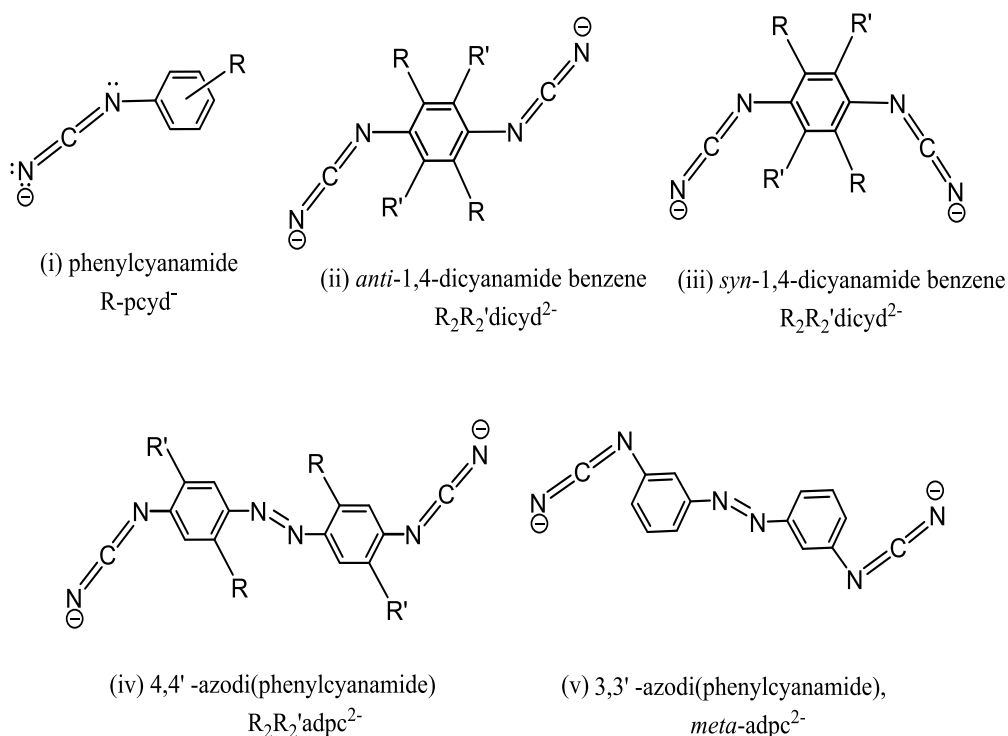
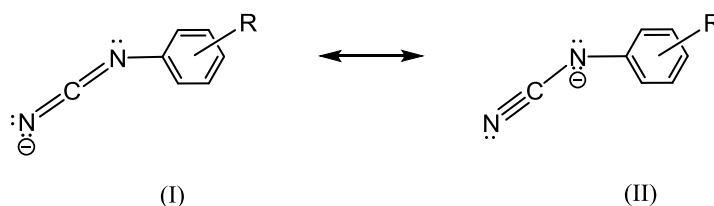


Figure 1.7: Structures of aromatic phenylcyanamide anion ligands. (i) phenylcyanamide monoanion (R-pcyd^-), (ii) *anti*- and *syn*- (iii) 1,4-dicyanamide benzene dianions ($\text{R}_2\text{R}_2'\text{dicyd}^{2-}$), (iv) 4,4'-azodi(phenylcyanamide) dianions ($\text{R}_2\text{R}_2'\text{adpc}^{2-}$), (v) 3,3'-azodi(phenylcyanamide) dianions (*meta*- adpc^{2-}).

The electronic structures of free anionic phenylcyanamide monoanion (pcyd^-) as well as 1,4-dicyanamidebenzene (dicyd^{2-}) and 4,4'-azodi(phenylcyanamide) dianion (adpc^{2-}) have been reported previously, using semi-empirical, HF *ab initio* or single-point DFT calculations.^{20,40b} As a preliminary work, restricted hybrid HF-DFT SCF calculations using the Spartan 14 Parallel suite program and the B3LYP/6-31G* model were performed on these ligands to obtain more precise description of the energy and symmetry of frontier molecular orbitals. Calculated frontier molecular orbitals are shown in the Figure 1.8.

X-ray crystallography of mononuclear Ru-phenylcyanamide complexes have shown that, the cyanamide group is approximately co-planar with the phenyl ring, a configuration which is favored by strong π -interaction between the cyanamide group and the phenyl ring.^{9,11,14} This provides an energetically favorable means by which a metal ion can couple into a conjugated organic π -system. Phenylcyanamide anion ligands are pseudohalides and exhibit both σ and π -donor properties with π -acid metal ions. The anionic ligand is stabilized by two resonance forms¹⁰ as shown below.



It has been observed that the resonance form (I) dominates when cyanamide ligand is bonded to Ru(III), while the resonance form (II) dominates in Ru(II)-phenylcyanamide complexes. Cyanamide anion (NCN^-) exhibits σ -bonding interaction with metal using one of the three lone pairs of electrons via amine or nitrile nitrogens, and there are

examples in the literature of both types of coordination.¹⁰ Transition metal complexes appear to prefer coordination to the nitrile nitrogen. This may be due to the π -back-bonding and donor properties of the nitrile group and the greater steric hindrance that would be experienced upon coordination to the amine of *N*-phenyl-substituted cyanamides. In addition to σ bonding, the anionic phenylcyanamide ligands also exhibit π -donor properties using two non-bonding electron pairs. These two non-bonding electron pairs give rise to two π -symmetry non-bonding molecular orbitals (HOMO and HOMO-3 in the Figure 1.8 a), that span the entire molecule and are of appropriate symmetry and close energy match with the $d\pi$ orbital on ruthenium ions. As seen in the Figure 1.8 a, the HOMO-3 is comprised of bonding interaction between the cyanamide group and the phenyl ring, while this interaction is antibonding in the HOMO, resulting in stabilization of the former by about 2.6 eV relative to the latter. This is in agreement with previous Hückel calculations that showed two non-degenerate non-bonding orbitals (π_{nb1} and π_{nb2}) of phenylcyanamide ligand and is consistent with two cyanamide-to-Ru(III) ligand-to-metal charge transfer transitions observed in Ru-phenylcyanamide complexes.¹⁰⁻¹²

Crystal structures⁴⁰ of unsubstituted and substituted 1,4-dicyanamidebenzene dianion ligands (R_2R_2' dicyd²⁻ where $R_2R_2' = Me_2-, Cl_2-$ and Cl_4-) have shown that both cyanamide groups are approximately co-planar with the phenyl ring, with terminal nitrile nitrogen being no more than 0.31 Å out of the plane of the central phenyl ring. Both cyanamide groups in these ligands are in *anti*-conformations relative to each other in these planar ligands. The planar nature of these anionic 1,4-dicyanamide benzene derivatives allows for continuous π -conjugation between cyanamide groups and the

phenyl ring. However, this is not the case for $\text{Me}_4\text{dicyd}^{2-}$ dianion where the repulsion between *ortho* methyl groups is enough to force the cyanamide group out of the plane while maintaining the *anti*-conformation. In all cases, cyanamide groups are almost linear, with NCN bond angle ranging from 168.8 to 177.5°. The relative *anti*-conformations of cyanamide groups as well as overall planarity of dicyanamide benzene ligand are still retained in their dinuclear ruthenium complexes, as evident from their crystal structures.¹⁵ However, there is an example of dinuclear ruthenium complex, in which both cyanamide groups of unsubstituted dicyd^{2-} ligand adopted the *syn*-conformation while still maintaining the coplanarity of cyanamide groups and the phenyl ring.¹⁶ The planar structure was also observed in the charge-transfer complexes with the stoichiometry $\text{Cu}(\text{DCNQI})_2$ where DCNQI is the two electron oxidation product (dicyd^0) of 1,4-dicyanamide benzene dianion (dicyd^{2-}), which exhibited metallic properties and high conductivity ($5 \times 10^5 \text{ Sm}^{-1}$) at 3.5 K and showed the ability to form π stacks in the solid state.^{40b,c} The one electron oxidation product ($\text{dicyd}^{\bullet-}$) of dicyd^{2-} also maintained the coplanarity of cyanamide groups and the phenyl ring in the silver or sodium salts of the radical anion $\text{dicyd}^{\bullet-}$.^{40d}

The 1,4-dicyanamidebenzene dianion represents a delocalized π -system through donor (NCN⁻)-acceptor (phenyl)-donor (NCN⁻) interactions. As seen in the Figure 1.8 b, both HOMO and HOMO-1 are π -based MOs having -NCN lone pair character together with contribution from the phenyl ring, while the HOMO-3 is localized on the cyanamide groups. On the other hand, LUMO is centred on the phenyl ring without any contribution from the cyanamide groups. It is to be noted that the π -HOMO (3.5 eV) of dicyd^{2-} ligand is significantly higher in energy than that of phenylcyanamide ligand (-0.30 eV), which is

likely to arise from the electron releasing effects of two donor cyanamide groups on the phenyl ring. The DFT calculated HOMO and LUMO orbitals are pictorially equivalent to those reported earlier using Hartree-Fock orbitals, however, the calculated HOMO-LUMO energy gap (4.0 eV) is significantly larger than that obtained in the earlier

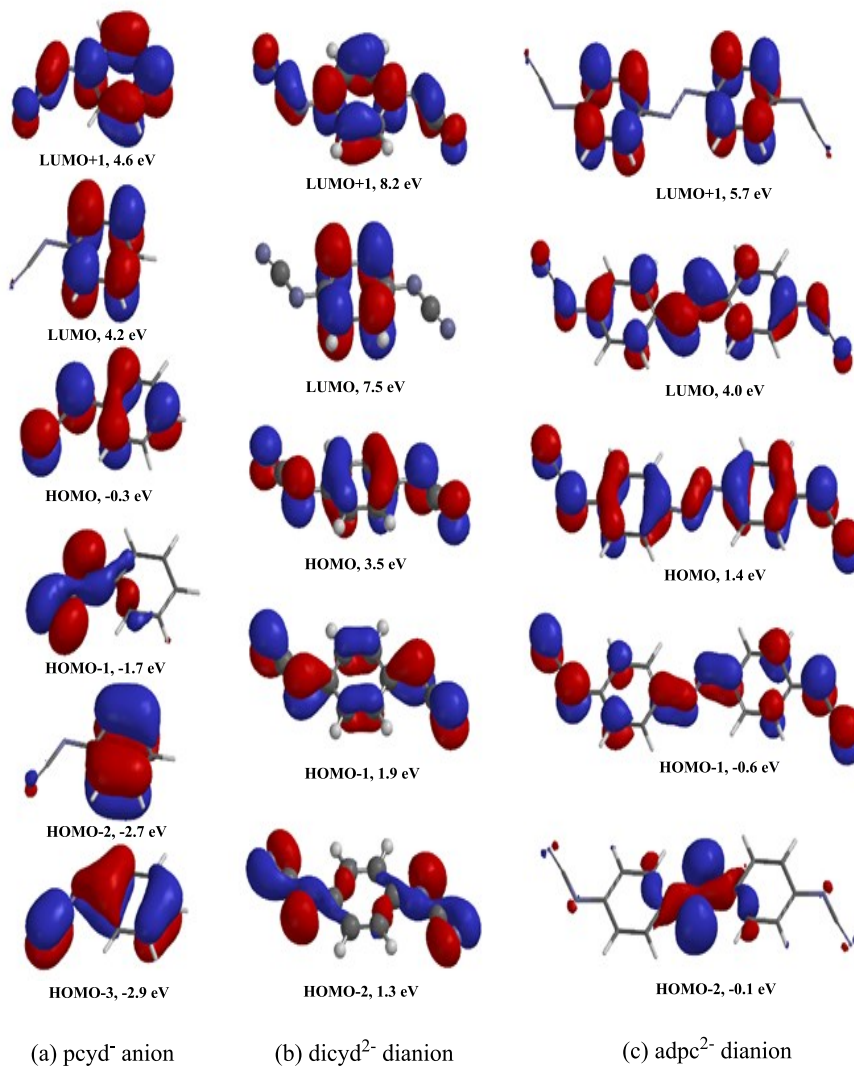


Figure 1.8: Selected frontier molecular orbitals of (a) phenylcyanamide monoanion (b) 1,4-dicyanamidebenzene dianion and (c) 4,4'-azodi(phenylcyanamide) as calculated by gas-phase DFT calculation using B3LYP/6-31G* model.

calculation (HF/6-311G**) using the Spartan 5.01 suite of programs.²⁰ The high energy continuous π -HOMO on the dicyd²⁻ anion are in close energy and symmetry match with the Ru $d\pi$ orbitals and provided an efficient π -pathway for metal-metal coupling in dinuclear mixed-valence complexes of bridging dicyd²⁻ ligand via hole-transfer superexchange mechanism. It is to be noted that the LUMO of the dicyd²⁻ anion is significantly higher in energy than the HOMO and only centered on the phenyl ring, which by symmetry, overlap and energy considerations, excludes the possibility of the electron-transfer metal-metal superexchange via the bridging dicyd²⁻ dianion. Due to presence of high energy filled π -HOMOs, dicyd²⁻ ligands are expected to be easily oxidized to their radical anions. Indeed, cyclic voltammetry determined L^{\bullet}/L^{2-} couples (-0.55 to -0.025 V versus NHE) of R_2R_2' dicyd²⁻ anions.¹⁵ However, incorporation of chloro-substituents stabilizes the π -HOMO significantly; the L^{\bullet}/L^{2-} couples being positively shifted by about 0.53 V for Cl_4 dicyd²⁻ relative to Me_2 dicyd²⁻.

Incorporation of an azo group between two phenylcyanamide moieties, as in 4,4'-azodi(phenylcyanamide) dianion ($adpc^{2-}$), is expected to provide an extended delocalized π -system via strong donor (NCN)-acceptor(azo)-donor(NCN) interactions and allow for metal-metal coupling over longer a metal-metal separation than the dicyd²⁻ anion.²⁰ Two phenyl rings in $adpc^{2-}$ can adopt both *cis* and *trans* configurations relative to the azo group, however, the crystal structure of dinuclear $[\{Ru(tpy)(bpy)\}_2(\mu-adpc)]^{2+}$ complex showed the *trans* conformation and an approximately planar $adpc^{2-}$ bridge, suggesting an effective π -conjugation of phenylcyanamide and the azo groups that span the entire molecule.²⁰ Like other dinuclear ruthenium complexes of bridging 1,4-dicyanamide benzene ligands, both cyanamide groups of the $adpc^{2-}$ adopted an *anti*-

conformation relative to each other in the $[\{\text{Ru}(\text{tpy})(\text{bpy})\}_2(\mu\text{-adpc})]^{2+}$ complex. As seen in the Figure 1. 8(c), both HOMO and HOMO-1 of the adpc^{2-} dianion are π -based continuous MOs having -NCN- nitrogen lone-pair character together with contributions from the phenyl and the azo group. While the azo group exhibits bonding interaction in the HOMO, it is antibonding in the HOMO-1 and in the LUMO. In addition, the HOMO is comprised of antibonding interaction between the phenyl ring and the azo nitrogens and the corresponding bonding interaction is present in the LUMO which is also a π -symmetry molecular orbital and spans the entire molecule. This leads to fully allowed HOMO-to-LUMO $\pi \rightarrow \pi^*$ type transition. Indeed, the HOMO-LUMO energy gap (2.6 eV) compares quite favourably with the energy of the visible absorption band (523 nm, 2.37 eV) of free adpc^{2-} dianion in DMF solution.²⁰ The HOMO-2 and HOMO-3 are mostly localized on the azo and cyanamide groups respectively and are significantly stabilized relative to the HOMO and HOMO-1 orbitals. The calculated frontier orbitals of adpc^{2-} are very similar in their appearance and energies to those calculated by a gas-phase DFT calculation reported previously.²¹ It is to be noted that the calculated HOMO-LUMO energy gap (2.6 eV) of the adpc^{2-} dianion is significantly reduced relative to that of dicyd^{2-} anion (4.0 eV) and unlike the dicyd^{2-} dianion, both HOMO and LUMO of adpc^{2-} dianion span the entire molecule and are of appropriate symmetry to interact with Ru $d\pi$ orbital. Therefore, by symmetry, overlap and energy considerations, both hole- and electron-transfer superexchange are viable for metal-metal coupling in dinuclear ruthenium complexes of bridging adpc^{2-} ligand. It is also notable that the π -HOMO of adpc^{2-} anion (1.4 eV) is significantly stabilized relative to that of the bridging dicyd^{2-} anion (3.5 eV), which is consistent with stabilization by the azo group, indicating greater

stability of adpc^{2-} dianion towards oxidation relative to the dicyd^{2-} anion. The relative stability of adpc^{2-} anion is also reflected in its $\text{L}^{2-}/\text{L}^{\bullet-}$ couple (0.48 V vs NHE), which is positively shifted by about 0.95 V relative to that of the dicyd^{2-} dianion.^{15,20}

1.4 Research Strategy and Goals

This thesis describes a comprehensive study of four families of mononuclear and dinuclear ruthenium complexes in which the redox *ambi-valence* of phenylcyanamide ligands is investigated by a series of electronic perturbations to ruthenium-phenylcyanamide bonds by the (i) σ/π donor/acceptor properties of ancillary ligands, (ii) donor strengths of the phenylcyanamide ligands and (iii) donor properties of solvents.

As mentioned previously, EPR studies by Bonvoisin⁶ *et al* showed that oxidation state of $[\{\text{Ru}(\text{tpy})(\text{thd})\}_2(\mu\text{-dicyd})]^+$ is best described by $\text{Ru}(\text{II})\text{-dicyd}^{\bullet-}\text{-Ru}(\text{II})$. This can be attributed to the stabilization of the $\text{Ru}(\text{III})$ $d\pi$ orbital relative to the π -HOMO of the bridging dicyd^{2-} ligand by the strong π -acceptor properties of the ancillary tpy/thd ligands. These studies suggested that the previously reported $[\{\text{Ru}(\text{tpy})(\text{bpy})\}_2(\mu\text{-dicyd})]^{3+}$ was also a radical-centred complex.⁴² However, the π -HOMO of the bridging ligand can be significantly perturbed by the variation of the donor strength of $\text{R}_2\text{R}_2'\text{dicyd}^{2-}$ ligands via incorporation of electron releasing methyl ($\text{R}_2\text{R}_2' = \text{Me}_2$ -) and withdrawing chloro ($\text{R}_2\text{R}_2' = \text{Cl}_2\text{-}, \text{Cl}_4\text{-}$) substituents and this may lead to a significant variation in the orbital composition of the SOMO. In Chapter 2, four dinuclear $[\{\text{Ru}(\text{ttpy})(\text{bpy})\}_2(\mu\text{-R}_2\text{R}_2'\text{dicyd})]^{2+}$ complexes of bridging $\text{R}_2\text{R}_2'\text{dicyd}^{2-}$ ligands are characterized and both singly and doubly oxidized forms of complexes

$[\{\text{Ru}(\text{tpy})(\text{bpy})\}_2(\mu\text{-R}_2\text{R}_2'\text{dicyd})]^{3+,4+}$ are investigated by EPR and ^1H NMR spectroscopies and IR and vis-NIR spectroelectrochemistry and theory to examine the degree of non-innocent behavior of $\text{R}_2\text{R}_2'\text{dicyd}^{2-}$ ligands.

In a previous study,²⁰ the complex $[\{\text{Ru}(\text{tpy})(\text{bpy})\}_2(\mu\text{-adpc})]^{3+}$ was described as a strongly coupled Class(III) mixed-valence species, $\text{Ru}(\text{II})\text{-adpc}^{2-}\text{-Ru}(\text{III})$, on the basis of a large comproportionation constant ($K_c = 10^{13}$) obtained from the cyclic voltammetry data of the complex, which was further supported by the presence of a fairly intense and broad MMCT band at 1920 nm in DMF. However, a gas-phase DFT calculation by Chisholm²¹ *et al* supported the ligand-centered valence configuration, $\text{Ru}(\text{II})\text{-R}_2\text{R}_2'\text{adpc}^{\bullet}\text{-Ru}(\text{II})$, of $[\{\text{Ru}(\text{tpy})(\text{bpy})\}_2(\mu\text{-adpc})]^{3+}$. Gas-phase DFT calculations are suspect because solvent effects can play an important role particularly with respect to electron density distributions as shown by DFT calculations of $[\{\text{Ru}(\text{NH}_3)_5\}_2(\mu\text{-dicyd})]^{3+,5}$. To investigate the dinuclear ruthenium adpc^{2-} system further, Chapter 3 describes the synthesis of a family of dinuclear $[\{\text{Ru}(\text{tpy})(\text{bpy})\}_2(\mu\text{-R}_2\text{R}_2'\text{adpc})]^{2+}$ complexes in which electron donating or withdrawing substituents on the bridging adpc^{2-} ligand are varied. These complexes were characterized by EPR spectroscopy and IR and vis-NIR spectroelectrochemistry and DFT calculations to examine the redox ambivalence of bridging $\text{R}_2\text{R}_2'\text{adpc}^{2-}$ ligands in both singly and doubly oxidized $[\{\text{Ru}(\text{tpy})(\text{bpy})\}_2(\mu\text{-R}_2\text{R}_2'\text{adpc})]^{3+/4+}$ complexes.

Widespread interest in the development of electronic devices based on molecular systems has concentrated on reversible and robust “photo-switches” for NIR telecommunication devices.⁴⁴ Mixed-valence complexes incorporating a fast “photo-switching” component can be thought of as simple models for these nano devices. In this

regard, ruthenium-polypyridyl sulfoxide complexes have shown efficient switching properties via ultra-fast photo-induced reversible S→O and O→S linkage isomerism of sulfoxide ligands, with a substantial variation of the Ru(III/II) couples in the *S*- and *O*-bound forms of sulfoxide ligands.^{45,46} If this ultra-fast (sub-picosecond) photo-switching component can be introduced into dinuclear mixed-valence complexes of bridging dicyd²⁻ or adpc²⁻ ligands, it could be possible to tune the intensity and energy of their NIR absorption bands by controlling metal-metal coupling via photo-induced fast and reversible S→O and O→S linkage isomerism of sulfoxide ligands. The resulting mixed-valence complex would be an effective NIR “photo-switch” that could turn on/off the transmission of NIR signals. However, before one can create a “photo-switch” mixed-valence complex, it is first necessary to find a mononuclear coordination environment that has the potential in a dinuclear complex to simultaneously express both properties of photoisomerism and mixed-valency. In Chapter 4, six mononuclear [Ru(bpy)₂(R-*pcyd*)(dms(*-S*))] ⁺ complexes of phenylcyanamide (R-*pcyd*⁻) ligands are prepared and investigated for both photo- and redox-induced reversible S→O and O→S linkage isomerism of the dms ligand in solutions as well as in solid polymer films by electronic absorption spectroscopy and cyclic voltammetry. The quantum yields of photo-induced S→O isomerism ($\Phi_{S\rightarrow O}$) and rates of thermal O→S reactions (k_{OS1}) are measured and correlated with the donor property of phenylcyanamide ligands (R-*pcyd*⁻).

Donor-acceptor polymeric materials have found applications in a number of devices such as Mach-Zehnder modulators,⁴⁷ solar energy cells⁴⁸ and polymer spintronics.⁴⁹ For modulator applications, the component donor-acceptor molecules must be neutral so that under the influence of a large potential field, their dipole moments

cause molecules to align in the host polymer and so express non-linear-optical (NLO) properties.^{50,51} In this regard, neutral mixed-valence complexes containing polarizable bridging ligands, for example, dicyd²⁻ or adpc²⁻ are well suited because the charge transfer transition of these molecules can give rise to hyperpolarizability.⁵⁰ In order to understand the electronics involved in mixed-valence systems, one has to first look at the mononuclear complexes which makes up the target system. To this effect, a family of mononuclear neutral complexes *trans*-[Ru(tpy)(R-pcyd)Cl₂] was prepared to model an acceptor moiety of a neutral mixed-valence complex. This provided an opportunity to examine the degree of non-innocence of phenylcyanamide ligand in a coordination sphere of strong π -acceptor tpy ligand and σ/π donor Cl⁻ ligands. In Chapter 5, the degree of non-innocent behavior of phenylcyanamide ligands in *trans*-[Ru(tpy)(R-pcyd)Cl₂] complexes is described as a function of the donor strength of phenylcyanamide ligands and solvents, by combined paramagnetic ¹H NMR, electronic absorption spectroscopy and DFT calculations, and correlated with observed electrochemical and spectroscopic properties of complexes.

1.5 References

1. (a) Kaim, W.; Schwederski, B. *Coord. Chem. Rev.* **2010**, *254*, 1580. (b) Lyons, C. T.; Stack, T. D. P. *Coord. Chem. Rev.* **2012**, *257*, 528.
2. (a) Boyer, J. L.; Rochford, J.; Tsai, W.-T.; Muckerman, J. T.; Fujita, E. *Coord. Chem. Rev.* **2010**, *254*, 309. (b) Lyaskovskyy, V.; de Bruin, B. *ACS Catal.* **2012**, *2*, 270.
3. Marder, S. R.; Kippelen, B.; Jen, A. K.-Y.; Peyghambarian, N. *Nature* **1997**, *388*, 845.
4. (a) Low, P. J., *Coord. Chem. Rev.*, **2013**, *257*,1507. (b) Das, A K; Sarkar, B.; Fiedler, J.; Zalis, S.; Hartenbach, I.; Strobel, S.; Lahiri, G. K.; Kaim, W., *J. Am. Chem. Soc.* **2009**, *131*, 8895. (c) Chakraborty, S.; Laye, R. H.; Paul, R. L.; Gonnade, R. G.; Puranik, V. G.; Ward, M. D.; Lahiri, G. K., *J. Chem. Soc., Dalton Trans.* **2002**, 1172. d) Ward, M. D.; McCleverty, J. A., *J. Chem. Soc., Dalton Trans.* **2002**, 275. (e) Kaim, W. *Inorg. Chem.* **2011**, *50*, 9752. (f) Kaim, W.; Lahiri, G. K. *Angew. Chem. Int. Ed.* **2007**, *46*, 1778. (g) Kaim, W. *Eur. J. Chem.* **2012**, 343.
5. Naklicki, M. L.; Gorelsky, S. I.; Kaim, W.; Sarkar, B.; Crutchley, R. J. *Inorg. Chem.* **2012**, *51* 1400.
6. Fabre, M.; Jaud, J.; Hliwa, M.; Launay, J.-P.; Bonvoisin, J. *Inorg. Chem.* **2006**, *45*, 9332.
7. (a) Potember, R. S.; Poehler, T. O.; Cowan, D. O.; *Appl. Phys. Lett.* **1979**, *34*, 405. (b) Guo, Y.; Langlois, J.-M.; Goddard, W. A. *Science* **1988**, *239*, 896. (c) Zhao, H.; Bazile Jr., M. J.; Dun-bar, *Angew. Chem.* **2003**; *115*, 1045. (d) Zhao,

- H.; Bazile Jr., M. J.; Dun-bar, *Angew. Chem. Int. Ed.* **2003**; *42*, 1015. (e) Harris, T. D.; Coulon, C.; Long, J. R. *J. Am. Chem. Soc.* **2011**, *133*, 123. (f) Geoffroy, G. L.; Wrighton, M. S. *Organometallic Photochemistry*; Academic Press: New York, **1979**.
8. Mahmoud, L.; Gorelsky, S. I.; Kaim, W.; Sarkar, B.; Crutchley, R. J. *Inorg. Chim. Acta* **2011**, *374*, 147.
 9. Harb, C.; Kravstov, P.; Choudhuri, M.; Sirianni, E. R.; Yap, G. P. A.; Lever, A. B. P.; Crutchley, R. J. *Inorg. Chem.* **2013**, *52*, 1621.
 10. Naklicki, M.; Crutchley, R. J.; *Inorg. Chem.* **1989**, *28*, 1955.
 11. Crutchley, R. J.; McCaw, K.; Lee, F. L.; Gabe, J. E. *Inorg. Chem.* **1990**, *29*, 2576.
 12. Saleh, A. A.; Crutchley, R. J. *Inorg. Chem.* **1990**, *29*, 2123.
 13. Evans, C. E. B.; Ducharme, D.; Naklicki, M.; Crutchley, R. J.; *Inorg. Chem.* **1995**, *34*, 1350.
 14. Mosher, P. J.; Yap, G. P. A.; Crutchley, R. J.; *Inorg. Chem.* **2001**, *40*, 550.
 15. (a) Aquino, M. A. S.; Lee, F. L.; Gabe, E. J.; Bensimon, C.; Greedan, J. E.; Crutchley, R. J. *J. Am. Chem. Soc.* **1992**, *114*, 5130. (b) Naklicki, M.; Crutchley, R. J. *Inorg. Chim. Acta* **1994**, *225*, 123.
 16. Rezvani, A. R.; Bensimon, C.; Crompton, B.; Reber, C.; Greedan, J. E.; Kondratiev, V. V.; Crutchley, R. J. *Inorg. Chem.* **1997**, *36*, 3322.
 17. Evans, C. E. B.; Naklicki, M. L.; Rezvani, A. R.; White, C. A.; Kondratiev, V. V.; Crutchley, R. J. *J. Am. Chem. Soc.* **1998**, *120*, 13096.
 18. De Rosa, M. C.; White, C. A.; Evans, C. E. B.; Crutchley, R. J. *J. Am. Chem. Soc.* **2001**, *123*, 1396.

19. Evans, C. E. B.; Yap, G. P. A.; Crutchley, R. J. *Inorg. Chem.* **1998**, *37*, 6161.
20. Mosher, P. J.; Yap, G. P. A.; Crutchley, R. J. *Inorg. Chem.* **2001**, *40*, 1189.
21. Chisholm, M. H.; D'Acchioli, J. S.; Hadad, C. M.; Patmore, N. J. *Inorg. Chem.* **2006**, *45*, 11035.
22. Jorgensen, C. K. *Coord. Chem. Rev.* **1966**, *1*, 164.
23. Wanat, A.; Schnepf, T.; Stochel, G.; van Eldik, R.; Bill, E.; Weighardt, K. *Inorg. Chem.* **2002**, *41*, 4.
24. Balzani, V.; Juris, A.; Barigelletti, F.; Campagna, S.; Belser, P.; Von Zelewsky, A. *Coord. Chem. Rev.* **1988**, *84*, 85.
25. Hughes, M. C.; Macero, D. J. *Inorg. Chem.* **1976**, *15*, 2041.
26. (a) Smith, D. A.; Bastanov, A. S.; Costuas, K.; Edge, R.; Apperley, D. C.; Collision, D.; Halet, J.-F.; Howard, J. A. K.; Deyar, P. W. *Angew. Chem.* **2010**, *122*, 7194. (b) Smith, D. A.; Bastanov, A. S.; Costuas, K.; Edge, R.; Apperley, D. C.; Collision, D.; Halet, J.-F.; Howard, J. A. K.; Deyar, P. W. *Angew. Chem. Int. Ed.* **2010**, *49*, 7040.
27. (a) Rall, J.; Wanner, M.; Albrecht, M.; Hornung, F. M.; Kaim, W. *Eur. J. Chem.* **1999**, *5*, 2802. (b) Rall, J.; Waldhor, E.; Schwederski, B.; Schwach, M.; Kohlmann, S.; Kaim, W. *Bioinorganic Chemistry: Transition Metals in Biology and Their Coordination Chemistry*; Trautwein, A. X., Ed.; VCH: Weinheim, Germany, **1997**, p476. (c) Kahn, O.; Prins, R.; Reedijk, J.; Thompson, J. S. *Inorg. Chem.* **1987**, *26*, 3557.
28. Gross, R.; Kaim, W. *Inorg. Chem.* **1987**, *26*, 3596.
29. Remenyi, C.; Kaupp, M. *J. Am. Chem. Soc.* **2005**, *127*, 11399.

30. (a) Krentzien, H.; Taube, H. *J. Am. Chem. Soc.* **1976**, *98*, 6379. (b) Hage, R.; Haasnoot, J. G.; Reedijk, J.; Wang, R.; Vos, J. G. *Inorg. Chem.* **1991**, *30*, 3263. (c) Haga, M.; Matsumara-Inoue, T.; Yamabe, S. *Inorg. Chem.* **1987**, *26*, 4148. (d) Beley, M.; Collin, J.-P.; Louis, R.; Metz, B.; Suavage, J.-P. *J. Am. Chem. Soc.* **1991**, *113*, 8521. (e) Kaim, W.; Kasack, V.; Binder, H.; Roth, E.; Jordanov, J. *Angew. Chem., Int. Ed. Engl.* **1988**, *27*, 1174. (f) Kaim, W.; Kasack, V. *Inorg. Chem.* **1990**, *29*, 4696. (g) Kasack, V.; Kaim, W.; Binder, H.; Jordanov, J.; Roth, E. *Inorg. Chem.* **1995**, *34*, 1924. (h) Jana, R.; Sarkar, B.; Bubrin, D.; Feidler, J.; Kaim, W. *Inorg. Chem. Commun.* **2010**, *13*, 1060.
31. (a) Hartmann, H.; Kaim, W.; Hartenbach, L.; Schleid, T.; Wanner, M.; Fiedler, J. *Angew. Chem.* **2001**, *113*, 2927. (b) Hartmann, H.; Kaim, W.; Wanner, M.; Klein, A.; Frantz, S.; Duboc-Toia, Fiedler, J. *Inorg. Chem.* **2003**, *42*, 7018. (c) Moscherosch, M.; Waldhor, E.; Binder, H.; Kaim, W.; Fiedler, J. *Inorg. Chem.* **1995**, *34*, 4326. (d) Waldhor, E.; Kaim, W.; Lawson, M.; Jordanov, J. *Inorg. Chem.* **1997**, *36*, 3248.
32. (a) Kaim, W. *Coord. Chem. Rev.* **1987**, *76*, 187. (b) Weil, J. A.; Bolton, J. T.; Wertz, J. E. *Electron Paramagnetic Resonance*; Willey: New York, **1994**. (c) Kaim, W.; Kasack, V. *Inorg. Chem.* **1990**, *29*, 4696. (d) Roy, S.; Sarkar, B.; Imrich, H.-G.; Fiedler, J.; Zalis, S.; Jimenez-Aparicio, R.; Urbanos, F. A.; Mobin, S. M.; Lahiri, G. K.; Kaim, W. *Inorg. Chem.* **2012**, *51*, 9273. (e) Remenyi, C.; Kaupp, M. *J. Am. Chem. Soc.* **2005**, *127*, 11399.
33. (a) Drago, R. *Physical Methods for Chemists, Second Ed.*; Surfside Scientific Publishers: Gainesville, **1992**. (b) Bertini, I.; Luchinat, C.; Parigi, G. *Current*

- Methods in Inorganic Chemistry, Solution NMR of Paramagnetic Molecules, Vol.2*; Elsevier, **2001**. (c) Kluiber, R. W.; Horrocks, W. D. *Inorg. Chem.* **1967**, *6*, 430. (d) Bertini, I.; Wilson, L. J. *J. Coord. Chem.* **1971**, *1*, 237. (e) Holm, R. H.; Chakravorty, A.; Dudek, G. O. *J. Am. Chem. Soc.* **1964**, *86*, 379.
34. Al-Noaimi, M.; Crutchley, R. J. *Inorg. Chim. Act.* **2007**, *360*, 3013.
35. Al-Noaimi, M.; Yap, G. P. A.; Crutchley, R. J. *Inorg. Chem.* **2004**, *43*, 1770.
36. Choudhuri, M. M. R.; Kaim, W.; Sarkar, B.; Crutchley, R. J. *Inorg. Chem.* **2013**, *52(19)*, 11060.
37. (a) Heilmann, M.; Frantz, S.; Kaim, W.; Kaim, W.; Fiedler, J. Duboc, C. *Inorg. Chim. Acta* **2006**, *359*, 821. (b) Maji, S.; Sarkar, B.; Patra, S.; Fiedler, J.; Mobin, S. M.; Puranik, V. G.; Kaim, W.; Lahiri, G. K. *Inorg. Chem.* **2006**, *45*, 1316. (c) Patra, S.; Sarkar, B.; Maji, S.; Ghumaan, S.; Fiedler, J.; Zaliz, S.; Kaim, W.; Lahiri, G. K. *Dalton Trans.* **2004**, 750.
38. (a) Hush, N. S. *Prog. Inorg. Chem.*, **1967**, *8*, 391. (b) Creutz, C.; Newton, M. D.; Sutin, N.; *J. Photochem. Photobiol. A: Chem.* **1994**, *82*, 47.
39. (a) Cano, J.; Ruiz, E.; Alvarez, S.; Verdeguer, M. *Comments Inorg. Chem.* **1998**, *20*, 27. (b) Johansson, M. P.; Sundholm, D.; Gerfen, G.; Wikstrom, M. *J. Am. Chem. Soc.* **2002**, *124*, 11771. (c) Ray, K.; Begum, A.; Weyhermueller, T.; Piligkos, S.; Van Slageren, J.; Nees, F.; Wieghardt, K. *J. Am. Chem. Soc.* **2005**, *127*, 4403.
40. (a) Aquino, M. A. S.; Crutchley, R. J.; Lee, F. L.; Gabe, E. J.; Bensimon, C. *Acta Cryst.* **1993**, *C49*, 1543. (b) Aumuller, A.; Erk, P.; Klebe, G.; Hunig, S.; Von Schutz, J. U.; Warner, H.-P. *Angew. Chem. Int. Ed. Engl.* **1986**, *25*, 740, 741. (c)

- Aumuller, A.; Hunig, S. *Justus Liebigs Ann. Chem.* **1986**, *155*, 142. (d) Hünig, H.; Bau, R.; Kemmer, M.; Meixner, H.; Metzenthin, T.; Peter, K.; Sinzger, K.; Gulbis, J. *Eur. J. Org. Chem.* **1998**, 335.
41. (a) Crutchley, R. J. *Coord. Chem. Rev.* **2001**, *125*, 219. (a) Crutchley, R. J. *Comp. Coord. Chem. II* **2003**, *2*, 785.
42. Rezvani, A. R.; Evans, C. E. B.; Crutchley, R. J. *Inorg. Chem.* **1995**, *34*, 4600.
43. Barrier, F.; Camire, N.; Geiger, W. E.; Mueller-Westerhoff, U. T.; Sanders, R. J. *Am. Chem. Soc.* **2002**, *124*, 7263.
44. (a) Irie, M. *Chem. Rev.* **2000**, *100(5)*, 1685. (b) Raymo, F. M.; Tomasulo, M. *Chem.* **2006**, *12(12)*, 3186.
45. Rack, J.J. *Coord. Chem. Rev.* **2009**, *253*, 78.
46. Rack, J., McClure, B.-A. *Eur. J. Inorg. Chem.* **2010**, 3895.
47. Marder, S. R.; Kippelan, B.; Jen, A. K.-Y.; Peyghambarian, N. *Nature* **1997**, 388, 845.
48. Gunes, S.; Neugebauer, H.; Sariciftci, N. S.; *Chem. Rev.* **2007**, *107*, 1324.
49. Yan, L.; Wu, Y.; Hu, B. *ACS Symp. Ser.* **2010**, *1061*, 85.
50. (a) Chemla, D. S., in: J. Zyss (Ed.) *Nonlinear Optical Properties of Organic Materials and Crystals, vols. 1 and 2*; Academic Press: New York, **1987**. (b) Prasad, P. N., Williams, D. J. (Eds.), *Introduction to Nonlinear Optical Effects in Molecules and Polymers*; Wiley: New York, **1991**. (c) Marder, S. R.; Sohn, J. E.; in: Stucky, G. D. (Ed.) *Material for Nonlinear Optics: Chemical Perspectives*, *ACS Symp. Ser.* **1991**, 455.
51. Kajzar, F.; Lee, K.-S.; Jen, A. K.-Y.; *Adv. Polym. Sci.* **1998**, *120*, 13096.

52. (a) Laidlaw, W. M.; Denning, R. G.; Verbiest, T.; Chauchard, Persoons, A. *Nature* **1993**, *363*, 58. (b) Coe, B. J.; Harris, J. A.; Jones, L. A.; Brunschwig, B. S.; Song, K.; Clays, K.; Garin, J.; Orduna, J.; Coles, S. J.; Hursthouse, M. B.; *J. Am. Chem. Soc.* **2005**, *127*, 4845.

Chapter 2: Non-Innocence of 1,4-Dicyanamidebenzene Ligands in Dinuclear Ruthenium Complexes.

2.1 Introduction

2.1.1 Research Objectives

The bridging 1,4-dicyanamidebenzene (dicyd^{2-}) is an efficient mediator of magnetic and electronic metal-metal coupling in dinuclear $[\{\text{Ru}(\text{NH}_3)_5(\mu\text{-R}_2\text{R}_2'\text{dicyd})\}^{3+,4+}]$ complexes due to close energy match between $\text{Ru(III)}d\pi$ and the π -HOMO of the bridging ligand that permits hole-transfer superexchange.¹⁻⁶ The dinuclear $[\{\text{Ru}(\text{NH}_3)_5(\mu\text{-R}_2\text{R}_2'\text{dicyd})\}^{3+,4+}]$ ions have been shown⁷ by EPR and ^1H NMR evidence to correspond to valence configurations, $\text{Ru(III)-dicyd}^{2-}\text{-Ru(II)}$ and $\text{Ru(III)-dicyd}^{2-}\text{-Ru(III)}$, respectively, with the bridging ligand remaining dicyd^{2-} . DFT calculations of $[\{\text{Ru}(\text{NH}_3)_5\}_2(\mu\text{-dicyd})]^{3+}$ in the gas phase gave a mostly ligand-based SOMO in disagreement with experiment and could only be reconciled with the EPR and ^1H NMR data by invoking a strong donor-acceptor interaction between solvent molecules and the ammine protons and cyanamide groups. In contrast, Bonvoisin⁸ *et al* provided EPR and crystallographic evidence that the complex $[\{\text{Ru}(\text{tpy})(\text{thd})\}_2(\mu\text{-dicyd})]^+$ where tpy is 2,2',6',2''-terpyridine and thd⁻ is 2,2,6,6-tetramethyl-3,5-heptanedione, possesses two Ru(II) ions bridged by a radical dicyd^{\bullet} ligand, corresponding to a valence configuration $\text{Ru(II)-dicyd}^{\bullet}\text{-Ru(II)}$. DFT calculations also provided supporting evidence for radical bridge in this complex. This apparent discrepancy in these two complexes in their redox behavior generates a question: why does replacing the ammines with tpy and thd cause the destabilizing the π -HOMO of dicyd^{2-} relative to Ru(II) ? Clearly, the solvent donor-acceptor interaction for $[\{\text{Ru}(\text{tpy})(\text{thd})\}_2(\mu\text{-dicyd})]^+$ is not as great compared to dinuclear

ammine complexes and Ru(II) state is stabilized by the tpy and thd⁻ coordination sphere. This stabilization should be even greater if thd⁻ is replaced by the neutral acceptor, 2,2'-bipyridine (bpy), and it is thus likely that the previously reported [$\{\text{Ru}(\text{tpy})(\text{bpy})\}_2(\mu\text{-dicyd})\]^{3+}$ is also a radical-centred Ru(II)-dicyd^{•-}-Ru(II) species.⁹

The highest occupied molecular orbital (π -HOMO) of the dicyd²⁻ bridging ligand can be significantly perturbed by electron donating or withdrawing substituents. Electrochemical data showed that the L^{•-}/L²⁻ couples of free anionic R₂R_{2'}dicyd²⁻ ligands are stabilized by about 0.53 V by the replacement of electron releasing dimethyl-(Me₂-) with electron withdrawing tetrachloro-(Cl₄-) substituents on the dicyd²⁻ ligand and this creates an opportunity to study a perturbed, mostly ligand-localized SOMO in [$\{\text{Ru}(\text{ttpy})(\text{bpy})\}_2(\mu\text{-dicyd})\]^{3+}$ complexes by spectroscopic methods. To this effect following research objectives can be stated:

- (i) To synthesize four dinuclear complexes [$\{\text{Ru}(\text{ttpy})(\text{bpy})\}_2(\mu\text{-R}_2\text{R}_2'\text{dicyd})\][\text{PF}_6]$, where ttpy = 4-(*tert*-butylphenyl)-2,2':6',2''-terpyridine, bpy = 2,2'-bipyridine and R₂R_{2'}dicyd = 2,5-dimethyl(Me₂-), 2,5-dichloro(Cl₂-), 2,3,4,5-tetrachloro(Cl₄-) and unsubstituted 1,4-dicyanamidebenzene dianion, and characterize the complexes by ¹H NMR, IR, electronic absorption spectroscopy and cyclic voltammetry.
- (ii) To examine the non-innocent behavior of bridging R₂R_{2'}dicyd²⁻ ligand and assign the most appropriate the oxidation state distributions of singly and oxidized complexes [$\{\text{Ru}(\text{ttpy})(\text{bpy})\}_2(\mu\text{-R}_2\text{R}_2'\text{dicyd})\]^{3+,4+}$ by combined EPR, IR, vis-NIR spectroelectrochemistry and semi-empirical PM3 calculations and correlate the degree non-innocence with the observed electrochemical and spectroscopic properties of complexes.

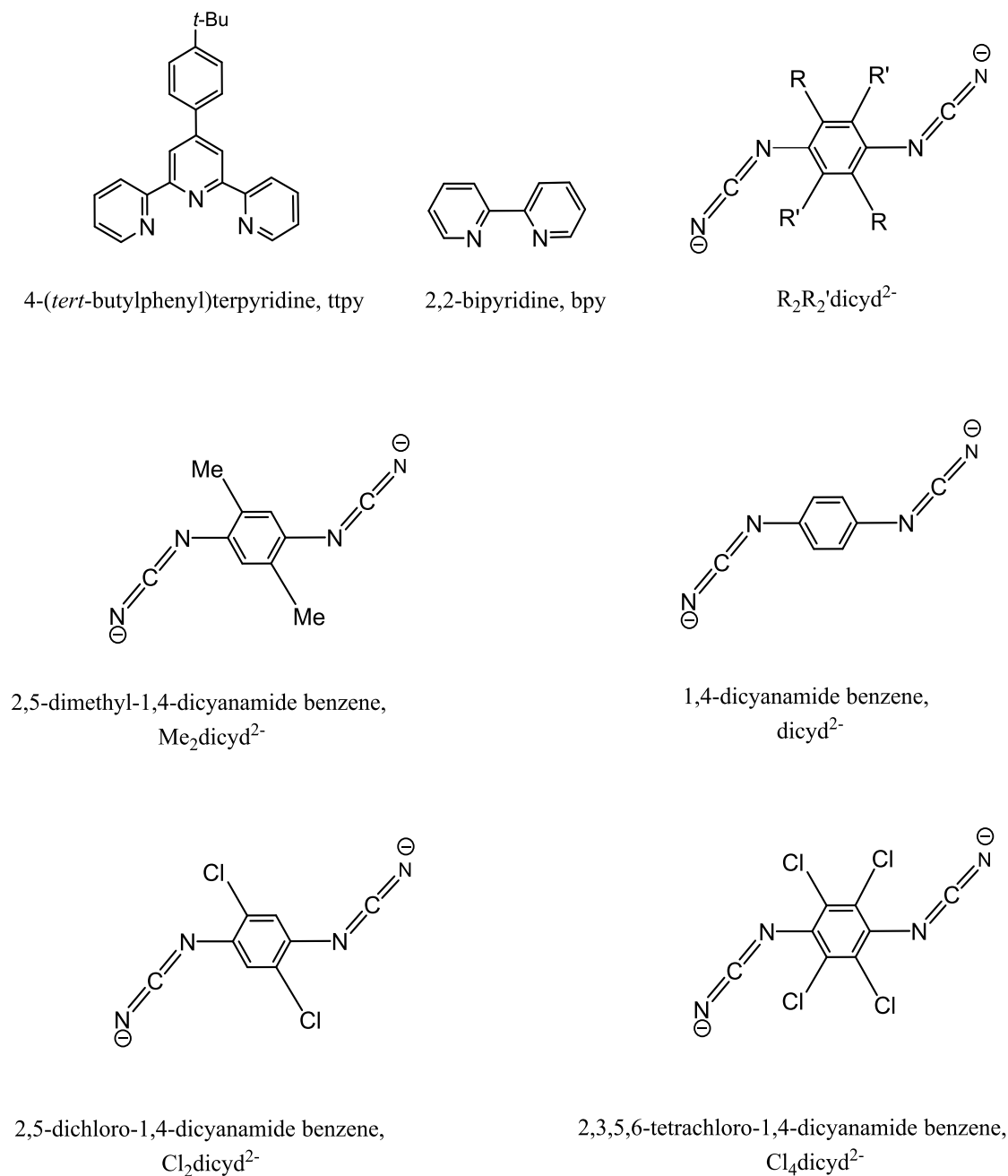


Figure 2.1.1: The bridging R_2R_2' dicyd²⁻ and ancillary ttpy and bpy ligands used in the synthesis of $[\{Ru(\text{ttpy})(\text{bpy})\}_2(\mu\text{-}R_2R_2'\text{dicyd})]^{2+}$ complexes (**1-4**).

2.2 Experimental

2.2.1 Starting Materials

Reagents for Ligand Synthesis

Acetyl chloride ($\geq 99.5\%$, Fluka), glacial acetic acid ($\leq 99.7\%$, ACS reagent grade, Anachemia), acetylpyridine, ammonium thiocyanate (ACS reagent grade, 97.5+%, Aldrich), Benzoyl chloride (99%, Aldrich), 4-*tert*-butylbenzaldehyde, lead(II) acetate trihydrate (ACS reagent grade, 99+%, Aldrich), sodium hydroxide (97%, ACS reagent grade, Caledon Labs.), sulfuric acid (ACS reagent grade, 98%, Anachemia), thallium (I) acetate ($\geq 99\%$, Sigma-Aldrich) (**Caution: highly toxic**), thallium (I) nitrate (BDH), were used as received without further purification.

Reagents for Complex Synthesis

Ammonium hexafluorophosphate (99.5%, Alfa Aesar), lithium chloride ($\geq 99\%$, Sigma-Aldrich), ruthenium (III) chloride hydrate (99.9%, Alfa Aesar), 2,2'-bipyridyl (Reagent plus, $\geq 99\%$, Sigma-Aldrich) were used as received.

Compressed gases

Argon (ultra high purity grade 5.0, PRAXAIR).

Adsorbent in Column Chromatography and Drying Agents

Aluminum oxide (activated, acidic, Brockman I) for column chromatography was deactivated to grade III by adding water and slowly shaking the mixture for 4 h. Phosphorus pentoxide (ACS reagent grade, 98+%, Anachemia) were used as received. Aluminum oxide (neutral, chromatography grade, Woelm) was activated by heating to 300 °C for several hours in a muffle furnace.

Electrochemistry Electrolytes and Internal References and

Tetrabutylammonium hexafluorophosphate (TBAH) was used as the supporting electrolyte in electrochemical experiments. The synthesis of TBAH (tetrabutylammonium hexafluorophosphate) was completed through the combination of a 0.1 M solution of tetrabutylammonium bromide (95+%, Aldrich) and a 0.1 M solution of ammonium hexafluorophosphate (ReagentPlus, 99%, Sigma-Aldrich). The resulting TBAH powder was recrystallized twice from 1:1 ethanol: water and vacuum dried at 110°C. Dicyclopentadienyliron (ferrocene) (reagent grade, J. T. Baker) was used as the internal reference and was purified by sublimation.

Solvents for Synthesis

N,N-dimethylformamide (99.8%, anhydrous, Sigma-Aldrich), anhydrous ethyl alcohol (Commercial Alcohols, absolute), glacial acetic acid (ACS reagent grade, ≤ 99.7%, Anachemia), methanol and toluene (Caledon Labs, reagent grade) were used as received. Acetone (Fisher Scientific, ACS reagent grade) was distilled under glass prior to use.

Solvents for NMR spectroscopy

Dimethyl-*d*₆ sulfoxide (99.9 atom % D, CDN Isotopes) was used as received.

Solvents for Electrochemistry

Acetonitrile (Chromosolv®Plus, 99.9%, HPLC grade, Sigma-Aldrich), *N,N*-dimethylformamide (Chromosolv®Plus, 99.9%, HPLC grade, Sigma-Aldrich) were used with no further purification or drying. The solvent was stored inside a polyethylene glove bag that was filled with argon when mixtures of TBAH and the solvent needed to be made in 20 mL glass vials.

Solvents for Quantitative Electronic Absorption Spectroscopy

N,N-Dimethylformamide (Caledon Labs, reagent grade) was used as received.

2.2.2 Synthesis

The Author is thankful to Professor Dr. Robert J. Crutchley for the synthesis of complexes studied in the present work. Syntheses of ligands and complexes are described in the following paragraphs.

Synthesis of R_2R_2' -dicydH₂ Ligands

1,4-Dicyanamidebenzene (dicydH₂) and its derivatives 2,5-dimethyl-(Me₂dicydH₂), 2,5-dichloro- (Cl₂dicydH₂) and 2,3,5,6-tetrachloro-1,4-dicyanamidobenzene (Cl₄dicydH₂) were prepared by literature methods.⁸ Both Cl₂dicydH₂ and Cl₄dicydH₂ possessed a significant impurity of the guanidine dimer as shown by a strong IR $\nu(C=N)$ band at approximately 1680 cm⁻¹. This dimer impurity reverts to a monomer in basic solutions and does not affect the isolation of the thallium salt of the ligand as discussed previously.¹

Synthesis of Tl₂[R₂R₂'-dicyd] Salts

Thallium salts (**Caution: highly toxic**) of dicyd²⁻ and its substituted derivatives were prepared by using the general method described below for Tl₂[Me₂dicyd]) and were used without further purification.

Preparation of Tl₂[Me₂dicyd]: Crude Me₂dicydH₂ (0.4 g) was dissolved in 100 mL of gently boiling 3:1 acetone: water and then filtered. Approximately 1.5 mL of triethylamine was added to the filtrate, followed quickly by a warm solution of 1.3 g of TlNO₃ in 25 mL of water. The slightly blue solution was gently boiled for five minutes forming a yellow precipitate which was filtered and washed with acetone and water and

finally acetone and allowed to dry. Yield: 0.7 g (54%). Anal. Calcd. for $C_{10}H_8N_4Tl_2$: C, 20.26; H, 1.36; N, 9.45. Found: C, 20.17; H, 1.16; N, 9.43. 1H NMR (DMSO- d_6): the poor solubility and oxidation to the radical by trace oxygen made Me_2dicyd^{2-} chemical shift assignment unreliable. IR (KBr): $\nu(NCN) = 2063$ and 2133 cm^{-1} .

Preparation of $Tl_2[dicyd]$: This compound was prepared in the same manner as $Tl_2[Me_2dicyd]$. Yield: 77 %. Anal. Calcd. for $C_8H_4N_4Tl_2$: C, 17.01; H, 0.71; N, 9.92. Found: C, 17.18; H, 0.58; N, 9.75. 1H NMR (DMSO- d_6): 6.32 (4H, s) ppm. IR (KBr): $\nu(NCN) = 2102$ and 2051 cm^{-1} .

Preparation of $Tl_2[Cl_2dicyd]$: This compound was prepared in the same manner as $Tl_2[Me_2dicyd]$. Yield: 60 %. Anal. Calcd. for $C_8H_2N_4Cl_2Tl_2$: C, 15.16; H, 0.32; N, 8.84. Found: C, 15.19; H, 0.33; N, 8.75. 1H NMR (DMSO- d_6): 6.73 (2H, s) ppm. IR (KBr): $\nu(NCN) = 2098\text{ cm}^{-1}$.

Preparation of $Tl_2[Cl_4dicyd] \cdot 0.25 [HN(CH_2CH_3)_3][NO_3]$: This compound was prepared in the same manner as $Tl_2[Me_2dicyd]$. Yield: 48 %. Anal. Calcd. for $C_{9.5}H_4N_{4.5}Cl_4O_{0.75}Tl_2$: C, 15.34; H, 0.54; N, 8.47. Found: C, 15.43; H, 0.3; N, 8.66. This procedure was repeated twice and the elemental analyses gave the same triethylammonium impurity whose presence was confirmed by 1H NMR. IR (KBr): $\nu(NCN) = 2086\text{ cm}^{-1}$.

Synthesis of 4-(*tert*-butylphenyl)-2,2':6',2''-terpyridine (tppy)

This compound has been prepared previously¹⁰ but the method described below eliminates the need to isolate the penta-1,5-dione derivative. 4-*tert*-Butylbenzaldehyde (5g) and 2-acetylpyridine (13g) were added to 800 mL of methanol in a 2L Erlenmeyer flask. To the stirred solution was added 330 mL of concentrated aqueous ammonia and

65 mL of 3.75 M NaOH. The Erlenmeyer flask was covered with a watch glass and the reaction solution allowed to stir for 4 days during which time the solution became yellow and then cloudy with the precipitation of the product. The reaction mixture was filtered and the light-green product washed with copious water and allowed to air dry. Recrystallization from acetone/water (4:1) yielded 3.0 g, (26%), of light-green flaky crystals. Anal. Calcd. for $C_{25}H_{23}N_3$: C, 82.16; H, 6.34; N, 11.50. Found: C, 82.13; H, 6.43; N, 11.51. 1H NMR (300 MHz, $CDCl_3$): 8.74 (4H, m); 8.68 (2H, d); 7.89(4H, dd); 7.53(2H, d); 7.35(2H, m); 1.56 (9H, s).

Synthesis of Precursor Metal Complexes

Preparation of $Ru(tpy)Cl_3 \cdot H_2O$: The reagent complex $Ru(tpy)Cl_3$ was prepared following the preparation¹¹ of $Ru(tpy)Cl_3$. The complex can be used without further purification. Anal. Calcd. for $C_{25}H_{25}N_3Cl_3ORu$: C, 50.81; H, 4.26; N, 7.11. Found: C, 50.53; H, 3.83; N, 6.94.

Preparation of $[Ru(tpy)(bpy)Cl][PF_6]$: $Ru(tpy)Cl_3$ (1 g) and 2,2'-bipyridine (0.27 g) were added to 200 mL of water/ethanol (2:1) and refluxed under argon for 14 h. The reaction solution was allowed to cool slightly before adding LiCl (1g) and refluxing for a further 1h. The reaction solution was filtered and to the hot filtrate was added 2 g of NH_4PF_6 , precipitating the desired product which was immediately filtered off, washed with water and allowed to air dry. Yield 1.2 g (86%). Anal. Calcd. for $C_{35}H_{31}N_5ClPF_6Ru$: C, 52.34; H, 3.89; N, 8.72. Found: C, 52.16; H, 3.78; N, 8.71. 1H NMR (300 MHz, $DMSO-d_6$): 10.10 (1H, d); 9.15 (2H, s); 8.91 (3H, d); 8.64 (1H, d); 8.36 (1H, t); 8.22 (2H, d); 8.12 – 7.95 (3H, m); 7.77 (1H, t); 7.71 (2H, d); 7.62 (2H, d); 7.42-7.36 (3H, m); 7.08 (1H, t); 1.41(9H, s).

Filtering off the complex from the hot solution keeps impurities in solution and yields an almost pure reagent complex. The reagent complex was used without further purification.

Synthesis of $\{Ru(ttpy)(bpy)\}_2(\mu-R_2R_2'dicyd)[PF_6]_2$ Complexes (1-4)

Preparation of $\{Ru(ttpy)(bpy)\}_2(\mu-Me_2dicyd)[PF_6]_2$ (1)

$[Ru(ttpy)(bpy)Cl][PF_6]$ (1.0 g) and $Tl_2[Me_2dicyd]$ (0.3 g) were placed in 175 mL of DMF and refluxed under argon for 40 h during which time the reaction solution changed color from violet-purple to a brownish-purple and $TlCl$ precipitated. The reaction mixture was gravity filtered through Celite and the filtrate's volume reduced to 5-10 mL. The crude complex was precipitated by the addition of ether (300 mL), filtered and allowed to air dry. Crude yield: 0.8 g. Separation of the dinuclear complex from monomer impurity was achieved by dissolving the complex in 20 mL of CH_3CN , filtering and to the filtrate slowly adding approximately 40 mL of toluene. The precipitated dinuclear complex was filtered, washed with toluene and then ether and vacuum dried. Yield: 0.35 g, 33%. Anal. Calcd. for $C_{80}H_{70}N_{14}P_2F_{12}Ru_2$: C, 55.88; H, 4.10; N, 11.40. Found: C, 55.39; H, 4.36; N, 11.75. 1H NMR (300 MHz, $DMSO-d_6$): 9.60 (d, 2H); 9.17 (s, 4H); 8.94 (d, 6H); 8.67 (d, 2H); 8.38 (t, 2H); 8.20 (d, 4H); 8.08-8.02 (m, 6H); 7.83 (t, 2H); 7.67-7.64 (m, 8H); 7.47 (d, 2H); 7.41 (t, 4H); 7.12 (t, 2H); 5.49 (s, 2H); 1.38 (s, 18H). IR (KBr): $\nu(NCN) = 2104\text{ cm}^{-1}$.

Preparation of $\{Ru(ttpy)(bpy)\}_2(\mu-dicyd)[PF_6]_2 \cdot (C_4H_{10}O)$ (2)

This complex (2) was prepared as for 1 and then recrystallized by ether diffusion into an acetonitrile solution of the complex. Yield: 0.40 g, 38%. Anal. Calcd. for $C_{89.2}H_{86.8}N_{14}O_4P_2F_{12}Ru_2$: C, 56.06; H, 4.58; N, 10.26. Found: C, 56.11; H, 4.19; N, 10.50.

^1H NMR (300 MHz, $\text{DMSO-}d_6$): 9.59 (d, 2H); 9.16 (s, 4H); 8.93 (d, 6H); 8.66 (d, 2H); 8.37 (t, 2H); 8.21 (d, 4H); 8.10-8.02 (m, 6H); 7.82 (t, 2H); 7.70 (d, 4H); 7.66 (d, 4H); 7.45 – 7.35 (m, 6H); 7.13 (t, 2H); 1.40 (s, 18H). IR (KBr): $\nu(\text{NCN}) = 2084$ and 2131 cm^{-1} .

Preparation of $\{[\text{Ru}(\text{ttpy})(\text{bpy})]_2(\mu\text{-Cl}_2\text{dicyd})\}[\text{PF}_6]_2$ (**3**)

$[\text{Ru}(\text{ttpy})(\text{bpy})\text{Cl}][\text{PF}_6]$ (1 g) and $\text{Ti}_2[\text{Cl}_2\text{dicyd}]$ (0.4 g) were placed in 175 mL of DMF and refluxed under argon for 60h during which time the reaction solution changed color from violet-purple to a brownish-purple and TiCl precipitated. The reaction mixture was gravity filtered through Celite and the filtrates volume reduced to 50 mL. The crude complex was precipitated by the addition of ether (300 mL), filtered and allowed to air dry. Crude yield: 0.7 g. Chromatography using alumina (Type III) and elution with CH_3CN : toluene 1:1 yielded an orange band, followed by a purple reagent band and finally a brown band. The latter was collected and the acetonitrile evaporated off yielding the desired product suspended in toluene. Yield 0.23 g (21%). Anal. Calcd. for $\text{C}_{78}\text{H}_{64}\text{N}_{14}\text{Cl}_2\text{P}_2\text{F}_{12}\text{Ru}_2$: C, 53.22; H, 3.66; N, 11.14. Found: C, 53.36; H, 3.43; N, 11.46. ^1H NMR (300 MHz, $\text{DMSO-}d_6$): 9.66 (d, 2H); 9.17 (s, 4H); 8.94 (d, 6H); 8.67 (d, 2H); 8.37 (t, 2H); 8.19 (d, 4H); 8.08-8.01 (m, 6H); 7.81 (t, 2H); 7.68-7.64 (m, 8H); 7.44-7.38 (m, 6H); 7.11 (t, 2H); 5.24 (s, 2H); 1.39 (s, 18H). IR (KBr): $\nu(\text{NCN}) = 2141\text{ cm}^{-1}$.

Preparation of $\{[\text{Ru}(\text{ttpy})(\text{bpy})]_2(\mu\text{-Cl}_4\text{dicyd})\}[\text{PF}_6]_2$ (**4**)

This complex (**4**) was prepared in the same manner as **3**. Yield: 15 %. Anal. Calcd. for $\text{C}_{83.5}\text{H}_{69}\text{N}_{15}\text{Cl}_4\text{P}_2\text{F}_{12}\text{Ru}_2$: C, 52.33; H, 3.63; N, 10.96. Found: C, 52.08; H, 3.54; N, 11.10. ^1H NMR (300 MHz, $\text{DMSO-}d_6$): 9.64 (d, 2H); 9.15 (s, 4H); 8.95-8.91 (m, 6H); 8.67 (d, 2H); 8.38 (t, 2H); 8.19 (d, 4H); 8.11 – 7.97 (m, 6H); 7.82 (t, 2H); 7.69-7.65 (m,

8H); 7.48 – 7.34 (m, 6H); 7.12 (t, 2H); 5.49 (s, 4H); 1.39 (s, 18H). IR (KBr): $\nu(\text{NCN}) = 2156 \text{ cm}^{-1}$.

2.3.3 Physical Measurements

Elemental Analyses

All elemental analyses were performed by Canadian Microanalytical Services, Ltd. in Delta, B. C., Canada.

Infrared Spectroscopy

Infrared spectroscopy was performed on a Bomem Michelson 120 FTIR spectrometer as KBr mulls. Data was analyzed using Bomem Grams/386 v3.04 Level II software.

NMR Spectroscopy

All standard diamagnetic 1-D and 2-D (COESY) ^1H NMR spectra were recorded using a Bruker AMX-400 NMR or Bruker 300 Ultra Shield spectrometers at room temperature in chloroform- d_3 and dimethyl- d_6 sulfoxide and all chemical shifts were referenced with respect to TMS (tetramethylsilane). The sample size consisted of 5-10 mg in 1.00 mL of chloroform- d_3 or dimethyl- d_6 sulfoxide and was measured in a Norell XR-55 NMR tube.

In order to investigate paramagnetic ^1H NMR spectroscopy, the dinuclear $[\{\text{Ru}(\text{ttpy})(\text{bpy})\}_2(\mu\text{-R}_2\text{R}_2'\text{dicyd})]^{2+}$ complexes were oxidized in their acetonitrile solutions by using $\text{NO}^+ \text{BF}_4^-$ as oxidant. Evaporation of acetonitrile left the crude oxidized complexes which were used without further purification.

Electronic Absorption Spectroscopy

The quantitative electronic absorption spectra of $[\{\text{Ru}(\text{ttpy})(\text{bpy})\}_2(\mu\text{-R}_2\text{R}_2'\text{dicyd})][\text{PF}_6]_2$ complexes (**1-4**) were recorded in *N,N'*-dimethylformamide (DMF) using a Varian Cary 5 UV-Vis-NIR Spectrophotometer at ambient temperatures using Quartz cells of 1.000 cm path length from Hellma (Canada) Limited. Runs were done at 1800 nm/min vs. solvent backgrounds, with a data interval of 0.333 nm, a spectral bandwidth of 2.00 nm, and a signal averaging time of 0.033 s.

Cyclic Voltammetry

Cyclic voltammetry studies were performed using a Ω Metrohm Autolab potentiostat/galvanostat PGSTAT30. *N,N*-Dimethylformamide (Sigma-Aldrich, Chromosolv®Plus, 99.9%, HPLC grade) was used for the studies. A three electrode arrangement consisting of a platinum disk electrode working electrode (BAS 1.6 mm diameter), a platinum wire auxiliary electrode, and a silver-wire quasi-reference electrode was used. The electrochemical cell consisted of a double jacketed glass container with an internal volume of 15 mL. Ferrocene ($E^\circ = 0.665$ V versus NHE)¹² was used as internal reference. TBAH (0.1M) was used as the supporting electrolyte. Argon gas was bubbled into the solutions for 10-15 minutes in order to degas them before scans were recorded. A scan rate of 0.1 V/s was used in order to record the background CV.

Vis-NIR and IR Spectroelectrochemistry

Vis-NIR spectroelectrochemistry of dinuclear $[\{\text{Ru}(\text{ttpy})(\text{bpy})\}_2(\mu\text{-R}_2\text{R}_2'\text{dicyd})][\text{PF}_6]_2$ complexes (**1-4**) were performed using an OTTLE (Optically Transparent Thin Layer Electrochemistry) cell based on the design of Hartl³⁰ using ITO (indium-tin oxide) coated glass as working and counter electrodes and Ag/AgCl as

reference electrode. Same cell was used for IR spectroelectrochemistry with the exception that gold-foil (500 line/inch, 60% Transmittance, Buckbee Mears) was used as working and counter electrodes instead of using the ITO glass. *N,N*-dimethylformamide (DMF) was used as the solvent and tetrabutylammonium hexafluorophosphate (TBAH, 0.1M) as supporting electrolyte (solvent information provided in section). Potentials were controlled using a BAS CV-27 potentiostat and varied between 0.00 and 1.10 V for the R_2R_2' -dicyd system. UV-vis-NIR spectra were obtained on the same Cary 5 Spectrophotometer as was used for electronic absorption spectroscopy vs. appropriate backgrounds of solvent and electrolyte at a scan rate of 1800 nm/min. IR spectra were taken on Bomem Michelson 120 FTIR spectrometer as was used for IR spectroscopy. At any given potential, the system was allowed to come to equilibrium ($i \approx 0 \mu\text{A}$) prior to acquisition of the spectrum.

EPR Spectroscopy

EPR spectra of the complexes were recorded in DMF at room temperature to 110 K by using a Bruker system EMX and a continuous flow cryostat ESR 900 of Oxford Instruments was used for this purpose. The author is thankful to Professor Wolfgang Kaim and Biprajit Sarkar of University of Stuttgart for performing EPR studies on singly oxidized forms of $[\text{Ru}(\text{tpy})(\text{bpy})(2,4\text{-Cl}_2\text{pcyd})][\text{PF}_6]$ and $[\{\text{Ru}(\text{tpy})(\text{bpy})\}_2(\mu\text{-}R_2R_2'\text{dicyd})][\text{PF}_6]_2$ complexes (**2,4**).

2.2.4 Theoretical Calculations

Restricted hybrid HF-DFT SCF calculation was performed on $[\{\text{Ru}(\text{tpy})(\text{bpy})\}_2(\mu\text{-dicyd})]^{2+}$ (**2**) in order to obtain the optimized geometry of the complex, using Wavefunction Inc., Spartan 14 Parallel suite program, with the Beck three

parameter hybrid exchange and Lee-Yang-Parr correlation functionals (B3LYP) and the 6-31G* basis set for C, H, N and LANL2DZ basis set for Ru atoms. DFT calculations on the oxidized complex $[\{\text{Ru}(\text{ttpy})(\text{bpy})\}_2(\mu\text{-dicyd})]^{3+,4+}$ were attempted but calculations would not converge. Semi-empirical restricted and unrestricted Hartree-Fock PM3D calculations were performed using Wavefunction Inc. Spartan 10 parallel Suite Program to obtain the optimized geometry and frontier orbital parentages of $[\{\text{Ru}(\text{tpy})(\text{bpy})\}_2(\mu\text{-R}_2\text{R}_2'\text{dicyd})]^{2+/4+}$ and $[\{\text{Ru}(\text{tpy})(\text{bpy})\}_2(\mu\text{-R}_2\text{R}_2'\text{dicyd})]^{3+}$, respectively. In order to simplify calculations, *t*-butylphenyl group on the tpy ligand was replaced with the H-atom.

complexes (1-4) varied between 17-38%. Elemental analyses of complexes are consistent with molecular formulations and purity of complexes was further confirmed by ^1H NMR spectroscopy.

2.3.2 Molecular Structure

A gas-phase DFT calculation using B3LYP/6-31G*-LANL2DZ gave the geometry optimized structure of the $[\{\text{Ru}(\text{ttpy})(\text{bpy})\}_2(\mu\text{-dicyd})][\text{PF}_6]_2$ complex (2), which is shown in the Figure 2.3.1.

In the symmetric dinuclear complex, the Ru(II) ion occupies a pseudo-octahedral coordination sphere of nitrogen donor atoms, where ttpy ligand occupies the

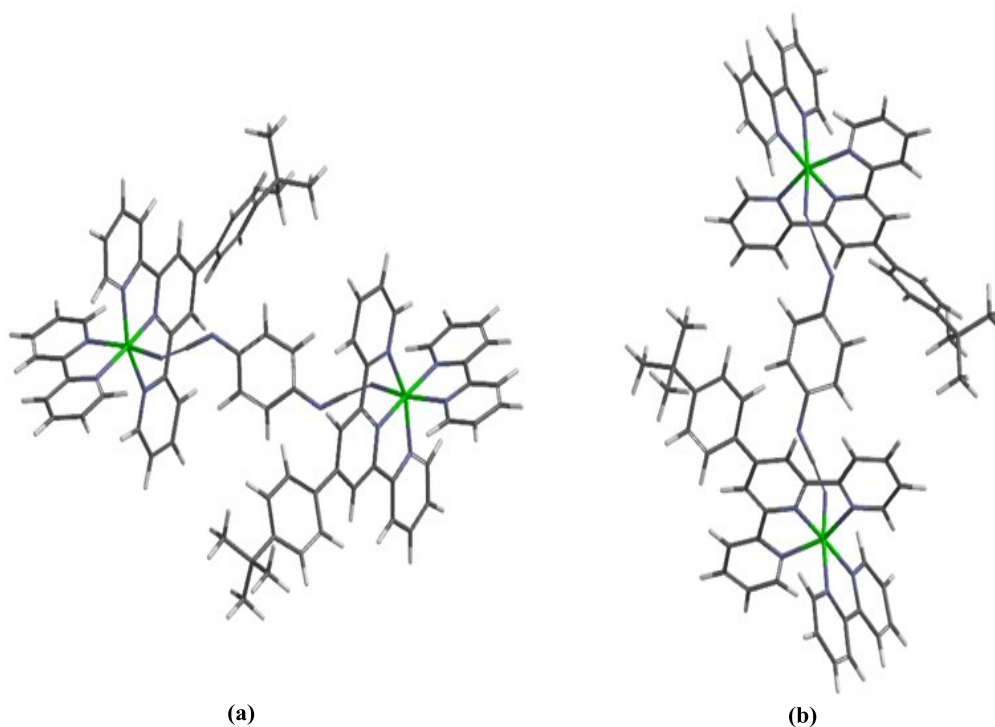


Figure 2.3.1: Geometry optimized structure of $[\{\text{Ru}(\text{ttpy})(\text{bpy})\}_2(\mu\text{-dicyd})][\text{PF}_6]_2$ complex. (a) horizontal and (b) vertical views.

equatorial plane and the cyanamide group of the dicyd^{2-} ligand is *trans* to a pyridine moiety of bipyridine ligand.

The bridging dicyd^{2-} ligand is approximately planar, with two cyanamide groups adopting stable *anti*-conformation. The planar conformation of dicyd^{2-} anion and its derivatives has also been observed in crystal structures of tetraphenylarsonium salts and Ru(III) complexes and has been suggested to allow for effective π -conjugation between the cyanamide groups and the phenyl ring. The cyanamide group is approximately linear with N-C-N angle of 173° . On the other hand, the angle describing ruthenium and cyanamide bond is significantly bent (133.14°). This bent geometry of metal-cyanamide bond is also observed in the crystal structures of $[\{\text{Ru}(\text{tpy})(\text{bpy})\}_2(\mu\text{-adpc})][\text{PF}_6]_2$ and palladium complexes of phenylcyanamide ligands.¹³⁻¹⁵ On the other hand, crystal structures of many Ru(III)-cyanamide complexes show approximately linear cyanamide group and it has been suggested that π -bonding is optimized when the bond between Ru(III) and cyanamide is linear, a condition which evidently relaxed when π -bonding is not as important.¹⁶ The calculated Ru-N(NCN) bond length (2.092 Å) for the bridging dicyd^{2-} ligand is comparable to those in other Ru(II)-phenylcyanamide complexes.¹³⁻¹⁵ In addition, calculated Ru-N bond lengths for two terminal and central pyridine rings of the tpy are 2.120 and 2.134 Å, respectively. These bond lengths are comparable to those observed in the crystal structures of other Ru(II)-polypyridyl-phenylcyanamide complexes.¹³⁻¹⁴ The terpyridine fragment of the tpy ligand is approximately planar, with the dihedral angle between the central and terminal pyridine rings being only 1.22° . As observed in other 4'-substituted free terpyridine ligands and their complexes,^{17a-d} the *t*-butylphenyl group is twisted about the terpyridine plane, with the dihedral angle between

them being 58.36°. The twisted geometry is a compromise between π -conjugation of the *t*-butylphenyl group with the terpyridine fragment and the steric repulsion between *ortho* proton on the phenyl ring and the 3' proton on the central pyridine ring of the terpyridine ligand.^{17a-b}

2.3.3 Electronic Structure

The gas phase semi-empirical PM3 calculations were performed on $[\{\text{Ru}(\text{tpy})(\text{bpy})\}_2(\mu\text{-dicyd})]^{2+/3+/4+}$ in order to obtain the electronic structures of complexes **2**, **2⁺** and **2²⁺**. DFT calculations were attempted but calculations would not converge.¹⁸ As *t*-butylphenyl group on tpy ligand has little influence on the energetic of the frontier orbitals, calculations were simplified by the replacement of *t*-butylphenyl group with the H-atom. The orbital energies and corresponding wave functions for $[\{\text{Ru}(\text{tpy})(\text{bpy})\}_2(\mu\text{-dicyd})]^{2+/3+/4+}$ complexes are shown in the Figure 2.3.2-2.3.4.

The Gas-phase PM3 calculation of the complex **2** shows that the HOMO and HOMO-1, are entirely centered on the bridging dicyd²⁻ ligand, without any contributions from the Ru($d\pi$) orbitals. This is consistent with EPR spectroscopic results on the singly oxidized complex **2⁺**, which suggested a mostly ligand-centered SOMO (*Vide infra*). On the other hand, the LUMO and the LUMO+1 are nearly degenerate and localized on tpy and bpy ligands.

As seen in Figure 2.3.3, the calculated β -HOMO (which is SOMO in this case) of **2⁺** is also localized on the bridging dicyd²⁻ ligand, implying a predominantly ligand-centered spin in **2⁺**, which is in agreement with EPR results. Like the β -HOMO, both β -HOMO-1 and β -HOMO-2 are predominantly of ligand character, with a little contribution from the Ru($d\pi$) orbital as well. On the other hand, the β -LUMO is

predominantly localized on the ttpy ligand with minor contribution from the bpy ligand. Like the singly oxidized complex 2^+ , semi-empirical calculations on the doubly oxidized

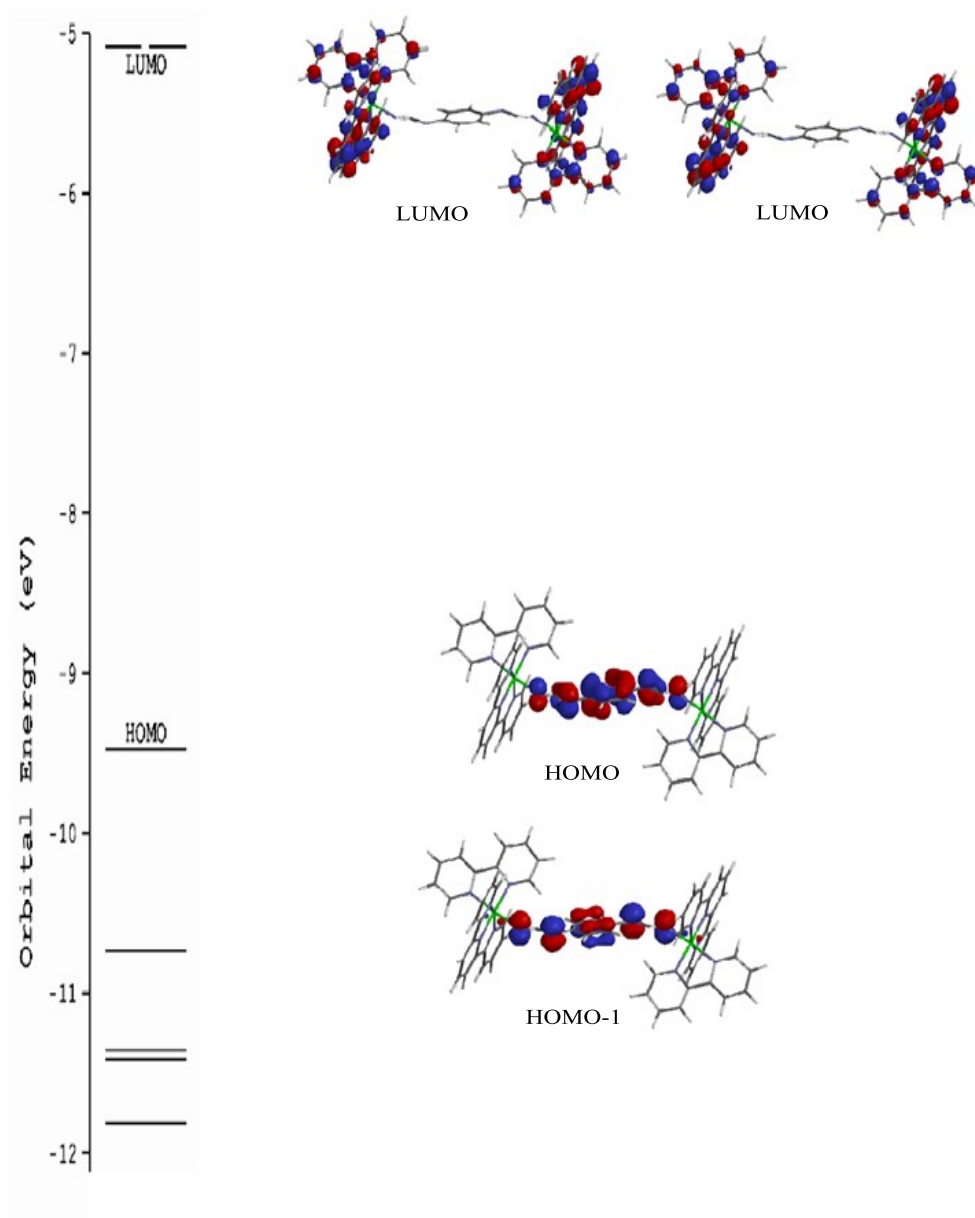


Figure 2.3.2: Gas-phase semi-empirical calculation (PM3) of the orbital energies and wavefunctions of $[\{\text{Ru}(\text{tpy})(\text{bpy})\}_2(\mu\text{-dicyd})]^{2+}$ (**2**).

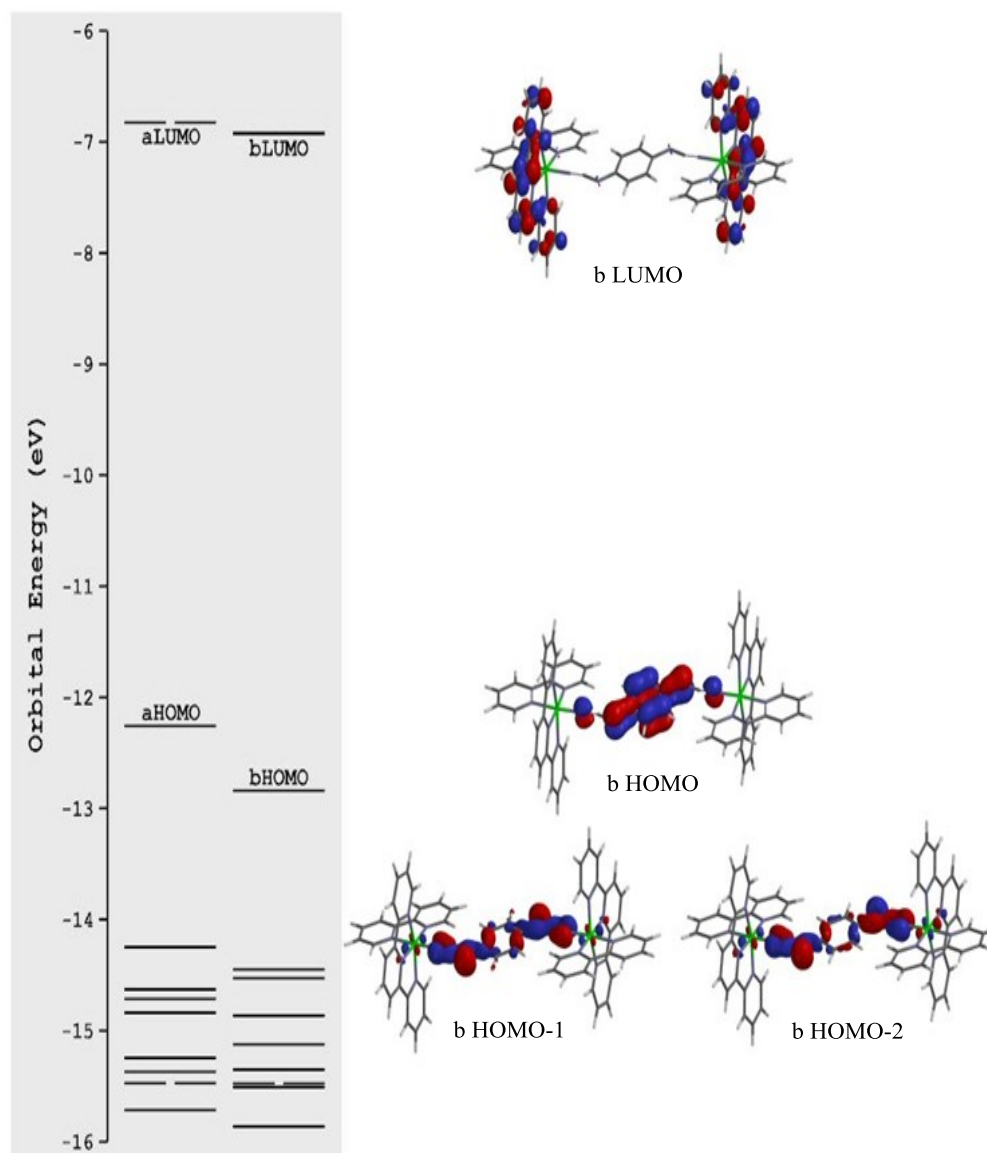


Figure 2.3.3: Gas phase semi-empirical calculation (PM3) of the orbital energies and β -wavefunctions of $[\{\text{Ru}(\text{tpy})(\text{bpy})\}_2(\mu\text{-dicyd})]^{3+}$ (2^+).

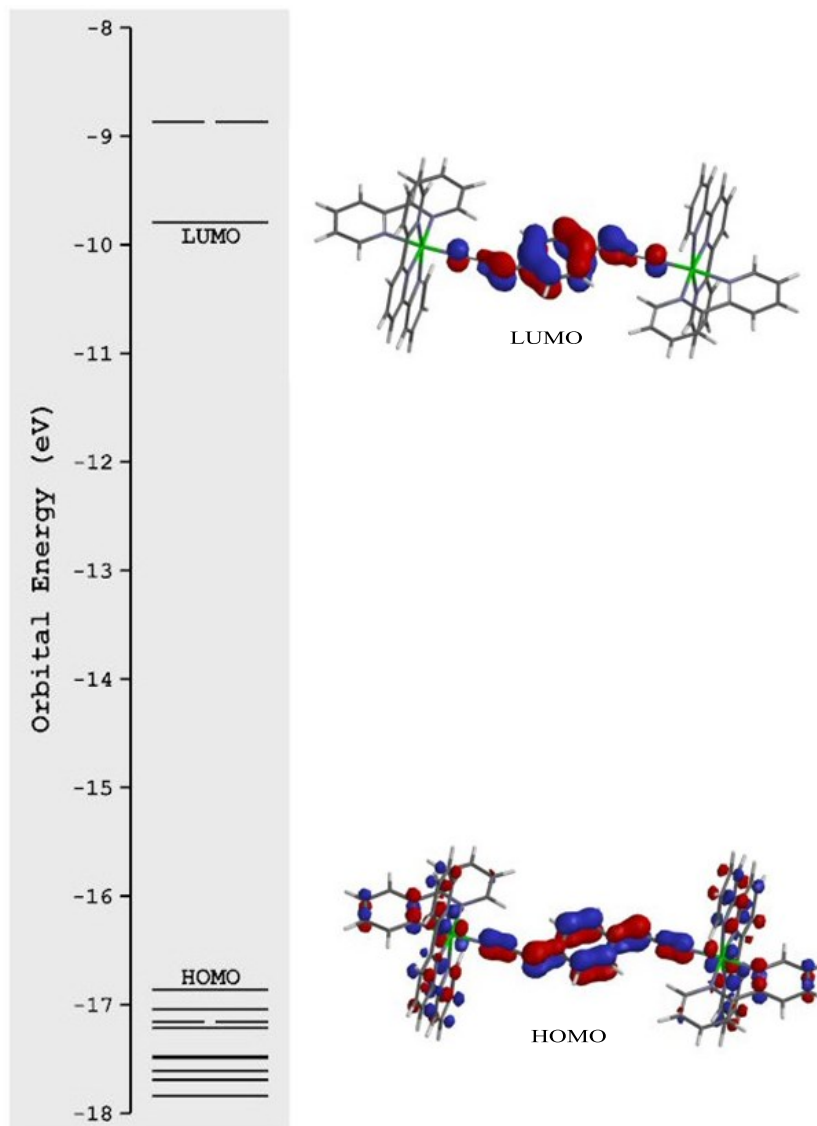


Figure 2.3.4: Gas phase semi-empirical calculation (PM3) of the orbital energies and LUMO and HOMO wavefunctions of $[\{\text{Ru}(\text{tpy})(\text{bpy})\}_2(\mu\text{-dicyd})]^{4+}$ (2^{2+}).

complex 2^{2+} , assuming a singlet ground state, $\text{Ru(II)-R}_2\text{R}_2'\text{dicyd}^0\text{-Ru(II)}$, also gave mostly a ligand-centered HOMO and LUMO (Figure 2.3.4). While the LUMO is predominantly of ligand character, the HOMO possesses minor contributions from Ru and tpy ligand.

2.3.4 IR Spectroscopy

The infrared spectra of neutral $\text{R}_2\text{R}_2'\text{dicydH}_2$ ligands, $\text{Ti}_2[\text{R}_2\text{R}_2'\text{dicyd}]$ salts and dinuclear $[\{\text{Ru}(\text{tpy})(\text{bpy})\}_2(\mu\text{-R}_2\text{R}_2'\text{dicyd})][\text{PF}_6]_2$ complexes (**1-4**) were taken on the KBr discs and the corresponding $\nu(\text{NCN})$ stretching frequencies are shown in the Table 2.3.1. The Figures 2.3.5-2.3.7 show the representative spectra of neutral $\text{Cl}_2\text{dicydH}_2$ ligand, its anionic form, $\text{Ti}_2[\text{Cl}_2\text{dicyd}]$ and the dinuclear complex, $[\{\text{Ru}(\text{tpy})(\text{bpy})\}_2(\mu\text{-Cl}_2\text{dicyd})][\text{PF}_6]_2$ complex (**3**).

IR spectra of $\text{R}_2\text{R}_2'\text{dicydH}_2$ ligands are characterized by a strong $\nu(\text{NCN})$ band in the range of $2224\text{-}2242\text{ cm}^{-1}$. The band positions are comparable to those of neutral phenylcyanamide ligands and vary only slightly with the electronic nature of the substituents on the bridging ligand.^{14,15,20-22} Both $\text{Cl}_2\text{dicydH}_2$ and $\text{Cl}_4\text{dicydH}_2$ possessed a significant impurity of the guanidine dimer as shown by a strong IR $\nu(\text{C=N})$ band at approximately 1680 cm^{-1} .¹⁹

The $\nu(\text{NCN})$ bands of anionic $\text{R}_2\text{R}_2'\text{dicyd}^{2-}$ ligands appear at $2033\text{-}2098\text{ cm}^{-1}$ while those of dinuclear $[\{\text{Ru}(\text{tpy})(\text{bpy})\}_2(\mu\text{-R}_2\text{R}_2'\text{dicyd})][\text{PF}_6]_2$ complexes (**1-4**) at $2085\text{-}2150\text{ cm}^{-1}$ and show a modest increase with the electron withdrawing substituents. The observed band positions again coincide with those for other anionic phenylcyanamide and 1,4-dicyanamide ligands as well as their complexes.^{1-9,13-16,20-22}

Table 2.3.1: Infrared Data of $\nu(\text{NCN})$ Bands in Free $\text{R}_2\text{R}_2'\text{dicydH}_2$, $\text{Tl}_2[\text{R}_2\text{R}_2'\text{dicyd}]$ and $[\{\text{Ru}(\text{ttpy})(\text{bpy})\}_2(\mu\text{-R}_2\text{R}_2'\text{dicyd})]^{2+}$ Complexes (1-4).^a

Substituents, $\text{R}_2\text{R}_2'$ -	NCN Stretches, ν/cm^{-1}		
	Neutral Ligand, $\text{R}_2\text{R}_2'\text{dicydH}_2$	Tl Salts, $\text{R}_2\text{R}_2'\text{dicyd}^{2-}$	Complexes
Me_2 -	2287,2231	2063,2033	2104
H_4 -	2224	2102, 2051	2132,2085
Cl_2 -	2264,2233,2122	2098	2132
Cl_4 -	2242,2126,1683	2086	2150

^aperformed on KBr disc.

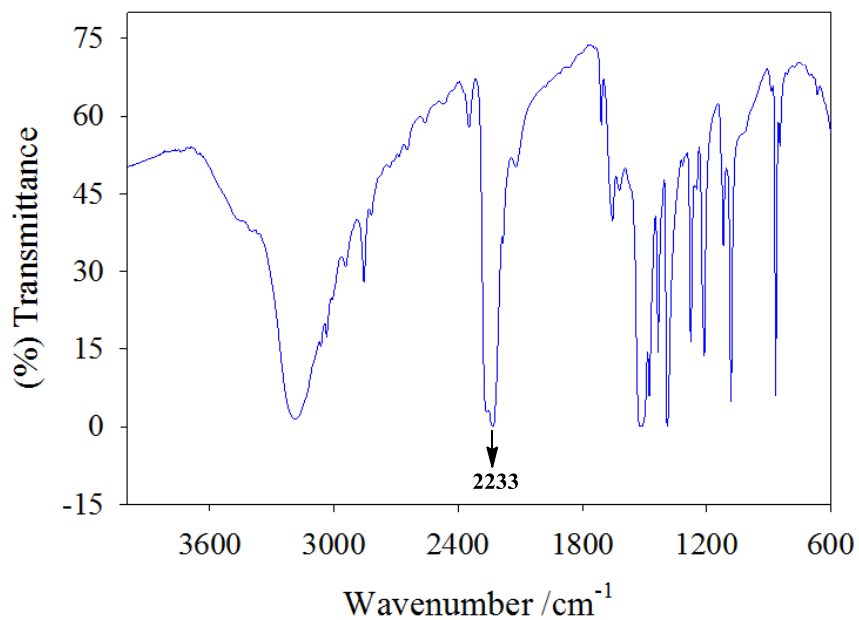


Figure 2.3.5: IR spectrum of $\text{Cl}_2\text{dicydH}_2$ ligand on KBr Disc.

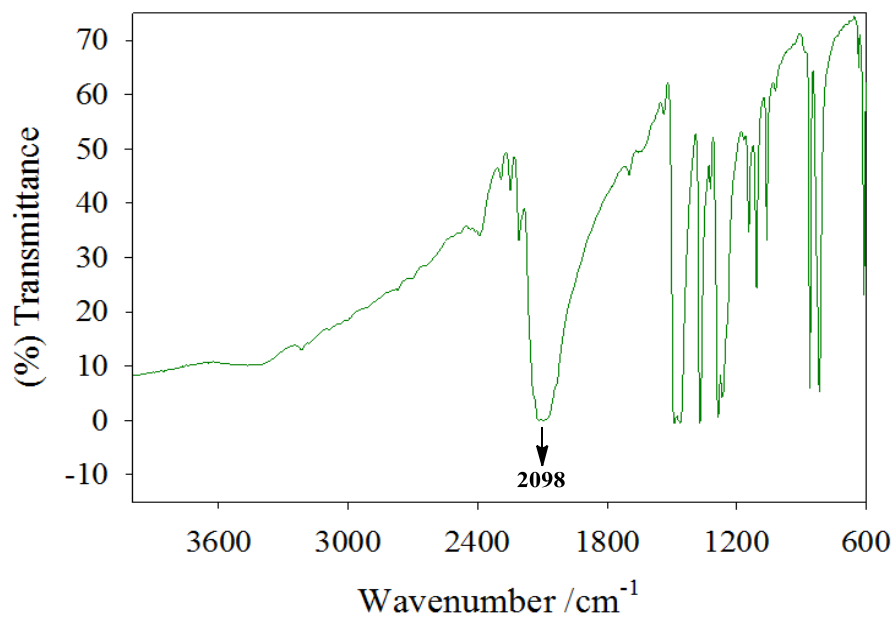


Figure 2.3.6: IR spectrum of $\text{Tl}_2[\text{Cl}_2\text{dicyd}_2]$ salt on KBr Disc.

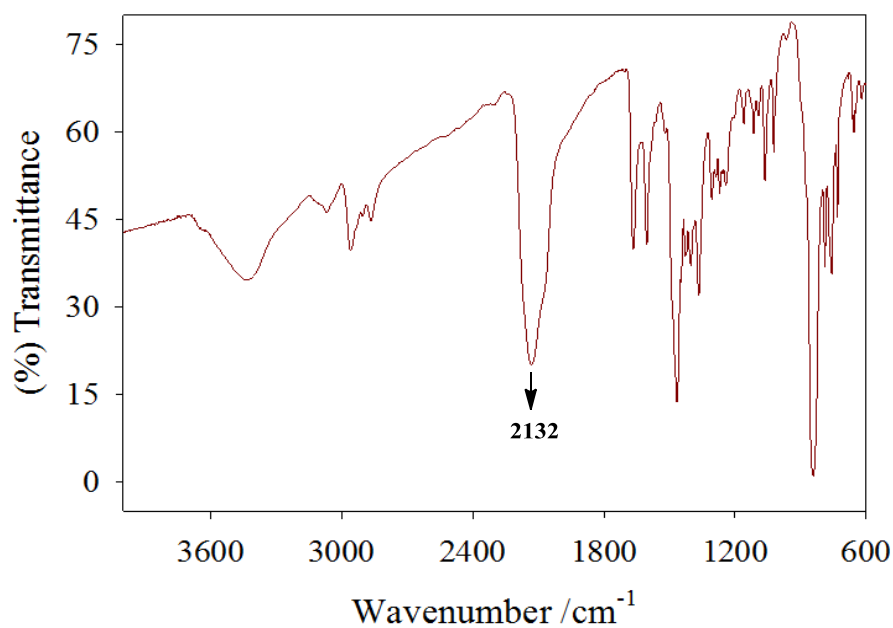


Figure 2.3.7: IR spectrum of $[\{\text{Ru}(\text{tpy})(\text{bpy})\}_2(\mu\text{-Cl}_2\text{dicyd})][\text{PF}_6]_2$ complex (**3**) on KBr Disc.

2.3.5 ^1H NMR Spectroscopy

The ^1H NMR spectra of precursor $[\text{Ru}(\text{ttpy})(\text{bpy})\text{Cl}][\text{PF}_6]$ and all dinuclear $[\{\text{Ru}(\text{ttpy})(\text{bpy})\}_2(\mu\text{-R}_2\text{R}_2'\text{dicyd})][\text{PF}_6]_2$ complexes (**1-4**) were recorded in $\text{DMSO-}d_6$ and the observed chemical shifts were referenced to TMS proton resonances. The ^1H NMR and ^1H - ^1H -COSY spectra $[\text{Ru}(\text{ttpy})(\text{bpy})\text{Cl}][\text{PF}_6]$ complex are shown in the Figure 2.3.8 and 2.3.9 respectively. On the hand, spectra of complexes (**1-4**) are shown in the Figure 2.3.10-2.3.17 and the corresponding data are provided in the Table 2.3.2. All proton peaks for ttpy, bpy and coordinated $\text{R}_2\text{R}_2'\text{dicyd}^{2-}$ ligands were assigned with the help of ^1H - ^1H COSY technique, coupling constants (J values) and integration values for respective peaks and compared with those reported in the literature.¹⁷

The precursor mononuclear $[\text{Ru}(\text{ttpy})(\text{bpy})\text{Cl}][\text{PF}_6]$ and all dinuclear $[\{\text{Ru}(\text{ttpy})(\text{bpy})\}_2(\mu\text{-R}_2\text{R}_2'\text{dicyd})][\text{PF}_6]_2$ complexes (**1-4**) exhibited a total of 15 signals consisting of seven signals from ttpy and eight signals from bpy protons in the region between $\delta 9.66$ - 7.11 ppm and a sharp singlet for *t*-butyl protons at $\delta 1.38$ ppm in their ^1H NMR spectra (Table 2.3.2). The signals for aromatic protons of bridging $\text{R}_2\text{R}_2'\text{dicyd}$ ligands in dinuclear complexes appear in the region between $\delta 5.24$ - 5.49 ppm. The numbering schemes used to assign the ttpy and bpy protons on $[\text{Ru}(\text{ttpy})(\text{bpy})\text{Cl}][\text{PF}_6]$ $[\{\text{Ru}(\text{ttpy})(\text{bpy})\}_2(\mu\text{-R}_2\text{R}_2'\text{dicyd})][\text{PF}_6]_2$ complexes (**1-4**) are shown in the Figure 2.3.18.

All seven signals from the ttpy ligand (A6, A5, A4, A3, B3, E2, and E3), are easily distinguished from those of bpy ligands on the basis of the integration ratios of corresponding protons, (ttpy : bpy = 1:2). The most deshielded singlet at $\delta 9.15$ - 9.17 ppm could be easily recognized as the signal from B3 protons on the ttpy ligand. This singlet

Table 2.3.2: 300 MHz ^1H NMR Data of $[\{\text{Ru}(\text{ttpy})(\text{bpy})\}_2(\mu\text{-R}_2\text{R}_2'\text{dicyd})][\text{PF}_6]_2$ Complexes (1-4) in $\text{DMSO-}d_6$.

Complexes	Chemical Shift (ppm)/type	<i>J</i> values (Hz)
Me ₂ dicyd (1)	9.66 (d, 2H) (C6)	5.2
	9.17 (s, 4H) (B3)	
	8.94 (d, 6H) (C3, A3)	8.0
	8.67 (d, 2H) (D3')	8.3
	8.37 (t, 2H) (C4)	7.9
	8.19 (d, 4H) (E2)	8.5
	8.08-8.01 (m, 6H) (C5, A4)	8.3
	7.81 (t, 2H) (D4')	
	7.68-7.64 (m, 8H) (E3, A6)	
	7.44-7.38 (m, 6H) (D6', A5)	6.7
	7.11 (t, 2H) (D5')	
	5.24 (s, 2H) (F1)	
	1.39 (s, 24H) (<i>t</i> -Bu, Me)	
dicyd (2)	9.64 (d, 2H) (C6)	5.2
	9.15 (s, 4H) (B3)	
	8.95-8.91 (m, 6H) (C3, A3)	8.2
	8.67 (d, 2H) (D3')	
	8.38 (t, 2H) (C4)	
	8.19 (d, 4H) (E2)	8.5
	8.11 – 7.97 (m, 6H) (C5, A4)	7.9
	7.82 (t, 2H) (D4')	
	7.69-7.65 (m, 8H) (E3, A6)	
	7.48 – 7.34 (m, 6H) (D6', A5)	7.2
	7.12 (t, 2H) (D5')	
	5.49 (s, 4H) (F1)	
	1.39 (s, 18H) (<i>t</i> -Bu)	

continued

Complexes	Chemical Shift (ppm)/type	<i>J</i> values (Hz)
Cl ₂ dicyd (3)	9.60 (d, 2H) (C6) 9.17 (s, 4H) (B3) 8.94 (d, 6H) (C3, A3) 8.67 (d, 2H) (D3') 8.38 (t, 2H) (C4) 8.20 (d, 4H) (E2) 8.08-8.02 (m, 6H) (C5, A4) 7.83 (t, 2H) (D4') 7.67-7.64 (m, 8H) (E3, A6) 7.47 (d, 2H) (D6') 7.41 (t, 4H) (A5) 7.12 (t, 2H) (D5') 5.49 (s, 2H) (F1) 1.38 (s, 18H) (<i>t</i> -Bu)	4.9 7.9 8.2 7.2 8.5 8.5 5.1 6.9 6.6
Cl ₄ dicyd (4)	9.59 (d, 2H) (C6) 9.16 (s, 4H) (B3) 8.93 (d, 6H) (C3, A3) 8.66 (d, 2H) (D3') 8.37 (t, 2H) (C4) 8.21 (d, 4H) (E2) 8.10-8.02 (m, 6H) (C5, A4) 7.82 (t, 2H) (D4') 7.70 (d, 4H) (E3) 7.66 (d, 4H) (A6) 7.45 – 7.35 (m, 6H) (D6', A5) 7.13 (t, 2H) (D5') 1.40 (s, 18H) (<i>t</i> -Bu)	5.1 8.2 8.3 8.0 8.5 8.5 8.5 4.8 7.1

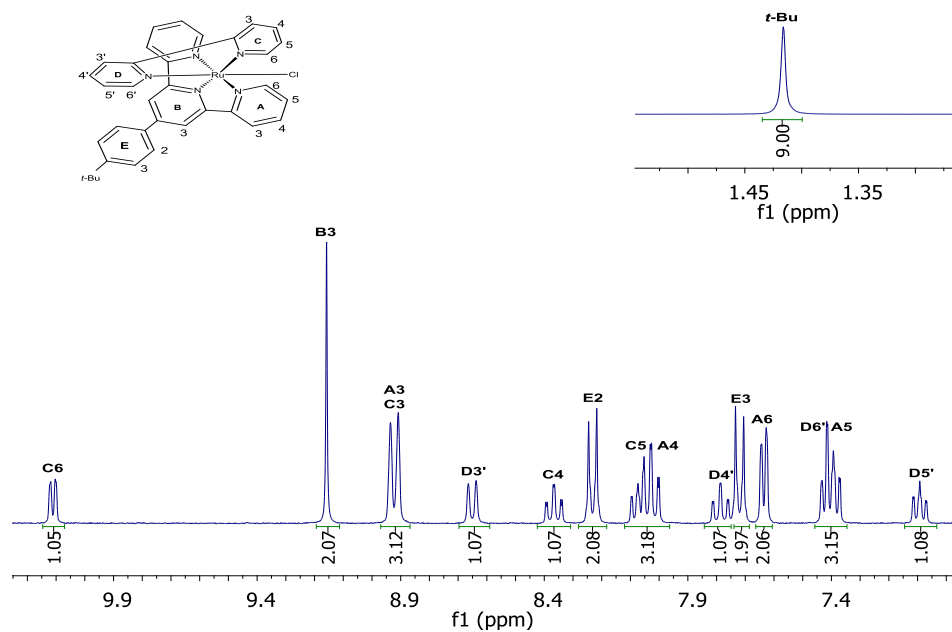


Figure 2.3.8: ^1H NMR spectrum of $[\text{Ru}(\text{tpy})(\text{bpy})\text{Cl}] [\text{PF}_6]$ complex in $\text{DMSO-}d_6$.

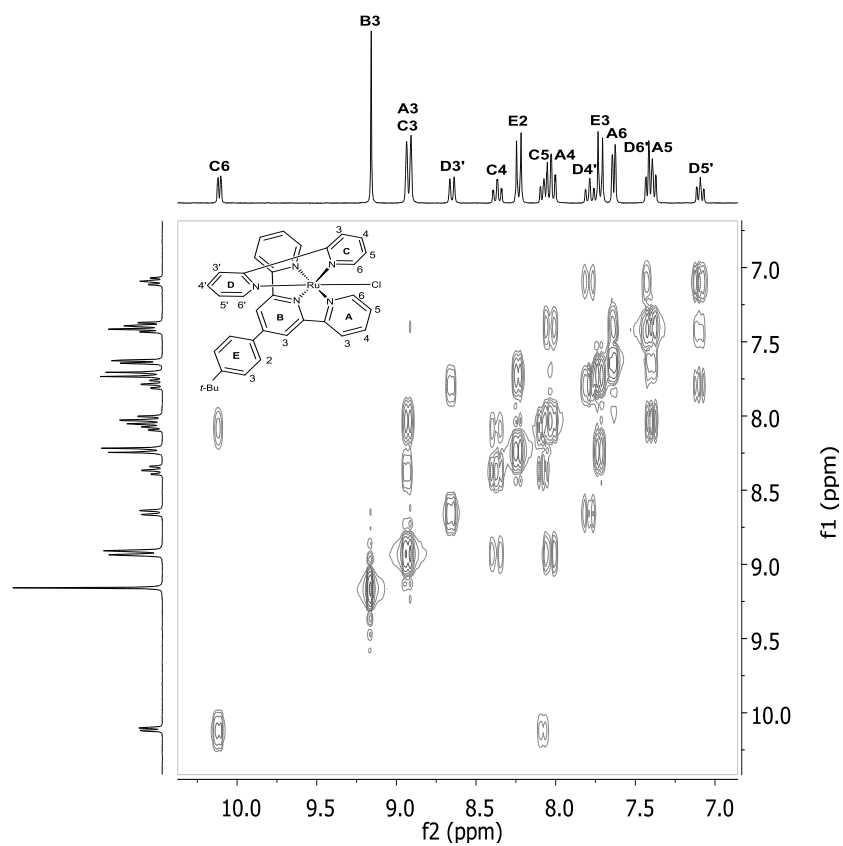


Figure 2.3.9: ^1H - ^1H COSY spectrum of $[\text{Ru}(\text{tpy})(\text{bpy})\text{Cl}] [\text{PF}_6]$ complex in $\text{DMSO-}d_6$.

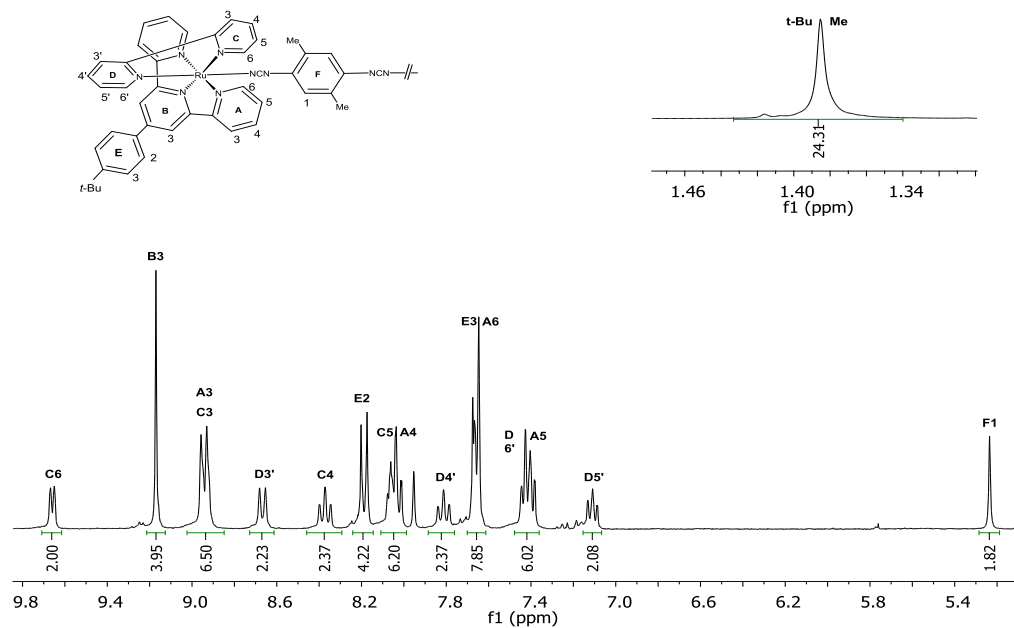


Figure 2.3.10: ^1H NMR spectrum of $[\{\text{Ru}(\text{ttpy})(\text{bpy})\}_2(\mu\text{-Me}_2\text{dicyd})] [\text{PF}_6]_2$ complex (1) in $\text{DMSO-}d_6$.

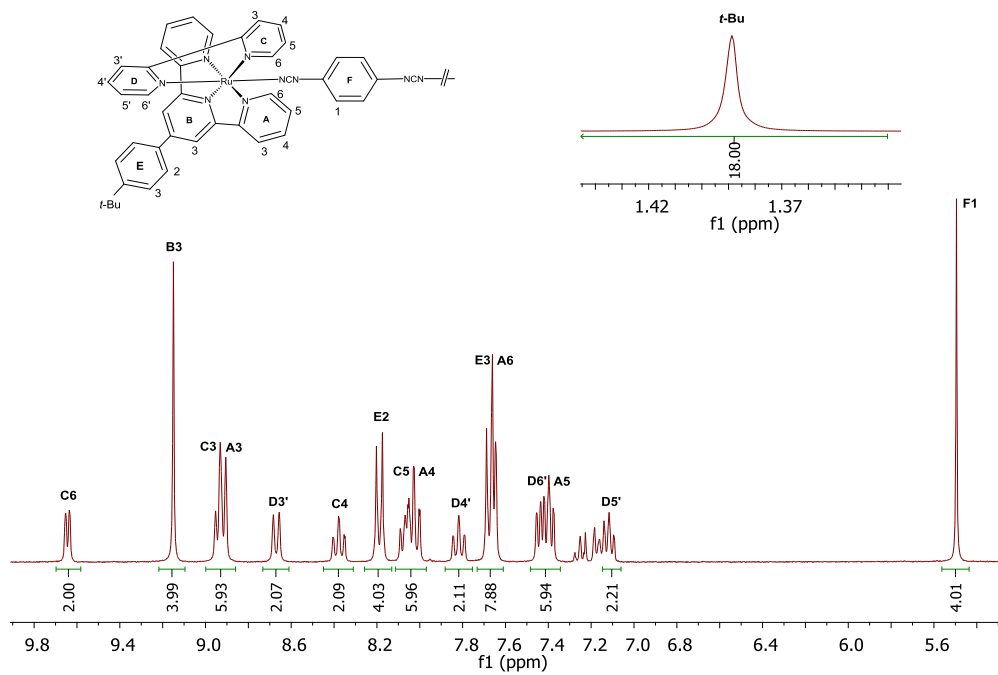


Figure 2.3.11: ^1H NMR spectrum of $[\{\text{Ru}(\text{ttpy})(\text{bpy})\}_2(\mu\text{-dicyd})] [\text{PF}_6]_2$ complex (2) in $\text{DMSO-}d_6$.

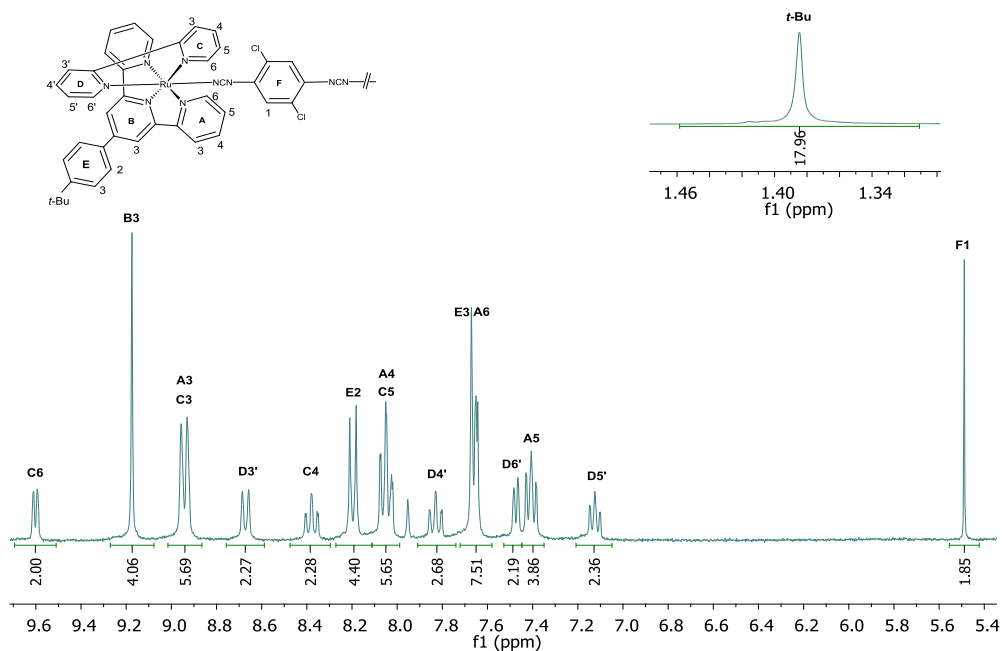


Figure 2.3.12: ^1H NMR spectrum of $[\{\text{Ru}(\text{ttpy})(\text{bpy})\}_2(\mu\text{-Cl}_2\text{dicyd})][\text{PF}_6]_2$ complex (3) in $\text{DMSO-}d_6$.

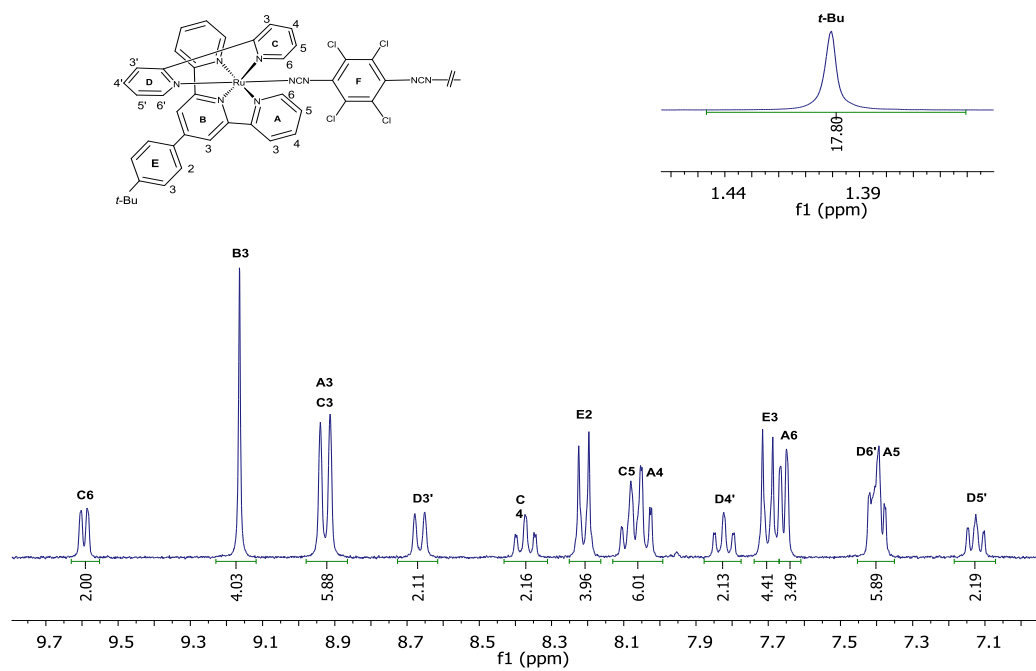


Figure 2.3.13: ^1H NMR spectrum of $[\{\text{Ru}(\text{ttpy})(\text{bpy})\}_2(\mu\text{-Cl}_4\text{dicyd})][\text{PF}_6]_2$ complex (4) in $\text{DMSO-}d_6$.

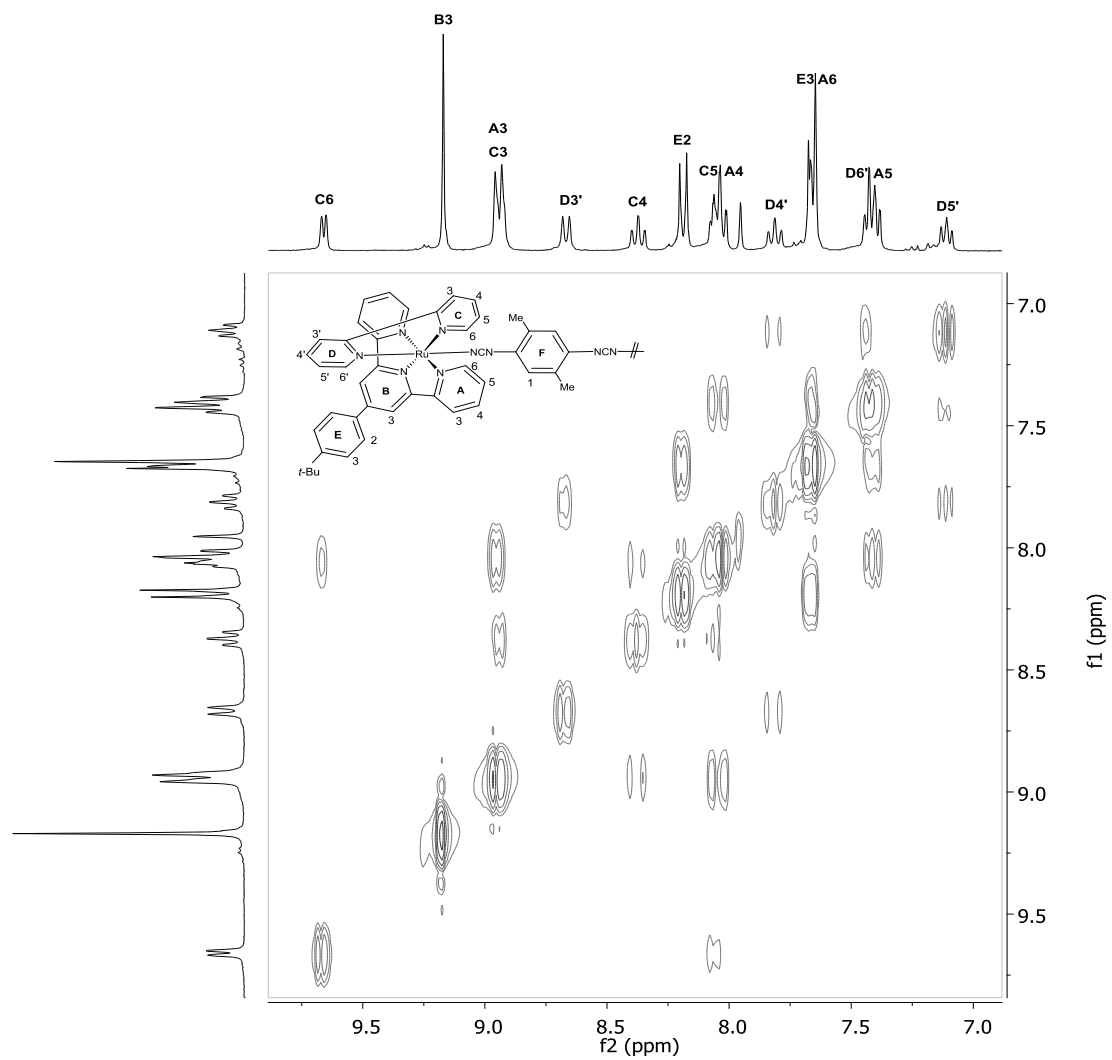


Figure 2.3.14: ^1H - ^1H COSY spectrum of $[\{\text{Ru}(\text{tpy})(\text{bpy})\}_2(\mu\text{-Me}_2\text{dicyd})][\text{PF}_6]_2$ complex (1) in $\text{DMSO-}d_6$.

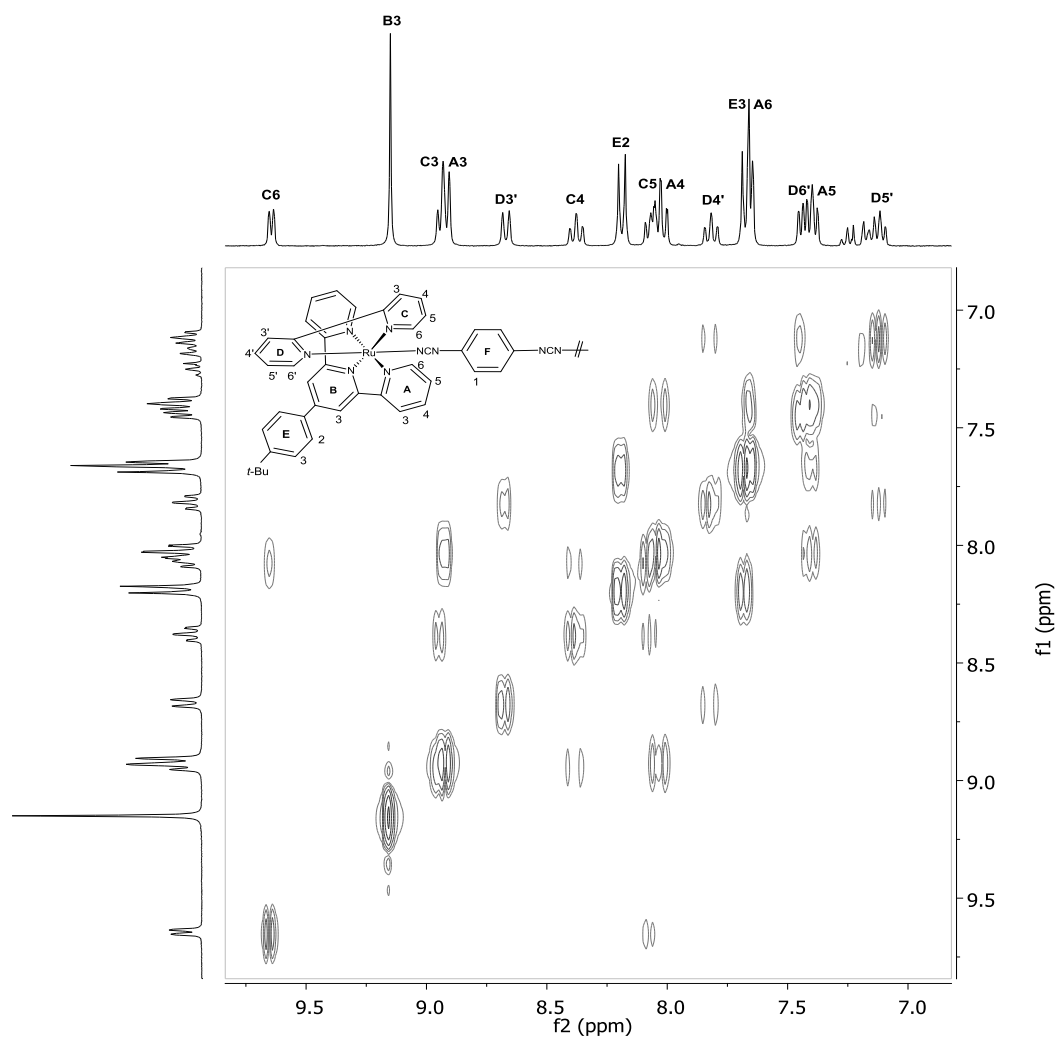


Figure 2.3.15: ^1H - ^1H COSY spectrum of $[\{\text{Ru}(\text{ttpy})(\text{bpy})\}_2(\mu\text{-dicyd})][\text{PF}_6]_2$ complex (2) in $\text{DMSO-}d_6$.

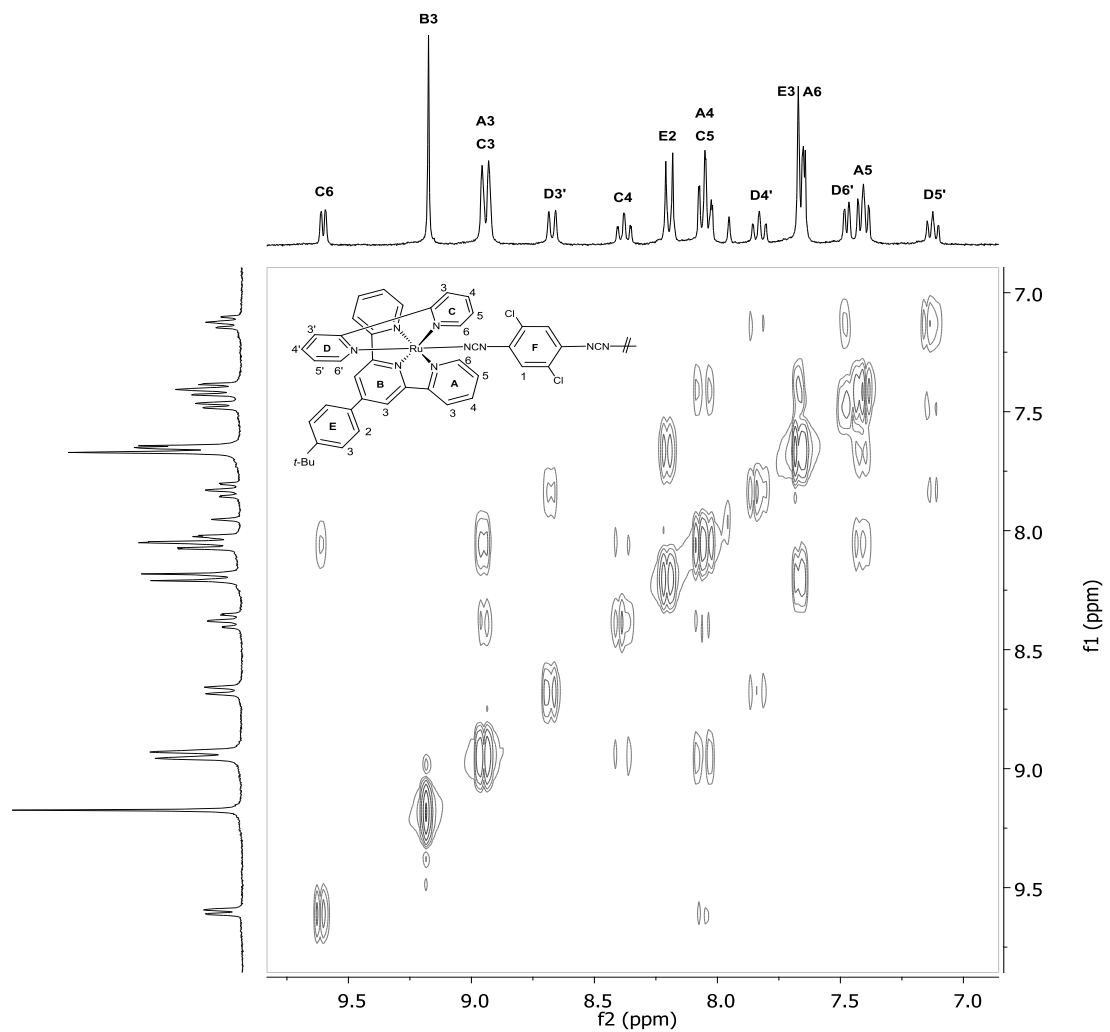


Figure 2.3.16: ^1H - ^1H COSY spectrum of $[\{\text{Ru}(\text{ttpy})(\text{bpy})\}_2(\mu\text{-Cl}_2\text{dicyd})][\text{PF}_6]_2$ complex (3) in $\text{DMSO-}d_6$.

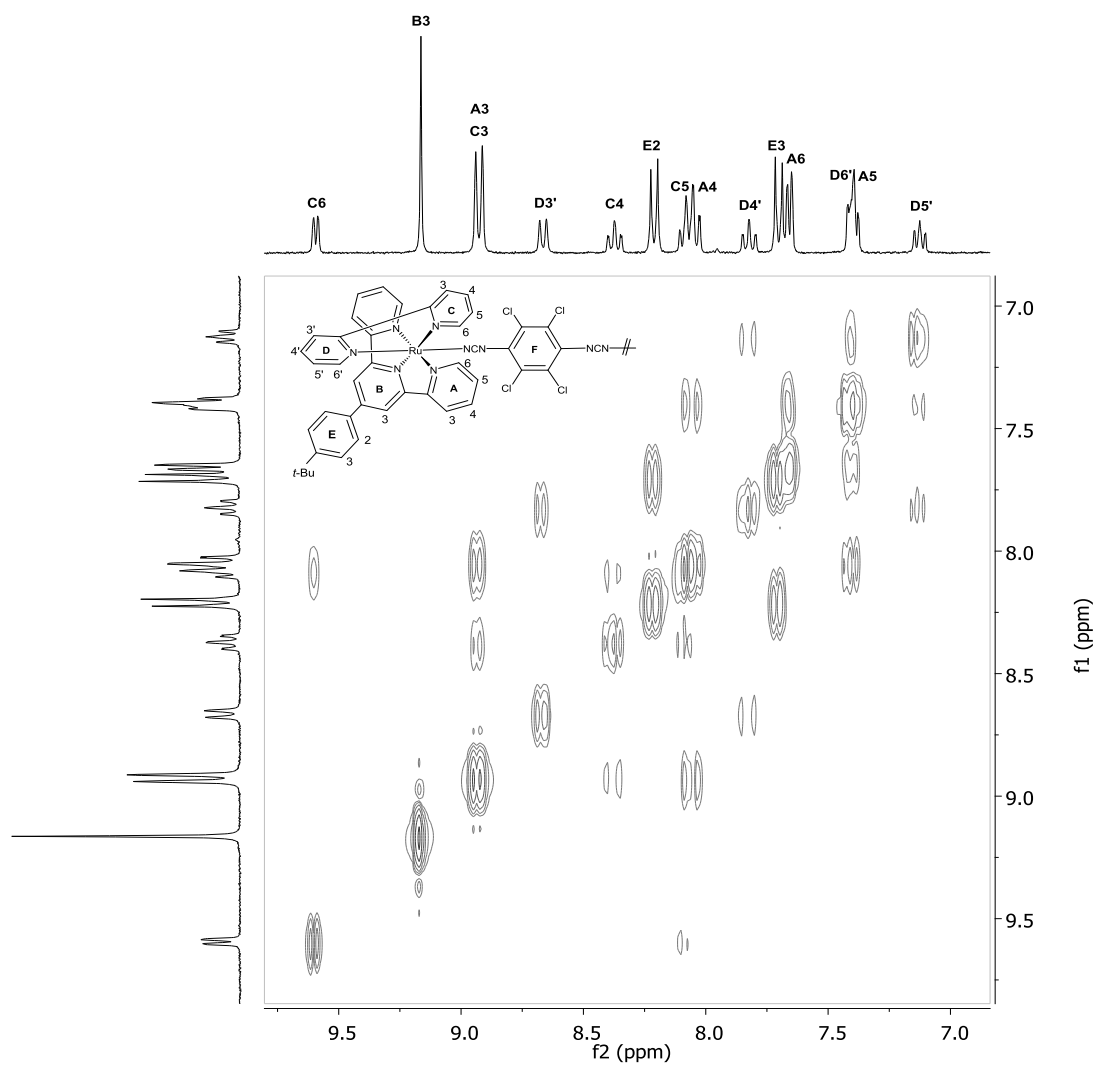


Figure 2.3.17: ^1H - ^1H COSY spectrum of $[\{\text{Ru}(\text{ttpy})(\text{bpy})\}_2(\mu\text{-Cl}_4\text{dicyd})][\text{PF}_6]_2$ complex (4) in $\text{DMSO-}d_6$.

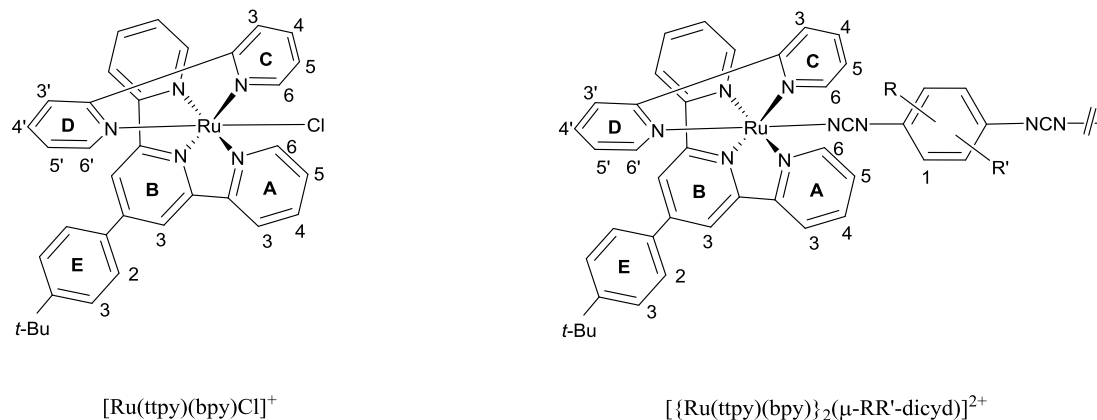


Figure 2.3.18: Numbering scheme used to assign ttpy and bpy proton resonances in $[\text{Ru}(\text{ttpy})(\text{bpy})\text{Cl}] [\text{PF}_6]$ and $[\{\text{Ru}(\text{ttpy})(\text{bpy})\}_2(\mu\text{-R}_2\text{R}_2'\text{dicyd})] [\text{PF}_6]_2$ complexes (**1-4**) in $\text{DMSO-}d_6$.

also appears as the most deshielded signal in the ^1H NMR spectra of $[\text{Ru}(\text{ttpy})_2]^{2+}$ (δ 9.15 ppm) and $[\text{Ru}(\text{ftpy})_2]^{2+}$ (δ 8.98 ppm) complexes where ftpy is 4-fluorophenyl-2,2':6',2''-terpyridine.^{17a-d} In these complexes, B3 protons experience a significant downfield shift relative to those in free ttpy ligand (δ 8.74 ppm), which is attributed to the conformational change of pyridine rings from *trans,trans* in the free ligand to *cis,cis* in the metal complexes, resulting in a significant through-space interaction between B3 protons and A3 protons on adjacent pyridine rings.^{17a-b} The integration value (6H) for the doublet signal at δ 8.91-8.94 ppm corresponds to two overlapping signals from ttpy and bpy ligands. The ttpy component of this signal was assigned to the A3 protons on the basis of characteristic coupling constant ($J = 8.0$ Hz) and the chemical shift values as observed in $[\text{Ru}(\text{ttpy})_2]^{2+}$ and $[\text{Ru}(\text{ftpy})_2]^{2+}$ complexes.^{17a-d} Further support of this assignment was obtained from $^1\text{H-}^1\text{H}$ COSY spectral correlations with other protons in the pyridine ring. The isolated doublet at δ 8.20-8.22 ppm appears exactly at the similar position of the E2 protons of the phenyl ring in $[\text{Ru}(\text{ttpy})_2]^{2+}$ and $[\text{Ru}(\text{ftpy})_2]^{2+}$ complexes

and is recognized by the characteristic coupling constant value ($J = 8.5$ Hz).^{17a-d} The distinction between E2 and E1 protons was made on the basis of the deshielding effect that E2 protons experience via through-space interaction with the B3 protons on the central pyridine ring.^{17a-b} The assignments of other protons on the ttpy ligand (A4, A5, A6 and E3) followed directly from the ^1H - ^1H COSY spectral correlations.

Two pyridine rings (C, D) on the bpy ligand are magnetically non-equivalent. The axial pyridine ring (D) overhanging the central pyridine ring (B) of the ttpy ligand experiences strong diamagnetic anisotropic field of aromatic ring current of the latter and the proton resonances corresponding to this ring (D) usually occur in the upfield region relative to those of the equatorial pyridine ring (C).^{17e-i} Thus the most *up-field* triplet at $\delta 7.15$ ppm was assigned to D5' protons due to their closest proximity to the diamagnetic ring current of the underlying pyridine ring of the ttpy ligand. The assignment of D6' protons was then made with the help of ^1H - ^1H COSY spectral correlation with D5' protons. The doublet signal in the most downfield region ($\delta 9.59$ - 9.66 ppm) was assigned to the C6 protons on the bpy ligand on the basis of the characteristic coupling constant value ($J = 5.1$ Hz) of the protons on the carbon adjacent to the nitrogen atom in the pyridine ring.^{17e-i} This assignment was further supported by ^1H - ^1H COSY spectroscopy. Like the terpyridine system, the C3 and D3' protons on the adjacent pyridine rings on the bpy ligand also experience through-space interaction and are deshielded. These two protons were identified by their characteristic coupling constant values ($J = 8.1$ Hz).^{17e-i} The assignments of C4, C5 and D4' protons were made directly from the coupling patterns observed in the ^1H - ^1H COSY spectrum of the complex.

The signal from the *t*-butyl protons was observed as a sharp singlet at δ 1.38-1.40 ppm which coincides with those in other known complexes.^{17b} The signals (δ 5.24-5.49 ppm) from phenyl ring protons on the bridging R_2R_2' dicyd²⁻ ligands are well-separated from those of ttpy and bpy ligands and could be assigned without any complication.

2.3.6 Electronic Absorption Spectroscopy

The quantitative electronic absorption spectra of all dinuclear $[\{Ru(tpy)(bpy)\}_2(\mu-R_2R_2'dicyd)]^{2+}$ complexes (**1-4**) in DMF are shown in the Figure 2.3.19 and the corresponding absorption data, including those of their oxidized forms (**1⁺-4⁺** and **1²⁺-4²⁺**), are provided in the Table 2.3.3.

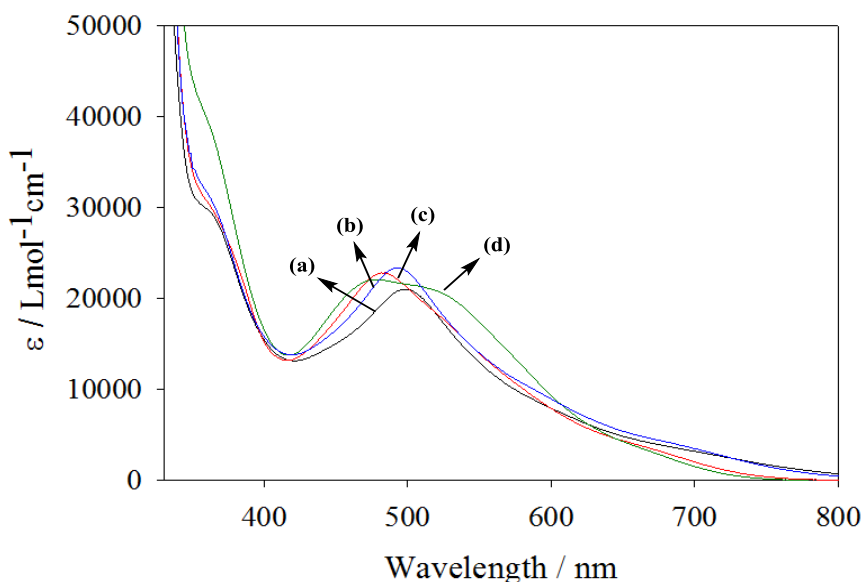


Figure 2.3.19: Quantitative electronic absorption spectra of $[\{Ru(tpy)(bpy)\}_2(\mu-R_2R_2'dicyd)] [PF_6]_2$ complexes in DMF. $R_2R_2'dicyd = Me_2-$ (a); unsubstituted, H_4- (b); Cl_2- (c); Cl_4- dicyd (d).

Table 2.3.3: Quantitative Electronic Absorption Data^a of [$\{\text{Ru}(\text{tpp})\}_2(\mu\text{-R}_2\text{R}'_2\text{dicyd})$][PF₆]₂ Complexes (**1-4**) and their Oxidized Forms (**1⁺-4⁺**, **1²⁺-4²⁺**) in DMF.^b

Complexes	Absorption / Wavelength, λ in nm (Molar Extinction Coefficient, ϵ / $\text{Lmol}^{-1}\text{cm}^{-1}$) ^a
$[\{\text{Ru}(\text{tpp})(\text{bpy})\}_2(\mu\text{-Me}_2\text{dicyd})]^{2+}$	364 (sh,29300), 498 (21000)
$[\{\text{Ru}(\text{tpp})(\text{bpy})\}_2(\mu\text{-Me}_2\text{dicyd})]^{3+}$	399 (sh,23900), 491 (22300), 1023 (13300)
$[\{\text{Ru}(\text{tpp})(\text{bpy})\}_2(\mu\text{-Me}_2\text{dicyd})]^{4+}$	463 (24200), 918(17100)
$[\{\text{Ru}(\text{tpp})(\text{bpy})\}_2(\mu\text{-dicyd})]^{2+}$	364 (sh,30600), 493(23400)
$[\{\text{Ru}(\text{tpp})(\text{bpy})\}_2(\mu\text{-dicyd})]^{3+}$	383 (sh,27800), 487 (25000), 1083(17700)
$[\{\text{Ru}(\text{tpp})(\text{bpy})\}_2(\mu\text{-dicyd})]^{4+}$	457 (26700), 959 (27500)
$[\{\text{Ru}(\text{tpp})(\text{bpy})\}_2(\mu\text{-Cl}_2\text{dicyd})]^{2+}$	364 (sh,29800), 482 (22800)
$[\{\text{Ru}(\text{tpp})(\text{bpy})\}_2(\mu\text{-Cl}_2\text{dicyd})]^{3+}$	358 (sh,30300), 426 (30000), 482(27000), 1265(18800)
$[\{\text{Ru}(\text{tpp})(\text{bpy})\}_2(\mu\text{-Cl}_2\text{dicyd})]^{4+}$	482(27000), 855 (9900)
$[\{\text{Ru}(\text{tpp})(\text{bpy})\}_2(\mu\text{-Cl}_4\text{dicyd})]^{2+}$	364 (sh, 38100), 485 (22200)
$[\{\text{Ru}(\text{tpp})(\text{bpy})\}_2(\mu\text{-Cl}_4\text{dicyd})]^{3+}$	430 (37000), 489 (sh,26300), 1376 (25200)
$[\{\text{Ru}(\text{tpp})(\text{bpy})\}_2(\mu\text{-Cl}_4\text{dicyd})]^{4+}$	489 (26000), 869 (8500), 1376 (6300)

^a Wavelength in nm, molar extinction coefficient ($\text{Lmol}^{-1}\text{cm}^{-1}$) in parentheses, ^b electrochemically oxidized spectra taken in 0.1M TBAH in DMF

The electronic absorption spectra of complexes **1-4** (Figure 2.3.19) are characterized by a strong absorption at 482-498 nm ($\epsilon = 21000-23400 \text{ Lmol}^{-1}\text{cm}^{-1}$) and a shoulder at 364 nm ($\epsilon = 27000-30600 \text{ Lmol}^{-1}\text{cm}^{-1}$). These bands are at the typical position of the Ru(II)d π to π^* (tpy/bpy) MLCT transitions and assigned accordingly.²² The MLCT band positions and intensities for complexes **1-4** are also comparable to those of mononuclear [Ru(tpy)(bpy)(R-pcyd)][PF₆] complexes.¹⁴

2.3.7 Cyclic Voltammetry

The Cyclic voltammetry of dinuclear complexes **1-4** and the mononuclear [Ru(tpy)(bpy)Cl][PF₆] complex were performed in DMF at scan rate of 0.1 V/s. The cyclic voltammograms of **1-4** are shown in the Figure 2.3.20 and the corresponding data are placed in the Table 2.3.4. Cyclic voltammetry data of [AsPh₄]₂[R₂R₂'dicyd] salts were reported previously¹ and included here for comparison.

The cyclic voltammetry of the precursor [Ru(tpy)(bpy)Cl][PF₆] complex resulted in a quasi-reversible wave at 1.05 V vs. NHE, which was assigned to the Ru(III/II) couple by comparison with that of the [Ru(tpy)(bpy)Cl][PF₆] complex.²⁹ The CV's of dinuclear complexes (**1-4**) display two quasi-reversible waves in the region between 0.23 V and 1.03 V vs. NHE (Figure 2.3.19). For each couple, the anodic and cathodic waves are of equal current but with peak to peak separation greater than 58 mV. The latter occurs when heterogeneous electron transfer is slow and identifies these one-electron oxidations as quasi-reversible processes. The first redox couple (E1) is positively shifted by about 430 mV while the second redox couple by 310 mV from electron releasing Me₂- to electron withdrawing Cl₄-substituents on the R₂R₂'dicyd²⁻ ligands,

Table 2.3.4: Cyclic Voltammetry Data^a of [Ru(tpy)(bpy)Cl][PF₆] and [{Ru(tpy)(bpy)}₂(μ-R₂R₂'dicyd)][PF₆]₂ Complexes and [AsPh₄]₂[R₂R₂'dicyd] Salts.^b

Ligands/Complex	E1 / V vs. NHE (Δ E _{ca} in mV)	E2 / V vs. NHE (Δ E _{ca} in mV)	ΔE = E2-E1 / V
[AsPh ₄] ₂ [Me ₂ dicyd]	-0.29 (130)	0.35 (60)	0.64
[AsPh ₄] ₂ [dicyd]	-0.21 (125)	0.46 (65)	0.67
[AsPh ₄] ₂ [Cl ₂ dicyd]	0.08 (75)	0.72 (60)	0.64
[AsPh ₄] ₂ [Cl ₄ dicyd]	0.23 (80)	0.83 (70)	0.60
[Ru(tpy)(bpy)Cl][PF ₆]	1.02 (85)	-	-
[{Ru(tpy)(bpy)} ₂ (μ-Me ₂ dicyd)][PF ₆] ₂	0.23 (71)	0.72 (71)	0.49
[{Ru(tpy)(bpy)} ₂ (μ-dicyd)][PF ₆] ₂	0.33 (83)	0.80 (73)	0.47
[{Ru(tpy)(bpy)} ₂ (μ-Cl ₂ dicyd)][PF ₆] ₂	0.54 (66)	0.96 (106)	0.42
[{Ru(tpy)(bpy)} ₂ (μ-Cl ₄ dicyd)][PF ₆] ₂	0.66 (66)	1.03 (110)	0.37

^a E in V vs. NHE, scan rate 0.1 V/s, in 0.1M TBAH in DMF, Fc⁺/Fc used as internal reference, ΔE_{ca} = E_a - E_c in mV, ΔE = E₂ - E₁ in V; ^b Data taken from ref (1)

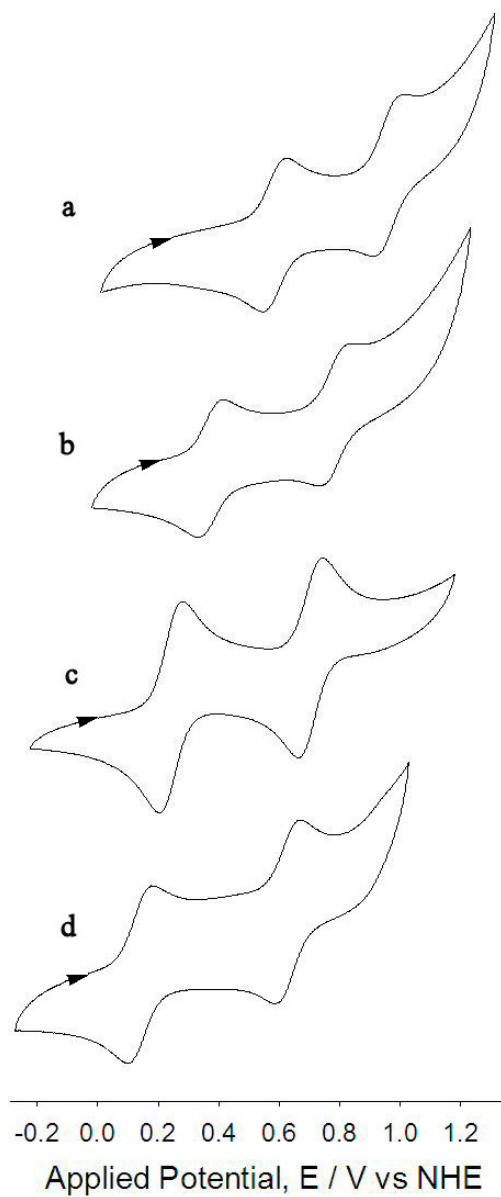


Figure 2.3.20: Cyclic Voltammograms of $[\{\text{Ru}(\text{ttpy})(\text{bpy})\}_2(\mu\text{-R}_2\text{R}'_2\text{dicyd})] [\text{PF}_6]_2$ Complexes (**1-4**) in DMF. Electrolyte 0.1 M TBAH, Scan Rate 0.1 V/s. $\text{R}_2\text{R}'_2\text{dicyd}^{2-} = \text{Cl}_4^-$ (a); Cl_2^- (b); unsubstituted, H_4^- (c); $\text{Me}_2\text{-dicyd}^{2-}$ (d).

indicating large stabilization of the redox orbitals on complexes by the electron withdrawing substituents on the bridging ligand. The EPR spectroscopy provided unambiguous assignment of the first redox couples (E1) of **1-4** to the $L^{\bullet-}/L^{2-}$ couples of the bridging R_2R_2' dicyd $^{2-}$ ligand while both semi-empirical (PM3) calculations and combined vis-NIR and IR spectroelectrochemical studies suggested the second couple (E2) belonging to the $L^0/L^{\bullet-}$ couple of the oxidized R_2R_2' dicyd $^{\bullet-}$ ligands in all dinuclear complexes.

2.3.8 EPR Spectroscopy

The EPR spectroscopic studies were performed on the singly oxidized $[\{Ru(tpy)(bpy)\}_2(\mu-R_2R_2'dicyd)]^{3+}$ complexes (**1⁺**, **2⁺**) in DMF at room temperature to 4 K. For comparison, EPR spectroscopic study was also performed on the mononuclear complex $[Ru(tpy)(bpy)(2,4-Cl_2pcyd)]^{2+}$ complex in DMF at 110 K and the corresponding

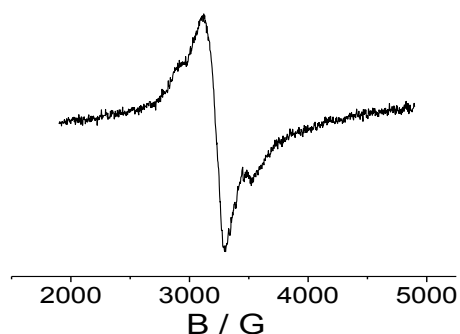


Figure 2.3.21: EPR spectrum of oxidized $[Ru(tpy)(bpy)(2,4-Cl_2pcyd)][PF_6]$ in DMF at 110K.

spectrum is shown in the Figure 2.3.21. The EPR spectra for singly oxidized complexes of unsubstituted (**2⁺**) and Cl_4dicyd^{2-} ligands (**4⁺**) are shown in the Figure 2.3.22 and 2.3.23 respectively.

The mononuclear complex $[\text{Ru}(\text{tpy})(\text{bpy})(2,4\text{-Cl}_2\text{pcyd})]^{2+}$ where tpy is 2,2':6',2''-terpyridine and $2,4\text{-Cl}_2\text{pcyd}^-$ is 2,4-dichlorophenylcyanamide, exhibited a broad EPR signal in DMF at 110 K, and gave anisotropic g values of $g_1, g_2, g_3 = 2.337, 2.100,$ and $1.923,$ respectively and $g_{\text{av}} = 2.127,$ g anisotropy $\Delta g = g_1 - g_3 = 0.414$ (Figure 2.3.21). This feature is very typical of a low spin d^5 Ru(III) ion.²⁴

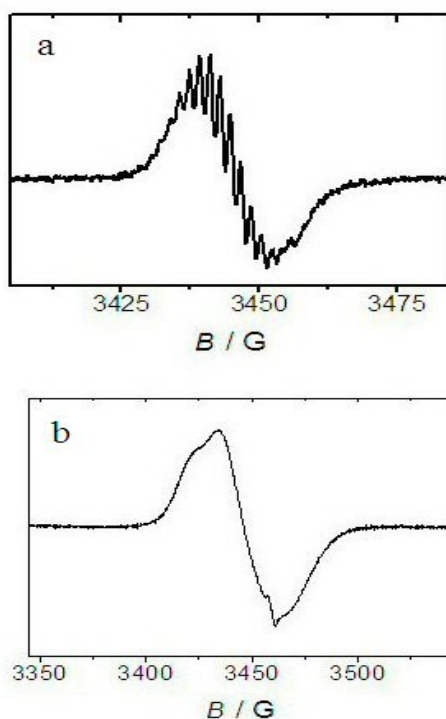


Figure 2.3.22: EPR spectra of $[\{\text{Ru}(\text{tpy})(\text{bpy})\}_2(\mu\text{-dicyd})]^{3+}$ (2^+) in DMF solution at a) room temperature and b) 110K, a weak signal from an organic impurity is observed at $g = 2.003$.

In contrast, the singly oxidized $[\{\text{Ru}(\text{tpy})(\text{bpy})\}_2(\mu\text{-dicyd})]^{3+}$ gave an isotropic EPR spectrum at room temperature with $g = 2.009$ and exhibited several hyperfine lines split by approximately 1.7 G (Figure 2.3.22). The splitting pattern is very similar to that observed in the EPR spectrum of potassium salt of $\text{dicyd}^{\bullet-}$, which is centered at $g = 2.0034$ and exhibited hyperfine coupling of around 1-5 G.^{24f} However, the EPR spectrum

taken at 110 K lacks the hyperfine pattern and shows a sharp and narrow signal with some g anisotropy ($g_1, g_2, g_3 = 2.025, 2.011$ and 1.999 respectively, $\Delta g = g_1 - g_3 = 0.026$). The spectral pattern is very similar to that observed in the EPR spectra of silver salt of 2,5-diiodo-1,4-dicyanamido benzene anion (DI-dicyd $^{\bullet-}$) and in that of ligand centered radical species [$\{\text{Ru}(\text{tpy})(\text{thd})\}_2(\mu\text{-dicyd})\]^+$ ($g = 2.02$) where, tpy is 2,2':6',2''-terpyridine and thd is 2,2,6,6-tetramethyl-3,5-heptanedione.^{8,24h,i} The lack of hyperfine coupling in these radical species has been explained by interaction between anion radical π - system and metallic d -orbitals. Although observed anisotropy in the 100 K EPR spectrum of [$\{\text{Ru}(\text{tppy})(\text{bpy})\}_2(\mu\text{-dicyd})\]^3+$ indicates little contribution of Ru(III) character to the singly occupied molecular orbital (SOMO), the average g value of 2.012 is still consistent with ligand-based radical anion.^{24a}

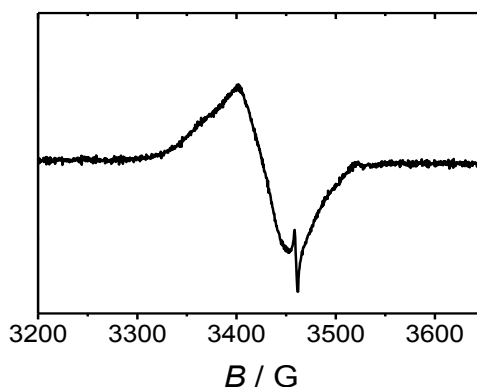


Figure 2.3.23: EPR spectra of [$\{\text{Ru}(\text{tppy})(\text{bpy})\}_2(\mu\text{-Cl}_4\text{dicyd})\]^3+$ in DMF solution at 110K. A weak signal from an organic impurity is observed at $g = 2.003$.

Incorporation of chloro substituents on the dicyd ligand should stabilize the ligand-based HOMO and would exhibit greater contribution of Ru(III) on the SOMO. Indeed, the EPR spectrum of [$\{\text{Ru}(\text{tppy})(\text{bpy})\}_2(\mu\text{-Cl}_4\text{dicyd})\]^3+$ complex at 110 K shows

comparatively broadened signal with significantly large g anisotropy ($g_1, g_2, g_3 = 2.063, 2.029$ and 2.022 respectively, $g_{av} = 2.038$ and g anisotropy $\Delta g = g_1 - g_3 = 0.041$), indicating increased metal character in the singly occupied molecular orbital (SOMO). However, the g values are still consistent with a dominant contribution of the bridging ligand and all singly oxidized $[\{\text{Ru}(\text{tpty})(\text{bpy})\}_2(\mu\text{-R}_2\text{R}_2'\text{dicyd})]^{3+}$ complexes are therefore best described by $\text{Ru}(\text{II})\text{-R}_2\text{R}_2'\text{dicyd}^{\bullet-}\text{-Ru}(\text{II})$. The $[\{\text{Ru}(\text{tpty})(\text{bpy})\}_2(\mu\text{-R}_2\text{R}_2'\text{dicyd})]^{3+/2+}$ couples can be then assigned to $\text{L}^{\bullet-}/\text{L}^{2-}$ couples of the bridging $\text{R}_2\text{R}_2'\text{dicyd}^{2-}$ ligand.

2.3.9 Paramagnetic ^1H NMR Study on Singly Oxidized Complexes

EPR spectroscopy is the method of choice for evaluating the non-innocence of metal complexes containing redox-active ligands and indeed, in this study, EPR has shown that $[\text{Ru}(\text{tpty})(\text{bpy})(2,4\text{-Cl}_2\text{pcyd})]^{2+}$ is a $\text{Ru}(\text{III})$ species with metal-centered spin while $[\{\text{Ru}(\text{tpty})(\text{bpy})\}_2(\mu\text{-R}_2\text{R}_2'\text{dicyd})]^{3+/2+}$ are radical complexes with ligand-centered spin. However, cost and availability of EPR instrumentation to researchers are significant disadvantages and some radical complexes can be EPR silent even at very low temperatures. In these cases, paramagnetic ^1H NMR spectroscopy may provide evidence of SOMO parentage. The oxidized complexes $\mathbf{1}^+ \text{-} \mathbf{4}^+$ were prepared by reacting $\mathbf{1-4}$ with $\text{NO}^+ \text{BF}_4^-$ in acetonitrile solution, checking for completeness by comparison to the spectra of $\mathbf{1}^+ \text{-} \mathbf{4}^+$ as obtained by spectroelectrochemical methods (*vide infra*).

The spectra of $\mathbf{1}^+ \text{-} \mathbf{4}^+$ showed broad, poorly resolved signals belonging to tpty ligand between 6-15 ppm that could not be assigned unambiguously. On the other hand, the *t*-butyl protons seem to be unaffected by oxidation and exhibited an insignificant *downfield* shift by 0.02 ppm relative to its diamagnetic value of 1.38 ppm.^{17b} This is

contrary to a large *upfield* shift of this signal to 1.09 ppm, observed in the ^1H NMR spectrum of Ru(III) centered oxidized $[\text{Ru}(\text{tpy})(\text{bpy})\text{Cl}]^{2+}$ complex. Assuming the pseudo-contact shift contribution is small, the contact shift in the latter complex must arise from spin density being placed on the *t*-butyl hydrogens via combination of both σ and π spin polarization of unpaired electron density originating on Ru (III).^{27,28} The small isotropic shift that is observed in the dinuclear $[\{\text{Ru}(\text{tpy})(\text{bpy})\}_2(\mu\text{-R}_2\text{R}_2'\text{dicyd})]^{3+}$ complexes is therefore not consistent with oxidized Ru(III), suggesting a SOMO which is centered on the bridging $\text{R}_2\text{R}_2'\text{dicyd}^{2-}$ ligand.

Electronic and IR spectroelectrochemistry were performed on the $[\{\text{Ru}(\text{tpy})(\text{bpy})\}_2(\mu\text{-R}_2\text{R}_2'\text{dicyd})]^{2+}$ complexes in order to gain a greater understanding of these complexes with non-innocent ligands and, more specifically, to see if the introduction of more metal character to the SOMO of $[\{\text{Ru}(\text{tpy})(\text{bpy})\}_2(\mu\text{-R}_2\text{R}_2'\text{dicyd})]^{3+}$ results in significantly perturbed electronic and IR spectra.

2.3.10 Vis-NIR Spectroelectrochemistry

Vis-NIR spectra of both singly and doubly oxidized complexes ($\mathbf{1}^+-\mathbf{4}^+$, $\mathbf{1}^{2+}-\mathbf{4}^{2+}$) were recorded in DMF solution using Optically Transparent Thin Layer Electrochemical (OTTLE) cell and are shown in the Figure 2.3.24-2.3.27. The vis-NIR spectroelectrochemical data on the free anionic dicyd^{2-} ligand was reported previously;⁹ and included here with those of the dinuclear complexes in the Table 2.3.3. All complexes show good reversibility upon single electron oxidation while the second oxidation is not very reversible (less than 90% recovery of the initial spectrum).

In general, the vis-NIR spectra of singly oxidized complexes $\mathbf{1}^+-\mathbf{4}^+$ feature a gradually developing NIR band at 1023-1376 nm (Figure 2.3.24 a – 2.3.27a). Upon

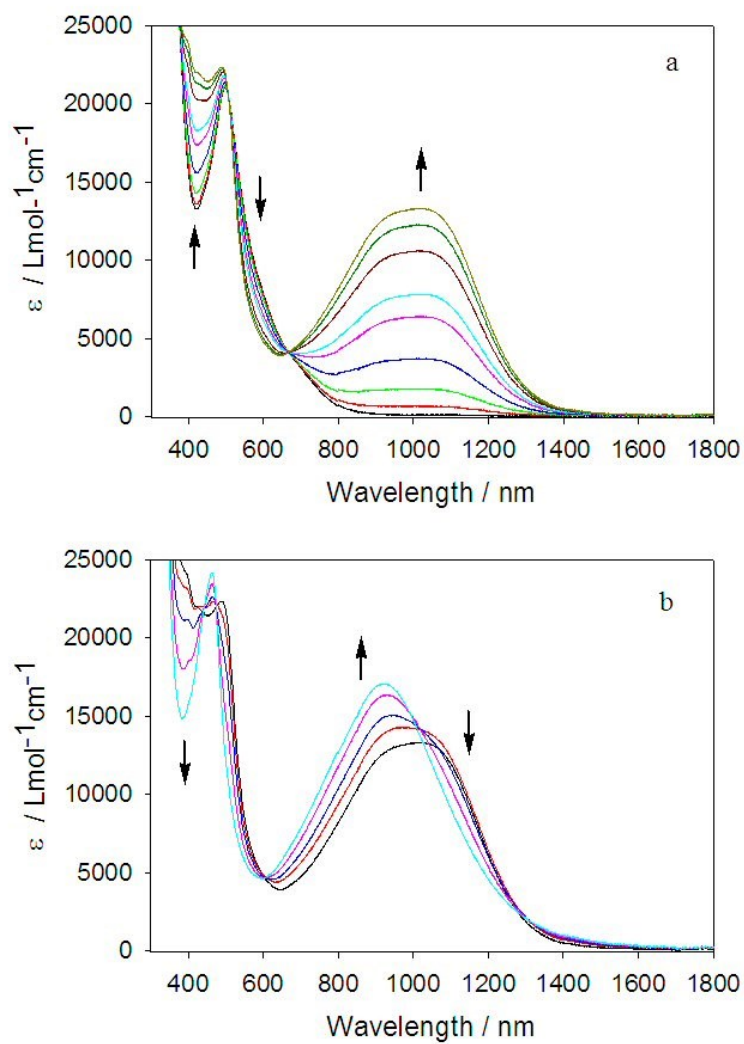


Figure 2.3.24: Vis-NIR spectroelectrochemical oxidation of $[\{\text{Ru}(\text{tpp})(\text{bpy})\}_2(\mu\text{-Me}_2\text{dicyd})]^{2+}$ to form a) $[\{\text{Ru}(\text{tpp})(\text{bpy})\}_2(\mu\text{-Me}_2\text{dicyd})]^{3+}$ and b) $[\{\text{Ru}(\text{tpp})(\text{bpy})\}_2(\mu\text{-Me}_2\text{dicyd})]^{4+}$ in DMF, 0.1 M TBAH. a) 0 – 0.44 V, b) 0.68 – 0.80 V vs. Ag / AgCl.

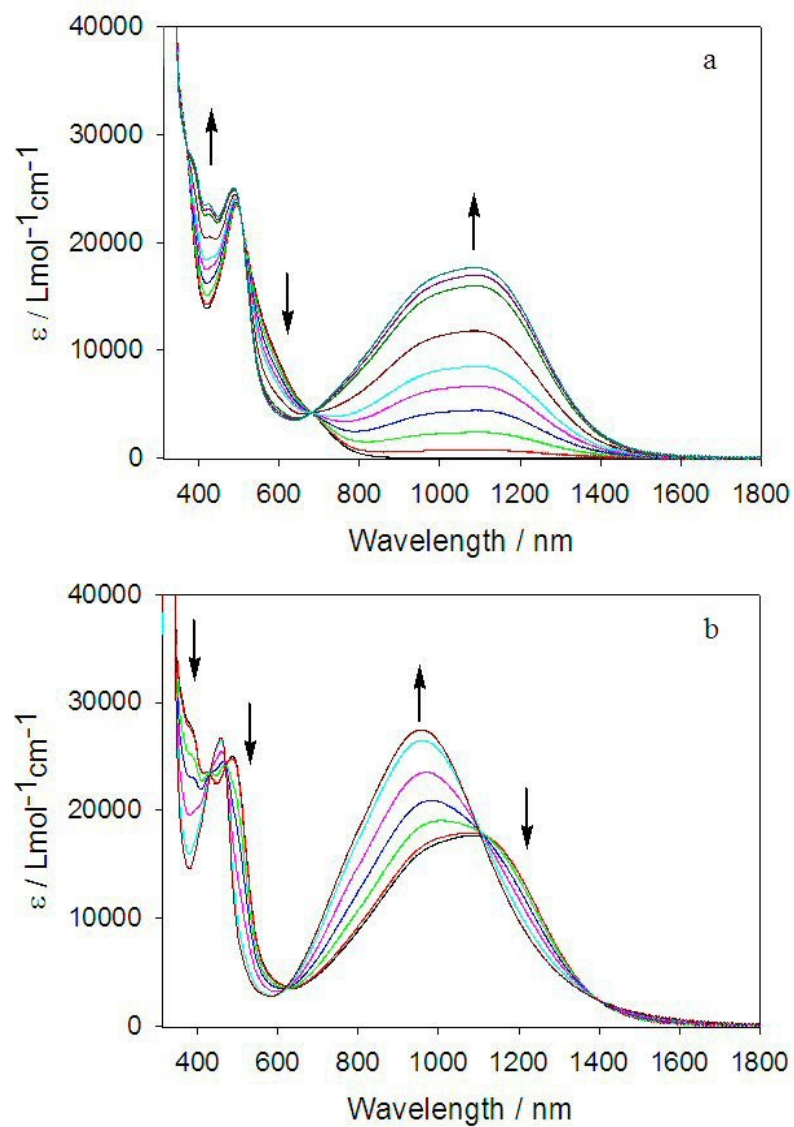


Figure 2.3.25: Vis-NIR spectroelectrochemical oxidation of $[\{\text{Ru}(\text{tpy})(\text{bpy})\}_2(\mu\text{-dicyd})]^{2+}$ to form a) $[\{\text{Ru}(\text{tpy})(\text{bpy})\}_2(\mu\text{-dicyd})]^{3+}$ and b) $[\{\text{Ru}(\text{tpy})(\text{bpy})\}_2(\mu\text{-dicyd})]^{4+}$ in DMF, 0.1 M TBAH. a) 0 – 0.66 V, b) 0.85 – 0.98 V vs. Ag / AgCl.

second oxidation to $\mathbf{1}^{2+}$ - $\mathbf{4}^{2+}$, the NIR band gradually loses its intensity with the growth of a high energy band at 855-959 nm (Figure 2.3.24 b– 2.3.27 b).

Single electron oxidation of $\mathbf{1-4}$ forming $\mathbf{1}^+$ - $\mathbf{4}^+$ resulted in a growth of a NIR band at 1023-1276 nm (Figure 2.3.24 a-2.3.27a), which are bathochromically shifted from electron releasing Me_2 - to electron withdrawing Cl_4 -substituents on the bridging ligand. The positions and intensities of the NIR bands are comparable to those of the $[\{\text{Ru}(\text{tpy})(\text{thd})\}_2(\mu\text{-dicyd})]^+$ complex containing the bridging $\text{dicyd}^{\bullet-}$ radical anion.⁸ As EPR spectroscopy suggested $\text{Ru}(\text{II})\text{-R}_2\text{R}_2'\text{dicyd}^{\bullet-}\text{-Ru}(\text{II})$ description of singly oxidized species, the electronic transition responsible for NIR absorption is likely to arise from $\text{Ru}(\text{II})\text{-to-R}_2\text{R}_2'\text{dicyd}^{\bullet-}$ MLCT or intra-ligand charge transfer (ILCT) transition involving $p\pi$ MO's in the oxidized $\text{R}_2\text{R}_2'\text{dicyd}^{\bullet-}$ ligand. In order to settle this issue, density functional (DFT) calculations were attempted, however, the calculations would not converge.¹⁸ Semi-empirical calculations on both neutral ($\mathbf{2}$) and singly oxidized ($\mathbf{2}^+$) complexes showed HOMOs which are predominantly localized on the bridging $\text{R}_2\text{R}_2'\text{dicyd}$ ligands (Figure 2.3.2 and 2.3.3) in agreement the EPR and paramagnetic ^1H NMR spectroscopic results. Calculation on the singly oxidized $\mathbf{2}^+$ is consistent with possible low energy transitions from filled $p\pi$ MO's of the $\text{dicyd}^{\bullet-}$ ligand thereby supporting a mostly ligand-centered transition. The relative low energy shift of the NIR band $\mathbf{3}^+$ and $\mathbf{4}^+$ with respect to those of $\mathbf{1}^+$ and $\mathbf{2}^+$ is consistent with the stabilization of ligand based frontier orbitals by the electron withdrawing chloro-substituents, narrowing the energy gap of electronic transition.

Although first oxidation gave similar Vis-NIR spectroelectrochemical feature for all complexes ($\mathbf{1}^+$ - $\mathbf{4}^+$), the spectral behaviors of doubly oxidized Me_2 - and

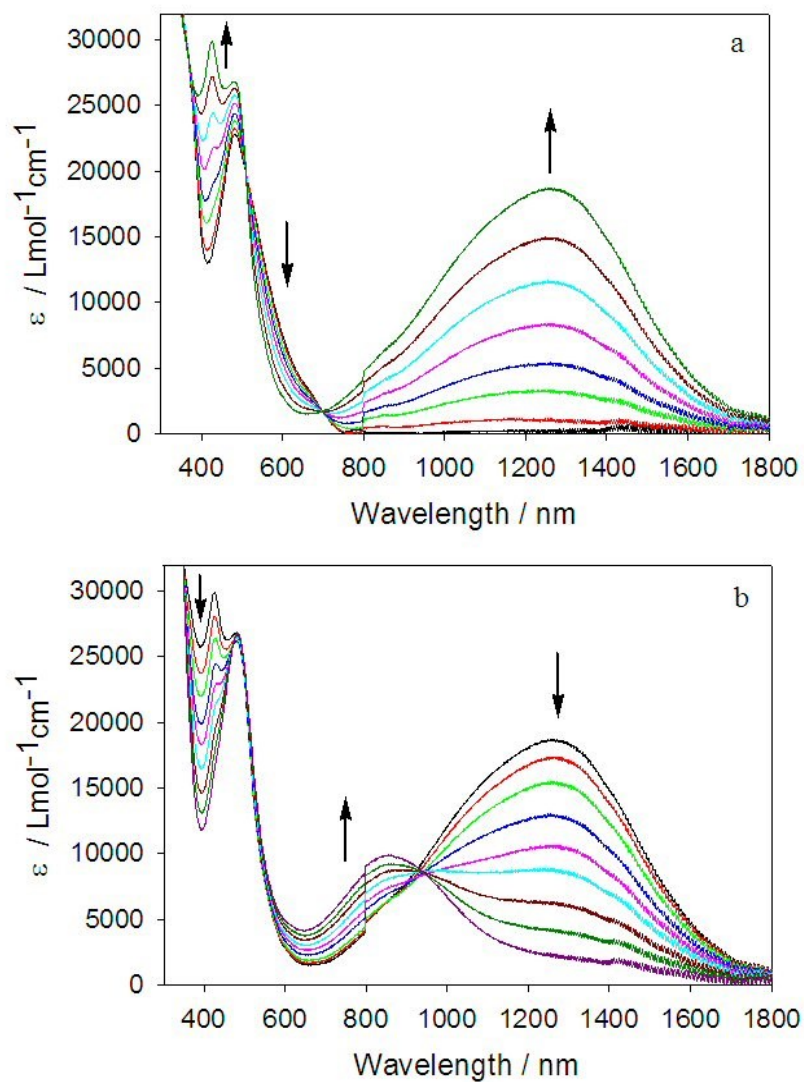


Figure 2.3.26: Vis-NIR spectroelectrochemical oxidation of $[\{\text{Ru}(\text{tpp})(\text{bpy})\}_2(\mu\text{-Cl}_2\text{dicyd})]^{2+}$ to form a) $[\{\text{Ru}(\text{tpp})(\text{bpy})\}_2(\mu\text{-Cl}_2\text{dicyd})]^{3+}$ and b) $[\{\text{Ru}(\text{tpp})(\text{bpy})\}_2(\mu\text{-Cl}_2\text{dicyd})]^{4+}$ in DMF, 0.1 M TBAH. a) 0 – 0.76 V, b) 0.90 – 1.03 V vs. Ag / AgCl.

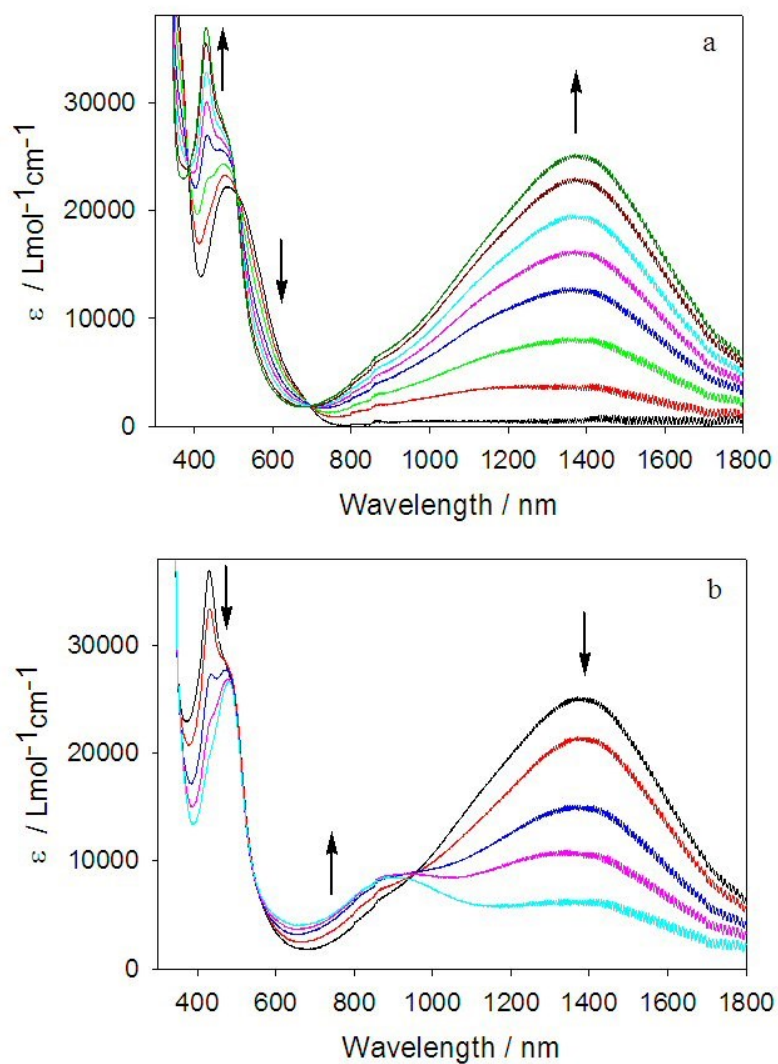


Figure 2.3.27: Vis-NIR Spectroelectrochemical Oxidation of $[\{\text{Ru}(\text{tpy})(\text{bpy})\}_2(\mu\text{-Cl}_4\text{dicyd})]^{2+}$ to form a) $[\{\text{Ru}(\text{tpy})(\text{bpy})\}_2(\mu\text{-Cl}_4\text{dicyd})]^{3+}$ and b) $[\{\text{Ru}(\text{tpy})(\text{bpy})\}_2(\mu\text{-Cl}_4\text{dicyd})]^{4+}$ in DMF, 0.1 M TBAH. a) 0 – 0.86 V, b) 0.97 – 1.0 V vs. Ag / AgCl.

unsubstituted dicyd²⁻ complexes (**1**²⁺, **2**²⁺) were found to be significantly different from that of Cl₂-, Cl₄dicyd complexes (**3**²⁺, **4**²⁺). The second oxidation forming **1**²⁺-**2**²⁺ resulted in an increase in intensity of the NIR band (1010-1023 nm) with slight shift of the band to the higher energies (918-959 nm) (Figure 2.3.24b-2.3.25b). Semi-empirical (PM3) calculation on the **2**²⁺ assuming a singlet ground state, Ru(II)-dicyd⁰-Ru(II), showed mostly a ligand-centered HOMO and LUMO (Figure 2.3.4), arising from the oxidized dicyd^{•-} radical anion to dicyd⁰. However, doubly oxidized diamagnetic *N,N'*-dicyanoquinone diimine (dicyd⁰ or DCNQI in the literature) and its substituted derivatives do not show any NIR absorption.²⁵ The NIR bands for doubly oxidized Me₂- and unsubstituted dicyd²⁻ complexes (**1**²⁺, **2**²⁺) are therefore not easily explained by a ligand-centered transition (ILCT), and it is suggested that, if the structure can be formally represented by Ru(II)-R₂R₂'dicyd⁰-Ru(II), this band is a mostly Ru(II)-to-R₂R₂'dicyd⁰ MLCT transition.

The second oxidation of both Cl₂- and Cl₄dicyd²⁻ complexes forming **3**²⁺ and **4**²⁺ were incomplete due to poor reversibility (Figures 2.3.26 b, 2.3.27 b), however, it resulted in a large shift of the NIR band (1254-1276 nm) to shorter wavelengths (855-888 nm) with significant decrease in intensity relative to those of Me₂- and dicyd²⁻ complexes **1**²⁺ and **2**²⁺. In addition, a low energy weak transition is also observed at 1200-1800 nm for the complexes **3**²⁺-**4**²⁺, which is very different from spectral change associated with the doubly oxidized **1**²⁺-**2**²⁺, and may arise from a significant contribution of the structure Ru(III)-R₂R₂'dicyd^{•-}-Ru(II), exhibiting Ru(II) to Ru(III) MMCT transitions.²⁶

Further evidence for the participation of ruthenium in the **3**⁺ and **4**⁺ complex's SOMO can be found in IR spectroelectrochemical studies.

2.3.11 IR Spectroelectrochemistry

IR spectra for the oxidized species of $[\text{AsPh}_4]_2[\text{Me}_2\text{dicyd}]$, $[\text{Ru}(\text{tpy})(\text{bpy})(2,4\text{-Cl}_2\text{pcyd})][\text{PF}_6]$ and dinuclear $[\text{Ru}(\text{ttpy})(\text{bpy})]_2(\mu\text{-R}_2\text{R}_2'\text{dicyd})][\text{PF}_6]_2$ complexes ($\mathbf{1}^+-\mathbf{4}^+$, $\mathbf{1}^{2+}\text{-}\mathbf{4}^{2+}$) in DMF solution have been taken in the region of $\nu(\text{NCN})$ band ($1800\text{-}2400\text{ cm}^{-1}$) using Optically Transparent Thin Layer Electrochemical (OTTLE) cell and are shown in the Figure 2.3.28-2.3.33. The complexes $\mathbf{1}\text{-}\mathbf{4}$ showed good reversibility upon single electron oxidation while the second oxidation is not very reversible (less than 90% recovery of the initial spectrum). The $\text{Cl}_4\text{dicyd}^{2-}$ complex $\mathbf{4}$ showed poorest reversibility on second oxidation and initial spectrum could not be regenerated even upon rapid reduction.

The IR spectrum of free anionic $\text{Me}_2\text{dicyd}^{2-}$ ligand in DMF solution shows an intense $\nu(\text{NCN})$ band at 2074 cm^{-1} and a far weaker band at 2110 cm^{-1} . Cyanamide groups can adopt *syn*- and *anti*-conformations and so a multiplicity of $\nu(\text{NCN})$ bands is not unexpected. Upon oxidation to the anion radical, the intensity of the band at 2070 cm^{-1} drops and new bands appear at 2120 and 2090 cm^{-1} (Figure 2.3.28 a). Further oxidation to $\text{Me}_2\text{dicyd}^0$ results in a decrease in intensity and new bands appearing at 2170 and 2220 cm^{-1} (Figure 2.3.28 b). Overall, oxidation of $\text{Me}_2\text{dicyd}^{2-}$ to $\text{Me}_2\text{dicyd}^{\bullet-}$ results in a decrease in intensity and a shift of $\nu(\text{NCN})$ to higher frequencies.

Electrochemical oxidation of the mononuclear complex $[\text{Ru}(\text{tpy})(\text{bpy})(2,4\text{-Cl}_2\text{pcyd})]^+$ results in a gradual decrease in $\nu(\text{NCN})$ band at 2160 cm^{-1} with the generation of a low energy band at 2047 cm^{-1} and a very weak band at 2265 cm^{-1} (Figure 2.3.29). The band at 2265 cm^{-1} is associated with decomposition of the complex and indeed only 85% reversibility to the original dication spectrum observed. As EPR spectroscopy has

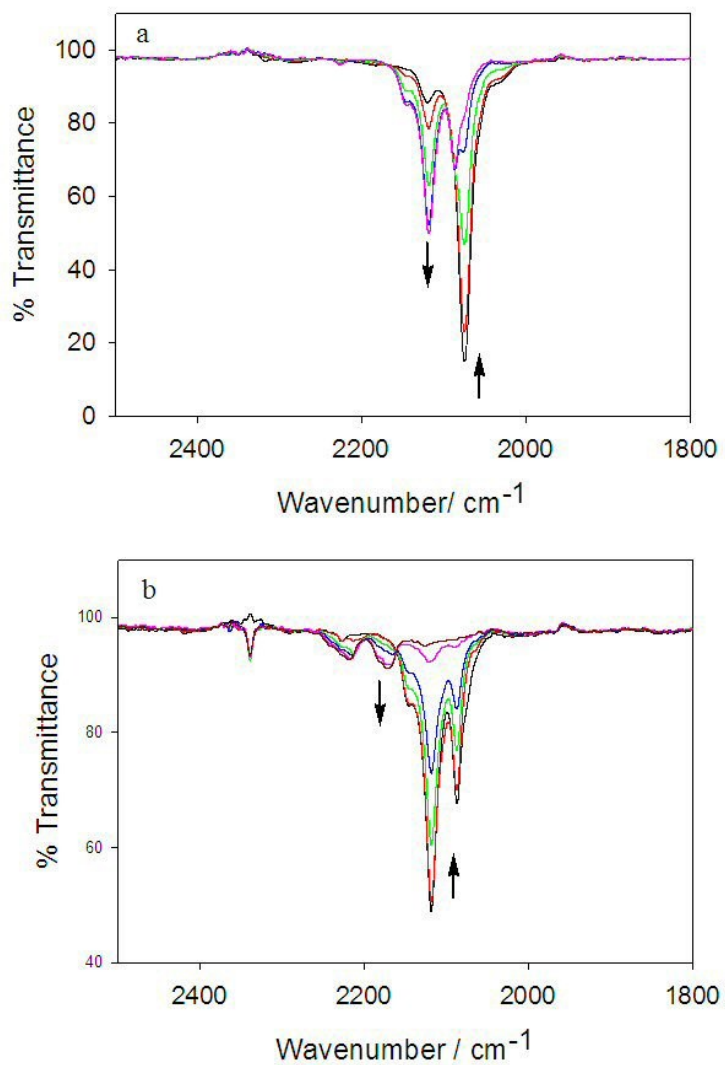


Figure 2.3.28: IR spectroelectrochemical oxidation of Me₂dicyd²⁻ a) to form Me₂-adpc⁻ radical anion and b) to form Me₂-adpc⁰ (Bottom) in DMF, 0.1 M TBAH in DMF, 0.1M TBAH. a) 0 – 0.10 V, b) 0.10 – 0.80 V vs. Ag/ AgCl

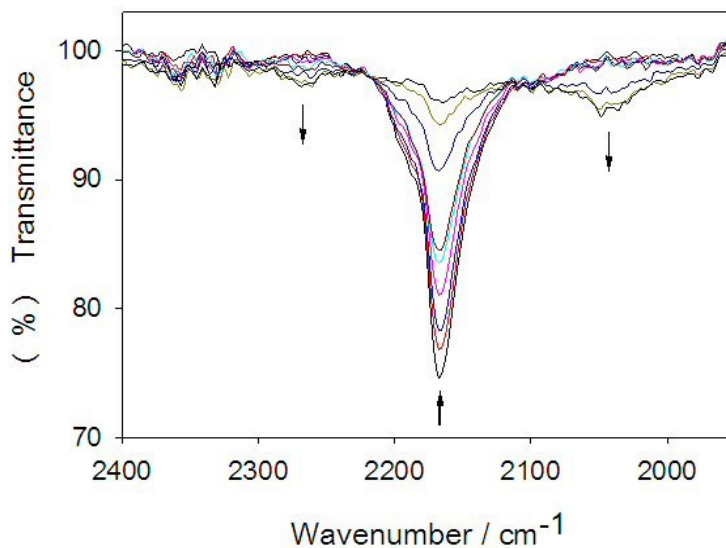
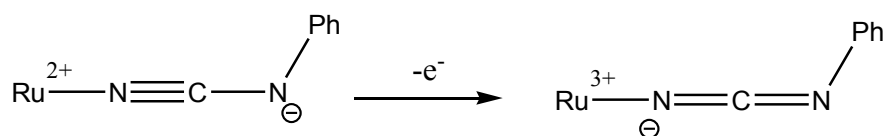


Figure 2.3.29: IR spectroelectrochemical oxidation of $[\text{Ru}(\text{tpy})(\text{bpy})(2,4\text{-Cl}_2\text{pcyd})]^+$ to form $[\text{Ru}(\text{tpy})(\text{bpy})(2,4\text{-Cl}_2\text{pcyd})]^{2+}$ in DMF, 0.1 M TBAH. 0 - 0.74 V vs. Ag / AgCl.

shown that the single electron oxidation of this complex is entirely metal-centered, the low energy 2047 cm^{-1} band is therefore assigned to the $\nu(\text{NCN})$ stretch of the anionic cyanamide ligand coordinated to the oxidized Ru (III) ion. This result is consistent with previous IR spectroscopic studies on $[\text{Ru}(\text{NH}_3)_5(2,3,5,6\text{-Cl}_4\text{pcyd})][\text{PF}_6]_2$ and $[\text{Ru}(\text{NH}_3)_3(\text{bpy})(2,3\text{-Cl}_2\text{pcyd})][\text{PF}_6]_2$ complexes which showed that the $\nu(\text{NCN})$ band shifts to lower frequencies upon oxidation of Ru(II) to Ru(III) because of a shift of cyanamide resonance forms as shown below.⁵



The initial IR spectra of both Me_2 - and unsubstituted dicyd complexes (**1-2**) in DMF show at least two overlapping $\nu(\text{NCN})$ bands at 2106 and 2126 cm^{-1} which are probably due to a mixture of *syn*- and *anti*-conformation in solution (Figure 2.3.30 a-

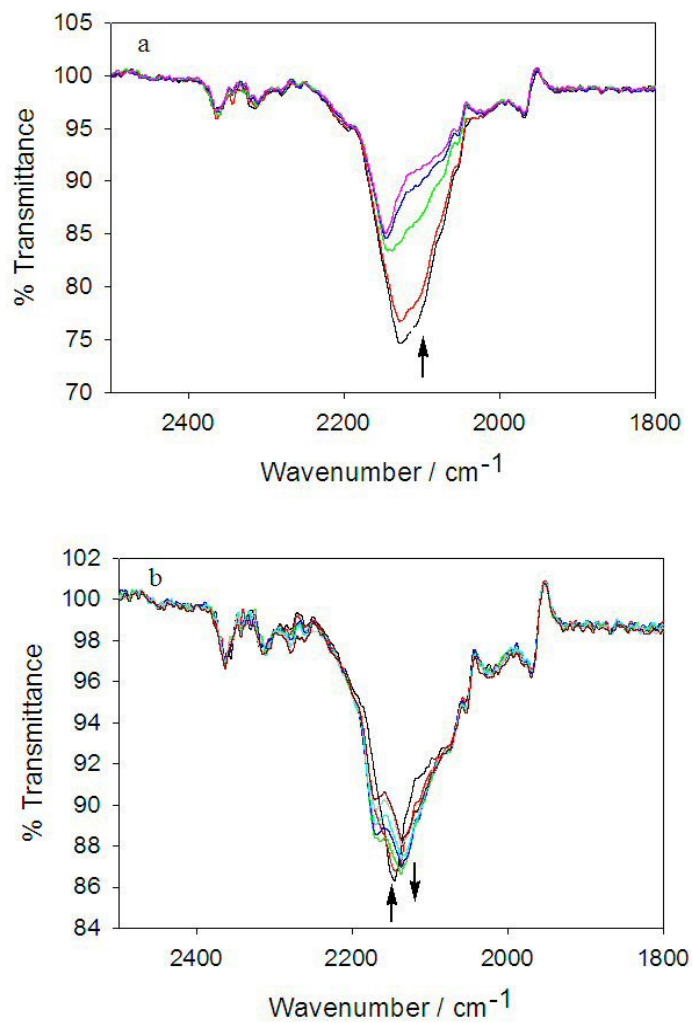


Figure 2.3.30: IR spectroelectrochemical oxidation of $[\{\text{Ru}(\text{tpy})(\text{bpy})\}_2(\mu\text{-Me}_2\text{dicyd})]^{2+}$ to form a) $[\{\text{Ru}(\text{tpy})(\text{bpy})\}_2(\mu\text{-Me}_2\text{dicyd})]^{3+}$ and b) $[\{\text{Ru}(\text{tpy})(\text{bpy})\}_2(\mu\text{-Me}_2\text{dicyd})]^{4+}$, in DMF, 0.1 M TBAH. a) 0 – 0.25 V, b) 0.25 – 0.87 V vs Ag / AgCl.

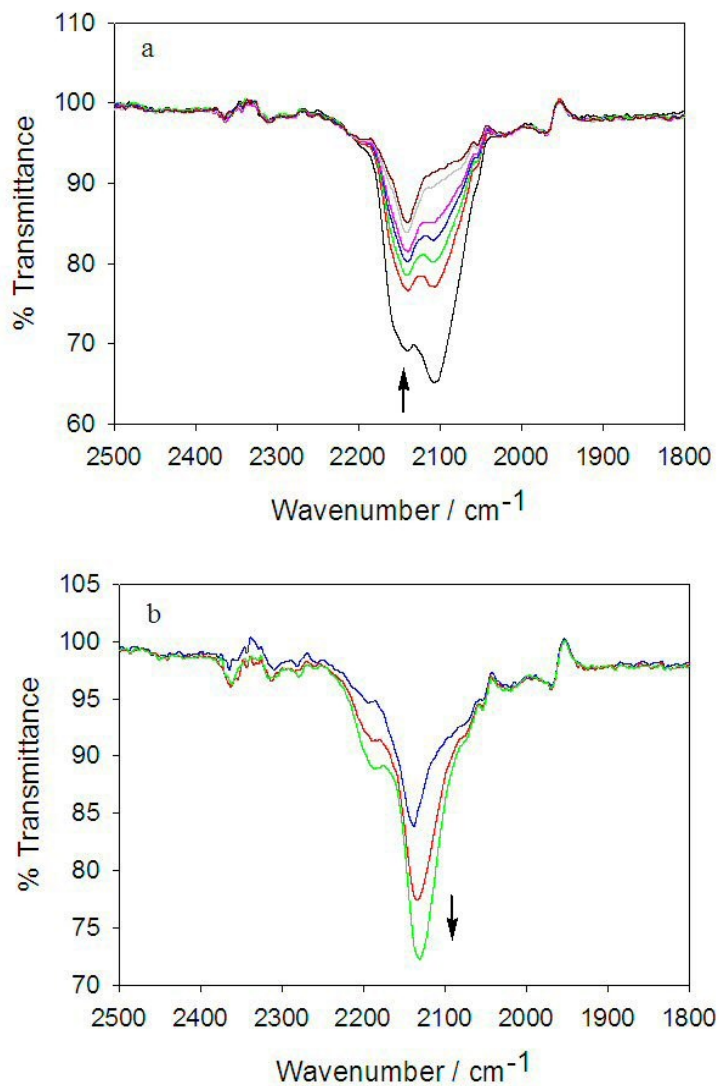


Figure 2.3.31: IR spectroelectrochemical oxidation of $[\{\text{Ru}(\text{tpp})\text{(bpy)}\}_2(\mu\text{-dicyd})]^{2+}$ to form a) $[\{\text{Ru}(\text{tpp})\text{(bpy)}\}_2(\mu\text{-dicyd})]^{3+}$ and b) $[\{\text{Ru}(\text{tpp})\text{(bpy)}\}_2(\mu\text{-dicyd})]^{4+}$, in DMF, 0.1 M TBAH. a) 0 – 0.50 V, b) 0.50 – 0.80 V vs Ag / AgCl.

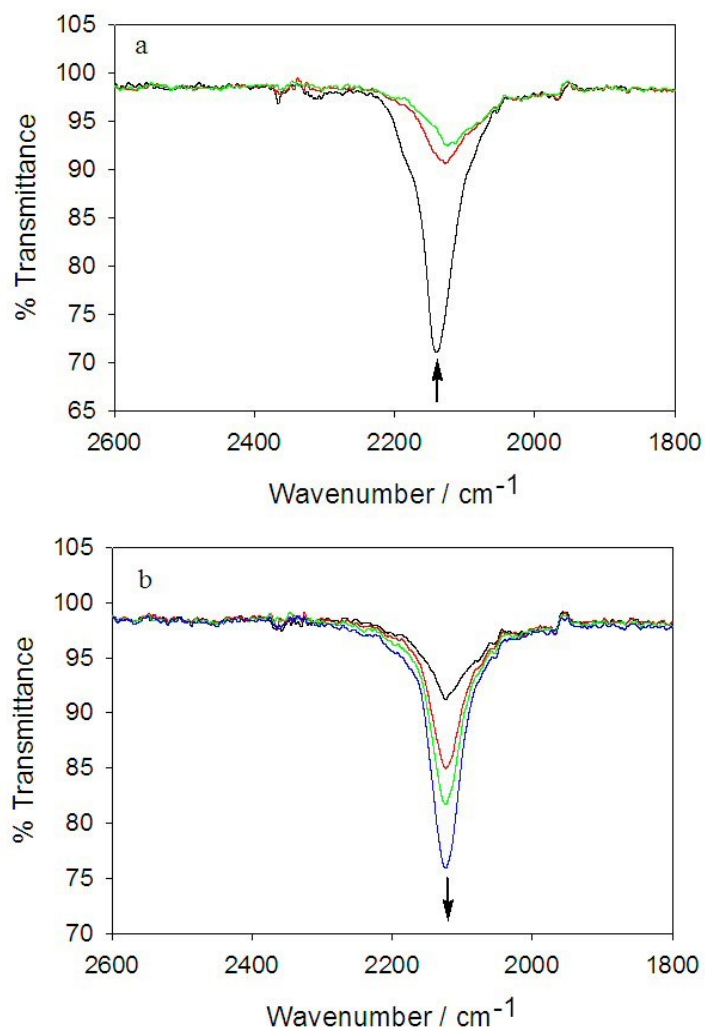


Figure 2.3.32: IR spectroelectrochemical oxidation of $[\{\text{Ru}(\text{tpp})\text{(bpy)}\}_2(\mu\text{-Cl}_2\text{dicyd})]^{2+}$ to form a) $[\{\text{Ru}(\text{tpp})\text{(bpy)}\}_2(\mu\text{-Cl}_2\text{dicyd})]^{3+}$ and b) $[\{\text{Ru}(\text{tpp})\text{(bpy)}\}_2(\mu\text{-Cl}_2\text{dicyd})]^{4+}$, in DMF, 0.1 M TBAH. a) 0 – 0.78 V, b) 0.78 – 0.92 V vs Ag / AgCl.

2.3.31 a). Crystal structure of dinuclear ruthenium complexes bridged by R_2R_2' dicyd²⁻ ligands have shown both *syn*- and *anti*-conformations, however, the most common structure is that of a planar *anti*-conformation. Upon single electron oxidation of **1-2** to **1⁺-2⁺**, the intensity of the $\nu(\text{NCN})$ bands (2106 and 2126 cm^{-1}) decreases with only a slight shift to higher frequencies (Figure 2.3.30 a- 2.3.31 a). Based on EPR results on the complex **2⁺**, the single $\nu(\text{NCN})$ band must be a consequence of a SOMO possessing equivalent contributions from the cyanamide groups of the bridging ligand. Further oxidation to **1²⁺-2²⁺** (Figure 2.3.30 b and 2.3.31 b), slightly shifts the $\nu(\text{NCN})$ band to lower frequency and increases its intensity. Comparing with the spectral change associated the oxidation the mononuclear $[\text{Ru}(\text{tpy})(\text{bpy})(2,4\text{-Cl}_2\text{pcyd})]^+$ (Figure 2.3.29), the low frequency shift of the $\nu(\text{NCN})$ band can be attributed to increased Ru(III) character in the doubly oxidized complexes **1²⁺-2²⁺**. However, as described above, semi-empirical calculation on **2⁺** gave a HOMO that is predominantly centered on the bridging ligand with minor contribution from the ruthenium ion (Figure 2.3.4), supporting a structure having oxidized bridging R_2R_2' dicyd⁰ ligand. The IR spectroelectrochemical oxidations of **3** forming the **3⁺** and **3²⁺** (Figure 2.3.32 a-b) are also very similar to results for **1-2** forming **1⁺-2⁺** and **1²⁺-2²⁺**, respectively. Oxidation of **4** shows significantly different behavior.

In Figure 2.3.33, the oxidation of **4** to **4⁺** in DMF causes a decrease in intensity of the $\nu(\text{NCN})$ band at 2150 cm^{-1} and the growth of a new band at 2100 cm^{-1} . This shift to lower frequencies is very different from that of **1⁺-2⁺** (Figure 2.3.30 a- 2.3.31 a) and it

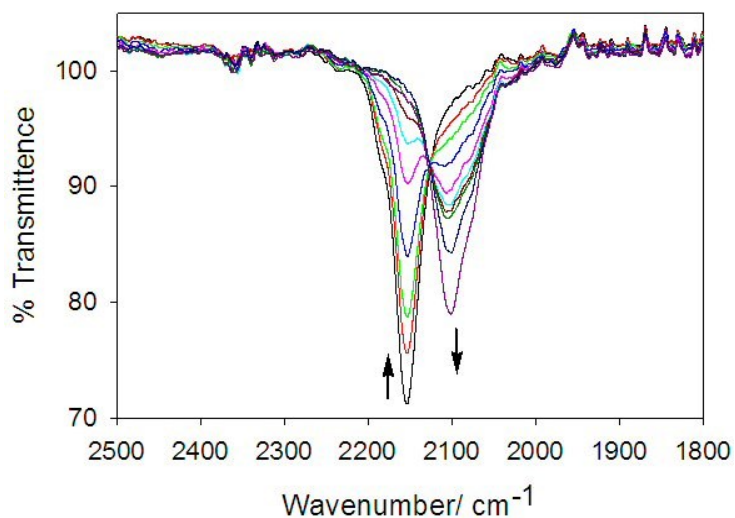


Figure 2.3.33: IR spectroelectrochemical oxidation of $[\{\text{Ru}(\text{tpp})\text{(bpy)}\}_2(\mu\text{-Cl}_4\text{dicyd})]^{2+}$ to form $[\{\text{Ru}(\text{tpp})\text{(bpy)}\}_2(\mu\text{-Cl}_4\text{dicyd})]^{3+}$ in DMF, 0.1 M TBAH. 0–0.90 V vs. Ag / AgCl.

is suggested to be due to a greater contribution of ruthenium character to the SOMO in 4^+ . A single band $\nu(\text{NCN})$ at 2100 cm^{-1} in Figure 2.3.33 is consistent with a delocalized state and indeed 2100 cm^{-1} is the average of Ru(II) and Ru(III) cyanamide stretching frequencies from the Figure 2.3.29. However, as already discussed, the EPR data do not support a ruthenium-centered SOMO and indicate the caution which must be invoked before making state assignments based on IR data alone.

2.4 Conclusion

Four dinuclear complexes $[\{\text{Ru}(\text{tpy})(\text{bpy})\}_2(\mu\text{-R}_2\text{R}_2'\text{dicyd})][\text{PF}_6]$ (**1-4**) were prepared and characterized by ^1H NMR, IR, electronic absorption spectroscopy and cyclic voltammetry. EPR spectra of the $\mathbf{1}^+\text{-4}^+$ ions show predominately organic radical features, confirming ligand-centered spins and thus the complexes' oxidation states are best formulated as $\text{Ru}(\text{II})\text{-R}_2\text{R}_2'\text{dicyd}^{\bullet-}\text{-Ru}(\text{II})$. The paramagnetic ^1H NMR study also supported ligand-centered radical description $\text{Ru}(\text{II})\text{-R}_2\text{R}_2'\text{dicyd}^{\bullet-}\text{-Ru}(\text{II})$ of $\mathbf{1}^+\text{-4}^+$. The EPR data indicates greater contribution of metal to the SOMO of the $\text{Cl}_2\text{-}$ and Cl_4dicyd complexes ($\mathbf{3}^+\text{-4}^+$), suggesting a significant contribution of $\text{Ru}(\text{II})\text{-R}_2\text{R}_2'\text{dicyd}^{2-}\text{-Ru}(\text{III})$ structure. Visible/NIR and IR spectra of $\mathbf{1}^+\text{-4}^+$ and $\mathbf{1}^{2+}\text{-4}^{2+}$ ions were obtained by spectroelectrochemical methods. For the singly oxidized complexes $\mathbf{1}^+\text{-4}^+$, spectral variations were rationalized in terms of the nature of the substituted bridging ligand $\text{R}_2\text{R}_2'\text{dicyd}$ and variable ruthenium d -orbital contributions to the mostly ligand-centered SOMO. Semi-empirical calculations in conjugation with vis-NIR spectroelectrochemistry also suggested a closed-shell valence configuration $\text{Ru}(\text{II})\text{-R}_2\text{R}_2'\text{dicyd}^0\text{-Ru}(\text{II})$ for doubly oxidized complexes $\mathbf{1}^{2+}\text{-4}^{2+}$ with increasing contribution of the triplet structure $\text{Ru}(\text{III})\text{-R}_2\text{R}_2'\text{dicyd}^{\bullet-}\text{-Ru}(\text{II})$ for $\mathbf{3}^{2+}\text{-4}^{2+}$. $[\{\text{Ru}(\text{tpy})(\text{bpy})\}_2(\mu\text{-R}_2\text{R}_2'\text{dicyd})]^{3+}$ showed tunable NIR absorption properties (1023-1376 nm) as a function of the electronic nature of the substituents which is suitable for applications in NIR signal processing devices and in NIR filters.

2.6 References

1. Aquino, M. A. S.; Lee, F. L.; Gabe, E. J.; Bensimon, C.; Greedan, J. E.; Crutchley, R. J. *J. Am. Chem. Soc.* **1992**, *114*, 5130.
2. Naklicki, M.; Crutchley, R. J. *Inorg. Chim. Acta* **1994**, *225*, 123.
3. Rezvani, A. R.; Bensimon, C.; Crompton, B.; Reber, C.; Greedan, J. E.; Kondratiev, V. V.; Crutchley, R. J. **1997**, *36*, 3322.
4. Evans, C. E. B.; Naklicki, M. L.; Rezvani, A. R.; White, C. A.; Kondratiev, V. V.; Crutchley, R. J. *J. Am. Chem. Soc.* **1998**, *120*, 13096.
5. De Rosa, M. C.; White, C. A.; Evans, C. E. B.; Crutchley, R. J. *J. Am. Chem. Soc.* **2001**, *123*, 1396.
6. Evans, C. E. B.; Yap, G. P. A.; Crutchley, R. J. *Inorg. Chem.* **1998**, *37*, 6161.
7. Naklicki, M. L.; Gorelsky, S. I.; Kaim, W.; Sarkar, B.; Crutchley, R. J. *Inorg. Chem.* **2012**, *51*, 1400.
8. Fabre, M.; Jaud, J.; Hliwa, M.; Launay, J.-P.; Bonvoisin, J. *Inorg. Chem.* **2006**, *45*, 9332.
9. Rezvani, A. R.; Evans, C. E. B.; Crutchley, R. J. *Inorg. Chem.* **1995**, *34*, 4600.
10. Constable, E. C.; Harverson, P.; Smlth, D. F.; Whall, L. A. *Tetrahedron* **1994**, *50*, 7799.
11. Hadda, T. B.; Bozec, H. L. *Inorg. Chim. Acta* **1993**, *204*, 103.
12. Gennett, T.; Milner, D. F.; Weaver, M. J. *J. Phys. Chem.* **1985**, *89*, 2787.
13. (a) Mosher, P. J.; Yap, G. P. A.; Crutchley, R. J. *Inorg. Chem.* **2001**, *40*, 1189. (b) Zhang, W.; Bensimon, C.; Crutchley, R. J. *Inorg. Chem.* **1993**, *32*, 5808.
14. Mosher, P. J.; Yap, G. P. A.; Crutchley, R. J.; *Inorg. Chem.* **2001**, *40*, 550.

15. Harb, C.; Kravstov, P.; Choudhuri, M.; Sirianni, E. R.; Yap, G. P. A.; Lever, A. B. P.; Crutchley, R. J. *Inorg. Chem.* **2013**, *52*, 1621.
16. Aquino, M. A. S.; Crutchley, R. J.; Lee, F. L.; Gabe, E. J.; Bensimon, C. *Acta Cryst.* **1993**, *C49*, 1543.
17. (a) Constable, E. C.; Lewis, J.; Liptrot, M. C.; Raithby, P. R. *Inorg. Chim. Acta*, **1990**, *178*, 47. (b) Constable, E. C.; Harverson, P.; Diane, R. S.; Whall, L. *Polyhedron*, **1997**, *16(20)*, 3615. (c) Lashgari, K.; Kritikos, M.; Norrestam, R.; Norrby, T. *Acta Cryst.* **1999**, *C55*, 64. (d) Norrby, T.; Borje, A.; Akermark, B.; Hammarstrom, L.; Alsins, J.; Lashgari, K.; Norrestam, R.; Martensson, J.; Stenhagen, G. *Inorg. Chem.* **1997**, *36*, 5850. (e) Lyttle, F. E.; Petrosky, L. M.; Carlson, L. R. *Anal. Chim. Acta* **1971**, *57*, 239. (f) Orellana, G.; Ibarra, C. A.; Santoro, J. *Inorg. Chem.* **1988**, *27*, 1025. (g) Heijden, M.; van Vliet, P. M.; Reedijk, J. *J. Chem. Soc. Dalton Trans.* **1993**, 3675. (h) Rutherford, T. J.; Reitsma, D. A.; Keene, F. R. *J. Chem. Soc. Dalton Trans.* **1994**, 3659. (i) Bryant, G. M.; Ferguson, J. *Aust. J. Chem.* **1971**, *24*, 441.
18. Serge Gorelsky, personal communication, April 4, 2013. Time-dependent DFT calculations at the B3LYP/DZVP level of theory failed to converge.
19. Crutchley, R. J. *Coord. Chem. Rev.* **2001**, *125*, 219.
20. Crutchley, R. J.; McCaw, K.; Lee, F. L.; Gabe, J. E. *Inorg. Chem.* **1990**, *29*, 2576.
21. Saleh, A. A.; Crutchley, R. J. *Inorg. Chem.* **1990**, *29*, 2123.
22. Evans, C. E. B.; Ducharme, D.; Naklicki, M.; Crutchley, R. J.; *Inorg. Chem.* **1995**, *34*, 1350.

23. Balzani, V.; Juris, A.; Barigelletti, F.; Campagna, S.; Belser, P.; Von Zelewsky, A. *Coord. Chem. Rev.* **1988**, *84*, 85.
24. (a) Kaim, W. *Coord. Chem. Rev.* **1987**, *76*, 187. (b) Weil, J. A.; Bolton, J. T.; Wertz, J. E. *Electron Paramagnetic Resonance*; Willey: New York, **1994**. (c) Kaim, W.; Kasack, V. *Inorg. Chem.* **1990**, *29*, 4696. (d) Roy, S.; Sarkar, B.; Imrich, H.-G.; Fiedler, J.; Zalis, S.; Jimenez-Aparcio, R.; Urbanos, F. A.; Mobin, S. M.; Lahiri, G. K.; Kaim, W. *Inorg. Chem.* **2012**, *51*, 9273. Patra, S.; Sarkar, B.; Mobin, S. M.; Kaim, W.; Lahiri, G. K. *Inorg. Chem.* **2003**, *42*, 6469. (e) Poppe, J.; Moscherosch, M.; Kaim, W. *Inorg. Chem.* **1993**, *32*, 2640. (f) Gerson, F.; Gescheidt, G.; Möckel, R.; Aumüller, A.; Erk, P.; Hünig, S. *Helv. Chim. Acta* **1988**, *71*, 1665. (g) Remenyi, C.; Kaupp, M. *J. Am. Chem. Soc.* **2005**, *127*, 11399. (h) Mori, T.; Inokuchi, H.; Kobayashi, A.; Kato, R.; Kobayashi, H. *Phys. Rev. B* **1988**, *38*, 5913. (i) Sakurai, T.; Nakagawa, N.; Okubo, S.; Ohta, H.; Kanoda, K.; Hiraki, K. *J. Phys. Soc. Jpn* **2001**, *70*(6), 1794.
25. (a) Aumüller, A.; Hünig, S. *Justus Liebigs Ann. Chem.* **1986**, 142. (b) Hünig, H.; Bau, R.; Kemmer, M.; Meixner, H.; Metzenthin, T.; Peter, K.; Sinzger, K.; Gulbis, J. *Eur. J. Org. Chem.* **1998**, 335.
26. (a) Creutz, C.; *Prog. Inorg. Chem.* **1983**, *30*, 1. (b) Crutchley, R. J. *Adv. Inorg. Chem.* **1994**, *41*, 273. (c) Ward, M. D.; *Chem. Soc. Rev.* **1995**, 121. (c) Hush, N. S. *Prog. Inorg. Chem.*, **1967**, *8*, 391. (d) Creutz, C.; Newton, M. D.; Sutin, N.; *J. Photochem. Photobiol. A: Chem.* **1994**, *82*, 47.
27. Distance from Ru(III) to the *t*-butyl group is ca. 10.5 Å and pseudo-contact shift is proportional to $1/r^3$.

28. (a) Drago, R. *Physical Methods for Chemists, Second Ed.*; Surfside Scientific Publishers: Gainsville, **1992**. (b) Bertini, I.; Luchinat, C.; Parigi, G. *Current Methods in Inorganic Chemistry, Solution NMR of Paramagnetic Molecules, Vol.2*; Elsevier, **2001**.
29. Takeuchi, K. J.; Thompson, M. S.; Pipes, D. W.; Meyer, T. J. *Inorg. Chem.* **1984**, *23*, 1845.
30. Krejcik, M.; Danek, M.; Hartle, F. *J. Electroanal. Chem.*, **1991**, *317*, 179

Chapter 3: Redox Ambi-valence of 4,4'-Azodi(phenylcyanamide) Ligands in Dinuclear Ruthenium Complexes

3.1 Introduction

3.1.1 Research Objectives

The bridging 4,4'-azodi(phenylcyanamide) dianion or adpc^{2-} possesses an extended π -conjugation via strong donor(NCN)-acceptor(phenylazo)-donor(NCN) π -interactions.^{1,2} DFT calculations showed that the π -HOMO of adpc^{2-} spans the entire molecule, and if the π -HOMO of adpc^{2-} is in close energy match with the $\text{Ru}(d\pi)$ orbital, an efficient hole-transfer superexchange metal-metal coupling, over longer a metal-metal separation than dicyd^{2-} is possible.^{1,3,4} In addition, unlike dicyd^{2-} , adpc^{2-} also possesses a low energy π -symmetry LUMO (HOMO-LUMO gap 2.6 eV).² that also spans the entire molecule,

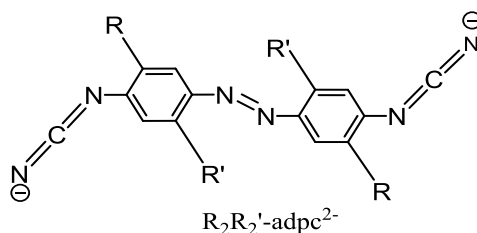


Figure 3.1.1: Substituted 4,4'-azodi(phenylcyanamide) dianion ($\text{R}_2\text{R}'_2\text{-adpc}^{2-}$).

therefore, both hole- and electron-transfer superexchange metal-metal coupling is viable.¹⁻⁴ In this regard, the dinuclear $[\{\text{Ru}(\text{tpy})(\text{bpy})\}_2(\mu\text{-adpc})]^{3+}$ complex has been described as a strongly coupled delocalized Class III mixed-valence molecule on the basis of large comproportionation constant $K_c = 10^{13}$ obtained from the electrochemical data and a low energy NIR inter-valence band (IT) observed at 1920 nm in DMF.¹ In

contrast to a mixed-valence description $\text{Ru}^{2.5+}\text{-R}_2\text{R}_2'\text{adpc}^{2-}\text{-Ru}^{2.5+}$ of these complexes, a gas-phase DFT calculation on the $[\{\text{Ru}(\text{tpy})(\text{bpy})\}_2(\mu\text{-adpc})]^{2+}$ complex strongly suggested that the singly oxidized $[\{\text{Ru}(\text{tpy})(\text{bpy})\}_2(\mu\text{-adpc})]^{3+}$ complex is a ligand-centred radical species $\text{Ru}(\text{II})\text{-adpc}^{\bullet-}\text{-Ru}(\text{II})$. However, assignments solely based on gas-phase DFT calculations are often misleading and unreliable. For example, in a previous study, EPR spectroscopy unambiguously assigned the oxidation state description $\text{Ru}(\text{II})\text{-dicyd}^{2-}\text{-Ru}(\text{III})$ to the $[\{\text{Ru}(\text{NH}_3)_5\}_2(\mu\text{-dicyd})]^{3+}$ complex even though gas-phase DFT calculations supported the dicyd radical description $\text{Ru}(\text{II})\text{-dicyd}^{\bullet-}\text{-Ru}(\text{II})$.⁵ DFT calculations on this molecule could only be reconciled with experimental results when specific solvent-solute donor-acceptor interactions were incorporated in the model. Obviously, $\text{Ru}(\text{II})d\pi$ orbitals are significantly stabilized in an inner coordination sphere of π -acceptor tpy/bpy ligands and it is possible to have a situation in which the π -HOMO of the bridging adpc^{2-} ligand is above the $\text{Ru}(\text{II})d\pi$ orbitals as in $[\{\text{Ru}(\text{ttpy})(\text{bpy})\}_2(\mu\text{-R}_2\text{R}_2'\text{dicyd})]^{3+}$ complexes (Chapter 2). However, electrochemical data show that the $L^{-/2-}$ couple of the free adpc^{2-} is about 0.95V more positive than that of the dicyd^{2-} dianion. In addition, gas-phase DFT calculations (Chapter 1) of free adpc^{2-} show that the π -HOMO of the free adpc^{2-} dianion is about 2.1 eV more stabilized than that of the dicyd^{2-} ligand. Incorporation of electron withdrawing chloro-substituents would further stabilize the π -HOMO of the adpc^{2-} ligand as we already noticed with the $[\{\text{Ru}(\text{ttpy})(\text{bpy})\}_2(\mu\text{-R}_2\text{R}_2'\text{dicyd})]^{3+}$ system (Chapter 2). We therefore questioned the DFT predicted radical-centred $\text{Ru}(\text{II})\text{-adpc}^{\bullet-}\text{-Ru}(\text{II})$ description² of the complex $[\{\text{Ru}(\text{tpy})(\text{bpy})\}_2(\mu\text{-adpc})]^{3+}$ and wished to examine the redox-ambiguity of the bridging $\text{R}_2\text{R}_2'\text{adpc}^{2-}$ ligands in dinuclear $[\{\text{Ru}(\text{tpy})(\text{bpy})\}_2(\mu\text{-R}_2\text{R}_2'\text{adpc})]^{3+/4+}$ as a function of the electronic nature of substituents

(R_2R_2' -) via incorporation of both electron donating and withdrawing substituents on the bridging ligand. Somewhat minor focus pertains to the effect of the bridging *meta* isomer of the $adpc^{2-}$ ligand on the electronics of the dinuclear complexes $[\{Ru(tpy)(bpy)\}_2(\mu\text{-}meta\text{-}adpc)]^{3+/4+}$. To this effect, four research objectives can be stated:

- (i) To synthesize substituted $R_2R_2'adpc^{2-}$ ligands where $R_2R_2'adpc^{2-} = 2,2':5,5'$ -tetramethyl(Me_4)-, $2,2'$ -dimethyl(Me_2)-, $3,3'$ -dichloro(Cl_2)-, $2,2':5,5'$ -tetrachloro(Cl_4)-, unsubstituted $4,4'$ -azodi(phenylcyanamide) and unsubstituted $3,3'$ -(*meta*-)azodi(phenylcyanamide) ligands and characterize by elemental analysis, IR, 1H NMR and electronic absorption spectroscopy.
- (ii) To synthesize dinuclear $[\{Ru(tpy)(bpy)\}_2(\mu\text{-}R_2R_2'adpc)]^{2+}$ complexes of bridging $R_2R_2'adpc^{2-}$ ligands and to characterize by elemental analysis, IR, 1H NMR and electronic absorption spectroscopy.
- (iii) To examine the degree of non-innocence of the bridging $R_2R_2'adpc^{2-}$ ligands and assign the most appropriate oxidation state distributions in singly and doubly oxidized dinuclear complexes $[\{Ru(tpy)(bpy)\}_2(\mu\text{-}R_2R_2'adpc)]^{3+,4+}$ complexes by combined EPR, IR, vis-NIR spectroelectrochemistry and DFT calculations, and correlate with the observed electrochemical and spectroscopic properties of complexes.

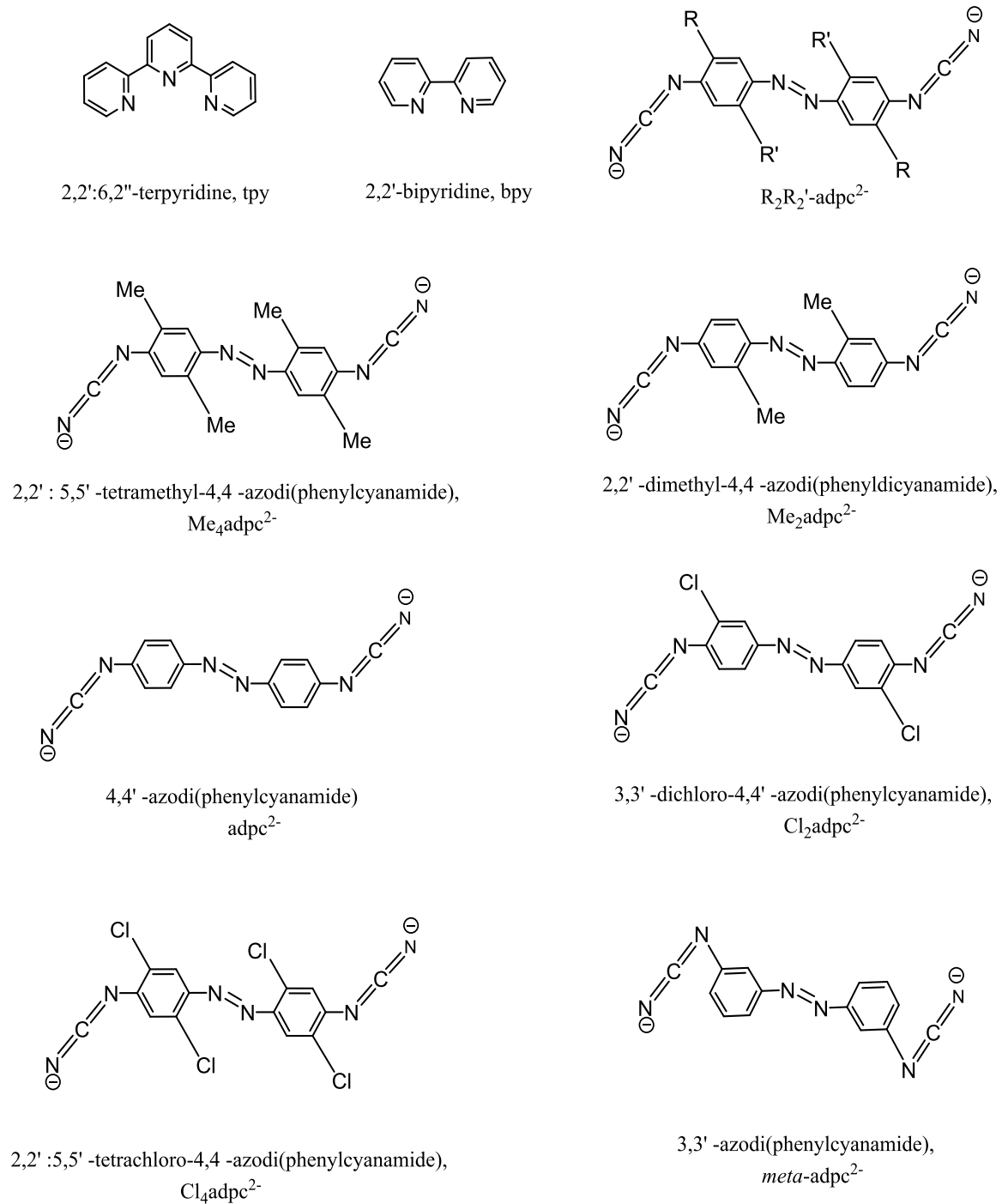
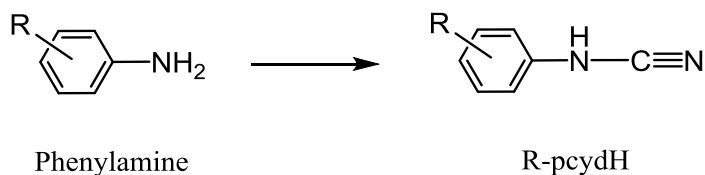


Figure 3.1.2: The bridging R_2R_2' adpc²⁻ and ancillary tpy and bpy ligands used in the synthesis of $[\{Ru(tpy)(bpy)\}_2(\mu-R_2R_2'adpc)]^{2+}$ complexes.

3.2 Synthesis of Substituted Azodicyd (R_2R_2' adpcH₂) Ligands

Syntheses of aromatic cyanamide ligands from phenylamines involve the cyanation of precursor amines following various synthetic protocols.^{19a, 20}

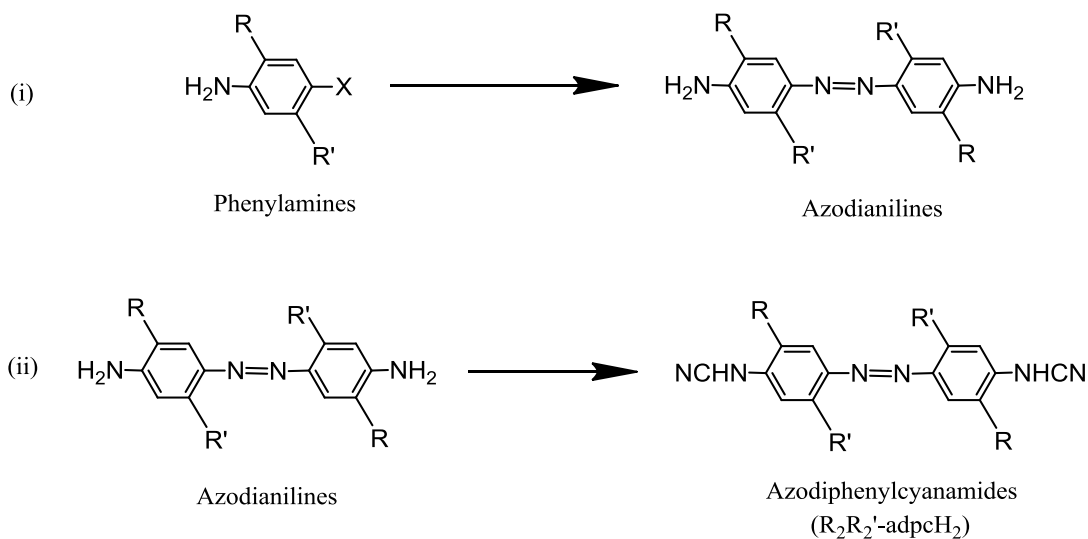
Scheme 3.2.1: Cyanation of Aromatic Amine forming Aromatic Cyanamide.



In the past, substituted phenylcyanamide (R-pcydH) and 1,4-dicyanamide benzene (dicydH₂) could be conveniently prepared from corresponding phenylamines via thiourea method, involving the formation of thiourea derivatives of corresponding phenylamines, followed by hydrolysis, desulfurization, and subsequent acidification of the anionic ligands.^{19a} However, due to commercial unavailability of precursor substituted azodianilines, syntheses of substituted R_2R_2' adpcH₂ ligands had to be performed in two major steps: (i) syntheses of precursor azodianilines from corresponding phenylamines (ii) cyanation of the precursor azodianilines (Scheme 3.2.2). This engendered a significant synthetic challenge because the syntheses of both substituted azodianilines and the corresponding R_2R_2' adpcH₂ ligands were complicated by the electronic nature of substituents, especially those with highly electron withdrawing (Cl₂- and Cl₄-) and releasing (Me₄-) substituents. The electron withdrawing substituents (Cl₂-, Cl₄-) complicated the syntheses of final azodicyd ligands from precursor azodianilines due to deactivation of the corresponding amines for cyanation reactions,

while the syntheses of precursor azodianilines were complicated by both highly electron withdrawing (Cl_2 -, Cl_4 -) and releasing (Me_4 -) substituents. For these particular

Scheme 3.2.2: (i) Preparation of $\text{R}_2\text{R}_2'$ -azodianilines from Phenylamine and (ii) Cyanation of Azodianilines to form Azodi(phenylcyanamide) ($\text{R}_2\text{R}_2'$ -adpcH₂).



compounds, available literature methods proved either inefficient or completely unworkable and this took a huge effort and time on the design and determination of workable and efficient reaction pathways for the syntheses of both substituted azodianilines and corresponding azodicyd ligands. However, this provided an opportunity to experience the synthetic organic chemistry of aromatic amines, nitro/ nitrosoarenes, azo-compounds and aromatic cyanamide ligands and indeed a good number of new precursor aromatic amines, nitroarenes, nitroso and azo compounds were prepared for the synthesis of substituted azodianilines and corresponding azodicyd ligands.

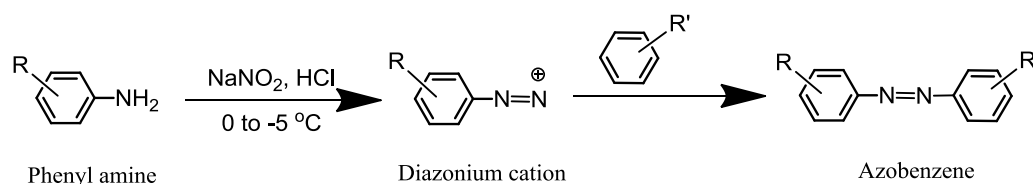
3.2.1 Reviews on the Synthesis of Azobenzene Derivatives

The syntheses of azobenezenes have been driven by their potential applications as dyes and pigments,^{21a} food additives, indicators,^{21b} radical reaction initiators,^{21c} and

recently, by their targeted applications in non-linear optics, optical storages^{21d} and photochemical molecular switches.^{21e} Azobenzenes are generally prepared by using classical azo coupling reaction,²² Mills reaction²³ and the Wallach reaction²⁴. Recently, many methods have been developed to prepare azobenzenes with a range of electron withdrawing and releasing substituents. A review by Merino²⁵ has covered all classical and recently developed methods for the synthesis of azobenzenes from various aromatic amines and nitro compounds.

The classical azo coupling reaction^{22a,b,c} involves initial diazotization of an aromatic amine at low temperature to form the electrophilic diazonium cation, which then undergoes substitution reaction with an activated arenes, usually at the *para* position of the phenyl ring, to form the azobenzene (Scheme 3.2.3).

Scheme 3.2.3: Synthesis of Azobenzenes via Azo Coupling Reaction. R = H, -NO₂; R' = NR₃⁻, -NH₂⁻, -OH.

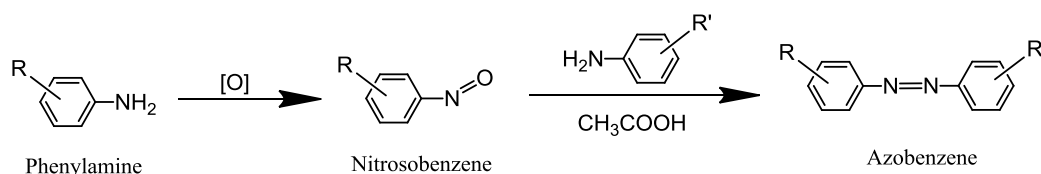


As the diazonium cation is a weak electrophile, it requires strong nucleophilic or activated arenes with donor substituents, like amino (-NH₂), alkyl (-R) or hydroxyl (-OH), for this coupling reaction to take place. The azo coupling reaction is very pH dependent and requires acidic conditions for the diazotization reaction of the precursor amine as well as for the following coupling reaction of the diazonium cation with the amino substituted arenes to prevent undesirable N-N coupling forming amino diazo compound.^{22d} Nucleophilic phenols should be used in their deprotonated forms

(phenoxide ion) to increase their reactivity towards the coupling reaction but highly alkaline conditions also result in the formation of an undesirable diazohydroxy compound which inhibits the coupling reaction.^{22d} Therefore, the coupling of phenols has to be done in mild basic conditions at controlled pH. Although the azo coupling reaction is not very suitable for the synthesis of azobenzenes with electron-withdrawing substituents and sometimes results in poor reaction yields due to the abovementioned side reactions, it is still one of the popular methods for the synthesis of a large number of asymmetric azobenzenes from highly activated aromatic amines.

The classical Mills reaction is another efficient route for the synthesis of a large number azobenzenes.²³ The reaction involves the condensation reaction of aromatic nitroso compounds with aromatic amines in glacial acetic acid. The nitroso derivative can be prepared by the oxidation of the aromatic amine, as shown in the Scheme 3.2.4.

Scheme 3.2.4: Synthesis of Azobenzenes via Mills Reaction.

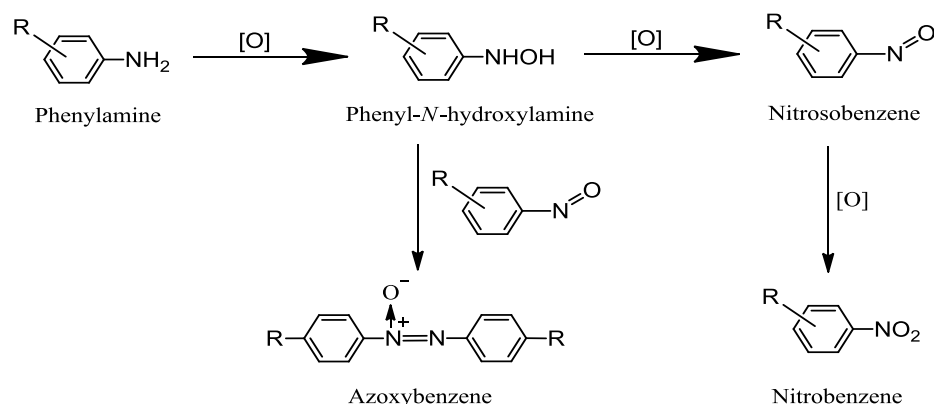


The oxidation of amine forming the precursor nitroso compound is the critical step in this reaction scheme. It involves the formation of intermediate *N*-arylhydroxylamine, which is further oxidized to form the nitroso compound, as shown in the Scheme 3.2.5.

The oxidation of aromatic amine is very sensitive to the reaction conditions, *e.g.*, temperature, solvents and the nature of oxidizing agents and catalysts. A large number of oxidizing agents *e.g.*, ferric chloride,^{23b} Caro's acid (H₂SO₅),^{23c} sodium or

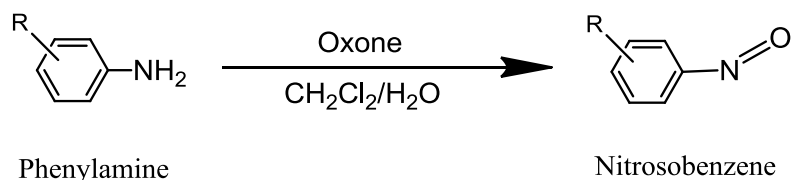
potassium dichromate/H₂SO₄,^{23d} acetic acid/H₂O₂^{23e} etc. have been used to generate the aromatic nitroso compounds with good overall yields. Oxidations using hydrogen peroxide in presence of rhenium,^{23f} tungsten^{23g} or molybdenum^{23h} catalysts also give nitrosoarenes with high reaction yields. However, this heterogeneous reaction is complicated by the instability of the nitroso compound, over-oxidation to nitro-derivative, or condensation of intermediate *N*-aryhydroxyl amine with the nitroso compound forming an undesirable azoxybenzene, as shown in the Scheme 3.2.5. These side reactions are commonly observed with deactivated amines having electron

Scheme 3.2.5: Oxidation of Phenylamine forming Nitrosobenzene: two major side reactions forming Azoxy- and Nitrobenzene.



withdrawing substituents in the *para* or *meta* position, and are favoured by prolonged reaction times as well. Recently, a two-phase heterogeneous system using Oxone in H₂O/CH₂Cl₂ has been used to synthesize nitrosoarenes in high purity and yields (70-80%) (Scheme 3.2.6).^{23i,k} This biphasic system secures the separation of the generally less water-soluble nitroso compound from the precursor anilines and *N*-aryhydroxyl amine intermediates and thereby, prevents the undesirable condensation reaction between the

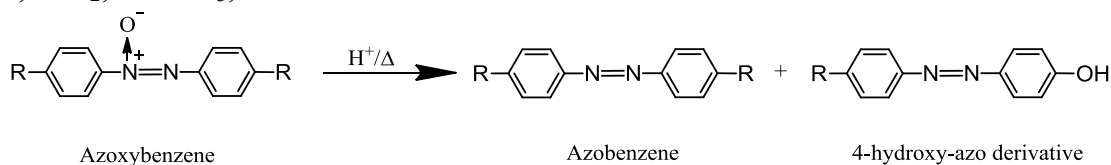
Scheme 3.2.6: Synthesis of Nitrosobenzene from Phenylamines using Oxone in $\text{CH}_2\text{Cl}_2/\text{H}_2\text{O}$ biphasic system. $\text{R} = -\text{CF}_3, -\text{NO}_2, -\text{H}, -\text{Br}$.



nitroso compound and *N*-arylhydroxylamine forming the azoxy compound or that between unreacted amine and nitroso compound forming the azo compound. Oxone biphasic oxidation method appears to be one of the cleanest and efficient methods for the synthesis of nitrosoarenes with electron withdrawing substituents.^{23k} In the present research work, two chloro-substituted nitrosobenzenes have been prepared following this method.

Azobenzenes are also prepared quite conveniently via Wallach reaction,²⁴ which involves the treatment of an azoxybenzene with an acid to form the corresponding azobenzene, as shown in the Scheme 3.2.6.^{24a} The precursor azoxybenzene can be prepared by the reduction of nitrobenzene using alcoholic KOH/acetaldehyde,^{24b} sodium amalgam,^{24c} MeONa,^{24e} H_2/PbO ^{24d} or by the oxidation of aniline using H_2O_2 or $\text{HMnO}_4/\text{HCHO}$.^{24f}

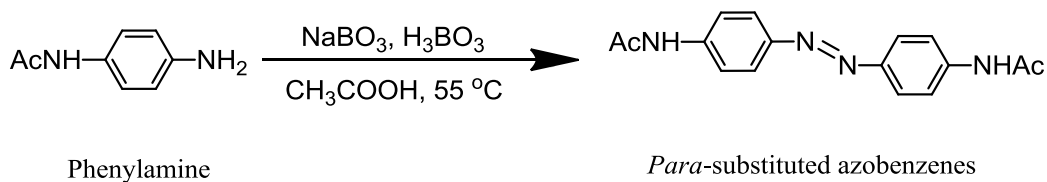
Scheme 3.2.7: Synthesis of Azobenzene from Azoxybenzene via Wallach Reaction. $\text{R} = -\text{H}, -\text{NO}_2, -\text{COCH}_3, -\text{COOH}$.



However, this reaction is very sensitive to the nature of the substituents on azoxybenzene and the product azobenzene often forms with substantial amount of side-products containing 2-hydroxy or 4-hydroxy azo derivatives.^{24g}

A large number of symmetrical substituted azobenzenes have been successfully prepared by direct oxidation of anilines under selective oxidation conditions.²⁵ The electrochemical oxidation of anilines usually gives low yields of azo compounds.^{26a} The aromatic amines are usually oxidized by using $\text{NaBO}_3/\text{acetic acid}$,^{26b} KMnO_4 supported on $\text{CuSO}_4 \cdot 5\text{H}_2\text{O}$,^{26c} $\text{H}_2\text{O}_2/\text{Na}_2\text{WO}_4/\text{Si}_2\text{Cl}_6$,^{26d} variety of metallic and non-metallic reagents like Ag_2CO_3 , AgMnO_4 , $\text{Pb}(\text{OAc})_4$, $\text{RuCl}_3/\text{H}_2\text{O}_2$, bispyridine silver permanganate, $[\text{PhI}(\text{OAc})_2]$ or under aerobic oxidation conditions and the resultant azobenzenes are usually obtained in high purity with average yields (30-50%).²⁵ Oxidation of aromatic amines using sodium perborate/acetic acid is a convenient method for the synthesis of *para*-substituted azobenzenes, as shown in the Scheme 3.2.8.^{26e}

Scheme 3.2.8: Synthesis of Azobenzenes via Perborate/Acetic acid Oxidation method.

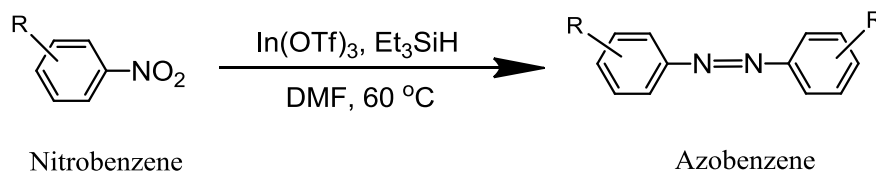


Previous studies have shown that sodium perborate first oxidizes solvent acetic acid to the peroxyacetic acid, which in turn, oxidizes the amine to the corresponding azo compound.^{25e,f} Presumably, the oxidation of amine proceeds through *in situ* formation of the corresponding nitroso compound which then undergoes Mills condensation reaction with the unreacted amine to form the azo compound. However, a successful synthesis of

azo compound following this route requires careful control of temperature and reaction time as well as the optimum oxidant-amine ratio.^{25f} Prolonged reaction time and higher concentration of perborate produces appreciable amount of azoxy compounds, following the formation of the azo compound. Too high reaction temperature (> 55 °C) also leads to the formation of azoxy compound by the condensation of intermediate *N*-arylhydroxyl amine with the nitroso compound. In the present work, the perborate oxidation method has been used to prepare Me₄-azodiacetanilide, the precursor for Me₄-azodianiline.

Another widely practiced method for the synthesis of azobenzenes is the reductive coupling of nitrobenzene using reducing agents, like LiAlH₄, NaBH₄, KOH, Zn/NaOH or sodium 2-hydroxy ethoxide, In(OTf)₃/Et₃SiH etc.,²⁵ as shown in the Scheme 3.2.9.²⁷

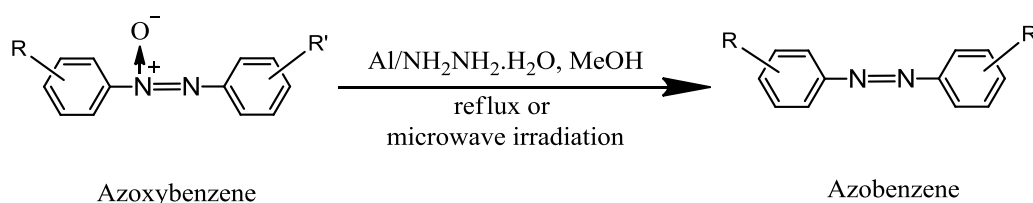
Scheme 3.2.10: Synthesis of Azobenzenes by Reductive coupling of Nitrobenzene. R = -H, -Me, -Cl, -Br, -CN, MeCO-, MeCO₂-.



The probable mechanism involves reduction of nitrobenzene to form the intermediate *N*-arylhydroxyl amine and nitroso radical anions which then undergo N-N coupling to form *N,N'*-dihydroxylamine intermediate. The dehydration of this species, followed by reduction leads to the formation of the azobenzene. This method is very useful for the synthesis of symmetrical azobenzenes with reaction yields of $\leq 90\%$.

Asymmetric azobenzenes can be conveniently prepared by the reduction of azoxybenzene.²⁵ A recently reported method involves the treatment of azoxyarenes with hydrazine in presence of Al in methanol or microwave irradiation, as shown in the Scheme 3.2.10.²⁸

Scheme 3.2.10: Synthesis of Azobenzene by Reduction of Azoxybenzene. R,R' = -H,-Me, -OMe, -OEt, -Cl.



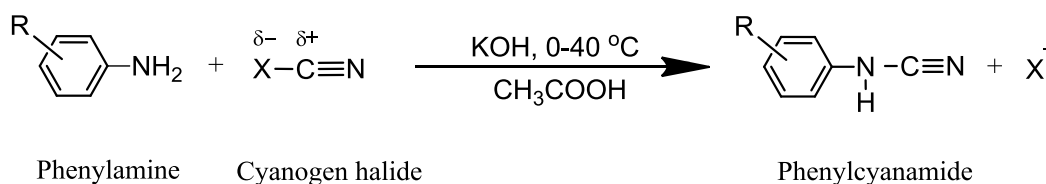
Other methods for the synthesis of azobenzenes include dehydrogenation of arylhydrazines, dimerisation of diazonium salts (Gatterman reaction using metallic Cu), triazine rearrangement, thermolysis of azides, metal catalyzed coupling of arylhydrazines etc.²⁵

3.2.2 Reviews on the Syntheses of Aromatic Cyanamide Ligands

The most frequently adopted method for the synthesis of cyanamide is the direct cyanation of amine using cyanogen halides, or its synthon (CN⁺).²⁰ The reagents capable of delivering electrophilic cyanogens (CN⁺) are the 2-chlorobenzylthiocyanate,^{20c} 1-cyanoimidazole,^{20d} 2-cyanopyridazine-3-(2H)-ones,^{20e} 1-cyanobenzotriazole and metal cyanide,^{20f} tosylcyanide,^{20g,h} thiocyanogen,²⁰ⁱ and cyanogen azide.^{20j} All these reagents have shown their cyanating ability on specific classes of aliphatic and aromatic amines and their applicability is often limited by the electronic nature of the amines as well as the

reaction conditions. The use of cyanogen bromide (CNBr) or cyanogen chloride (CNCl) for cyanating amines can be dated back to the early 20th century and since then a large number of aliphatic and aromatic cyanamides have been prepared using these reagents (Scheme 3.2.11).^{20a}

Scheme 3.2.11: Synthesis of Phenylcyanamide from Phenylamine using Cyanogen Halide Method.



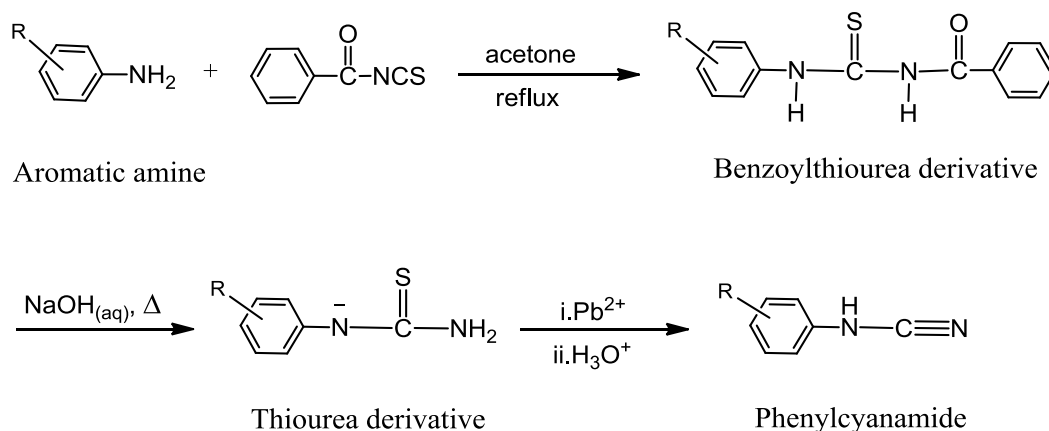
The reaction mechanism involves the nucleophilic attack of amine on the positively charged carbon on cyanogen halide to form the corresponding cyanamide with the elimination HX as a by-product (Scheme 3.2.21). In order to prevent deactivation of the unreacted amine as well as to prevent toxic evolution of hydrogen halide gas, an auxiliary base (*e.g.*, KOH, NaOH, sodium or potassium carbonates, bicarbonates) is used to scavenge HX. This reaction is particularly suitable for activated amines, having basicity or nucleophilicity equal or greater than 2-nitroaniline and 4-nitroaniline.^{20a} The standard procedure involves addition of cyanogen halide to a homogeneous solution of the amine in acetic acid in presence of an auxiliary base at temperature between -20 to 40 °C. The reaction is very sensitive to the reaction conditions *i.e.*, homogeneity of the amine solution, reagent ratio and temperature etc. A patent by Fauss and Riebel,^{20a} outlined various factors affecting the overall yields of the reaction using cyanogen chloride and provided optimum conditions for the synthesis of a large number of aromatic cyanamides

in high purity. According to their suggestions, the solution needs to be homogeneous in order to prevent co-precipitation of amine with the product, and depending on the solubility of the amine, a solvent mixture of acetic acid/alcohol, acetic acid/ water, acetic acid/DMF etc. could be used. In order to achieve the maximum yield, the amine: cyanogen chloride: base ratio should be kept within 1:1-2:1.05-1.15 and the base should be added in such a way that the pH of the solution is maintained slightly acidic throughout the reaction. The synthesis of aryl cyanamides using cyanogen halide often results in low yields of the products due to some side reactions like saponification reaction of cyanogen halide, or further reaction of cyanamide with unreacted amine to form guanidine or polymeric secondary products. The latter reactions are more prominent with highly activated amines at moderately high temperature. In order to prevent this, the reactions should be performed at very low temperature. The toxicity of the reagent cyanogen halide as well as the hydrogen halide gas generated in the reaction is a safety issue and special care should be taken handling those chemicals. In order to prevent elimination of hydrogen halide gas and volatile cyanogen chloride or decomposition of cyanogen bromide and other side reactions, the reaction should be carried out at low to moderate temperatures (-20 to 40 °C). In spite of the toxicity associated with the chemicals, this is the most direct method for cyanating the activated aromatic amines and requires less work-up compared to other known methods for the preparation of aromatic cyanamides. Although the reaction is not suitable for the synthesis of aromatic cyanamides with highly electron withdrawing substituents, it has been found to be very efficient method for the synthesis of phenylcyanamide with electron releasing substituents. This method gave the best yields for the unsubstituted and Me₂adpcH₂

ligands prepared in the present work. The *meta*-adpcH₂ ligand was prepared by following this method.

The most widely used route for the synthesis of phenylcyanamide derivatives from the corresponding anilines is the thiourea method, as shown in the Scheme 3.2.12.^{19a} Within the Crutchley lab, this reaction scheme has been extensively used for the synthesis of phenylcyanamide and bridging 1,4-dicyanamidobenzene (dicydH₂) ligands with various electron releasing and withdrawing substituents.¹⁹ This simple method involves the nucleophilic attack of a phenylamine on the carbonyl carbon of benzoyl thiocyanate to form the corresponding benzoyl thiourea derivative. Subsequent base hydrolysis of benzoyl thiourea gives the corresponding thiourea, which after desulfurization using lead acetate, followed by acidification, gives the protonated phenylcyanamide ligand.

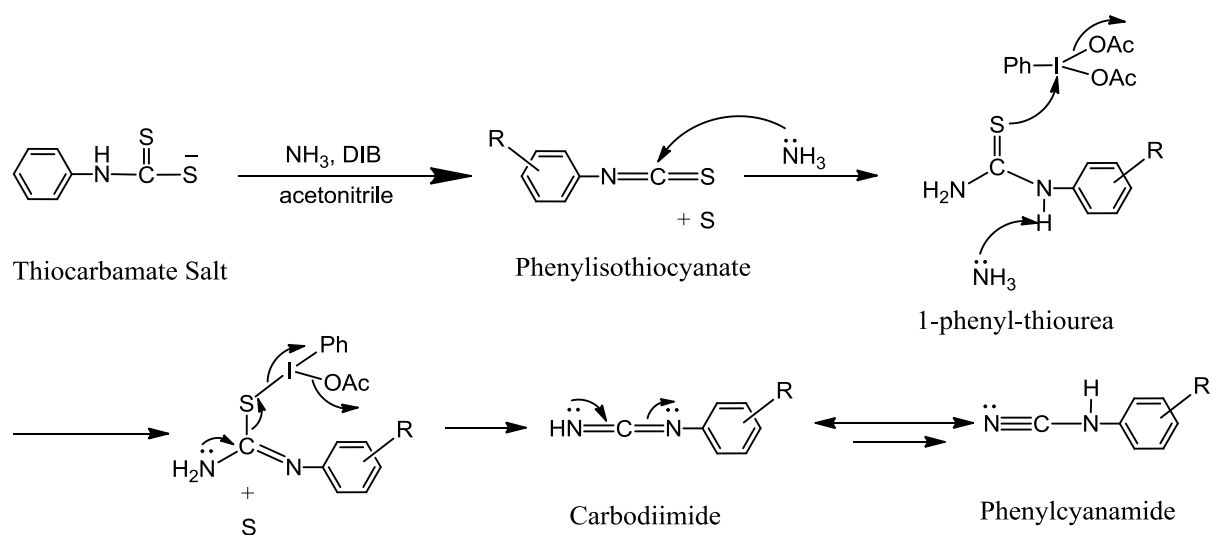
Scheme 3.2.12: Synthesis of Phenylcyanamide from Phenylamine using Thiourea method.



Experience has shown that, the formation of benzoyl thiourea derivative is usually complete within 30 minutes, however, for highly deactivated amines, it needs longer reflux time in presence of the excess amount of benzoyl thiocyanate. The hydrolysis step forming the anionic thiourea usually requires 10 minutes of boiling in 10% aqueous

dithiocarbamate salt requires a moderately activated amine to undergo nucleophilic attack on the weakly electrophilic carbon on carbon disulfide. In the case of deactivated aromatic amines, it is often convenient to deprotonate the amine using very strong base like BuLi, however, special care should be taken while handling this pyrophoric reagent. Although there are many desulfurising agents available in the literature, most of them are toxic mercury, lead, and thallium based reagents. Recently, desulfurising ability of compounds containing hypervalent (III) iodine has been explored.^{20b,m} In this regard, deacetoxyiodobenzene (DIB) has shown its potential in desulfurising many aromatic dithiocarbamates in the preparation of their phenylcyanamide derivatives. This non-metallic, non-toxic and eco-friendly hypervalent iodine (III) reagent enabled a high yielding (70-85%), ‘one-pot’ synthesis of phenylcyanamide ligands from their

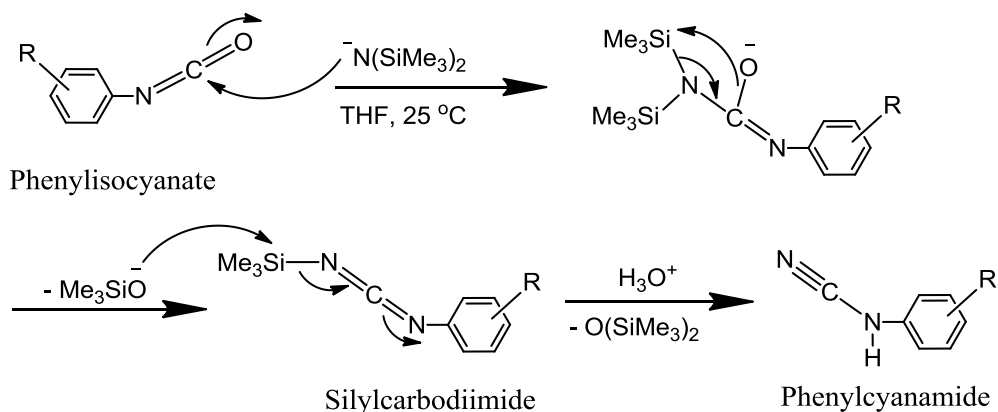
Scheme 3.2.14: Proposed Mechanism for the Synthesis of Phenylcyanamide from the Dithiocarbamate salt using DIB and Concentrated NH₃.



corresponding dithiocarbamic acid salts in presence of concentrated ammonia.^{20.b} The mechanism of the reaction, as shown in the Scheme 3.2.14,^{20b} involves initial desulfurization of dithiocarbamate anion by DIB and concentrated NH₃ to form its

basic conditions.^{29b,c} Sodium bis(trimethylsilyl) amide is a strong nitrogen base, a potential deoxygenating reagent and is occasionally used to add nitrogen atom to many organic compounds.^{29a} A plausible mechanism of its action forming the phenylcyanamide from the corresponding isocyanate is shown in the Scheme 3.2.16.^{29a}

Scheme 3.2.16: Proposed Mechanism for the Synthesis of Phenylcyanamide from Isocyanate using $\text{NaN}(\text{SiMe}_3)_2$.



According to this scheme, phenylisocyanate undergoes nucleophilic substitution by the $(\text{SiMe}_3)_2\text{N}^-$ anion to form an adduct which undergoes 1,2-elimination at Si-N-C-O^- to form silylcarbodiimide and Me_3SiO^- and the nucleophilic attack of the later on the former results in the formation of corresponding phenylcyanamide. This scheme provided an efficient method for the synthesis of phenylcyanamides from their corresponding isocyanates with a range of electron withdrawing and releasing substituents ($-\text{Cl}$, $-\text{NO}_2$, $-\text{Me}$, $-\text{OMe}$ etc.) with an overall yields of 70-97%.^{29b} In another recent method, cyanamides have been prepared from N,N' -disubstituted glycyamide using penta-valent iodine reagent in the presence of tetraethylammonium bromide at ambient temperature.^{29d} Aromatic cyanamides have also been prepared from organic isocyanides and

trimethylsilyl azide via a Si-N bond cleavage catalyzed by [$\{\eta^3\text{-C}_3\text{H}_5\}\text{PdCl}\}_2$].^{29e} Other less frequently adopted methods for the synthesis of aromatic cyanamides include Tiemann rearrangement of aldoximes and alkaline decomposition of 1-aryltetrazoles in DMSO.^{29f}

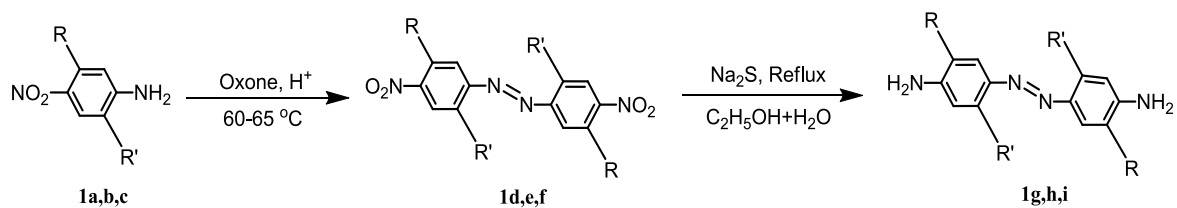
3.2.3 Synthetic Strategy

Substituted Azodianilines

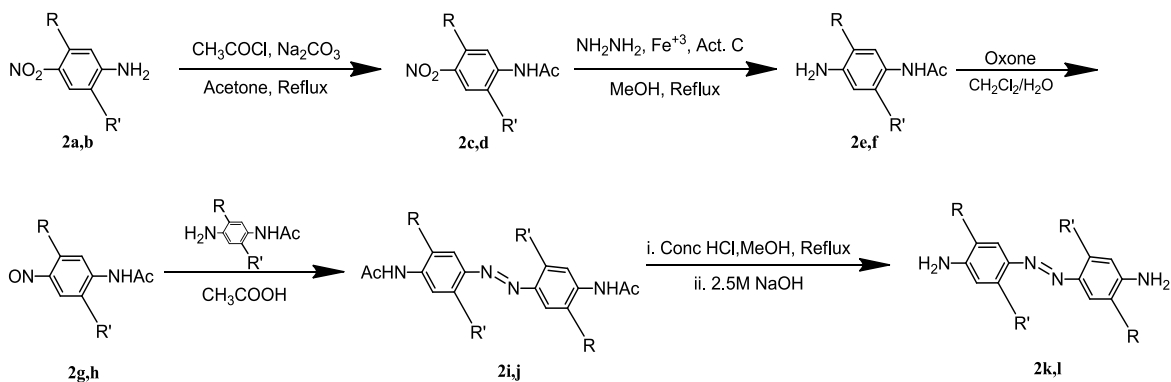
Six precursor $\text{R}_2\text{R}_2'$ -azodianilines (**1g-I**, **2i-j**, **3f**), where $\text{R}_2\text{R}_2' = \text{H}_2\text{-}$, $\text{Me}_2\text{-}$; $\text{H}_4\text{-}$; *meta*- $\text{H}_4\text{-}$, $\text{Cl}_2\text{-}$, $\text{H}_2\text{-}$; $\text{Cl}_4\text{-}$, and $\text{Me}_4\text{-}$ have been prepared by following Schemes 3.2.17-3.2.19. For simplicity, we will label $\text{R}_2\text{R}_2'$ -azodianilines as $\text{Me}_2\text{-}$, unsubstituted, *meta*-, $\text{Cl}_2\text{-}$, $\text{Cl}_4\text{-}$ and $\text{Me}_4\text{-}$ azodianilines, respectively in this chapter. The $\text{Me}_2\text{-}$, unsubstituted- and *meta*-azodianiline (**1g**, **1h** and **1i**) have been prepared by following the Scheme 3.2.17, which was developed in the current research work. This method involves the azocoupling reaction of precursor nitroanilines (**1a**, **1b**, **1c**) using slightly warm (55 °C) and acidic solution of Oxone (potassium peroxomonosulphate) in water forming the corresponding dinitroazo compound (**1d**, **1e**, **1f**), which after hydrolysis using sodium sulfide gave the desired azodianilines (**1g**, **1h**, **1i**). However, this method proved inefficient for the synthesis of azodianilines with highly electron withdrawing $\text{Cl}_2\text{-}$, $\text{Cl}_4\text{-}$ (**2k**, **2l**) or releasing $\text{Me}_4\text{-}$ substituents (**3f**) due to deactivation of amines in presence of nitro group for the former and over-reaction to dinitrobenzene derivatives for the latter. On the other hand, azodianilines with $\text{Cl}_2\text{-}$ and $\text{Cl}_4\text{-}$ substituents (**2k**, **2l**) could be prepared by following the Scheme 3.2.18. In this method, the amine group on the precursor nitroaniline (**2a**, **2b**) was first protected by *N*-acylation (**2c**, **2d**), followed by

reduction of the nitro group to corresponding amines (**2e**, **2f**). These amines (**2e**, **2f**) were then converted to the corresponding nitroso compounds (**2g**, **2h**), followed by Mills condensation reaction in glacial acetic acid,²³ giving the corresponding azodiacetanilide derivatives (**2i**, **2j**) which after hydrolysis in acidic methanol/ethanol gave the desired azodianilines (**2k**, **2l**). On the other hand, this method was still found to be inefficient for the synthesis of Me₄-azodianiline (**3f**) due to over-oxidation of the corresponding nitroso compound to the nitro derivative in presence of highly electron releasing methyl groups. However, the Me₄-azodianiline (**3f**) could be successfully prepared by following the Scheme 3.2.19. In this method, the reagent phenylamine (**3a**) was nitrated first to precursor nitroaniline (**3b**). This nitroaniline (**3b**) was *N*-acylated first (**3c**), followed by the reduction of the nitro group to corresponding amine (**3d**) which under mild oxidation condition following perborate oxidation method^{26e} gave the desired azidiacetanilide derivative (**3e**). The Me₄-azodianiline (**3f**) was then obtained by acid hydrolysis of the corresponding azodiacetanilide (**3e**) in methanol. All precursor R₂R₂'-azodianilines were elementally analyzed and the purity was further confirmed by ¹H NMR spectroscopy.

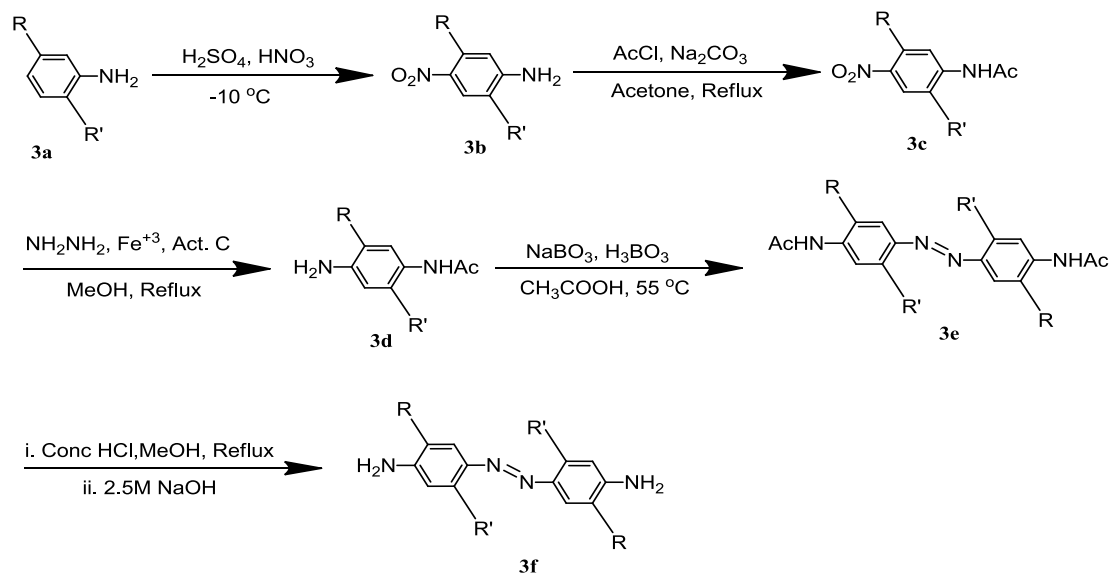
Scheme 3.2.17: Synthesis of R₂R₂'-azodianilines. R₂R₂' = H₂-, Me₂- ; H₄- ; *meta*-H₄-.



Scheme 3.2.18: Synthesis of R_2R_2' -azodianilines. $R_2R_2' = Cl_2-, H_2-, Cl_4-$.



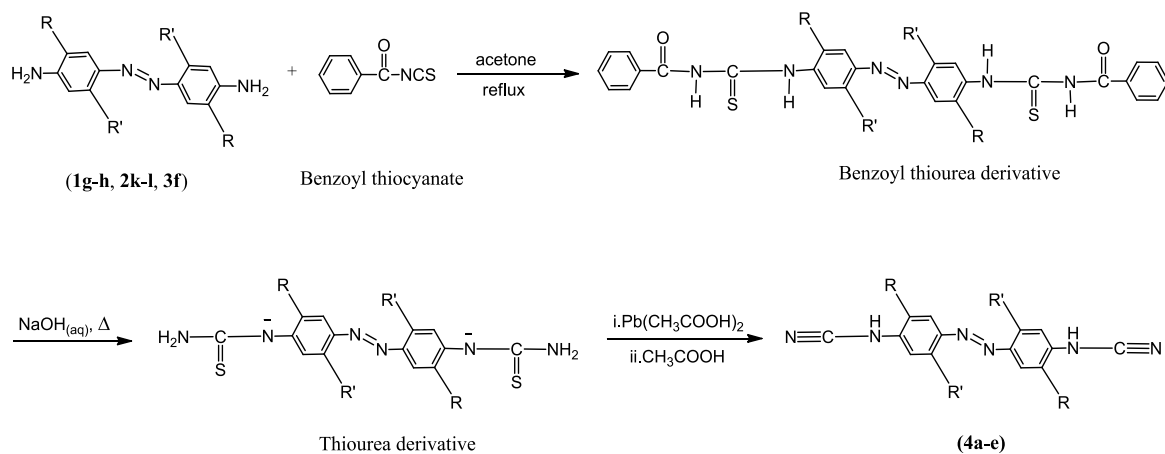
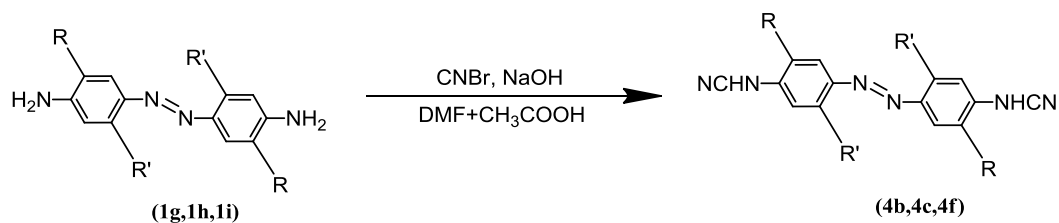
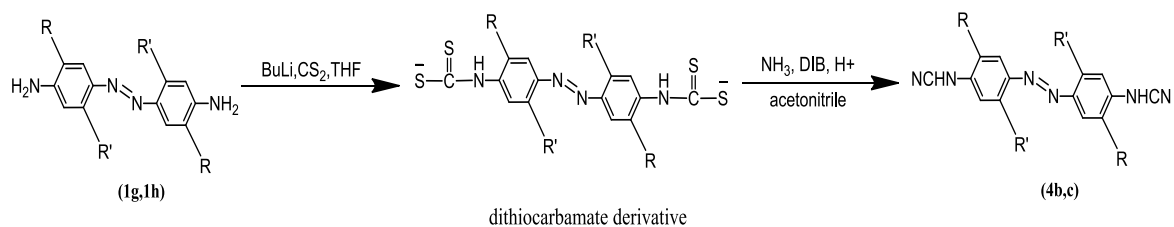
Scheme 3.2.19: Synthesis of R_2R_2' -azodianilines. $R_2R_2' = Me_4-$



Substituted Azodicyd Ligands

All six azodi(phenylcyanamide) (R_2R_2' adpcH₂) ligands (**4a-4f**), where $R_2R_2' = Me_4-, H_2-, Me_2-, H_4-, Cl_2-, H_2-, Cl_4-, meta-H_4-$ have been prepared from their precursor R_2R_2' -azodianilines by following the reaction Schemes 3.2.20-3.2.22. For simplicity, we will label R_2R_2' adpcH₂ ligands as $Me_4-, Me_2-, unsubstituted-, Cl_2-, Cl_4-$ and *meta*-adpcH₂

respectively. In general, all R_2R_2' adpcH₂ ligands (**4a-4e**) except the *meta*-adpcH₂ ligand (**4f**) could be prepared via thiourea method¹⁹ with an overall yield of 50-55% (Scheme 3.2.20). This method involves initial reaction between corresponding azodianilines with benzoyl thiocyanate forming the intermediate benzoyl thiourea derivatives which after base hydrolysis, followed by desulfurization using lead acetate and subsequent acidification gave the desired azodicyclid ligands (**4a-4e**). However, this reaction was complicated by the nucleophilicity of the deactivated amines on azodianilines with highly electron withdrawing Cl₂- and Cl₄- substituents (**4d**, **4e**), resulting in a substantial amount of monocyanamide derivatives. By systematic manipulation of the reaction condition, Cl₂adpcH₂ ligand (**4d**) could be obtained in pure form, however, the corresponding Cl₄adpcH₂ (**4e**) could not be obtained in pure form after all efforts and contained a substantial amount of monocyanamide impurities. However, purity of this ligand (**4e**) was improved in the formation of thallium salt and final dinuclear complex (**7e**) was obtained in the elementally pure form. The thiourea method (Scheme 3.2.20) also proved inefficient for the synthesis of the *meta*-adpcH₂ ligand (**4f**). In order to improve the purity of Cl₄adpcH₂ (**4e**) and prepare ligands with more electron withdrawing trifluoromethyl substituents and *meta*-adpcH₂ (**4f**) ligands other synthetic methods have been attempted, which provided two efficient routes for the syntheses of adpcH₂ (**4c**) and Me₂adpcH₂ (**4b**) and *meta*-adpcH₂ (**4f**) ligands, as shown in the Scheme 3.2.21 and 3.2.22. The *meta*-adpcH₂ ligand (**4f**) could only be prepared and high yields (98%) following the cyanogen bromide route involving direct cyanation of the amines using cyanogen bromide, after a significant modification of the reaction conditions described in the literature (Scheme 3.2.21).^{20a} The Me₂- and unsubstituted adpcH₂ ligands (**4b**, **4c**) could also be prepared in

Scheme 3.2.20: Synthesis of R_2R_2' adpcH₂. $R_2R_2' = H_2-, Me_2-, H_4-, Me_4-, Cl_2-, H_2-, Cl_4-$.**Scheme 3.2.21:** Synthesis of R_2R_2' adpcH₂. $R_2R_2' = H_4-, H_2-, Me_2-, meta-H_4-$.**Scheme 3.2.22:** Synthesis of R_2R_2' adpcH₂. $R_2R_2' = H_4-, H_2-, Me_2-$.

high purity with excellent yields by following the cyanogen bromide (Scheme 3.2.21) and thiocarbamate (Scheme 3.2.22) routes.^{20a,b} The thiocarbamate route^{20b} (Scheme 3.2.22)

required the initial deprotonation of the amine using a very strong base *i.e.* BuLi, followed by the reaction with carbon disulfide forming the intermediate dithiocarbamate salts which after hydrolysis using ammonia and desulfurization using DIB, gave an excellent yield (95-98%) of corresponding azodicyclid ligands (**4b**, **4c**) (Scheme 3.2.22). However, both Schemes proved inefficient for the synthesis of azodicyclid ligands with electron withdrawing Cl₂-, Cl₄- and (CF₃)₂-substituents and this limited our study with the highly electron withdrawing (CF₃)₂-substituents. Except for the Cl₄adpcH₂ (**4e**), all R₂R₂'adpcH₂ ligands were elementally analyzed and their purity was further confirmed by ¹H NMR spectroscopy.

3.2.4 Synthesis of Precursor Compounds for Substituted Azodianilines

Precursors for 3,3'-dichloro-4,4'-azodianiline, **2k**

(i) *2-chloro-4-nitro acetanilide, 2c*: A mixture of 2-chloro-4-nitro aniline (**2a**) (30.0 g, 0.174 mol), Na₂CO₃ (18.45 g, 0.174 mol) and acetyl chloride (13.66 g, 0.174 mol) was brought to reflux in 300 ml of distilled acetone with mechanical stirring. The reflux continued for 1 h during which time the suspended yellow particles went into solution. After the end of reflux, the yellow solution was added instantaneously to 500 ml of distilled water to afford precipitation of the crude yellow product, which was then filtered, washed with 1.5 L of distilled water and dried overnight. The crude product was recrystallized from 600 mL ethanol-water (1:1) mixture to obtain 28.7 g of pure light yellow crystalline compound (**2c**). Yield: 77%. ¹H NMR (300 MHz, DMSO-*d*₆): 9.87 (s, 1H); 8.36 (d, 1H); 8.20-8.29 (m, 2H); 2.22 (s, 3H).

(ii) *2-chloro-4-amino acetanilide, 2e*: The compound (**2e**) was prepared following the same procedure as described in literature³⁰ with little modifications: A

mixture of 2-chloro-4-nitro acetanilide (**2c**) (14.8 g, 69 mmol), active carbon (1.54 g, 128 mmol) and $\text{FeCl}_3 \cdot 6\text{H}_2\text{O}$ (0.1 g) was refluxed for 15 min in 100 ml of methanol. About 5.3 mL (110 mmol) of hydrazine hydrate was added drop wise to the refluxing mixture for 1 h, after which reflux continued for additional 3 h. The colorless filtrate was collected and concentrated to 10 ml. To the concentrate was added about 50 mL of CH_2Cl_2 to afford precipitation of the white product, which after washing with water, followed by vacuum drying gave 11.0 g of the pure white solid compound (**2e**). Yield: 86.4%. ^1H NMR (300 MHz, $\text{DMSO}-d_6$): 9.19 (1H, s); 7.09 (1H, d); 6.64 (1H, s); 6.49 (1H, d); 5.31 (2H, s); 1.99 (3H, s). Mass spectrum: m/z 214.5 (M^+).

(iii) *2-chloro-4-nitroso acetanilide*, **2g**: This nitroso compound (**2g**) was prepared by following the same procedure as described in literature^{23k} with some modifications: A mixture of 2-chloro-4-amino acetanilide (**2e**) (2.0 g, 9.3 mmol) and Oxone (11.46 g, 18.6 mmol) in $\text{CH}_2\text{Cl}_2 / \text{H}_2\text{O}$ biphasic system (1:1, 120 mL) was stirred vigorously at room temperature for 10 mins during which time all white solids disappeared with the formation of lime green solution of the nitroso compound in the organic layer. The lime green CH_2Cl_2 layer was collected, washed with 2 x 50 mL of distilled water and dried with anhydrous MgSO_4 . After removal of the MgSO_4 , the filtrate was rotaevaporated to dryness to obtain 1.51 g of the pure lime green nitroso compound, **2g**. Yield: 70 %. ^1H NMR (300 MHz, $\text{DMSO}-d_6$): 9.86 (1H, s); 8.45 (1H, d); 8.11 (1H, d); 7.97 (1H, s); 2.26 (3H, s). Mass Spectrum (EI): m/z 198.5 (M^+).

(iv) *3,3'-dichloro-4,4'-azodiacetanilide*, **2i**: This azodiacetanilide compound (**2i**) was prepared by following the same procedure as described in literature²³ with some modifications: A mixture of 2-chloro-4-nitrosoacetanilide (**2g**) (1.58 g, 7.96 mmol) and

2-chloro-4-amino acetanilide (**2e**) (1.71 g, 7.96 mmol) was stirred in 60 mL of glacial acetic acid at room temperature. An orange yellow precipitate formed within 30 min and the precipitation completed in about 6 h. The resulting solid was filtered, washed with 150 ml of distilled water until the pH of the washings reached about 7.0, dried overnight to obtain 1.85 g of the pure yellow-orange product (**2i**). Yield: 64 %. ¹H NMR (300 MHz, DMSO-*d*₆): 9.73 (2H, s); 8.16 (2H, d); 8.00 (2H, s); 7.92 (2H, d); 2.20 (6H, s). Mass Spectrum: *m/z* 365 (M⁺).

Precursors for 2,2': 5,5'-tetrachloro-4,4'-azodianiline, 2l

(i) *2,5-dichloro-4-nitro acetanilide, 2d*: This compound (**2d**) was prepared from 2,5-dichloro-4-nitro aniline (**2b**) following the same procedure as described above for the synthesis of **2c**. Yield: 75%. ¹H NMR (300 MHz, DMSO-*d*₆): 9.92 (s, 1H); 8.36 (s, 2H); 2.20 (s, 3H).

(ii) *2,5-dichloro-4-amino acetanilide, 2f*: This compound (**2f**) was prepared from 2,5-dichloro-4-nitro acetanilide (**2d**) by following exactly the same procedure as described above for the synthesis of **2e**. Yield: 95%. ¹H NMR (300 MHz, DMSO-*d*₆): 9.31 (1H, s); 7.37 (1H, s); 6.87 (1H, s); 5.53 (2H, s); 2.00 (3H, s).

(iii) *2,5-dichloro-4-nitroso acetanilide, 2h*: This compound (**2h**) was prepared from 2,5-dichloro-4-amino acetanilide (**2f**) by following the same procedure as described for the synthesis of **2g**, except that the reaction mixture was stirred at 35-45 °C for 2 h to yield the desired nitroso compound (**2h**). Yield: 80%. ¹H NMR (300 MHz, DMSO-*d*₆): 9.90 (1H, s); 8.72 (1H, d); 8.11(1H, d); 6.52 (1H, s); 2.26 (3H, s).

(iv) *2,2':5,5'-tetrachloro-4,4'-azodiacetanilide, 2j*: This compound (**2j**) was prepared from 2,5-dichloro-4-amino acetanilide (**2f**) and 2,5-dichloro-4-nitroso

acetanilide (**2h**) by following the same procedure as described for the synthesis of **2i**, with little modifications: the reactant mixture in glacial acetic acid was stirred at 30-35 °C for 18 h . Yield: 51%. ¹H NMR (300 MHz, DMSO-*d*₆): 9.84 (2H, s); 8.41 (2H, s); 7.77 (2H, s); 2.21 (6H, s).

Precursors for 2,2':5,5'-tetramethyl-4,4'-azodianiline, **3f**

(i) *2,5-dimethyl-4-nitroaniline, 3b*: This compound (**3b**) is prepared from 2,5-dimethylaniline (**3a**) by following the same procedure as described in literature.³¹ Yield: 22 %. ¹H NMR (300 MHz, DMSO-*d*₆): 7.83 (1H, s); 6.47 (1H, s); 6.30 (2H, s); 2.45 (3H, s); 2.07 (3H, s).

(ii)-*2,5-dimethyl-4-nitroacetanilide, 3c*: The acylation of 2,5-dimethyl-4-nitroaniline (**3b**) was carried out by following the same procedure as described for the synthesis of **2c** and **2d**, except that the reaction mixture of **3b** (15 g, 90 mmol), acetyl chloride (7.5 g, 90 mmol), Na₂CO₃ (9.54 g, 90 mmol) in acetone (150 mL) was refluxed for about 18 h to obtain a substantial amount of the product (**3c**).Yield: 16.27g, 76 %.¹H NMR (300 MHz, DMSO-*d*₆): 9.48 (1H, s); 7.93 (1H, s); 7.77 (1H, s); 2.49 (3H, s); 2.29 (3H, s); 2.14 (3H, s).

(iii)-*2,5-dimethyl-4-aminoacetanilide, 3d*: This compound (**3d**) was prepared from 2,5-dimethyl-4-nitroacetanilide (**3c**) by following the same procedure as described for the synthesis of **2e** and **2f**, except that the reduction of **3c** (16g, 68 mmol) was carried out in refluxing ethanol for 16 h to obtain 12 g of the pure off-white solid compound (**3d**). Yield: 85%. ¹H NMR (300 MHz, DMSO-*d*₆): 8.94 (1H, s); 6.77 (1H, s); 6.42 (1H, s); 4.65 (2H, s); 2.00 (3H, s); 1.98 (3H, s); 1.95 (3H, s).

(iv)-2,2': 5,5'-tetramethyl-4,4'-azodiacetanilide, **3e**: This compound (**3e**) was prepared from 2,5-dimethyl-4-aminoacetanilide (**3d**) by following the same procedure as described elsewhere^{26e} with some modifications: A mixture of 2,5-dimethyl-4-aminoacetanilide (**3d**) (8.0 g, 39 mmol), NaBO₃ (8.12 g) and H₃BO₃ (2.03 g) of was stirred in glacial acetic acid at 45-50 °C for about 5.5 h. The resulting orange yellow precipitate was filtered, washed with distilled water and dried overnight to obtain 2.61 g of the pure compound (**3e**). Yield: 33 %. ¹H NMR (300 MHz, DMSO-*d*₆): 9.34 (2H, s); 7.63 (2H, s); 7.43 (2H, s); 2.63 (6H, s); 2.25 (6H, s); 2.11 (6H, s).

3.2.5 Synthesis of Substituted Azodianilines

2,2'-dimethyl-4,4'-azodianiline, **1g**

2-methyl-4-nitroaniline (**1a**) (5 g, 27.3 mmol) was suspended in a mixture of 12.5 mL H₂SO₄ and 42.5 mL water. About 20 g of Oxone (32.5 mmol) was gradually added to the reaction mixture with continuous stirring in about 1 h at 60-65 °C. After the addition was complete, the reaction mixture was stirred for another 1 h at the same temperature. The yellow brown precipitate was filtered, washed with copious amount of water and recrystallized from glacial acetic acid (40 mL) to afford red needle shaped crystals of 3,3'-dimethyl-4,4'-dinitroazobenzene (**1d**). About 40 g of Na₂S was added to the solution of **1d** in a solvent mixture of water and ethanol (1:3, 160 mL) and the resulting mixture was refluxed for 30 min during which a red orange precipitate of the product was formed. The crude product was filtered, washed with a copious amount of water and dried overnight. Recrystallization from ethanol afforded 2.16 g of the pure red orange compound (**1g**). Yield: (55 %). Anal. Calcd for C₁₄H₁₆N₄ (M_w=240.3): C, 69.97;

H, 6.71; N, 23.32. Found: C, 69.67; H, 6.96; N, 23.07. ^1H NMR (300 MHz, DMSO- d_6): 7.41 (2H, d), 6.44 (2H, s), 6.41 (2H, d), 5.60 (4H, s), 2.50 (6H, s).

4,4'-azodianiline, 1h

This compound (**1h**) was prepared from 4-nitroaniline (**1b**) by following the same procedure as described above for the synthesis of **1g**. Yield: 64%. Anal. Calcd for 4,4'-azodianiline·1/4 H₂O (C₁₂H_{12.5}N₄O_{2.5}, M_w = 216.8): C, 66.49; H, 5.81; N, 25.85. Found: C, 66.30; H, 5.32; N, 25.59. ^1H NMR (300 MHz, CHCl₃- d): 7.76 (4H, d); 6.73 (4H, d); 3.97 (4H, s).

3,3'-azodianiline, 1i

This compound (**1i**) was prepared from 3-nitroaniline (**1c**) by following the same procedure as described above for the synthesis of **1g** and **1h**. Yield: 62%. Anal. Calcd for 3,3'-azodianiline·1/7 (C₂H₅OH) (C_{12.3}H_{12.9}N₄O₁, M_w=218.8): C, 67.43; H, 5.92; N, 25.60. Found: C, 67.05; H, 5.49; N, 25.32. ^1H NMR (300 MHz, DMSO- d_6): 7.22(t, 2H); 7.02(4H, d); 6.73 (2H, d); 5.39 (4H, s).

3,3'-dichloro-4,4'-azodianiline, 2k

This compound (**2k**) was prepared from 3,3'-dichloro-4,4'-azodiacetanilide (**2i**) by following the same procedure as described elsewhere,²³ with some modifications: 3,3'-dichloro-4,4'-azodiacetanilide (**2i**) (2.0 g, 5.58 mmol) was hydrolyzed under refluxing condition in a mixture of methanol (200 mL) and conc. HCl (280 mL) for 3.5 h during which time the yellowish orange suspension turned dark red. The suspension was cooled at room temperature and filtered to obtain the dark red solid. The damp solid was then suspended in 300 mL of distilled water and to the suspension was added 2.5 M NaOH

solution drop-wise to the until the pH of the solution reached about 12. The mixture was then stirred with gentle warming for about 30 min and the resulting green solid was filtered on a glass frit, washed with 200 mL of distilled water and 50 mL of hexane, dried overnight to obtain 1.25 g of the orange product (**2k**). Yield: 81 %. Anal. Calcd for 3,3'-dichloro-4,4'-azodianiline·1/4(H₂O) (C₁₂H_{10.5}N₄Cl₂O_{0.25}, M_w = 218.8): C, 50.46; H, 3.71; N, 19.61. Found: C, 50.63; H, 3.65; N, 19.41. ¹H NMR (300 MHz, DMSO-*d*₆): 7.69 (2H, s); 7.59 (2H, d); 6.89 (2H, d); 6.10 (4H, s). Mass spectrum: *m/z* 281 (M⁺).

2,2': 5,5'-tetrachloro-4,4'-azodianiline, 2l

This compound (**2l**) was prepared by following the same procedure as described for the synthesis of **2k**, except that the hydrolysis of the 2,2':5,5'-tetrachloro-4,4'-azodiacetanilide (**2j**) was carried out in a mixture of refluxing ethanol and conc. HCl (1:2, 500 mL) for 48 h. Repeated hydrolysis was needed to achieve a substantial conversion of **2k** to the corresponding azodianiline (**2l**). The crude product (1.0 g) was purified by using an alumina column (350g, grade III, Brockman acidic) and CH₂Cl₂ and acetonitrile as eluents. The first yellow band, eluted with CH₂Cl₂ and 10-20 % acetonitrile in CH₂Cl₂, gave a mixture of unreacted azodiacetanilides and partially converted amines. The second yellow orange band was eluted with 100 % acetonitrile, which after removal of the solvent gave 0.5 g of the pure orange compound (**2l**). Yield: 50 %. Anal. Calcd for 2,2':5,5'-tetrachloro-4,4'-azodianiline·1/4(H₂O) (C₁₂H_{8.5}N₄Cl₄O_{0.25}, M_w = 218.8): C, 50.46; H, 3.71; N, 19.61. Found: C, 50.63; H, 3.65; N, 19.41. ¹H NMR (300 MHz, DMSO-*d*₆): 7.62 (2H, s); 7.00 (2H, s); 6.47 (4H, s).

3.2.6 Synthesis of Azodicyd Ligands (4a-4f)

3,3'-dichloro-4,4'-azodi(phenylcyanamide)·0.25H₂O, 4d

A boiling solution of benzoyl chloride (2 g, 14.2 mmol) in 20 mL of acetone was added drop-wise to a refluxing solution of NH₄SCN (1.08 g, 14.2 mmol) in 20 mL of acetone for 30 min. To the mixture was added a boiling solution of 3,3'-dichloro-4,4'-azodianiline, **2k** (1.25 g, 4.7 mmol) in acetone (100 mL) and the reflux continued for 12 h. The resulting suspension was added to 1 L of distilled water to afford precipitation of orange benzoylthiourea derivative of **2k** which was then filtered, washed with water and then added to a boiling solution of 2M NaOH (400 mL) and stirred vigorously for about 20 minutes until a deep red solution formed. The solution was cooled to 60-65 °C and treated with a solution of lead acetate (5.36 g, 14.2 mmol) in distilled water (20 mL) while stirring to effect precipitation of black PbS. After 5 min., the reaction mixture was filtered through a Buchner funnel into an ice-cooled suction flask. The dark red filtrate was then acidified with glacial acetic acid (100 g, 1.67 mol) precipitating the dark-green product. Recrystallization from 1.6 L of boiling acetone afforded 1.05 g yellowish-green product, **4d**. Yield: 71.3 %. Anal. Calcd for C₁₄H_{8.5}N₆O_{0.25}Cl₂: C, 50.10; H, 2.55; N, 25.04. Found: C, 50.25; H, 2.64; N, 25.00. ¹H NMR (300 MHz, DMSO-*d*₆): 10.51 (2H, s); 7.96 (2H, d); 7.93 (2H, dd); 7.39 (2H, d). IR(KBr): ν(NCN) 2248 cm⁻¹. Mass spectrum: m/z 331 (M⁺).

2,2':5,5'-tetrachloro-4,4'-azodi(phenylcyanamide), 4e

The synthesis was similar to that of **4d** with some modification: Four equivalents of NH₄SCN and benzoyl chloride were used for the preparation of benzoyl thiocyanate, which was then refluxed with one equivalent of 2,2':5,5'-tetrachloro-4,4'-

azodianiline, **2i** in almost double the volume of acetone for 36 h to generate the crude product, **4e**. ^1H NMR showed the crude to be made of mostly **4e** (~80%) and an impurity (likely the monocyanamide). The poor solubility of **4e** frustrated attempts at purification and so the compound was used as isolated to make its thallium salt (see below). ^1H NMR (300 MHz, DMSO- d_6): 7.71 (2H, s); 7.27 (2H, s). IR(KBr): $\nu(\text{NCN})$ 2251 cm^{-1} .

2,2':5,5'-tetramethyl-4,4'-azodi(phenylcyanamide)·0.4(acetone)·0.2(CH₃COOH), 4a

The compound (**4a**) was prepared by following the same procedure as outlined for the synthesis of **4d** except that crude **4a** was recrystallized from acetone/water/glacial acetic acid (1:1:1) to give yellow crystalline flakes in 50% final yield. Anal. Calcd for C_{19.6}H_{21.2}N₆O_{0.8}: C, 66.57; H, 6.04; N, 23.77. Found: C, 66.35; H, 5.69; N, 23.70. ^1H NMR (300 MHz, DMSO- d_6): 9.67 (2H,s) ; 7.45 (2H, s); 7.04 (2H, s); 2.65 (6H, s); 2.21 (6H, s). IR(KBr): $\nu(\text{NCN})$ 2233 cm^{-1} . Mass spectrum: m/z 318 (M^+).

4,4'-azodi(phenylcyanamide) 4c

The ligand (**4c**) has been prepared previously using Method 1 (Scheme 3.2.20)^{1,19} and gave a reported yield of 50%. Two alternative methods (Scheme 3.2.21 and 3.2.22) are presented below.

Method 2 (Scheme 3.2.21): This method follows some modifications of the literature procedure.^{20a} To 4,4'-azodianiline, **1h** (1.0 g, 4.7 mmol) in 60 mL 40% DMF in glacial acetic acid was added one-half of a solution of CNBr (1.20 g, 11.3 mmol) in 20 mL of 40% DMF in glacial acetic acid and stirred at -10 to -15 °C for 30 min. The rest of the CNBr solution was then added to the reaction mixture followed by the drop-wise addition of 20 mL of 1M NaOH solution over an hour period. The reaction mixture was

permitted to rise to room temperature and stirred for 24 h precipitating golden-yellow microcrystalline **4c** which was filtered, washed with copious amount of water and dried overnight. Yield: 1.21 g, 98%. Anal. Calcd for **4c**·H₂O, C₁₄H₁₂N₆O: C, 59.99; H, 4.32; N, 29.98. Found: C, 59.70; H, 4.39; N, 29.76. ¹H NMR (300 MHz, DMSO-*d*₆): 10.61 (2H, s); 7.88 (4H, d); 7.12 (4H, d). IR(KBr): ν(NCN) 2225 cm⁻¹ in agreement with literature.¹

Method 3 (Scheme 3.2.22): This method follows some modifications of the literature procedure:^{20a,n,o} To a solution of 4,4'-azodianiline, **1h** (1.0 g, 4.7 mmol) in THF (100 mL) was added dropwise about 4.5 mL (10.62 mmol) of 2.5M BuLi solution in hexane at -30 to -40 °C and the mixture was stirred for 30 minutes during which the dark brown solution turned red due to formation of the corresponding amide. The solution was then brought to room temperature and CS₂ (0.7 mL, 11.2 mmol) was added. The resulting mixture was then stirred at room temperature for 24 h during which an orange precipitate was formed. The precipitate was filtered, washed with THF and dried overnight to obtain 0.85 g of pure lithium dithiocarbamate (Yield: 48%). To a solution of dithiocarbamate (0.3 g, 0.80 mmol) in acetonitrile (50 mL) was added conc. NH₃ (30 mL) and temperature of the solution was brought down to 0 to -5 °C. Diacetoxyiodobenzene (DIB) (0.26 g, 0.80 mmol) was added portion-wise to the solution over a period of 30 min during which a light yellow precipitate of sulfur started to separate out and the mixture was stirred for 2h at room temperature. The rest of DIB (0.26 g, 0.80 mmol) was added again over a period of 30 min and stirring continued for 12 h to effect complete precipitation of yellow sulfur. The orange red filtrate, collected after removal of sulfur, was added to 500 mL water and acidified with glacial acetic acid to afford very fine yellow-orange precipitate

of **4c**. The yellow precipitate was filtered, washed with water and dried overnight to obtain 0.2 g of the pure product, **4c**. Yield: 95%. ^1H NMR spectrum was identical to that of **4c** using Method 2.

2,2'-dimethyl-4,4'-azodi(phenylcyanamido)·0.1H₂O, 4b

Method 1: Same as for **4c**. Yield: 55%. Method 2: Same as for **4c**. Yield: 97%. Method 3: Same as for **4c**. Yield: 95%. Anal. Calcd for $\text{C}_{16}\text{H}_{14.2}\text{N}_6\text{O}_{0.1}$: C, 65.78; H, 4.90; N, 28.77. Found: C, 65.74; H, 4.86; N, 28.48. ^1H NMR (300 MHz, $\text{DMSO-}d_6$): 10.54 (2H, s); 7.65 (2H, d); 6.96 (2H, s); 6.90 (2H, dd); 2.67 (6H, s). IR(KBr): $\nu(\text{NCN})$ 2243 cm^{-1} .

3,3'-azodi(phenylcyanamide)·1.1H₂O, 4f

Method 2 procedure to prepare **4c** was followed with minor modification: 3,3'-azodianiline, **1i** (1.0 g, 4.7 mmol) was treated with CNBr (1.20 g, 11.3 mmol) in 60% CH_3COOH in DMF (total reaction volume 120 mL) in presence of gradually added 1M NaOH (20 mL) solution to give a reddish brown precipitate of the crude product which after recrystallisation from a boiling mixture of acetone and water (3:2, 1000 mL) afforded 1.04 g of pure reddish brown product, **4f**. Yield: 85 %. Anal. Calcd for $\text{C}_{14}\text{H}_{12.2}\text{N}_6\text{O}_{1.1}$: C, 59.61; H, 4.36; N, 29.79. Found: C, 59.62; H, 4.10; N, 28.51. ^1H NMR (300 MHz, $\text{DMSO-}d_6$): 10.51 (2H, s); 7.60 (4H, dd); 7.41 (2H, s); 7.17 (2H, d). IR(KBr): $\nu(\text{NCN})$ 2236 cm^{-1} .

3.2.7 Concluding Remarks

The syntheses of all precursor $\text{R}_2\text{R}'_2$ -azodianilines have been performed by using the Schemes 3.2.17-3.2.19. The formation of the azoderivatives of the

corresponding anilines appeared to be the crucial steps in the synthesis of R_2R_2' -azodianilines and depended on the electronic nature of the substituents on the precursor anilines. The Scheme 3.2.17 using Oxone in acidic aqueous medium is suitable for *in-situ* generation of Me_2 -, unsubstituted and *meta*-azoderivatives, while the Oxone method in CH_2Cl_2/H_2O biphasic media (Scheme 3.2.18) provided an efficient way to isolate the highly pure nitroso compounds of the anilines with electron withdrawing Cl and Cl_2 -substituents, which could be then easily reacted with the equimolar amount of the amines in glacial acetic to form the Cl_2 - and Cl_4 - substituted azo derivatives. Finally, perborate oxidation method (Scheme 3.2.19) has been found to be the most convenient method for the synthesis of Me_4 -azodianiline.

Three reaction Schemes (3.2.20-3.2.22) have been developed for the synthesis of Me_4 -, Me_2 -, Cl_2 -, Cl_4 - and unsubstituted $adpcH_2$ and *meta*- $adpcH_2$ ligands. The syntheses of ligands with highly electron withdrawing Cl_2 -, Cl_4 -, $(CF_3)_2$ -substituents were found to be increasingly difficult due to the deactivation of amine groups on corresponding R_2R_2' azodianilines. In general, the thiourea method is suitable for the synthesis of all R_2R_2' $adpcH_2$ ligands with electron releasing and withdrawing substituents (**4a-4e**) with an overall yield of about 50-55%. The Cl_4adpcH_2 ligand (**4e**) obtained by thiourea method was not pure enough for elemental analysis, however, purity improved upon formation of the thallium salt and the elementally pure dinuclear complex of this ligand was obtained without any complication (*vide infra*). The synthesis of $(CF_3)_2adpcH_2$ was unsuccessful and this limited the range of electronic perturbations introduced by the nature of the bridging ligand. The *meta*- $adpcH_2$ ligand (**4f**) could only be prepared by following the cyanogen bromide method in high yields (98%). Both

cyanogen bromide and thiocarbamate methods appear to be very efficient and clean methods for the synthesis of Me₂- and unsubstituted adpH₂ ligands (**4b**, **4c**) with excellent reaction yields (95-98%). These two schemes could be successfully used to make any phenylcyanamide and 1,4-dicyanamide ligands as well as moderately activated adpcH₂ ligands in bulk quantities.

3.3 Experimental

3.3.1 Starting Materials

Reagents

Acetyl chloride ($\geq 99.5\%$, Fluka), glacial acetic acid ($\leq 99.7\%$, ACS reagent grade, Anachemia), ammonium thiocyanate (ACS reagent grade, 97.5+%, Aldrich), 2,5-Dimethylaniline (99%, Aldrich), 3-nitroaniline (98%, Aldrich), 4-nitroaniline ($\geq 97.5\%$, Sigma), 2-chloro-4-nitroaniline (99%, Aldrich), 2,5-dichloro-4-nitroaniline (97%, Aldrich), 2-methyl-4-nitroaniline (97%, Aldrich), (diacetoxyiodo)benzene (98%, Aldrich), benzoyl chloride (99%, Aldrich), boric acid (ACS reagent grade, Fisher), carbon disulfide ($\geq 99\%$, anhydrous, Aldrich), activated charcoal (Commercial), cyanogen bromide (97%, Aldrich), hydrazine monohydrate (98%, Aldrich), hydrochloric acid (ACS reagent grade, 36.5 - 38.0%, Anachemia), iron (III) chloride hexahydrate ($\geq 98\%$, Aldrich), *n*-butyllithium solution (2.5M in hexane, Aldrich), Lead(II) acetate trihydrate (ACS reagent grade, 99+%, Aldrich), potassium peroxomonosulphate (Oxone) (4.5% active oxygen, Acros), sodium perborate tetrahydrate (Aldrich), sodium carbonate (ACS reagent grade, Caledon Labs), sodium hydroxide (97%, ACS reagent grade, Caledon Labs.), sulfuric acid (ACS reagent grade, 98%, Anachemia), thallium(I) hexafluorophosphate (97%, Strem), thallium (I) acetate ($\geq 99\%$, Sigma-Aldrich) (**Caution: highly toxic**), were used as received without further purification. Ammonium hexafluorophosphate (99.5%, Alfa Aesar), lithium chloride ($\geq 99\%$, Sigma-Aldrich), ruthenium (III) chloride hydrate (99.9%, Alfa Aesar), 2,2': 6',2'' terpyridine (98%, Sigma-Aldrich), 2,2'-bipyridyl (Reagent plus, $\geq 99\%$, Sigma-Aldrich) were used as received.

Compressed Gases

Argon (ultra high purity grade 5.0, PRAXAIR)

Adsorbent in Column Chromatography and Drying Agents

Aluminum oxide (activated, acidic, Brockman I) for column chromatography was deactivated to grade III by adding water and slowly shaking the mixture for 4h. Phosphorus pentoxide (ACS reagent grade, 98+%, Anachemia) were used as received. Aluminum oxide (neutral, chromatography grade, Woelm) was activated by heating to 300 °C for several hours in a muffle furnace.

Electrochemistry Internal References and Electrolytes

TBAH (tetrabutylammonium hexafluorophosphate) was synthesized by combining a 0.1 M solution of tetrabutylammonium bromide (95+%, Aldrich) with a 0.1 M solution of ammonium hexafluorophosphate (ReagentPlus, 99%, Sigma-Aldrich). The resulting TBAH precipitate was isolated and recrystallized twice from 1:1 ethanol:water and vacuum dried at 110°C. Ferrocene (reagent grade, J. T. Baker) was purified by sublimation.

Solvents for Synthesis

N,N-dimethylformamide (99.8%, anhydrous, Sigma-Aldrich), anhydrous ethyl alcohol (Commercial Alcohols, absolute), dichloromethane (Caledon Labs, Laboratory Grade), hexanes (Caledon Labs, ACS spectro grade), glacial acetic acid (ACS reagent grade, ≤ 99.7%, Anachemia), anhydrous ethyl ether, methanol and toluene (Caledon Labs, reagent grade) were used as received. Acetone (Fisher Scientific, ACS reagent grade) was distilled under glass prior to use. Tetrahydrofuran (Fisher Scientific) was

dried by vacuum distillation using metallic sodium as drying agent and dried solvent was stored in a sealed bottle and kept under argon prior to use.

Solvents for NMR spectroscopy

Chloroform- d_3 and dimethyl- d_6 sulfoxide (99.9 atom % D, CDN Isotopes) were used as received.

Solvents for Electrochemistry

Acetonitrile (Chromosolv®Plus, 99.9%, HPLC grade, Sigma-Aldrich), *N,N*-dimethylformamide (Chromosolv®Plus, 99.9%, HPLC grade, Sigma-Aldrich) were used with no further purification or drying. The solvent was stored inside a polyethylene glove bag that was filled with argon when mixtures of TBAH and the solvent needed to be made in 20 mL glass vials.

Solvents for Quantitative Electronic Absorption Spectroscopy

N,N-Dimethylformamide (Caledon Labs, reagent grade) was used as received.

3.3.2 Metal Complex Precursor Synthesis

Preparation of Ru(tpy)Cl₃·3H₂O, 6a: This complex (**6a**) was prepared by following the same procedure as described elsewhere,³² with minor modifications: A mixture of RuCl₃·3H₂O (1.22 g, 4.66 mmol) and 2,2': 6',2'' terpyridine (1.08 g, 4.29 mmol) was refluxed in 180 mL of absolute ethanol for 4 h and allowed to cool to room temperature. The greenish brown solid was filtered, washed with 3 x 30 mL of ethanol, 3 x 30 mL of water, and 100 ml of diethyl ether. The wet product was then dried under vacuum to obtain 1.87 g of the pure compound, Ru(tpy)Cl₃·3H₂O (**6a**). Yield: 92%.

Preparation of [Ru(tpy)(bpy)Cl][PF₆], 6b: The complex was prepared by following literature method³³ with some modification: A mixture of Ru(tpy)Cl₃·3H₂O (1.85 g, 3.73 mmol) and 2,2-bipyridine (0.66 g, 4.19 mmol) was refluxed in water-ethanol mixture (4:1, 400 mL) for 5 h during which time the initial light brown solution turned more darker. At the end of reflux, LiCl (1.37 g, 32 mmol) was added to the reaction mixture and reflux continued for another 30 min. To the hot solution was added solid NH₄PF₆ (0.685 g, 4.2 mmol) and stirring continued for another 30 min. The reaction mixture was then concentrated to 200 mL and chilled overnight at -20 °C. The dark brown shiny crystals of the product were filtered, washed with water (100 mL), dried overnight to obtain 2.00 g of the pure [Ru(tpy)(bpy)Cl][PF₆] complex (**6b**). Yield: 80%. ¹H NMR (300 MHz, DMSO-*d*₆): 10.10 (1H, d); 8.91 (1H, d); 8.82 (2H, d); 8.70 (2H, d); 8.64 (1H, d); 8.36 (1H, t); 8.22 (1H, t); 8.07 (1H, t); 7.99 (2H, t); 7.78 (1H, t); 7.63 (2H, d); 7.38 (2H, t); 7.32 (1H, d); 7.08 (1H, t).

3.3.3 Synthesis of R₂R₂'adpcH₂ Ligands and Tl₂[R₂R₂'adpc] Salts

The syntheses of all R₂R₂'adpcH₂ and *meta*-R₂R₂'adpcH₂ (**4a-4f**) ligands have been described in the Section 3.2.4. Five Tl₂[R₂R₂'-adpc] salts (**5a-e**), where R₂R₂' = H₂-, Me₂-; H₄-; Cl₂-, H₂-; Cl₄-; *meta*-H₄-, have been prepared from corresponding R₂R₂'adpcH₂ ligands (**4b-4f**) by following procedure outlined elsewhere with some modifications.¹ However, Tl₂[Cl₄adpc] salt (**5d**) prepared from the crude Cl₄adpcH₂ ligand (**4e**) was not elementally pure and was used as isolated for the synthesis of the dinuclear complex [{Ru(tpy)(bpy)}₂(μ-Me₄adpc)][PF₆]₂ (**7e**). All attempts to make the thallium or tetraphenylarsonium (AsPh₄) salt of Me₄adpcH₂ ligand (**4a**) were unsuccessful, due to increased basicity of electron releasing Me₄adpc²⁻ anion. Me₄adpcH₂

ligand (**4a**) was deprotonated in DMF solution using BuLi, prior to synthesis of the dinuclear complex [$\{\text{Ru}(\text{tpy})(\text{bpy})\}_2(\mu\text{-Me}_4\text{adpc})\][\text{PF}_6]_2$ (**7a**).

Preparation of $\text{Tl}_2[\text{Me}_2\text{adpc}]$, **5a:** $\text{Me}_2\text{adpcH}_2$ ligand (**4b**) (0.25g, 0.93mmol) was dissolved in boiling acetone-water mixture (2:1, 300 mL) and about 1 mL of triethylamine was added. An orange precipitate quickly formed upon addition of a solution of thallium acetate (0.45 g, 1.86 mmol) in acetone-water mixture (2:1, 50 mL). The resulting mixture was then boiled for additional 5 min and slowly cooled at $-20\text{ }^\circ\text{C}$. Filtration afforded a bright red-orange microcrystalline solid which was washed with cold water-acetone mixture and dried overnight to obtain 0.46 g of the pure $\text{Tl}_2[\text{Me}_2\text{adpc}]$ (**5a**). Yield: 71%. Anal. Calcd for $\text{C}_{16}\text{H}_{12}\text{N}_6\text{Tl}_2$: C, 27.55; H, 1.74; N, 12.06. Found: C, 27.48; H, 1.52; N, 11.91. ^1H NMR (300 MHz, $\text{DMSO-}d_6$): 7.36 (2H, d); 6.49 (2H, s); 6.40 (2H, d); 2.45 (6H, s). IR(KBr): $\nu(\text{NCN})$ 2083 and 2061 cm^{-1} .

Preparation of $\text{Tl}_2[\text{adpc}]$, **5b:** This compound (**5b**) was prepared by following the same procedure as described elsewhere.¹

Preparation of $\text{Tl}_2[\text{Cl}_2\text{adpc}]$, **5c:** This compound (**5c**) was prepared following the method used for **5a**. Yield: 55%. Anal. Calcd for $\text{C}_{14}\text{H}_6\text{N}_6\text{Tl}_2$: C, 22.77; H, 0.82; N, 11.39. Found: C, 22.92; H, 1.19; N, 11.37. ^1H NMR (300 MHz, $\text{DMSO-}d_6$): 7.55 (2H, d); 7.44 (2H, dd); 6.96 (2H, d). IR (KBr): $\nu(\text{NCN})$ 2099 cm^{-1} .

Preparation of $\text{Tl}_2[\text{Cl}_4\text{adpc}]$ **5d:** This compound (**5d**) was prepared following the method used for **5a**. This salt did not give acceptable elemental analysis. ^1H NMR (300 MHz, $\text{DMSO-}d_6$): 7.59 (2H, s); 6.95 (2H, s). IR(KBr): $\nu(\text{NCN})$ 2115 cm^{-1} .

Preparation of $\text{Tl}_2[\text{meta-adpc}]\cdot 0.30(\text{CH}_3\text{COCH}_3)$, **5e:** This compound (**5e**) was prepared by following the method used for **5a** and **5b**, except the ratio of acetone-water mixture is maintained 1:1 and total reaction volume is reduced by one third of that used for making **5a** and **5b**. Yield: 60%. Anal. Calcd for $\text{C}_{14.9}\text{H}_{9.8}\text{N}_6\text{O}_{0.3}\text{Tl}_2$: C, 26.07; H, 1.44; N, 12.24. Found: C, 26.35; H, 1.24; N, 12.64. ^1H NMR (300 MHz, $\text{DMSO-}d_6$): 7.09 (4H, m); 6.92 (2H, d); 6.72 (2H, d). IR(KBr): $\nu(\text{NCN})$ 2104 cm^{-1} .

Preparation of $[\text{AsPh}]_2[\text{adpc}]$, (5f**):** This compound (**5f**) was prepared by following the same procedure as described in the literature.¹

Preparation of $[\text{AsPh}]_2[\text{Me}_2\text{adpc}]$, (5g**):** $\text{Me}_2\text{-adpcH}_2$ ligand (**4b**) (0.10g, 0.93mmol) was dissolved in 50 mL of 2 M NaOH_{aq} . To this was added a solution of $[\text{AsPh}_4]\text{Cl}\cdot\text{H}_2\text{O}$ (0.35 g, 0.80 mmol) in 20 mL of water, and the mixture was stirred for 15 min. The red precipitate was collected and washed with 30 mL of water. Recrystallisation from boiling acetonitrile gave red needle-shaped X-ray quality crystals of $[\text{AsPh}]_2[\text{Me}_2\text{adpc}]$ (**5f**). Yield: 0.25 g, 60%. ^1H NMR (300 MHz, $\text{DMSO-}d_6$): 7.36 (2H, d); 6.49 (2H, s); 6.40 (2H, d); 2.45 (6H, s). IR(KBr): $\nu(\text{NCN})$ 2083 and 2061 cm^{-1} .

3.3.4 Synthesis of $[\{\text{Ru}(\text{tpy})(\text{bpy})\}_2(\mu\text{-R}_2\text{R}_2'\text{adpc})][\text{PF}_6]_2$ Complexes (**7a-7f**)

$[\{\text{Ru}(\text{tpy})(\text{bpy})\}_2(\mu\text{-Me}_4\text{adpc})][\text{PF}_6]_2\cdot\text{H}_2\text{O}$, **7a:** To a solution of $\text{Me}_4\text{adpcH}_2$ (**4a**) (0.10 g, 0.314 mmol) in anhydrous DMF (90 mL) was added 2.5 M BuLi in hexane (0.3 mL, 0.698 mmol) under inert atmosphere at -40°C and the mixture was stirred for 30 mins at the same temperature. The resulting dark red solution was then brought to room temperature, treated with $[\text{Ru}(\text{tpy})(\text{bpy})\text{Cl}][\text{PF}_6]$ (0.42 g, 0.628 mmol) and TIPF_6 (0.22 g, 0.628 mmol) and refluxed under inert atmosphere for 2 days. The resulting mixture was

chilled overnight at $-20\text{ }^{\circ}\text{C}$ and filtered to remove fine white precipitate of TiCl_4 . The dark brown filtrate was rota-evaporated to dryness, re-dissolved in acetone (30 mL) and added to anhydrous ether (1L) to precipitate 0.40 g of the crude product. The dinuclear complex was purified using an alumina column (Grade III, Brockman acidic, 330 g) and toluene/acetonitrile, DMF as eluents. The first three bands containing starting materials and mononuclear impurities were eluted by 1:1, 1:2 and 1:3 toluene/acetonitrile. The fourth reddish brown band was identified as the dinuclear complex and eluted with 1:1 DMF/acetonitrile. The resulting mass after removal of the solvent was re-dissolved in acetone (20 mL), filtered and treated with anhydrous ether (300 mL) to precipitate the dark brown product. Recrystallisation of the complex from its saturated solution in DMF by slow diffusion of ether, followed by vacuum drying, afforded 0.20g of the pure complex, **7a**. Yield: 38%. Anal. Calcd for $\text{C}_{68}\text{H}_{56}\text{N}_{16}\text{P}_2\text{F}_{12}\text{ORu}_2$: C, 50.88; H, 3.52; N, 13.96. Found: C, 51.07; H, 3.87; N, 14.19. ^1H NMR (300 MHz, $\text{DMSO-}d_6$): 9.68 (2H, d); 8.97 (2H, d); 8.92 (4H, d); 8.80 (4H, d); 8.70 (2H, d); 8.41 (2H, t); 8.33 (2H, t); 8.11 (6H, dd); 7.86 (2H, t); 7.75 (4H, d); 7.55 – 7.39 (6H, m); 7.20-7.13 (2H, m); 7.12 (2H, s); 5.61 (2H, s); 2.21 (6H, s); 1.80 (6H, s). IR(KBr): $\nu(\text{NCN})$ 2152 cm^{-1} .

[{Ru(tpy)(bpy)}₂(μ -Me₂adpc)][PF₆]₂·H₂O, 7b: A mixture of $[\text{Ru}(\text{tpy})(\text{bpy})\text{Cl}][\text{PF}_6]$ (0.38g, 0.56 mmol) and $\text{Ti}_2[\text{Me}_2\text{adpc}]$ (0.20 g, 0.28 mmol) was refluxed in DMF (50 mL) for 48 h. The reaction mixture was then chilled at $-20\text{ }^{\circ}\text{C}$ and filtered through cellite to remove fine white precipitate of TiCl_4 . The dark brown filtrate was then rotaevaporated to dryness to yield 0.51 g of the crude product which after recrystallisation from its saturated solution in DMF by slow diffusion of ether, followed by filtration and vacuum drying, gave 0.41g of the pure dark brown complex, **7b**. Yield:

93%. Anal. Calcd for $C_{66}H_{52}N_{16}P_2F_{12}ORu_2$: C, 50.26; H, 3.32; N, 14.21. Found: C, 50.27; H, 3.13; N, 13.86. 1H NMR (300 MHz, DMSO- d_6): 9.69 (2H, d); 9.00 (2H, d); 8.94 (4H, d); 8.82 (4H, d); 8.73 (2H, d); 8.44 (2H, t); 8.35 (2H, t); 8.13 (6H, dd); 7.89 (2H, t); 7.77 (4H, d); 7.49 (6H, dd); 7.18 (4H, dd); 5.95 (2H, d); 5.87 (2H, s); 2.31 (6H, s). IR(KBr): $\nu(NCN)$ 2164 cm^{-1} .

[{Ru(tpy)(bpy)}₂(μ -adpc)][PF₆]₂, 7c: This complex (**7c**) was prepared by following the same procedure as described elsewhere.¹

[{Ru(tpy)(bpy)}₂(μ -Cl₂adpc)][PF₆]₂·DMF, 7d: A mixture of [Ru(tpy)(bpy)Cl][PF₆] (0.61 g, 0.91 mmol) and Ti₂[Cl₂adpc] (0.33 g, 0.45 mmol) in 100 mL of DMF was refluxed for 48 hrs. After removing the fine white precipitate of TiCl₄, the dark brown filtrate was concentrated to 20 mL and added to diethyl ether (600 mL) to precipitate the crude product (0.71 g). About 0.41 g of the crude product was then dissolved in 80 mL of 1:1 acetonitrile/toluene, and purified by column chromatography using an alumina column (50 cm x 3 cm, Grade III, Brockman acidic, 250 g). The first three bands containing starting materials and mononuclear impurities were eluted with 1:1 and 2:1 acetonitrile/toluene. The 4th dark brown band containing the target compound was eluted with 3:1 acetonitrile/toluene, filtered and evaporated to dryness to obtain the dark brown solid. Recrystallisation was achieved by slow diffusion of ether into a saturated solution of the complex in DMF (30 ml) which after filtration and vacuum drying gave 0.36 g of the pure dark brown compound, **7d**. Yield: 36%. Anal. Calcd for $C_{67}H_{51}N_{17}Cl_2P_2F_{12}ORu_2$: C, 48.09; H, 3.07; N, 14.23. Found: C, 47.97; H, 3.45; N, 14.26. 1H NMR (300 MHz, DMSO- d_6): 9.67 (2H, d); 8.98 (2H, d); 8.93 (4H, d); 8.81

(4H, d); 8.72 (2H, d); 8.50-8.30 (4H, m); 8.12 (6H, m); 7.89 (2H, t); 7.76 (4H, d); 7.49 (6H, m); 7.24 (2H, dd); 7.18 (2H, t); 5.88 (2H, d). IR(KBr): $\nu(\text{NCN})$ 2164 cm^{-1} .

[{Ru(tpy)(bpy)}₂(μ -Cl₄adpc)][PF₆]₂·5H₂O, 7e: This complex (**7e**) was prepared by following the same method as described above for the synthesis of **7d**, with some modification: A mixture of [Ru(tpy)(bpy)Cl] (0.58 g, 0.43 mmol) and crude Tl₂[Cl₄adpc] (0.35 g) was refluxed in DMF (130 mL) for 4 days to yield 0.69g of the crude product. Column chromatography of the 0.30 g of crude product was performed using an alumina column (Grade IV, Brockman acidic, 300 g). The fourth deep purple band was eluted with pure acetonitrile and 10% methanol (in acetonitrile) to yield a dark brown complex that lacks [PF₆] anion (recognized by IR for $\nu(\text{PF}_6)$: 842 cm^{-1}). This complex was then stirred in the boiling mixture of DMF and water (1:1, 40 mL) in presence of excess NH₄PF₆ (5 equivalents) for 10 minutes and the resulting mixture was cooled down to room temperature to obtain [PF₆] salt of the complex. Pure dark brown compound, **7e** (0.1 g) was obtained by slow diffusion of ether into a saturated solution of the complex in DMF. Yield: 13%. Anal. Calcd for C₆₄H₅₂N₁₆Cl₄P₂F₁₂O₅Ru₂: C, 43.70; H, 2.98; N, 12.74. Found: C, 43.85; H, 3.10; N, 13.00. ¹H NMR (300 MHz, DMSO-*d*₆): 9.64 (2H, d); 8.97 (2H, d); 8.93 (4H, d); 8.81 (4H, d); 8.71 (2H, d); 8.50-8.28 (4H, m); 8.12 (6H, m); 7.88 (2H, t); 7.76 (4H, d); 7.48 (6H, m); 7.43 (2H, s); 7.18 (2H, t); 5.88 (2H, s). IR(KBr): $\nu(\text{NCN})$ 2166 cm^{-1} .

[{Ru(tpy)(bpy)}₂(μ -*meta*-adpc)][PF₆]₂·2H₂O, 7f: This complex (**7f**) was prepared by following the same method as described above for the synthesis of **7d** with minor modification: A mixture of [Ru(tpy)(bpy)Cl][PF₆] (0.60 g,) and Tl₂[*meta*-adpc] (0.30 g,) in 100 mL of DMF gave 0.67 g of the crude product after 48 h of reflux. The

crude dark brown product (0.35 g) was purified using an alumina column (50 cm x 3 cm, Grade IV, Brockman acidic, 350 g) and acetonitrile/toluene as eluent. The fourth dark red band was identified as the pure dinuclear complex and was eluted with pure acetonitrile and 10% methanol in acetonitrile. The product obtained after removing the solvent, was recrystallised by slow diffusion of ether into a DMF solution of **7f**. Yield: 0.10 g, 17%. Anal. Calcd for $C_{64}H_{50}N_{16}P_2F_{12}O_2Ru_2$: C, 49.05; H, 3.22; N, 14.30. Found: C, 48.83; H, 3.10; N, 14.12. 1H NMR (300 MHz, DMSO- d_6): 9.68 (2H, d); 8.96 (2H, d); 8.86(4H, d); 8.74 (4H, d); 8.69 (2H, d); 8.39 (2H, t); 8.27 (2H, t); 8.14 - 7.98 (6H, m); 7.85 (2H, t); 7.73 (4H, d); 7.47 – 7.35 (6H, m); 7.14 (2H, t); 7.00 (2H, t); 6.91 (2H, d); 6.53 (2H, s); 6.08 (2H, d). IR(KBr): $\nu(NCN)$ 2158 cm^{-1} .

3.3.4 Physical Measurements

Elemental Analyses

All elemental analyses were performed by Canadian Microanalytical Services, Ltd. in Delta, B. C., Canada.

X-ray Crystallography

The determination of X-ray crystal structure of $[AsPh]_2[Me_2adpc]$ salt was conducted by Dr. Glenn P. A. Yap at the University of Delaware. The complex data were collected on a 1K Siemens Smart CCD using Mo-K α radiation ($\lambda = 0.71073 \text{ \AA}$) at 203(2) K using an ω -scan technique and corrected for absorptions using equivalent reflections.

No symmetry higher than triclinic was observed and the solution in the centric space group option yielded chemically reasonable and computationally stable results of refinement. Direct methods were used to solve the structures and refinement was done with full-matrix least-squares procedures. Anisotropic refinement was performed on all

non-hydrogen atoms. Calculations were performed for all hydrogen atoms. Scattering factors are contained in the SHELXTL version 5.1 program libraries. Tables of complete listing of all bond lengths and angles are listed in the Table C.1 in the Appendix C.

Spectroscopy and Electrochemistry

Infrared, ^1H NMR and electronic absorption spectroscopy and cyclic voltammetry of free protonated $\text{R}_2\text{R}_2'\text{-adpcH}_2$ ligands (**4a-4f**), thallium salts of anionic ligands $\text{Tl}_2[\text{R}_2\text{R}_2'\text{-adpc}]$ (**5a-5e**), and $[\{\text{Ru}(\text{tpy})(\text{bpy})\}_2(\mu\text{-R}_2\text{R}_2'\text{-adpc})][\text{PF}_6]_2$ complexes (**7a-7f**) were performed using the same instruments as described in the Section 2.3.3 (Chapter 2). EPR, IR, and vis-NIR spectroelectrochemistry on oxidized complexes $[\{\text{Ru}(\text{tpy})(\text{bpy})\}_2(\mu\text{-R}_2\text{R}_2'\text{-adpc})]^{3+,4+}$ (**7a⁺-7f⁺**, **7a²⁺-7f²⁺**) were performed following the same procedure and using the same instruments as described in the Section 2.3.3 (Chapter 2)

Oscillator Strength Calculations

The oscillator strength of a band in electronic absorption spectrum, assuming Gaussian shape, can be calculated by using the Eq. 3.3.1.

$$f = 4.61 \times 10^{-9} \varepsilon_{\max} \Delta\nu_{1/2} \quad (3.3.1)$$

where ε_{\max} represents the maximum extinction coefficient in $\text{M}^{-1}\text{cm}^{-1}$ and $\Delta\nu_{1/2}$ represents the bandwidth at half peak height in cm^{-1} . Due to the non Gaussian nature of the NIR bands resulting from $[\{\text{Ru}(\text{tpy}(\text{bpy}))\}_2(\mu\text{-R}_2\text{R}_2'\text{-adpc})][\text{PF}_6]_2$ complexes, the use of Eq. 3.3.1 for calculating the oscillator strength of the band would generate an inexact value. In order to obtain an exact value of the oscillator strength, multiple Gaussian bands were fitted on the NIR band envelope using Jandel Scientific peakfitTM v 3.0 software. The

fitting procedure is illustrated in Figure 3.3.1 and was done on the low energy NIR band of $[\{\text{Ru}(\text{tpy})(\text{bpy})\}_2(\mu\text{-Me-adpc})][\text{PF}_6]_2$.

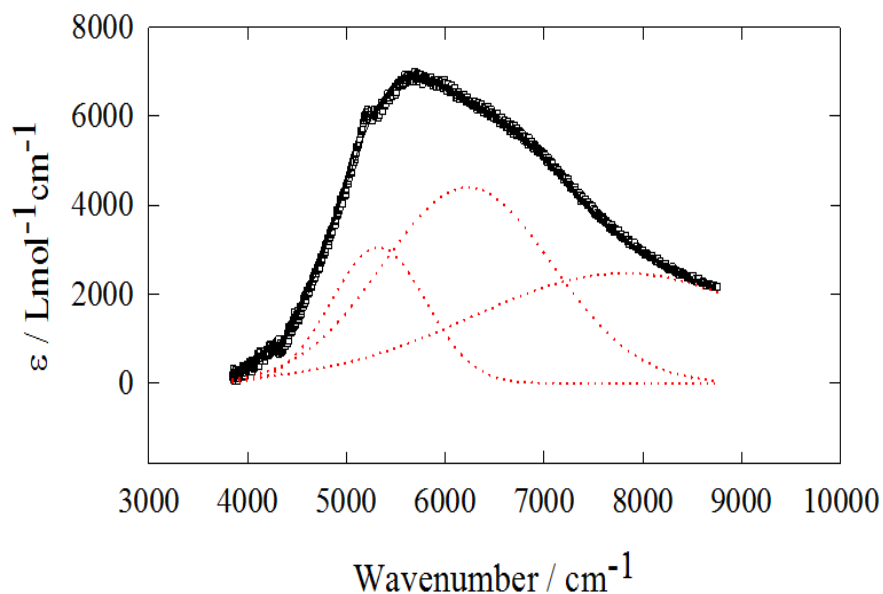


Figure 3.3.1: The low energy NIR band of $[\{\text{Ru}(\text{tpy})(\text{bpy})\}_2(\mu\text{-Me}_2\text{adpc})]^{3+}$ (**7b⁺**) in DMF showing the best fit of the three Gaussian curves (dashed lines) used for the calculation of the oscillator strength.

In this treatment, electronic transitions or vibrational features are not represented by the number of Gaussian bands. The NIR band oscillator strength was then calculated according to equation (13), which results in the sum of the contribution to the oscillator strength from each of the Gaussian bands.

$$f = 4.61 \times 10^{-9} \sum_i \varepsilon_i \cdot \Delta\nu_i \quad (3.3.2)$$

In the above equation, ε is the extinction coefficient at λ_{max} for each Gaussian peak and $\Delta\nu$ is the Gaussian band width at half peak height in cm^{-1} .

3.3.6 Theoretical Calculations

Restricted hybrid HF-DFT SCF calculation was performed on $[\{\text{Ru}(\text{tpy})(\text{bpy})\}_2(\mu\text{-adpc})]^{2+}$ (**7c**) to obtain the optimized geometry, orbital energy of the complex, using Wavefunction Inc., Spartan'14 Parallel suite program, with the Beck three parameter hybrid exchange and Lee-Yang-Parr correlation functionals (B3LYP) and the 6-31G* basis set for C, H, N and LANL2DZ basis set for Ru atoms. Geometry optimization was performed in C_1 symmetry with subsequent vibrational frequency analysis to confirm that each stationary point was a minimum on the potential energy surface. Tight SCF convergence criteria (10^{-8} a.u.) were used for the calculation. Unrestricted HF-DFT SCF calculations were performed to obtain optimized geometry, orbital energy and spin density distributions in oxidized complexes $[\{\text{Ru}(\text{tpy})(\text{bpy})\}_2(\mu\text{-R}_2\text{R}_2'\text{adpc})]^{3+}$ (**7a⁺** -**7e⁺**), using the same model.

Density functional theory (DFT) calculations on doubly oxidized complexes $[\{\text{Ru}(\text{tpy})(\text{bpy})\}_2(\mu\text{-R}_2\text{R}_2'\text{adpc})]^{4+}$ (**7c²⁺** and **7e²⁺**) have been performed using the *Gaussian 09* program.³⁵ The author is thankful to Professor Serge I. Gorelsky, Ottawa University who performed DFT calculations on these complexes. The structures of all species were optimized using the B3LYP exchange-correlation functional^{36,37} with the DZVP³⁸ basis set for Ru and the triple-zeta basis set (TZVP)³⁹ on all other atoms. Geometry optimizations were performed both in the gas phase and in solvent (the SMD implicit solvation model⁴⁰ with methanol as a solvent). Tight SCF convergence criteria (10^{-8} a.u.) were used for all calculations. For all open-shell calculations, the spin-unrestricted molecular orbital treatment was employed. Wave function stability calculations were performed to confirm that the calculated wave functions corresponded

to the electronic ground state. Time-dependent DFT (TD-DFT)^{41,42} calculations at the B3LYP/DZVP level of theory were used to calculate the energies and intensities of 30 lowest-energy spin-allowed electronic transitions. The absorption spectra were calculated using the *SWizard* program,^{43,44} using the pseudo-Voigt model (50% gaussian and 50% lorentzian functions). The half-bandwidths were taken to be equal to 3000 cm⁻¹.

3.4 Results

3.4.1 Synthesis of Complexes:

Dinuclear $[\{Ru(tpy)(bpy)\}_2(\mu-R_2R_2'adpc)][PF_6]_2$ complexes (**7b-7f**), where $R_2R_2'adpc = Me_2-$, unsubstituted, Cl_2- , Cl_4- , and *meta*-adpc, have been prepared by refluxing corresponding thallium salts, $Tl_2[R_2R_2'adpc]$ (**5a-5e**), with two equivalents of $[Ru(tpy)(bpy)Cl][PF_6]$ complex (**6b**) in DMF for 48 h. The $Tl_2[Cl_4adpc]$ salt (**5e**) could not be obtained in the elementally pure form and was used as isolated for the synthesis of its dinuclear complex (**7e**). The reaction mixture had to be refluxed for a relatively longer time (96 h) in order to obtain a substantial amount of the dinuclear complex (**7e**). The protonated neutral form of the ligand Me_4adpcH_2 (**4a**) was used for the synthesis of dinuclear Me_4adpc complex (**7a**). In the actual synthesis of this complex (**7a**), the Me_4adpcH_2 ligand (**4a**) was deprotonated initially in DMF solution at low temperature by using BuLi. Two equivalents of $Tl(PF_6)$ and $[Ru(tpy)(bpy)Cl][PF_6]$ were then added and finally, the reaction mixture was heated to reflux under inert atmosphere. The Me_2adpc complex (**7b**) was isolated from the reaction mixture almost in pure form, which after recrystallization from DMF by slow diffusion of ether, gave an elementally pure dinuclear complex (**7b**) in 93 % yield. Other dinuclear complexes (**7a**, **7c-f**) were purified by column chromatography using alumina column (Grade III, Brockman acidic) as adsorbent and solvent mixtures containing toluene, acetonitrile and DMF as eluents. Further purification was achieved by recrystallizing these complexes from their saturated solutions in DMF by slow diffusion of ether. Dinuclear complexes (**7a**, **7c-f**) showed specific binding properties to the alumina column which reduced their yields significantly

(15-35%). However, complexes **7a-7f** were obtained in elementally pure forms, and purity of **7a-7f** was further confirmed by ^1H NMR spectroscopy.

3.4.2 X-ray Crystallography

X-ray quality needle shaped crystals of tetraphenylarsonium salt of $\text{Me}_2\text{adpcH}_2$ ligand, $[\text{AsPh}_4][\text{Me}_2\text{adpc}]$ (**5g**), were grown from boiling acetonitrile solution of the salt. All attempts to grow crystals of dinuclear $[\{\text{Ru}(\text{tpy})(\text{bpy})\}_2(\mu\text{-R}_2\text{R}'_2\text{adpc})][\text{PF}_6]_2$ complexes (**7a-7b, 7d-7f**) were unsuccessful. The crystallography data, bond lengths and angles for anionic $\text{Me}_2\text{adpc}^{2-}$ are reported in the Table 3.4.1 and 3.4.2 respectively. An ORTEP drawing of the anionic $\text{Me}_2\text{adpc}^{2-}$ (**5g**) is shown in the Figure 3.4.1.

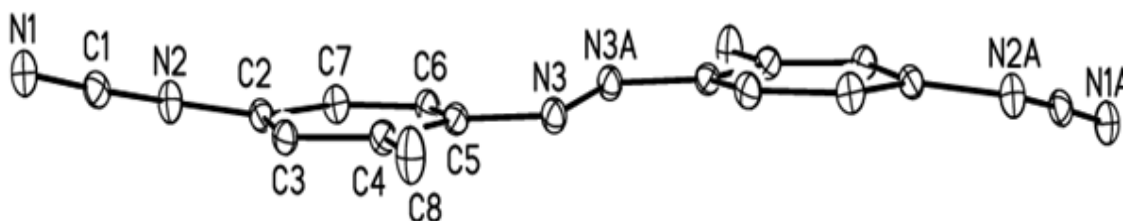


Figure 3.4.1: ORTEP drawing of anionic $\text{Me}_2\text{adpc}^{2-}$ ligand (**5g**). The solvent of crystallization and hydrogen atoms have been omitted for clarity. Ellipsoids are depicted at 30 % probability.

The $\text{Me}_2\text{adpc}^{2-}$ anion (**5g**) is approximately planar, where two cyanamide groups are in *anti*-conformation relative to each other and the azo group is in thermodynamically stable *trans*- conformation. The conformations of the cyanamide and azo groups in free $\text{Me}_2\text{adpc}^{2-}$ ligand are identical to those of adpc^{2-} in the crystal structure of $[\{\text{Ru}(\text{tpy})(\text{bpy})\}_2(\mu\text{-adpc})]^{2+}$ (**7c**).¹ The cyanamide group in $\text{Me}_2\text{adpc}^{2-}$ is only slightly out

Table 3.4.1: Crystal Data and Structure Refinement for [AsPh₄]₂[Me₂adpc](**5g**).

Empirical Formula	C ₃₂ H ₂₆ As N ₃
Formula Weight	527.48 g/mol
Temperature	120 (2) K
Wavelength	0.71073 Å
Crystal System	Triclinic
Space Group	P2 (1) / c
Unit Cell Dimensions	a = 8.992 (5) Å alpha = 90.00° b = 10.885 (6) Å beta = 90.605(8)° c = 26.000 (14) Å gamma = 90.00°
Volume, Z	2545.2 (3) Å ³ , 4
Density (calculated)	1.377 Mg/m ³
Absorption Coefficient	1.362 mm ⁻¹
F (000)	1088
Crystal Size	0.38 x 0.33 x 0.29
Theta range for data collection	2.74 to 27.27°
Limiting Indices	-11 ≤ h ≤ 11, -13 ≤ k ≤ 14, -33 ≤ l ≤ 34
Reflections Collected	5774
Absorption Correction	multi-scan
Max. And Min. Transmission	0.6927 and 0.6250
Refinement Method	Full-matrix Least-squares on F ²
Data/ Restraints/ Parameters	5774/ 0 /326
Goodness-of-fit on F ²	1.027
R1 ^a	0.0337
wR2 ^b	0.0937

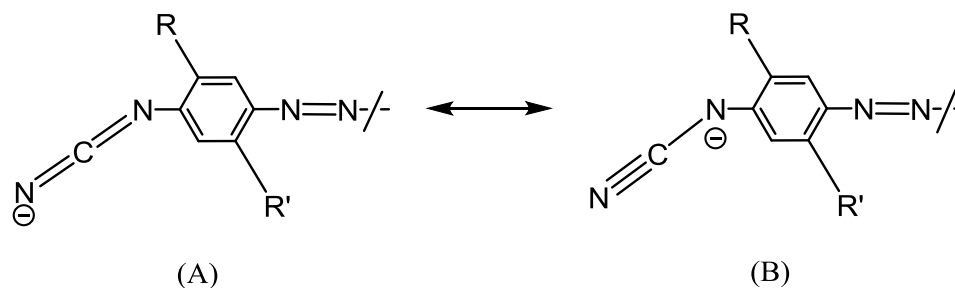
$${}^a\text{R1} = \frac{\sum ||F_o| - |F_c||}{\sum |F_o|}$$

$${}^b\text{wR2} = \left(\frac{\sum w(|F_o| - |F_c|)^2}{\sum w|F_o|^2} \right)^{1/2}$$

Table 3.4.2: Selected Crystal Structure Data for [AsPh₄]₂[Me₂adpc](5g).

Bond Lengths ^a / angstroms		Bond Angles ^a / deg.	
N1-C1	1.164 (2)	N1-C1-N2	174.59 (17)
N2-C1	1.313 (2)	C1-N2-C2	117.50 (13)
N2-C2	1.385 (2)	N2-C2-C3	124.55 (14)
N3-C5	1.411 (2)	N2-C2-C7	118.06 (13)
N3-N3 (A)	1.272 (3)	N3-C5-C6	124.09 (14)
-		N3-C5-C4	116.76 (13)
-		N3(A)-N3-C5	114.28 (16)
-		C8-C4-C5	120.85 (13)

of the plane of the phenyl ring (no more than 0.3 Å), while the azo group maintains coplanarity with the phenyl group even in presence of two bulky methyl groups *ortho* to the azo group. It has been suggested that the planar geometry allows for effective π -delocalization of the cyanamide group with the phenylazo groups. Like other phenylcyanamide and 1,4-dicyanamide benzene anions, the cyanamide group in Me₂adpc²⁻ is approximately linear (174.59 (17)°).⁴⁴ The terminal nitrile bond length in Me₂adpc²⁻ anion (1.164 (2) Å) is smaller than that of corresponding 2,5-Me₂dicyd²⁻ anion (1.18 (3) Å) and comparable to that of 2,3,4,5-Cl₄dicyd²⁻ anion (1.167 (4)).⁴⁴ This is consistent with large electron withdrawing effect of the phenylazo group that increases more triple bond character in the terminal nitrile (CN) bond by favouring the resonating structure B, as shown below.



This resonance effect is also reflected in the relatively smaller bond length between the phenyl ring and the cyanamide group in $\text{Me}_2\text{adpc}^{2-}$ anion (1.385 (2) Å) than that in 2,5- $\text{Me}_2\text{dicyd}^{2-}$ anion (1.426 (22) Å). The $-\text{N}=\text{N}-$ bond length (1.272 (3) Å) in $\text{Me}_2\text{adpc}^{2-}$ anion also falls in the expected region for aromatic azo compounds.

3.4.3 Infrared Spectroscopy

The infrared spectra of $\text{R}_2\text{R}_2'\text{adpcH}_2$ ligands (**4a-4f**), $\text{Tl}_2[\text{R}_2\text{R}_2'\text{adpc}]$ salts (**5a-5e**) and all dinuclear $[\{\text{Ru}(\text{tpy})(\text{bpy})\}_2(\mu\text{-R}_2\text{R}_2'\text{adpc})][\text{PF}_6]_2$ complexes (**7a-7f**) were taken on the KBr discs and the corresponding $\nu(\text{NCN})$ stretches are shown in the Table 3.4.3. The Figures 3.4.3-3.4.5 show representative spectra of neutral $\text{Me}_2\text{adpcH}_2$ ligand, its anionic form $\text{Tl}_2[\text{Me}_2\text{adpc}]$ and **7b**.

4a-4f exhibit strong $\nu(\text{NCN})$ stretches in the region between 2225 and 2251 cm^{-1} and show only a little variation with the electronic nature of the substituents. The observed $\nu(\text{NCN})$ stretching frequencies are comparable to those of other neutral phenylcyanamide and 1,4-dicyanamide ligands.⁷⁻¹⁸ The $\nu(\text{NCN})$ bands of **5a-5e** and **7a-7f** appear at 2042-2115 cm^{-1} and 2153-2165 cm^{-1} , respectively and coincide with those of other anionic phenylcyanamide, 1,4-dicyanamide ligands and their complexes.⁷⁻¹⁸

Table 3.4.3: Infrared Data for $\nu(\text{NCN})$ Bands of Free Ligands (**4a-4f**, **5a-5e**) and $[\{\text{Ru}(\text{tpy})(\text{bpy})\}_2(\mu\text{-R}_2\text{R}_2'\text{adpc})]^{2+}$ Complexes (**7a-7f**).^a

Substituents, $\text{R}_2\text{R}_2'$ -	$\nu(\text{NCN})$ Stretches / cm^{-1}		
	Neutral Ligand, $\text{R}_2\text{R}_2'\text{-adpcH}_2$	TI Salts, $\text{R}_2\text{R}_2'\text{-adpc}^{2-}$	Complexes
$\text{Me}_4\text{-}$	2241	2111	2156
$\text{Me}_2\text{-}$	2243	2062	2154
$\text{H}_4\text{-}$	2225	2078, 2042	2161
$\text{Cl}_2\text{-}$	2249	2113	2153
$\text{Cl}_4\text{-}$	2251	2115	2165
<i>meta</i> - $\text{H}_4\text{-}$	2236	2104	2158

^aperformed on KBr disc.

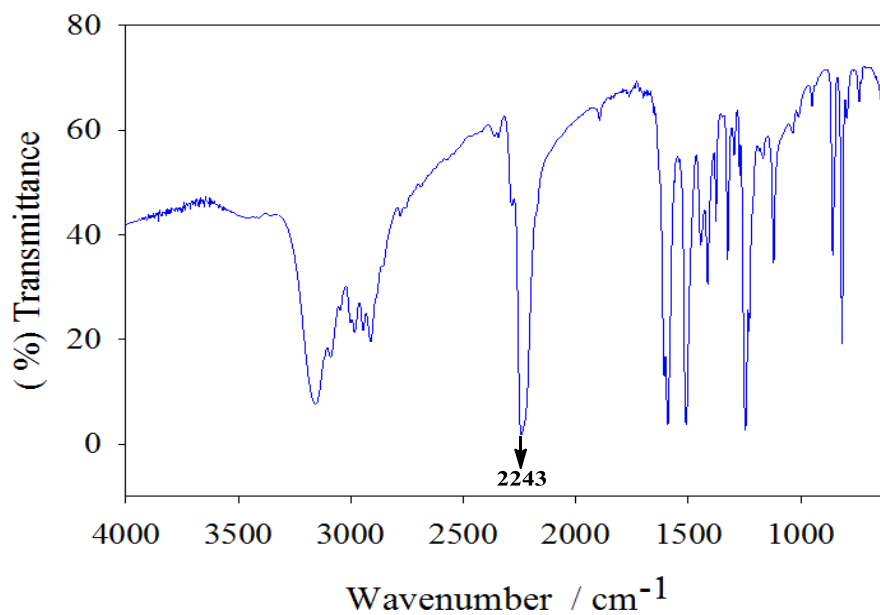


Figure 3.4.3: IR spectrum of $\text{Me}_2\text{adpcH}_2$ ligand (**4b**) on KBr Disc.

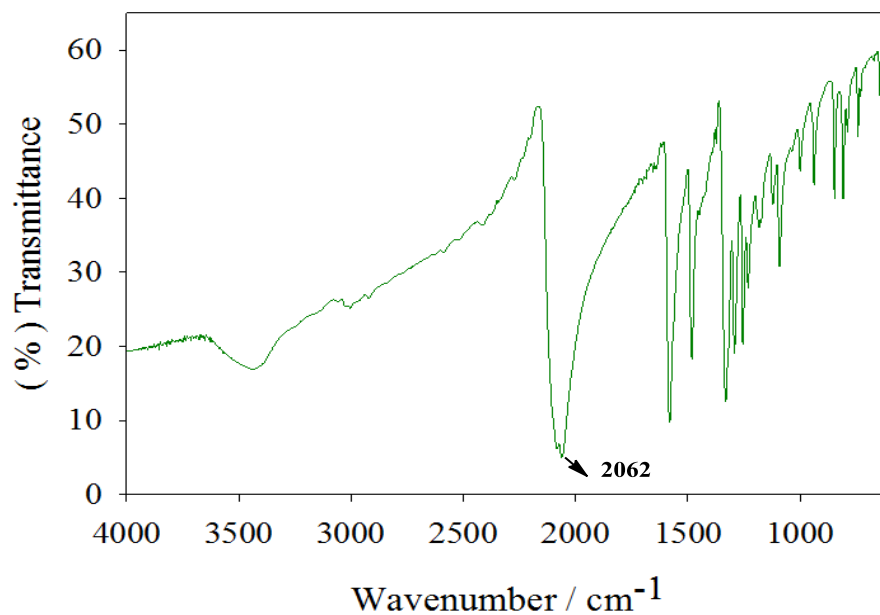


Figure 3.4.4: IR spectrum of $\text{Tl}_2[\text{Me}_2\text{adpc}]$ salt (**5a**) on KBr Disc.

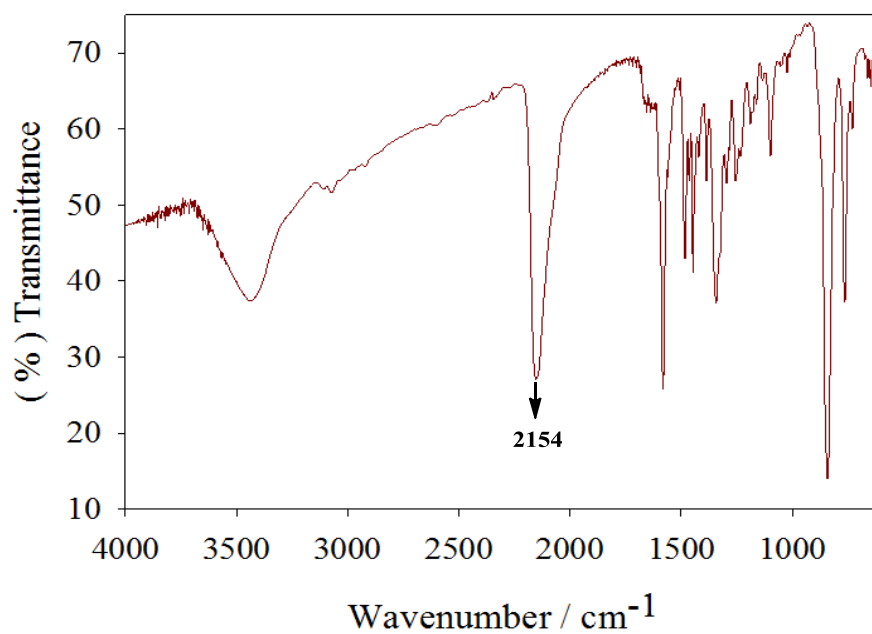


Figure 3.4.5: IR spectrum of $[\{\text{Ru}(\text{tpy})(\text{bpy})\}_2(\mu\text{-Me}_2\text{adpc})] [\text{PF}_6]_2$ (**7b**) in KBr.

Table 3.4.4: 300 MHz ^1H NMR Data of $\text{R}_2\text{R}'_2\text{adpcH}_2$ (**4a-4f**) in $\text{DMSO}-d_6$.

$\text{R}_2\text{R}'_2\text{adpcH}_2$ Ligands	Chemical Shift (ppm)/ type	J values (Hz)
$\text{Me}_4\text{adpcH}_2$	9.67 (s, 2H) (H5, N-H) 7.45 (s, 2H) (H1, Ph-H) 7.04 (s, 2H) (H2, Ph-H) 2.65 (s, 6H) (H3, CH_3 -H) 2.21 (s, 6H) (H4, CH_3 -H)	
$\text{Me}_2\text{adpcH}_2$	10.54 (s, 2H) (H4, N-H) 7.65 (d, 2H) (H2, Ph-H) 6.97 (d, 2H) (H1, Ph-H) 6.90 (dd, 2H) (H3, Ph-H) 2.67 (s, 6H) (H5, CH_3 -H)	8.7 2.3 8.8, 2.4
adpcH_2	10.61 (s, 2H) (H3, N-H) 7.88 (d, 4H) (H1, Ph-H) 7.12 (d, 4H) (H2, Ph-H)	8.8 8.8
$\text{Cl}_2\text{adpcH}_2$	10.40 (s, 2H) (H4, N-H) 7.96 (d, 2H) (H1, Ph-H) 7.93 (dd, 2H) (H2, Ph-H) 7.39 (d, 2H) (H3, Ph-H)	2.0 8.6, 2.2 8.5
<i>meta</i> - adpcH_2	10.54 (s, 2H) (H5, N-H) 7.67 – 7.54 (m, 4H) (H2, H3, Ph-H) 7.41 (d, 2H) (H1, Ph-H) 7.17 (dt, 2H) (H4, Ph-H)	1.8 7.1, 2.0

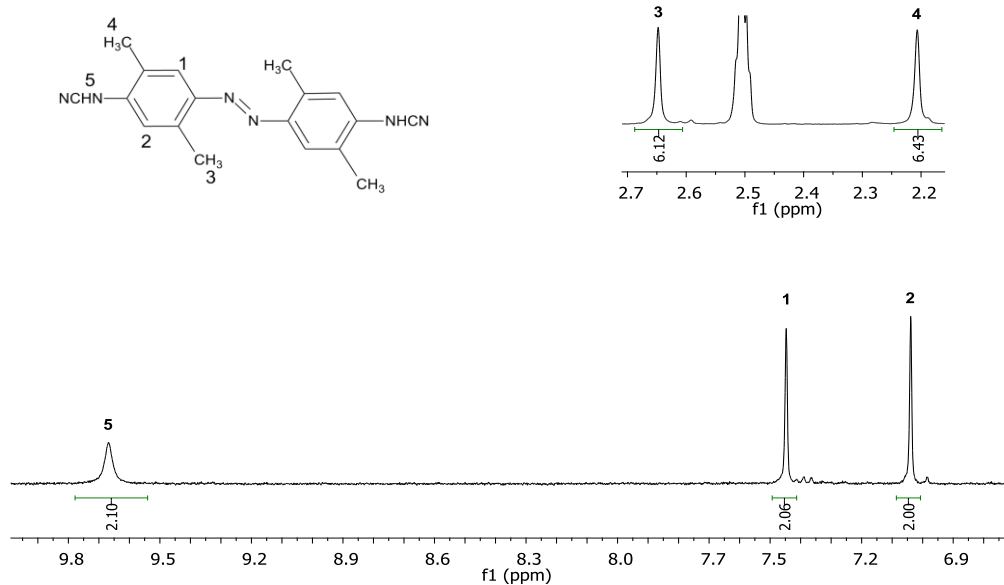


Figure 3.4.7: ^1H NMR spectrum of $\text{Me}_4\text{adpcH}_2$ ligand (**4a**) in $\text{DMSO-}d_6$

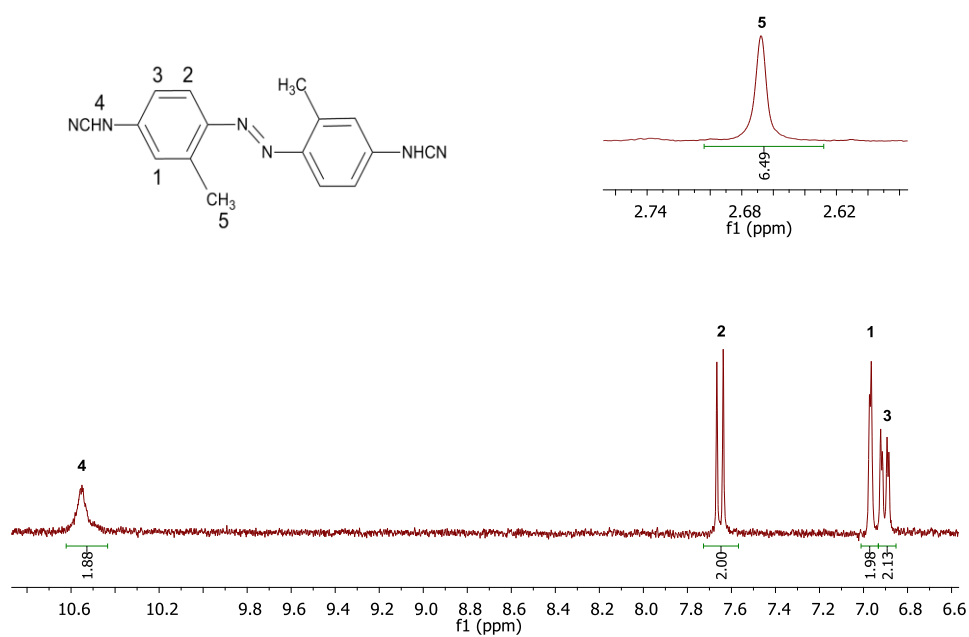


Figure 3.4.8: ^1H NMR spectrum of $\text{Me}_2\text{adpcH}_2$ ligand (**4b**) in $\text{DMSO-}d_6$

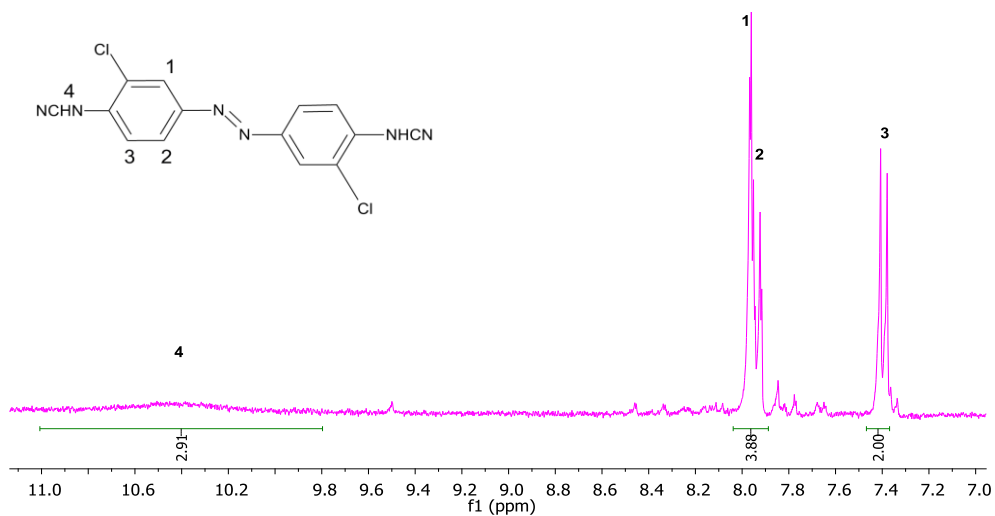


Figure 3.4.9: ^1H NMR spectrum of $\text{Cl}_2\text{adpcH}_2$ ligand (**4e**) in $\text{DMSO-}d_6$

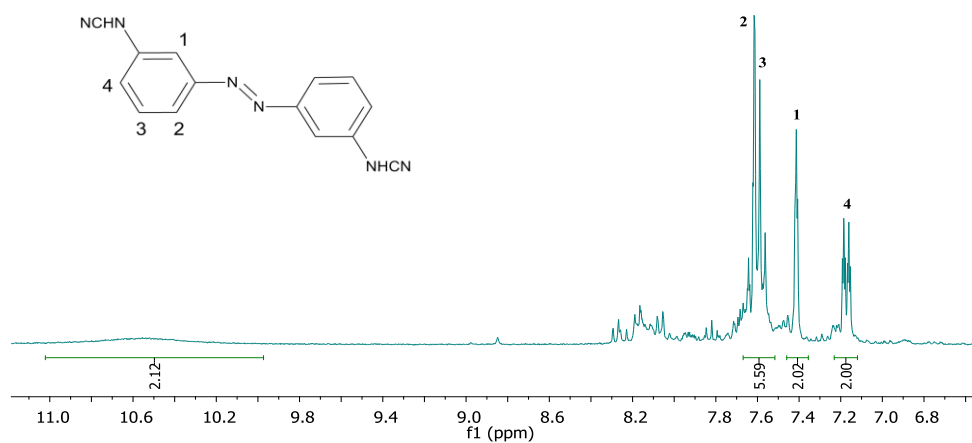
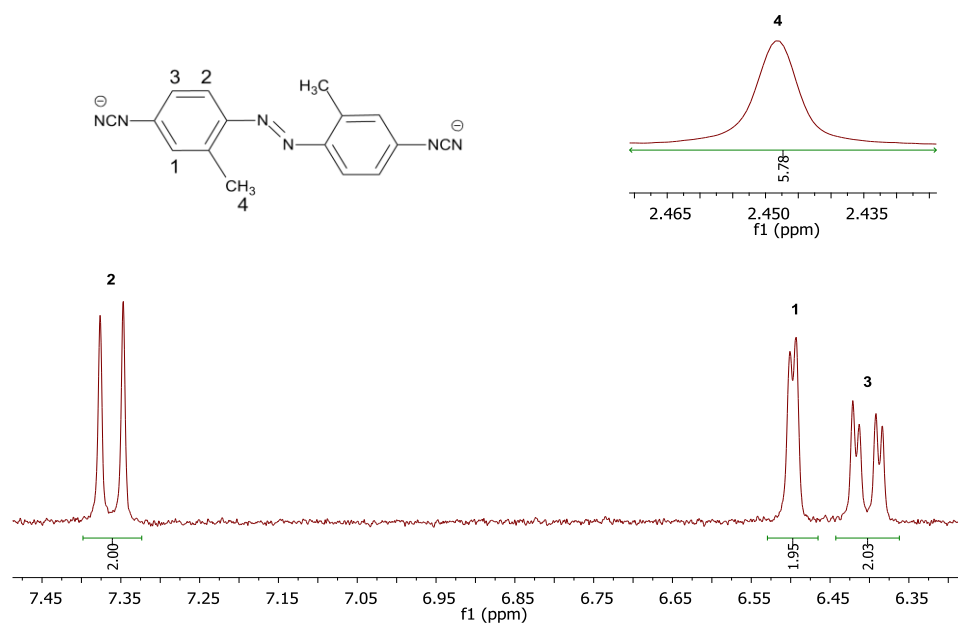


Figure 3.4.10: ^1H NMR spectrum of *meta*- adpcH_2 ligand (**4f**) in $\text{DMSO-}d_6$

Table 3.4.5: 300 MHz ^1H NMR Data of $\text{Tl}_2[\text{R}_2\text{R}'_2\text{adpc}]$ (**5a-5e**) in $\text{DMSO-}d_6$.

$\text{R}_2\text{R}'_2\text{adpc}^{2-}$	Chemical Shift (ppm)/ type	J values (Hz)
$\text{Me}_2\text{adpc}^{2-}$	7.36 (d, 2H) (H2, Ph-H) 6.49 (s, 2H) (H1, Ph-H) 6.40 (d, 2H) (H3, Ph-H) 2.45 (s, 6H) (H4, CH_3 -H)	8.8 11.2
adpc^{2-}	7.41 (d, 4H) (H1, Ph-H) 6.62 (d, 4H) (H2, Ph-H)	8.8 8.8
$\text{Cl}_2\text{adpc}^{2-}$	7.55 (d, 2H) 7.44 (dd, 2H) 6.96 (d, 2H)	
$\text{Cl}_4\text{adpc}^{2-}$	7.59 (s, 2H) 6.95 (s, 2H)	
<i>meta</i> - adpc^{2-}	7.13 – 7.02 (m, 4H) (Ph-H1, H3) 6.88 (ddd, 2H) (Ph-H2) 6.68 (ddd, 2H) (Ph-H4)	7.6, 2.0, 1.1 7.9, 2.4, 1.1

**Figure 3.4.11:** ^1H NMR spectrum of $\text{Tl}_2[\text{Me}_2\text{adpc}]$ (**5a**) in $\text{DMSO-}d_6$

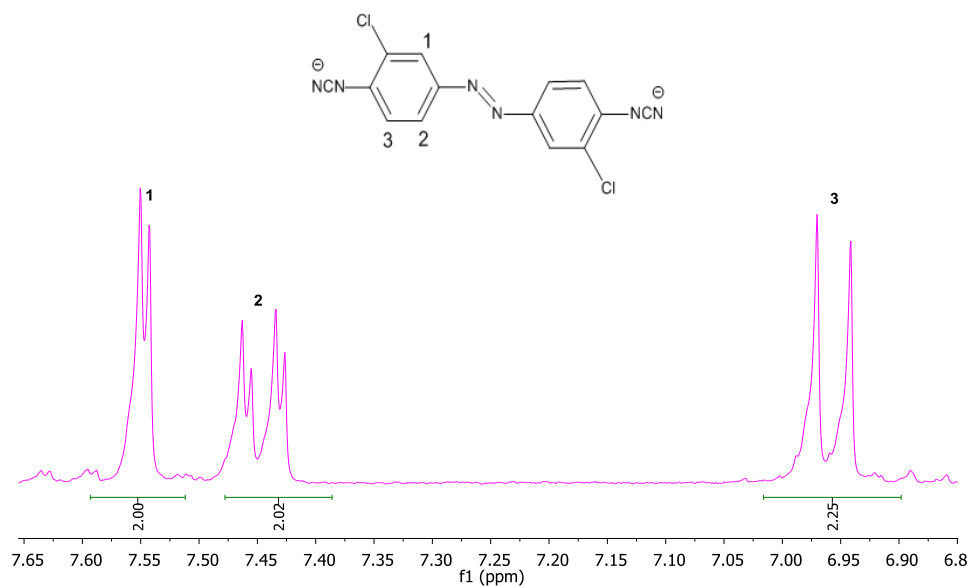


Figure 3.4.12: ^1H NMR spectrum of $\text{Tl}_2[\text{Cl}_2\text{adpc}]$ (**5c**) in $\text{DMSO-}d_6$

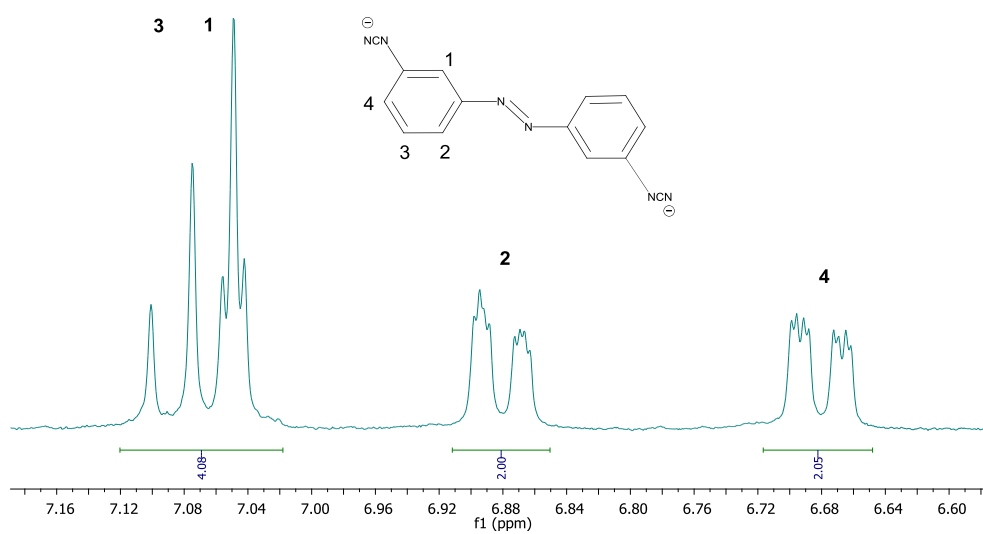


Figure 3.4.13: ^1H NMR spectrum of $\text{Tl}_2[\text{meta-adpc}]$ (**5e**) in $\text{DMSO-}d_6$.

Table 3.4.6: 300 MHz ^1H NMR data for $[\{\text{Ru}(\text{tpy})(\text{bpy})\}_2(\mu\text{-R}_2\text{R}_2'\text{adpc})](\text{PF}_6)_2$ complexes (**7a-7f**) in $\text{DMSO-}d_6$

$\text{R}_2\text{R}_2'\text{adpc}$	Chemical Shift (ppm)/type	J values (Hz)
Me_4adpc	9.68 (d, 2H) (C6) 8.97 (d, 2H) (C3) 8.92 (d, 4H) (B3') 8.80 (d, 4H) (A3) 8.70 (d, 2H) (D3') 8.41 (t, 2H) (C4) 8.33 (t, 2H) (B4') 8.11 (dd, 6H) (C5, A4) 7.86 (t, 2H) (D4') 7.75 (d, 4H) (A6) 7.55 – 7.39 (m, 6H) (D6', A5) 7.20 – 7.13 (t, 2H) (D5') 7.12 (s, 2H) (E1) 5.61 (s, 2H) (E2) 2.21 (s, 6H) (E3) 1.80 (s, 6H) (E4)	5.4 8.3 8.1 8.0 8.0 7.9 8.1 14.5, 6.9 7.8 5.0
Me_2adpc	9.69 (d, 2H) (C6) 9.00 (d, 2H) (C3) 8.94 (d, 4H) (B3') 8.82 (d, 4H) (A3) 8.73 (d, 2H) (D3') 8.44 (t, 2H) (C4) 8.35 (t, 2H) (B4') 8.13 (dd, 6H) (C5, A4) 7.89 (t, 2H) (D4') 7.77 (d, 4H) (A6) 7.49 (dd, 6H) (D6', A5) 7.18 (dd, 4H) (D5', E3) 5.95 (d, 2H) (E2) 5.87 (s, 2H) (E1) 2.31 (s, 6H)	4.9 8.3 8.1 8.0 8.2 7.9 8.1 15.8, 7.9 7.9 5.4 11.5, 6.1 7.3, 4.9 8.8

Continued

R₂R₂'adpc	Chemical Shift (ppm)/type	J values (Hz)
Me ₄ adpc	9.68 (d, 2H) (C6) 8.97 (d, 2H) (C3) 8.92 (d, 4H) (B3') 8.80 (d, 4H) (A3) 8.70 (d, 2H) (D3') 8.41 (t, 2H) (C4) 8.33 (t, 2H) (B4') 8.11 (dd, 6H) (C5, A4) 7.86 (t, 2H) (D4') 7.75 (d, 4H) (A6) 7.55 – 7.39 (m, 6H) (D6',A5) 7.20 – 7.13 (t, 2H) (D5') 7.12 (s, 2H) (E1) 5.61 (s, 2H) (E2) 2.21 (s, 6H) (E3) 1.80 (s, 6H) (E4)	5.4 8.3 8.1 8.0 8.0 7.9 8.1 14.5, 6.9 7.8 5.0
Me ₂ adpc	9.69 (d, 2H) (C6) 9.00 (d, 2H) (C3) 8.94 (d, 4H) (B3') 8.82 (d, 4H) (A3) 8.73 (d, 2H) (D3') 8.44 (t, 2H) (C4) 8.35 (t, 2H) (B4') 8.13 (dd, 6H) (C5, A4) 7.89 (t, 2H) (D4') 7.77 (d, 4H) (A6) 7.49 (dd, 6H) (D6', A5) 7.18 (dd, 4H) (D5', E3) 5.95 (d, 2H) (E2) 5.87 (s, 2H) (E1) 2.31 (s, 6H)	4.9 8.3 8.1 8.0 8.2 7.9 8.1 15.8, 7.9 7.9 5.4 11.5, 6.1 7.3, 4.9 8.8

Continued

R₂R₂'adpc	Chemical Shift (ppm)/type	J values (Hz)
Cl₄adpc	9.64 (d, 2H) (C6) 8.97 (d, 2H) (C3) 8.93 (d, 4H) (B3') 8.81 (d, 4H) (A3) 8.71 (d, 2H) (D3') 8.50 – 8.28 m, 4H)(C4,B4') 8.12 (m, 6H) (C5, A4) 7.88 (t, 2H) (D4') 7.76 (d, 4H) (A6) 7.48 (t, 6H) (D6', A5) 7.43 (s, 2H)(E1) 7.17 (t, 2H)(D5') 5.88 (s, 2H)(E2)	5.1 8.4 8.1 7.9 8.4 7.0 7.3 5.1 5.9 6.9
meta-adpc	9.68 (s, 2H) (C6) 8.96 (d, 2H) (C3) 8.86 (d, 4H) (B3') 8.74 (d, 4H) (A3) 8.69 (d, 2H) (D3') 8.39 (t, 2H) (C4) 8.27 (t, 2H) (B4') 8.14 – 7.98 (m, 6H)(C5, A4) 7.85 (t, 2H) (D4') 7.73 (d, 4H) (A6) 7.47 – 7.35 (m, 6H)(D6', A5) 7.14 (t, 2H) (D5') 7.00 (t, 2H) (E3) 6.91 (d, 2H) (E2) 6.53 (d, 2H) (E1) 6.08 (d, 2H) (E4)	4.8 8.1 8.1 8.1 8.2 6.8 8.1 7.2 5.3 7.1 6.5 8.2 4.0 8.8

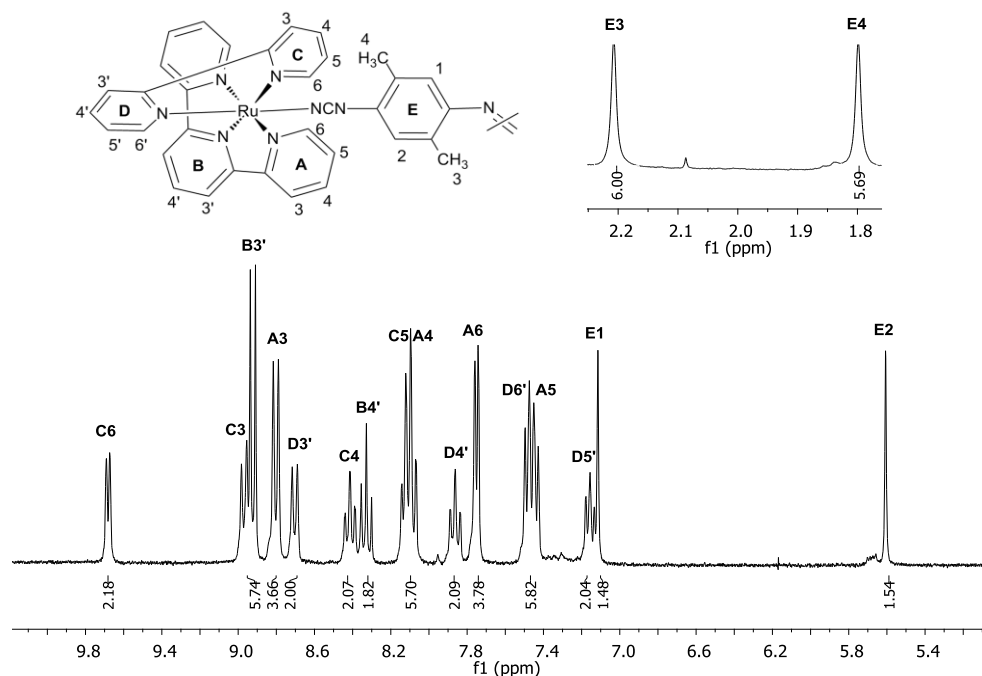


Figure 3.4.14: ^1H NMR spectrum of $[\{\text{Ru}(\text{tpy})(\text{bpy})\}_2(\mu\text{-Me}_4\text{adpc})][\text{PF}_6]_2$ complex (7a) in $\text{DMSO-}d_6$.

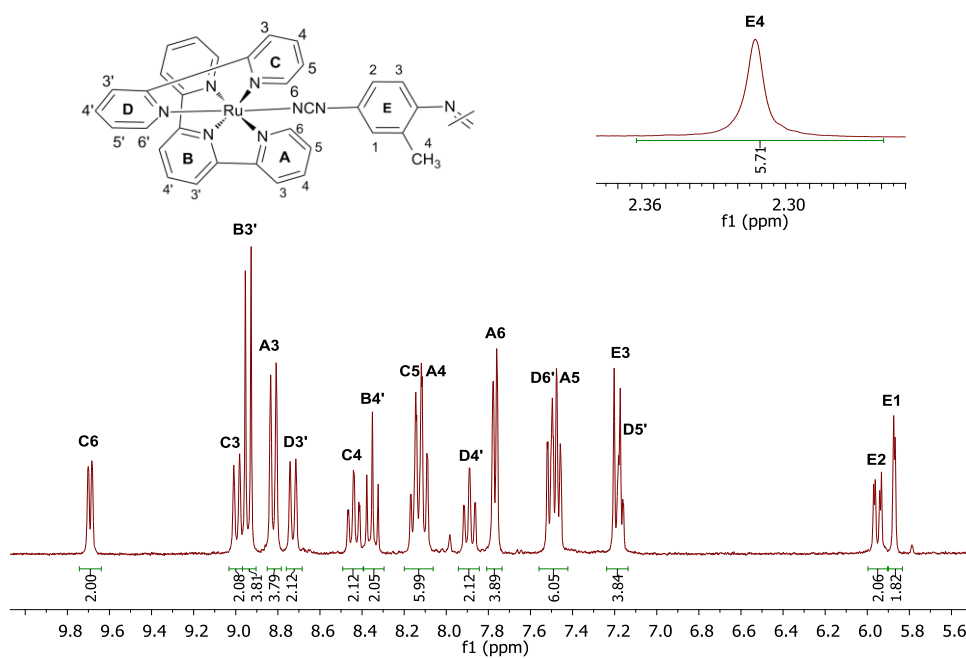


Figure 3.4.15: ^1H NMR spectrum of $[\{\text{Ru}(\text{tpy})(\text{bpy})\}_2(\mu\text{-Me}_2\text{adpc})][\text{PF}_6]_2$ complex (7b) in $\text{DMSO-}d_6$.

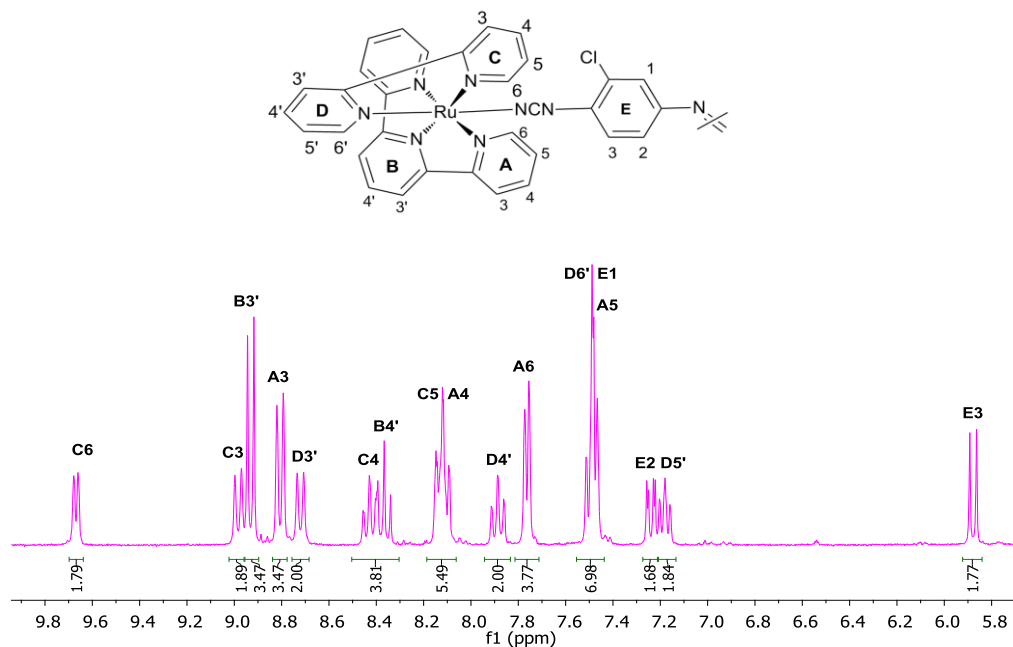


Figure 3.4.16: ^1H NMR spectrum of $[\text{Ru}(\text{tpy})(\text{bpy})]_2(\mu\text{-Cl}_2\text{adpc}) [\text{PF}_6]_2$ complex (7d) in $\text{DMSO-}d_6$.

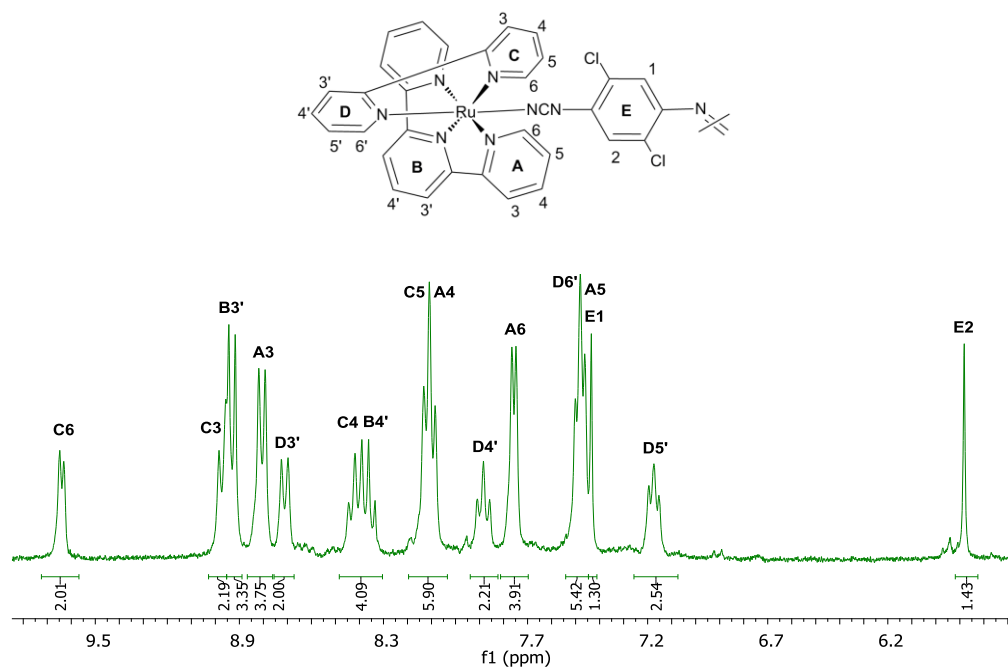


Figure 3.4.17: ^1H NMR spectrum of $[\text{Ru}(\text{tpy})(\text{bpy})]_2(\mu\text{-Cl}_4\text{adpc}) [\text{PF}_6]_2$ complex (7e) in $\text{DMSO-}d_6$.

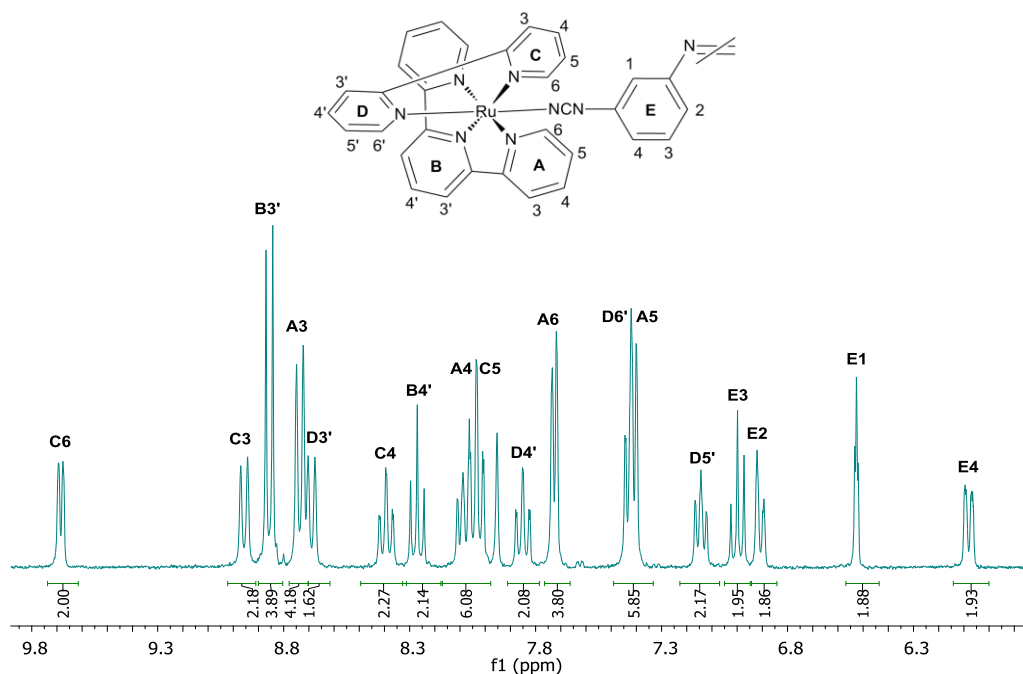


Figure 3.4.18: 1H NMR spectrum of $[Ru(tpy)(bpy)]_2(\mu\text{-meta-adpc}) [PF_6]_2$ complex (**7f**) in $DMSO-d_6$.

3.4.5. The 1H NMR and 1H - 1H -COSY spectra of **7a-7b**, **7d-7f** are shown in the Figures 3.4.14-3.4.22 and the corresponding data for **7a-7f** have been included in the Table 3.4.6. The 1H NMR spectral data for unsubstituted $adpcH_2$ ligand (**4c**), its thallium salt (**5b**) and dinuclear complex (**7c**) have been reported previously,¹ and reproduced in the present work. The chemical shift values of $Tl[Cl_4adpc]$ salt (**5d**) have been taken from the 1H NMR spectrum of the slightly impure thallium salt and included in the Table 3.4.5 for comparison. All proton peaks for tpy, bpy and coordinated R_2R_2' adpc ligands have been assigned with the help of 1H - 1H COSY technique, coupling constants (J values) and integration values for respective peaks and compared with those reported in the literature.

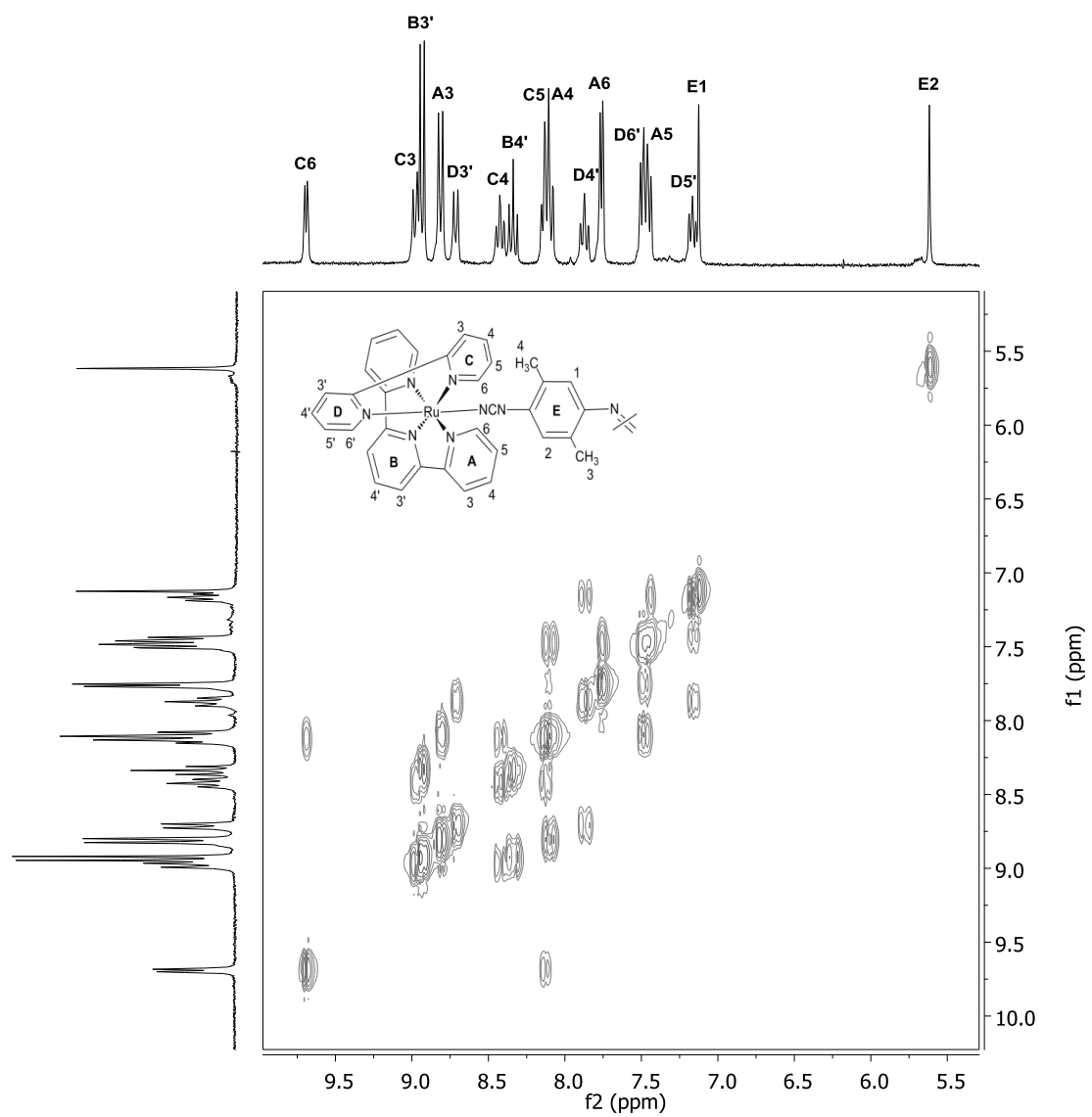


Figure 3.4.19: ^1H - ^1H COSY spectrum of $[\{\text{Ru}(\text{tpy})(\text{bpy})\}_2(\mu\text{-Me}_4\text{adpc})][\text{PF}_6]_2$ complex (7a) in $\text{DMSO-}d_6$.

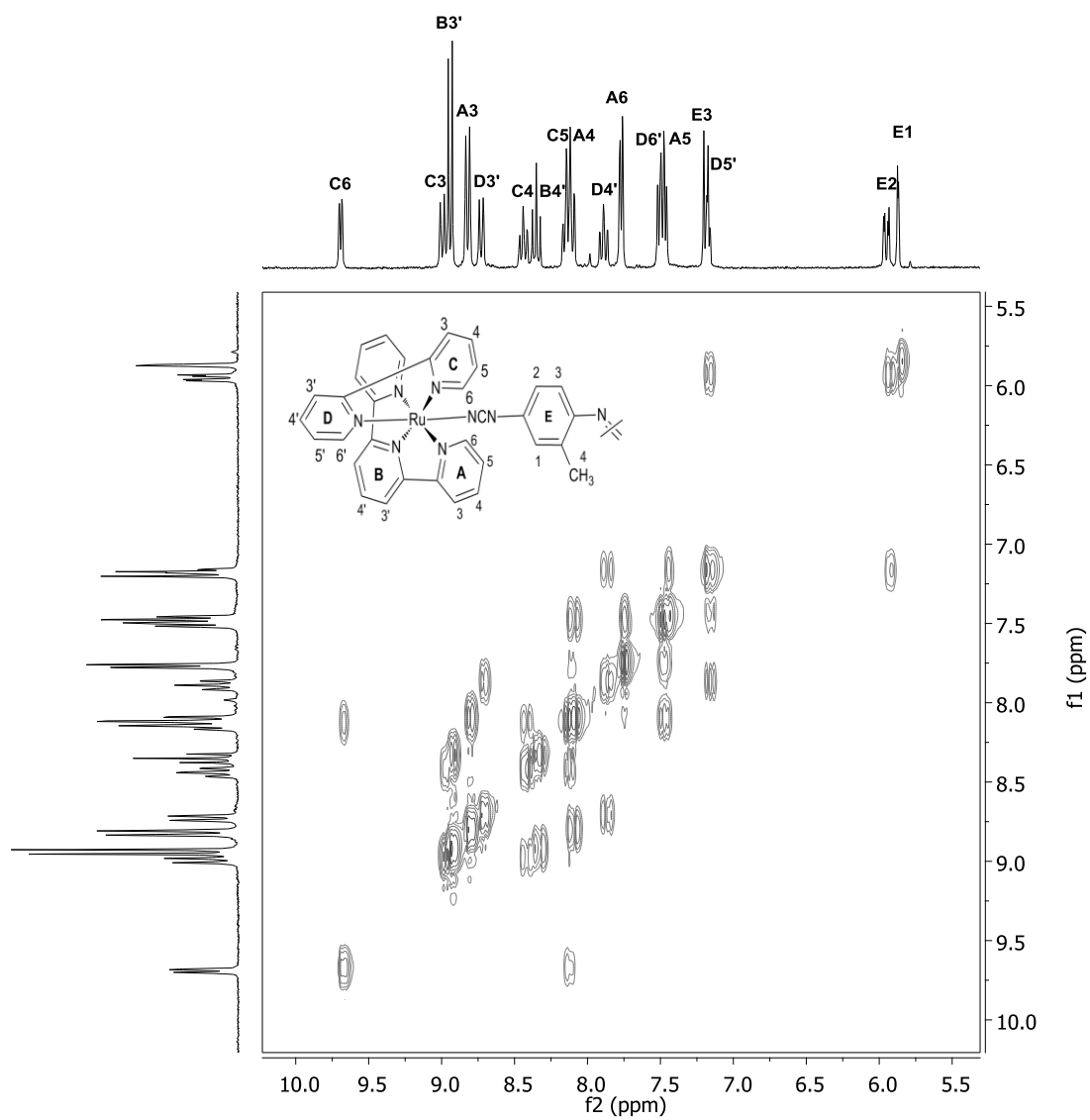


Figure 3.4.20: ^1H - ^1H COSY spectrum of $[\{\text{Ru}(\text{tpy})(\text{bpy})\}_2(\mu\text{-Me}_2\text{adpc})][\text{PF}_6]_2$ complex (7b) in $\text{DMSO-}d_6$.

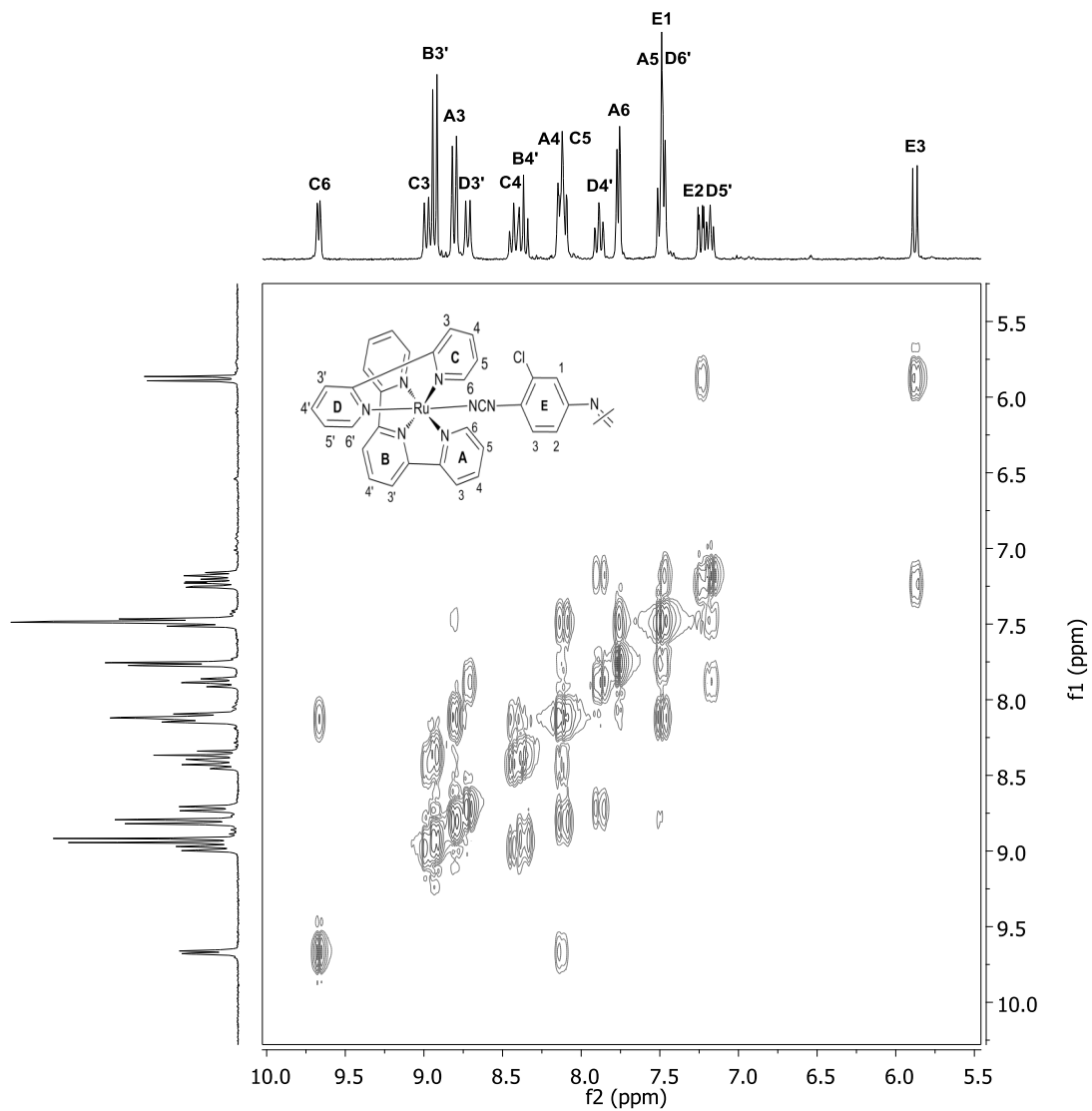


Figure 3.4.21: ^1H - ^1H COSY spectrum of $[\{\text{Ru}(\text{tpy})(\text{bpy})\}_2(\mu\text{-Cl}_2\text{adpc})][\text{PF}_6]_2$ complex (**7d**) in $\text{DMSO-}d_6$.

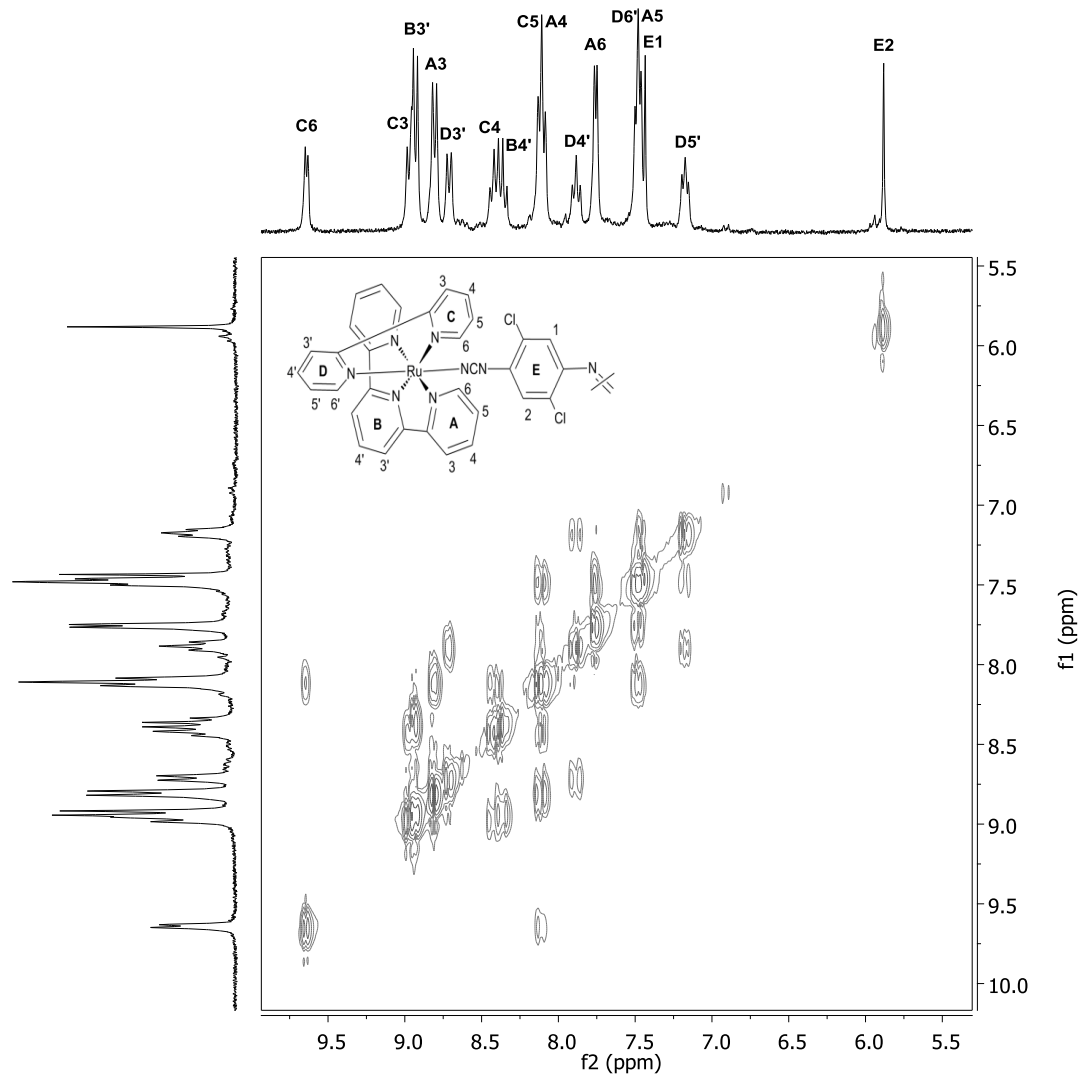


Figure 3.4.22: ^1H - ^1H COSY spectrum of $[\{\text{Ru}(\text{tpy})(\text{bpy})\}_2(\mu\text{-Cl}_4\text{adpc})] [\text{PF}_6]_2$ complex (**7e**) in $\text{DMSO-}d_6$.

All dinuclear $[\{\text{Ru}(\text{tpy})(\text{bpy})\}_2(\mu\text{-R}_2\text{R}'_2\text{adpc})] [\text{PF}_6]_2$ complexes (**7a-7f**), exhibited a total of 14 signals for tpy and bpy protons in the region between $\delta 9.70$ - 7.15 ppm (Table 2.4.5), while the signals for aromatic protons on the bridging $\text{R}_2\text{R}'_2\text{adpc}^{2-}$

ligands appear in the region between $\delta 7.20$ - 5.65 ppm. The numbering schemes used to assign protons from tpy and bpy ligands in **7a-7f** are shown in the Figure 3.4.23.

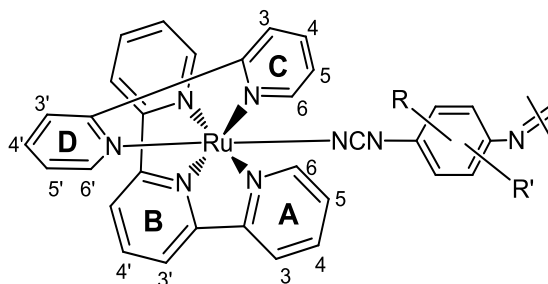


Figure 3.4.23: Numbering scheme used to assign tpy and bpy proton resonances in $[\{\text{Ru}(\text{tpy})(\text{bpy})\}_2(\mu\text{-R}_2\text{R}'_2\text{adpc})][\text{PF}_6]_2$ complex (**7a-7f**) in $\text{DMSO-}d_6$.

As the X-ray crystal structure of $[\{\text{Ru}(\text{tpy})(\text{bpy})\}_2(\mu\text{-adpc})]^{2+}$ (**7c**) shows, each Ru(II) ion occupies a pseudo-octahedral coordination sphere of nitrogen donor atoms, where tpy ligand occupies an equatorial plane and a cyanamide group of the adpc^{2-} ligand is *trans*- to one of the pyridine rings of bpy. With this arrangement of ligands, one would expect to observe a total of six signals from the tpy ligand consisting of three triplets and three doublets for protons on the terminal and the central pyridine rings (A, B). On the other hand, pyridine rings (C, D) on the bpy ligand are magnetically non-equivalent and would exhibit a total of eight signals consisting of two sets of two doublets and two triplets. Both tpy and bpy ligands are therefore expected to give a total of 14 signals in the ^1H NMR spectra of **7a-7f**.

With the exception of B4' protons, signals for A6, A5, A4, A3, B3' protons on the tpy ligand could be easily distinguished from those of bpy ligands on the basis of the integration ratios of tpy and bpy signals (tpy : bpy = 1:2). The most deshielded signals at

δ 8.92 and δ 8.80 ppm have been assigned to B3' and A3 protons on the basis of their characteristic coupling constant values ($J \sim 8.1$ Hz).^{46a-d} These two protons on the adjacent pyridine rings have been assigned as the most deshielded protons on the tpy ligand in other Ru(II)-terpyridine complexes and they are significantly deshielded in complexes relative to free ligands (ref).^{46a-d} These studies have shown that the terminal and central pyridine rings undergo conformational change from *trans,trans* in the free ligand to *cis,cis* in complexes, which causes significant through-space interaction between A3 and B3' protons on the adjacent pyridine rings, rendering them the most deshielded protons in the coordinated tpy ligand.^{46a,b} The distinction between A3 and B3' protons was made by combined analysis of coupling patterns of these two protons in ¹H-¹H COSY spectra and integration values of their correlated protons. As seen in the Figure 3.4.23, B3' protons would have correlation with the B4' protons which would give a triplet signal with an integration value half of those of other protons on the tpy ligand. Indeed, the doublet signal at δ 8.92 ppm is correlated with the triplet at δ 8.35 ppm, which gives an integration value half of that of the former (see Figures 3.4.15 and 3.4.20, for example), suggesting the assignments of the signals at δ 8.92 and δ 8.35 ppm to B3' and B4' protons, respectively. The deshielded doublet signal at δ 8.80 ppm is therefore assigned to A3. The assignments of the rest of the tpy protons (A4, A5, A6) were directly made from the coupling patterns observed in the ¹H-¹H COSY spectra of complexes (Figure 3.4.20-3.4.22).

Two pyridine rings (C, D) on the bpy ligand are magnetically inequivalent. The axial pyridine ring (D) overhanging the central pyridine ring (B) of the tpy ligand experiences strong diamagnetic anisotropic field of aromatic ring current of the latter and

proton resonances corresponding to this ring (D) usually occur in the *upfield* region with respect to those of the pyridine ring (C).^{46e-i} The most *upfield* doublet and triplet signals for the bpy ligand (δ 7.50 and δ 7.15 ppm respectively) could be assigned to D6' and D5' protons respectively, as they were expected to experience the most shielding effect due to their close proximities to the diamagnetic ring current of the underlying pyridine ring (B) of the tpy ligand. These assignments were further supported by the coupling patterns observed in the ^1H - ^1H COSY spectra of complexes. On the other hand, the doublet in the most *downfield* region ($\delta \sim 9.65$ ppm) was assigned to C6 proton on the basis of the characteristic coupling constant value ($J = 5.1$ Hz) of the proton on the carbon adjacent to the nitrogen atom in the pyridine system.^{46e-i} This assignment was further supported by the coupling pattern of C6 proton observed in the ^1H - ^1H COSY spectra of complexes. Like the terpyridine system, the C3 and D3' protons on the adjacent pyridine rings on the bpy ligand also experience through space interaction and are deshielded. These two protons were identified by their characteristic coupling constant values ($J = 8.1\text{Hz}$).^{46e-i} The C4, C5 and D4' protons were assigned directly from the observed coupling patterns in the ^1H - ^1H COSY spectra of complexes.

Aromatic protons on the bridging $\text{R}_2\text{R}_2'\text{adpc}^{2-}$ ligands in complexes exhibits signals in the more *upfield* region (δ 7.20-5.65 ppm) relative to those of tpy and bpy ligands. The assignments of these protons were made with the help of ^1H - ^1H COSY spectroscopy. The observed chemical shifts are comparable to those of other Ru(II)-phenylcyanamide complexes.^{1,3,4,13,18}

3.4.5 Electronic Absorption Spectroscopy

The quantitative electronic absorption spectra of $Tl_2[R_2R_2'adpc]$ salts (**5a-5c**) and dinuclear $[\{Ru(tpy)(bpy)\}_2(\mu-R_2R_2'adpc)]^{2+}$ complexes (**7a-7f**) in DMF are shown in the Figure 3.4.20 and 3.4.21 respectively, while that for $Tl_2[meta-adpc]$ salt (**5e**) is shown in the Figure C.7 in the Appendix-C. The quantitative electronic absorption data of all anionic ligands (**5a-5c**, **5e**) and **7a-7f**, including those of their oxidized forms, have been included in the Table 3.4.7. The electronic absorption data of unsubstituted free anionic $adpc^{2-}$ ligand (**5b**), its dinuclear complex (**7c**) and their oxidized forms have been reported previously¹ and reproduced in the present research work.

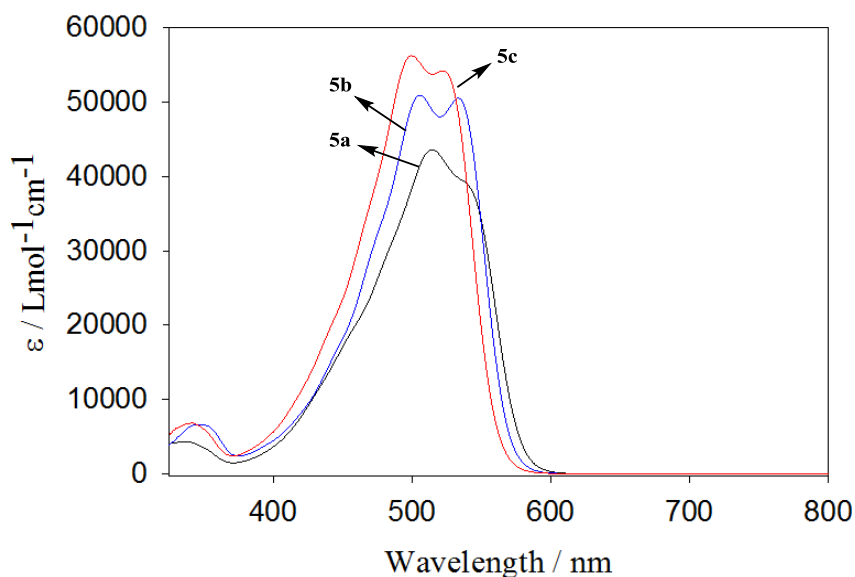


Figure 3.4.24: Quantitative electronic absorption spectra of $Tl_2[R_2R_2'adpc]$ (**5a-5c**) in DMF. $R_2R_2'adpc = Me_2-$ (**5a**); unsubstituted, H_4- (**5b**) and Cl_2adpc (**5c**).

Free anionic $R_2R_2'adpc^{2-}$ (**5a-5c**) show intense absorption at 500-545 nm ($\epsilon = 43600-51000 \text{ Lmol}^{-1}\text{cm}^{-1}$), which can be assigned to cyanamide-to-phenylazo intra-ligand charge transfer (ILCT) transitions. The splitting pattern in the band is likely to be

vibronic in origin.¹⁷ The intensity of the visible band ($\lambda_{\text{max}} = 480 \text{ nm}$, $\epsilon = 2070 \text{ Lmol}^{-1}\text{cm}^{-1}$) for free anionic *meta*-adpc²⁻ ligand (**5e**) is significantly reduced relative to its *para* analogues (**5a-5c**) (Table 3.4.7, Figure C.7 in the Appendix-C), indicating poor π -overlap between *meta*-cyanamide with the phenylazo group. The complexes **7a-7e** exhibit two strong absorptions at 317-321 nm ($\epsilon = 58500\text{-}72100 \text{ Lmol}^{-1}\text{cm}^{-1}$) and 490-534 nm ($\epsilon = 58500\text{-}72100 \text{ Lmol}^{-1}\text{cm}^{-1}$), respectively. The $[\{\text{Ru}(\text{tpy})(\text{bpy})\}_2(\mu\text{-meta-adpc})]^{2+}$ complex (**7f**) also exhibits these two absorptions; however, the intensity of the low energy band ($\lambda_{\text{max}} = 490 \text{ nm}$, $\epsilon = 17400 \text{ Lmol}^{-1}\text{cm}^{-1}$) is significantly reduced relative to those other dinuclear complexes (**7a-7e**).

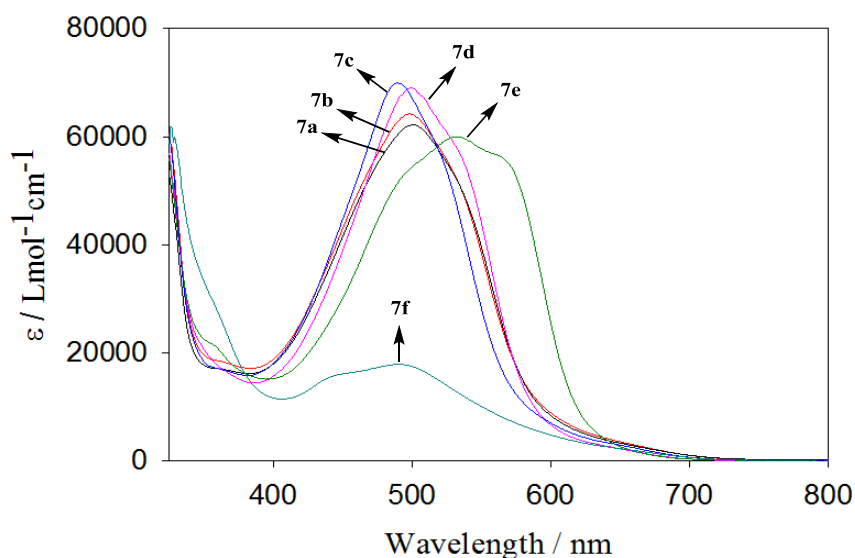


Figure 3.4.25: Quantitative electronic absorption spectra of $[\{\text{Ru}(\text{tpy})(\text{bpy})\}_2(\mu\text{-R}_2\text{R}'_2\text{adpc})] [\text{PF}_6]_2$ complexes (**7a-7f**) in DMF. $\text{R}_2\text{R}'_2\text{adpc} = \text{Me}_4\text{-}$ (**7a**); $\text{Me}_2\text{-}$ (**7b**); unsubstituted, $\text{H}_4\text{-}$ (**7c**); $\text{Cl}_2\text{-}$ (**7d**); $\text{Cl}_4\text{-}$ (**7e**) and *meta*-adpc (**7f**).

Table 3.4.7: Quantitative Electronic Absorption Data^a for $Tl_2[R_2R_2'adpc]$ Salts (**5a-5c**, **5e**) and $[Ru(tpy)(bpy)]_2(\mu-R_2R_2'adpc)[PF_6]_2$ (**7a-7f**) complexes and their Oxidized forms^b in DMF.

Compounds	Absorption / Wavelength, λ in nm (Molar Extinction Coefficient, ϵ / $Lmol^{-1}cm^{-1}$)
Me_2adpc^{2-}	338 (4345); 515 (43600); 545 (37400)
$Me_2adpc^{\bullet-}$	430 (12000); 514 (33900); 667 (2440); 726 (9100); 1118 (760); 1256 (1780)
$adpc^{2-}$	340 (6700); 500 (54400); 523 (51500)
$adpc^{\bullet-}$	421 (8400); 498 (31100); 658 (5030); 714 (17400); 1310 (3900)
Cl_2adpc^{2-}	346 (6600); 506 (51000); 533(50600)
$Cl_2adpc^{\bullet-}$	426 (15000); 505 (37600); 663 (2910); 719 (9130); 1175 (928), 1341 (2060)
<i>meta</i> - $adpc^{2-}$	326 (14200); 480 (2070)
<i>meta</i> - $adpc^{\bullet-}$	326 (12400); 480 (1430); 811 (100)
$[Ru(tpy)(bpy)]_2(\mu-Me_4adpc)^{2+}$	319 (58500); 501(62300)
$[Ru(tpy)(bpy)]_2(\mu-Me_4adpc)^{3+}$	486 (42500); 652 (11300); 820 (10500); 1678 (5300)
$[Ru(tpy)(bpy)]_2(\mu-Me_4adpc)^{4+}$	453 (42000); 696 (14500); 1678 (610)
$[Ru(tpy)(bpy)]_2(\mu-Me_2adpc)^{2+}$	321 (62000); 499 (69100)
$[Ru(tpy)(bpy)]_2(\mu-Me_2adpc)^{3+}$	479 (44500); 652 (12800); 823 (12200); 1758 (7000)
$[Ru(tpy)(bpy)]_2(\mu-Me_2adpc)^{4+}$	452 (44700); 788 (8168); 1758 (490)
$[Ru(tpy)(bpy)]_2(\mu-adpc)^{2+}$	293 (81900); 317(72100); 490 (69100)
$[Ru(tpy)(bpy)]_2(\mu-adpc)^{3+}$	292 (86900); 314(73700); 471 (41300); 652 (13900); 812 (12700); 1920 (11,000)
$[Ru(tpy)(bpy)]_2(\mu-adpc)^{4+}$	312 (73400); 456 (41900); 856 (12200)

continued

Compounds	Absorption / Wavelength, λ in nm (Molar Extinction Coefficient, ϵ / $\text{Lmol}^{-1}\text{cm}^{-1}$)
$[\{\text{Ru}(\text{tpy})(\text{bpy})\}_2(\mu\text{-Cl}_2\text{adpc})]^{2+}$	321 (62000); 499 (69100)
$[\{\text{Ru}(\text{tpy})(\text{bpy})\}_2(\mu\text{-Cl}_2\text{adpc})]^{3+}$	482(42300); 667 (13100); 833(8700); 1923 (10400)
$[\{\text{Ru}(\text{tpy})(\text{bpy})\}_2(\mu\text{-Cl}_2\text{adpc})]^{4+}$	487 (25000); 1124 (11500); 1923 (2620)
$[\{\text{Ru}(\text{tpy})(\text{bpy})\}_2(\mu\text{-Cl}_4\text{adpc})]^{2+}$	321 (63700); 534 (60000)
$[\{\text{Ru}(\text{tpy})(\text{bpy})\}_2(\mu\text{-Cl}_4\text{adpc})]^{3+}$	517 (35900); 677(7900); 876 (7700); 1923 (6600)
$[\{\text{Ru}(\text{tpy})(\text{bpy})\}_2(\mu\text{-Cl}_4\text{adpc})]^{4+}$	462 (31700); 1120 (7020); 1923 (1790)
$[\{\text{Ru}(\text{tpy})(\text{bpy})\}_2(\mu\text{-meta-adpc})]^{2+}$	326 (62000); 491 (17400)
$[\{\text{Ru}(\text{tpy})(\text{bpy})\}_2(\mu\text{-meta-adpc})]^{3+}$	457(17300); 837 (1240); 1100 (2450)
$[\{\text{Ru}(\text{tpy})(\text{bpy})\}_2(\mu\text{-meta-adpc})]^{4+}$	457 (15000); 1120 (9600)
$[\{\text{Ru}(\text{tpy})(\text{bpy})\}_2(\mu\text{-Me}_4\text{adpc})]^{3+}$	486 (42500); 652 (11300); 820 (10500); 1678 (5300)

^aWavelength in nm, molar extinction coefficient ($\text{Lmol}^{-1}\text{cm}^{-1}$) in parentheses,

^belectrochemically oxidized spectra taken in 0.1M TBAH in DMF

The high energy 317-321 nm band of **7a-7f** can be assigned to typical π to π^* transitions in tpy/bpy ligands, which may overlap with similar transitions in the bridging $\text{R}_2\text{R}'_2\text{adpc}^{2-}$ ligand.¹ On the other hand, the low energy visible band (490-534 nm) appears at the typical position of Ru(II) $d\pi$ to π^* (tpy/bpy) metal-to-ligand charge transfer (MLCT) transitions in ruthenium (II)-polypyridyl complexes.⁴⁷ However, in **7a-7f**, the cyanamide-to-phenylazo intra-ligand charge transfer (ILCT) transitions may also occur in the similar region of the MLCT transitions.¹

3.4.6 Cyclic Voltammetry

Cyclic voltammetry of all $[\{\text{Ru}(\text{tpy})(\text{bpy})\}_2(\mu\text{-R}_2\text{R}_2'\text{adpc})][\text{PF}_6]_2$ (**7a-7e**) complexes were performed in acetonitrile at a scan rate of 0.1 V/s, while those of $[\{\text{Ru}(\text{tpy})(\text{bpy})\}_2(\mu\text{-meta-adpc})][\text{PF}_6]_2$ complex (**7f**) and $\text{Tl}_2[\text{R}_2\text{R}_2'\text{adpc}]$ salts (**5a-5c**) have been performed in DMF. Voltammetric study of $\text{Tl}_2[\text{meta-adpc}]$ was unsuccessful due to its poor solubility in known electrochemical solvents. Cyclic voltammograms of all dinuclear complexes are shown in the Figure 3.4.22 (a-f) and those of **5a-5c** have been placed in the Figure C.6 in the Appendix C. Cyclic voltammetric data of **7a-7e** and **5a-5c** have been placed in the Table 3.4.8. Electrochemical data of free unsubstituted anionic adpc^{2-} ligand (**5b**), its dinuclear complex (**7c**) have been reported previously and reproduced in the present work.¹

The CVs of **5a-5c** in DMF are characterized by two closely spaced waves between 0.30 – 0.70 V (vs. NHE). Both couples are positively shifted by about 200 mV from electron releasing Me_2 to electron withdrawing Cl_2 - substituents, which is consistent with greater stabilization of the redox orbital on anionic $\text{R}_2\text{R}_2'\text{adpc}^{2-}$ ligand by the electron withdrawing chloro-substituents. The $E_{1/2}$ couples of $\text{R}_2\text{R}_2'\text{adpc}^{2-}$ anions are positively shifted by about 70 mV relative to those of $\text{R}_2\text{R}_2'\text{dicyd}^{2-}$ anions in agreement with greater stabilization of redox orbitals on $\text{R}_2\text{R}_2'\text{adpc}^{2-}$ anions by electron withdrawing azo group.

The CV's of dinuclear $[\{\text{Ru}(\text{tpy})(\text{bpy})\}_2(\mu\text{-R}_2\text{R}_2'\text{adpc})][\text{PF}_6]_2$ complexes (**7a-7e**), in acetonitrile present two quasi-reversible waves in the region between 0.60 V and 1.70 V vs NHE, (**a-e** in the Figure 2.4.22). The first redox couple (E_1) is stabilized by about 400 mV from electron releasing Me_4 - to electron withdrawing Cl_4 -substituents,

Table 3.4.8: Cyclic Voltammetry Data^a of $\text{Tl}_2[\text{R}_2\text{R}'_2\text{adpc}]^b$ and $[\{\text{Ru}(\text{tpy})(\text{bpy})\}_2(\mu\text{-R}_2\text{R}'_2\text{adpc})][\text{PF}_6]_2$ (**7a-7e**).^c

Ligands/Complex	$E_1 / \text{V vs NHE}$ (ΔE_{ca} in mV)	$E_2 / \text{V vs NHE}$ (ΔE_{ca} in mV)	$\Delta E = E_2 - E_1 / \text{V}$
$\text{Tl}_2[\text{Me}_2\text{adpc}]$	0.29 (17)	0.43 (22)	0.14
$\text{Tl}_2[\text{adpc}]$	0.40 (32)	0.54 (26)	0.14
$\text{Tl}_2[\text{Cl}_2\text{adpc}]$	0.47 (25)	0.62 (22)	0.15
$[\text{AsPh}_4]_2[\text{adpc}]$	0.48	0.63	0.15
$[\{\text{Ru}(\text{tpy})(\text{bpy})\}_2(\mu\text{-Me}_4\text{adpc})][\text{PF}_6]_2$	0.67 (54)	1.59 (73)	0.92
$[\{\text{Ru}(\text{tpy})(\text{bpy})\}_2(\mu\text{-Me}_2\text{adpc})][\text{PF}_6]_2$	0.70 (49)	1.56 (85)	0.86
$[\{\text{Ru}(\text{tpy})(\text{bpy})\}_2(\mu\text{-adpc})][\text{PF}_6]_2$	0.80 (39)	1.56 (69)	0.76
$[\{\text{Ru}(\text{tpy})(\text{bpy})\}_2(\mu\text{-Cl}_2\text{adpc})][\text{PF}_6]_2$	0.94 (66)	1.60 (89)	0.66
$[\{\text{Ru}(\text{tpy})(\text{bpy})\}_2(\mu\text{-Cl}_4\text{adpc})][\text{PF}_6]_2$	1.06 (110)	1.61 (80)	0.55
$[\{\text{Ru}(\text{tpy})(\text{bpy})\}_2(\mu\text{-meta-adpc})][\text{PF}_6]_2$	0.98	-	-

^a In 0.1M TBAH, scan rate 0.1 V/s, Fc^+/Fc used as internal reference, $\Delta E_{\text{ca}} = E_a - E_c$ in mV, $\Delta E = E_2 - E_1$ in V; ^b all thallium and tetraphenylarsonium salts in DMF; ^c all dinuclear complexes in acetonitrile, except *meta*-adpc complex (**7f**) in DMF.

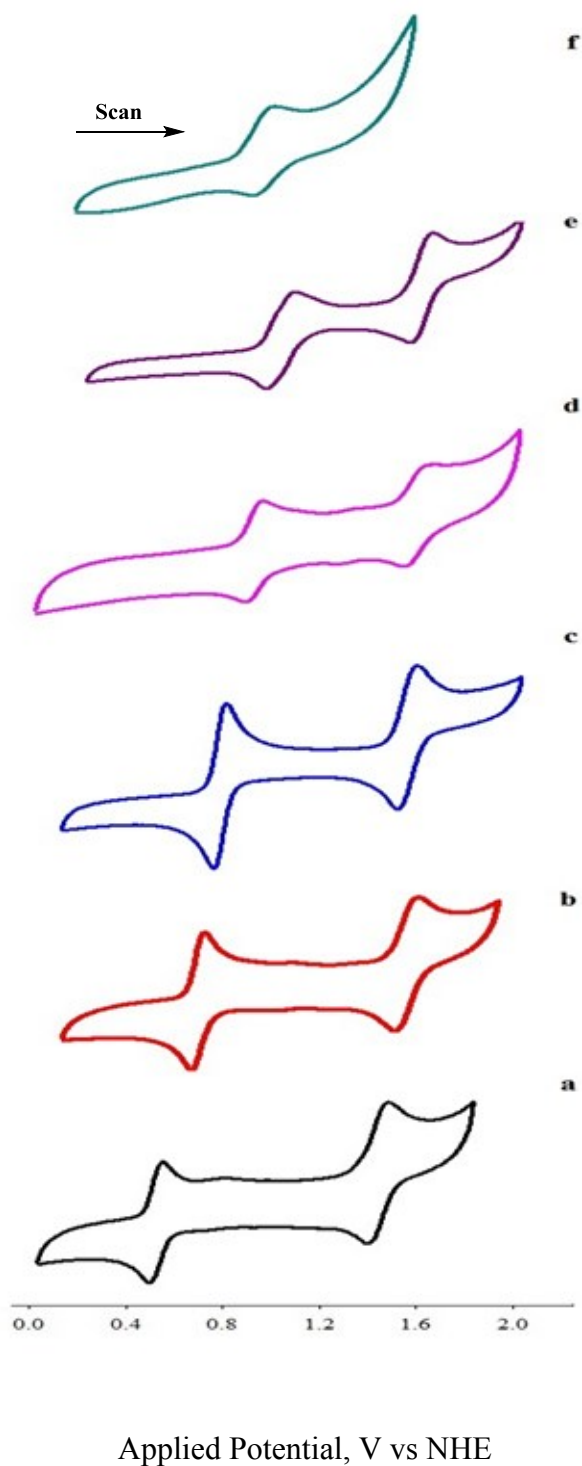


Figure 3.4.26: Cyclic voltammograms of $[\{\text{Ru}(\text{tpy})(\text{bpy})\}_2(\mu\text{-R}_2\text{R}'_2\text{adpc})] [\text{PF}_6]_2$ complexes in 0.1 M TBAH in acetonitrile at scan rate 0.1 V / s. $\text{R}_2\text{R}'_2\text{adpc} = \text{Me}_4\text{-}$ (a); $\text{Me}_2\text{-}$ (b); unsubstituted, $\text{H}_4\text{-}$ (c); $\text{Cl}_2\text{-}$ (d); $\text{Cl}_4\text{-}$ (e) and *meta*-adpc (f).

while the second redox couples (E2) show insignificant variations with the substituents on the bridging R_2R_2' adpc ligands. The assignments of both couples (E1 and E2) will be determined by combined EPR, IR and vis-NIR spectroelectrochemical analysis as well as theoretical calculations on oxidized dinuclear complexes $[\{Ru(tpy)(bpy)\}_2(\mu-R_2R_2'adpc)]^{3+/4+}$ ($7a^+$ - $7f^+$ and $7a^{2+}$ - $7e^{2+}$) (discussed below).

3.4.7 EPR Spectroscopy

The EPR spectroscopic studies were performed on the singly oxidized dinuclear $[\{Ru(tpy)(bpy)\}_2(\mu-R_2R_2'adpc)]^{3+}$ complexes ($7a^+$, $7d^+$ and $7f^+$) where $R_2R_2' = Me_4-$, Cl_2- and Cl_4- , respectively, in acetonitrile at room temperature to 10 K. The spectra are shown in the Figure 3.4.24. Unfortunately, the singly oxidized Me_2- , unsubstituted adpc and *meta*-adpc complexes ($7b^+$, $7c^+$ and $7f^+$) remained EPR silent even at liquid helium temperature (4K).

The dinuclear $[\{Ru(tpy)(bpy)\}_2(\mu-Me_4adpc)]^{3+}$ ($7a^+$) gave a room temperature isotropic spectrum in acetonitrile (Figure 3.4.27 a), which is relatively narrow with $g = 1.96$. This is very similar to EPR spectrum of the potassium salt of the 1,4-dicyanamide radical anion in which $g = 2.0023$.⁴⁸ These results strongly suggested a singly occupied molecular orbital (SOMO) which is localized on the bridging ligand in $7a^+$.

On the other hand, singly oxidized $[\{Ru(tpy)(bpy)\}_2(\mu-Cl_2adpc)]^{3+}$ ($7d^+$) remained EPR silent at room temperature. However, it gave a broad anisotropic EPR signal at 110 K in acetonitrile (Figure 3.4.27 b) with $g_1, g_2, g_3 = 2.162, 2.094, 1.963$

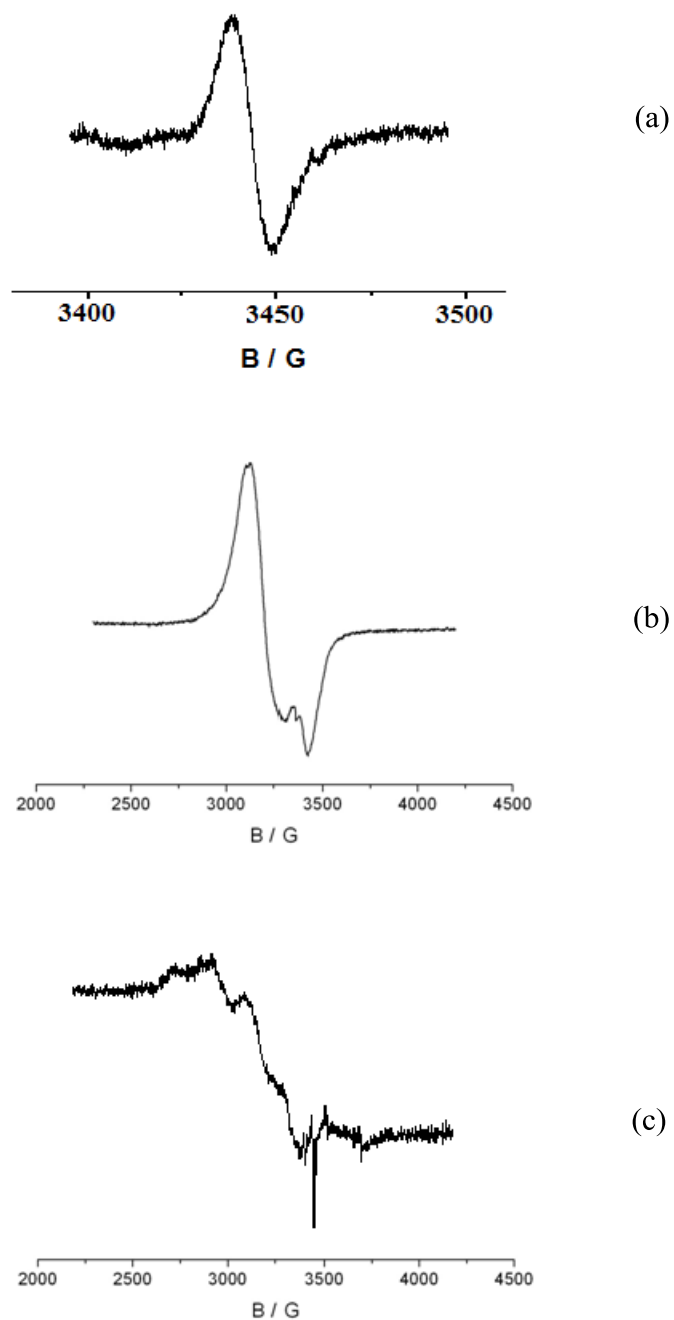


Figure 3.4.27: EPR spectra of $[\{\text{Ru}(\text{tpy})(\text{bpy})\}_2(\mu\text{-R}_2\text{R}'_2\text{adpc})]^{3+}$ in acetonitrile. $\text{R}_2\text{R}'_2 = \text{Me}_4^-$ at 295 K (a); Cl_2^- at 10 K (b); Cl_4^- at 110 K (c).

respectively, and $g_{\text{av}} = 2.075$ and g anisotropy $\Delta g = g_1 - g_2 = 0.199$. The spectral pattern is very similar to that of mononuclear $[\text{Ru}(\text{tpy})(\text{bpy})(2,4\text{-Cl}_2\text{pcyd})]^{2+}$ (Figure 2.3.21, Chapter 2), suggesting a singly occupied molecular orbital (SOMO) which is

predominantly of Ru(III) character in $7d^+$. $[\{\text{Ru}(\text{tpy})(\text{bpy})\}_2(\mu\text{-Cl}_4\text{adpc})]^{3+}$ ($7e^+$) was EPR silent at room temperature, however, a very weak signal is observed at 110 K, which may be due to impurities (Figure 3.4.27 c). Nevertheless, a broad anisotropic feature is evident which is consistent with Ru(III) character in the singly occupied molecular orbital (SOMO) of $7e^+$.

3.4.8 IR Spectroelectrochemistry

IR spectroelectrochemical studies of the $\nu(\text{NCN})$ region (2300-1700 cm^{-1}) showing the formation of $[\text{Ru}(\text{tpy})(\text{bpy})(2,4\text{-Cl}_2\text{pcyd})]^{2+}$, free $\text{adpc}^{\bullet-}$ radical anion ($5b^+$), and $[\text{Ru}(\text{tpy})(\text{bpy})_2(\mu\text{-R}_2\text{R}_2'\text{adpc})]^{3+/4+}$ ($7a^+$ - $7f^+$ and $7a^{2+}$ - $7e^{2+}$) were performed in DMF with 0.1 M TBAH using an OTTLE cell and are shown in the Figures 3.4.28-3.4.34. Generally, good reversibility was observed for single electron oxidation, while the second oxidation is not very reversible (80 - 90% recovery of the initial spectrum).

Electrochemical oxidation of the mononuclear $[\text{Ru}(\text{tpy})(\text{bpy})(2,4\text{-Cl}_2\text{pcyd})]^+$ complex resulted in a gradual decrease of the $\nu(\text{NCN})$ band at 2160 cm^{-1} with the generation of a low energy band at 2047 cm^{-1} and a very weak band at 2265 cm^{-1} (Figure 3.4.28 A). Previous IR spectroelectrochemical studies on $[\text{Ru}(\text{NH}_3)_5(2,3,5,6\text{-Cl}_4\text{pcyd})][\text{PF}_6]_2$ and $[\text{Ru}(\text{NH}_3)_3(\text{bpy})(2,3\text{-Cl}_2\text{pcyd})][\text{PF}_6]_2$ have shown that $\nu(\text{NCN})$ shifts to lower frequencies upon a change in oxidation state of ruthenium from Ru(II) to Ru(III).¹⁰ The low energy $\nu(\text{NCN})$ band at 2047 cm^{-1} in the IR spectra of $[\text{Ru}(\text{tpy})(\text{bpy})(2,4\text{-Cl}_2\text{pcyd})]^{2+}$ is therefore consistent with the anionic cyanamide ligand attached to a Ru(III) ion in agreement with EPR studies. The weak high energy band at

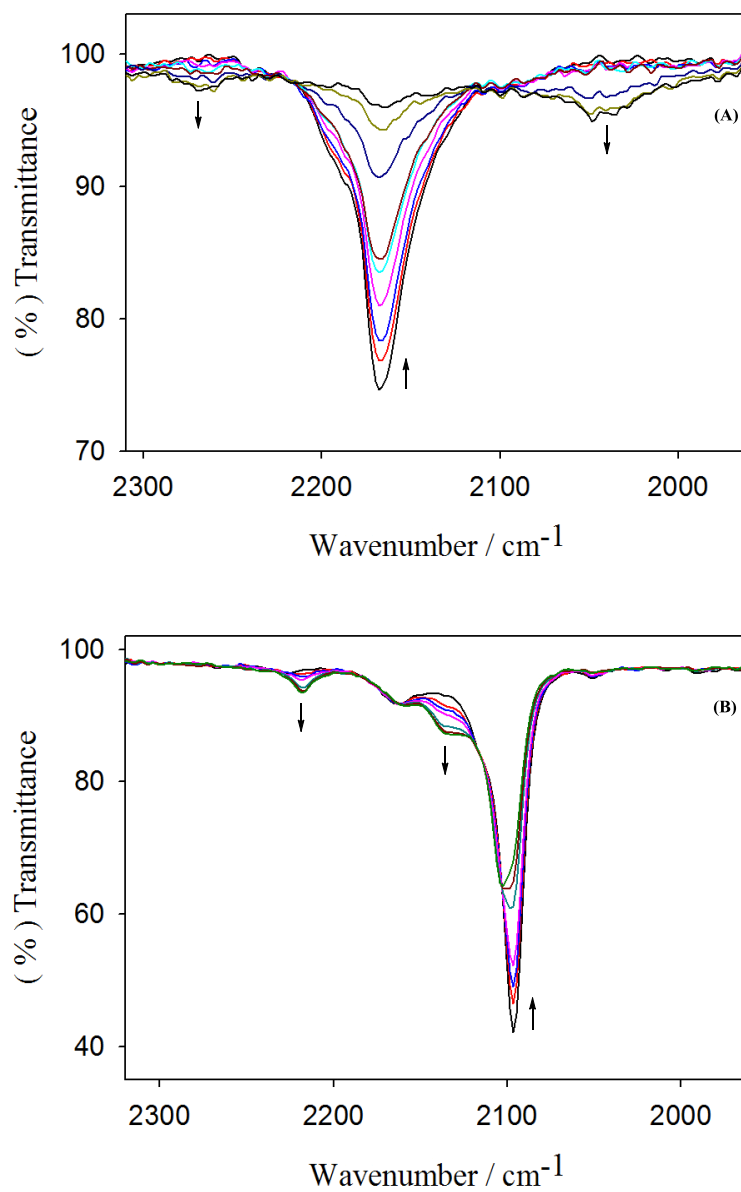


Figure 3.4.28: IR spectroelectrochemical oxidation of A) $[\text{Ru}(\text{tpy})(\text{bpy})(2,4\text{-Cl}_2\text{pcyd})]^+$ to form $[\text{Ru}(\text{tpy})(\text{bpy})(2,4\text{-Cl}_2\text{pcyd})]^{2+}$ and B) adpc^{2-} anion (**5b**) to form $\text{adpc}^{\bullet-}$ radical anion (**5b**⁺) in DMF, 0.1 M TBAH. A) 0 - 0.74 V, B) 0 - 0.20 V vs. Ag / AgCl

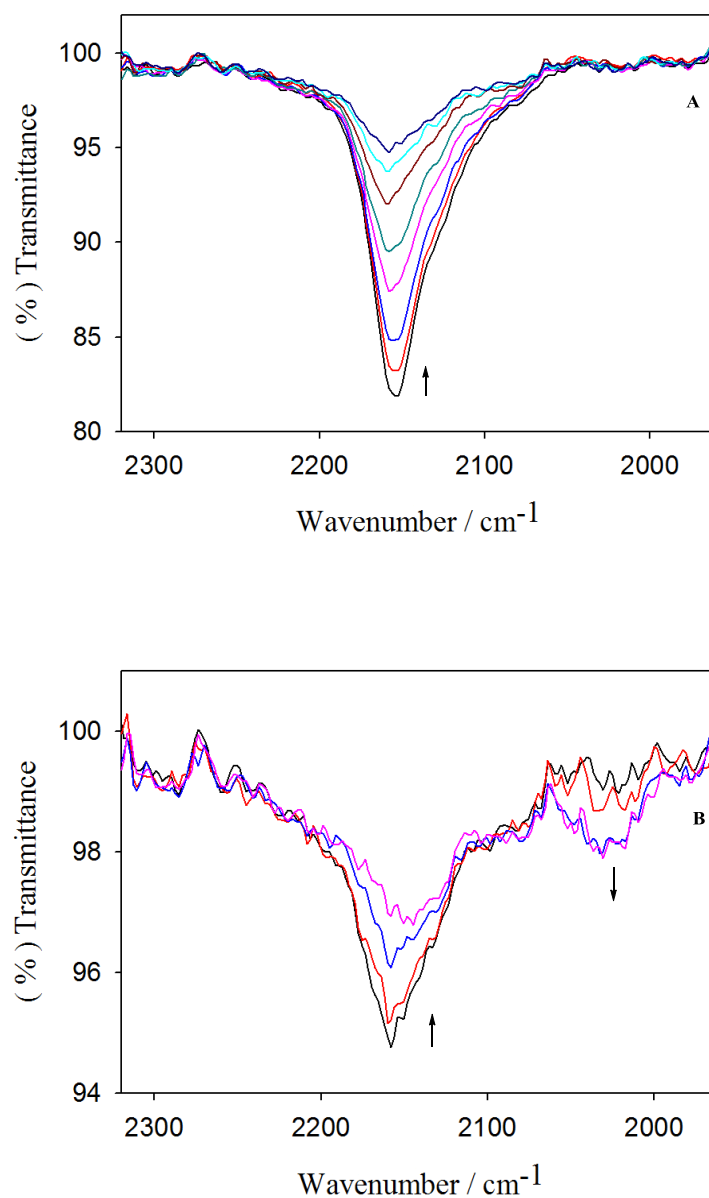


Figure 3.4.29: IR spectroelectrochemical oxidation of $[\{\text{Ru}(\text{tpy})(\text{bpy})\}_2(\mu\text{-Me}_4\text{adpc})\}_2]^{2+}$ (**7a**) to form A) $[\{\text{Ru}(\text{tpy})(\text{bpy})\}_2(\mu\text{-Me}_4\text{adpc})\}_3]^{3+}$ (**7a**⁺) and B) $[\{\text{Ru}(\text{tpy})(\text{bpy})\}_2(\mu\text{-Me}_4\text{adpc})\}_4]^{4+}$ (**7a**²⁺) in DMF, 0.1 M TBAH. A) 0 - 0.58 V, B) 0.58 - 0.70 V vs. Ag / AgCl.

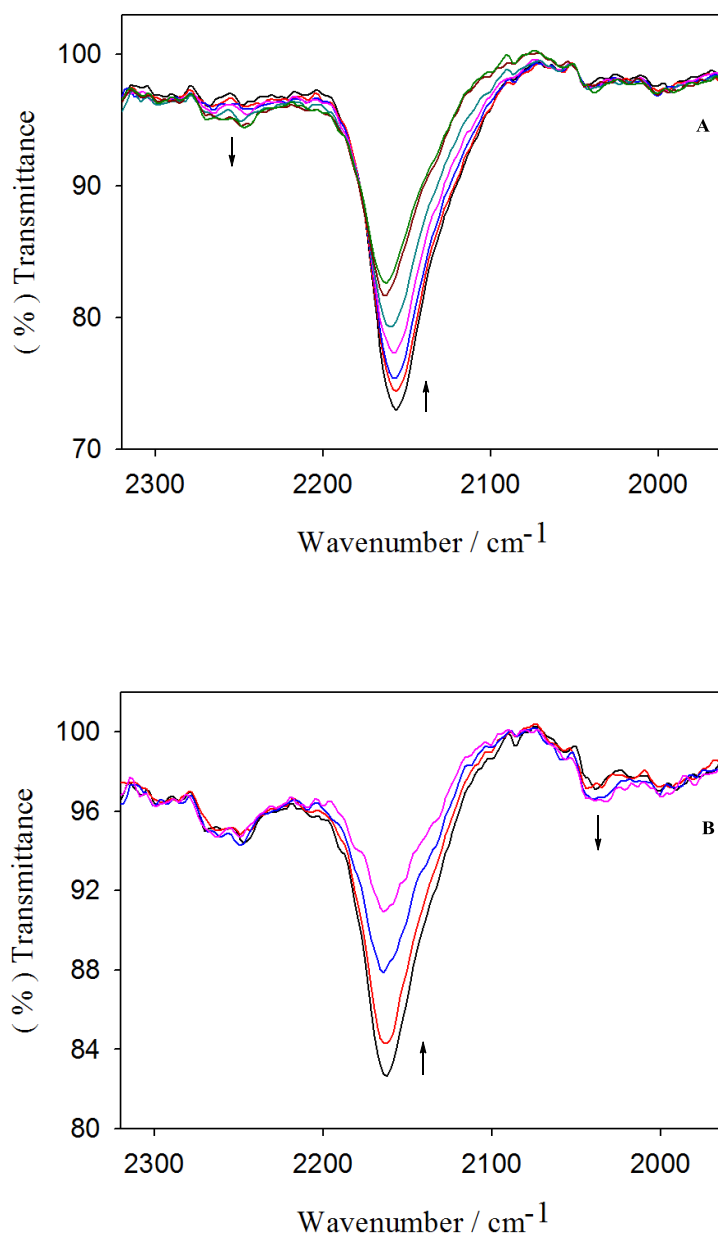


Figure 3.4.30: IR spectroelectrochemical oxidation of $[\{\text{Ru}(\text{tpy})(\text{bpy})\}_2(\mu\text{-Me}_2\text{adpc})]^{2+}$ (**7b**) to form A) $[\{\text{Ru}(\text{tpy})(\text{bpy})\}_2(\mu\text{-Me}_2\text{adpc})]^{3+}$ (**7b⁺**) and B) $[\{\text{Ru}(\text{tpy})(\text{bpy})\}_2(\mu\text{-Me}_2\text{adpc})]^{4+}$ (**7b²⁺**) in DMF, 0.1 M TBAH. A) 0 - 0.64 V, B) 0.64 - 0.72 V vs. Ag / AgCl.

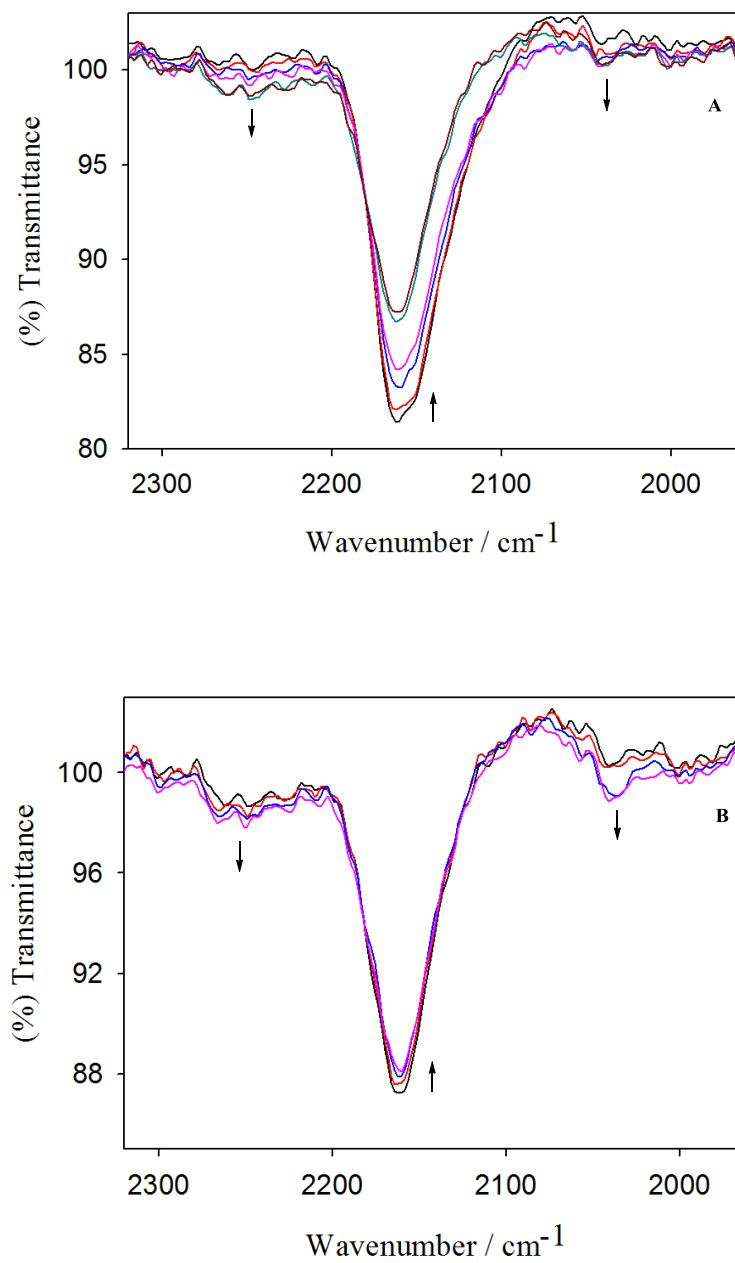


Figure 3.4.31: IR spectroelectrochemical oxidation of $[\{\text{Ru}(\text{tpy})(\text{bpy})\}_2(\mu\text{-adpc})]^{2+}$ (**7c**) to form A) $[\{\text{Ru}(\text{tpy})(\text{bpy})\}_2(\mu\text{-adpc})]^{3+}$ (**7c⁺**) and B) $[\{\text{Ru}(\text{tpy})(\text{bpy})\}_2(\mu\text{-adpc})]^{4+}$ (**7c²⁺**) in DMF, 0.1 M TBAH. A) 0-0.66 V, B) 0.66 - 0.80 V vs. Ag / AgCl.

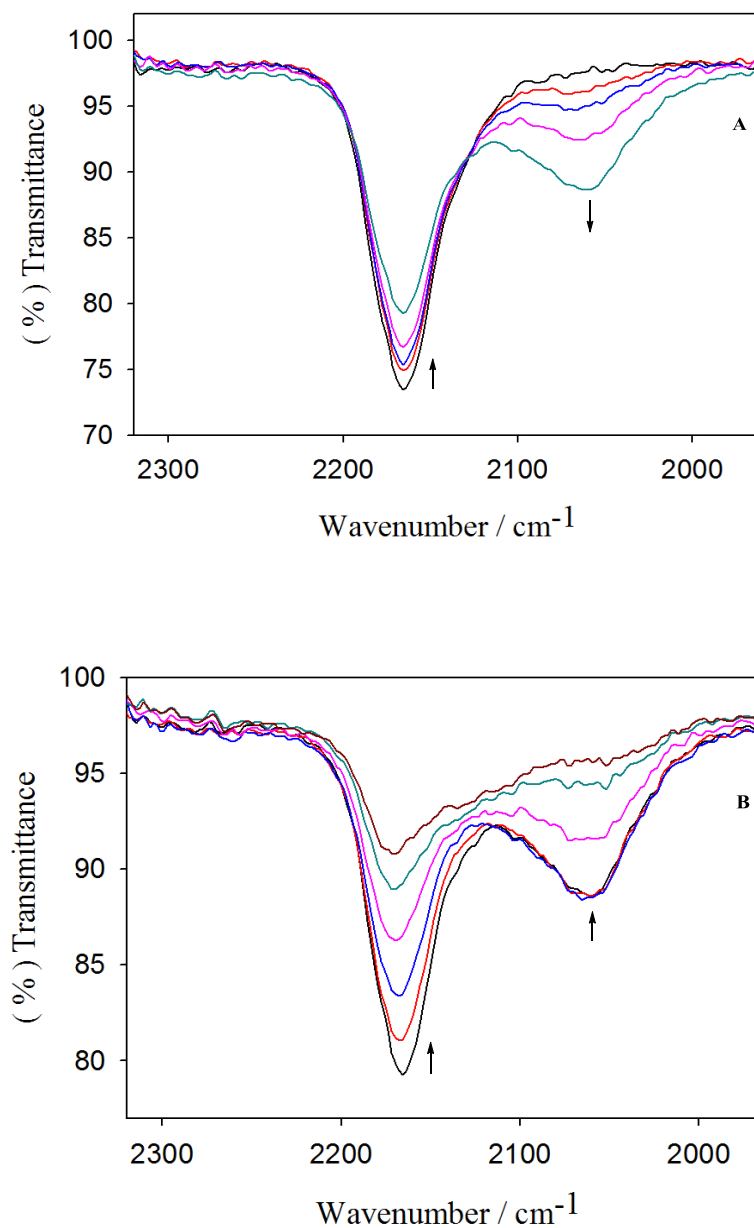


Figure 3.4.32: IR spectroelectrochemical oxidation of $[\{\text{Ru}(\text{tpy})(\text{bpy})_2(\mu\text{-Cl}_2\text{adpc})\}]^{2+}$ (**7d**) to form A) $[\{\text{Ru}(\text{tpy})(\text{bpy})_2(\mu\text{-Cl}_2\text{adpc})\}]^{3+}$ (**7d**⁺) and B) $[\{\text{Ru}(\text{tpy})(\text{bpy})_2(\mu\text{-Cl}_2\text{adpc})\}]^{4+}$ (**7d**²⁺) in DMF, 0.1 M TBAH. A) 0 - 0.66 V, B) 0.66 - 0.82 V vs. Ag / AgCl.

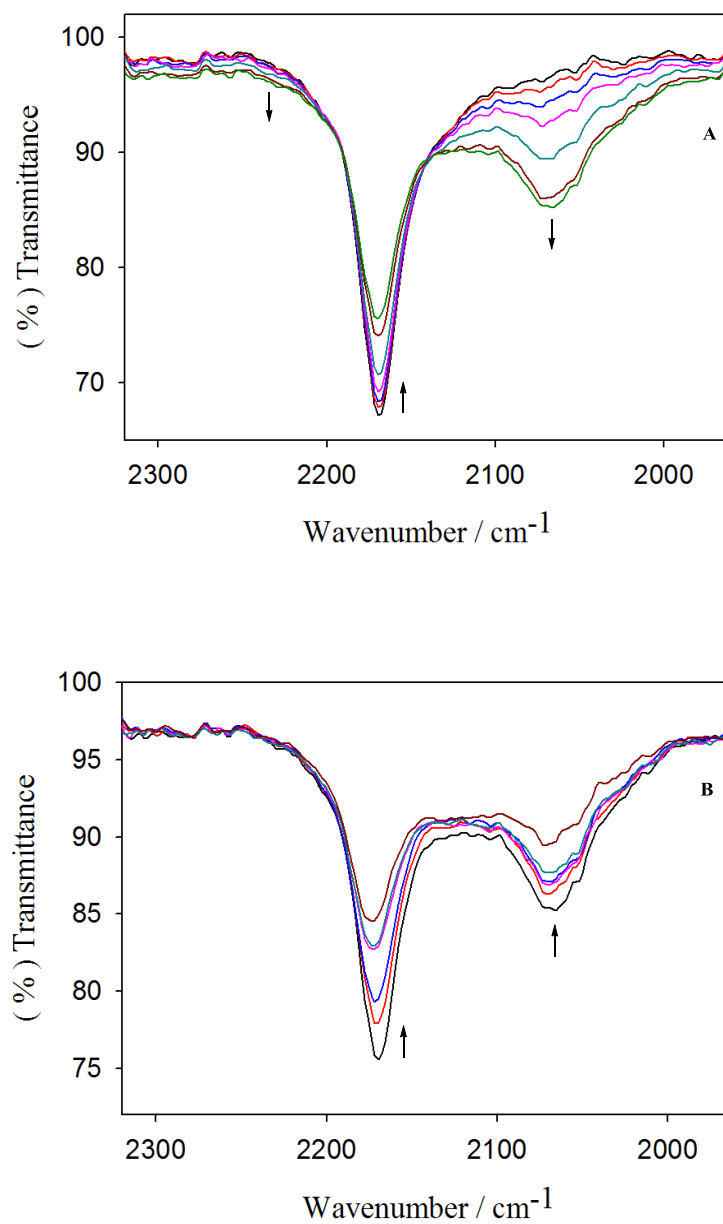


Figure 3.4.33: IR spectroelectrochemical oxidation of $[\{\text{Ru}(\text{tpy})(\text{bpy})\}_2(\mu\text{-Cl}_4\text{adpc})]^{2+}$ (**7e**) to form A) $[\{\text{Ru}(\text{tpy})(\text{bpy})\}_2(\mu\text{-Cl}_4\text{adpc})]^{3+}$ (**7e⁺**) and B) $[\{\text{Ru}(\text{tpy})(\text{bpy})\}_2(\mu\text{-Cl}_4\text{adpc})]^{4+}$ (**7e²⁺**) in DMF, 0.1 M TBAH. A) 0 - 0.80 V, B) 0.80 - 0.90 V vs. Ag / AgCl.

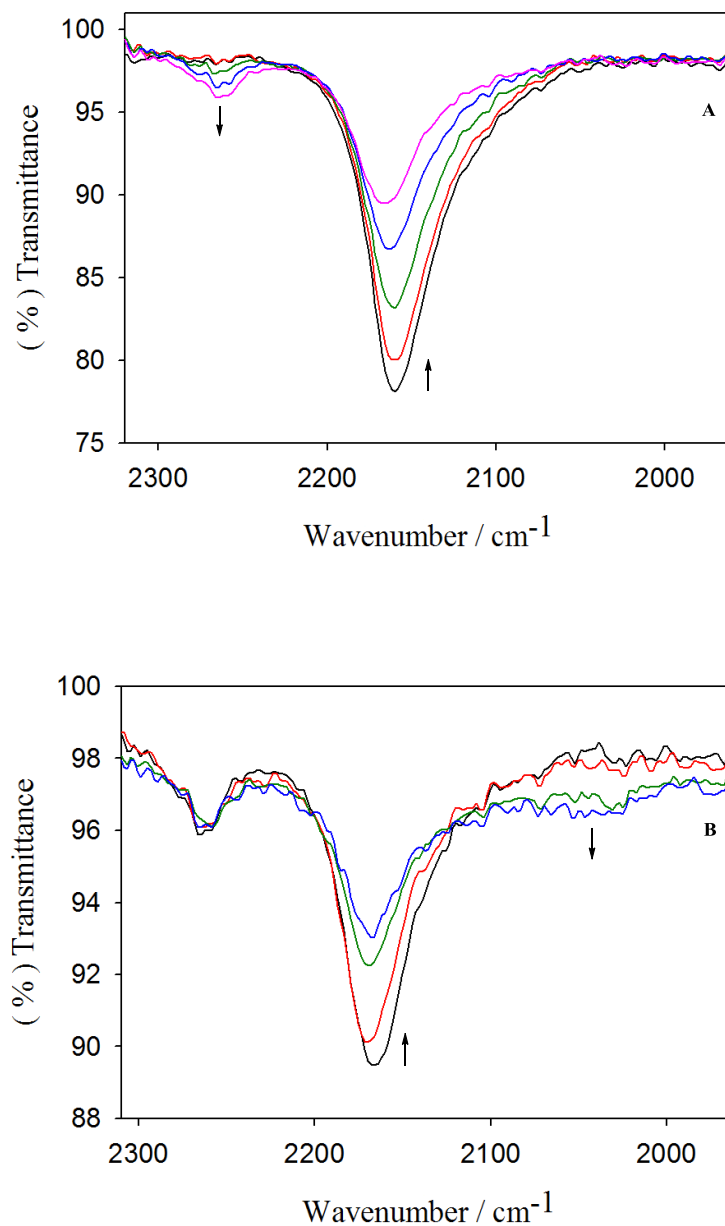


Figure 3.4.34: IR spectroelectrochemical oxidation of $[\{\text{Ru}(\text{tpy})(\text{bpy})\}_2(\mu\text{-meta-adpc})]^{2+}$ (**7f**) to form A) $[\{\text{Ru}(\text{tpy})(\text{bpy})\}_2(\mu\text{-meta-adpc})]^{3+}$ (**7f⁺**) and B) $[\{\text{Ru}(\text{tpy})(\text{bpy})\}_2(\mu\text{-meta-adpc})]^{4+}$ (**7f²⁺**) in DMF, 0.1 M TBAH. A) 0 - 0.50 V, B) 0.50 - 0.65 V vs. Ag / AgCl.

2265 cm^{-1} may arise from decomposition of the complex and indeed only 85% reversibility to the original dication spectrum was observed. The IR spectrum of free adpc^{2-} **5b** (Figure 3.4.28 B) in DMF shows an intense $\nu(\text{NCN})$ band at 2096 cm^{-1} and a far weaker band at 2162 cm^{-1} . Cyanamide groups can adopt *syn*- and *anti*-conformations and so multiple $\nu(\text{NCN})$ bands are not unexpected. A similar multiplicity of $\nu(\text{NCN})$ bands is observed in the IR spectrum of free $\text{Me}_2\text{dicyd}^{2-}$ in DMF.⁴⁹ Single electron oxidation of **5b** forming the radical anion **5b**⁺, resulted in a gradual decrease of the $\nu(\text{NCN})$ band at 2096 cm^{-1} and the growth of two very weak high energy bands at 2136 and 2217 cm^{-1} (Figure 3.4.28 B). Further oxidation of **5b**⁺ to **5b**²⁺ resulted in decomposition of the ligand.

IR spectroelectrochemical oxidation of complexes [$\{\text{Ru}(\text{tpy})(\text{bpy})\}_2(\mu\text{-Me}_4/\text{Me}_2\text{adpc})\}]^{2+}$ (**7a-7b**) forming the **7a**⁺-**7b**⁺, resulted in a gradual decrease of the $\nu(\text{NCN})$ band at 2160 cm^{-1} and a slight shift of this band to higher frequencies, (Figure 3.4.26A and 3.4.27A). This spectral feature is very similar to that of **5b**⁺ (Figure 3.4.25 B), suggesting a SOMO which is predominantly localized on the bridging ligand and is agreement with EPR studies of **7a**⁺. Although **7b**⁺ remained EPR silent even at liquid He temperature, the similar IR spectroelectrochemical results of both **7a**⁺ and **7b**⁺ suggests a ligand-centered SOMO for **7b**⁺ as well. The observed single $\nu(\text{NCN})$ band is also consistent with a SOMO delocalized in the bridging ligand with equivalent cyanamide groups. Oxidation of **7a**⁺ and **7b**⁺ forming **7a**²⁺ and **7b**²⁺, (Figure 3.4.29 B and 3.4.30 B, respectively), resulted in the growth of a low energy band at 2040 cm^{-1} , a feature which is very similar to IR spectra of $[\text{Ru}(\text{tpy})(\text{bpy})(2,4\text{-Cl}_2\text{pcyd})]^{2+}$ (Figure 3.4.28 A), suggesting

a significant contribution of Ru(III) to the highest occupied molecular orbital (HOMO) in **7a**²⁺ and **7b**²⁺.

In contrast, both [$\{\text{Ru}(\text{tpy})(\text{bpy})\}_2(\mu\text{-Cl}_2/\text{Cl}_4\text{adpc})\]^{2+} complexes (**7d**-**7e**), exhibited significantly different IR spectroelectrochemical behaviour. Single electron oxidation forming **7d**⁺ and **7e**⁺ (Figures 3.4.32 A and 3.4.33 A, respectively) resulted in the growth of a low energy band at 2040 cm⁻¹ with a gradually decreasing, but non-diminishing, band at 2160 cm⁻¹. Like mononuclear $[\text{Ru}(\text{tpy})(\text{bpy})(2,4\text{-Cl}_2\text{pcyd})]^{2+}$, the low energy 2040 cm⁻¹ band indicates a significantly large Ru(III) character in the SOMOs of **7d**⁺ and **7e**⁺. This is in agreement with EPR results, which also suggested a predominantly metal-centered SOMO in both complexes. Overall, IR spectra of **7d**⁺ and **7e**⁺ feature two $\nu(\text{NCN})$ bands, which is consistent with a localized (valence-trapped) mixed-valence system where two cyanamide groups on the bridging ligand experience the electronic effect of isolated Ru(II) and Ru(III) ions on IR time scale.¹⁰ The second oxidation forming **7d**²⁺ and **7e**²⁺ (Figures 3.4.32 B and 3.4.33 B, respectively) resulted in a gradual decrease of both 2040 and 2160 cm⁻¹ bands with slight shift of the latter band to higher frequencies, suggesting a greater contribution of radical $\text{Cl}_2/\text{Cl}_4\text{-adpc}^{\bullet}$ species in **7d**²⁺ and **7e**²⁺.$

The IR spectrum of [$\{\text{Ru}(\text{tpy})(\text{bpy})\}_2(\mu\text{-adpc})\]^{2+} (**7c**) in DMF shows a single $\nu(\text{NCN})$ band at 2160 cm⁻¹. Single electron oxidation forming **7c**⁺ resulted in a slight decrease in intensity of the 2160 cm⁻¹ band and the growth of two very weak bands at 2040 and 2250 cm⁻¹ respectively (Figure 3.4.31 A). The weak high frequency band at 2250 cm⁻¹ is likely to arise from different conformations of cyanamide groups in solution or from decomposition of the complex.⁴⁹ The low frequency 2040 cm⁻¹ band is absent in$

the IR spectra of ligand-centered radical complexes $7a^+$ and $7b^+$ and it is more prominent in the IR spectra of the mostly metal-centered mixed-valence complexes $7d^+$ and $7e^+$. This suggested that the SOMO in $7c^+$ is intermediate between mostly ligand and mostly Ru(III) character. The strong single $\nu(\text{NCN})$ band at 2160 cm^{-1} for $7c^+$ suggests a mostly delocalized SOMO; however, the low frequency 2040 cm^{-1} band also indicates some localized nature of the SOMO. Overall, IR spectroelectrochemical behavior of $7c^+$ is consistent with a delocalized system having significant Ru(III) character. Vis-NIR spectroelectrochemical study on $7c^+$ provided more insight into the SOMO parentage in $7c^+$ (described below). Oxidation of $7c^+$ to $7c^{2+}$, resulted in a more pronounced increase in the low energy band at 2040 cm^{-1} without any significant change in the 2160 cm^{-1} band (Figure 3.4.31 B), suggesting again a delocalized system having significant metal character on the highest occupied molecular orbital (HOMO).

The IR spectroelectrochemical behaviour of $[\{\text{Ru}(\text{tpy})(\text{bpy})\}_2(\mu\text{-meta-adpc})]^{2+}$ ($7f$) is shown in Figure 3.4.34. Single electron oxidation forming $7f^+$ resulted in a gradual decrease of the band at 2160 cm^{-1} (Figure 3.4.34 A) while oxidation to $7f^{2+}$ resulted in the growth of a low energy band at 2040 cm^{-1} (Figure 3.4.34 B). $7f^+$ is EPR silent however Figure 3.4.34 A is consistent with *meta-adpc*²⁻ oxidation to the radical anion. In agreement, a gas-phase DFT calculation of $7f^+$ showed spin density mostly located on the phenylcyanamide fragments. However, cyclic voltammetry and visible-NIR spectroelectrochemistry suggested a Ru(III)-centred spin in $7f^+$, which will be discussed below.

3.4.9 Vis-NIR Spectroelectrochemistry

Vis-NIR spectroelectrochemical oxidation on $\text{Tl}_2[\text{R}_2\text{R}_2'\text{adpc}]$ salts (**5a**, **5c**, **5e**) and dinuclear $[\text{Ru}(\text{tpy})(\text{bpy})\}_2(\mu\text{-R}_2\text{R}_2'\text{adpc})][\text{PF}_6]_2$ complexes (**7a-7f**) have been performed in 0.1 M TBAH in DMF. The vis-NIR spectra **5a**⁺ and **5c**⁺ are shown in the Figure 3.4.35, while that of **5e**⁺ is shown in the Figure C.8 in the Appendix C. The spectra for dinuclear complexes **7a**⁺-**7f**⁺ and **7a**²⁺-**7e**²⁺ are shown in the Figures 3.4.36-3.4.41. Vis-NIR spectroelectrochemical data for **5a**⁺-**5c**⁺ and **5e**⁺ and **7a**⁺-**7f**⁺ and **7a**²⁺-**7e**²⁺ are compiled in Table 3.4.7. The data for **5b**⁺ and **7c**⁺ and **7c**²⁺ have been reported previously and reproduced in the present work.¹ All dinuclear complexes **7a-7f** show good reversibility upon single electron oxidation while the second oxidation is not very reversible (less than 90% recovery of the initial spectrum). On the other hand, the *meta*-adpc complex **7f** exhibited poor reversibility on second oxidation and the initial spectrum could not be regenerated even upon rapid reduction. The low energy NIR band properties for the singly oxidized dinuclear complexes **7a**⁺-**7e**⁺ have been placed in Table 3.4.9 and the corresponding bands are shown in the Figure 3.4.42.

Spectroelectrochemical oxidation of **5a** and **5c** forming the radicals **5a**⁺ and **5c**⁺ resulted in a gradual decrease in the intra-ligand charge transfer (ILCT) bands at 500 nm and the growth of two weak bands at 715 and 1315 nm (Figure 3.4.32). The spectral features of **5a**⁺ and **5c**⁺ are very similar to that reported for the free adpc^{•-} radical anion.¹ Single electron oxidation of *meta*-adpc²⁻ forming **5e**⁺ also resulted in a gradual decrease of the 470 nm band with the development of a NIR band at 800 nm. No significant absorption was observed at ca. 1315 nm, however, the intensity of the 800 nm band is considerably reduced relative to those of its *para* analogues (Table 3.4.7). The spectral

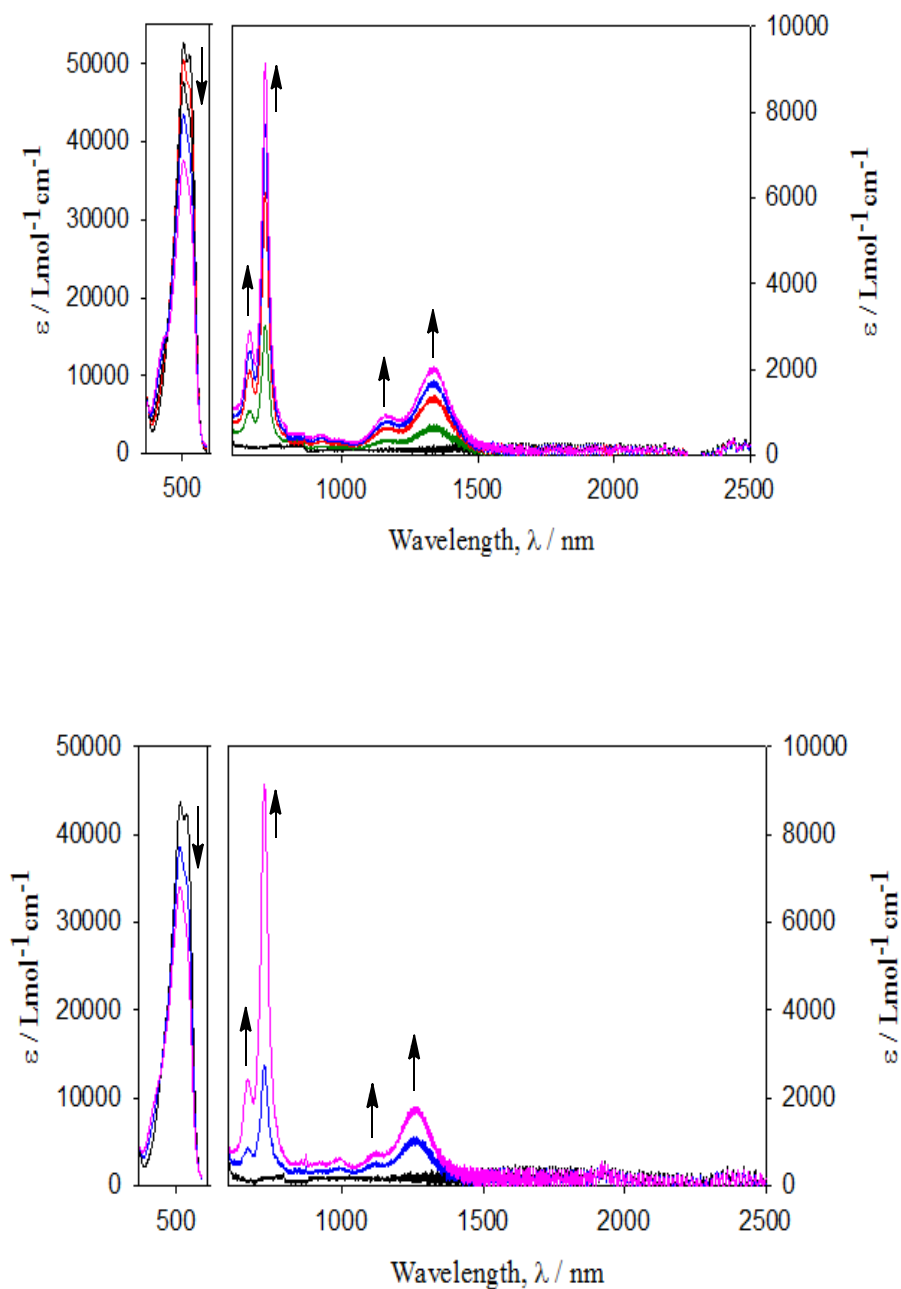


Figure 3.4.35: Vis-NIR spectroelectrochemical oxidation of $\text{Cl}_2\text{adpc}^{2-}$ (**5c**) forming $\text{Cl}_2\text{adpc}^{\bullet-}$ radical anion (**5c**⁺) (top) and $\text{Me}_2\text{adpc}^{2-}$ (**5a**) forming $\text{Me}_2\text{adpc}^{\bullet-}$ radical anion (**5a**⁺) (bottom) in DMF, 0.1 M TBAH. (Top) 0 - 0.80 V and (Bottom) 0 - 0.18 V vs. Ag / AgCl.

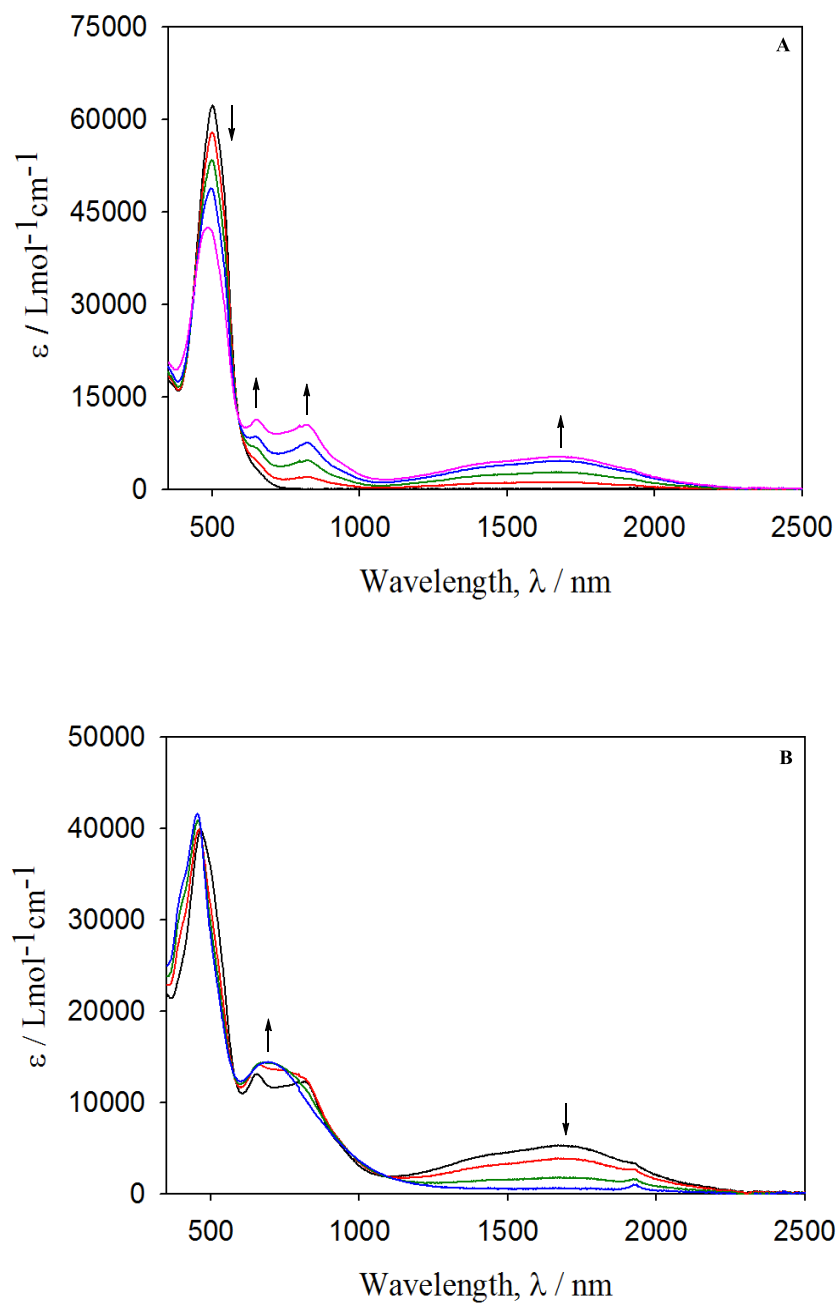


Figure 3.4.36: Vis-NIR spectroelectrochemical oxidation of $[\{\text{Ru}(\text{tpy})(\text{bpy})_2(\mu\text{-Me}_4\text{adpc})\}]^{2+}$ (7a) forming A) $[\{\text{Ru}(\text{tpy})(\text{bpy})_2(\mu\text{-Me}_4\text{adpc})\}]^{3+}$ (7a^+) and B) $[\{\text{Ru}(\text{tpy})(\text{bpy})_2(\mu\text{-Me}_4\text{adpc})\}]^{4+}$ (7a^{2+}) in DMF, 0.1 M TBAH. A) 0 - 0.48V, B) 0.50 - 0.58 V vs. Ag / AgCl.

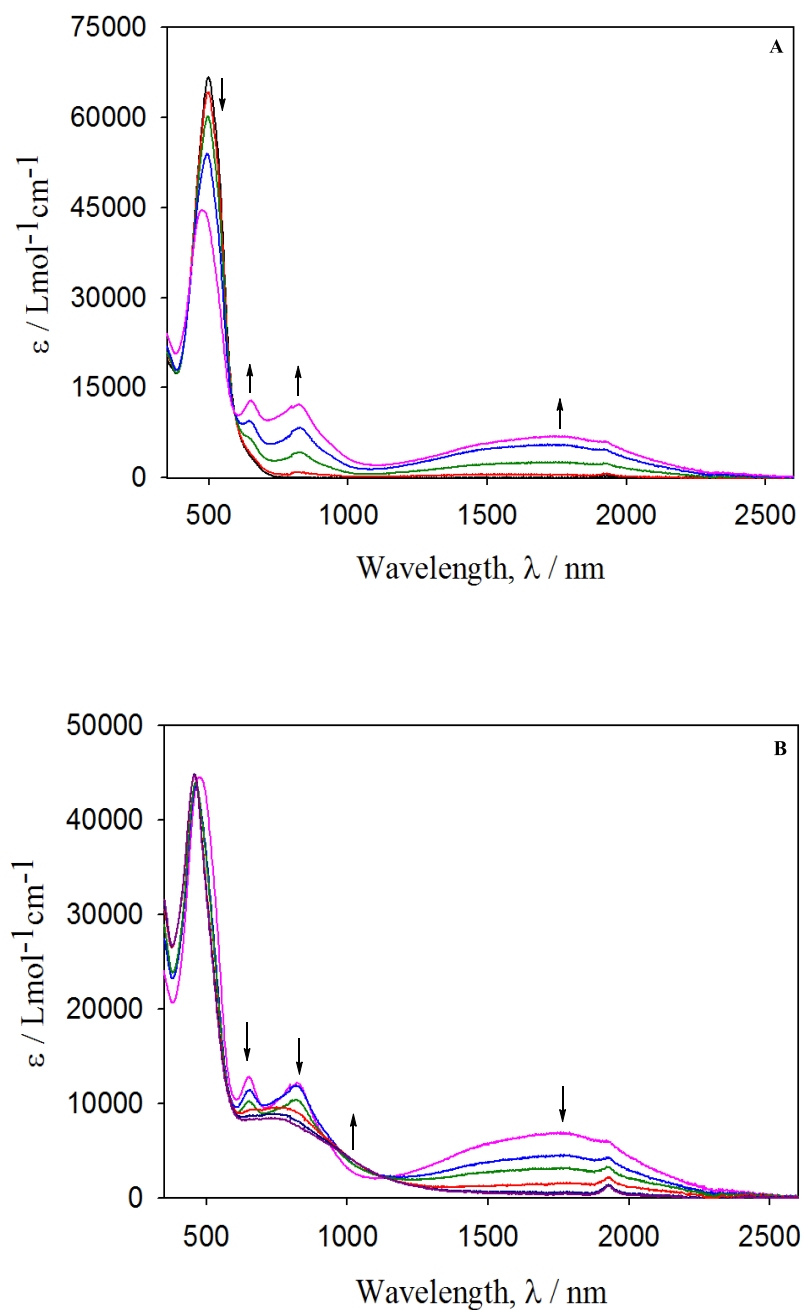


Figure 3.4.37: Vis- NIR spectroelectrochemical oxidation of $[\{\text{Ru}(\text{tpy})(\text{bpy})_2(\mu\text{-Me}_2\text{adpc})\}]^{2+}$ (**7b**) forming A) $[\{\text{Ru}(\text{tpy})(\text{bpy})_2(\mu\text{-Me}_2\text{adpc})\}]^{3+}$ (**7b**⁺) and (B) $[\{\text{Ru}(\text{tpy})(\text{bpy})_2(\mu\text{-Me}_2\text{adpc})\}]^{4+}$ (**7b**²⁺) in DMF, 0.1 M TBAH. A) 0 - 0.56 V, B) 0.56 - 0.66 V vs. Ag / AgCl.

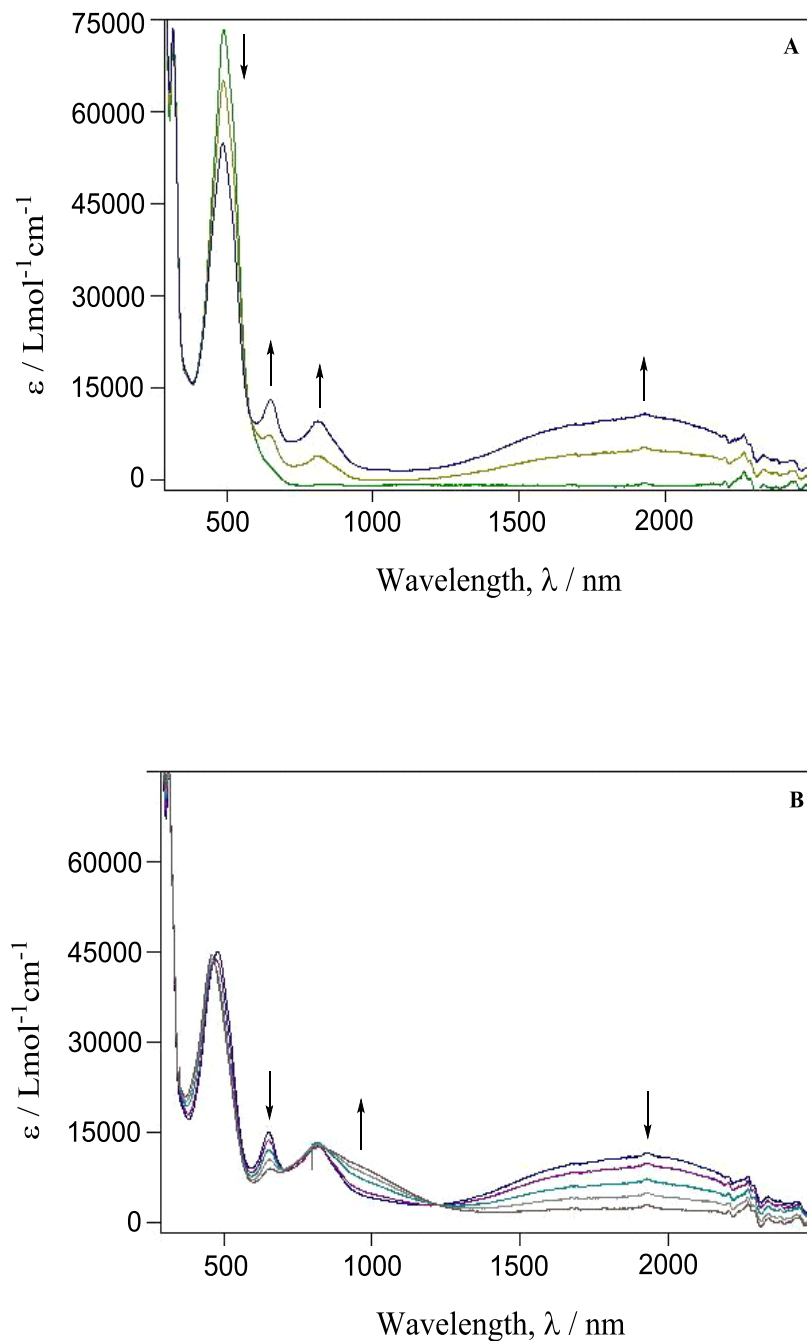


Figure 3.4.38: Vis- NIR spectroelectrochemical oxidation of $[\{\text{Ru}(\text{tpy})(\text{bpy})_2(\mu\text{-adpc})\}]^{2+}$ (7c) forming A) $[\{\text{Ru}(\text{tpy})(\text{bpy})_2(\mu\text{-adpc})\}]^{3+}$ (7c^+) and B) $[\{\text{Ru}(\text{tpy})(\text{bpy})_2(\mu\text{-adpc})\}]^{4+}$ (7c^{2+}) in DMF, 0.1 M TBAH. A) 0 - 0.75 V, B) 0.80 - 1.00 V vs. Ag / AgCl.

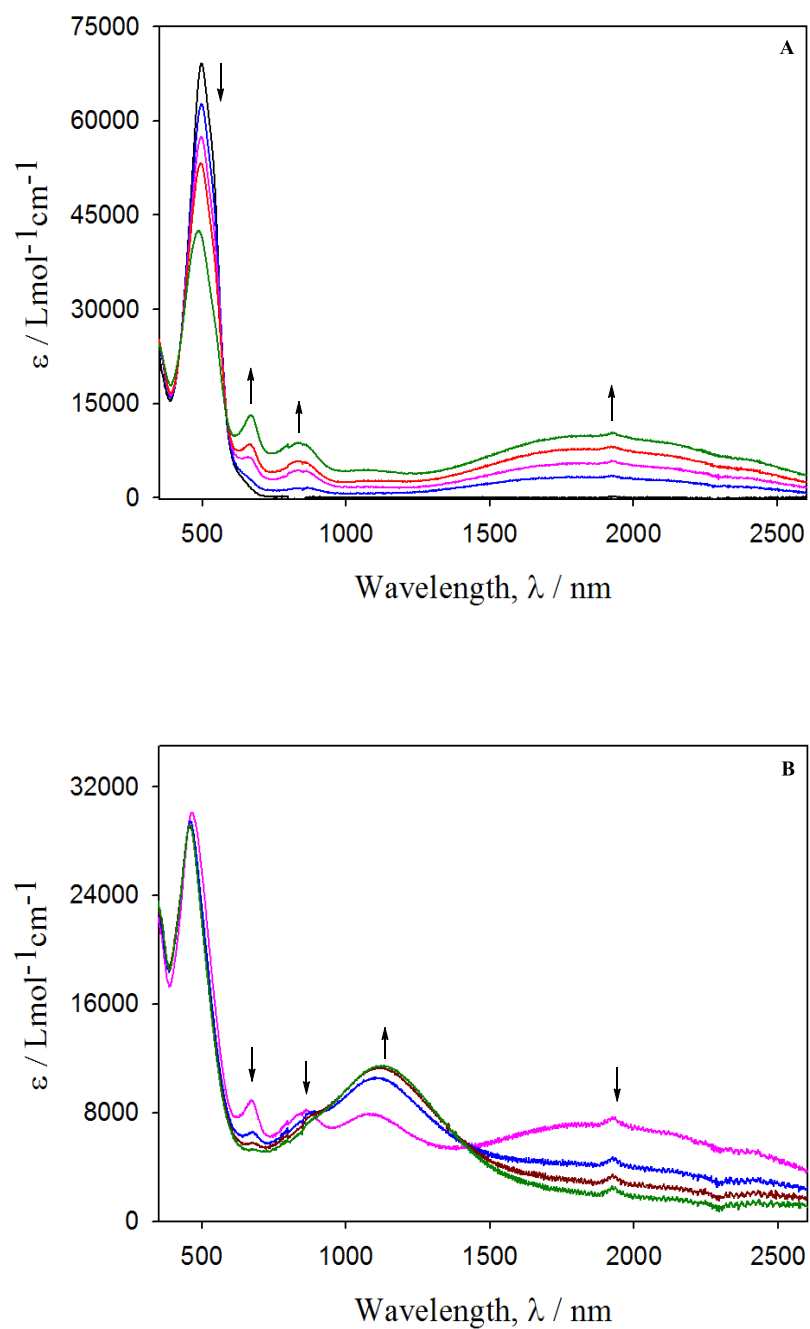


Figure 3.4.39: Vis-NIR spectroelectrochemical oxidation of $[\{\text{Ru}(\text{tpy})(\text{bpy})\}_2(\mu\text{-Cl}_2\text{adpc})]^{2+}$ (7d) forming A) $[\{\text{Ru}(\text{tpy})(\text{bpy})\}_2(\mu\text{-Cl}_2\text{adpc})]^{3+}$ (7d^+) and B) $[\{\text{Ru}(\text{tpy})(\text{bpy})\}_2(\mu\text{-Cl}_2\text{adpc})]^{4+}$ (7d^{2+}) in DMF, 0.1 M TBAH. A) 0 - 0.78 V, B) 0.81 - 0.98 V vs. Ag / AgCl.

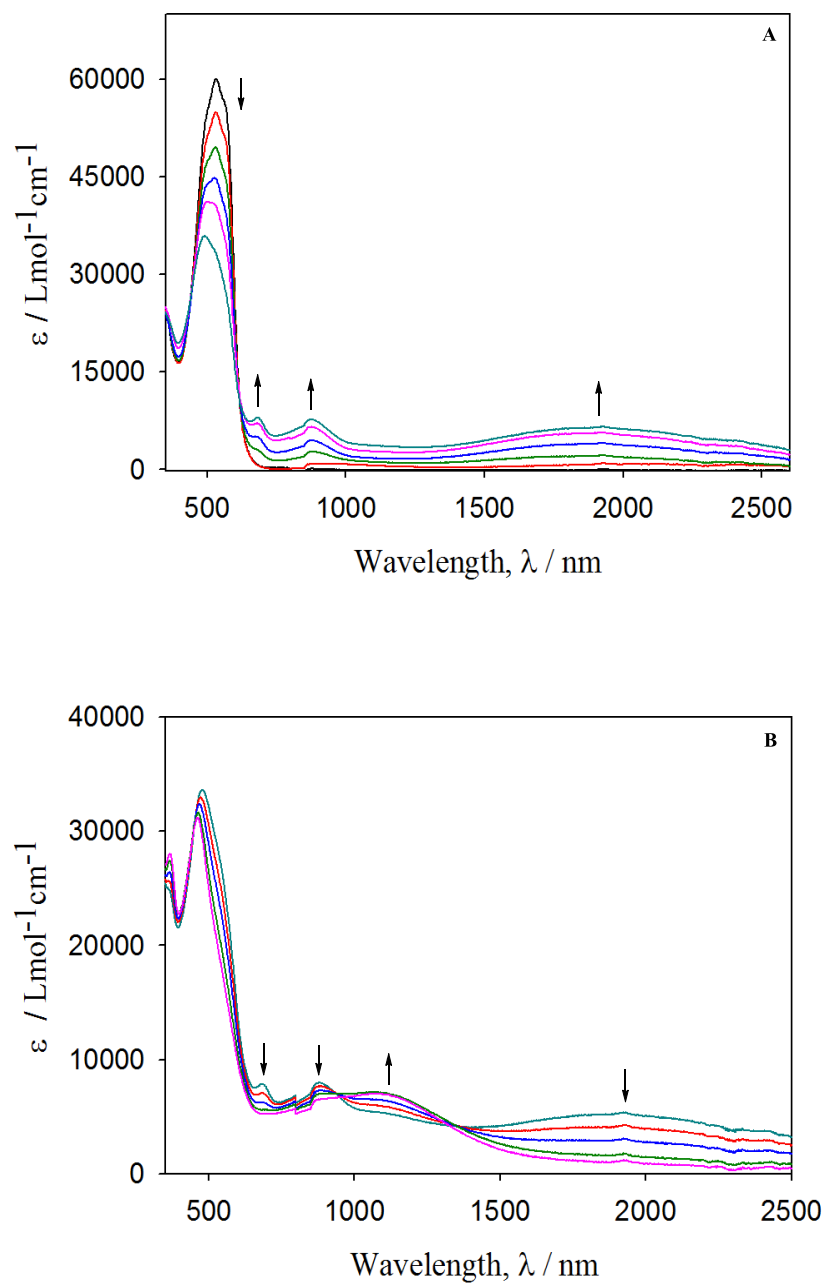


Figure 3.4.40: Vis-NIR spectroelectrochemical oxidation of $[\{\text{Ru}(\text{tpy})(\text{bpy})_2(\mu\text{-Cl}_4\text{adpc})\}]^{2+}$ (7e) forming A) $[\{\text{Ru}(\text{tpy})(\text{bpy})_2(\mu\text{-Cl}_4\text{adpc})\}]^{3+}$ (7e^+) and B) $[\{\text{Ru}(\text{tpy})(\text{bpy})_2(\mu\text{-Cl}_4\text{adpc})\}]^{4+}$ (7e^{2+}) in DMF, 0.1 M TBAH. A) 0 - 0.78 V; B) 0.81 - 0.98 V vs. Ag / AgCl.

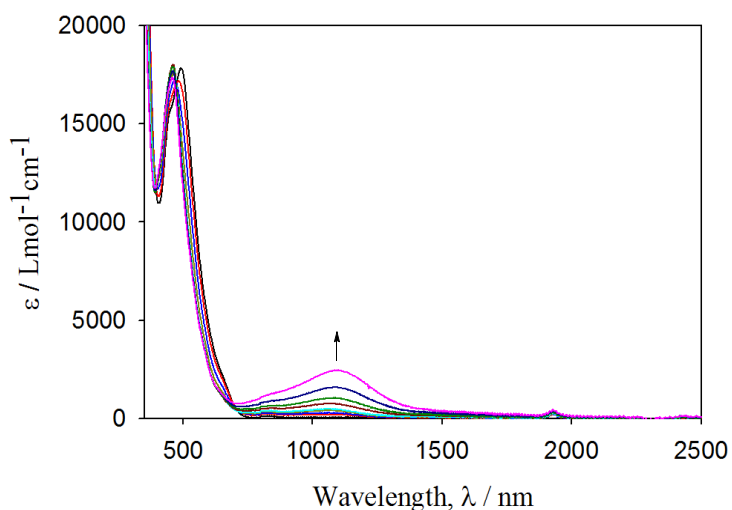


Figure 3.4.41: Vis-NIR spectroelectrochemical oxidation of $[\{\text{Ru}(\text{tpy})(\text{bpy})\}_2(\mu\text{-meta-adpc})]^{2+}$ (**7f**) forming $[\{\text{Ru}(\text{tpy})(\text{bpy})\}_2(\mu\text{-meta-adpc})]^{3+}$ (**7f**⁺) in DMF, 0.1 M TBAH. 0 - 1.27 V vs Ag / AgCl.

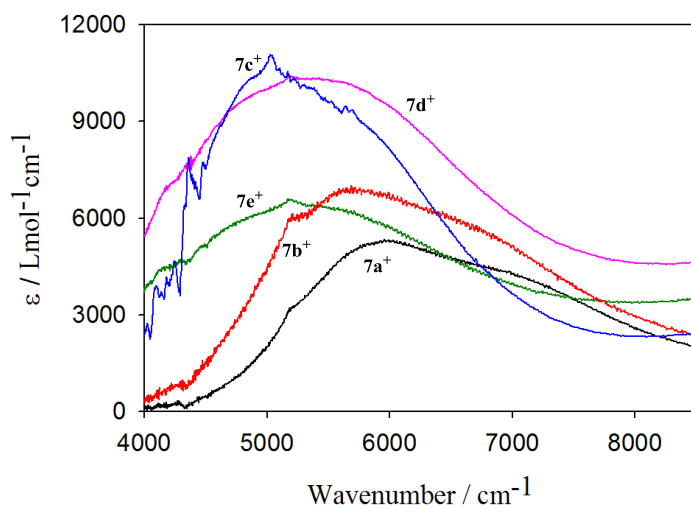


Figure 3.4.42: Low energy NIR bands of $[\{\text{Ru}(\text{tpy})(\text{bpy})\}_2(\mu\text{-R}_2\text{R}'_2\text{adpc})]^{3+}$ complexes (**7a**⁺-**7e**⁺). $\text{R}_2\text{R}'_2\text{adpc} = \text{Me}_4\text{-}$ (**7a**⁺); $\text{Me}_2\text{-}$ (**7b**⁺); Unsubstituted, $\text{H}_4\text{-}$ (**7c**⁺); $\text{Cl}_2\text{-}$ (**7d**⁺); $\text{Cl}_4\text{-}$ (**7e**⁺).

Table 3.4.9. Low Energy NIR Band Properties of $\{\text{Ru}(\text{tpy})(\text{bpy})\}_2(\mu\text{-R}_2\text{R}_2'\text{adpc})]^{3+}$ complexes (**7a**⁺-**7e**⁺).

Complexes	NIR band Energy / cm^{-1}	Intensity, $\epsilon / \text{Lmol}^{-1} \text{cm}^{-1}$	Oscillator Strength, f
Me_4adpc (7a ⁺)	5960	5300	0.074
Me_2adpc (7b ⁺)	5668	7000	0.098
adpc (7c ⁺)	5208	11000	0.141
Cl_2adpc (7d ⁺)	5200	10400	0.167
Cl_4adpc (7e ⁺)	5200	6600	0.118

change for singly oxidized radical anion $\text{R}_2\text{R}_2'\text{adpc}^{\bullet-}$ is reversible if reduction is performed rapidly. However further oxidation is not reversible, as even partial regeneration of $\text{R}_2\text{R}_2'\text{adpc}^{2-}$ spectra was not achieved.

Vis-NIR spectroelectrochemical behaviour of $[\{\text{Ru}(\text{tpy})(\text{bpy})\}_2(\mu\text{-meta-adpc})]^{2+}$ (**7f**) is quite different from **7a-7e**. Single electron oxidation forming **7f**⁺ resulted in the growth of a NIR band at 1100 nm without any significant change in the Ru(II)-to tpy/bpy MLCT band at 491 nm (Figure 3.4.38). The NIR band is significantly red shifted relative to that of *meta*-adpc^{•-} (Figure C.8), but is coincident with the Ru(III)-cyanamide LMCT band of $[\text{Ru}(\text{tpy})(\text{bpy})(2,4\text{-Cl}_2\text{pcyd})]^{2+}$,¹⁸ suggesting a Ru(III)-centred spin in this uncoupled complex (**7f**⁺) in disagreement with the gas-phase DFT calculations (Figure C.2 a, discussed below). This is further supported by the redox couple **7f**⁺/**7f** (0.98V vs.

NHE, Table 3.4.8) of the complex **7f**, which is significantly low relative to the L^0/L^- couple (1.64 V vs. NHE) but coincident with the Ru(III/II) couple (1.00 V vs. NHE) of the mononuclear $[\text{Ru}(\text{tpy})(\text{bpy})(2,4\text{-Cl}_2\text{pcyd})]^+$ complex.¹⁸ Oxidation to **7f**²⁺ resulted in decomposition of the complex and the initial spectrum could not be regenerated even upon rapid reduction.

In general, the vis-NIR spectra of **7a**⁺-**7e**⁺ featured three bands at 652-677, 812-876, and 1678-1925 nm and Ru(II)d π -to- π^* (tpy/bpy) MLCT bands at 470-535 nm (Figure 3.4.36 A-3.4.40A) of decreased intensity compared to those of **7a**-**7e**. The lowest energy NIR bands in spectra of **7c**⁺-**7e**⁺ (Table 3.4.9) are significantly broadened and bathochromically shifted ($\Delta\lambda_{\text{max}} = 247$ nm), with respect to those of **7a**⁺-**7b**⁺, suggesting a transition in the nature of the SOMO in these two sets of complexes. The assignment of the NIR bands of **7a**⁺-**7e**⁺ depends on the parentage of the SOMO. If the SOMO possesses significant Ru(III) character, the assignment would be Ru(II)-to-Ru(III) MMCT and the vis-NIR band would be properly assigned to cyanamide-to-Ru(III) LMCT transitions.^{1,18} This is suggested to be the case for **7c**⁺-**7e**⁺. On the other hand, if the SOMO possesses significant $R_2R_2'\text{adpc}^{\bullet}$ character, the dominant transitions would be ligand-centered transitions involving $\pi\pi$ orbitals of the oxidized ligand, as observed in the radical spectra of $R_2R_2'\text{adpc}^{\bullet}$ (Figure 3.4.35). In dinuclear complexes, there is also possibility of Ru(II)-to- $R_2R_2'\text{adpc}^{\bullet}$ -MLCT transition in the NIR.⁵¹ These would be the appropriate assignments to consider for **7a**⁺-**7b**⁺.

Oxidation to **7a**²⁺ - **7e**²⁺ resulted in the disappearance of three bands (652-677 nm, 812-876 nm and 1678-1923 nm) and the growth of a fairly intense band at 696-1124 nm (Figure 3.4.36 B-3.4.40 B). This new band is bathochromically shifted by $\Delta\lambda_{\text{max}} =$

428 nm (Table 3.4.7) from $7a^{2+}$ to $7e^{2+}$ and must be related to the nature of the substituents on R_2R_2' adpc²⁻. Electronic state calculations were used to understand the origin of this band.

3.4.10 DFT Calculations

Restricted and unrestricted hybrid HF-DFT SCF gas phase calculations on **7c** and the singly oxidized complexes $7a^+$ - $7e^+$, respectively, were performed using the B3LYP/6-31G*-LANL2DZ model. Calculated orbital energies and selected frontier orbitals of **7c** and β -wavefunctions of $7a^+$, $7c^+$ and $7e^+$ are shown in the Figures 3.4.43-3.4.46, while the corresponding α -wavefunctions of $7a^+$, $7c^+$ and $7e^+$ are shown in the Figure C.3-C.5 in the Appendix-C. Calculated spin density distributions for $7a^+$, $7c^+$, $7e^+$ are shown in the Figure 3.4.47. On the other hand, calculated orbital energies and selected frontier orbitals of *meta*-adpc²⁻(**5e**) and the β -wavefunctions and the corresponding spin density distribution of the dinuclear complex **7f^{tr}** are shown in the Figure C.1-C.2 in the Appendix-C. The atomic coordinates of all geometry optimized structures are provided in the Table C.2-C6 in the Appendix-C.

As seen in the Figure 3.4.43, the HOMO and HOMO-1 of **7c** are predominantly bridge-based HOMOs of the adpc²⁻ ligand, with a very small contribution from Ru($d\pi$) orbitals which is slightly more in the HOMO-1 relative to the HOMO. In the HOMO, the azo N-N contribution is π -bonding while antibonding in HOMO-1. However, the azo antibonding π^* contribution interacts in a bonding manner with the phenyl ring carbon in the HOMO-1, while the bonding π -contribution of the azo group interacts in an antibonding manner with the phenyl ring carbon in the HOMO. The interaction between Ru($d\pi$) and π -HOMO of the bridge is antibonding as expected for filled-filled interaction.

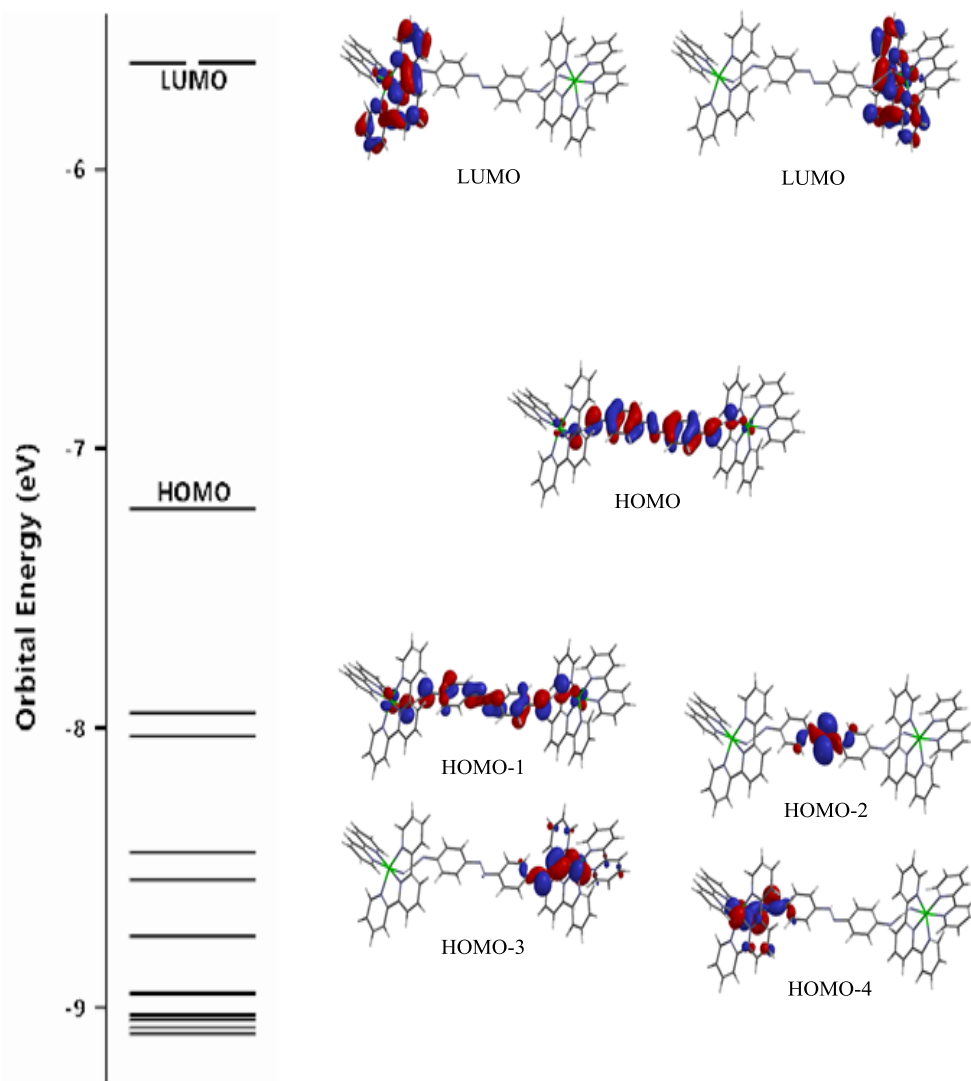


Figure 3.4.43: DFT calculation of orbital energies and selected molecular orbitals of $[\text{Ru}(\text{tpy})(\text{bpy})_2(\mu\text{-adpc})]^{2+}$ (7c).

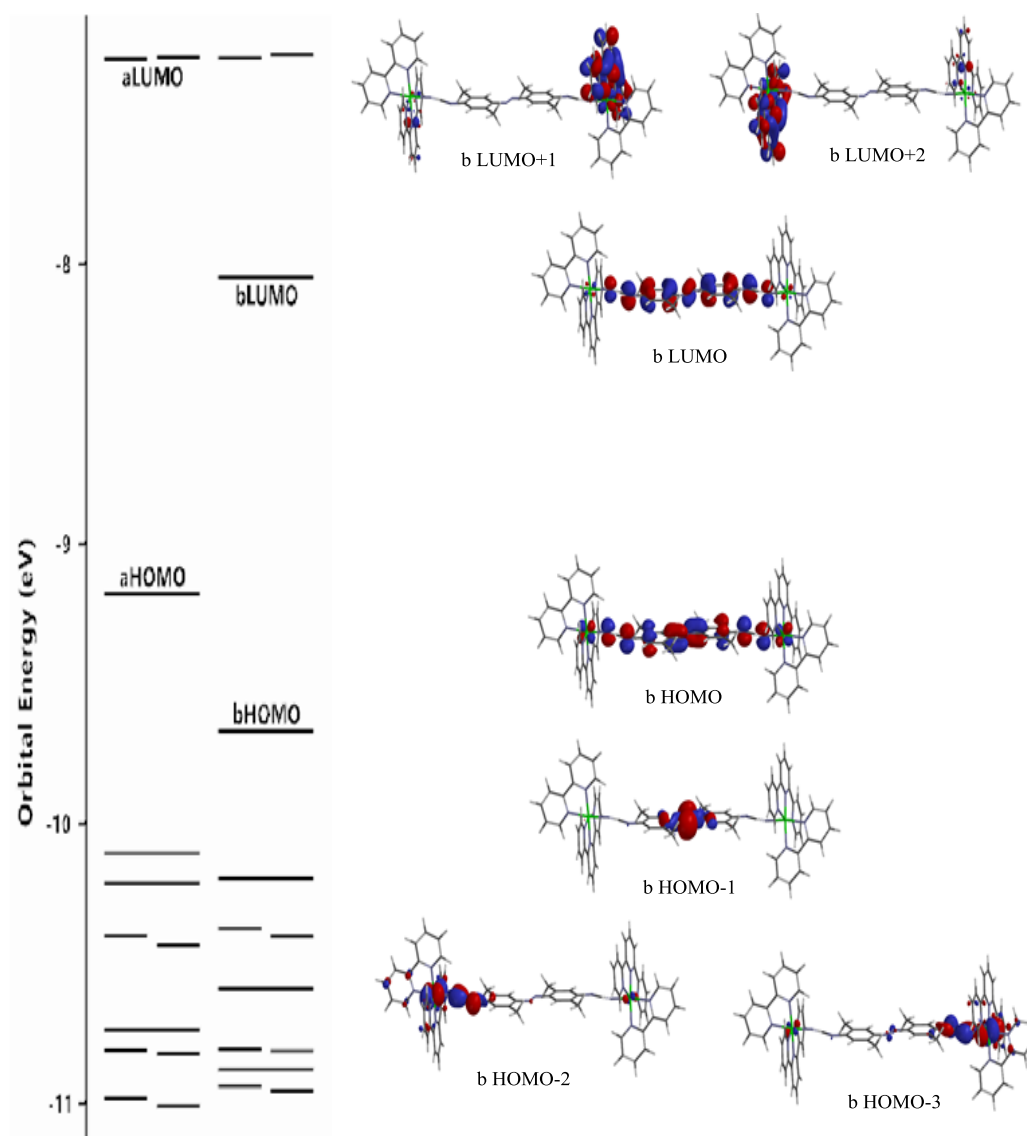


Figure 3.4.44: DFT calculation of orbital energies and selected β -molecular orbitals of $[\text{Ru}(\text{tpy})(\text{bpy})_2(\mu\text{-Me}_4\text{adpc})]^{3+}$ (7a^+).

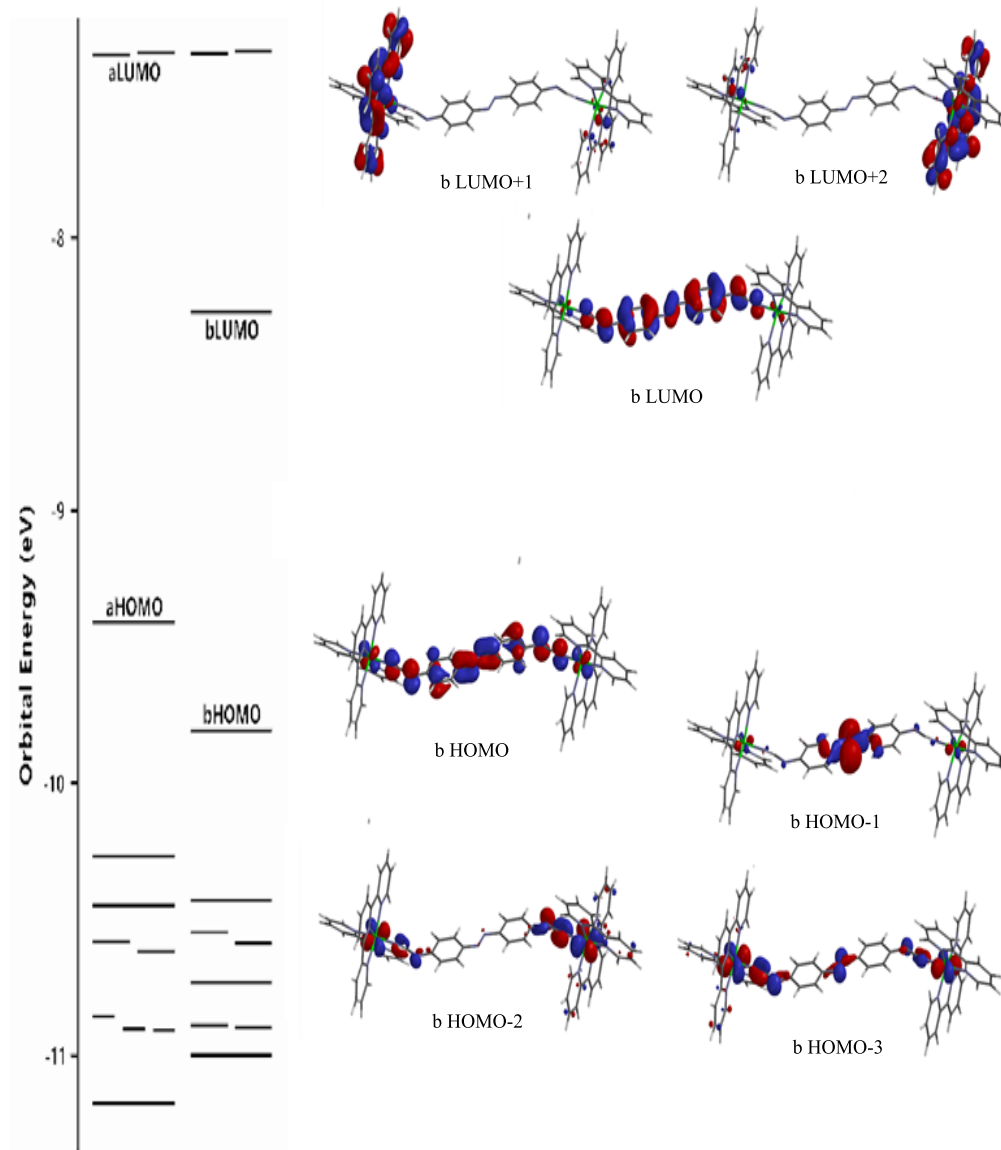


Figure 3.4.45: DFT calculation of orbital energies and selected β -molecular orbitals of $[\text{Ru}(\text{tpy})(\text{bpy})_2(\mu\text{-adpc})]^{3+}$ (7c^+).

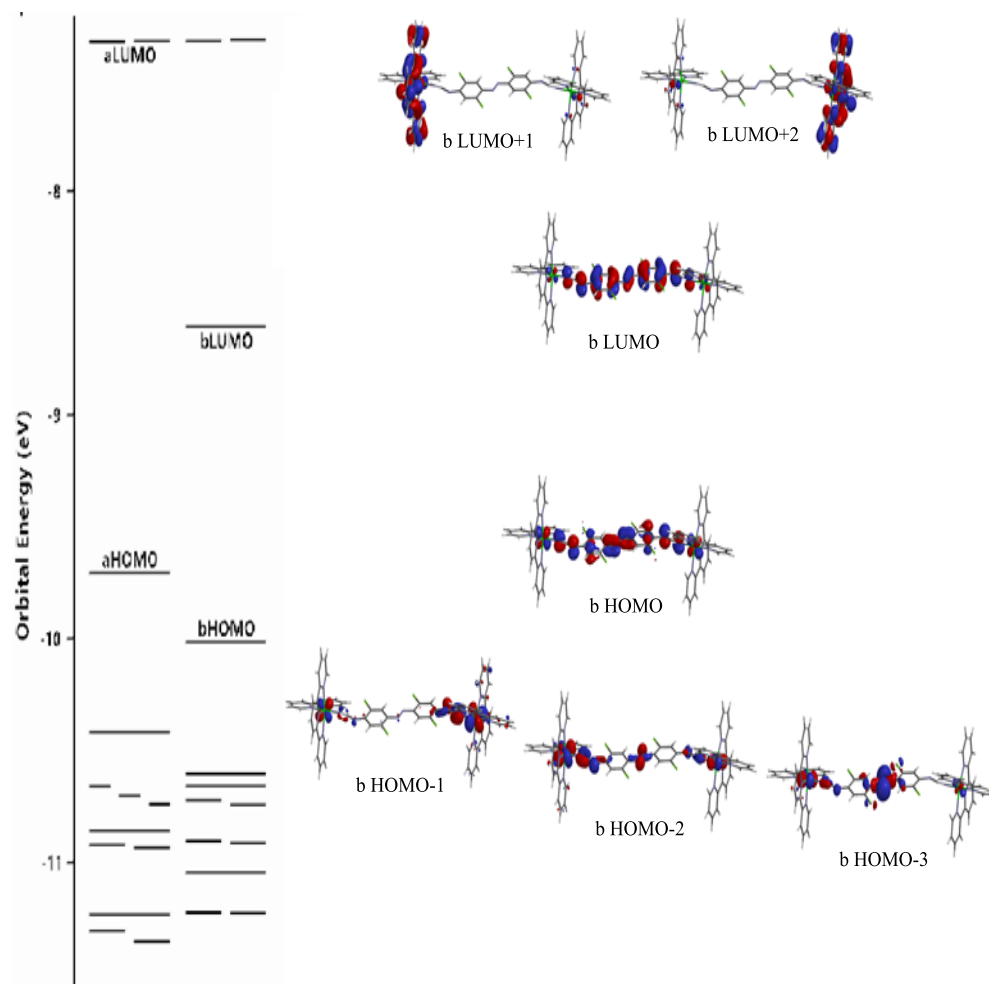


Figure 3.4.46: DFT calculation of orbital energies and selected β -molecular orbitals of $[\{\text{Ru}(\text{tpy})(\text{bpy})\}_2(\mu\text{-Cl}_4\text{adpc})]^{3+}$ ($7e^+$).

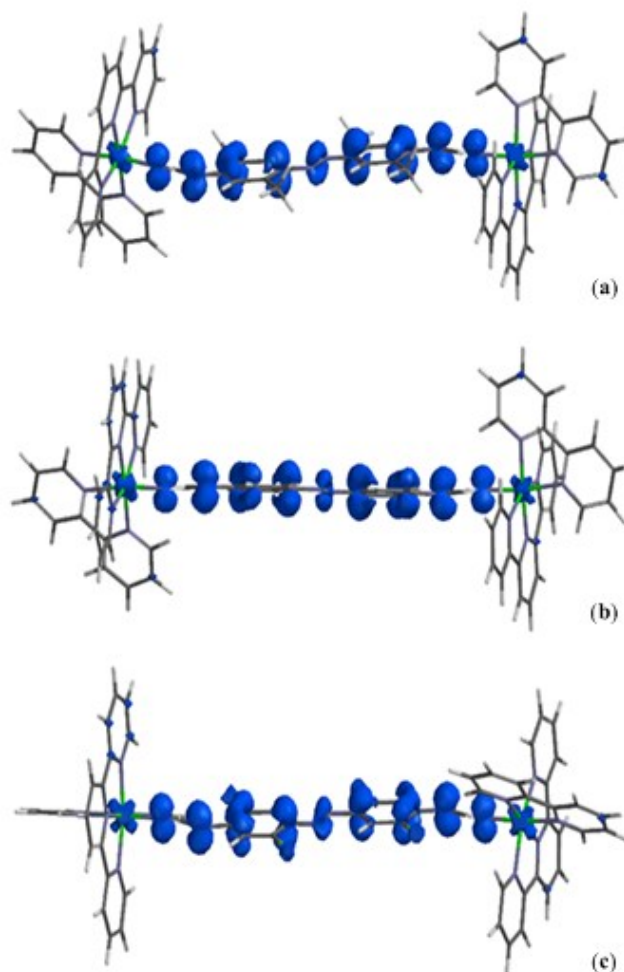


Figure 3.4.47: DFT calculation of spin density distribution of $[\{\text{Ru}(\text{tpy})(\text{bpy})\}_2(\mu\text{-R}_2\text{R}'_2\text{adpc})]^{3+}$ complexes (**7a⁺**, **7c⁺** and **7e⁺**). $\text{R}_2\text{R}'_2\text{adpc} = \text{Me}_4\text{-}$ (**7a⁺**), unsubstituted (**7c⁺**) and Cl_4adpc (**7e⁺**).

The HOMO-2 is predominantly an in-plane azo-nitrogen lone-pair combination. Below this comes the two closely spaced HOMO-3 and HOMO-4, which are the first to be seen that have significant metal character and show bonding interaction between $\text{Ru}(d\pi)$ and cyanamide nitrogen $p\pi$ lone pairs. Two degenerate LUMOs are mainly based on the tpy π^* orbital as expected for a strong π -acceptor ligand that stabilizes filled $\text{Ru}(\text{II})$ $d\pi$ orbital. This gas phase DFT calculation is qualitatively similar to a gas-phase DFT calculation

reported by Chisholm² *et al*, in so far as the predominance of bridging ligand character on the HOMOs are concerned. The other complexes also displayed similar frontier orbital parentages, with a slight increase in metal character in those orbitals as the number of electron withdrawing chloro-substituents increases on adpc²⁻.

The DFT calculations on the singly oxidized [$\{\text{Ru}(\text{tpy})(\text{bpy})\}_2(\mu\text{-R}_2\text{R}'_2\text{adpc})\]^{3+}$ gave the α - and β -wavefunctions (Figure 3.4.44-3.4.46 and Figure C.3-C.5), which are very similar in nature except that the molecular orbital centred on the azo group (β -HOMO-1) is more stabilized in the α -wavefunctions (α -HOMO-2 in Me₄- and unsubstituted adpc complexes and α -HOMO-3, α -HOMO-4 in Cl₄adpc complexes). Both α and β -wavefunctions of **7a**⁺, **7c**⁺ and **7e**⁺ show the similar feature as **7a**, **7c** and **7e** in their frontier orbital parentages, the HOMOs being predominantly centred on the bridging R₂R'₂'adpc ligand, with a slight increase in Ru(III) character in the singly oxidized species. The predominance of the bridging ligand in the SOMOs is also reflected in the spin density distributions of **7a**⁺, **7c**⁺ and **7e**⁺ as shown in the Figure 3.4.47 a-c. The spin density distributions, however, do show a slight increase in spin density on ruthenium upon moving from Me₄- to Cl₄adpc complexes.

Gas-phase DFT calculations of the free *meta*-adpc²⁻ (**5e**) and the complex **7f**⁺ showed a discontinuity in the π -conjugation in the HOMO and the SOMO, respectively, (Figure C.1-C.2) on the bridging ligand, suggesting an uncoupled **7f**⁺ consisting of two isolated Ru(tpy)(bpy) units. However, like its *para* analogues (**7a**⁺-**7e**⁺), gas-phase DFT calculations on the **7f**⁺ (Figure C.2 a) showed that the spin density is mainly located on the discontinuous phenylcyanamide fragments.

Overall, gas phase DFT calculations showed predominately bridging-ligand character of the SOMO and indicates preferential oxidation of the bridging R_2R_2' adpc²⁻ ligand over Ru(II) in the formation of $7a^+$ - $7f^+$, which is in disagreement with the EPR and IR and vis-NIR spectroelectrochemical results. More sophisticated calculations ($7a^+$ - $7f^+$) including solvents were attempted, however, calculations wouldn't converge.

DFT gas phase calculations of the doubly oxidized complexes $7c^{2+}$ and $7d^{2+}$ indicate that the lowest energy state of both complexes corresponds to a closed-shell singlet state with a $[Ru(II)-R_2R_2'$ adpc⁰-Ru(II)]⁴⁺ valence configuration. The triplet state that corresponds to the $[Ru(III)-R_2R_2'$ adpc²⁻-Ru(III)]⁴⁺ and $[Ru(III)-R_2R_2'$ adpc^{•-}-Ru(II)]⁴⁺ valence configurations lies above the ground singlet state.

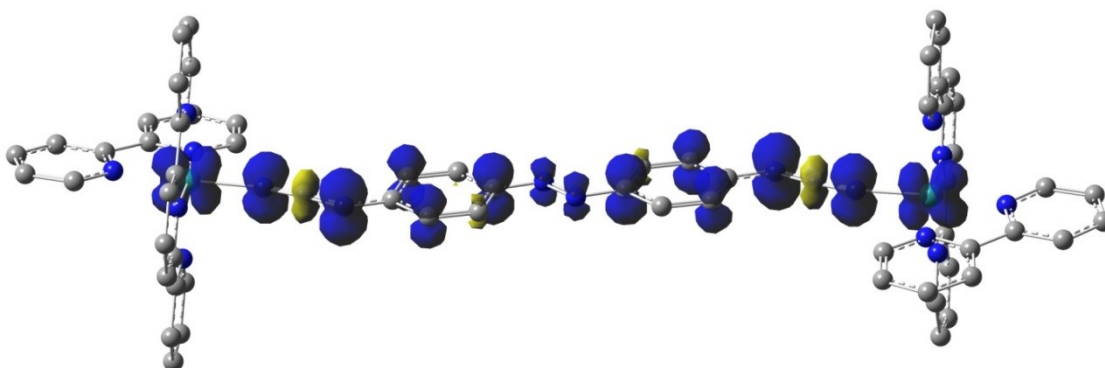


Figure 3.4.48: Spin density distribution in the lowest energy triplet state of the $[\{Ru(tpy)(bpy)\}_2(\mu\text{-adpc})]^{4+}$ cation ($7c^{2+}$). H atoms are not shown for clarity. Isosurface contour value for the spin density is 0.004 a.u.

Figure 3.4.48 shows the spin distribution for this triplet state in the $7c^{2+}$. In the gas-phase, the singlet-triplet energy gap is 6.4 kcal mol⁻¹ and 5.8 kcal mol⁻¹ for complexes $7c^{2+}$ and $7d^{2+}$, respectively. Solvent effects can significantly decrease the singlet-triplet energy gap and cause a spin crossover from the singlet ground state to triplet ground

state. This is shown by the DFT calculations of $7\mathbf{c}^{2+}$, which showed a reduction in the singlet-triplet energy gap from $6.4 \text{ kcal mol}^{-1}$ in the gas phase to $2.4 \text{ kcal mol}^{-1}$ in methanol. For $7\mathbf{d}^{2+}$, the change is more pronounced. In methanol, the triplet state becomes the lowest energy state with closed-shell singlet state lying $1.7 \text{ kcal mol}^{-1}$ above the triplet state for $7\mathbf{d}^{2+}$.

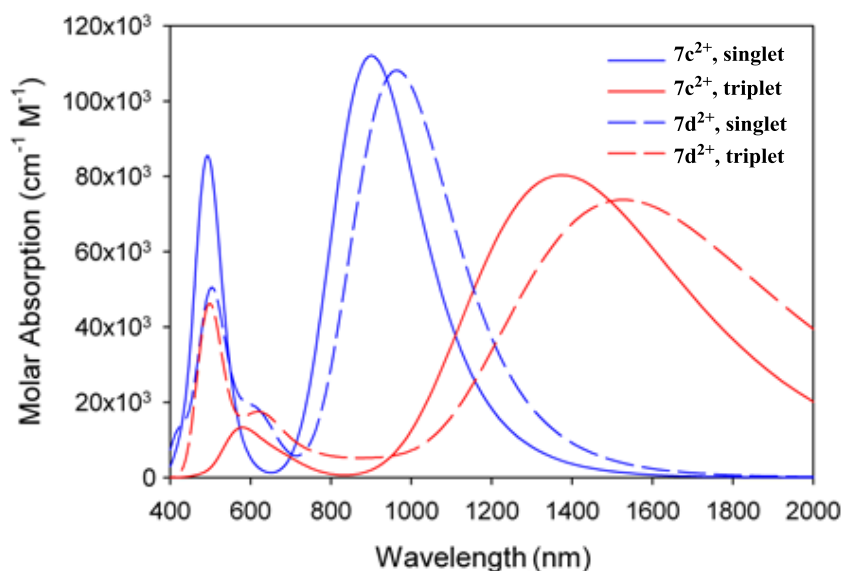


Figure 3.4.49: TD-DFT calculated spectra of $[\{\text{Ru}(\text{tpy})(\text{bpy})\}_2(\mu\text{-adpc})]^{4+}$ ($7\mathbf{c}^{2+}$) and $[\{\text{Ru}(\text{tpy})(\text{bpy})\}_2(\mu\text{-Cl}_2\text{adpc})]^{4+}$ ($7\mathbf{d}^{2+}$) in both singlet and triplet ground states.

TD-DFT calculated spectra of $7\mathbf{c}^{2+}$ and $7\mathbf{d}^{2+}$ in both spin singlet and triplet ground states are shown in the Figure 3.4.49. The spectra of both complexes in the singlet ground state possess a low energy, intense band at 910-1000 nm due to electronic excitations from the HOMO and HOMO-2 to the LUMO and a high energy, fairly intense band at ca. 450 nm. The low energy bands (910-1000 nm) of both complexes are of equal intensity and the band for $7\mathbf{d}^{2+}$ is slightly bathochromically shifted relative to that of $7\mathbf{c}^{2+}$. On the other hand, the intensity of the high energy band (450 nm) for $7\mathbf{d}^{2+}$ is significantly reduced relative to that of $7\mathbf{c}^{2+}$. The triplet ground state spectra of both complexes feature

an intense low energy band at ca. 1400 nm (7000 cm^{-1}) due to electronic excitations from the β -spin HOMO and β -spin HOMO-5 to the β -spin LUMO. As seen in Figure 3.4.38 (B) and 3.4.39 (B) and in Table 3.4.7, both fully oxidized complexes ($7\mathbf{c}^{2+}$ and $7\mathbf{d}^{2+}$) possess an equally intense low energy band at 856 -1124 nm without any significant absorption at ca. 1400 nm, and a high energy band at 456-487 nm, the intensity of which band is significantly reduced for $\text{Cl}_2\text{-adpc}^{2-}$ complex ($7\mathbf{d}^{2+}$) relative to that of adpc^{2-} complex ($7\mathbf{c}^{2+}$). This is in agreement with calculations and a singlet ground state of both complexes ($7\mathbf{c}^{2+}$ and $7\mathbf{d}^{2+}$) with a $[\text{Ru(II)-R}_2\text{R}'_2\text{adpc}^0\text{-Ru(II)}]^{4+}$ valence configuration.

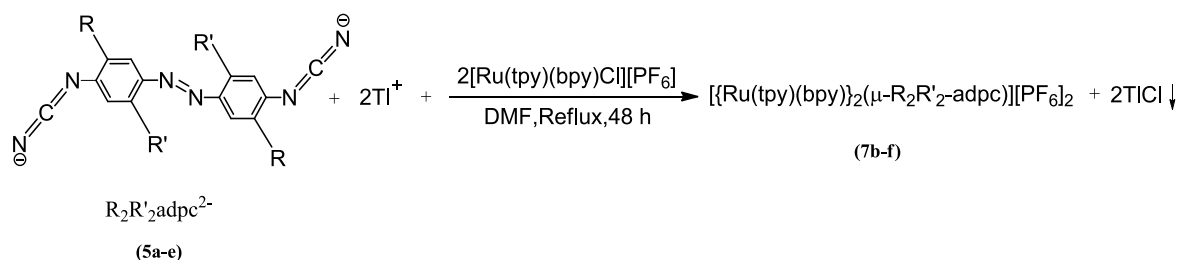
Like unsubstituted adpc^{2-} and $\text{Cl}_2\text{adpc}^{2-}$ complexes ($7\mathbf{c}^{2+}$ and $7\mathbf{d}^{2+}$), $\text{Me}_4\text{-,Me}_2\text{-}$ and Cl_4adpc complexes ($7\mathbf{a}^{2+}$, $7\mathbf{b}^{2+}$ and $7\mathbf{e}^{2+}$) also featured a pronounced vis-NIR absorption at 696-1124 nm without any significant absorptions at ca. 1400 nm (Figure 3.4.36 B-3.4.40 B), which suggested a predominantly closed-shell singlet ground state description $[\text{Ru(II)-R}_2\text{R}'_2\text{adpc}^0\text{-Ru(II)}]^{4+}$ for $7\mathbf{a}^{2+}$ - $7\mathbf{e}^{2+}$. The low energy NIR band of $[\{\text{Ru(tpy)(bpy)}\}_2(\mu\text{-R}_2\text{R}'_2\text{adpc})]^{4+}$ complexes ($7\mathbf{a}^{2+}$ - $7\mathbf{e}^{2+}$) is, therefore, mostly a Ru(II)-to- adpc^0 MLCT transition. However, the low energy tail (1200-2000 nm) of the NIR band gradually gains some intensity from $\text{Me}_4\text{-}$ to $\text{Cl}_4\text{-adpc}^{2-}$ complexes (Figure 3.4.36 B-3.4.40 B), indicating a minor but gradually increasing contribution of open shell triplet structures $[\text{Ru(III)-R}_2\text{R}'_2\text{adpc}^{2-}\text{-Ru(III)}]^{4+}$ and $[\text{Ru(III)-R}_2\text{R}'_2\text{adpc}^{\bullet-}\text{-Ru(II)}]^{4+}$ to the predominant singlet structure $[\text{Ru(II)-R}_2\text{R}'_2\text{adpc}^0\text{-Ru(II)}]^{4+}$. This is also consistent with theoretical prediction that suggested a possible spin switch-over from the singlet to the triplet ground state for $\text{Cl}_2\text{adpc}^{2-}$ complex ($7\mathbf{c}^{2+}$) in solution.

3.5 Discussion

3.5.1 Synthesis

The dinuclear $[\{\text{Ru}(\text{tpy})(\text{bpy})\}_2(\mu\text{-R}_2\text{R}'_2\text{adpc})][\text{PF}_6]_2$ complexes (**7b-7f**), where $\text{R}_2\text{R}'_2\text{adpc} = \text{Me}_4\text{-}, \text{Me}_2\text{-}$, unsubstituted, $\text{Cl}_2\text{-}$, $\text{Cl}_4\text{-}$, and *meta*-adpc, have been prepared by the metathesis reaction of $[\text{Ru}(\text{tpy})(\text{bpy})\text{Cl}][\text{PF}_6]$ with thallium salts **5a-5e** in refluxing DMF for 48 h, according to the Scheme 3.5.1. The synthesis of the Cl_4adpc complex (**7e**) required refluxing in DMF for 96 h to obtain a substantial amount of the dinuclear complex, because of the deactivation of $\text{Cl}_4\text{adpc}^{2-}$ towards ligand substitution.

Scheme 3.5.1: Synthetic Scheme used to prepare **7b-7f**.



The thallium salt of $\text{Me}_4\text{adpc}^{2-}$, could not be prepared and so the synthesis of **7a** required *in situ* deprotonation of $\text{Me}_4\text{adpcH}_2$ using BuLi, according to (Scheme 3.5.2)

Scheme 3.5.2: Synthetic Scheme used to prepare **7a**



7b was obtained in high yield (93%) by recrystallization of the crude complex from DMF by ether diffusion. On the other hand, **7a**, **7c-7f** required purification by column chromatography before recrystallization and this decreased the yields to 13-15%.

3.5.2 Spectroscopic Analysis, Cyclic Voltammetry and Theory

The principal stimulus of this research project was a publication by Chisholm *et al*² in which gas phase DFT calculations of the mixed-valence [$\{\text{Ru}(\text{tpy})(\text{bpy})\}_2(\mu\text{-adpc})\]^{3+}$ complex supported bridging ligand oxidation and an oxidation state description of Ru(II)-adpc^{•-}-Ru(II), in disagreement with literature.¹ Previous EPR studies⁶ of [$\{\text{Ru}(\text{tpy})(\text{thd})\}_2(\mu\text{-dicyd})\]^+$ had demonstrated the non-innocence of dicyd²⁻ and so oxidation of adpc²⁻ was a reasonable possibility. However, the ligand oxidation couple of adpc²⁻ is 0.95 V more positive than that of dicyd²⁻ and DFT calculations that neglect solvent effects can give erroneous results. For the latter, ¹H NMR and EPR spectroscopic data conclusively showed that mixed-valence [$\{\text{Ru}(\text{NH}_3)_5\}_2(\mu\text{-dicyd})\]^{3+}$ possessed an oxidation state description Ru(III)-dicyd²⁻-Ru(II), a result that could only be modelled by DFT calculations that included explicit electrostatic interactions between solute and solvent. To resolve this question in the case of [$\{\text{Ru}(\text{tpy})(\text{bpy})\}_2(\mu\text{-adpc})\]^{3+}$, EPR and IR and vis-NIR spectroscopic studies were performed on the family of complexes [$\{\text{Ru}(\text{tpy})(\text{bpy})\}_2(\mu\text{-R}_2\text{R}_2'\text{adpc})\]^{2+/3+/4+}.$

EPR spectroscopy provides the strongest evidence for the orbital parentage of a SOMO and in the case of the [$\{\text{Ru}(\text{tpy})(\text{bpy})\}_2(\mu\text{-R}_2\text{R}_2'\text{adpc})\]^{3+}$ complexes, where R₂R₂' = Me₄ (**7a**⁺), Me₂ (**7b**⁺) H₄ (**7c**⁺) Cl₂ (**7d**⁺) and Cl₄ (**7e**⁺), Figure 3.4.24 shows that while **7d**⁺ has an oxidation state description Ru(III)-Cl₂adpc²⁻-Ru(II), that for **7a**⁺ is best described by Ru(II)-Me₄adpc^{•-}-Ru(II). The energetics of the dπ orbitals of the Ru²⁺(tpy)(bpy) moiety and the π-HOMO orbital of adpc²⁻ are therefore closely matched so that the perturbation of a phenyl ring substituent is enough to push the SOMO from being mostly metal to mostly ligand centred. Unfortunately, **7b**⁺, **7c**⁺ and **7e**⁺ were either

EPR silent or gave a weak EPR signal. Nevertheless, the parentage of the SOMO could be established by a comparison of IR and vis-NIR spectroelectrochemical studies for these complexes with those of **7a**⁺ and **7d**⁺. The IR spectroelectrochemical oxidation of **7a** and **7b** (Figure 3.4.26A and 3.4.27A) resulted in similar changes to the $\nu(\text{NCN})$ band that were consistent with the oxidation of the bridging ligand; the band decreased in intensity and shifted slightly to higher frequencies. A single $\nu(\text{NCN})$ band is seen in this case because $\text{R}_2\text{R}_2'\text{adpc}^{\bullet-}$ is a delocalized radical with equivalent cyanamide groups. In contrast, while the IR spectroelectrochemical oxidation of **7d** and **7e** (Figure 3.4.29A and 3.4.30A) resulted in decreasing intensity of the $\nu(\text{NCN})$ band, the band frequency remained the same and a new $\nu(\text{NCN})$ band appeared at lower frequencies. This result is consistent with an oxidation state distribution of $\text{Ru(III)-R}_2\text{R}_2'\text{adpc}^{2-}\text{-Ru(II)}$ in which the growth of the lower frequency band is due to cyanamide coordinated to Ru(III). Thus, both **7d**⁺ and **7e**⁺ must be considered valence-trapped mixed-valence complexes on the IR timescale (10^{13} s^{-1}) despite a presumably large free energy of comproportionation $\Delta G_c = -\Delta E$, in Table 3.4.8. The trend in ΔE in Table 3.4.8 decreases from **7a**⁺ to **7e**⁺ and this might be interpreted as due to a decrease in metal-metal coupling. However, ΔE for both **7d**⁺ and **7e**⁺ is too large to be consistent with a valence-trapped mixed-valence complex. For comparison, the Creutz-Taube ion $[\{\text{Ru}(\text{NH}_3)_5\}_2(\mu\text{-pyrazine})]^{5+}$ is considered to be a borderline delocalized case and has only $\Delta G_c = -0.39 \text{ V}$.⁵² This discrepancy can be rationalized if the second oxidation to form **7d**²⁺ and **7e**²⁺ is not Ru(III/II) but is ligand centred and therefore the value of ΔE Table 3.4.8 is not a true measure of ΔG_c . Indeed, the IR spectroelectrochemical oxidation forming **7d**²⁺ and **7e**²⁺ (Figure 3.4.29B and 3.4.30B, respectively) shows a decrease of the lower frequency band that is assigned to

cyanamide coordinated to Ru(III) rather than an increase as would be expected if Ru(III)-adpc²⁻-Ru(III) formed. A delocalized case is suggested to apply to mixed-valence **7c**⁺. This complex has only a single $\nu(\text{NCN})$ band (Figure 3.4.28), and it is suggested to be best described by the oxidation state distribution, Ru(II^{1/3})-adpc^{1^{2/3}-}-Ru(II^{1/3}). The complexes **7a**⁺-**7e**⁺ all possess an intense NIR band (Figure 3.4.39) but only in the case of **7d**⁺ and **7e**⁺ can this band be described as mostly metal-to-metal charge transfer. The true electronic state description of this NIR transition must await theoretical methods that can properly account for solvent effects. Unrestricted gas phase DFT calculations of **7a**⁺-**7e**⁺ supported an oxidation state description Ru(II)-R₂R₂'adpc^{•-}-Ru(II) in disagreement with the experimental results of **7d**⁺ and **7e**⁺. For the doubly oxidized species **7a**²⁺ - **7e**²⁺, TD-DFT calculations which included solvent (methanol) determined the spectra of **7c**²⁺ and **7d**²⁺ (Figure 3.4.46) and supported a singlet state description Ru(II)-R₂R₂'adpc⁰-Ru(II). However, a low energy tail (1200 to 2000 nm) of the NIR band (Figure 3.4.33 B-3.4.37 B) gains intensity from **7a**²⁺ and **7e**²⁺ and may indicate a minor but gradually increasing contribution of open shell triplet structures Ru(III)-R₂R₂'adpc²⁻-Ru(III) and Ru(III)-R₂R₂'adpc^{•-}-Ru(II).

The *meta*-adpc complex **7f** was prepared to see the effect of positional isomer of the bridging adpc²⁻ ligand on the metal-metal coupling in the dinuclear mixed-valence complex **7f**⁺. However, DFT calculations of the *meta*-adpc²⁻ ligand and **7f**⁺ showed a discontinuity in π -conjugation. Unlike its *para* analogue (**7c**), the cyclic voltammetry of the **7f** showed only a single reversible wave (0.98V) close to the Ru(III/II) couple of mononuclear [Ru(tpy)(bpy)(2,4-Cl₂pcyd)]⁺ and the NIR band (1100 nm) that is observed

for the $7f^+$ also coincides with the Ru(III)-cyanamide LMCT band of the oxidized $[\text{Ru}(\text{tpy})(\text{bpy})(2,4\text{-Cl}_2\text{pcyd})]^+$, supporting a Class I mixed-valence behaviour of the $7f^+$.

3.6 Conclusion

The bridging $\text{R}_2\text{R}_2'\text{adpc}^{2-}$ ligands exhibited substituent dependent non-innocent behavior in dinuclear $[\{\text{Ru}(\text{tpy})(\text{bpy})\}_2(\mu\text{-R}_2\text{R}_2'\text{adpc})]^{3+,4+}$ complexes ($7a^+$ - $7f^+$ and $7a^{2+}$ - $7e^{2+}$). Gas-phase DFT calculations showed mostly ligand-centred radical description $\text{Ru(II)-R}_2\text{R}_2'\text{adpc}^{\bullet-}\text{-Ru(II)}$ of the singly oxidized dinuclear complexes $[\{\text{Ru}(\text{tpy})(\text{bpy})\}_2(\mu\text{-R}_2\text{R}_2'\text{adpc})]^{3+}$. However, EPR spectroscopy, supported by IR and Visible-NIR spectroelectrochemical studies strongly suggested a ligand-centered radical description, $\text{Ru(II)-R}_2\text{R}_2'\text{adpc}^{\bullet-}\text{-Ru(II)}$ of complexes $[\{\text{Ru}(\text{tpy})(\text{bpy})\}_2(\mu\text{-Me}_4/\text{Me}_2\text{adpc})]^{3+}$ ($7a^+$, $7b^+$) and a delocalized mixed-valence description, $\text{Ru}^{2.5}\text{-adpc}^{2-}\text{-Ru}^{2.5}$, of unsubstituted $[\{\text{Ru}(\text{tpy})(\text{bpy})\}_2(\mu\text{-adpc})]^{3+}$ ($7c^+$) and more localized mixed-valence descriptions, $\text{Ru(II)-R}_2\text{R}_2'\text{adpc}^{2-}\text{-Ru(III)}$, of $[\{\text{Ru}(\text{tpy})(\text{bpy})\}_2(\mu\text{-Cl}_2/\text{Cl}_4\text{adpc})]^{3+}$ ($7d^+$, $7e^+$). DFT calculations in conjugation with vis-NIR spectroelectrochemical studies gave the most appropriate closed shell singlet description, $\text{Ru(II)-R}_2\text{R}_2'\text{adpc}^0\text{-Ru(II)}$, of $[\{\text{Ru}(\text{tpy})(\text{bpy})\}_2(\mu\text{-R}_2\text{R}_2'\text{adpc})]^{4+}$ ($7a^{2+}$ - $7e^{2+}$) with increasing contribution of triplet structures, $\text{Ru(III)-R}_2\text{R}_2'\text{adpc}^{2-}\text{-Ru(III)}$ and $\text{Ru(II)-R}_2\text{R}_2'\text{adpc}^{\bullet-}\text{-Ru(III)}$, in unsubstituted, Cl_2 - and Cl_4adpc complexes ($7c^{2+}$ - $7e^{2+}$). DFT calculations and cyclic voltammetry of $[\{\text{Ru}(\text{tpy})(\text{bpy})\}_2(\mu\text{-meta-adpc})]^{3+}$ complex ($7f^+$) are consistent with an uncoupled system and both electrochemical and vis-NIR feature suggested Ru(III)-centred spin. Finally, dinuclear complexes $[\{\text{Ru}(\text{tpy})(\text{bpy})\}_2(\mu\text{-R}_2\text{R}_2'\text{adpc})]^{3+}$ ($7a^+$ - $7e^+$) exhibited fairly intense NIR charge transfer absorption at 1650-1920 nm, which can fit them well as variable

optical attenuator (electro-optic switching) in NIR telecommunication devices as well as in smart windows to filter-out the radiant heat whilst transmitting visible light.

3.7 References

1. Mosher, P. J.; Yap, G. P. A.; Crutchley, R. J. *Inorg. Chem.* **2001**, *40*, 1189.
2. Chisholm, M. H.; D'Acchioli, J. S.; Hadad, C. M.; Patmore, N. J. *Inorg. Chem.* **2006**, *45*, 11035.
3. Al-Noaimi, M.; Crutchley, R. J. *Inorg. Chim. Act.* **2007**, *360*, 3013.
4. Al-Noaimi, M.; Yap, G. P. A.; Crutchley, R. J. *Inorg. Chem.* **2004**, *43*, 1770.
5. Naklicki, M. L.; Gorelsky, S. I.; Kaim, W.; Sarkar, B.; Crutchley, R. J. *Inorg. Chem.* **2012**, *51* 1400.
6. Fabre, M.; Jaud, J.; Hliwa, M.; Launay, J.-P.; Bonvoisin, J. *Inorg. Chem.* **2006**, *45*, 9332.
7. (a) Aquino, M. A. S.; Lee, F. L.; Gabe, E. J.; Bensimon, C.; Greedan, J. E.; Crutchley, R. J. *J. Am. Chem. Soc.* **1992**, *114*, 5130. (b) Naklicki, M.; Crutchley, R. J. *Inorg. Chim. Acta* **1994**, *225*, 123.
8. Rezvani, A. R.; Bensimon, C.; Crompton, B.; Reber, C.; Greedan, J. E.; Kondratiev, V. V.; Crutchley, R. J. **1997**, *36*, 3322.
9. Evans, C. E. B.; Naklicki, M. L.; Rezvani, A. R.; White, C. A.; Kondratiev, V. V.; Crutchley, R. J. *J. Am. Chem. Soc.* **1998**, *120*, 13096.
10. De Rosa, M. C.; White, C. A.; Evans, C. E. B.; Crutchley, R. J. *J. Am. Chem. Soc.* **2001**, *123*, 1396.
11. Evans, C. E. B.; Yap, G. P. A.; Crutchley, R. J. *Inorg. Chem.* **1998**, *37*, 6161.

12. Mahmoud, L.; Gorelsky, S. I.; Kaim, W.; Sarkar, B.; Crutchley, R. J. *Inorg. Chim. Acta* **2011**, *374*, 147.
13. Harb, C.; Kravstov, P.; Choudhuri, M.; Sirianni, E. R.; Yap, G. P. A.; Lever, A. B. P.; Crutchley, R. J. *Inorg. Chem.* **2013**, *52*, 1621.
14. Naklicki, M.; Crutchley, R. J.; *Inorg. Chem.* **1989**, *28*, 1955.
15. Crutchley, R. J.; McCaw, K.; Lee, F. L.; Gabe, J. E. *Inorg. Chem.* **1990**, *29*, 2576.
16. Saleh, A. A.; Crutchley, R. J. *Inorg. Chem.* **1990**, *29*, 2123.
17. Evans, C. E. B.; Ducharme, D.; Naklicki, M.; Crutchley, R. J.; *Inorg. Chem.* **1995**, *34*, 1350.
18. Mosher, P. J.; Yap, G. P. A.; Crutchley, R. J.; *Inorg. Chem.* **2001**, *40*, 550.
19. (a) Crutchley, R. J. *Coord. Chem. Rev.* **2001**, *125*, 219. (b) Hollebhone, B. R.; Nyholm, R. S.; *J. Chem. Soc. A* **1971**, 332. (c) Hollebhone, B. R. *J. Chem. Soc. A* **1971**, 481. (d) Hollebhone, B. R.; Stillman, M. J. *Inorg. Chim. Acta* **1980**, *42*, 169 (e) Crutchley, R. J. *Comp. Coord. Chem. II* **2003**, *2*, 785. (f) Rasmussen, C. R.; Villani Jr., F. J.; Weaner, L. E.; Reynolds, B. E.; Hood, A.R.; Hecker, L. R.; Nortey, S. O.; Hanslin, A.; Costanzo, M. J.; Powell, E. T.; Molinari, A. J. *Synthesis Papers* **1987**, 456.
20. (a) Fauss, R.; Riebel, H.-J. CA 1256898, C 19890723. (b) Ghosh, H.; Yella, R.; Ali, A. R.; Sahoo, S. K.; Patel, B. K. *Tetrahedron Lett.* **2009**, *50*, 2407. (c) Wheland, R. C.; Martin, E. L.; *J. Org. Chem.* **1975**, *40*, 3101. (d) Wu, Y.-Q.; Limburg, D. C.; Wilkinson, D. E.; Hamilton, G. S. *Org. Lett.* **2000**, *2*, 795. (e) Kim, J.-J.; Kweon, D.-H.; Cho, S.-D.; Kim, H.-K.; Jung, E.-Y.; Lee, S.-G.; Falck, J. R.; Yoon, Y.-J. *Tetrahedron* **2005**, *61*, 5889. (f) Hughes, T. V.; Hammond, S.

- D.; Cava, M. P. *J. Org. Chem.* **1998**, *63*, 401. (g) Davis, W. A.; Cava, M. P. *J. Org. Chem.* **1983**, *48*, 2774. (h) Kahne, D.; Collum, D. *Tetrahedron Lett.* **1981**, *22*, 5015. (i) Boltz, K. H.; Dell, H. D.; *Justus Liebigs Ann. Chem.* **1967**, *709*, 63. (j) Hermes, M. E.; Marsh, F. D. *J. Org. Chem.* **1972**, *37*, 2969. (k) Emami, S.; Foroumadi, A. *Chin. J. Chem.* **2006**, *24*, 791. (l) Sattigeri, V. J.; Soni, A.; Singhal, S.; Khan, S.; Pandya, M.; Bhateza, P.; Mathur, T.; Rattan, A.; Khanna, J. M.; Mehta, A. *Arkivoc* **2005**, *2*, 46. (m) Ghosh, H.; Yella, R.; Nath, J.; Patel, B. K. *Eur. J. Org. Chem.* **2008**, 6189. (n) Humeres, E.; Debacher, N. A.; Franco, J. D.; Lee, B. S.; Martendal A. *J. Org. Chem.* **2002**, *67*, 3662. (o) Hlasiwetz.; Kachler. *Libig's Annelan*, 166.142.
21. (a) Hunger, K.; *Industrial Dyes: Chemistry, Properties, Applications*; ed: Wiley-VCH: Weinheim, Germany, **2003**. (b) Ashutosh, P. N. D.; Mehrotra, J. K. *Colourage* **1979**, *26*, 25. (c) Athey Jr., R. D.; *Eur. Coat. J.* **1998**, *3*, 146. (d) Ikeda, T.; Tsutsumi, O. *Science*, **1995**, *268*, 1873. (e) Feringa, B. L.; Van Delden, R. A.; Koumura, N.; Geertsema, E. M.; *Chem. Rev.* **2000**, *100*, 1789.
22. (a) Hegarty, A. F.; ed: Patai, S. *The Chemistry of Diazonium and Diazo Group Part 2*; Wiley: New York, **1978**, 545. (b) Zollinger, H.; *Diazo Chemistry I. Aromatic and Heteroaromatic Compounds*; VCH: New York, **1994**. (c) Zollinger, H.; *Azo and Diazo Chemistry Aliphatic and Aromatic Compounds*; Interscience: New York, **1961**, 294. (d) Svele, I.; Zollinger, H. *Top. Curr. Chem.* **1983**, *112*, 1.
23. (a) Bacon, E. S.; Richardson, D. H.; *J. Chem. Soc.* **1932**, 884. (b) Entwistle, I. D.; Gilkerson, T.; Johnstone, R. A. W.; Telford, R. P. *Tetrahedron*, **1978**, *34*, 213. (c) Caro, H. *Angew. Chem.* **1898**, *11*, 845. (d) Haworth, R. D.; Lapworth, A.; *J.*

- Chem. Soc.* **1921**, *119*, 768. (e) Ibne-Rasa, K. M.; Lauro, C. G.; Edwards, J. O. J. *Am. Chem. Soc.* **1963**, *85*, 1165. (f) Zhu, Z.; Espenson, J. H. *J. Org. Chem.* **1995**, *60*, 1326. (g) Melnikov, E. B.; Suboch, G. A.; Belyaev, E. Y. *Zh. Org. Khim.* **1995**, *31*, 1849. (h) Dafoin, A. *Synthesis*, **2004**, 706. (i) Yu, B. C.; Shirai, Y.; Tour, G. M. *Tetrahedron*, **2006**, *62*, 10303. (j) Davey, H. H.; Lee, R. D.; Marks, T. J. *J. Org. Chem.* **1999**, *64*, 4976. (k) Priewisch, B.; Ruck-Braun, K. *J. Org. Chem.* **2005**, *70*, 2350. (l) Meenakshisundaram, S.; Selvaraju, M.; Gowda, N. M. M.; Rangappa, K. S. *Effects of Substituents on the Rate of Oxidation of Anilines with Peroxomonosulphate Monoanion in Aqueous Acetonitrile: A Mechanistic Study*; Wiley Periodicals, May, **2005**. (m) Karr, J. A. *Chem. Rev.* **1966**, *66*, 465.
24. (a) Shimao, I.; Matsumura, S. *Bull. Chem. Soc. Jpn.* **1976**, *49*, 2294. (b) Bacon, E. S.; Richardson, D. H.; *J. Chem. Soc.* **1932**, 884. (c) Moltchanoffsky, N. *J. Russ. Chem. Soc.* 18882, 224. (d) Henki, C. O.; Brown, O. W.; *J. Phys. Chem.* **1922**, *26*, 324. (e) Fry, H. S.; *J. Am. Chem. Soc.* **1930**, *52*, 1531. (f) Bigelow, H. E.; Palmer, *Org. Synth.* **1931**, *11*, 16. (g) Shimao, I.; Oae, S. *Bull. Chem. Soc. Jpn.* **1983**, *56*, 643.
25. Merino, E. *Chem. Soc. Rev.* **2011**, *40*, 3835.
26. (a) Wawzonek, S.; McIntyre, T. W. *J. Electrochem. Soc.* **1972**, *119*, 1350. (b) Karunakaran, C.; Palanysamy, P. N. *J. Mol. Catal. A.: Chem.* 2001, *172*, 9. (c) Noureldin, N. A.; Bellegarde, J. W. *Synthesis* **1999**, 939. (d) Olsen, H.; Snyder, J. P. *J. Am. Chem. Soc.* **1977**, *99*, 1524. (e) Santurri, P.; Robbins, F. *Org. Synth.* **1960**, *40*, 341. (f) Huestis, L. *J. Chem. Ed.* **1977**, *54(5)*, 327.

27. Sakai, N.; Fujii, K.; Nabeshima, S.; Ikeda, R.; Konakahara, T. *Chem. Commun.* **2010**, *46*, 3173.
28. Nanjundaswami, H. M.; Pasha, M. A. *Synth. Commun.* **2005**, *35*, 2163.
29. (a) Wong, F. F.; Chen, C.-Y.; Yeh, M.-Y. *Synlett.* **2006**, *4*, 559. (b) Charalambides, Y. C.; Moratti, S. *Synth. Commune.* **2007**, *37*, 1037. (c) Collman, J. P.; Wang, Z.; Straumanis, A. *J. Org. Chem.* **1998**, *63(8)*, 2424. (d) Chaudhuri, K. H.; Mahajan, U. S.; Bhalerao, D. S. *Synlett.* **2007**, 2815. (e) Kamijo, S.; Jin, T.; Yamamoto, Y. *Angew. Chem. Int. Ed.* **2002**, *41*, 1780. (f) Bakunov, S. A.; Rukavishnikov, A. V.; Tkachev, A. V. *Synthesis* **2000**, 1148. (g) Voitekhovich, S. V.; Vorob'ev, A. N.; Gaponik, P. N.; Ivashkevich, O. A. *Chem. Hetero. Comp.* **2005**, *41(9)*, 999.
30. Hirashima, T.; Manabe, O. *Chemistry Letters* **1975**, 259.
31. Terc, J.; Bartos, A.; Pokorny, M.; Vojtisek, V.; Zima, J. CS 255228 B1 19880215.
32. Hadda, T. B.; Bozec, H. L. *Inorg. Chim. Acta* **1993**, *204*, 103.
33. Takeuchi, K. J.; Thompson, M. S.; Pipes, D. W.; Meyer, T. J. *Inorg. Chem.* **1984**, *23*, 1845.
34. Gennett, T.; Milner, D. F.; Weaver, M. J. *J. Phys. Chem.* **1985**, *89*, 2787.
35. Frisch, M. J.; Trucks, G. W.; Schlegel, H. B.; Scuseria, G. E.; Robb, M. A.; Cheeseman, J. R.; Scalmani, G.; Barone, V.; Mennucci, B.; Petersson, G. A.; Nakatsuji, H.; Caricato, M.; Li, X.; Hratchian, H. P.; Izmaylov, A. F.; Bloino, J.; Zheng, G.; Sonnenberg, J. L.; Hada, M.; Ehara, M.; Toyota, K.; Fukuda, R.; Hasegawa, J.; Ishida, M.; Nakajima, T.; Honda, Y.; Kitao, O.; Nakai, H.; Vreven, T.; Montgomery, J., J. A.; Peralta, J. E.; Ogliaro, F.; Bearpark, M.; Heyd, J. J.;

- Brothers, E.; Kudin, K. N.; Staroverov, V. N.; Kobayashi, R.; Normand, J.; Raghavachari, K.; Rendell, A.; Burant, J. C.; Iyengar, S. S.; Tomasi, J.; Cossi, M.; Rega, N.; Millam, J. M.; Klene, M.; Knox, J. E.; Cross, J. B.; Bakken, V.; Adamo, C.; Jaramillo, J.; Gomperts, R.; Stratmann, R. E.; Yazyev, O.; Austin, A. J.; Cammi, R.; Pomelli, C.; Ochterski, J. W.; Martin, R. L.; Morokuma, K.; Zakrzewski, V. G.; Voth, G. A.; Salvador, P.; Dannenberg, J. J.; Dapprich, S.; Daniels, A. D.; Farkas, Ö.; Foresman, J. B.; Ortiz, J. V.; Cioslowski, J.; Fox, D. J. *Gaussian 09*, Revision A.02; Gaussian Inc.: Wallingford, CT, 2009.
36. Becke, A. D., *Journal of Chemical Physics* **1993**, 98, 5648.
37. Lee, C.; Yang, W.; Parr, R. G., *Physical Reviews* **1988**, B37, 785.
38. Godbout, N.; Salahub, D. R.; Andzelm, J.; Wimmer, E., *Canadian Journal of Chemistry* **1992**, 70, 560-571.
39. Schafer, A.; Huber, C.; Ahlrichs, R., *Journal of Chemical Physics* **1994**, 100, (8), 5829-5835.
40. Marenich, A. V.; Cramer, C. J.; Truhlar, D. G., *J. Phys. Chem. B* **2009**, 113, 6378-6396.
41. Casida, M. E., In *Recent Advances in Density Functional Methods*, Chong, D. P., Ed. World Scientific: Singapore, 1995; pp 155-192.
42. Stratmann, R. E.; Scuseria, G. E.; Frisch, M. J., *J. Chem. Phys.* **1998**, 109, 8218-8224.
43. Gorelsky, S. I. *SWizard, Version 4*, <http://www.sg-chem.net>, 2008.
44. Aquino, M. A. S.; Crutchley, R. J.; Lee, F. L.; Gabe, E. J.; Bensimon, C. *Acta Cryst.* **1993**, C49, 1543.

45. Kurzar, F.; Douraghi-Zadeh, K. *Chem. Rev.* **1967**, *67*, 107.
46. (a) Constable, E. C.; Lewis, J.; Liptrot, M. C.; Raithby, P. R. *Inorg. Chim. Acta*, **1990**, *178*, 47. (b) Constable, E. C.; Harverson, P.; Diane, R. S.; Whall, L. *Polyhedron*, **1997**, *16(20)*, 3615. (c) Lashgari, K.; Kritikos, M.; Norrestam, R.; Norrby, T. *Acta Cryst.* **1999**, *C55*, 64. (d) Norrby, T.; Borje, A.; Akermark, B.; Hammarstrom, L.; Alsins, J.; Lashgari, K.; Norrestam, R.; Martensson, J.; Stenhagen, G. *Inorg. Chem.* **1997**, *36*, 5850. (e) Lyttle, F. E.; Petrosky, L. M.; Carlson, L. R. *Anal. Chim. Acta* **1971**, *57*, 239. (f) Orellana, G.; Ibarra, C. A.; Santoro, J. *Inorg. Chem.* **1988**, *27*, 1025. (g) Heijden, M.; van Vliet, P. M.; Reedijk, J. *J. Chem. Soc. Dalton Trans.* **1993**, 3675. (h) Rutherford, T. J.; Reitsma, D. A.; Keene, F. R. *J. Chem. Soc. Dalton Trans.* **1994**, 3659. (i) Bryant, G. M.; Ferguson, J. *Aust. J. Chem.* **1971**, *24*, 441.
47. Balzani, V.; Juris, A.; Barigelletti, F.; Campagna, S.; Belser, P.; Von Zelewsky, A. *Coord. Chem. Rev.* **1988**, *84*, 85.
48. Gerson, F.; Gescheidt, G.; Möckel, R.; Aumüller, A.; Erk, P.; Hünig, S. *Helv. Chim. Acta* **1988**, *71*, 1665.
49. Choudhuri, M. M. R.; Kaim, W.; Sarkar, B.; Crutchley, R. J. *Inorg. Chem.* **2013**, *52(19)*, 11060.
50. (a) Creutz, C.; *Prog. Inorg. Chem.* **1983**, *30*, 1. (b) Crutchley, R. J. *Adv. Inorg. Chem.* **1994**, *41*, 273. (c) Ward, M. D.; *Chem. Soc. Rev.* **1995**, 121. (c) Hush, N. S. *Prog. Inorg. Chem.*, **1967**, *8*, 391. (d) Creutz, C.; Newton, M. D.; Sutin, N.; *J. Photochem. Photobiol. A: Chem.* **1994**, *82*, 47.

51. (a) Kaim, W. *Coord. Chem. Rev.* **1987**, *76*, 187. (b) Weil, J. A.; Bolton, J. T.; Wertz, J. E. *Electron Paramagnetic Resonance*; Wiley: New York, **1994**. (c) Kaim, W.; Kasack, V. *Inorg. Chem.* **1990**, *29*, 4696. (d) Roy, S.; Sarkar, B.; Imrich, H.-G.; Fiedler, J.; Zalis, S.; Jimenez-Aparicio, R.; Urbanos, F. A.; Mobin, S. M.; Lahiri, G. K.; Kaim, W. *Inorg. Chem.* **2012**, *51*, 9273. (e) Remenyi, C.; Kaupp, M. *J. Am. Chem. Soc.* **2005**, *127*, 11399. (h) Mori, T.; Inokuchi, H.; Kobayashi, A.; Kato, R.; Kobayashi, H. *Phys. Rev. B* **1988**, *38*, 5913. (i) Sakurai, T.; Nakagawa, N.; Okubo, S.; Ohta, H.; Kanoda, K.; Hiraki, K. *J. Phys. Soc. Jpn* **2001**, *70(6)*, 1794.

Chapter 4: Phenylecyanamide Ligand Control of Linkage Isomerism in Ruthenium-Sulfoxide Complexes

4.1 Introduction

4.1.1 Scope of Research

Photo-switchable bistable molecules have received special attention in recent years due to their potential applications in optical molecular information storage, optical switching and molecular sensing devices.^{1,2} In this regard, photochromic compounds are of particular interest because of their ability to undergo light induced fast (sub-picosecond) reversible transformation between two isomeric forms that have distinctly different electronic absorption ($\Delta\nu \gg 100 \text{ cm}^{-1}$) properties. These properties are well-suited for applications in all optical networks such as ultrafast optical switches,³ logic gates for molecular computing application,⁴ or for high-density volume data storage.^{5,6} For applications in optical information and communication technology (ICT), the desired materials need to fulfill certain requirements: (i) two or more optically distinctive states, (ii) an efficient and fast light-induced conversion between these states and (iii) specific lifetime of molecules in these states. The photo-induced conversion should be triggered by excitation using UV/Vis light, whereas the spectral range of the photochromic response should either be in UV/Vis for high-density storage^{5,6} or in NIR for photo-switches³ and logic gates.⁴ In recent years several coordination compounds like nitroprussides (NO)¹, sulfoxides (SO)⁹, as well as several organic molecules like diarylethenes^{3a} have shown excellent photofunctionality towards applications in molecular photonic devices.

The coordination compounds like nitroprussides (NO), sulfoxides (SO) have shown their photofunctionality via light-induced ultrafast reversible linkage isomerism of bound nitrosyl (NO) and sulfoxide (SO) ligands.^{1,9} In this regard, dimethylsulfoxide (dmsO) ligand in $[\text{Ru}(\text{tpy})(\text{bpy})(\text{dmsO}-S)]^{2+}$, where tpy is 2,2':6',2''-terpyridine and bpy is 2,2'-bipyridine, has been showed to undergo rapid photo-induced linkage isomerism $\text{Ru-dmsO}(-S) \rightarrow \text{Ru-dmsO}(-O)$ followed by a far slower thermal $\text{Ru-dmsO}(-O) \rightarrow \text{Ru-dmsO}(-S)$ reaction in solution, crystals and films.⁷ The excited state responsible for this rearrangement arises from a metal-to-ligand charge transfer (MLCT) transition and it is therefore not surprising that the electrochemical oxidation of Ru(II) to Ru(III) induces the same rearrangement with Ru(II)-dmsO(-S) and Ru(III)-dmsO(-O) being the stable bonding modes of dmsO.⁸ Recent transient absorption studies of ruthenium(II) dimethylsulfoxide complexes⁹⁻²⁷ have revealed that photo-induced linkage isomerism occurs in the picosecond timescale from a previously populated ³MLCT excited state.

In past studies, metal-metal coupling in dinuclear ruthenium complexes bridged by aromatic cyanamide ligands has been shown to be sensitive to the nature of the inner coordination sphere and the solvent.²⁸⁻²⁹ If these changes in metal-metal coupling could be induced photochemically, it would have significant photonics applications particularly in the case of mixed-valence complexes that possess intense intervalence bands which overlap the low-loss region of optical fibers in the NIR region. This is because transmission in the NIR region could be turned on/off by the changing energy and intensity of intervalence bands with the magnitude of metal-metal coupling. However, before one can create a “photo-switch” mixed-valence complex, it is first necessary to find a mononuclear coordination environment that has the potential in a dinuclear

complex to simultaneously express both properties of photoisomerism and mixed-valency. The focus this research is centred on the synthesis and characterization of a family of mononuclear ruthenium complexes of phenylcyanamide ligands $[\text{Ru}(\text{bpy})_2(\text{R-pcyd})(\text{dmsO-S})]^+$ to examine the photo- and electrochemically induced linkage isomerism of dimethyl sulfoxide ligand and correlate these properties with the donor property of phenylcyanamide ligands.

Prior to considering the linkage isomerism in mononuclear ruthenium-phenylcyanamide-dmsO complexes that forms the subject of this project, a detailed discussion regarding linkage isomerism of sulfoxide ligands in transition metal complexes will be given in following sections.

4.1.2 Transition Metal-sulfoxide Complexes

The Lewis base properties of sulfoxides have been known for a long time, yet the coordination chemistry of these interesting ligands remained largely unexplored until a renaissance period began in the early 1960s. During this period it was recognized that sulfoxides are capable of acting as ambidentate ligands, coordinating to specific metal via either sulfur (*S*-) or oxygen (*O*-) atom. A comprehensive review by Reynolds³⁰ illustrated these binding modes ($\eta^1\text{-S}$ and $\eta^1\text{-O}$) for dimethyl sulfoxide ligands in many transition metal complexes. A recent review by Calligaris^{31a} illustrated other binding modes of sulfoxide ligands in a variety of mononuclear and dinuclear transition metal complexes (Figure 4.1.1) and provided an account of theoretical and experimental values of S-O and M-S, M-O bond lengths in these complexes.

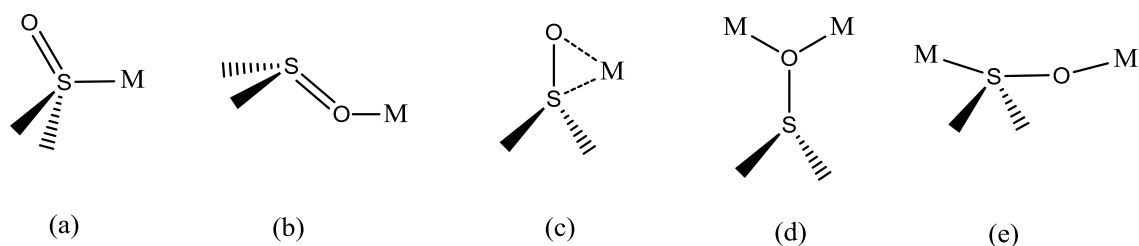


Figure 4.1.1: Binding modes of sulfoxide ligand in metal-sulfoxide complexes: (a) η^1 -S-binding, (b) η^1 -O-binding, (c) Side-on (η^2 -S,O)-symmetric or asymmetric binding, (d) μ -O-bridging type, (e) μ -S,O-bridging type.

Direct coordination via sulfur or oxygen atom (η^1 -S and η^1 -O) is the most common binding mode of sulfoxide ligands in transition metal complexes.^{30,31} The preference for *S*- or *O*-bound form has been rationalized by Hard-Soft-Acid-Base (HSAB) theory. In general, metal ions having large positive charge (3^+ or larger, smaller in size) or those whose *d*-electrons are relatively unavailable for π -bonding are less polarizable (hard acids) and prefer coordination through small, highly electronegative and less polarizable oxygen atom (hard base) on sulfoxide ligands. The alkaline earth ions, Al^{3+} , Cr^{3+} , Mn^{2+} , Fe^{3+} , Co^{3+} etc. fall into this category. On the other hand, metals having less positive charge (*mono*- or *di*-cation) or whose *d*-electrons or orbitals are available for π -bonding, are polarizable (soft acid) and prefer binding to large, less electronegative and polarizable sulfur atom (soft base) on sulfoxides. The diffuse nature of the orbitals on both soft acids (metal) and bases (*S* atom) favours efficient orbital overlap between the donor and the acceptor. Most of the second and third row transition metal ions having 45 or more electrons and especially platinum group metals fall into this category. Some metal ions like Fe^{2+} , Co^{2+} , Cu^{2+} , Zn^{2+} , Ru^{2+} etc., called the borderline metal ions, may exhibit both *S*- and *O*- coordination both *S*- and *O*- coordination (η^1 -S

and η^1 -O) depending on the electronic and steric environment of metal and ligands in their sulfoxide complexes.^{7-27,30,31}

Besides the most common *S*- or *O*- (η^1 -S and η^1 -O) coordination modes of sulfoxide ligands, there are also situations (Figure 4.1.1) where sulfoxide ligand exhibit side-on (η^2 -S,O) binding mode, for example, in some ruthenium-polypyridyl-sulfoxide complexes.^{7,9,10} Although only η^1 -S binding mode is observed for *S*-coordination, some bridging μ -O metal-sulfoxide complexes were also observed, in addition to the most common η^1 -O complexes.^{31a,b} Interestingly, three crystallographically characterized complexes have been reported recently, where sulfoxide acts as μ -S,O-bridging bidentate ligands connecting two ruthenium atoms.^{31c}

4.1.3 Linkage Isomerism in Ruthenium-Sulfoxide Complexes

According to HSAB rationale, the hard acid Ru(III) ion would preferentially bind to *O*-atom of the sulfoxide ligand and exclusively form Ru(III)-sulfoxide(-*O*) complexes, while the low valent Ru(II), being a softer acid, would prefer coordination through soft *S*-atom and form stable Ru(II)-sulfoxide(-*S*) complexes. This rationale suggested that, the S→O and O→S linkage isomerism of sulfoxide (SO) ligands can be possibly induced by the redox transformations Ru(II)→Ru(III) and Ru(III)→ Ru(II), which could be achieved via electrochemical oxidation-reduction cycles of Ru-sulfoxide(-*S/O*) complexes (Figure 4.1.2). Much of the early work in this field was focused on electrochemically induced linkage isomerism of sulfoxide ligands.⁸

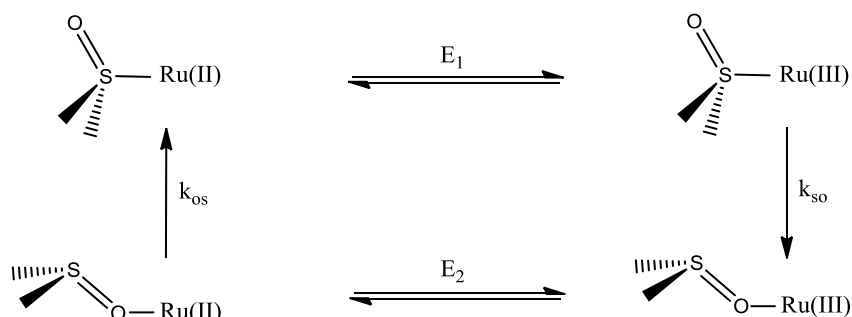


Figure 4.1.2: Electrochemically induced linkage isomerism in Ruthenium-sulfoxide complexes (ECEC square-scheme mechanism).

On the other hand, the Ru(II)→Ru(III) state can be formally generated by MLCT excitation of Ru(II)-Sulfoxide (-S) and recent studies on Ru-polypyridyl-sulfoxide complexes have shown that the ultra-fast (sub picosecond) S→O isomerism can be induced photochemically via MLCT excitation of thermodynamically stable Ru(II)-sulfoxide(-S) complexes⁹⁻²⁷. The photogenerated Ru(II)-sulfoxide(-O) complexes are thermodynamically unstable and slowly reverts back to the stable S-bound form or in some systems, this O→S transformation can be induced via MLCT excitation of Ru(II)-sulfoxide(-O) complexes²⁰ (Figure 4.1.3).

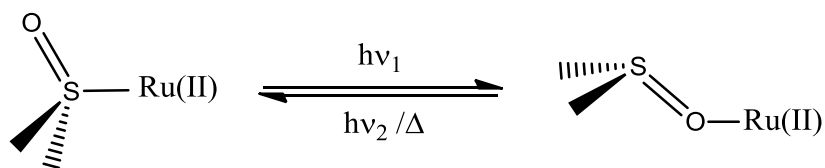


Figure 4.1.3: Photoinduced linkage isomerism in ruthenium-sulfoxide complexes

Here we provide a brief account of initial studies on the linkage isomerism of sulfoxide ligands and then, based on the most recent work, the mechanistic aspects as

well as the factors affecting the linkage isomerism of sulfoxide ligands in ruthenium-polypyridyl-sulfoxide complexes.

4.1.4 Initial Studies on Sulfoxide Isomerism

The redox-induced Ru-S→Ru-O and Ru-O→Ru-S linkage isomerism was first demonstrated in an electrochemical study on $[\text{Ru}(\text{NH}_3)_5(\text{dmsO-S})]^{2+}$ by Henry Taube et al.,^{8a} in the early 1980's. The cyclic voltammogram of this complex was characterized by two Ru(III/II) couples separated by $\Delta E = 900$ mV, where the couple at $E_{1/2} = 0.1$ V vs. NHE grew in only after oxidation at $E_{1/2} = 1.0$ V vs. NHE. When $[\text{Ru}(\text{NH}_3)_5(\text{dmsO-S})]^{2+}$ is oxidized, dmsO rapidly rearranges to form $[\text{Ru}(\text{NH}_3)_5(\text{dmsO-O})]^{3+}$. The latter complex is reduced at more negative potential and this is followed by O→S isomerism to form the stable Ru(II)-dmsO(-S) isomer. The electrochemical behavior was consistent with the well-known ECEC mechanism (Figure 4.1.2). Using the equations developed by Nicholson and Shain^{8c}, the rate constants (see Scheme 4.1.2), $k_{\text{SO}} = 0.07$ s⁻¹ and $k_{\text{OS}} = 40$ s⁻¹, were determined.²¹⁻²²

Sano^{8d-8g} and his coworkers expanded this study in dinuclear pentaammine complexes with a bridging 1,5-dithiocyclooctane ligand. Following the oxidation of one of the thioether linkages (forming sulfoxide), the dinuclear complex featured a reversible couple for Ru-S_{thioether} and an irreversible couple for Ru-S_{sulfoxide}, where irreversibility of the latter was attributed to S→O isomerism. These complexes showed important viability for application in information storage devices. This group also studied the effect of steric bulk on the sulfoxide by replacing one of the methyl groups on dmsO by *t*-butyl group and found about 10⁵ times increase in k_{SO} on Ru(III), while the corresponding k_{OS} remained almost unchanged.

During this time Deutsch⁸ⁱ *et al* reported a complex $[\text{Ru}(\text{tpy})(\text{bpy})(\text{dmsO}-S)]^{2+}$, whose electrochemical behavior was very similar to the complex $[\text{Ru}(\text{NH}_3)_5(\text{dmsO})]^{2+}$, reported by Taube^{8a}. They suggested that the irreversible anodic wave at 1.63 V vs. SCE was due to S→O isomerization following the oxidation of Ru(II) and the irreversible cathodic wave was due to O→S isomerization following the reduction of Ru(III). Although the data did not fit with the ECEC square-scheme mechanism, the rate $k_{\text{SO}} \geq 25 \text{ s}^{-1}$ was estimated from the scan rate dependence of the ratio of cathodic and anodic current (I_a/I_c ratios), corresponding to the Ru(III/II) couple of the *S*-bonded isomer.

In another study by Roeker and Meyer,^{8h} the reaction between $[(\text{bpy})_2(\text{py})\text{Ru}(\text{IV})=\text{O}]^{2+}$ and dimethylsulfide gave a Ru(II)-dmsO(-*O*) complex that reverted back to the *S*-bonded isomer intramolecularly and spontaneously. The *S*- and *O*-bonded isomers were characterized by UV-visible and NMR spectroscopy. NMR spectra of *S*- and *O*-bonded isomers were characterized by a distinguished feature of chemical shift values of methyl protons on dmsO, appearing as two singlets at δ 2.61 and 2.35 ppm, respectively in the *S*-bonded isomer, while as a sharp singlet at δ 2.32 ppm in the *O*-bonded isomer.

The photochemical and electrochemical behaviour of coordinated dimethyl sulfoxide in *cis,cis,cis*- and *cis,cis,trans*- $[\text{RuCl}_2(\text{dmsO})_2(\text{tbpy})_2]$ complexes, where tbpy is *t*-butylpyridine were reported in a number of papers in 1990s. These complexes were prepared by MLCT irradiated photo-substitution of dmsO on $[\text{RuCl}_2(\text{dmsO})_4]$ by tbpy ligand and both isomers were isolated after chromatographic separation. The *cis,cis,cis*-isomer exhibited S→O isomerism following the oxidation of Ru(II) and O→S isomerism following reduction of Ru(III). No indication of photochemical activity has been reported

for this isomer. On the other hand, the cyclic voltammogram of *cis,cis,trans*-isomer, in which two dmsoligands are in a *trans*-disposition relative to two chloride ligands, revealed a reversible Ru(III/II) couple ($E_{1/2} = 1.12$ V vs. NHE), indicating that isomerization was not triggered by oxidation of Ru(II) in this complex. This study demonstrated a geometric dependence of linkage isomerism.

4.1.5 Recent Studies on Sulfoxide Isomerism

In 2001, Gray and Wrinkler⁷ provided a comprehensive report on the photo-induced linkage isomerism (S→O and O→S) of dimethylsulfoxide ligand in the complex $[\text{Ru}(\text{tpy})(\text{bpy})(\text{dmsol-S})]^{2+}$ where tpy = 2,2':6',2''-terpyridine and bpy = 2,2'-bipyridine. The initial *S*-bound dmsol has been shown to undergo rapid photo-induced linkage isomerism $\text{Ru-dmsol}(-\text{S}) \rightarrow \text{Ru-dmsol}(-\text{O})$ ($\Phi = 0.024$), followed by a far slower thermal $\text{Ru-dmsol}(-\text{O}) \rightarrow \text{Ru-dmsol}(-\text{S})$ reaction in solution, crystals and polymer films.

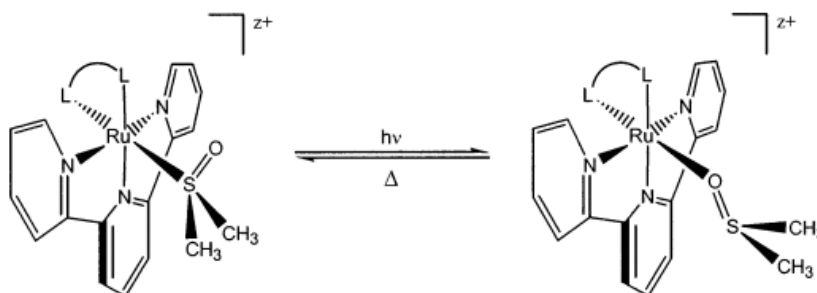


Figure 4.1.4: Photo-induced S→O and thermal O→S linkage isomerism of dimethyl sulfoxide (dmsol) ligand in $[\text{Ru}(\text{tpy})(\text{L2})(\text{dmsol})]$ complexes. L2 = bidentate ligand. Adapted from ref. (14)

The excited state responsible for this rearrangement was attributed to a metal-to-ligand charge transfer (MLCT) excitation. Rack^{7,14} and his group extended this study

on a family of $[\text{Ru}(\text{tpy})(\text{L2})(\text{dmsO-S})]^{2+}$ complexes (L2 is a bidentate σ/π donor-acceptor ligand), which also exhibited electrochemically induced S \rightarrow O isomerization.¹⁴

Rack⁹⁻²⁷ and his group have provided the most comprehensive and systematic studies on the linkage isomerism of both chelating and non-chelating sulfoxide ligands in ruthenium-polypyridyl-sulfoxide complexes throughout the last decade. Their studies have revealed the mechanistic aspects of the excited state sulfoxide isomerism, dependency of linkage isomerism on the electronic nature of ancillary ligands, steric factors, nature of sulfoxide ligands (chelating and non-chelating) as well as on solvents in ruthenium-polypyridyl-sulfoxide complexes. These findings will be briefly described in the following paragraphs.

Ligand Field State vs. Charge Transfer State in Photoisomerism

Ultrafast-transient absorption spectroscopy revealed that photo-triggered S \rightarrow O isomerism in ruthenium-polypyridyl-sulfoxide complexes occurs on picosecond timescale with quantum yields ($\Phi \sim 0.80$) much larger than those of photosubstitution reaction ($\Phi \sim 10^{-3}$).^{14,20} These studies showed that the S \rightarrow O isomerization occurs from the excited metal-to-ligand charge transfer (MLCT) potential energy surfaces without any necessity of the involvement of ligand field (LF) states.

Figure 4.1.5 shows the qualitative MO scheme for the excited state description in the octahedral ruthenium-polypyridyl complex, where the highest occupied molecular orbitals (HOMO) generally consist of Ru $d\pi$ orbitals (π_M) while the low-lying occupied donor orbitals (σ_L and π_L) are localized polypyridyl ligands. On the other hand, the unoccupied molecular orbitals are mainly localized on π^* acceptor orbital of the polypyridyl ligand and ruthenium $d\sigma^*$ orbitals (σ_M^*). The promotion of an electron from

Rud π (π_M) orbital to π_L^* ligand orbitals give rise to metal-to-ligand charge transfer (MLCT) excited states, while the promotion of an electron from π_M to σ_M^* metal orbitals gives rise to metal-centred excited ligand field (LF^*) states. Ligand-centered excited state can be obtained by the promotion of an electron from π_L to π_L^* ligand orbitals. All these excited states may have singlet and triplet multiplicity, although spin-orbit coupling

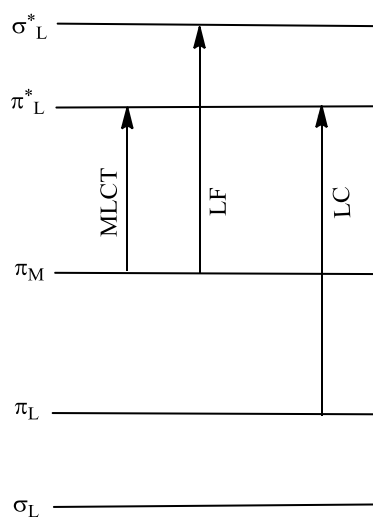


Figure 4.1.5: Qualitative MO scheme showing possible electronic transition in octahedral Ru-polypyridyl complexes. Adapted from the ref. (33).

causes singlet-triplet mixing in the MLCT and LF states. The initially formed short lived singlet, 1LF or 1MLCT states undergo rapid intersystem crossing to the comparatively long lived triplet 3LF or 3MLCT excited states. The metal-centered ligand field (LF) state of d^6 octahedral complex is strongly displaced with respect to the ground state geometry along metal-ligand vibration coordinate. When the lowest excited state is metal-centered 3LF state, it undergoes fast radiationless deactivation to the ground state and/or ligand dissociation reaction. As a consequence, the excited state lifetime for lowest energy 3LF state is very short, and so no luminescence emission are observed and no bimolecular

reaction can take place. On the other hand, when the lowest excited state is $^3\text{MLCT}$, it does not undergo fast radiationless decay to the ground state and luminescence emission is usually observed, except at high temperature when the thermally accessible ligand field states deactivate the excited $^3\text{MLCT}$ states.

The photochemistry and photophysics of transition metal-polypyridyl complexes are dominated by the interaction of the lowest energy $^3\text{MLCT}$ (metal-to-ligand charge transfer) states with the thermally accessible ^3LF states. For most Ru(II)-polypyridyl complexes, the lowest energy excited state is a $^3\text{MLCT}$ state which undergoes relatively slow radiationless transitions and thus exhibit long lifetime and intense luminescence emission. Thermal population of the ligand field states is the principal mechanism for depopulation of the $^3\text{MLCT}$ excited state and subsequent decrease in the lifetime of the excited state. This deactivation is undesirable, since much of the motivation of the work in this area is to access the potential energy stored in the excited MLCT state, as this energy may be used to drive other reactions. The relative energies of $^3\text{MLCT}$ and ^3LF excited states depend on the ligand field strength, the redox properties of metal and ligands, and intrinsic properties of the ligands. Ligand field states are, in general, thermally inaccessible for stronger N-donor ligands due to large ligand field splitting, while accessible for weaker O-donor ligands that deactivate the excited MLCT state, resulting in small and non-existent quantum yields for photochemical processes.

The works of Mcmillin³⁴ and others have shown that the photosubstitution reaction in transition metal-polypyridyl complexes is a dissociative process involving the population the Ru-L $d\sigma^*$ ligand field (LF) states and the corresponding quantum yields should be on the order of 10^{-3} . Indeed, the photoinduced S→O isomerization can be

thought of as intramolecular photosubstitution reaction and if the isomerization involves the ligand field (LF) states, one would expect the same order of magnitude of the quantum yield for isomerization as that for photosubstitution (10^{-3}). For example, the photosubstitution quantum yield of CH_3CN by pyridine in $[\text{Ru}(\text{tpy})(\text{bpy})(\text{CH}_3\text{CN})]^{2+}$ complex in acetonitrile is 0.0016, which is in agreement with the mechanism involving the ligand field (LF) state. A similar osmium complex¹⁴ did not show any photosubstitution reaction, supporting again the involvement of ligand field state in photosubstitution reaction because the ligand-field splitting is larger in Os(II) complexes relative to Ru(II) due to larger spin-orbit coupling effect in the former. In contrast, quantum yields for S \rightarrow O photoisomerization ($\Phi_{\text{S}\rightarrow\text{O}}$) in $[\text{Ru}(\text{tpy})(\text{bpy})(\text{dmsO})]^{2+}$, $[\text{Ru}(\text{tpy})(\text{pic})(\text{dmsO})]^+$ and $[\text{Ru}(\text{bpy})_2(\text{OSO})]^{2+}$ complexes^{14,20} (where tpy = terpyridine, bpy = bipyridine, pic = pyridine carboxylate, OSO = 2-methylsulfinyl benzoate) were found to be 0.024, 0.25 and 0.45, respectively, which are about 10 to 10^2 times larger than those of photosubstitution reaction. These large quantum yields indicated an efficient conversion of photonic energy to potential energy and suggested that the state responsible for S \rightarrow O isomerization is different from LF state, as proposed for photosubstitution reaction. Furthermore, if photoisomerization occurred from the LF state, the large ligand field splitting would prohibit photoisomerization on Os(II) complex as it did for the photosubstitution reaction. In contrast, $[\text{Os}(\text{bpy})_2(\text{dmsO})_2]^{2+}$ has been shown to undergo photoinduced S \rightarrow O linkage isomerism with a large quantum yield ($\Phi_{\text{S}\rightarrow\text{O}} = 0.042$)¹⁴. This study clearly showed that the sulfoxide isomerization does not necessarily involve ligand field (LF) states and that excited MLCT states are likely responsible for S \rightarrow O isomerism of sulfoxide ligand. Indeed ultra-fast transient absorption studies on

ruthenium-polypyridyl-sulfoxide complexes established that excited state $S \rightarrow O$ isomerization occurs from the MLCT manifold.¹⁶⁻²⁰

Excited State Mechanism

Transient absorption spectroscopy revealed two different excited state mechanisms for the linkage isomerism of non-chelating and chelating sulfoxides in ruthenium-polypyridyl-sulfoxide complexes involving excited MLCT states.^{16,20}

Studies on non-chelating dmsO complexes $[\text{Ru}(\text{tpy})(\text{bpy})(\text{dmsO})]^{2+}$ and $[\text{Ru}(\text{tpy})(\text{pic})(\text{dmsO})]^+$ complexes have shown that $S \rightarrow O$ isomerization occurs directly on the *S*-bonded $^3\text{MLCT}$ state surface to the *O*-bonded $^3\text{MLCT}$ state surface as depicted in the Figure 4.1.5 (A). The isomerization follows the adiabatic mechanism, in which progression along the reaction coordinate is maintained through the lowest electronically excited $^3\text{MLCT}$ potential energy surface (PES), analogous to any ground state thermal reaction. In this case, isomerization preceded relaxation to the ground state PES and the driving force for isomerization may be viewed in parallel to the electrochemical reaction in which the charge-transfer (CT) state is described as formally oxidized metal center Ru(III) and formally reduced tpy ligand, resulting in the *O*-bonded form being thermodynamically more stable than the *S*-bonded form in the excited state.

On the other hand, transient absorption studies on the chelating sulfoxide complex $[\text{Ru}(\text{bpy})_2(\text{OSO})]^{2+}$ where OSO = 2-methylsulfinyl benzoate, have shown that irradiation of the initial *S*-bonded isomer triggers $S \rightarrow O$ isomerization that occurs not along the $^3\text{MLCT}$ surface, but rather directly from the *S*-bonded $^3\text{MLCT}$ excited state to the *O*-bonded singlet ground state on a picosecond timescale, as shown in the Figure 4.1.5 (B). The mechanism was described as non-adiabatic, suggesting presence of a

conical intersection between the *S*-bonded $^3\text{MLCT}$ PES with the *O*-bonded singlet ground state PES.

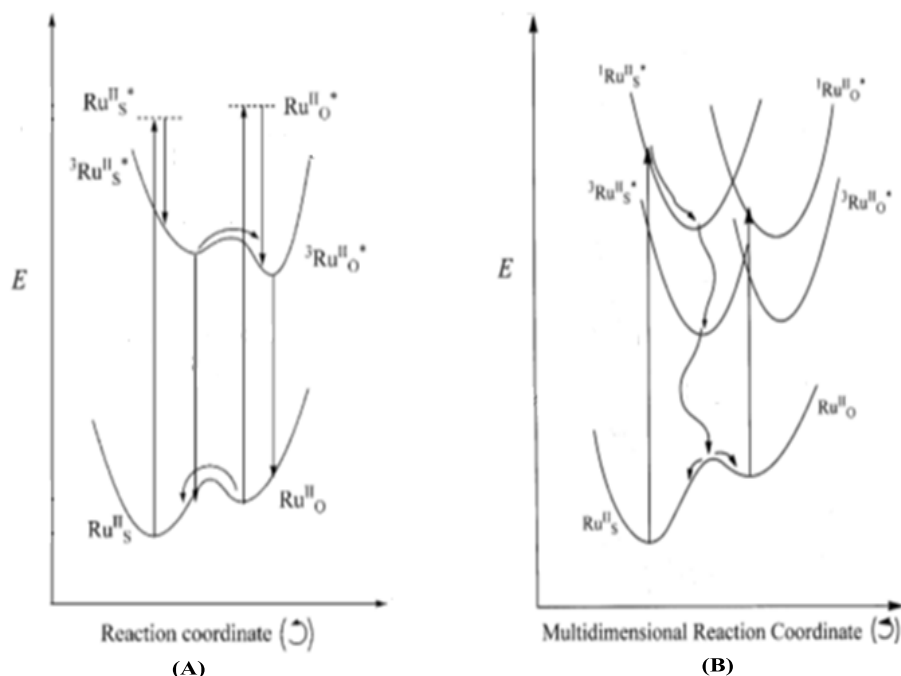


Figure 4.1.6: Electronic state diagram of (A) $[\text{Ru}(\text{tpy})(\text{bpy})(\text{dmsO})]^{2+}$ and (B) $[\text{Ru}(\text{bpy})_2(\text{OSOR})]^{2+}$ where OSOR is 2-methylsulfinyl benzoate. Adapted from ref. (16,20).

An important difference in the excited state potential energy surfaces of these complexes is that, in contrast to non-chelating dmsO complex $[\text{Ru}(\text{tpy})(\text{bpy})(\text{dmsO})]^{2+}$, the *O*-bonded $^3\text{MLCT}$ state is thermodynamically less stable than the *S*-bonded $^3\text{MLCT}$ state. In both chelating and non-chelating complexes, the thermally equilibrated *S*-bonded $^3\text{MLCT}$ feature large reorganization energy, significant change in the nuclear configuration with respect to Franck-Condon state and the geometry of the this thermally equilibrated *S*-bonded $^3\text{MLCT}$ state has been described as either η^2 or asymmetric η^2 coordination (side-on SO). Unlike $[\text{Ru}(\text{tpy})(\text{bpy})(\text{dmsO})]^{2+}$, the *O*-bonded $^3\text{MLCT}$ state in $[\text{Ru}(\text{bpy})_2(\text{OSO})]^{2+}$ complex is thermodynamically unstable with respect to the η^2 -excited

state, probably due to greater stabilization of Ru $d\pi$ orbitals by chelating sulfoxide in the ground state that is also translated into additional stabilization of the excited state structure. The relative stability of the n^2 -excited state in chelating sulfoxide complex results in rapid deactivation to the *O*-bonded singlet ground state without transforming along the *O*-bonded 3 MLCT state, exhibiting the non-adiabatic mechanism.

4.1.6 Characterization of Linkage Isomerism

The linkage isomerism of sulfoxide ligands can be probed by various spectroscopic techniques. The electronic absorption spectroscopy is traditionally used to monitor the photo-induced linkage isomerism of ruthenium-polypyridyl-sulfoxide complexes and distinguish the *S*- and *O*-bonded isomers by their distinct spectral properties. The Infrared spectroscopy probes the *S*- and *O*-bonded forms of the complex by their corresponding $\nu(\text{S-O})$ stretching frequencies. The X-ray crystallography provides direct evidence of binding modes of sulfoxide ligands and corresponding Ru-S/O or S-O bond lengths in complexes. ^1H NMR spectroscopy may provide further insight into the binding modes of sulfoxide ligands under specific situations. Theoretical calculations provide an insight into the geometry optimized structure as well as the electronic structure of both *S*- and *O*-bonded isomers. The ground state *S*→*O* and *O*→*S* isomerism can be induced electrochemically via oxidation of Ru(II)-*S* to Ru(III)-*S* and reduction of Ru(III)-*O* to Ru(II)-*O*, which can be probed by cyclic voltammetry and from the scan rate dependence voltammograms it is possible to estimate ground state-linkage isomerism rates. The quantum yields of photochemical reactions can be measured by chemical actinometry while the excited state linkage isomerization rates and the mechanism can be probed by ultra-fast transient absorption spectroscopy.

Electronic Absorption Spectroscopy

Electronic absorption spectroscopy is the most commonly used physical technique to probe $S \rightarrow O$ and $O \rightarrow S$ isomerism of sulfoxide ligands in ruthenium-polypyridyl-sulfoxide complexes.^{7,8-27}

The S -bonded isomers are thermodynamically more stable than the O -bonded isomers in ruthenium-polypyridyl-sulfoxide complexes. The electronic absorption spectrum of the S -bonded isomer is characterized by an intense absorption in the UV-visible region (400-480 nm) due to $Ru(II)d\pi$ -to- π^* (polypyridyl) metal-to-ligand charge transfer (MLCT) transitions.¹⁴⁻²⁷ On the other hand, these MLCT bands of O -bonded isomers are significantly bathochromically shifted ($\Delta\lambda \approx 80$ -100 nm) relative to those of the S -isomers and appear in the range 480-530 nm.

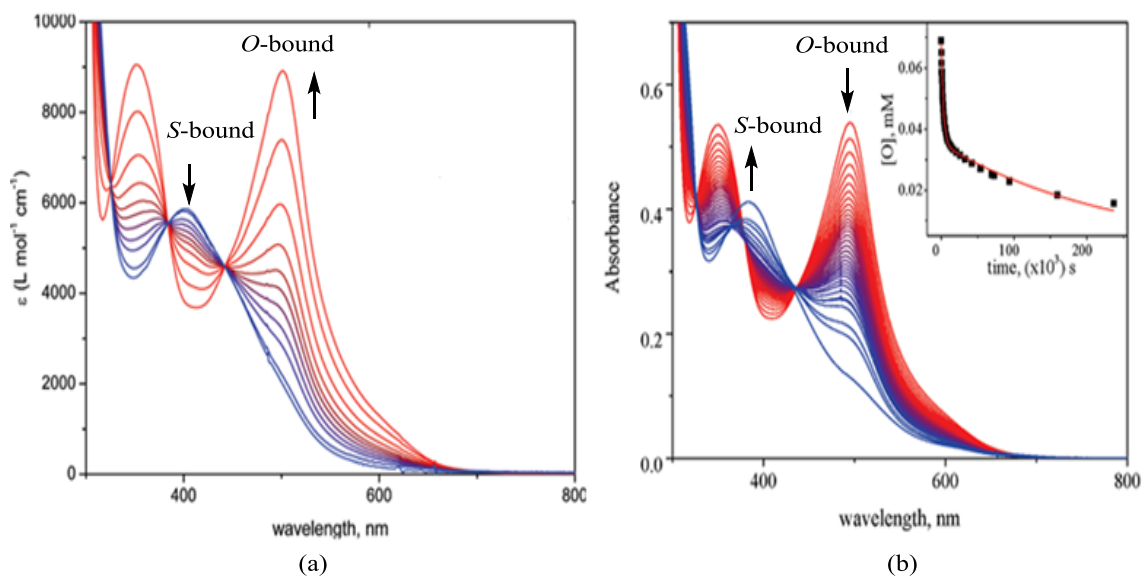


Figure 4.1.7: (a) MLCT excitation of S - $[Ru(bpy)_2(OSOR)]^+$ (blue traces) forming its linkage isomer O - $[Ru(bpy)_2(OSOR)]^+$ (red traces), (b) thermal reversion of O - $[Ru(bpy)_2(OSOR)]^+$ to initial S - $[Ru(bpy)_2(OSOR)]^+$ (blue traces) in methanol. Insert shows the decay profile of O -bound isomer. Adapted from ref. (19, 20).

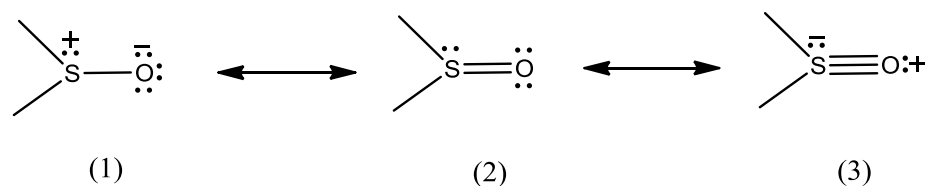
This large absorption shift between two isomers is attributed to the strong π -acceptor property of “soft” *S*-bonded sulfoxide ligand that stabilizes Ru(II) $d\pi$ orbital significantly, relative to “hard” *O*-bonded sulfoxide ligands. However, the absorption maxima of both *S*- and *O*- bonded isomer may slightly vary with the electronic nature of both ancillary and sulfoxide ligands, and solvents. For example, the MLCT bands of [Ru(tpy)(L2)(dmsO-S)] complexes appear at around 419-502 nm and show slight bathochromic shifts, as the donor property of bidentate ligands increases. Upon photoirradiation, the absorption maxima of these complexes are shifted to 500-540 nm due to the photogenerated *O*-bonded isomers. Similar spectral variation is observed in complexes with chelating sulfoxide ligands. As seen in the Figure 4.1.7 (a), the MLCT excitation of the initial *S*-[Ru(bpy)₂(OSOR)]⁺ isomer results in a gradual decrease in its MLCT band at 400 nm (blue trace) with the evolution of a low energy band at 495 nm (red traces) for the *O*-[Ru(bpy)₂(OSOR)]⁺ isomer. The (Figure 4.1.7 (b)) shows the thermal reversion of the *O*-bonded isomer to the initial *S*-bonded form. It is possible to determine slow thermal *O*→*S* reaction rates from the decay profile of the *O*-bonded isomer, as shown in the insert of Figure 4.1.7 (b).

Infrared Spectroscopy

Infrared spectroscopy provides valuable information on the binding modes of sulfoxide ligands in their metal complexes by the variation of corresponding $\nu(\text{SO})$ frequencies of coordinated ligands. The $\nu(\text{SO})$ band of free sulfoxide ligand is typically observed at 1055 cm^{-1} , while it is shifted to 1080-1154 cm^{-1} and 862-997 cm^{-1} for *S*- and *O*-coordinated ligand, respectively.^{31a} This variation is related to the SO bond order and bond lengths in the various forms of sulfoxide ligands. Recent statistical analysis of X-

ray crystallography data of free sulfoxides and their *S*- and *O*-coordinated metal complexes have shown that the average S-O bond length in free sulfoxide in the solid state is 1.492(1) Å, which is reduced by about 0.018 Å upon *S*-coordination (average $d = 1.4738(7)$ Å), while increased by about 0.036 Å upon *O*-coordination (average $d = 1.528(1)$ Å).^{31a,d,e} The observed trend in S-O bond distances and corresponding $\nu(\text{S-O})$ stretching frequencies can be rationalized on the basis of the electronegativity equalization concept,^{31a,d,e} considering the electron density redistribution passing from free to coordinated sulfoxides.

The structure of a sulfoxide group can be considered as a resonance hybrid of three canonical forms, as shown below



X-ray data^{31a} showed that free sulfoxide molecule is polarized with sulfur atom bearing a large positive charge, favouring the structure (I) relative to the structure (2) and (3) in the free ligand. Upon *S*-coordination to metal, *S*-atom becomes more electronegative due to increase in positive charge and withdraws electron density from the filled $p\pi$ orbitals on the oxygen atom to its low lying empty $d\pi$ orbital, resulting in a significant double bond character of the S-O bond (Structure 2) and a high frequency shift of the $\nu(\text{S-O})$ stretch relative to the free ligand. On the other hand, upon *O*-coordination to metal, the *O* atom becomes more electronegative, which reduces the transfer of π -electron density from *O* atom to the *S* atom relative to that in the free ligand, resulting in an increase in S-O bond

length and decrease in the $\nu(\text{S-O})$ frequencies (structure I is more pronounced in the *O*-bonded isomer than in the free ligand).

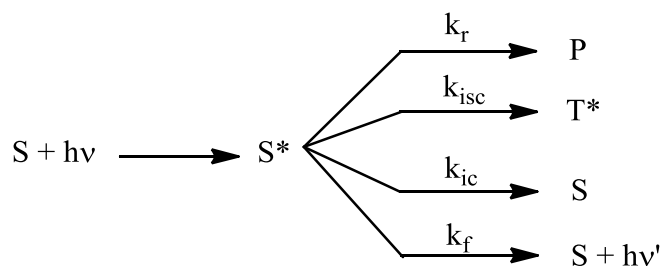
In ruthenium-polypyridyl complexes, the $\nu(\text{SO})$ bands are generally observed in the expected range for the *S*- and *O*-bonded isomers, however, the photogenerated *O*-bonded isomers, sometimes, exhibit the $\nu(\text{SO})$ stretches at slightly higher frequencies than the expected range. For example, in $O\text{-[Ru(bpy)(biq)(OSO)]}^+$ and $O\text{-[Ru(bpy)}_2\text{(OSOR)]}^+$ complexes (*Vide supra*), the $\nu(\text{SO})$ stretch appears at 1006 and 1022 cm^{-1} , respectively, and this high frequency shift was attributed to possible symmetric or antisymmetric ($\eta^2\text{-SO}$) binding modes of sulfoxide ligands.^{20,35} Besides the $\nu(\text{SO})$ bands, the IR spectroscopy also provides useful information about $\nu(\text{Ru-S})$ and $\nu(\text{Ru-O})$ stretching frequencies in the *S*- and *O*-bonded isomers respectively. In ruthenium sulfoxide complexes, the Ru(II)-S are typically observed at 410-430 cm^{-1} , while the Ru(II)-O at 460-490 cm^{-1} , which is consistent with the variation in the corresponding bond lengths (average $d_{\text{Ru-S}} = 2.260(2), 2.329(5)$ Å and average $d_{\text{Ru-O}} = 2.10(1)$ Å).

11,31a,h

Quantum Yield of Photochemical Reactions

Light absorption produces an excited state species that inevitably loses its energy through various photophysical and photochemical pathways. The photophysical deactivation processes include spontaneous emission (fluorescence, phosphorescence), internal conversion (IC), intersystem crossing (ISC) (singlet-triplet) while photochemical processes include isomerization, rearrangement, bond breaking and formation etc. The scheme shows multiple pathways for deactivation of the initially photo-excited reactive singlet species (S^*).

Scheme 4.1.1: Deactivation Pathways for Photo-excited Singlet Species with Rates (k_i 's): Photochemical Reaction (k_r), Singlet-Triplet Intersystem Crossing (k_{isc}), Internal Conversion (k_{ic}), Luminescence (k_f)



The quantum yield (Φ_i) of a light induced process can be simply defined by Eq.

4.1.3.

$$\Phi_i = \frac{\text{Number of events for the } i_{\text{th}} \text{ process}}{\text{Total number of photons absorbed by the Photoreactive Substance(S)}} \quad (4.1.3)$$

It represents the efficiency of any photochemical or photophysical process. The primary quantum yield for the i_{th} process is the fraction of molecules absorbing which decompose by that process and represents the yield of chemical species produced directly from the initially formed excited singlet state (S^*). The chemical species can be a radical or an intermediate and is not necessarily the end photoproduct. The integral (total) quantum yield (Φ_r) for a photoreaction can be defined by the Eq. 4.1.4

$$\Phi_r = \frac{n_r}{n_\Phi} \quad (4.1.4)$$

where n_r is the number of moles of reactant (S) consumed or product (P) formed and n_Φ is the number of moles of photons absorbed by the photoreactive substance (S) in a specific time, t . On the other hand, the differential quantum yield can be defined by the Eq. 4.1.5,

$$\Phi_r = \frac{\nu_r}{I_a} = \frac{-\frac{d[S]}{dt}}{I_a} = \frac{\frac{d[P]}{dt}}{I_a} \quad (4.1.5)$$

where, ν_r is the rate of consumption of reactant or formation of products and I_a is the number of quanta (Einstein) of light absorbed by the photoreactive substrate (S) per unit concentration per unit time.

If the multiple deactivation pathways (Scheme 4.1.4) are characterized by the rate constants (k_i 's) corresponding to unimolecular irreversible processes, the quantum yield for the photochemical reaction (Φ_r) can be expressed as

$$\Phi_r = \frac{k_r}{k_f + k_{ic} + k_{isc} + k_r} = \frac{k_r}{k_T} \quad (4.1.6)$$

The quantum yield for other processes can be defined in the same way giving sum of all quantum yields equal to unity. The quantum yield for the photoreaction (Φ_r) can be, therefore, interpreted as the fraction of singlet excited molecules (S^*) that undergo chemical transformation, *i. e.*, the ratio of the number of molecules reacting to the total number of S^* . Because there are several routes to deactivation of excited state species, the quantum yield (Φ_r) rather than the absolute rate constant (k_r) must be used to compare the efficiencies of photochemical conversion for different reactive system.

The quantum yields ($\Phi_{S \rightarrow O}$) of photo-induced linkage isomerism of sulfoxide ligands are typically measured by ferrioxalate actinometry.^{14,40} The Section 4.2 will describe the experimental details of the measurement of quantum yields ($\Phi_{S \rightarrow O}$) of photo-induced S \rightarrow O isomerization for *cis*-[Ru(bpy)₂(R-*pcyd*)(*dmsO-S*)] [PF₆] complexes.

4.1.7 Research Objectives

The focus of this research is centred on the synthesis and investigation of photo- and redox-induced S→O and O→S linkage isomerism of dimethyl sulfoxide (dmsO) ligand in mononuclear *cis*-[Ru(bpy)₂(R-*pcyd*)(dmsO-*S*)]⁺[PF₆]⁻ complexes and correlate the experimental observations with the electronic nature of phenylcyanamide (R-*pcyd*) ligands. In this regard, *trans*-[Ru(*tpy*)(*pic*)(dmsO-*S*)]⁺ complex where *pic* = 2-pyridinecarboxylato, has been shown to undergo ultrafast photo-induced S→O linkage isomerism forming the metastable *trans*-[Ru(*tpy*)(*pic*)(dmsO-*O*)]⁺ with $\Phi_{S \rightarrow O} = 0.25$. A slow thermal back reaction re-formed *trans*-[Ru(*tpy*)(*pic*)(dmsO-*S*)]⁺ with rate $k_{OS1} = 1 \times 10^{-3} \text{ s}^{-1}$.¹⁴ The cyclic voltammetry of the complex also demonstrated redox-induced ground-state S→O and O→S linkage isomerism. The coordination sphere of the designed mononuclear complex *cis*-[Ru(bpy)₂(R-*pcyd*)(dmsO-*S*)]⁺[PF₆]⁻ was deliberately chosen to be similar to that of *trans*-[Ru(*tpy*)(*pic*)(dmsO-*S*)]⁺. Both complexes possess a Ru(II) coordination sphere of four pyridine moieties, dmsO and a pseudohalide donor atoms. Similar chemistry is expected for the *cis*-[Ru(bpy)₂(R-*pcyd*)(dmsO-*S*)]⁺ complexes and will be examined with respect to the changing electron donor properties of the phenylcyanamide ligand. To this effect, following research objectives can be stated:

- (i) To synthesize six *cis*-[Ru(bpy)₂(R-*pcyd*)(dmsO-*S*)]⁺[PF₆]⁻ complexes, where bpy = 2,2'-bipyridine, R-*pcyd*⁻ = pentachloro-(Cl₅*pcyd*⁻), 2,3,5,6-tetrachloro-(Cl₄*pcyd*⁻), 2,4,5-trichloro-(Cl₃*pcyd*⁻), 2,4-dichloro-(Cl₂*pcyd*⁻), 4-chloro-(Cl*pcyd*⁻) and unsubstituted (*pcyd*⁻) phenylcyanamide and characterize by elemental analysis, ¹H NMR, IR, electronic absorption spectroscopy, cyclic voltammetry and DFT calculations.

- (ii) To investigate the photo-induced S→O linkage isomerism of cis -[Ru(bpy)₂(R-*pcyd*)(dms(-S))]⁺ complexes in solutions and solid polymer films by electronic absorption spectroscopy, measure the S→O isomerization quantum yields in solutions by ferrioxalate actinometry and the thermal O→S back reaction rates by electronic absorption spectroscopy and correlate the observed properties with the electronic nature of phenylcyanamide ligands
- (iii) To investigate redox-induced S→O and O→S linkage isomerism of cis -[Ru(bpy)₂(R-*pcyd*)(dms(-S))]⁺ complexes by cyclic voltammetry.

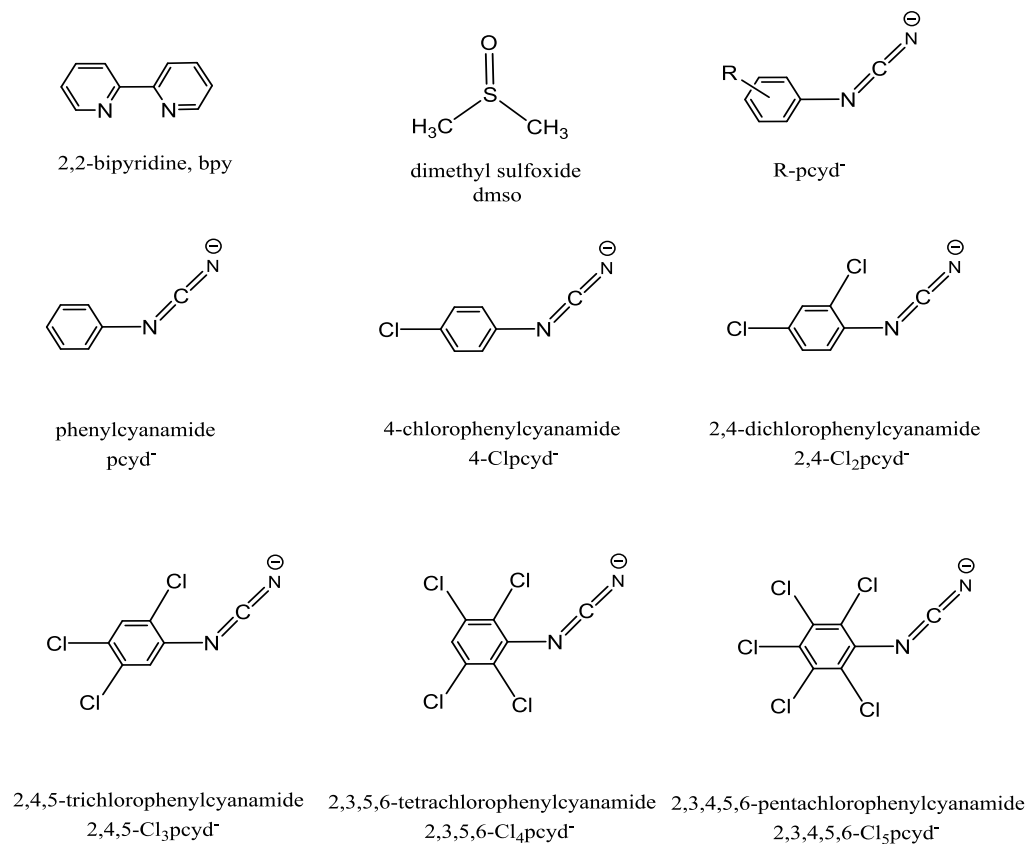


Figure 4.1.8: The R-*pcyd* and ancillary bpy and dms ligands used in the synthesis of cis -[Ru(bpy)₂(R-*pcyd*)(dms(-S))]⁺ complexes (**4a-4f**).

4.2 Experimental

4.2.1 Starting Materials

Reagents for Ligand Synthesis

Glacial Acetic acid ($\leq 99.7\%$, ACS reagent grade, Anachemia), ammonium thiocyanate (ACS reagent grade, 97.5+%, Aldrich), aniline ($\geq 99.5\%$, ACS reagent grade, Aldrich), 4-chloroaniline(98%, Aldrich), 2,4-dichloroaniline (99%, Aldrich), 2,4,5-trichloroaniline (95%, Aldrich), 2,3,5,6-tetrachloroaniline (97%, Aldrich), 2,3,4,5,6-pentachloroaniline (95%, Aldrich), benzoyl chloride (99%, Aldrich), triethyl amine (99.5%, Fluka), lead(II) acetate trihydrate (ACS reagent grade, 99+%, Aldrich), thallium (I) acetate ($\geq 99\%$, Sigma-Aldrich) (**Caution: highly toxic!**), were used as received without further purification.

Reagents for Complex Synthesis

Ammonium hexafluorophosphate (99.5%, Alfa Aesar), ruthenium (III) chloride hydrate (99.9%, Alfa Aesar), 2,2'-bipyridyl (Reagent plus, $\geq 99\%$, Sigma-Aldrich), dimethyl sulfoxide (Anhydrous, $\geq 99.5\%$, Sigma-Aldrich) were used as received.

Polymer for Polymer Film of Complexes

Poly(methyl methacrylate) (PMMA) (Average Mw = 15,000) was purchased from Aldrich and used as received.

Compressed Gases

Argon (ultra-high purity grade 5.0, PRAXAIR)

Adsorbent in Column Chromatography and Drying Agents

Aluminum oxide (activated, acidic, Brockman I) for column chromatography was deactivated to grade V by adding water and slowly shaking the mixture for 4h. Phosphorus pentoxide (ACS reagent grade, 98+%, Anachemia) were used as received. Aluminum oxide (neutral, chromatography grade, Woelm) was activated by heating at 300 °C for several hours in a muffle furnace.

Electrochemistry Internal References and Supporting Electrolytes

Tetrabutylammonium hexafluorophosphate (TBAH) was used as internal reference. The synthesis of TBAH was completed through the combination of a 0.1 M solution of tetrabutylammonium bromide (95+%, Aldrich) and a 0.1 M solution of ammonium hexafluorophosphate in water (ReagentPlus, 99%, Sigma-Aldrich). The resulting precipitate of TBAH powder was recrystallized twice from 1:1 ethanol: water and vacuum dried at 110°C for a day. Dicyclopentadienyliron (ferrocene) (reagent grade, J. T. Baker) was purified by sublimation.

Solvents for Synthesis

Anhydrous ethyl alcohol (Commercial Alcohols, absolute), *N,N*-dimethylformamide, anhydrous diethyl ether, acetonitrile, dichloromethane (Caledon Labs, reagent grade) were used as received. Acetone (Fisher Scientific, ACS reagent grade) was distilled under glass prior to use.

Solvents for NMR Spectroscopy

Dimethyl-*d*₆-sulfoxide (99.9 atom % D, CDN Isotopes) was used as received.

Solvents for Electrochemistry

Acetonitrile (Chromosolv®Plus, 99.9%, HPLC grade, Sigma-Aldrich), Dimethyl sulfoxide (Anhydrous, $\geq 99.5\%$, Sigma-Aldrich), Propylene carbonate (Anhydrous, 99.7%, Aldrich) were used with no further purification or drying. The solvent was stored inside a polyethylene glove bag that was filled with argon when mixtures of TBAH and the solvent needed to be made in 20 mL glass vials.

Solvents for Quantitative Electronic Absorption Spectroscopy

Dimethyl sulfoxide (Anhydrous, $\geq 99.5\%$, Sigma-Aldrich) and Propylene carbonate (Anhydrous, 99.7%, Aldrich) were used as received.

4.2.2 Synthesis of Precursor Ligands and Complexes

Synthesis of R-pcydH Ligands and Tl[R-pcyd] Salts

Phenylcyanamide (pcydH) and its derivatives 4-chloro- (4-ClpcydH), 2,4-dichloro- (2,4-Cl₂pcydH), 2,4,5-trichloro- (2,4,5-Cl₃pcydH), 2,3,5,6-tetrachloro- (2,3,5,6-Cl₄pcydH), 2,3,4,5,6-pentachloro-phenylcyanamide (2,3,4,5,6-Cl₅pcydH) (**1a-f**) and their corresponding thallium salts (**2a-f**) were prepared by literature methods.³⁶ Both Cl₄pcydH and Cl₅pcydH possessed a significant impurity of the guanidine dimer as shown by a strong IR $\nu(\text{C}=\text{N})$ band at approximately 1680 cm⁻¹. This dimer impurity reverts to a monomer in basic solutions and does not affect the isolation of the thallium salt of the ligand as discussed previously.³⁷

Synthesis of *cis*-Ru(bpy)Cl₂

This complex was prepared by following the procedure as described elsewhere.³⁸

Synthesis of Precursor *cis*-[Ru(bpy)₂(R-pcyd)₂] Complexes (3a-f)

The precursor *cis*-[Ru(bpy)₂(R-pcyd)₂] complexes were prepared from *cis*-Ru(bpy)₂Cl₂ complex by following the same procedure as described elsewhere but with some modifications.³⁶

Preparation of *cis*-[Ru(bpy)₂(pcyd)₂] (3a): This complex was prepared by following the same procedure as described elsewhere: A mixture of *cis*-Ru(bpy)₂Cl₂ (726 mg, 1.5 mmol) and Tl[pcyd] (964.2 mg, 3.0 mmol), after refluxing in 60 ml of DMF and subsequent chilling at -20 °C, filtering off the TlCl using Celite and addition of 1500 mL of diethyl ether to the filtrate, yielded 780 mg of the pure dark brown solid product (**3a**). Yield: 80 %. ¹H NMR (300 MHz, DMSO-*d*₆) : 9.50 (2H, d); 8.78 (2H, d); 8.65 (2H, d); 8.21 (2H, t); 7.92-7.84 (4H, m); 7.72 (2H, d); 7.27 (2H, t); 6.82 (4H, t); 6.41 (2H, t); 6.21 (4H, d). IR (KBr): ν(NCN) 2168 cm⁻¹.

Preparation of *cis*-[Ru(bpy)₂(4-Clpcyd)₂] (3b): This complex was prepared by following the same procedure as above with minor modification: A mixture of *cis*-Ru(bpy)₂Cl₂ (571 mg, 1.24 mmol), Tl[4-Clpcyd] (840 mg, 1.18 mmol) in 20 ml of DMF was refluxed for 3 h after which was chilled overnight at -20 °C. After removal of the fine white precipitate of TlCl using Celite, the deep purple filtrate was evaporated using a rotavap to dryness and the solid residue was digested in 10 mL of acetone. Upon addition of 300 mL of diethyl ether to the acetone digest, a deep purple precipitate of the pure compound (0.80g) was obtained (**3b**). Yield: 90 %. ¹H NMR (300 MHz, DMSO-*d*₆) : 9.45 (2H, d); 8.79 (2H, d); 8.65 (2H, d); 8.23 (2H, t); 7.95-7.83(4H, m); 7.73 (2H,d); 7.28 (2H, t); 6.81 (4H, t); 6.14 (2H, t). IR (KBr): ν(NCN) 2163 cm⁻¹.

Preparation of *cis*-[Ru(bpy)₂(2,4-Cl₂pcyd)₂] (3c): This complex was prepared by the same procedure as above for the synthesis of (3b) with following reagent amount: *cis*-Ru(bpy)₂Cl₂ (242 mg, 0.5 mmol), Ti[2,4-Cl₂pcyd] (390.4 mg, 1.0 mmol) in 20 ml of DMF and 500 mL of diethyl ether to crash out 282.6 mg of pure product (3c). Yield: 72 %. ¹H NMR (300 MHz, DMSO-*d*₆): 9.67 (2H, d); 8.73 (2H, d); 8.60 (2H, d); 8.21 (2H, t); 7.96-7.89 (4H, m); 7.03(2H, d); 6.73 (2H, d); 6.35 (2H, d). IR (KBr): ν(NCN) 2165 cm⁻¹.

Preparation of *cis*-[Ru(bpy)₂(2,4,5-Cl₃pcyd)₂] (3d): Same as above for the synthesis of (3b) with the following reagent amount: *cis*-Ru(bpy)₂Cl₂ (242 mg, 0.5 mmol), Ti[2,4,5-Cl₃pcyd] (426 mg, 1.0 mmol) in 20 ml of DMF and 500 mL of diethyl ether to crash out 300 mg of pure product (3d). Yield: 70 %. ¹H NMR (300 MHz, DMSO-*d*₆): 9.44 (2H, d); 8.83 (2H, d); 8.69 (2H, d); 8.26 (2H, t); 7.93 (4H, t); 7.76 (2H, t); 7.31(2H, s); 7.29 (2H, t); 6.12 (2H, s). IR (KBr): ν(NCN) 2174 cm⁻¹.

Preparation of *cis*-[Ru(bpy)₂(2,3,4,5-Cl₄pcyd)₂] (3e): A mixture of *cis*-Ru(bpy)₂Cl₂ (588 mg, 1.21 mmol) and Ti[Cl₄pcyd] (1140 mg, 2.43 mmol) in 20 ml of DMF was refluxed for 3 h after which the reaction mixture was chilled overnight at -20 °C. After removal of TiCl₄ using Celite, the volume of the reaction mixture was reduced to 60 mL and 1L of diethyl ether was added to crash out 1.1 g of pure dark brown compound (3e). Yield: 98 %. ¹H NMR (300 MHz, DMSO-*d*₆): 9.42 (2H,d); 8.77 (2H,d); 8.64 (2H,d); 8.23 (2H,t); 7.94 (2H,t); 7.90 (2H,t); 7.67 (2H,d); 7.31(2H,s); 7.29 (2H,t); 6.98 (2H,s). IR (KBr): (νNCN) 2176 cm⁻¹.

Preparation of *cis*-[Ru(bpy)₂(2,3,4,5,6-Cl₅pcyd)₂] (3f): The synthesis following the above procedure gave a mixture of products. However, the purest form of

the compound was obtained by the following modifications: A mixture of *cis*-Ru(bpy)₂Cl₂ (484 mg, 1.00 mmol) and Ti[Cl₅-pcyd] (988 mg, 1.14 mmol) was refluxed in 200 mL of DMF for 3h after which the reaction mixture was chilled at – 20 °C. After removal of the white ppt of TiCl₄, the volume of the reaction mixture was reduced to 50 mL to which was added 2L of diethyl ether and the reaction mixture was again chilled at -20 °C. The purple solid precipitate was redissolved in 50 mL of DMF, which upon addition of diethyl ether (1 L) yielded 800 mg of the pure dark brown compound (**3f**). Yield: 41%. ¹H NMR (300 MHz, DMSO-*d*₆): 9.41 (2H, d); 8.77 (2H, d); 8.64 (2H, d); 8.24 (2H, t); 7.94 (2H, t); 7.91 (2H, t); 7.67 (2H, d); 7.29 (2H, t). IR (KBr): ν(NCN) 2178 cm⁻¹.

4.2.3 Synthesis of *cis*-[Ru(bpy)₂(dmsO)(R-pcyd)][PF₆] Complexes (**4a-f**)

Preparation of *cis*-[Ru(bpy)₂(pcyd)(dmsO-S)][PF₆]·1.5H₂O** (**4a**):** A mixture of *cis*-[Ru(bpy)₂(pcyd)₂] (**3a**) (0.72 g, 1.11 mmol) and NH₄PF₆ (0.18 g, 1.12 mmol) in dimethylsulfoxide (20 mL) was refluxed under inert atmosphere for 20 min during which time the reaction solution color changed from purple to yellow-orange. The volume of the solution was then reduced under vacuum at temperature of ~100 °C to almost dryness (prolonged heating may result in some *bis*-dmsO by-product). The residue was dissolved in 10 mL of acetone, filtered and to the filtrate was added 200 mL of diethyl ether, precipitating the yellow-orange product (**4a**). Yield: 0.80 g, 89 %. Anal. Calcd. for C₂₉H₃₀N₆PF₆RuSO_{2.5} (M_w = 780.67): C, 44.62; H, 3.87; N, 10.76. Found: C, 44.70; H, 3.54; N, 10.84. ¹H NMR in ppm (300 MHz, dimethylsulfoxide-*d*₆): 10.02 (d, 1H), 9.14 (d, 1H), 8.88 (d, 1H), 8.83 (d, 1H), 8.78 (d, 1H), 8.72 (d, 1H), 8.43 (t, 1H), 8.34 (t, 1H), 8.16 (t, 1H), 8.08 (t, 1H), 8.03-7.92 (m, 2H), 7.90 (d, 1H), 7.51 (t, 1H), 7.44 (t, 1H), 7.23

(d, 1H), 6.86 (d, 2H), 6.07 (d, 2H), 3.18 (s, 3H), 2.23 (s, 3H). IR (KBr): $\nu(\text{NCN})$, 2171 and 2142; $\nu(\text{S=O})$ 1090 cm^{-1} .

Preparation of *cis*-[Ru(bpy)₂(4-Clpcyd)(dmsO-S)][PF₆] \cdot H₂O (4b): This complex (**4b**) was prepared by following the same procedure as above with modification. A mixture of *cis*-[Ru(bpy)₂(Clpcyd)₂] (**3b**) (0.80 g, 1.12 mmol) and NH₄PF₆ (0.18 g, 1.12 mmol) in 20 mL dimethylsulfoxide was refluxed under argon for 1h. The volume of the reaction solution was reduced as described above and after dissolving the residue in acetone and precipitation with diethyl ether gave 0.8 g of crude product. This was purified by chromatography through an alumina column (350 g, grade V) using CH₂Cl₂ and acetone as eluents. The second dark-brown band containing the desired product was eluted with 100% acetone. After removal of the solvent, the dry solid was digested in 15 mL acetonitrile and filtered. The dark-brown filtrate was reduced using a rotavap and the residue re-dissolved in 10 mL of acetone. The addition of 200 mL of diethyl ether to this acetone solution precipitated the dark-orange product (**4b**), which was filtered and vacuum dried. Yield: 0.30 g, 35%. Anal. Calcd. for C₂₉H₂₈N₆ClPF₆RuSO₂ (M_w = 806.11): C, 43.21; H, 3.50; N, 10.43. Found: C, 43.13; H, 3.18; N, 10.41. ¹H NMR in ppm (300 MHz, dimethylsulfoxide-*d*₆): 10.02 (d, 1H), 9.14 (d, 1H), 8.88 (d, 1H), 8.83 (d, 1H), 8.78 (d, 1H), 8.72 (d, 1H), 8.43 (t, 1H), 8.34 (t, 1H), 8.16 (t, 1H), 8.08 (t, 1H), 8.03-7.92 (m, 2H), 7.90 (d, 1H), 7.51 (t, 1H), 7.44 (t, 1H), 7.23 (d, 1H), 6.86 (d, 2H), 6.07 (d, 2H), 3.18 (s, 3H), 2.23 (s, 3H). IR (KBr): $\nu(\text{NCN})$, 2171 and 2142; $\nu(\text{S=O})$ 1090 cm^{-1} .

Preparation of *cis*-[Ru(bpy)₂(2,4-Cl₂pcyd)(dmsO-S)][PF₆] (4c): This complex (**4c**) was prepared by following the same procedure as above with some modification. A mixture of *cis*-[Ru(bpy)₂(Cl₂pcyd)₂] (**3c**) (1.16 g, 1.48 mmol) and NH₄PF₆ (0.25 g, 1.53

mmol) was refluxed in 20 mL of dimethylsulfoxide under argon for 30 min. The volume of the reaction solution was reduced as described above and after dissolving the residue in acetone and precipitation with diethyl ether gave 1.18 g of crude product. A portion (0.65 g) of the crude product was purified by chromatography through an alumina column (400 g, grade V) using CH₂Cl₂, acetone and DMF as eluents. The second dark-brown band containing the desired product was eluted with 10-20% DMF in acetone. After removal of the solvent, the dry solid was digested in 15 mL acetonitrile and filtered. The dark-brown filtrate was reduced using a rotavap and the residue re-dissolved in 10 mL of acetone. The addition of 200 mL of diethyl ether to this acetone solution precipitated the dark-orange product (**4c**) which was filtered and vacuum dried. Yield: 0.20 g, 30%. Anal. Calcd. for C₂₉H₂₅N₆Cl₂PF₆RuSO (M_w = 822.56): C, 42.35; H, 3.06; N, 10.22. Found: C, 42.62; H, 3.03; N, 10.20. ¹H NMR in ppm (300 MHz, dimethylsulfoxide-*d*₆): 10.01 (d, 1H), 9.16 (d, 1H), 8.88 (d, 1H), 8.84 (d, 1H), 8.78 (d, 1H), 8.72 (d, 1H), 8.44 (t, 1H), 8.35 (t, 1H), 8.17 (t, 1H), 8.09 (t, 1H), 7.97 (dt, 2H), 7.90 (d, 1H), 7.51 (t, 1H), 7.44 (t, 1H), 7.24 (d, 1H), 7.14 (d, 1H), 6.83 (d, 1H), 5.92 (d, 1H), 3.20 (s, 3H), 2.25 (s, 3H). IR (KBr): ν(NCN), 2172; ν(S=O), 1098 cm⁻¹.

Preparation of *cis*-[Ru(bpy)₂(2,4,5-Cl₃pcyd)(dmsO-S)][PF₆]₂·H₂O (4d**):** This complex (**4d**) was prepared by following the same procedure as above with some modification. A mixture of *cis*-[Ru(bpy)₂(Cl₃pcyd)₂] (**3d**) (0.85 g, 1.0 mmol) and NH₄PF₆ (0.16 g, 1.0 mmol) was refluxed in 20 mL of dimethylsulfoxide under argon for 30 min. The volume of the reaction solution was reduced as described above and after dissolving the residue in acetone and precipitation with diethyl ether gave 0.64 g of crude product. The pure compound was isolated by passing the crude product through the

alumina column (300 g, grade V) using CH_2Cl_2 and acetone as eluents. The second dark-brown band containing the desired product was eluted with 10% acetone in CH_2Cl_2 . After removal of the solvent, the dry solid was digested in 15 mL acetonitrile and then filtered. The dark-brown filtrate was reduced using a rotavap and the residue re-dissolved in about 10 mL of acetone. The addition of 200 mL of diethyl ether to this acetone solution precipitated the dark-orange product (**4d**) which was filtered and vacuum dried. Yield: 0.20 g, 23%. Anal. Calcd. for $\text{C}_{29}\text{H}_{26}\text{N}_6\text{Cl}_3\text{PF}_6\text{RuSO}_2$ ($M_w = 875.02$): C, 39.81; H, 2.99; N, 9.63. Found: C, 39.78; H, 2.62; N, 9.63. ^1H NMR in ppm (300 MHz, dimethylsulfoxide- d_6): 10.00 (d, 1H), 9.17 (d, 1H), 8.87 (dd, 2H), 8.80 (d, 1H), 8.72 (d, 1H), 8.44 (t, 1H), 8.36 (t, 1H), 8.18 (t, 1H), 8.09 (t, 1H), 7.98 (dt, 2H), 7.90 (d, 1H), 7.51 (t, 1H), 7.44 (t, 1H), 7.25 (d, 1H), 7.35 (s, 1H), 6.02 (s, 1H), 3.19 (s, 3H), 2.27 (s, 3H). IR (KBr): $\nu(\text{NCN})$ 2174; $\nu(\text{S=O})$ 1094 cm^{-1} .

Preparation of *cis*-[Ru(bpy) $_2$ (2,3,5,6-Cl $_4$ pcyd)(dmsO-S)][PF $_6$] (4e): A mixture of *cis*-[Ru(bpy) $_2$ (Cl $_4$ pcyd) $_2$] (**3e**) (0.10 g, 0.11 mmol) and NH_4PF_6 (0.018 g, 0.11 mmol) in dimethylsulfoxide (5 mL) was refluxed under argon for 17 min during which time the purple solution turned dark orange-yellow. After removal of dimethylsulfoxide at elevated temperature (~ 100 °C) under vacuum, the sticky solid was digested in 10 ml acetone to which was added about 200 mL diethyl ether, precipitating the dark-orange product (**4e**) which was filtered and vacuum dried. Yield: 0.067 g, 68 %. Anal. Calcd. for $\text{C}_{29}\text{H}_{23}\text{N}_6\text{Cl}_4\text{PF}_6\text{RuSO}$ ($M_w = 891.45$): C, 39.07; H, 2.60; N, 9.43. Found: C, 38.73; H, 2.31; N, 9.33. ^1H NMR in ppm (300 MHz, dimethylsulfoxide- d_6): 10.00 (d, 1H), 9.14 (d, 1H), 8.87 (d, 1H), 8.83 (d, 1H), 8.77 (d, 1H), 8.71 (d, 1H), 8.44 (t, 1H), 8.34 (t, 1H), 8.15 (t, 1H), 8.08 (t, 1H), 8.01 (t, 1H), 7.95 (t, 1H), 7.80 (d, 1H), 7.50 (t, 1H), 7.43 (t, 1H),

7.23 (d, 1H), 7.07 (s, 1H), 3.22 (s, 3H), 2.23 (s, 3H). IR (KBr): $\nu(\text{NCN})$, 2178; $\nu(\text{S=O})$ 1089 cm^{-1} .

Preparation of *cis*-[Ru(bpy)₂(Cl₅pcyd)(dmsO-S)][PF₆] \cdot H₂O (4f): This complex (4f) was prepared by following the same procedure as above with some modification. A mixture of *cis*-[Ru(bpy)₂(Cl₅pcyd)₂] (3f) (0.1 g, 0.10 mmol) and NH₄PF₆ (0.016 g, 0.10 mmol) in dimethylsulfoxide (5 mL) was refluxed under argon for 12 min. The dark-orange product (4f) was isolated as above. Yield: 0.057 g, 60 %. Anal. Calcd. for C₂₉H₂₄N₆Cl₅PF₆RuSO₂ (M_w= 943.91): C, 36.90; H, 2.56; N, 8.90; Cl, 18.78. Found: C, 37.09; H, 2.24; N, 8.99; Cl, 18.49. ¹H NMR in ppm (300 MHz, dimethylsulfoxide-*d*₆): 9.99 (d, 1H), 9.14 (d, 1H), 8.87 (d, 1H), 8.83 (d, 1H), 8.77 (d, 1H), 8.71 (d, 1H), 8.44 (t, 1H), 8.34 (t, 1H), 8.16 (t, 1H), 8.08 (t, 1H), 8.01 (t, 1H), 7.95 (t, 1H), 7.80 (d, 1H), 7.51 (t, 1H), 7.43 (t, 1H), 7.23 (d, 1H), 3.21 (s, 3H), 2.24 (s, 3H). IR (KBr): $\nu(\text{NCN})$, 2181; $\nu(\text{S=O})$ 1094 cm^{-1} .

4.2.4 Physical Measurements

Elemental Analyses

All elemental analyses were performed by Canadian Microanalytical Services, Ltd. in Delta, B. C., Canada.

Infrared Spectroscopy

Infrared spectroscopy of *S*-bonded complexes was performed on a Bomem Michelson 120 FTIR spectrometer as KBr mulls and data were analyzed using Bomem Grams/386 v3.04 Level II software. The data for *O*-bonded complexes were obtained by

evaporating the partially photolyzed solution of complexes in chloroform onto KBr pellet.

NMR Spectroscopy

All standard 1-D and 2-D (COSY) ^1H NMR spectra were recorded using a Bruker AMX-400 NMR or Bruker 300 Ultra Shield spectrometers at room temperature in dimethyl- d_6 sulfoxide and all chemical shifts were referenced with respect to TMS (tetramethylsilane). The sample size consisted of 5-10 mg in 1.00 mL of dimethyl- d_6 sulfoxide and the spectrum was measured in a Norell XR-55 NMR tube. NMR of the partially photolysed solution was taken after irradiation of the solution of the initial *S*-bonded form for 1h in white light from Xe-150 watt arc lamp.

Electronic Absorption Spectroscopy

UV-Vis spectra were recorded using a Varian Cary 5 UV-Vis-NIR Spectrophotometer at ambient temperatures using Quartz cells of 1.00 cm path length from Hellma (Canada) Limited.

Cyclic Voltammetry

Cyclic voltammetry studies were performed using a Metrohm Autolab potentiostat/galvanostat PGSTAT30. The cell was configured for a working volume of ~15 mL and it was fitted with a Teflon cap through which the electrodes and argon bubbler were introduced to the cell via pre-drilled holes. The electrodes themselves consisted of platinum disk working and counter electrodes (BAS, 1.6 mm diameter) and a silver wire pseudo-reference electrode with ferrocene ($E^\circ = 0.665$ V vs. NHE in acetonitrile)³⁹ added as the internal reference and 0.1 M TBAH as the supporting

electrolyte. The CVs for all complexes in their initial *S*-bonded forms were performed in DMSO as well as in acetonitrile under dark condition. In order to obtain CVs for photochemically generated *O*-bound forms in DMSO, the initial CV solutions were irradiated by intense white light from a Xe-150 W arc lamp for about 30 min. A scan rate of 1.0 V/s was used in order to record the background CV in DMSO and acetonitrile. Scan rate dependence of CV was performed in acetonitrile in the range 0.05-20.0 V/s using the same instrument. The information about the solvent and internal reference has been provided above in the section 4.2.1.

Photochemical Measurements

Instrumentation

Photolysis for NMR spectroscopy and cyclic voltammetry was performed using Oriel-Xe-150 watt arc lamp fitted with Oriel-68806 Basic Power Supply (50-200 watts). The Xe-arc lamp provided intense visible light with significant contribution of low energy UV. The solution of the complex was taken in 1.0 cm path length quartz cell, which was placed in a thermally jacketed sample holder at a distance of 50 cm from the light source. An infrared filter was placed in between the light source and the sample to prevent unwanted heating of the solution.

The experimental set-up for the quantum yield measurement is schematically shown in the Figure 4.2.1

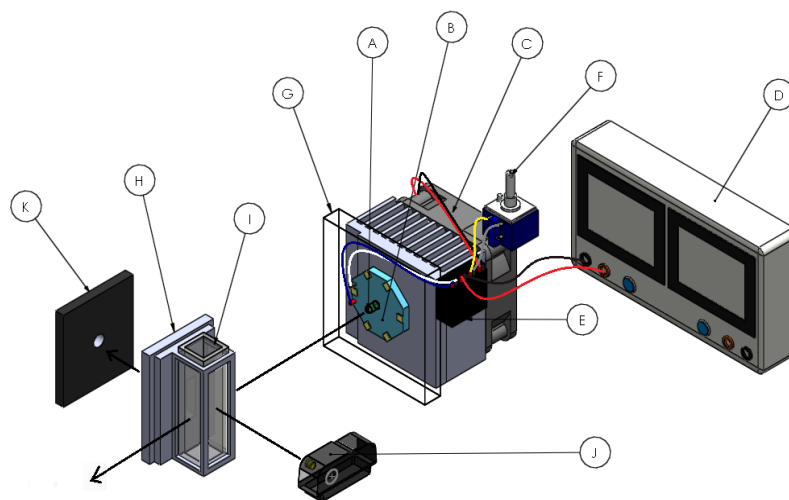


Figure 4.2.1: Instrumental arrangement for quantum yield measurement: (A) LED light, (B) Tristar Coolbase, (C) Heat-Sink, (D) DC Power Supply, (E) Buck Puck DC Driver, (F) Dimmable Potentiometer, (G) Neutral Density Filter, (H) Quartz Cell Holder, (I) Quartz Cell, (J) Light source in the Spectrophotometer, (K) Detector in the Spectrophotometer.

The photolysis for quantum yield measurement was performed using a Luxeon Rebel LED light source (Royal Blue, $\lambda = 447.5$ nm). The LED light (A) was mounted on 20 mm Tristar Coolbase (B) which provided thermal interface between the light source and the heat sink (D-E-700) (C). A Harrison 6205B Dual DC Power Supply (D) provided operating voltage of 12 V through a Buck Puck DC driver (E). The DC driver is extremely dimmable and puts up to 700 mA current for LED light through a potentiometer (5 kohm) (F). The potentiometer served to control the intensity of the LED light and the maximum power output was expected to be 2520 mW. The time required to reach the maximum power output for LED is quite fast (~ 50 μ s) and suitable for fast photochemical measurements.

During the quantum yield measurement, the LED light source was clamped in the sample compartment of the UV-Vis spectrophotometer (Cary 5) at a distance of 10 cm from the front face of the cuvette (Figure 4.2.1) and a neutral density filter (G) was placed between the light source and cuvette containing the solution of the complex. The cuvette holder (H) was drilled on four sides so that the sample solution could be irradiated from a direction perpendicular to the incident light beam used for subsequent absorption measurements in the spectrophotometer. A one cm path length quartz cell (I), transparent on four sides, provided an irradiation volume of 3 mL for solution containing the complex. Each time dependent absorbance data point was collected for a fresh solution of the complex. In a typical measurement, a degassed and stirred solution of the complex was irradiated for a specific period of time (1-120 s) and the absorbance of the solution was measured immediately after irradiation. The spectrophotometer was operated in the absorbance mode and stirring turned off before measuring the absorbance of the solution. After collecting sufficient data points for quantum yield measurement, the solution containing the complex was replaced by the actinometer solution and intensity of the incident light was measured following the method described below.

Ferrioxalate Actinometry

The intensity of the LED light source, used for quantum yield measurements, was measured by ferrioxalate actinometry.⁴⁰ The ferrioxalate actinometer is the most frequently used standard chemical actinometer. It has the advantage of constant quantum efficiency and high absorption factor over a wide range of wavelengths and of total radiation dose ($\lambda = 250\text{-}500\text{ nm}$, $\Phi_{\text{Fe}^{2+}} = 1.25\text{-}0.9$), high sensitivity and precision, coupled with simplicity of operation and availability of the photochemical material in the standard

form. It is also the primary standard against which are calibrated most other actinometers and is the most accurate of the chemical actinometers. The photochemical reaction involved is the reduction of Fe(III) to Fe(II) as shown below.



Figure 4.2.2: Photo generation of Fe(II) from Fe(III) used in ferrioxalate actinometry

The basic principle used in ferrioxalate actinometry involved the irradiation of the standard $\text{K}_3[\text{Fe(III)(C}_2\text{O}_4)_3]$ solution for a specific period of time, followed by spectrophotometric determination of the photoproduct, Fe(II), by measuring absorbance at 510 nm. The intensity of the incident radiation, I_0 (Einstein $\text{s}^{-1}\text{cm}^{-2}$) on the front surface of the cuvette containing solution was calculated by using the Eq. 4.2.1. ^{40b}

$$I_0 = \frac{A_{\text{Fe(II),510}} \times m}{(1 - 10^{-A_{\text{Fe(III),450}}}) \times 1000 \times \epsilon_{\text{Fe(II),510}} \times \Phi_{\text{Fe(II)}} \times t} \quad (4.2.1)$$

where $A_{\text{Fe(II),510}}$ = Absorbance of diluted photogenerated Fe(II) solution at 510 nm.

m = Dilution factor for the photogenerated Fe(II) solution = 25.

$A_{\text{Fe(III),450}}$ = Absorbance of standard Fe(III) solution at irradiation wavelength.

$\epsilon_{\text{Fe(II),510}}$ = Molar extinction co-efficient for Fe(II) solution at 510 nm = 11,300.

$\Phi_{\text{Fe(II)}}$ = Average quantum yield for the photogeneration of Fe(II) at 450 nm = 0.96. ^{42b}

t = Irradiation time.

All experiments involved in ferrioxalate actinometry were performed in the red light as recommended.^{40c} The intensity of the incident radiation from the LED light source ($\Delta\lambda = 440\text{-}460\text{ nm}$) on the front face of the cuvette (1 cm path length) containing the actinometer solution was measured by following the general protocol, as described by Hatchard^{40a} and Parker, which is outlined below.

A. Preparation of Calibration Curve for Fe(II) solution

A stock solution of 250 mL 0.1M FeSO₄ in 0.1N H₂SO₄ was prepared and standardized against 0.033M K₂Cr₂O₇ solution using diphenylaminesulphonate as indicator following standard procedure.

A series of calibration solutions were prepared by (a) transfer of 0, 0.5, 1.0, 1.5, 2.0, 2.5, 3.0 mL of the standard 0.12 M Fe(II) solution in 25 mL volumetric flasks, (b) addition of sufficient amount of 0.1N H₂SO₄ solution to each flask to make a total volume of each solution approximately 10 mL, (c) Addition of 5 mL of sodium acetate buffer (buffer solution prepared by mixing 150 mL of 0.1M Na(CH₃COO) with 90 mL of 1N H₂SO₄, diluted by water to 250 mL to each flask, (d) Addition of 2 mL of 0.1%(w/w) 1,10-phenanthroline solution in water to each flask), (e) dilution of each solution by water to 25 mL. All solutions were then kept in the dark (1,10-phenanthroline undergoes photodecomposition in the room fluorescent light) for 1h.

The absorbance of each solution was measured at 510 nm and from the slope of the plot of A vs [Fe(II)] was determined the molar extinction coefficient for Fe(II) ($\epsilon_{\text{Fe(II)},510} = 11,300\text{ Lmol}^{-1}\text{cm}^{-1}$).

B. Preparation of Standard Fe(III) Actinometer Solution

The solid $\text{K}_3[\text{Fe(III)(C}_2\text{O}_4)_3]\cdot 3\text{H}_2\text{O}$ was prepared by mixing 1.5M $\text{K}_2\text{C}_2\text{O}_4$ (300 mL) and 1.5 M FeCl_3 (100 mL). The pure green precipitate of the product was recrystallized three times from warm water (150 mL), dried in the air and stored in the dark. A 50 mL 0.15M Fe(III) solution was prepared by dissolving 3.71 g (7.55 mmol) of $\text{K}_3[\text{Fe(III)(C}_2\text{O}_4)_3]\cdot 3\text{H}_2\text{O}$ in 5 mL of 0.1N H_2SO_4 + 45 mL H_2O and stored in the dark.

The absorption spectrum of the standard Fe(III) solution was recorded and average absorbance at irradiation wavelengths ($\Delta\lambda = 440\text{-}460$ nm, $\lambda_{\text{max}} = 450$ nm) was measured ($A_{\text{Fe(III),450}} = 1.71$)

C. Measurement of Incident Light Intensity (I_0)

The standard Fe(III) solution (3 mL) in a 1 cm path length quartz cell was irradiated by the light from the LED source ($\Delta\lambda = 440\text{-}460$ nm, $\lambda_{\text{max}} = 450$ nm) with the same arrangement used for the measurement of the quantum yield for a specific period of time (5-15 s). After irradiation was transferred 1 ml of solution to a 25 mL volumetric flask for the analysis of photogenerated Fe(II) species. To this was added 9 mL of 0.1N H_2SO_4 , followed by a 5 mL of sodium acetate buffer and 2 mL of 0.1 % (w/w) 1,10-phenanthroline and the solution volume was made 25 mL finally by addition of water. The absorbance ($A_{\text{Fe(II),510}}$) of this solution was measured for photogenerated Fe(II) species and corrected against the blank (non-irradiated) Fe(III) solution. The intensity of the incident light, I_0 , (in Einstein $\text{s}^{-1}\text{cm}^{-2}$) was then calculated by using the Eq. 4.2.1. The intensity of incident light from LED light source was measured at three different irradiation times and averaged.

In practice, the light intensity was measured immediately after acquisition of data for quantum yield measurements. The intensity of incident light was found to vary slightly ($6.71\text{-}8.28 \times 10^{-8}$ Einstein $\text{s}^{-1}\text{cm}^{-1}$) in different quantum yield measurements, probably due to voltage fluctuation or slight variation in the relative position of cuvette in the sample holder and the light source.

Measurement of Quantum Yield for S→O Isomerization

Quantum yields for S→O isomerization for all complexes were determined by following the method described in the literature.¹³ All measurements were performed in dmso with the concentration of complexes in the range $7.15\text{-}9.61 \times 10^{-5}$ M. In a typical measurement, ten solutions (3 mL each and same concentration) of a complex were irradiated for specific periods of time (1-600 s) at the low energy isosbestic point wavelength ($\lambda = 431\text{-}444$ nm) and the absorbance (A) of the solutions were measured at two pre-selected wavelengths immediately after irradiation. For Cl_5^- , Cl_4^- , and $\text{Cl}_3\text{-pcyd}^-$ complexes, complete isomerization to O-bonded forms was obtained in 120 seconds of irradiation, while it took longer for Cl_2^- , Cl^- and unsubstituted pcyd^- complexes (~ 600 seconds). The concentration of the photogenerated O-bonded isomer (C_P) was determined by solving simultaneous Eq. 4.2.2 and 4.2.3 from the absorbance of the solution at wavelengths, $A(\lambda_1)$ and $A(\lambda_2)$.^{34e}

$$A(\lambda_1) = \varepsilon_{R,\lambda_1} C_R + \varepsilon_{P,\lambda_1} C_P \quad (4.2.2)$$

$$A(\lambda_2) = \varepsilon_{R,\lambda_2} C_R + \varepsilon_{P,\lambda_2} C_P \quad (4.2.3)$$

where, C_R and C_P are concentrations of S- and O- bonded isomers after an irradiation time of t , and $\varepsilon_{R,\lambda_1}$, $\varepsilon_{R,\lambda_2}$ and $\varepsilon_{P,\lambda_1}$, $\varepsilon_{P,\lambda_2}$ are molar extinction coefficients of S-

and O-bonded isomers at wavelengths, λ_1 and λ_2 , obtained from the quantitative absorption spectra of pure S-bonded and O-bonded isomers. The quantitative electronic absorption spectra for O-bonded isomers could be obtained after complete photoisomerization of the standard solutions of initial S-bonded isomers. The concentration of the photogenerated O-bonded isomer (C_p) as a function of irradiation time (t) provided data for the first order plot of $\ln(C_T) - \ln(C_T - C_p)$ versus t and the quantum yield ($\Phi_{S \rightarrow O}$) of S \rightarrow O isomerization was calculated from the corresponding slope, according to the Eq. 4.2.4.^{13,34a-e}

$$\Phi_{S \rightarrow O} = \frac{C_T V}{I_0(1 - 10^{-\varepsilon C_T l})} \times \frac{[\ln(C_T) - \ln(C_T - C_p)]}{t} \quad (4.2.4)$$

where, I_0 is the intensity of the incident light in E/s/cm², determined by ferrioxalate actinometry (*Vide supra*), C_p and C_T are product and total concentrations respectively, ε is the low energy isosbestic point extinction co-efficient, V is the volume of the irradiated solution (3 mL). The second factor on the right hand side of the equation (4.2.4) was determined from the slope of the plot of $\ln(C_T) - \ln(C_T - C_p)$ versus t . A good linear behavior was observed for the data collected for 50-80% conversion to the O-bonded isomer.

The initial quantum yields were also calculated from the initial slope of the plot of product concentration (C_p) versus irradiation time (t) for less than 30% conversion to the O-bonded isomers, using the Eq. 4.2.5, where the terms carry the usual meaning as above.^{40d,34a-e}

$$\Phi = \frac{\frac{dC_P}{dt}}{\left(\frac{I_0}{V}\right) (1-10^{-\epsilon C_T l})} \quad (4.2.5)$$

Both methods gave almost similar values of quantum yields for complexes of the present study and the final values were reported for those obtained by the equation 4.2.4. The raw and derived data used for calculating the quantum yield ($\Phi_{S \rightarrow O}$) for a representative complex *cis*-[Ru(bpy)₂(Cl₅pcyd)(dmsO-S)][PF₆] (**4f**) are placed in the Table D.6., Figure D.7 in the Appendix-D.

Kinetics of the Thermal Back Reaction

Kinetic studies of the dark back reaction (O→S) for all complexes were carried out in dmsO. In a typical experiment, the initial *S*-bonded isomer was irradiated until complete conversion to the *O*-bonded isomer and subsequent decay was measured in the dark by monitoring absorbance for the *O*-bonded isomer ($\lambda_{\max} \sim 512$ nm) as a function of time. The data were fitted to the first order plot of $\ln(A_t - A_\alpha)$ versus t and the corresponding slope gave the rate constants (k_{OS1}) for dark back reaction, according to the Eq. 4.2.6.^{40e}

$$\ln(A_t - A_\alpha) = \ln(A_0 - A_\alpha) - k_{OS1}t \quad (4.2.6)$$

where A_t is the absorbance at λ_{\max} for *O*-bonded isomer at time t , A_0 is the absorbance at $t = 0$ and A_α is the absorbance at infinite time, which was obtained from the absorption spectrum of initial *S*-bonded isomer before irradiation. The experimental data for a representative complex, *cis*-[Ru(bpy)₂(Cl₅pcyd)(dmsO-S)][PF₆] is placed in the Table D.7, Figure D.8-D.10 in the Appendix-D. The kinetics of dark back reaction for the same

complex was also studied in non-coordinating solvent, propylene carbonate and compared with that in dmsO.

Linkage Isomerism in Polymer Film

The photo-induced $S \rightarrow O$ and the subsequent thermal $O \rightarrow S$ for $[\text{Ru}(\text{bpy})_2(\text{Cl}_5\text{pcyd})(\text{dmsO}-S)][\text{PF}_6]$ complex were also studied in poly(methyl methacrylate) (PMMA) polymer film.

A. Preparation of PMMA Film of $[\text{Ru}(\text{bpy})_2(\text{Cl}_5\text{pcyd})(\text{dmsO}-S)][\text{PF}_6]$ (4f)

A 10% solution of PMMA ($M_w = 15,000$) was prepared in CHCl_3 . About ~ 3.0 mg of the complex (4f) was dissolved in 3 mL of the PMMA solution. The solution containing the complex was then evenly spread out onto a commercial glass slide using a Pasteur pipette and the slide was allowed to stand on a plane surface for 30 min during which time a homogeneous PMMA film of the complex was formed on the glass slide by the slow evaporation of the solvent.

B. Photo induced $S \rightarrow O$ and Thermal $O \rightarrow S$ Isomerism in PMMA Film

The absorption spectrum of the initial S -bonded complex in PMMA film (dark yellow) on the glass slide was measured ($\lambda_{\text{max}} = 412$ nm). Upon irradiation by the LED light, the film turned red and the absorption band was shifted to 510 nm for the photo-generated O -bonded isomer.

The rate (k_{OS1}) of the thermal back reaction $O \rightarrow S$ was determined from the decay profile of the photogenerated O -bonded isomer at the absorption maximum ($\lambda_{\text{max}} = 510$ nm), using the Eq. 4.2.6.

4.2.5 Theoretical Calculations

Restricted hybrid HF-DFT SCF calculations were performed on $[\text{Ru}(\text{bpy})_2(\text{Rpcyd})(\text{dmsO}-S/O)]^+$ complexes in order to obtain equilibrium geometry, orbital energy as well as IR spectra of complexes using Wavefunction Inc., Spartan'14 Parallel suite program, with the Beck three parameter hybrid exchange and Lee-Yang-Parr correlation functionals (B3LYP) and the 6-31G* basis set for C, H, N, S and LANL2DZ basis set for Ru atoms.^{53,54} All geometry optimization was performed in C_1 symmetry with subsequent vibrational frequency analysis to confirm that each stationary point was a minimum on the potential energy surface. Wave function stability calculations were performed to confirm that the calculated wave function corresponded to the electronic ground state. Tight SCF convergence criteria (10^{-8} a.u.) were used for all calculations. Unrestricted HF-DFT SCF calculations were performed to obtain spin density distributions in oxidized $[\text{Ru}(\text{bpy})_2(\text{Rpcyd})(\text{dmsO}-S/O)]^{2+}$ complexes using the same model.

4.3 Results

4.3.1 Synthesis

Six mononuclear complexes *cis*-[Ru(bpy)₂(R-pcyd) (dmsO-*S*)]⁺[PF₆⁻] (**4a-4f**) were prepared by refluxing a slightly acidic solution (using NH₄PF₆) of precursor *cis*-[Ru(bpy)₂(R-pcyd)₂] complexes (**3a-3f**) in anhydrous dimethyl sulfoxide under inert atmosphere for 10-30 minutes. By controlling the reflux time (10-30 min) and volume of the reaction mixture (5-20 mL), all complexes could be obtained in high purity with substantial yields (30-90%). Prolonged reflux and drying time (for the removal of solvents) resulted in a substantial amount of the undesired *bis*-dmsO or *trans*-complexes (confirmed by NMR spectroscopy), particularly for Cl₅⁻ and Cl₄pcyd⁻ complexes (**4e**, **4f**). However, syntheses at smaller scale and reduced reflux (10-15 min) and drying (20-30 min) time gave highly pure complexes (**4e**, **4f**). No further purification by column chromatography was required for these complexes. On the other hand, Cl⁻, Cl₂⁻ and Cl₃⁻pcyd⁻ complexes (**4b**, **4d**, **4e**) required the use of column chromatography (alumina, grade V) to obtain elementally pure compounds. These complexes showed specific binding properties to the alumina column, which reduced their yields significantly (23-35%). The unsubstituted pcyd⁻ complex (**4a**) could be obtained in high purity with the highest yield (90%) among other complexes (**4a-4f**), simply by refluxing the precursor complex (**3a**) in dmsO (20 mL) for 30 minutes.

4.3.2 Molecular Structure

DFT calculations on the *cis*-[Ru(bpy)₂(pcyd)(dmsO-*S*)]⁺ (**4a**) and *cis*-[Ru(bpy)₂(pcyd)(dmsO-*O*)]⁺ assuming C₁ symmetry and a spin multiplicity of 1 gave the geometry optimized structures of both complexes shown in the Figure 4.3.1 a and 4.3.1 b

respectively. The atomic coordinates of geometry optimized structures are provided in the Table D.1-D.2 in the Appendix-D.

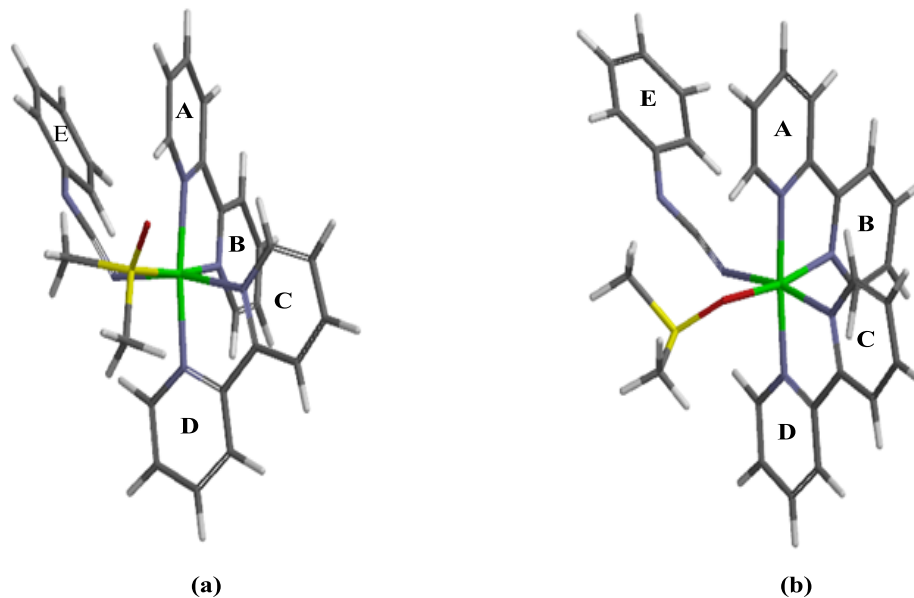


Figure 4.3.1: Geometry optimized structures of (a) cis -[Ru(bpy)₂(pcyd)(dmsO-*S*)]⁺ (**4a**) and (b) cis -[Ru(bpy)₂(pcyd)(dmsO-*O*)]⁺ complexes.

As seen in the Figure 4.3.1 a, two methyl groups on dmsO are in a non-equivalent environment in the *S*-bonded complex cis -[Ru(bpy)₂(pcyd)(dmsO-*S*)]⁺: one pointing towards the aromatic clouds of pyridine rings, C and D, while the other pointing towards the π -clouds of the cyanamide group on the phenylcyanamide ligand. Similar orientations of the methyl groups of the dmsO ligand were observed in the crystal structure of *S*-bonded complex cis -[Ru(bpy)₂(dmsO-*S*)Cl]⁺, which resulted in non-equivalent ¹H NMR chemical shifts of methyl groups on the *S*-bonded dmsO ligand.^{52b} The calculated Ru-S (2.373 Å) and S-O (1.511 Å) bond lengths in **4a** are in fairly good agreement with the average Ru-S (2.26-2.28 Å) and S-O (1.4738(1) Å) bond lengths in other ruthenium-sulfoxide complexes, although the values are slightly overestimated in

DFT calculations.^{31a,52a} Like the *cis*-[Ru(bpy)₂(dmsO)Cl]⁺ complex, the oxygen atom of the dmsO ligand in the complex *cis*-[Ru(bpy)₂(pcyd)(dmsO-*S*)]⁺ (**4a**) is also in close proximity to the H6 proton of the pyridine ring A (O-H₆ (A) = 2.110 Å), suggesting that a hydrogen bonding interaction between them is also present in the complex **4a**.^{52a}

On the other hand, two methyl groups of the dmsO ligand in the *O*-bonded isomer appear to be out of the influence of pyridine rings C and D and experience similar magnetic environment in the complex (Figure 4.3.1 b). Unlike the *S*-bonded isomer, the phenyl ring of the pcyd ligand in the *O*-isomer adopted a perpendicular orientation with respect to the plane of the pyridine rings A and B. The calculated S-O bond length (1.568 Å) in the *O*-isomer is larger than that of the *S*-isomer, which is in agreement with the change in binding modes of sulfoxide ligands.^{31a} Like the *S*-isomer, DFT calculated S-O bond length in the *O*-isomer is also slightly larger than the average S-O bond lengths (1.528(1) Å) in other metal-sulfoxide (*-O*) complexes.^{31a} The calculated Ru-O bond length (2.193 Å) is significantly shorter than the corresponding Ru-S bond (2.379 Å), as expected for the smaller size of the oxygen atom. It is also notable that the distance between the *O* atom on the dmsO ligand and the H6 proton on the pyridine ring A (O-H₆ (A) = 2.412 Å) is larger in the *O*-isomer, which suggested that the H-bonding interaction between them in the former is not as pronounced as in the *S*-isomer.^{51a}

In both *S*- and *O*- bonded complexes *cis*-[Ru(bpy)₂(pcyd)(dmsO-*S/O*)]⁺, the phenylcyanamide ligand is almost planar. The planar geometry of phenylcyanamide ligand is a common feature of ruthenium-phenylcyanamide complexes and has been ascribed to π -mixing between the cyanamide group and the phenyl ring.⁴¹⁻⁴⁴ Cyanamide groups of the phenylcyanamide ligands are approximately linear, with the NCN bond

angle being 172.78° and 170.35° in both *S*- and *O*-bonded isomers, respectively. The Ru-N(NCN) bond lengths (2.110 Å and 2.104 Å for *S*- and *O*-bonded isomers, respectively) fall within the expected range of Ru(II)-N(cyanamide) bond lengths (2.040-2.088 Å) in other Ru(II)-phenylcyanamide complexes.⁴²⁻⁴⁴ However, the angle describing the Ru(II)-cyanamide bond is significantly bent in both *S*-bonded (129.70°) and *O*-bonded (132.19°) isomers which is similar to that of the Pd(II)-phenylcyanamide bond ($137.9(4)^\circ$) in $[\text{Pd}(\text{tpy})(2,6\text{-dichlorophenylcyanamide})]^+$.⁴⁵ Similar bent structures have also been observed in other Ru(II)-phenylcyanamide complexes and it was suggested that the π -bonding is optimized when the angle between Ru(III) and cyanamide is linear, a condition which is evidently relaxed when π -bonding is not as important.

The Ru-N(bpy) bond lengths and angles between Ru and pyridine rings are comparable to those of other Ru(II)-polypyridyl-sulfoxide complexes.^{14,19,20,52b}

4.3.3 Electronic Structures

Restricted HF DFT calculations were performed on *cis*- $[\text{Ru}(\text{bpy})_2(\text{pcyd})(\text{dmsO-S})]^+$ (**4a**) and *cis*- $[\text{Ru}(\text{bpy})_2(\text{pcyd})(\text{dmsO-O})]^+$ complexes and corresponding frontier molecular orbitals and their energies of are shown in Figure 4.3.2 and 4.3.3, respectively.. On the other hand, unrestricted HF DFT calculations were performed on singly oxidized complexes *cis*- $[\text{Ru}(\text{bpy})_2(\text{pcyd})(\text{dmsO-S})]^{2+}$ and *cis*- $[\text{Ru}(\text{bpy})_2(\text{pcyd})(\text{dmsO-O})]^{2+}$ to obtain spin density distributions in both *S*- and *O*- bonded isomers, which are shown in Figure 4.3.4. The atomic coordinates of the geometry optimized structures complexes are provided in the Table-D.1-D5 in the Appendix-D.

The highest occupied molecular orbitals (HOMOs) of *cis*- $[\text{Ru}(\text{bpy})_2(\text{pcyd})(\text{dmsO-S})]^+$ (**4a**) and *cis*- $[\text{Ru}(\text{bpy})_2(\text{pcyd})(\text{dmsO-O})]^+$ complexes are of

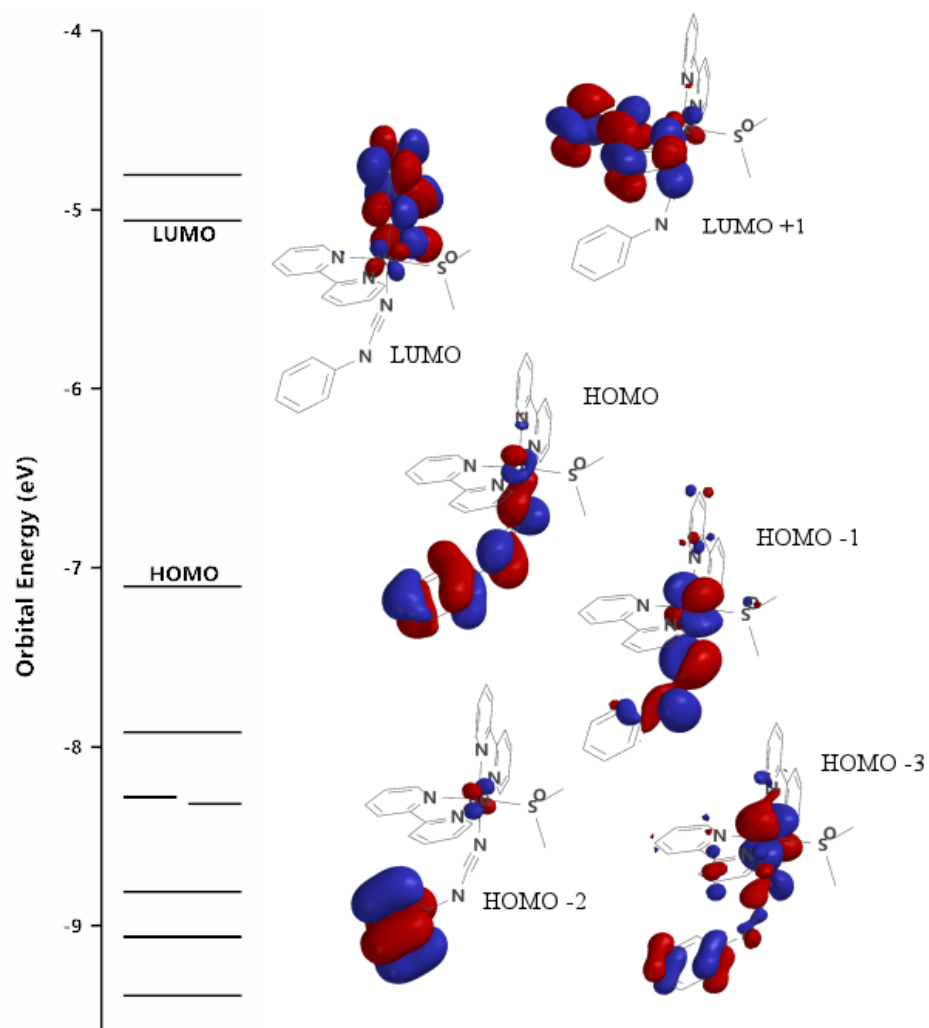


Figure 4.3.2: DFT calculation of orbital energies and selected molecular orbitals of $[\text{Ru}(\text{bpy})_2(\text{pcyd})(\text{dmsO-S})]^+$.

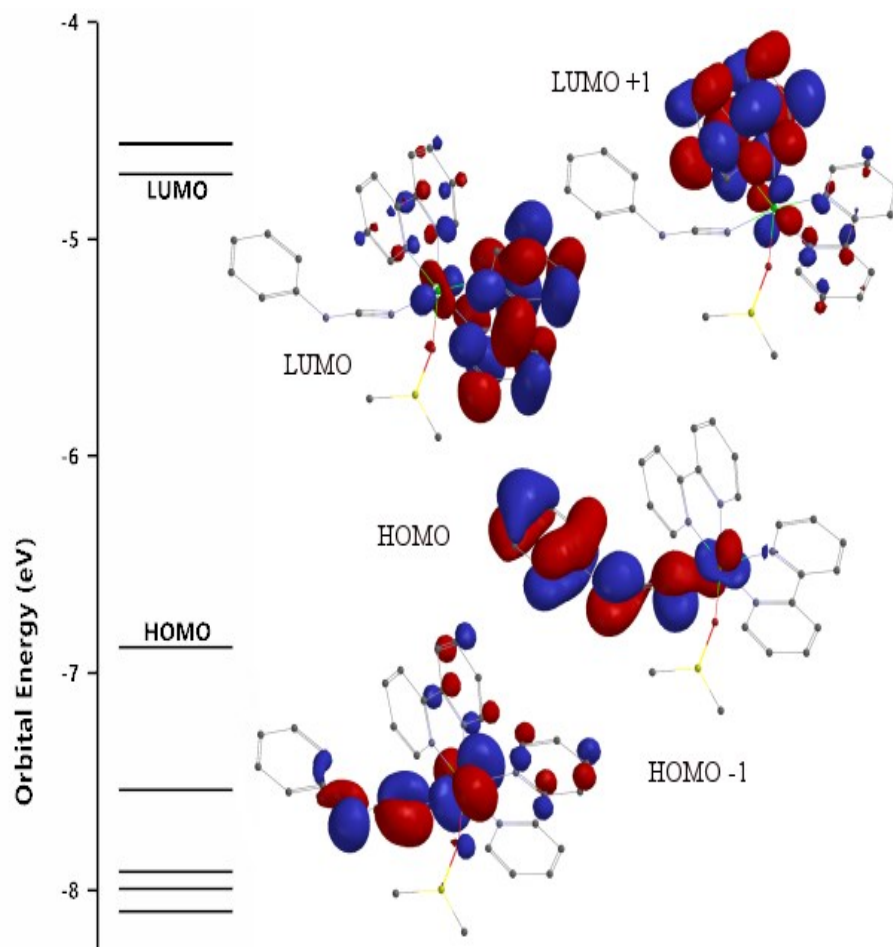


Figure 4.3.3: DFT calculation of orbital energies and selected molecular orbitals of $[\text{Ru}(\text{bpy})_2(\text{phen})(\text{dmsO}-O)]^+$.

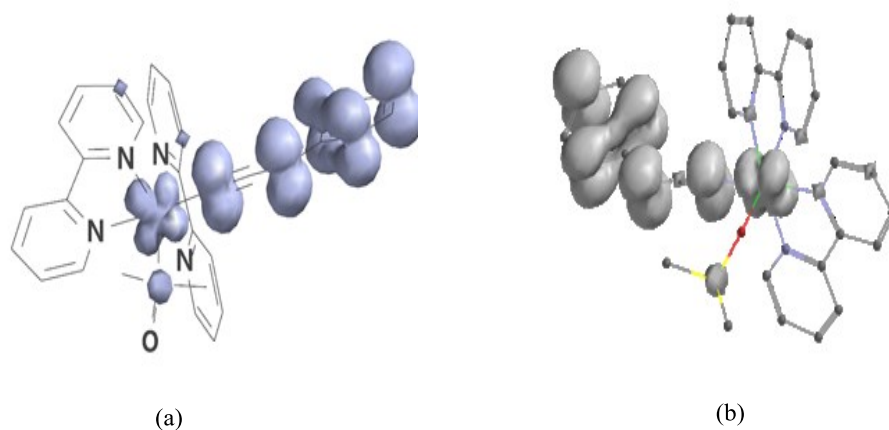


Figure 4.3.4: Spin density distribution of (a) $cis-[Ru(bpy)_2(pcyd)(dmsO-S)]^{2+}$ and (b) $cis-[Ru(bpy)_2(pcyd)(dmsO-O)]^{2+}$.

mostly phenylcyanamide ligand character (Figure 4.3.2 and 4.3.3). The HOMOs of other complexes (4b-4f) are also very similar to those of 4a, comprises mostly the π -HOMO of the phenylcyanamide ligand. It is therefore expected that upon oxidation considerable spin density should reside on the phenylcyanamide ligand. Indeed, Figure 4.3.4 (a) shows the spin density distribution of the oxidized complex $cis-[Ru(bpy)_2(pcyd)(dmsO-S)]^{2+}$, which places more than 80% of the spin on the phenylcyanamide ligand. A similar spin density distribution is seen for the *O*-bonded $[Ru(bpy)_2(pcyd)(dmsO-O)]^{2+}$ (Figure 4.3.4 b). DFT calculations, therefore, indicate that the phenylcyanamide ligand is non-innocent in both *S*- and *O*-bonded isomers $[Ru(bpy)_2(R-pcyd)(dmsO-S)]^{2+}$ and $[Ru(bpy)_2(R-pcyd)(dmsO-O)]^{2+}$.

A DFT calculation of molecular orbitals and energies was also performed on $cis-[Ru(bpy)_2(Cl_5pcyd)(dmsO-S)]^+$ (**4f**) (Figure D.1 in the Appendix D). In comparison to $cis-[Ru(bpy)_2(pcyd)(dmsO-S)]^+$ (**4a**), the molecular orbitals look much the same except that those of $cis-[Ru(bpy)_2(Cl_5pcyd)(dmsO-S)]^+$ are generally more stable. For example, the HOMO of the Cl_5pcyd^- complex (**4f**) is -0.4 eV more stable than that of the $pcyd^-$ (**4a**)

complex and this must be due to the electron-withdrawing properties of the chloro substituents.

4.3.4 Infrared Spectroscopy

Infrared data of six mononuclear $[\text{Ru}(\text{bpy})_2(\text{R-pcyd})(\text{dmsO})][\text{PF}_6]$ complexes (**4a-4f**) in both *S*- and *O*-bonded forms have been placed in the Table 4.3.1 and a representative IR-spectrum of the initial *S*-bonded isomer $[\text{Ru}(\text{bpy})_2(\text{Cl}_5\text{-pcyd})(\text{dmsO-}S)][\text{PF}_6]$ (**4f**) is shown in the Figure 4.3.5. IR spectra of all *S*-bonded complexes were taken on KBr pellet. On the other hand, spectra of *O*-bonded isomers were very difficult to obtain in the solid state and the data reported here were obtained by evaporating the partially photolyzed solution of complexes in chloroform onto KBr pellet and subsequently measuring the IR spectrum on the KBr pellet. An IR spectrum (Figure D.2 in the Appendix-D) of partially photolyzed complex *cis*- $[\text{Ru}(\text{bpy})_2(\text{Cl}_5\text{-pcyd})(\text{dmsO-}S)][\text{PF}_6]$ (**4f**) on KBr is placed in the Appendix- 3. DFT calculated IR spectra of both *S*- and *O*- bonded isomers of $[\text{Ru}(\text{bpy})_2(\text{pcyd})(\text{dmsO-}S/O)][\text{PF}_6]$ are shown in the Figure 4.3.6-4.3.7.

All $[\text{Ru}(\text{bpy})_2(\text{R-pcyd})(\text{dmsO})][\text{PF}_6]$ complexes (**4a-4f**) exhibited strong $\nu(\text{NCN})$ stretches at 2142-2181 cm^{-1} for coordinated R- pcyd^- ligands, as observed in other mononuclear and dinuclear ruthenium-phenylcyanamide complexes.⁴¹⁻⁵¹ The position and intensity of the $\nu(\text{NCN})$ band do not show significant substituent effect, only slightly shifted to higher frequencies as the number of chloro-substituent increased on R- pcyd ligand and also remain almost unchanged in both *S*- and *O*- bonded isomers. The intense $\nu(\text{P-F})$ band for the hexafluorophosphate anion is located at 840 cm^{-1} for all

complexes. The IR spectra of ruthenium-polypyridyl-sulfoxide complexes are characterized by a

Table 4.3.1: IR Data of *cis*-[Ru(bpy)₂(R-pcyd)(dmsO)][PF₆] Complexes.^{a,b}

R-pcyd ⁻	$\nu(\text{NCN})/\text{cm}^{-1}$	$\nu(\text{SO})/\text{cm}^{-1}$ <i>S</i> -bound	$\nu(\text{SO})/\text{cm}^{-1}$ <i>O</i> -bound	$\nu(\text{Ru-S})/\text{cm}^{-1}$	$\nu(\text{Ru-O})/\text{cm}^{-1}$
Cl ₅ pcyd ⁻	2181	1094	1020	430	451
Cl ₄ pcyd ⁻	2178 (2206) ^b	1089 (1090) ^b	1023 (907) ^b	428 (403) ^b	451 (460) ^b
Cl ₃ pcyd ⁻	2174	1094	1022	430	451
Cl ₂ pcyd ⁻	2172	1098	1023	427	452
Clpcyd ⁻	2171,2142	1090	1021	429	450
pcyd ⁻	2175,2147 (2164) ^b	1092 (1090) ^b	1022 (907) ^b	428 (403) ^b	449 (465) ^b

^a Experimental IR data on KBr pellet. ^b DFT Calculated IR data of *S*- and *O*- bonded forms of Cl₄pcyd (4e) and unsubstituted pcyd (4a) complexes.

fairly intense $\nu(\text{SO})$ band at 1080-1154 cm⁻¹ and 862-997 cm⁻¹ for *S*- and *O*-bonded sulfoxide ligands, respectively.^{31a} The *S*- and *O*- bonded isomers also exhibit relatively weak $\nu(\text{Ru-S})$ and $\nu(\text{Ru-O})$ bands at 410-430 cm⁻¹ and 460-490 cm⁻¹ respectively.^{11,31} In agreement with reported ranges, the IR spectra of all [Ru(bpy)₂(R-pcyd)(dmsO-S)][PF₆] complexes (4a-4f) also show characteristic $\nu(\text{S-O})$ and $\nu(\text{Ru-S})$ stretches at 1089-1098 cm⁻¹ and 427-432 cm⁻¹, respectively (Table 4.3.1, Figure 4.3.5). The calculated IR

spectrum (Table 4.3.1, Figure 4.3.6) of $[\text{Ru}(\text{bpy})_2(\text{pcyd})(\text{dmsO-S})][\text{PF}_6]$ (**4a**) is also in good agreement with the experimental spectra, in so far as the band positions of $\nu(\text{NCN})$,

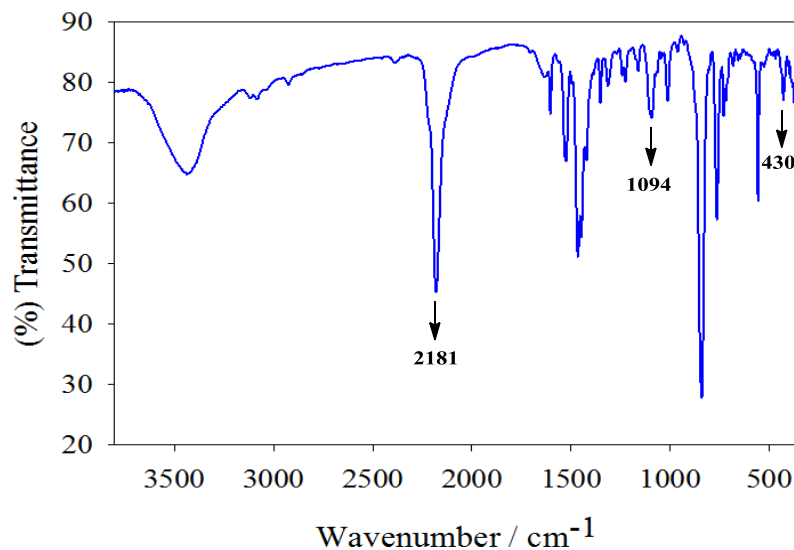


Figure 4.3.5: IR spectrum of *cis*- $[\text{Ru}(\text{bpy})_2(\text{Cl}_5\text{-pcyd})(\text{dmsO-S})][\text{PF}_6]$ complex (**4f**) on KBr.

$\nu(\text{S-O})$ and $\nu(\text{Ru-S})$ are concerned. On the other hand, the partially photolyzed spectra of these complexes are characterized by a decrease in intensity of the $\nu(\text{S-O})$ and $\nu(\text{Ru-S})$ bands with concomitant development of bands at 1020 cm^{-1} and 450 cm^{-1} , respectively and by comparison with the reported values, we assigned them to $\nu(\text{S-O})$ and $\nu(\text{Ru-O})$ for *O*-bonded isomers. However, the $\nu(\text{S-O})$ bands of the *O*-bonded isomers are slightly more positively shifted relative to the expected experimental range and the calculated range as well (Figure 4.3.7). This is not uncommon as recently reported IR spectra of photo-generated *O*-bonded complexes $O\text{-}[\text{Ru}(\text{bpy})(\text{biq})(\text{OSOR})]^+$ and $O\text{-}[\text{Ru}(\text{bpy})_2(\text{OSOR})]^+$ (where biq is 2,2-biquinoline and OSOR is 2-methylsulfinyl benzoate) exhibited positively shifted $\nu(\text{SO})$ stretches at 1006 and 1022 cm^{-1} , respectively, and this high frequency shift relative to the expected range was attributed to

possible symmetric or anti-symmetric (η^2 -SO) binding modes of sulfoxide ligands in the partially photolyzed complexes.^{20,35}

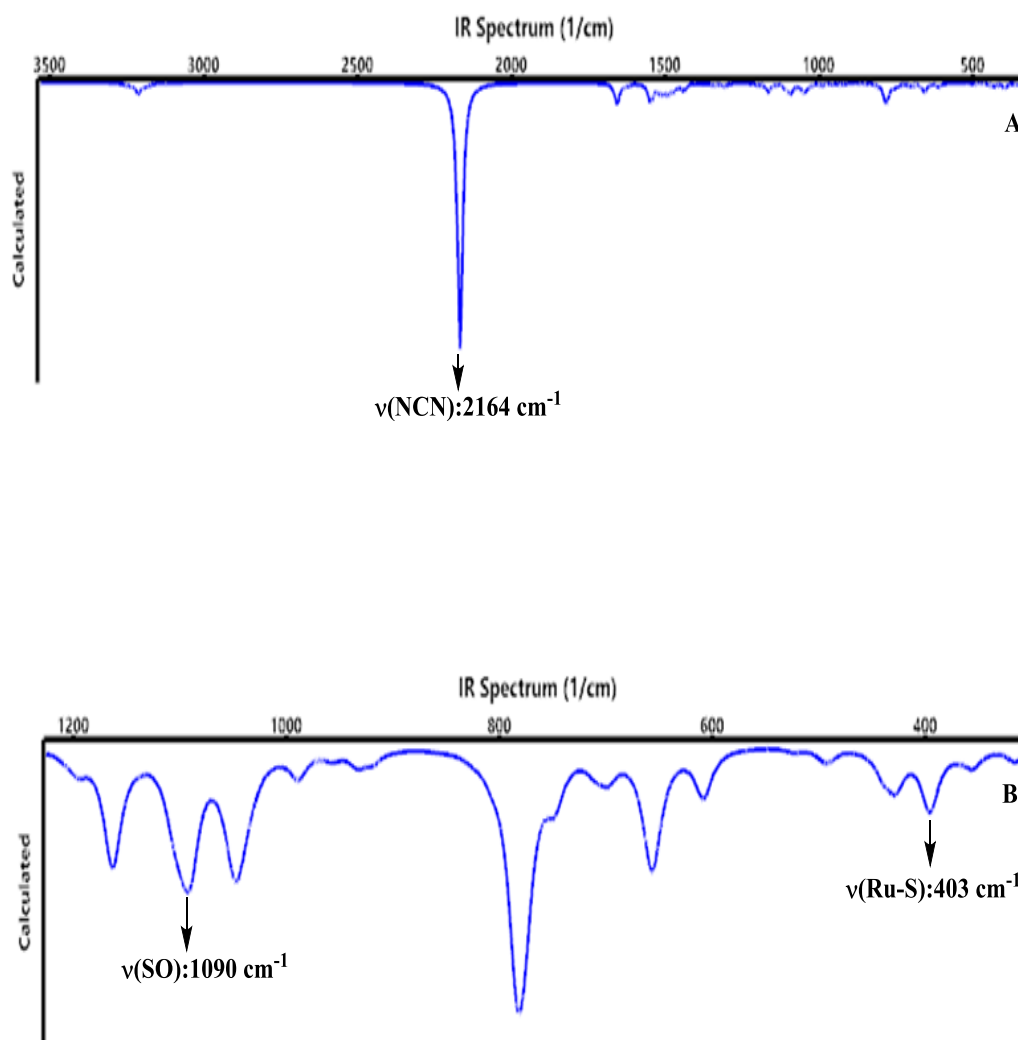


Figure 4.3.6: Calculated IR spectrum of $[\text{Ru}(\text{bpy})_2(\text{pecy}) (\text{dmsO-S})][\text{PF}_6]$ complex (4a) showing (A) $\nu(\text{NCN})$ (top) and (B) $\nu(\text{SO}, \text{Ru-S})$ (bottom) bands.

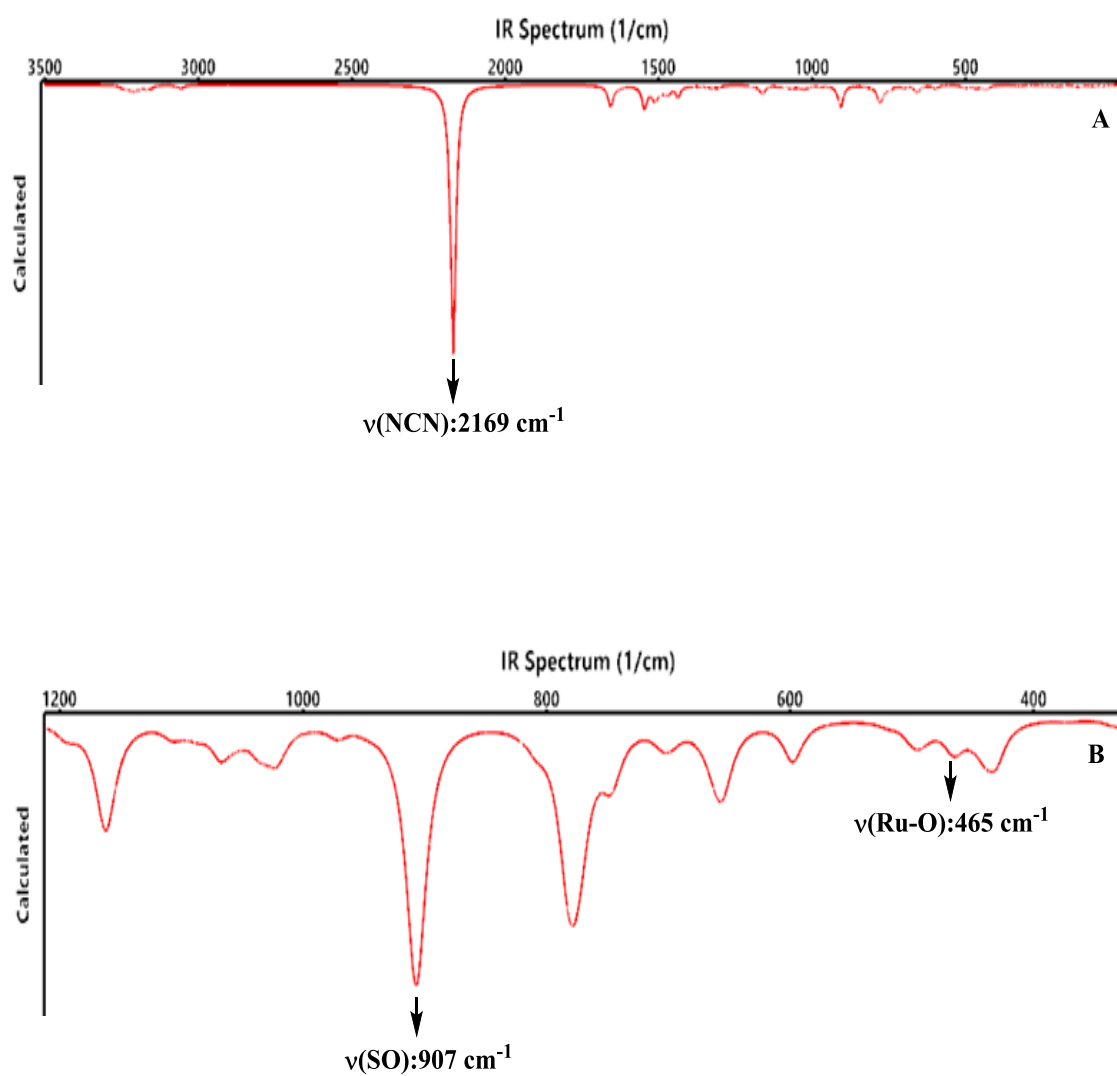


Figure 4.3.7: Calculated IR spectrum of [Ru(bpy)₂(pecy) (dmsO-O)][PF₆] complex (4a) showing (A) $\nu(\text{NCN})$ (top) and (B) $\nu(\text{SO}, \text{Ru-O})$ (bottom) bands.

4.3.5 NMR Spectroscopy

The ^1H NMR and ^1H - ^1H COSY spectra of complexes *cis*- $[\text{Ru}(\text{bpy})_2(\text{R-pcyd})(\text{dmsO-S})][\text{PF}_6]$ (**4a-4f**) in $\text{dmsO-}d_6$ are shown in the Figure 4.3.10-4.3.21 and corresponding data have been placed in the Table 4.3.2. Figure 4.3.8-4.3.9 show the representative ^1H NMR and ^1H - ^1H COSY spectra for the precursor complex *cis*- $[\text{Ru}(\text{bpy})_2(\text{Cl}_4\text{pcyd})_2]$. The ^1H NMR spectrum of partially photolyzed solution of *cis*- $[\text{Ru}(\text{bpy})_2(\text{Cl}_4\text{pcyd})(\text{dmsO-S})][\text{PF}_6]$ complex is also shown in the Figure 4.3.22. All proton peaks for bpy, R-pcyd and coordinated dimethylsulfoxide (dmsO) ligands were assigned with the help of ^1H - ^1H COSY technique, coupling constant and integration values for respective peaks and compared with the reported proton chemical shifts of structurally similar *cis*- $[\text{Ru}(\text{bpy})_2(\text{dmsO-S})\text{Cl}]^+$ complex.⁴¹ The numbering schemes used to assign the bpy and dmsO protons on the precursor *cis*- $\text{Ru}(\text{bpy})_2(\text{R-pcyd})_2$ as well as $[\text{Ru}(\text{bpy})_2(\text{R-pcyd})(\text{dmsO-S})][\text{PF}_6]$ complexes are shown in the Figure 4.3.23.

The bipyridine ligands in the precursor *cis*- $\text{Ru}(\text{bpy})_2(\text{Cl}_4\text{pcyd})_2$ complex (Figure 4.3.8-4.3.9) have two magnetically non-equivalent pyridine moieties (A and B rings) and exhibit a total of eight signals (in the region δ 9.50-7.25 ppm) consisting of two sets of two doublets and two triplets in the ^1H NMR spectrum of the complex. Both Cl_4pcyd anions occupy magnetically equivalent coordination environments in the complex, which is evident from a sharp singlet at 6.98 ppm and with an integration of two protons. The most downfield signal for bpy ligand could be for either A6' or B6 protons and was identified by the characteristic coupling constant value ($J= 5.1$ Hz) for proton adjacent to nitrogen atom on the pyridine ring.^{52c-g} However, in asymmetric *bis*-bidentate polypyridine complexes, the B6 proton lies above the shielding cone of the pyridine ring

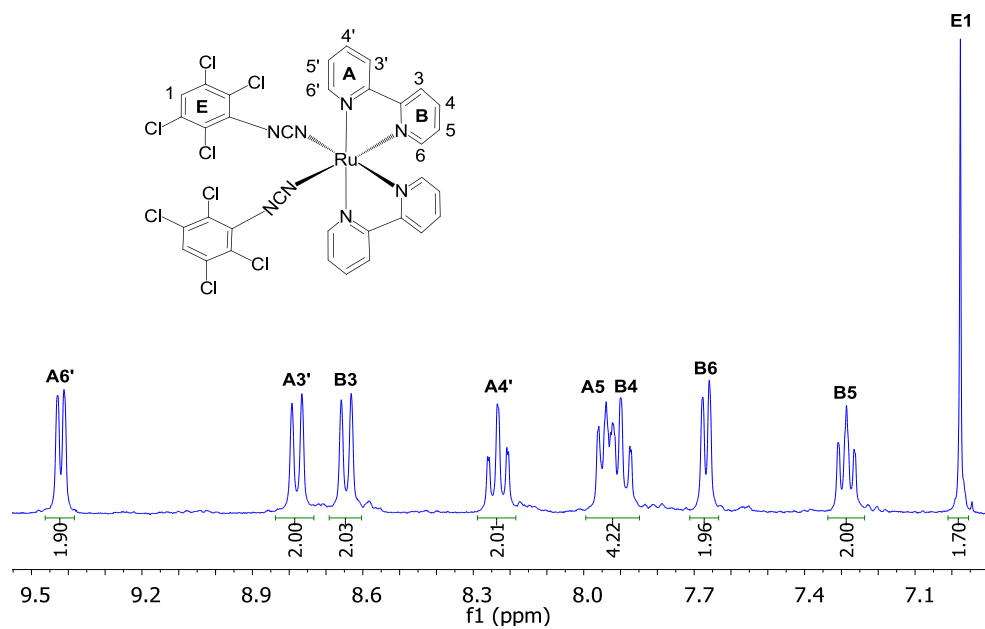


Figure 4.3.8: ¹H NMR spectrum of *cis*-[Ru(bpy)₂(Cl₄pcyd)₂] in dms0-d₆.

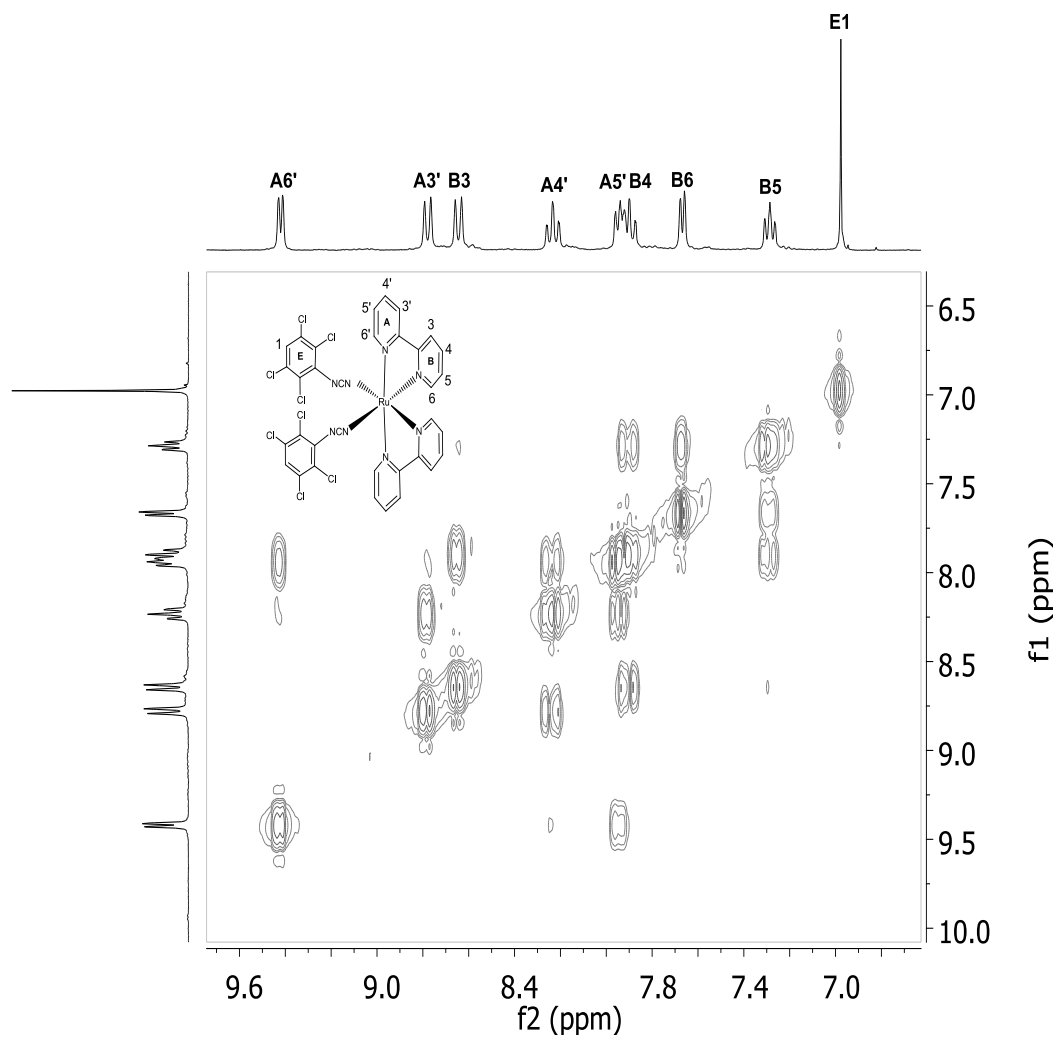


Figure 4.3.9: ^1H - ^1H COSY spectrum of *cis*-[Ru(bpy)₂(Cl₄pcyd)₂] in dms0-*d*₆.

Table 4.3.2: ^1H NMR Data of *cis*-[Ru(bpy) $_2$ (R-pcyd)(dms-*S*)] Complexes (**4a-4f**) in dms-*d* $_6$.

Complex	Chemical Shift (ppm)/ Coupling Constants/ type		
	bpy	R-pcyd	dms- <i>S</i>
4f	9.99 (d, $J = 5.7$ Hz, 1H), D6' 9.14 (d, $J = 5.6$ Hz, 1H), A6' 8.87 (d, $J = 7.9$ Hz, 1H), A3' 8.83 (d, $J = 8.0$ Hz, 1H), D3' 8.77 (d, $J = 8.1$ Hz, 1H), C3 8.71 (d, $J = 8.2$ Hz, 1H), B3 8.44 (t, $J = 7.9$ Hz, 1H), A4' 8.34 (t, $J = 7.9$ Hz, 1H), D4' 8.16 (t, $J = 7.9$ Hz, 1H), C4 8.08 (t, $J = 8.0$ Hz, 1H), B4 8.01(t, 1H), A5' 7.95 (t, $J = 6.6$ Hz, 1H), D5' 7.80 (d, $J = 5.1$ Hz, 1H), B6 7.51(t, 1H), C5 7.43 (t, 1H), B5 7.23 (d, $J = 4.6$ Hz, 1H), C6		3.21 (s, 3H), Me1 2.24 (s, 3H), Me2
4e	10.00 (d, $J = 4.7$ Hz, 1H), D6' 9.14 (d, $J = 4.7$ Hz, 1H), A6' 8.87 (d, $J = 8.1$ Hz, 1H), A3' 8.83 (d, $J = 7.7$ Hz, 1H), D3' 8.77 (d, $J = 8.1$ Hz, 1H), C3 8.71 (d, $J = 8.1$ Hz, 1H), B3 8.44 (t, $J = 7.9$ Hz, 1H), A4' 8.34 (t, $J = 7.9$ Hz, 1H), D4' 8.15 (t, $J = 7.9$ Hz, 1H), C4 8.08 (t, $J = 7.9$ Hz, 1H), B4 8.01 (t, 1H), A5' 7.95 (t, $J = 6.6$ Hz, 1H), D5' 7.80 (d, $J = 4.9$ Hz, 1H), B6 7.50 (t, 1H), C5 7.43 (t, 1H), B5 7.23 (d, $J = 5.6$ Hz, 1H), C6	7.07 (s, 1H), E1	3.22 (s, 3H), Me1 2.23 (s, 3H), Me2

Continued

Complex	Chemical Shift (ppm)/ Coupling Constants/ type		
	bpy	R-pcyd	dmsO
4d	10.00 (d, $J = 5.8$ Hz, 1H), D6' 9.17 (d, $J = 5.5$ Hz, 1H), A6' 8.87 (dd, $J = 7.9$ Hz, 2H), A3', D3' 8.80 (d, $J = 8.1$ Hz, 1H), C3 8.72 (d, $J = 7.9$ Hz, 1H), B3 8.44 (t, $J = 7.9$ Hz, 1H), A4' 8.36 (t, $J = 7.9$ Hz, 1H), D4' 8.18 (t, $J = 7.8$ Hz, 1H), C4 8.09 (t, $J = 7.9$ Hz, 1H), B4 7.98 (dt, $J = 6.1, 5.0$ Hz, 2H), A5', D5' 7.90 (d, $J = 5.5$ Hz, 1H), B6 7.51 (t, 1H), C5 7.44 (t, 1H), B5 7.25 (d, $J = 5.6$ Hz, 1H), C6	7.35 (s, 1H), E1 6.02 (s, 1H), E2	3.19 (s, 3H), Me1 2.27 (s, 3H), Me2
4c	10.01 (d, $J = 5.7$ Hz, 1H), D6' 9.16 (d, $J = 6.3$ Hz, 1H), A6' 8.88 (d, $J = 8.1$ Hz, 1H), A3' 8.84 (d, $J = 7.8$ Hz, 1H), D3' 8.78 (d, $J = 8.1$ Hz, 1H), C3 8.72 (d, $J = 8.1$ Hz, 1H), B3 8.44 (t, $J = 7.9$ Hz, 1H), A4' 8.35 (t, $J = 7.8$ Hz, 1H), D4' 8.17 (t, $J = 7.9$ Hz, 1H), C4 8.09 (t, $J = 7.9$ Hz, 1H), B4 7.97 (dt, $J = 7.7, 4.4$ Hz, 2H), A5', D5' 7.90 (d, $J = 4.8$ Hz, 1H), B6 7.51 (t, 1H), C5 7.44 (t, 1H), B5 7.24 (d, $J = 4.8$ Hz, 1H), C6	7.14 (d, $J = 2.5$ Hz, 1H), E1 6.83 (d, $J = 8.6$ Hz, 1H), E2 5.92 (d, $J = 8.6$ Hz, 1H), E3	3.20 (s, 3H), Me1 2.25 (s, 3H), Me2

Continued

Complex	Chemical Shift (ppm)/ Coupling Constants/ type		
	bpy	R-pcyd	dmsO
4b	10.02 (d, $J = 4.8$ Hz, 1H), D6' 9.14 (d, $J = 6.0$ Hz, 1H), A6' 8.88 (d, $J = 8.0$ Hz, 1H), A3' 8.83 (d, $J = 8.1$ Hz, 1H), D3' 8.78 (d, $J = 8.1$ Hz, 1H), C3 8.72 (d, $J = 8.1$ Hz, 1H), B3 8.43 (t, $J = 7.3$ Hz, 1H), A4' 8.34 (t, $J = 7.8$ Hz, 1H), D4' 8.16 (t, $J = 7.8$ Hz, 1H), C4 8.08 (t, $J = 7.3$ Hz, 1H), B4 8.03 – 7.92 (m, 2H), A5', D5' 7.90 (d, $J = 5.5$ Hz, 1H), B6 7.51 (t, 1H), C5 7.44 (t, 1H), B5 7.23 (d, $J = 4.9$ Hz, 1H), C6	6.86 (d, $J = 8.7$ Hz, 2H), E1 6.07 (d, $J = 8.7$ Hz, 2H), E2	3.18 (s, 3H), Me1 2.23 (s, 3H), Me2
4a	10.04 (d, $J = 5.6$ Hz, 1H), D6' 9.17 (d, $J = 4.8$ Hz, 1H), A6' 8.88 (d, $J = 8.0$ Hz, 1H), A3' 8.82 (d, $J = 7.9$ Hz, 1H), D3' 8.77 (d, $J = 8.1$ Hz, 1H), C3 8.72 (d, $J = 8.2$ Hz, 1H), B3 8.44 (t, $J = 7.9$ Hz, 1H), A4' 8.32 (t, $J = 7.8$ Hz, 1H), D4' 8.16 (t, 1H), C4 8.07 (t, $J = 7.2$ Hz, 1H), B4 8.03 – 7.92 (m, 1H), A5', D5' 7.90 (d, $J = 5.5$ Hz, 1H), B6 7.51 (t, 1H), C5 7.43 (t, 1H), B5 7.23 (d, $J = 5.6$ Hz, 1H), C6	6.85 (t, $J = 8.9$ Hz, 1H), E2 6.49 (t, $J = 6.7$ Hz, 1H), E3 6.11 (d, $J = 8.5$ Hz, 1H), E1	3.19 (s, 3H), Me1 2.22 (s, 3H), Me2

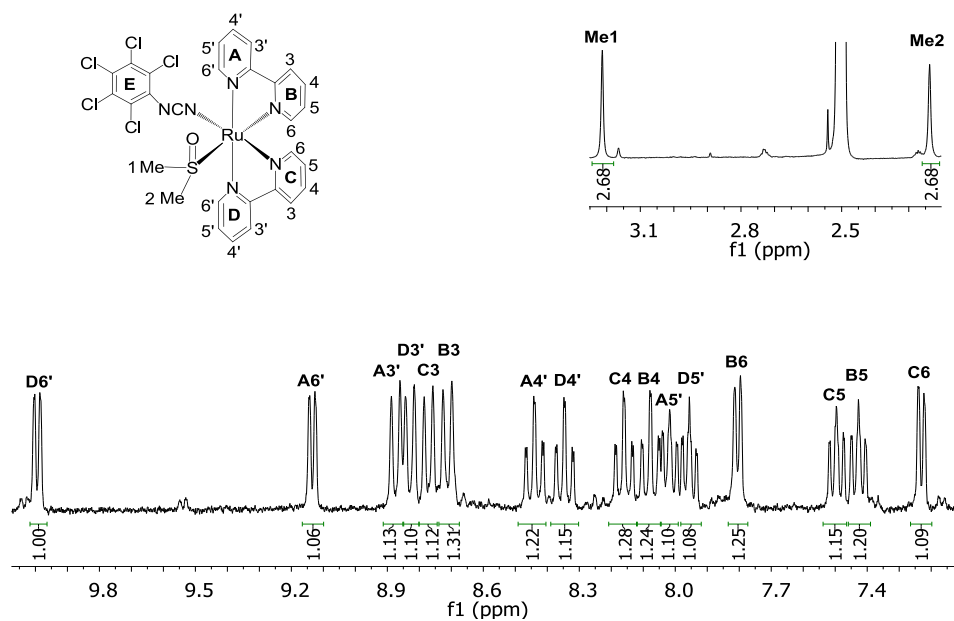


Figure 4.3.10: ^1H NMR spectrum of $\text{cis-}[\text{Ru}(\text{bpy})_2(\text{Cl}_5\text{pcyd})(\text{dms0-S})][\text{PF}_6]$ complex (4f) in $\text{DMSO-}d_6$.

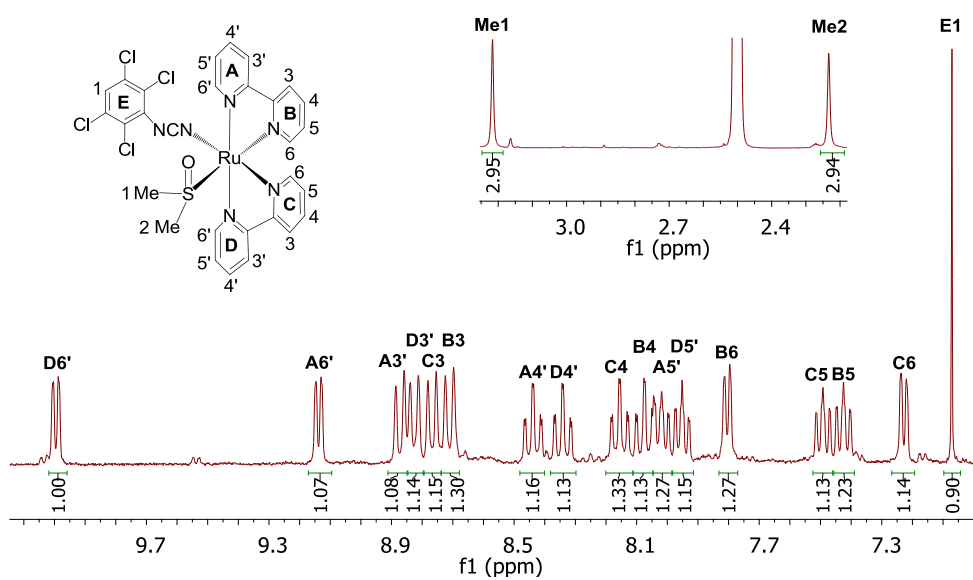


Figure 4.3.11: ^1H NMR spectrum of $\text{cis-}[\text{Ru}(\text{bpy})_2(\text{Cl}_4\text{pcyd})(\text{dms0-S})][\text{PF}_6]$ complex (4e) in $\text{dms0-}d_6$.

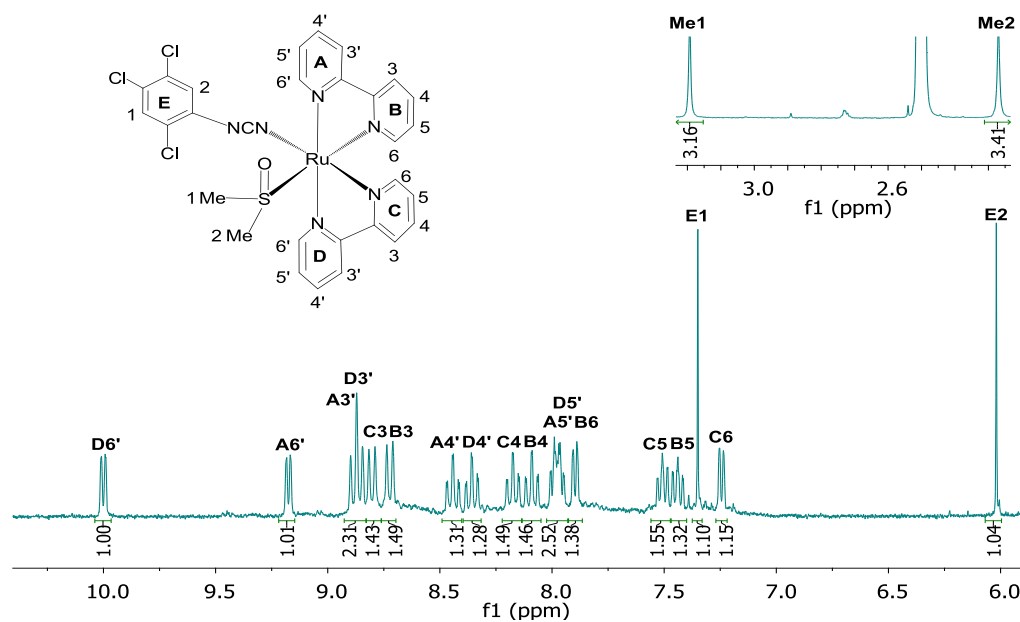


Figure 4.3.12: ^1H NMR spectrum of *cis*-[Ru(bpy) $_2$ (Cl $_3$ pcyd)(dmsO-S)]PF $_6$ complex (4d) in $\text{dmsO-}d_6$.

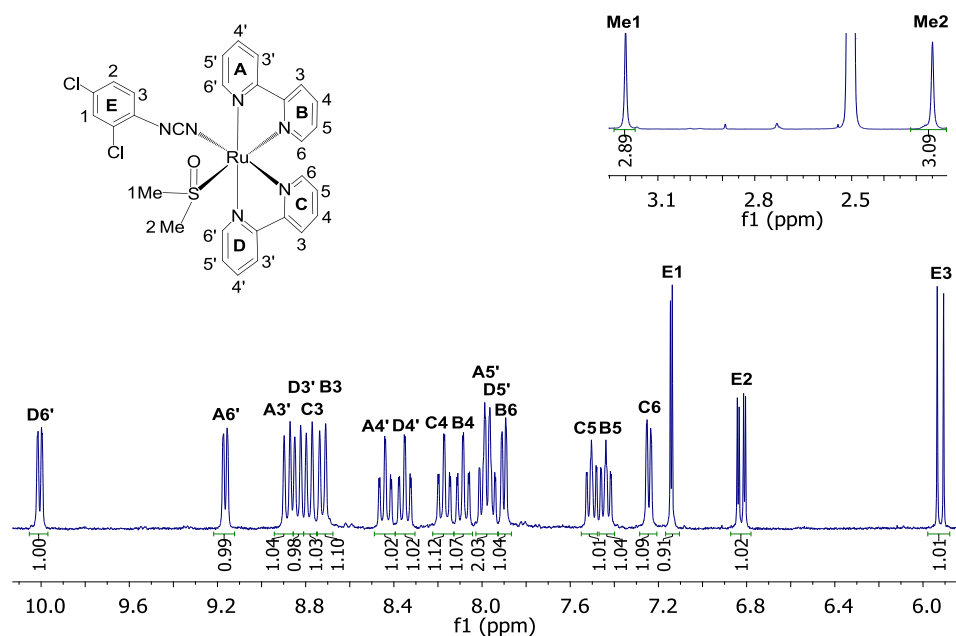


Figure 4.3.13: ^1H NMR spectrum of *cis*-[Ru(bpy) $_2$ (Cl $_2$ pcyd)(dmsO-S)]PF $_6$ complex (4c) in $\text{dmsO-}d_6$.

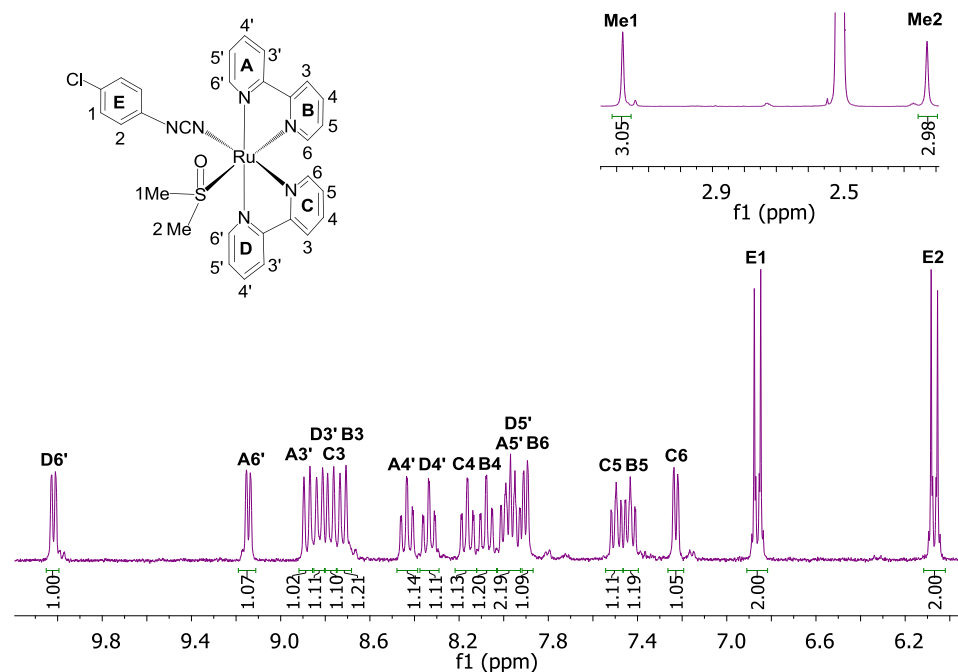


Figure 4.3.14: ^1H NMR spectrum of $\text{cis-}[\text{Ru}(\text{bpy})_2(\text{Clpcyd})(\text{dmsos})]^+[\text{PF}_6]^-$ complex (4b) in $\text{dms-}d_6$.

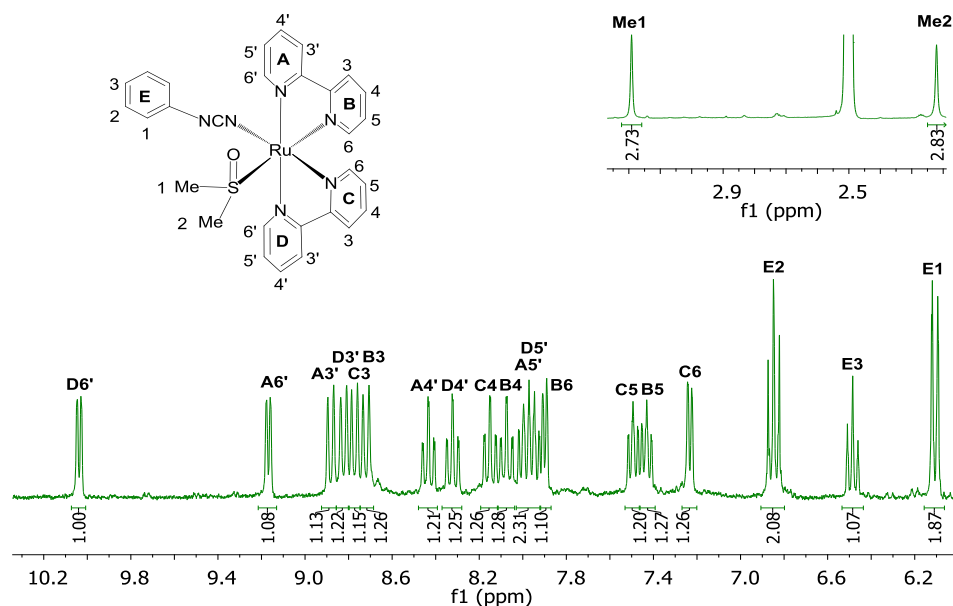


Figure 4.3.15: ^1H NMR spectrum of $\text{cis-}[\text{Ru}(\text{bpy})_2(\text{dmsos})(\text{pcyd})]^+[\text{PF}_6]^-$ complex (4a) in $\text{dms-}d_6$.

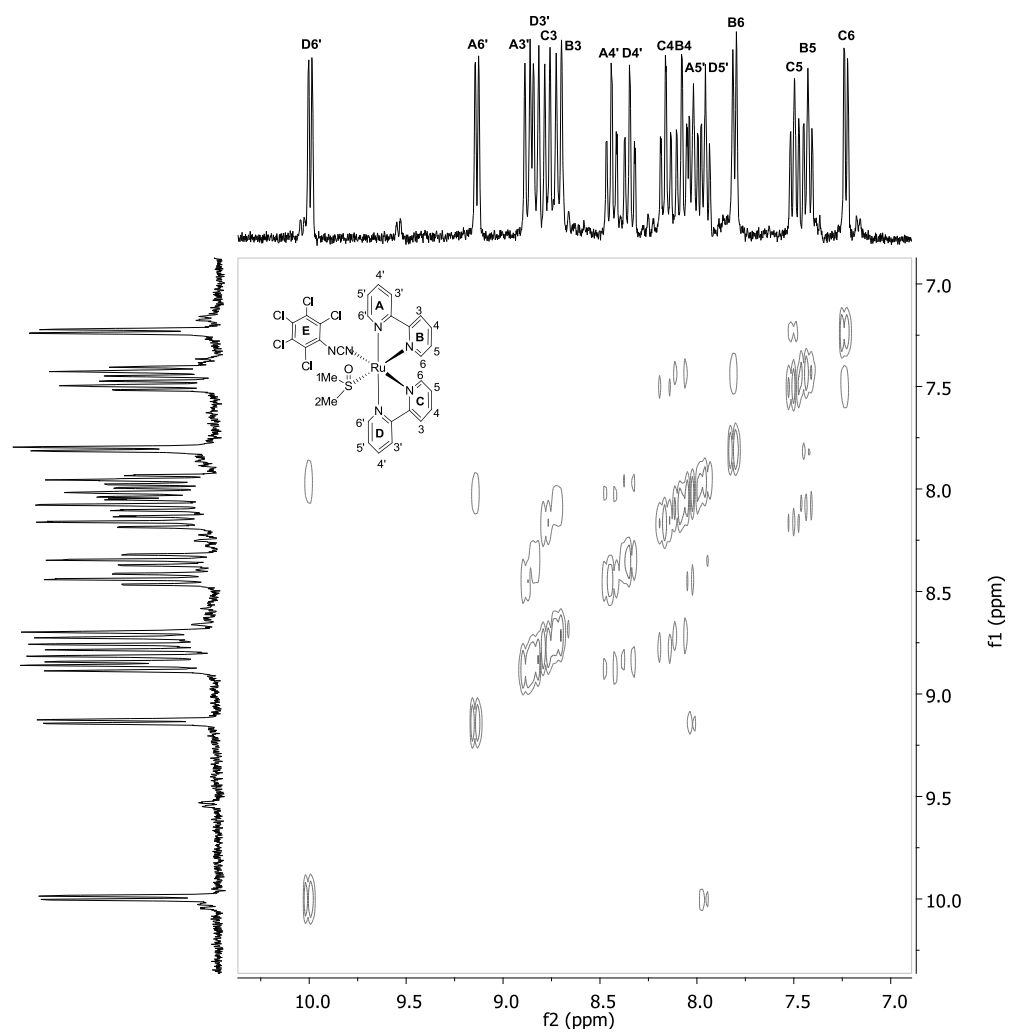


Figure 4.3.16: ^1H - ^1H COSY spectrum of *cis*-[Ru(bpy) $_2$ (Cl $_3$ pcyd)(dms0-S)][PF $_6$] complex (**4f**) in dms0- d_6 .

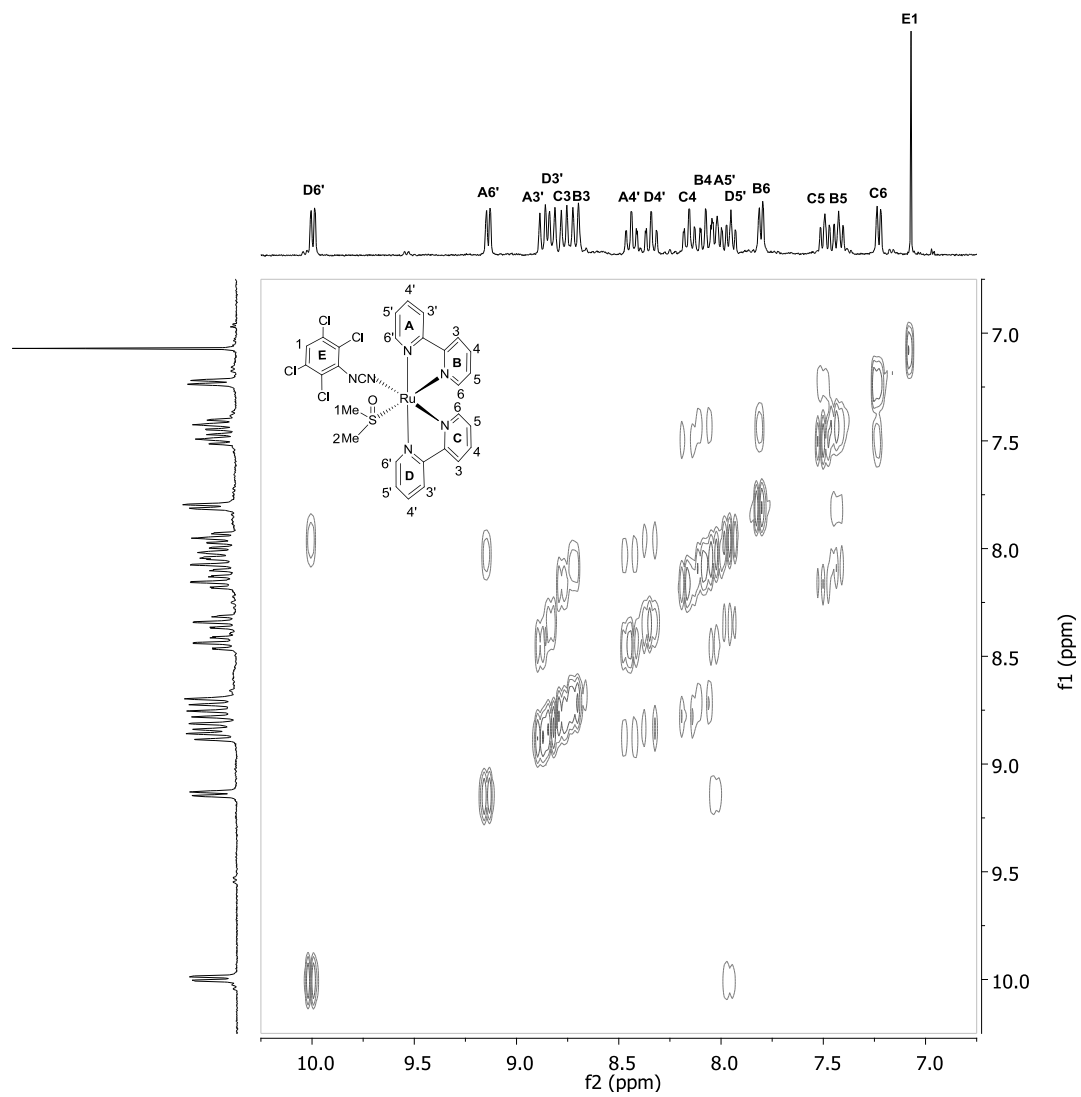


Figure 4.3.17: ^1H - ^1H COSY spectrum of *cis*-[Ru(bpy)₂(Cl₄pcyd)(dmsoS)]PF₆ complex (4e) in dmsO-*d*₆.

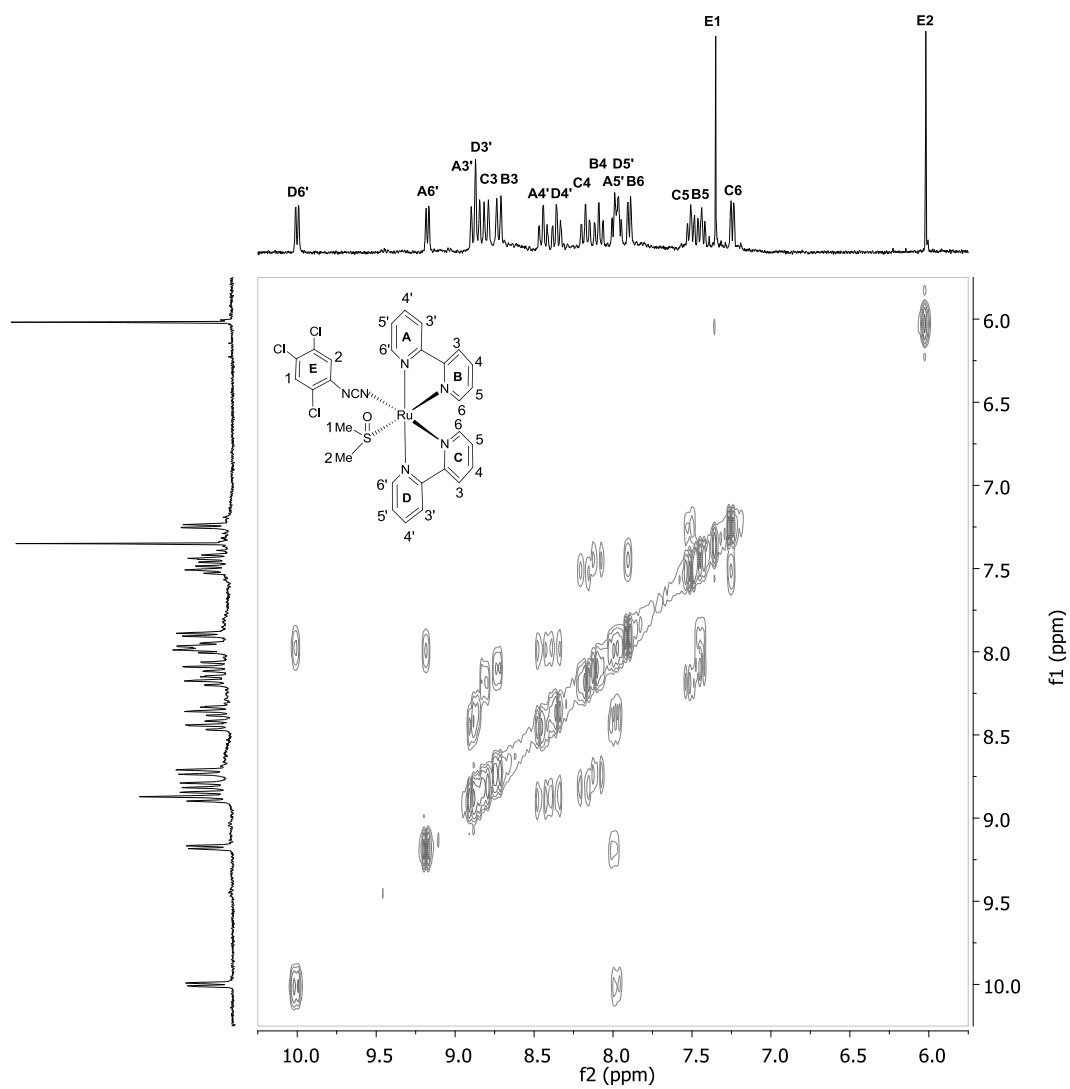


Figure 4.3.18: ^1H - ^1H COSY spectrum of *cis*-[Ru(bpy)₂(Cl₃pcyd)(dmsoS)]PF₆ complex (**4d**) in dmsO-*d*₆.

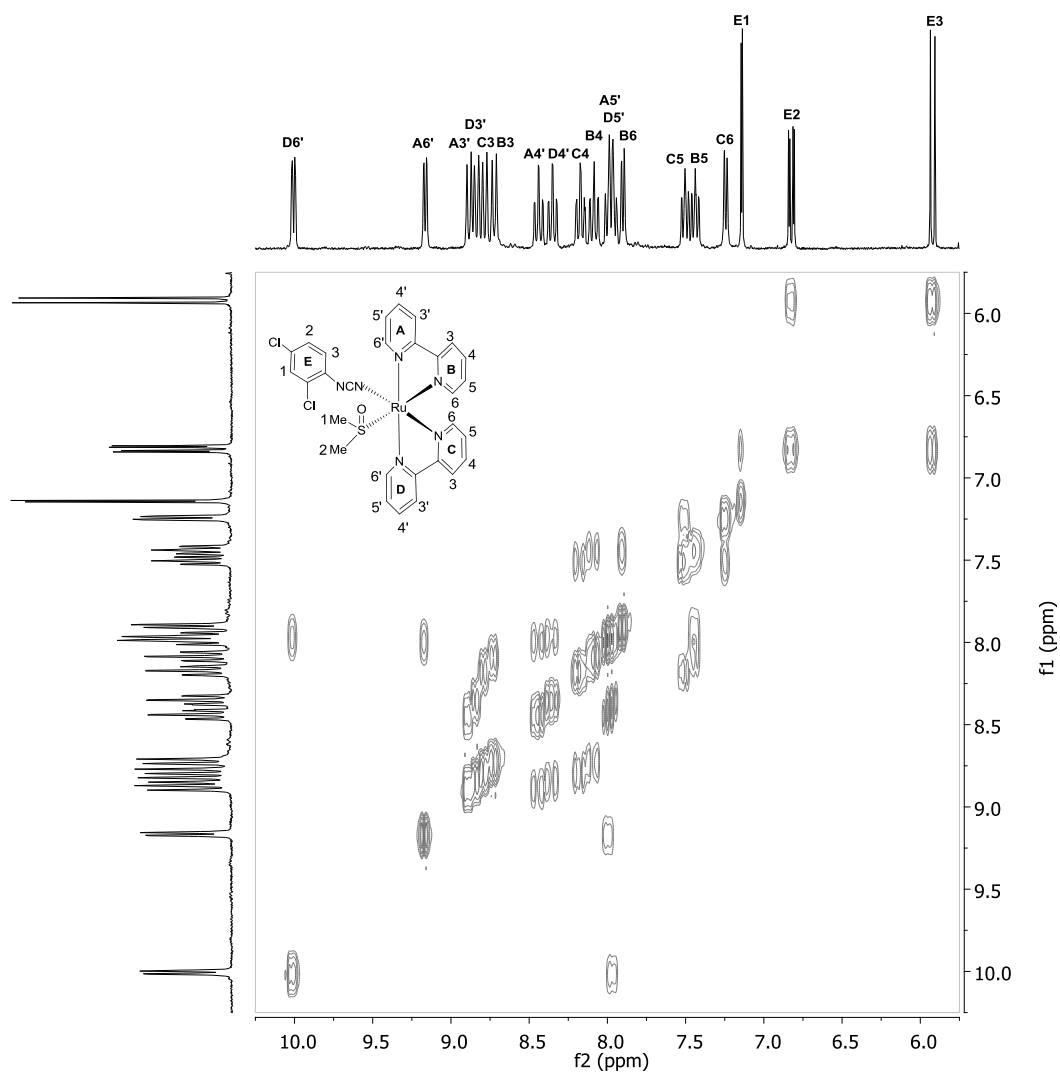


Figure 4.3.19: ^1H - ^1H COSY spectrum of *cis*-[Ru(bpy)₂(Cl₂pcyd)(dmsO-S)]PF₆ complex (4c) in dmsO-*d*₆.

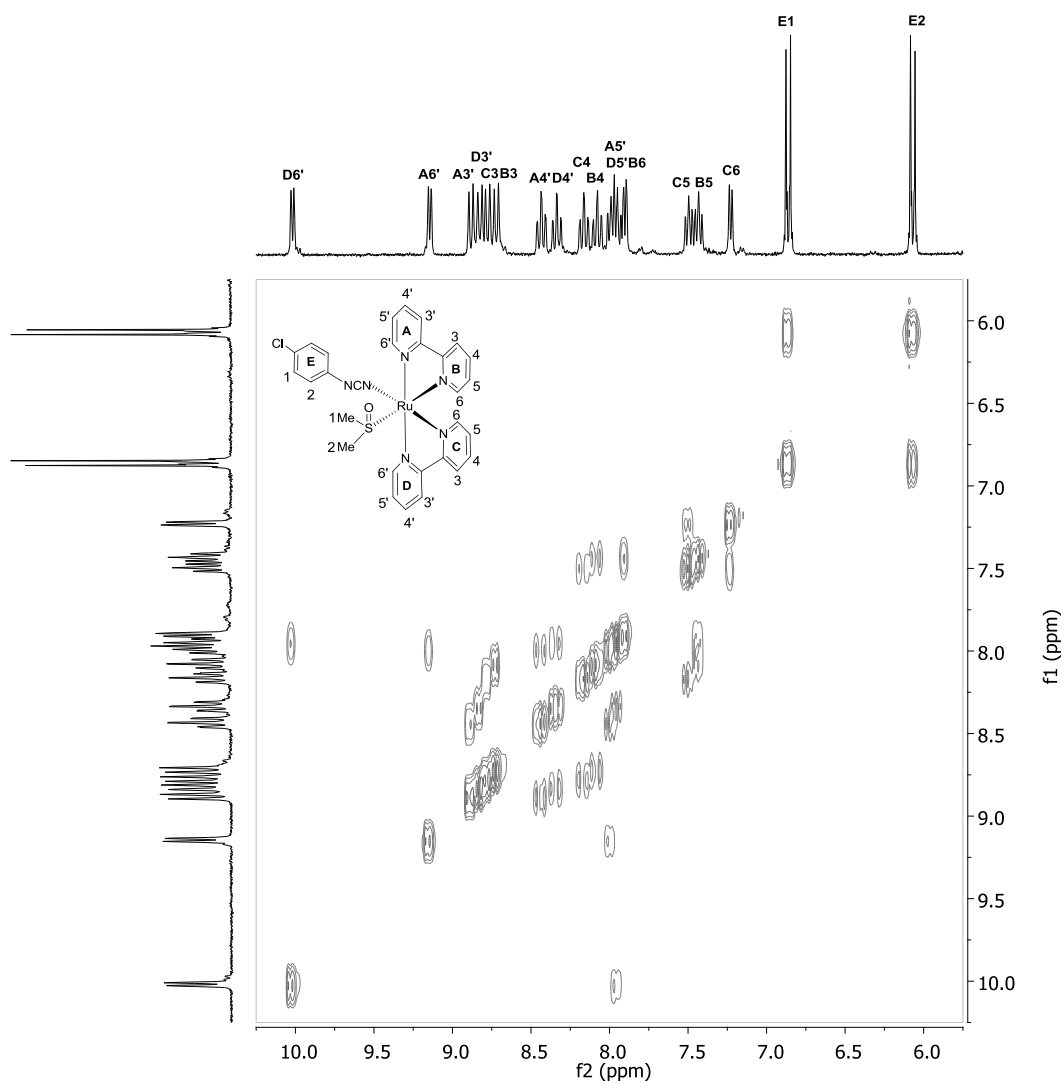


Figure 4.3.20: ^1H - ^1H COSY spectrum of *cis*-[Ru(bpy)₂(Clpcyd)(dmsO-S)] [PF₆] complex (4b) in dmsO-*d*₆.

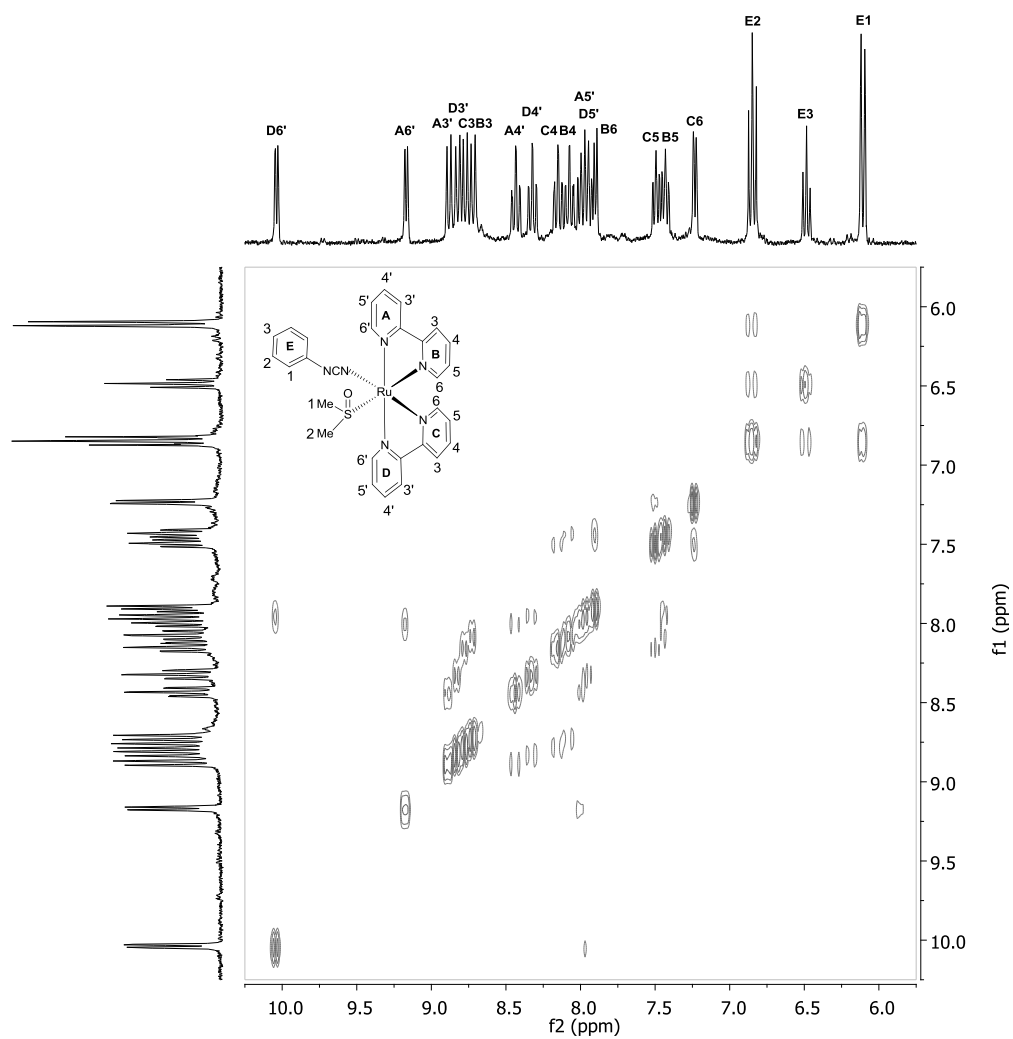


Figure 4.3.21: ^1H - ^1H COSY spectrum of *cis*-[Ru(bpy)₂(pcyd)(dmsoS)]PF₆ complex (**4a**) in dms-*d*₆.

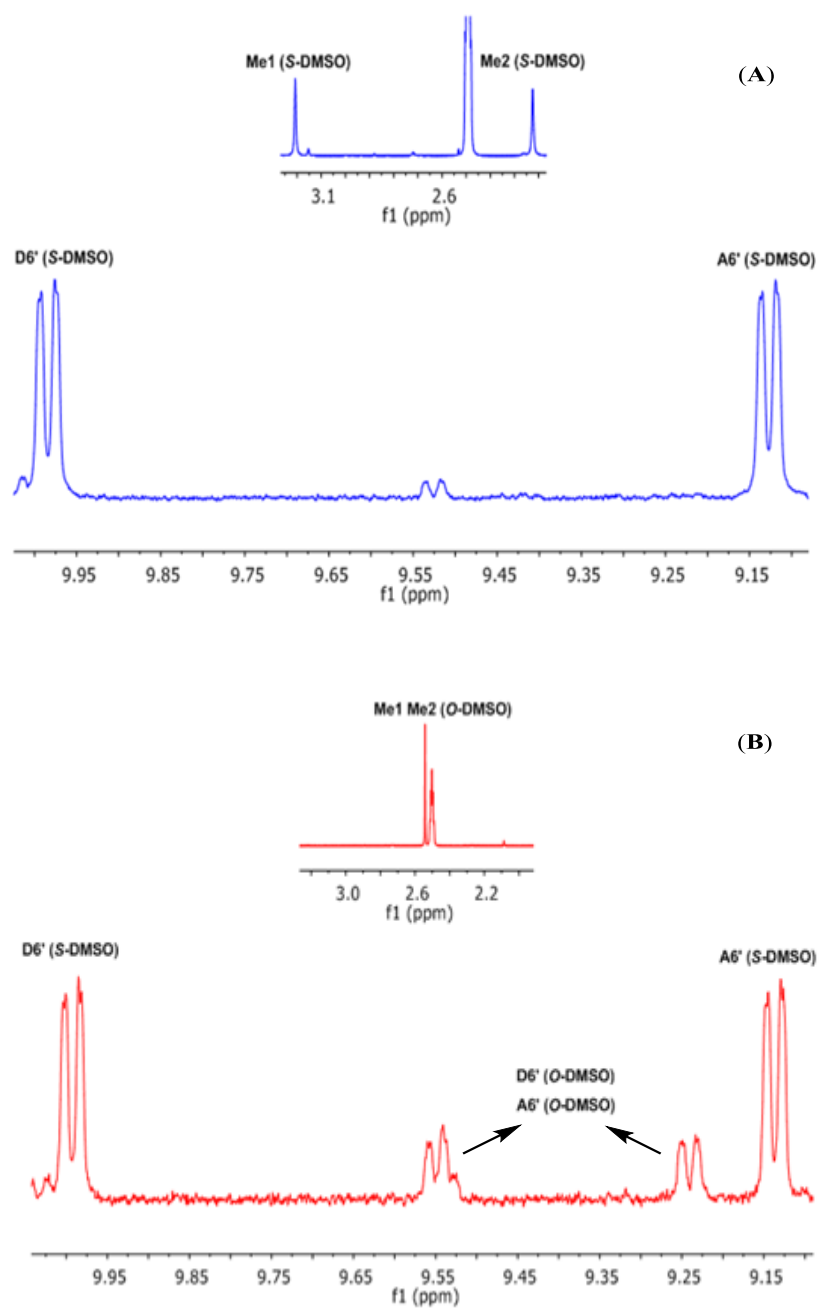


Figure 4.3.22: ^1H NMR spectra of $[\text{Ru}(\text{bpy})_2(\text{Cl}_4\text{pcyd})(\text{dmsO})][\text{PF}_6]$ complex (4e) in $\text{dmsO}-d_6$ (A) initial S-isomer (blue), (B) partially photolyzed (red).

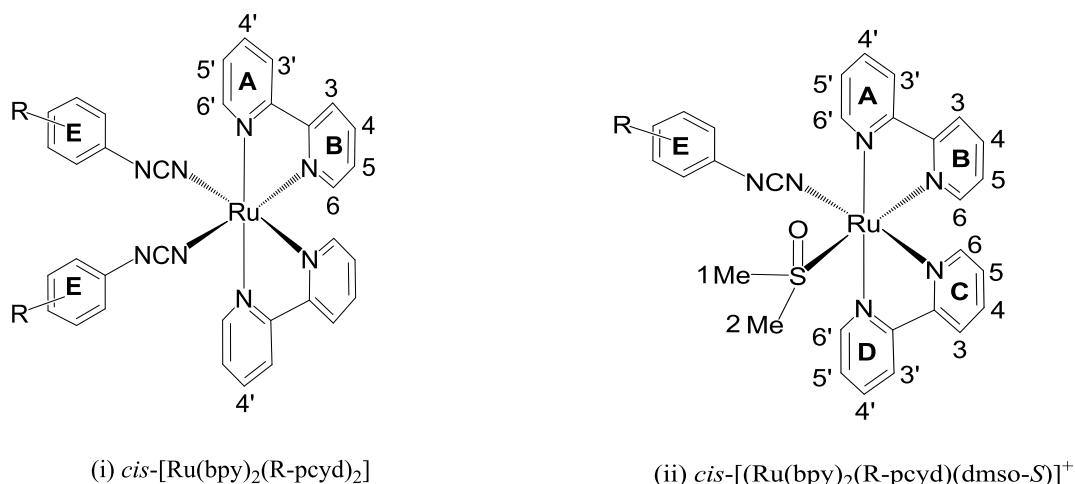


Figure 4.3.23: Numbering schemes used for the assignment of bpy and dmsO proton resonances in (i) precursor $cis\text{-}[\text{Ru}(\text{bpy})_2(\text{R}\text{-pcyd})_2]$ and (ii) $[\text{Ru}(\text{bpy})_2(\text{R}\text{-pcyd})(\text{dmsO}\text{-S})]^+$ complexes (**4a-4f**).

of the other bpy ligand and hence is shielded by 1-3 ppm, depending on the electronic nature of the system.^{52e-g} This leaves the assignment of the most *downfield* peak to A6' while the other *downfield* peak near δ 7.6 ppm is assigned to B6 protons. The A3' and B3 protons on bpy ligands have been cited to experience deshielding due to through-space steric interaction and are recognized by characteristic coupling constant values ($J \approx 8.1\text{-}8.6$).^{52c-d} Accordingly, the signals at δ 8.88 ppm and δ 8.72 ppm were assigned to A3' and B3 protons, respectively. The remainder protons A4', A5', B4, and B5 were readily assigned from the observed coupling pattern in the COSY spectrum.

The ^1H NMR spectra of $cis\text{-}[\text{Ru}(\text{bpy})_2(\text{R}\text{-pcyd})(\text{dmsO}\text{-S})][\text{PF}_6]$ complexes (**4a-4f**) are characterized a total of sixteen signals consisting of eight doublets and eight triplets in the low-field region between δ 7.23 and δ 10.02 ppm for bpy protons, which indicates non-equivalence of four pyridine rings (A,B,C,D) corresponding the *cis* geometry of two bpy ligands. Two equal integration singlets in the aliphatic region of the

spectra, one in the *downfield* (δ 3.19-3.22 ppm) and the other in the *upfield* (δ 2.22-2.27 ppm) region, have been assigned to two non-equivalent methyl groups on the coordinated dmso. On the other hand, the signals for phenyl protons on R-pcyd ligands were well-separated from those of bpy ligands and could be easily recognized in the region between δ 5.92 and δ 7.35 ppm.

The ^1H NMR spectral patterns of coordinated bpy and dmso ligands in complexes (**4a-4f**) are very similar to those in *cis*-[Ru(bpy)₂(dmso-*S*)Cl][PF₆] complex, in terms of the number of peaks and their chemical shift values and assigned accordingly.^{52a-b} Like the precursor complex *cis*-[Ru(bpy)₂(R-pcyd)₂], the coupling constant values of two most down-field doublets (δ 10.1-9.65 ppm) in the ^1H NMR spectra of **4a-4f** indicate that they belong to H6/H6' protons ($J = 5.1$ ppm) rather than to H3'/H3 protons ($J = 8.1$ ppm).^{52c-g} The B6 and C6 protons experience shielding by the anisotropic ring current of the underlying pyridine rings C and B,^{52c-g} suggesting the assignment of most downfield doublet signals to A6'/D6 protons. By analogy with complex *cis*-[Ru(bpy)₂(dmso-*S*)Cl][PF₆], we assigned the most downfield signal (~ 10.1 ppm) to D6 and the signal at 9 ppm to A6' protons.^{52a} The next four doublets (δ 8.87-8.72 ppm) were identified as D3'/A3'/B3/C3 protons by their characteristic coupling constant values ($J \sim 8.1$ Hz), as cited for H3/H3' protons on coordinated bpy ligands^{52c-d} and assigned from the coupling pattern observed in the COSY spectrum. The remainder of the signals was simply assigned by peak integrations, coupling constant values and correlation by COSY spectroscopy.

The assignment of phenyl protons were made with the help of COSY spectra and the corresponding chemical shifts were compared with those reported for other ruthenium-polypyridyl-phenylcyanamide complexes.⁴²⁻⁴⁴

Like *cis*-[Ru(bpy)₂(dms-*S*)Cl][PF₆], the two methyl groups on dms-*S* ligand in **4a-4f** showed non-equivalence with their chemical shift values, one appearing more *downfield* (δ 3.22-3.19 ppm for Me₂) while the other more *upfield* (δ 2.27-2.22 ppm for Me₁), relative to those on free dms-*S* (δ 2.52 ppm). The X-ray crystal structure^{41a,b} of the complex *cis*-[Ru(bpy)₂(dms-*S*)Cl]⁺ as well as the geometry optimized structure (Figure 4.3.1 a) of **4a** show that one of the methyl groups (Me₂) experiences the shielding effect of the anisotropic ring current of the pyridine rings C and D, while the other (Me₁) pointing towards the Cl / phenylcyanamide ligands, resulting in non-equivalence in their chemical shift values.

Upon partial photolysis of the ¹H NMR dms-*d*₆ solution of the *S*-bonded Cl₄pcyd complex (**4e**), the initial yellow solution turned red and two signals for methyl groups merged to a sharp singlet at δ 2.54 ppm (close to the residual solvent peak in DMSO-*d*₆), with a significant decrease in the separation between two most down field signals (D6' and A6') (Figure 4.3.23). The color (red) of the solution is indicative of S→O linkage isomerism (discussed below) and so the ¹H NMR spectral change in the aliphatic region can be ascribed to the formation of the *O*-bonded isomer in which two methyl groups on the dms-*S* ligand become equivalent as a result of linkage isomerism. Indeed, DFT calculated geometry optimized structure of the *O*-bonded complex *cis*-[Ru(bpy)₂(pcyd)(dms-*O*)] shows the equivalence of two methyl groups on the dms-*O* ligand (Figure 4.3.1 b). Similar spectral shift of methyl protons were observed upon

photo-irradiation of the initial *S*-bonded isomer of $cis\text{-}[\text{Ru}(\text{bpy})_2(\text{dmsO})_2]^{2+}$ complex in the deuterated dmsO and was attributed the formation of the *O*-bonded isomer.^{11,12} The spectral variation in the low field region (separation between D6' and A6') in the Figure 4.3.23 may be the consequence of both electronic and steric factors that changed upon linkage isomerism.

4.3.6 Electronic Absorption Spectroscopy and Photo-induced Linkage Isomerism

The solutions of complexes $cis\text{-}[\text{Ru}(\text{bpy})_2(\text{R-pcyd})(\text{dmsO-S})][\text{PF}_6]$ (**4a-4f**) are photochromic and in ambient light readily undergo significant photo-induced linkage $\text{S} \rightarrow \text{O}$ isomerism which can be monitored by electronic absorption spectroscopy. The metastable $cis\text{-}[\text{Ru}(\text{bpy})_2(\text{R-pcyd})(\text{dmsO-O})]^+$ complexes slowly revert back to $cis\text{-}[\text{Ru}(\text{bpy})_2(\text{R-pcyd})(\text{dmsO-S})]^+$ with first-order rate k_{OS1} (Figure 4.3.24).

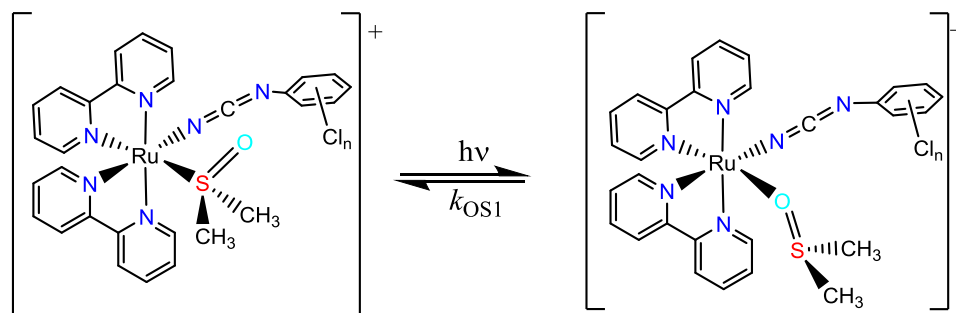


Figure 4.3.24: Photo-induced $\text{S} \rightarrow \text{O}$ and thermal $\text{O} \rightarrow \text{S}$ linkage isomerism of $cis\text{-}[\text{Ru}(\text{bpy})_2(\text{R-pcyd})(\text{dmsO-S})]^+$ complexes (**4a-4f**).

The photochromic nature of complexes **4a-4f** is very similar to previously reported $[\text{Ru}(\text{tpy})(\text{L2})(\text{dmsO-S})]$ complexes, where L2 is a bidentate ligand.^{14,16,21,25}

Electronic Absorption Spectroscopy

The quantitative electronic absorption spectra of both *S*- and *O*-bonded isomers of complexes $[\text{Ru}(\text{bpy})_2(\text{R-pcyd})(\text{dmsO})][\text{PF}_6]$ (**4a-4f**) were recorded in their dmsO solutions. The spectra for the *O*-bonded isomers were recorded after complete photolysis of the standard solutions of initial *S*-bonded isomers. The electronic absorption data of both *S*- and *O*-bonded complexes $[\text{Ru}(\text{bpy})_2(\text{R-pcyd})(\text{dmsO-}S/O)][\text{PF}_6]$ are compiled in the Table 4.3.3 and representative absorption spectra of $[\text{Ru}(\text{bpy})_2(\text{Cl}_5\text{pcyd})(\text{dmsO-}S/O)][\text{PF}_6]$ complexes are shown in the Figure 4.3.25.

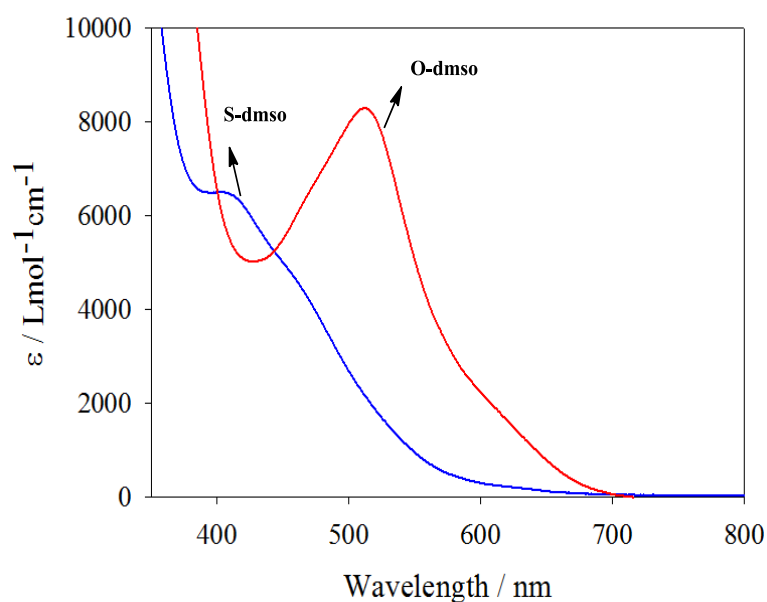


Figure 4.3.25: Quantitative electronic absorption spectra of *cis*- $[\text{Ru}(\text{bpy})_2(\text{Cl}_5\text{pcyd})(\text{dmsO-}S)][\text{PF}_6]$ (blue) and $[\text{Ru}(\text{bpy})_2(\text{Cl}_5\text{pcyd})(\text{dmsO-}O)][\text{PF}_6]$ (red) in dmsO.

The electronic absorption spectra of complexes $[\text{Ru}(\text{bpy})_2(\text{R-pcyd})(\text{dmsO-}S)]^+$ (**4a-4f**) are characterized by a sharp intense band in the UV region (284-294 nm, $\epsilon = 50,500\text{-}65,900 \text{ M}^{-1} \text{ cm}^{-1}$) and a fairly intense visible band at 400-406 nm, $\epsilon = 5200\text{-}6500$

Table 4.3.3: Electronic Absorption Data of *cis*-[Ru(bpy)₂(R-pcyd)(dmsO-S/O)][PF₆] Complexes in dmsO. R-pcyd is a Phenylcyanamide Ligand.

R-pcyd ⁻	Wavelength, λ / nm (Molar Extinction Coefficient, ϵ / M ⁻¹ cm ⁻¹)		
	dmsO-S	dmsO-O	Isosbestic Points
Cl ₅ pcyd ⁻	294 (61200), 405 (6500), 470 (s, 4100)	512 (8300)	398 (6500), 443 (5300)
Cl ₄ pcyd ⁻	296 (59900), 409 (6100), 465 (s, 4400)	506 (8000)	399 (6000), 444 (5100)
Cl ₃ pcyd ⁻	293 (62000), 405 (6200), 515 (s, 2930)	506 (6900)	396 (6400), 438 (5100)
Cl ₂ pcyd ⁻	288 (49500), 405 (5600), 470 (s, 3400)	513 (5900)	399 (5600), 439 (4500)
Clpcyd ⁻	287 (65900), 409 (5700), 468 (s, 3800)	505 (4300)	402 (5700), 444 (4600)
pcyd ⁻	284 (50500), 400 (5200), 470 (s, 3700)	517 (3700)	404 (5500), 431 (4700)

M⁻¹ cm⁻¹), with a weak shoulder at 470-515 nm in dmsO. The sharp intense band at 284-294 nm can be assigned to typical π to π^* transitions in bpy ligands.³³ The fairly intense visible band at 400-406 nm is at the typical position of Ru (II) $d\pi$ to π^* (bpy) metal-to-ligand charge transfer (MLCT) band of ruthenium-polypyridyl-sulfoxide-S complexes.¹⁴⁻²⁷ The MLCT energies showed little variation with the number of chloro-substituents on phenylcyanamide ligand, indicating an insignificant effect of the π -donor properties of

phenylcyanamide ligands on the relative energies of Ru(II) $d\pi$ and $bpy-\pi^*$ orbitals. Upon photo-irradiation of the initial *S*-bonded isomer, the MLCT band at 400-406 nm diminished with the development of a low energy band at 505-517 nm ($\epsilon = 8300-3700 \text{ M}^{-1} \text{ cm}^{-1}$), which is consistent with the formation of *O*-bonded isomer. By analogy other ruthenium-polypyridyl-sulfoxide complexes, we assign this band to Ru(II) $d\pi$ to π^* (*bpy*) metal-to-ligand charge transfer transition (MLCT) of the *O*-bonded isomers $[\text{Ru}(\text{bpy})_2(\text{R-}p\text{cyd})(\text{dmsO-}O)]^+$.¹⁴⁻²⁷

Photo-induced Linkage Isomerism

MLCT excitations of *cis*- $[\text{Ru}(\text{bpy})_2(\text{R-}p\text{cyd})(\text{dmsO-}S)][\text{PF}_6]$ complexes (**4a-4f**) using blue light ($450 \pm 20 \text{ nm}$ from the LED light source) induced *S*→*O* linkage isomerism in solution (dmsO, propylene carbonate) as well as on PMMA polymer films and the photogenerated *O*-bonded isomers slowly reverted back (*O*→*S* linkage isomerism) to the initial *S*-bonded isomer with rates k_{OS1} . Spectral changes are represented by those of $[\text{Ru}(\text{bpy})_2(\text{Cl}_5p\text{cyd})(\text{dmsO-}S)][\text{PF}_6]$ and are shown in the Figure 4.3.26-4.3.31. The quantum yields ($\Phi_{\text{S} \rightarrow \text{O}}$) of photo induced *S*→*O* linkage isomerism were measured in dmsO and calculated by using Eq. 4.2.4. The thermal *O*→*S* back reactions rates k_{OS1} for all complexes (**4a-4f**) were measured in dmsO and calculated by using Eq. 4.2.6. The thermal *O*→*S* back reaction rates were also measured in propylene carbonate and solid PMMA polymer film for the complex $[\text{Ru}(\text{bpy})_2(\text{dmsO})(\text{Cl}_5p\text{cyd})][\text{PF}_6]$ (**4f**) and reported here for comparison. The results of both quantum yield ($\Phi_{\text{S} \rightarrow \text{O}}$) measurements and thermal back reactions rates (k_{OS1}) are compiled in the Table 4.3.4. The experimental and derived data for a representative

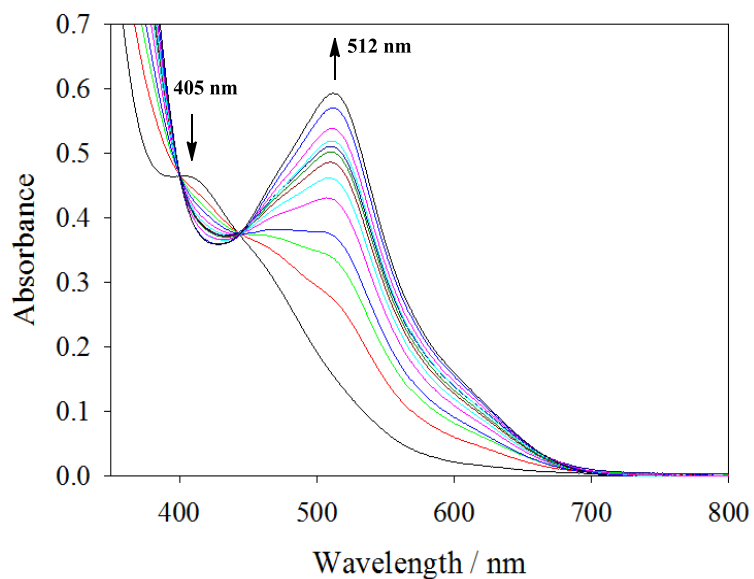


Figure 4.3.26: Photo-induced S→O isomerization of *cis*-[Ru(bpy)₂(Cl₅pcyd)(dms-*S*)]⁺[PF₆]⁻ complex (**4f**) in dms-*S* showing gradual depletion of the 405 nm band of the *S*-bonded isomer with concomitant development of a band at 512 nm for the *O*-bonded isomer. Irradiation time: 0-120 s.

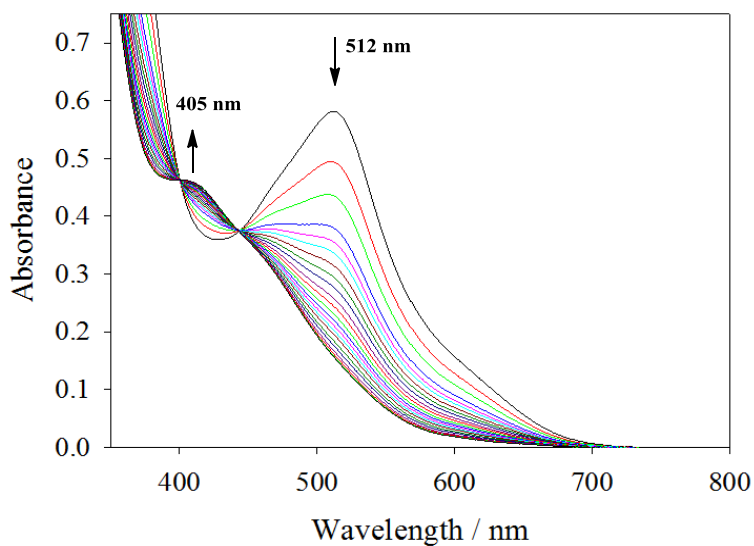


Figure 4.3.27: Thermal O→S isomerization of photogenerated *cis*-[Ru(bpy)₂(Cl₅pcyd)(dms-*O*)]⁺[PF₆]⁻ complex in dms-*O* with gradual depletion of the 512 nm band of the *O*-bonded isomer with concomitant development of the 405 nm band of the *S*-bonded isomer. Reaction time: 0-1498 s.

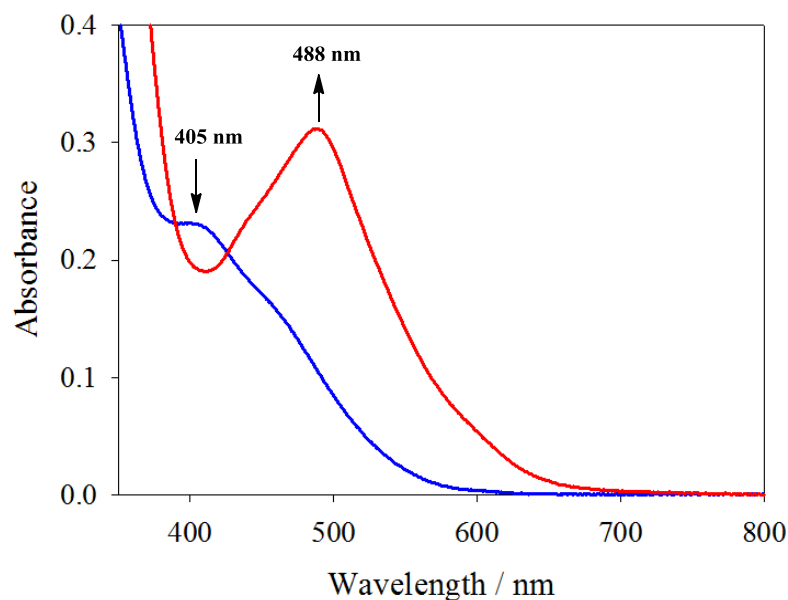


Figure 4.3.28: Photo-induced S→O isomerization of *cis*-[Ru(bpy)₂(Cl₅pcyd) (dmsO-S)]⁺ (**4f**) in propylene carbonate: time = 0, *cis*-[Ru(bpy)₂(Cl₅pcyd) (dmsO-S)]⁺ (blue line) and after 120 s irradiation, *cis*-[Ru(bpy)₂(Cl₅pcyd) (dmsO-O)]⁺ (red line).

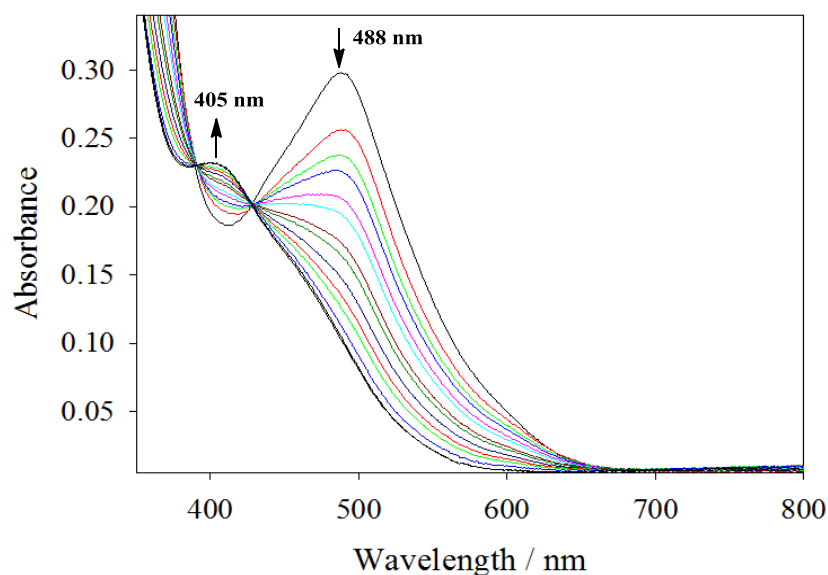


Figure 4.3.29: Thermal O→S isomerization of photogenerated *cis*-[Ru(bpy)₂(Cl₅pcyd) (dmsO-O)][PF₆]⁻ complex in propylene carbonate showing gradual depletion of the 488 nm band of the O-bonded isomer with concomitant development of the 405 nm band of the S-bonded isomer. Reaction time: 0-11700 s.

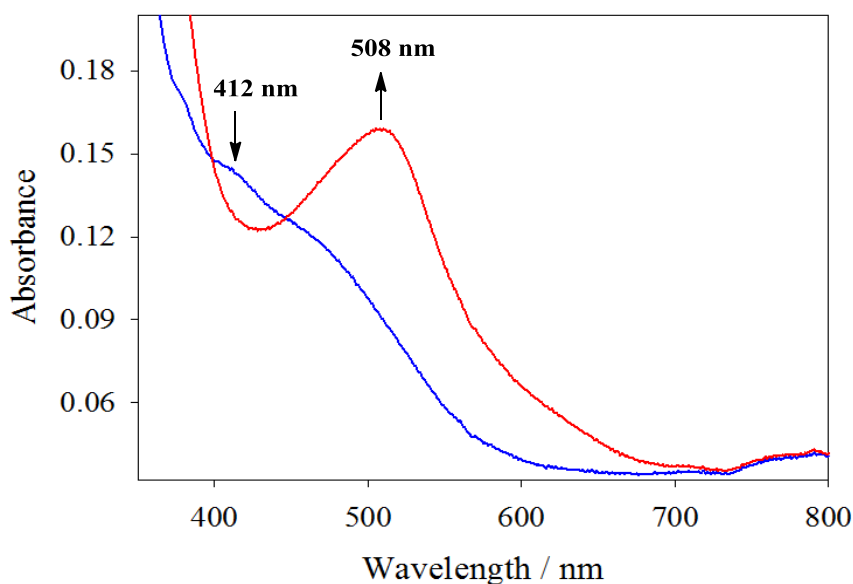


Figure 4.3.30: Photo-induced S→O isomerization of cis -[Ru(bpy)₂(Cl₅pcyd)]⁺ (**4f**) in PMMA polymer film: time = 0, cis -[Ru(bpy)₂(Cl₅pcyd)]⁺ (blue line) and after 120 s irradiation, cis -[Ru(bpy)₂(Cl₅pcyd)]⁺ (dmsO-*O*)⁺ (red line).

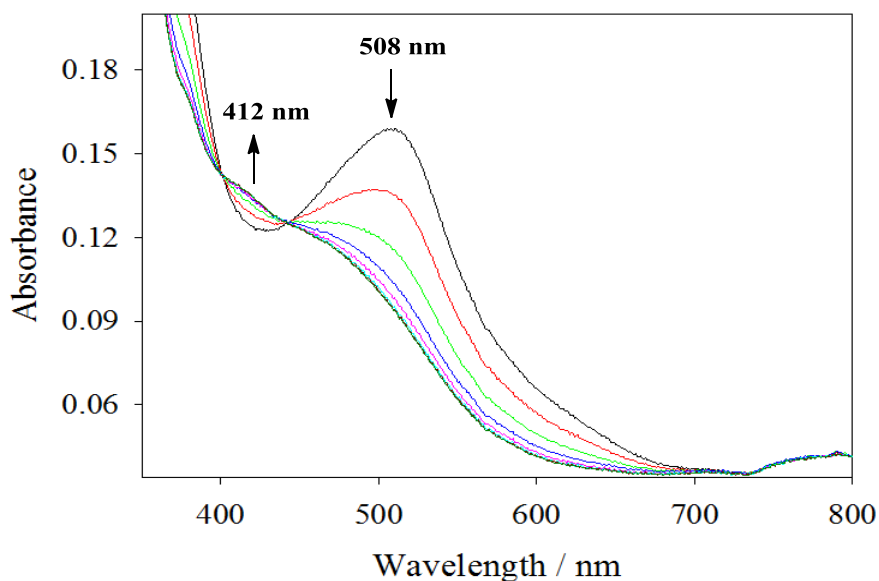


Figure 4.3.31: Thermal O→S isomerization of photogenerated cis -[Ru(bpy)₂(Cl₅pcyd)]⁺[PF₆]⁻ complex in PMMA polymer film showing gradual depletion of the 508 nm band of the *O*-bonded isomer with concomitant development of the 412 nm band of the *S*-bonded isomer. Reaction time: 0- 600 s.

Table 4.3.4: Photochemical Data of *cis*-[Ru(bpy)₂(R-pcyd)(dmsO)][PF₆] Complexes (**4a-4f**) in dmsO.

R-pcyd ⁻	Quantum Yield/ $\Phi_{S \rightarrow O}$	Thermal O→S Rates/ $k_{OS1} \times 10^3 /s$
Cl ₅ pcyd ⁻	0.43 (± 0.01)	2.61 ± 0.03 (0.19± 0.03) ^a (2.41±0.01) ^b
Cl ₄ pcyd ⁻	0.34 (±0.005)	2.31 ± 0.01
Cl ₃ pcyd ⁻	0.28 (±0.01)	2.41 ± 0.02
Cl ₂ pcyd ⁻	0.12 (±0.005)	2.84 ± 0.04
Clpcyd ⁻	0.10 (±0.005)	4.30 ± 0.07
pcyd ⁻	0.06 (±0.003)	4.50 ± 0.10

^aIn propylene carbonate. ^bIn PMMA polymer film

complex *cis*-[Ru(bpy)₂(dmsO)(Cl₅pcyd)][PF₆] (**4f**) are provided in the Table D.6-D.7 and corresponding plots are shown in Figure D.7-D.10 in the Appendix-D.

Charge transfer excitation of *cis*-[Ru(bpy)₂(R-pcyd)(dmsO-S)][PF₆] complexes (**4a-4f**) in solutions (dmsO, propylene carbonate) and in polymer film resulted in a gradual decrease in intensity of the MLCT band at 400-409 nm with the gradual development a low energy band at 505-517 nm in dmsO, 485 nm in propylene carbonate and 510 nm in PMMA film for the *O*-bonded isomer. The red *O*-bonded isomer thermally reverts back to the initial orange *S*-bonded isomers with the retention of isosbestic points, showing reversibility of the *S*→*O* and *O*→*S* linkage isomerization of dmsO in *cis*-[Ru(bpy)₂(R-pcyd)(dmsO-S)][PF₆] complexes (**4a-4f**). However, in highly donor and hydroxy solvents such as methanol, acetone, ethanol, acetonitrile the photo generated *O*-bonded isomers failed to regenerate the initial *S*-bonded isomers. Similar behavior was

observed after photoirradiation of $[\text{Ru}(\text{tpy})(\text{L2})(\text{dmsO})]^{n+}$ complexes in these hydroxyl and donor solvents and it was attributed to the formation of solvent adducts following the S→O isomerization.¹⁴ However, like $[\text{Ru}(\text{tpy})(\text{L2})(\text{dmsO})]^{n+}$ complexes, the photo-induced S→O and O→S linkage isomerism of complexes *cis*- $[\text{Ru}(\text{bpy})_2(\text{R-pcyd})(\text{dmsO-S})][\text{PF}_6]$ complexes (**4a-4f**) are reversible in other non-coordinating solvents propylene carbonate, chloroform, and in solid PMMA polymer films, suggesting that the linkage isomerism occurs *intramolecularly* in *cis*- $[\text{Ru}(\text{bpy})_2(\text{R-pcyd})(\text{dmsO-S})][\text{PF}_6]$ complexes (**4a-4f**).¹⁴

The quantum yields of photo-induced S→O isomerization of *cis*- $[\text{Ru}(\text{bpy})_2(\text{R-pcyd})(\text{dmsO-S})][\text{PF}_6]$ complexes (**4a-4f**) in dmsO are quite large and decreased dramatically with a decrease in the number of chloro-substituents on the phenylcyanamide ligand ($\Phi = 0.43-0.06$) (Table 4.3.4). The values are at least one order of magnitude larger than similar non-chelating dmsO complexes $[\text{Ru}(\text{tpy})(\text{L2})(\text{dmsO})]^{n+}$ and comparable to complexes containing chelating sulfoxides.^{12,14,16,20,26} The large quantum yield values indicate efficient conversion of photonic energy to potential energy that drives the following S→O isomerization in *cis*- $[\text{Ru}(\text{bpy})_2(\text{R-pcyd})(\text{dmsO-S})][\text{PF}_6]$ complexes. The dramatic variation in quantum yields that is observed in this family of complexes must be associated with the π -donor property of the redox-active phenylcyanamide ligands that resulted in a significant perturbation of the electronic structure of the ruthenium ion affecting the S→O isomerization rates in the excited state.

The thermal O→S back-reactions of complexes **4a-4e** are relatively slow compared to the fast excited state S→O isomerization and the corresponding rate constants ($k_{\text{OS1}} = 2.61- 4.50 \times 10^{-3} \text{ s}^{-1}$ in Table 4.3.4) are of the same order of magnitude

as those of $[\text{Ru}(\text{tpy})(\text{L}2)(\text{dmsO})]^{n+}$ and other ruthenium-polypyridyl-sulfoxide complexes.¹⁴⁻²⁷ Unlike the quantum yields of S→O isomerization, the thermal O→S reaction rates follow an opposite trend with the electronic nature of phenylcyanamide ligands, decreasing as the π -donor strength of phenylcyanamide ligand decreases, however, the variation is not as dramatic as observed in quantum yield values of complexes **4a-4f**. The thermal back reaction rates of *cis*- $[\text{Ru}(\text{bpy})_2(\text{Cl}_5\text{-pcyd})(\text{dmsO-S})][\text{PF}_6]$ (**4f**) (Table 4.3.4) show only a moderate variation in dmsO, propylene carbonate and in the PMMA polymer film, of in PMMA film, which is consistent with the *intramolecular* nature of sulfoxide isomerism in ruthenium-polypyridyl sulfoxide complexes^{12,14}.

4.3.7 Cyclic Voltammetry and Redox-induced Linkage Isomerism

Cyclic voltammetry of complexes **4a-4f** were performed in dmsO and acetonitrile. The voltammetric data for the *O*-bonded isomers in dmsO were collected by partial photolysis of initial voltammetric solutions containing the *S*-bonded isomers. The voltammetric data of complexes **4a-4f** in dmsO and acetonitrile are compiled in the Table 4.3.5 and 4.3.6, respectively. The voltammograms of a representative complex *cis*- $[\text{Ru}(\text{bpy})_2(\text{Cl}_5\text{pcyd})(\text{dmsO-S})][\text{PF}_6]$ (**4f**) in dmsO and acetonitrile at scan rate 1.0 V/s are shown in the Figure 4.3.32 and 4.3.33, respectively. The scan rate dependent voltammograms of **4f** in acetonitrile are shown in the Figure 4.3.34. The voltammograms of other complexes (**4a-4e**) in dmsO and in acetonitrile are provided in the Figure D.3-D.6 in the Appendix-D.

Cyclic voltammograms of solutions of *cis*- $[\text{Ru}(\text{bpy})_2(\text{dmsO-S})(\text{R-pcyd})][\text{PF}_6]$ complexes (**4a-4f**) in dmsO are characterized by a quasi-reversible wave (E1) ranging

from 0.90 to 1.29 V vs. NHE, shifted positively as the number of chloro substituents increase on the phenylcyanamide ligand. The reversibility of this wave was found to increase with an increase in the number of chloro-substituents on the phenylcyanamide ligand. The unsubstituted pcyd⁻ complex (**4a**) showed the poorest reversibility for which only the potential of an anodic wave is reported (Table 4.3.5).

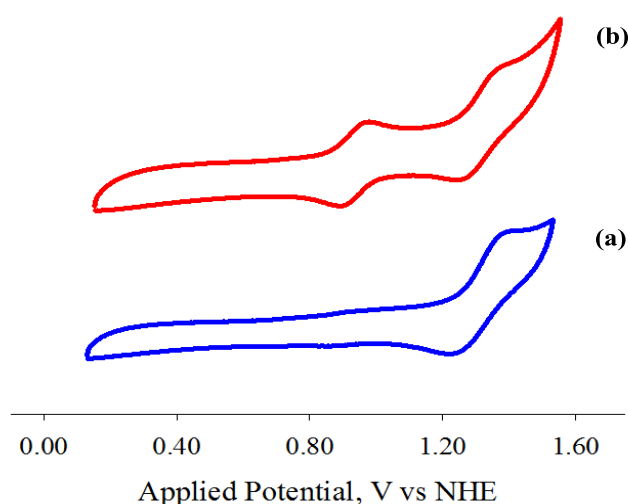


Figure 4.3.32: Cyclic voltammograms of *cis*-[Ru(bpy)₂(Cl₅pcyd)(dmsO-S)][PF₆] complex (**4f**) (a, blue) and after partial photolysis (b, red), in dmsO, 0.1 M TBAH, Scan rate 1.0 V/s.

However, unlike [Ru(tpy)(pic)(dmsO-S)]⁺,¹⁴ the oxidation wave of the E1 couple (Figure 4.3.32a, blue) did not generate any cathodic wave of Ru(III/II) couple for the *O*-bonded isomer within the potential window of the solvent dmsO. As DFT calculation shows that the spin on the singly oxidized *cis*-[Ru(bpy)₂(dmsO-S)(R-pcyd)]²⁺ complexes are located on the phenylcyanamide ligand (Figure 4.3.4 a), the E1 couple is assigned to L⁰/L⁻ couple of the phenylcyanamide ligand in the Ru(II)-dmsO(-S)-L⁻ complex. On the other hand, voltammograms obtained after partial photolysis of initial *S*-bonded complexes (**4a-4f**) in dmsO solutions exhibited a new quasi-reversible wave (E2) at 0.77-

Table 4.3.5: Cyclic Voltammetry Data of *cis*-[Ru(bpy)₂(R-pcyd)(dmsO)][PF₆] Complexes (**4a-4f**) in dmsO.^a

R-pcyd ⁻	Ru-(dmsO- <i>S</i>) isomer	Ru-(dmsO- <i>O</i>) isomer ^b	
	E1	E1	E2
Cl ₅ pcyd ⁻	1.29	1.29	0.90
Cl ₄ pcyd ⁻	1.27	1.27	0.89
Cl ₃ pcyd ⁻	1.23	1.23	0.89
Cl ₂ pcyd ⁻	1.16	1.16	0.86
Clpcyd ⁻	1.07	1.07	0.82
pcyd ⁻	0.90 ^c	0.90 ^c	0.77

^a In V vs. NHE, scan rate 1.0 V/s, in 0.1M TBAH, Fc⁺/Fc as internal reference, performed in the dark. ^b data obtained after irradiating the CV solutions of *S*-bonded complexes in dmsO, ^cirreversible, anodic wave reported.

0.90 V vs. NHE, in addition to the wave (E1) at 0.90-1.29 V (Figure 4.3.32 b, red). On the basis of DFT calculations (Figure 4.3.4 b), we also assign the E2 couple to L⁰/L⁻ couple of the non-innocent phenylcyanamide ligand on the Ru(II)-dmsO(-*O*)-L⁻ isomer.

In order to perform cyclic voltammetry at higher positive potential and observe the Ru(III/II) couple responsible for ground state S→O isomerism, cyclic voltammetry of complexes **4a-4f** were performed in acetonitrile. The cyclic voltammetry of complexes (**4a-4f**) in acetonitrile was complicated by either decomposition (Clpcyd⁻ and pcyd⁻ complexes, **4a-4b**) or poor reversibility (Cl₄pcyd⁻ complex, **4e**) at large positive potentials. However, Cl₅pcyd⁻ complex (**4f**) showed the highest stability and best reversibility among other complexes, while the Cl₃- and Cl₂pcyd⁻ complexes (**4d**, **4c**)

showed an intermediate stability and reversibility towards oxidation (Table 4.3.5). The electrochemical behavior of complexes (**4c**, **4d**, **4f**) in acetonitrile regarding redox-induced linkage isomerism is discussed here for *cis*-[Ru(bpy)₂(Cl₅pcyd)(dmsO-S)][PF₆] (**4f**). All potentials mentioned below are reported in V vs. NHE.

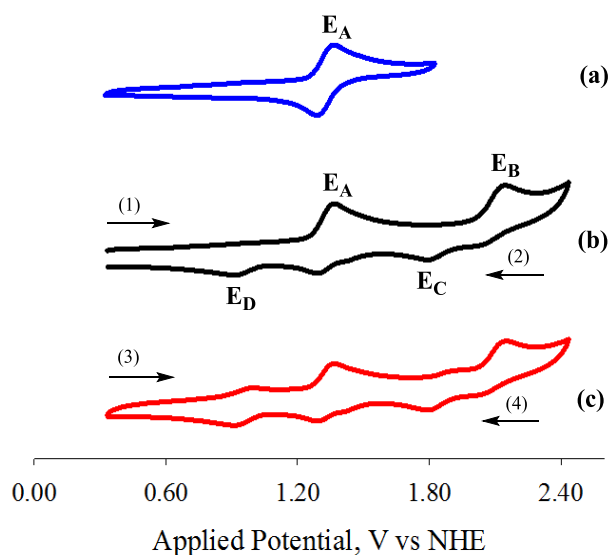


Figure 4.3.33: Cyclic voltammograms of *cis*-[Ru(bpy)₂(dmsO)(Cl₅pcyd)][PF₆] (**4f**) (a) scan range (0-1.80 V) (b) scan range (0-2.40 V), first redox cycle, (c) scan range (0.2-2.40 V), second redox cycle, in acetonitrile, 0.1 M TBAH, scan rate 1.0 V/s, arrows show scan direction, numbers show consecutive oxidative and reductive scans.

As seen in the Figure 4.3.32, the voltammogram (a, blue) of the complex **4f** in acetonitrile at scan rate 1.0 V only features the L⁰/L⁻ couple (E_A) of phenylcyanamide ligand at 1.31 V, which coincides well with the ligand couple obtained in dmsO. However, scanning towards more positive potentials, close to the solvent window of acetonitrile, resulted in additional redox waves in the voltammogram of the complex **4f** (b, black, c, red). The growth of these additional waves was completed in three consecutive oxidative-reductive-oxidative scans of two complete voltammetric cycles

Table 4.3.6: Cyclic Voltammetry Data of *cis*-[Ru(bpy)₂(R-pcyd)(dmsO)] Complexes (**4a-4f**) in Acetonitrile.^a

R-pcyd ⁻	Ru-(dmsO- <i>S</i>) isomer		Ru-(dmsO- <i>O</i>) isomer	
	E _A (V)	E _B (V)	E _C (V)	E _D (V)
Cl ₅ pcyd ⁻	1.31	2.09	1.79	0.95
Cl ₄ pcyd ⁻	1.30	2.22 ^b	-	-
Cl ₃ pcyd ⁻	1.24	2.02	1.69	0.95
Cl ₂ pcyd ⁻	1.15	1.93	1.71	0.90
Clpcyd ⁻	1.04 ^c	-	-	-
pcyd ⁻	1.01 ^b	-	-	-

^a In V vs. NHE, in acetonitrile, 0.1 M TBAH, scan rate 1.0 V/s, ^b irreversible, anodic peak potential. ^c partially reversible.

(labeled as steps 1, 2, 3 in the Figure 4.3.32 b-c). In the first cycle (b, black), scanning from 0.0 V to + 2.50 V (step 1) resulted in the oxidation wave of the reversible ligand couple L⁰/L⁻ couple (E_A) at 1.35 V, followed by an anodic wave of the irreversible couple (E_B) at 2.15 V. Reversing the polarity and scanning from +2.50 V to 0.0 V (step 2) resulted in a weak cathodic wave of the E_B couple at 2.02 V, followed by three cathodic waves at 1.79, 1.27 and 0.98 V for E_C, E_A and E_D couples, respectively. The anodic waves corresponding to the E_C and E_D couples are observed in the second cycle by reversing the polarity and scanning again from 0.0 V to +2.50 V (step 3). The scan rate dependent voltammograms (Figure 4.3.34) of the complex provided insight into the assignment of the additional waves (E_B, E_C, E_D), which could be interpreted by the redox-induced linkage isomerism shown in the Scheme 4.3.1.

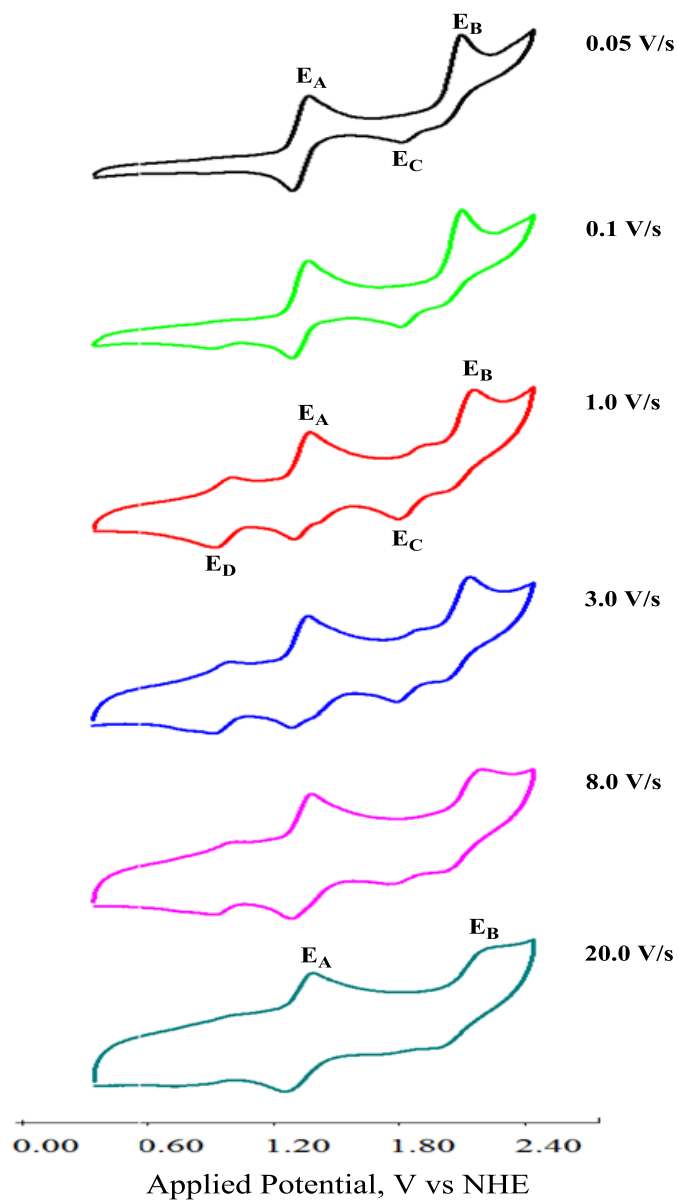
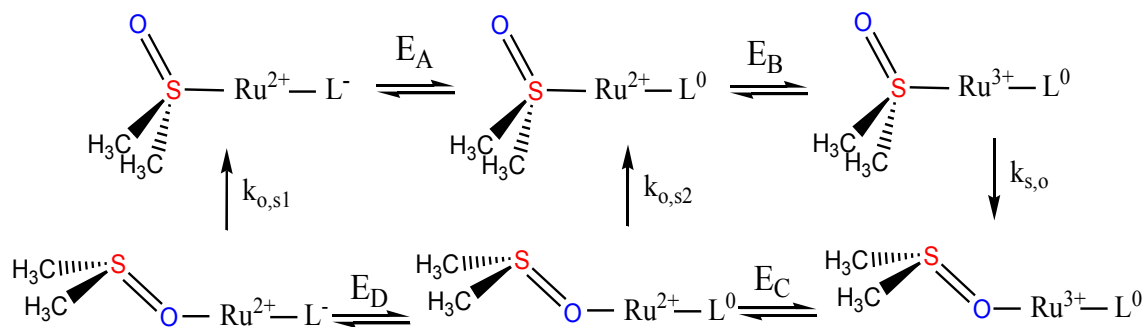


Figure 4.3.34: Cyclic voltammograms of *cis*-[Ru(bpy)₂(Cl₅pcyd)(dmsO-S)][PF₆] complex (4f) in acetonitrile, 0.1 M TBAH, at scan rates from 0.05 to 20 V/s.

Scheme 4.3.1: Assignment of the Redox Couples and Rates of Linkage Isomerism.

At all scan rates (0.05 V-20 V/s), the voltammograms (Figure 4.3.34) of the complex **4f** show a common feature in the initial anodic scans: an oxidation wave of the ligand couple L^0/L^- (E_A) at 1.35 V followed by an oxidation wave of the E_B couple at 2.15 V. We assign the more positive wave to the oxidation wave of the Ru(III/II) couple forming the *S*-bonded isomer Ru(III)-dms(-*S*)- L^0 . The position of this couple at such high energy is again consistent with greater stabilization of Ru(II) by π -back-bonding interaction with the dms and comparable to those reported for other ruthenium(II)-sulfoxide-*S* complexes.¹⁴ The Ru(III/II) couples (E_B) are irreversible at low scan rates (0.05- 8.0 V/s), which is consistent with the Ru(III) induced $\text{S} \rightarrow \text{O}$ isomerization (k_{SO}) of Ru(III)-dms(-*S*)- L^0 following the oxidation of Ru(II),¹⁴⁻²⁷ generating the *O*-bonded isomer Ru(III)-dms(-*O*)- L^0 , with the oxidized phenylcyanamide ligand L^0 (Scheme 4.3.1). At very low scan rate (0.05 V/s, Figure 4.3.34), the weak cathodic wave of the Ru(III/II) couple is followed by the cathodic waves of the E_C and E_A couples 1.79 V and 1.27 V, respectively. However, the reduction of the E_C couple must be followed by a chemical process that would recover the *S*-bonded complex Ru(II)-dms(-*S*)- L^0 in order to achieve a cathodic peak current of the L^0/L^- couple (E_A). This is consistent with the

reduction of Ru(III) on the *O*-bonded isomer Ru(III)-dmsO(-*O*)-L⁰ at 1.79 V forming the Ru(II)-dmsO(-*O*)-L⁰ species which then undergoes O→S isomerism with the rate k_{OS2} to generate the Ru(II)-dmsO(-*S*)-L⁰ species for the cathodic wave of the E_A couple (Scheme 4.3.1). This low scan rate data thus provided an estimation of $k_{OS2} \approx 0.2 \text{ s}^{-1}$ from the corresponding voltammogram. On the other hand, the cathodic wave (0.98 V) of the E_D couple is only observed at intermediate scan rates (0.1 V- 0.8 V/s) and appears at the similar position of the ligand couple (E₂ couple) of the photogenerated *O*-bonded isomer in dmsO solution (as described above). We therefore assign the cathodic wave of the E_D couple to the reduction of the ligand L⁰ on the *O*-bonded isomer Ru(II)-dmsO(-*O*)-L⁰. The species Ru(II)-dmsO(-*O*)-L⁻, formed after the reduction at 0.98 V must undergoes O→S isomerization (k_{OS1}) to recover the *S*-bonded complex Ru(II)-dmsO(-*S*)-L⁻ in order to achieve the anodic peak current of the L⁰/L⁻ couple (E_A). Finally, if the scan rate is much faster than the linkage isomerism rate k_{SO} , no Ru(III)-(dmsO-*O*)-L⁻ species will be generated and the cyclic voltammetry is that of Ru(II)-(dmsO-*S*)-L⁻ species (only E_A and E_B couples) (Figure 4.3.34, scan rate 20.0 V/s). From this high scan rate voltammogram, it was possible to estimate the ground-state S→O isomerism rate $k_{SO} \approx 50 \text{ s}^{-1}$.

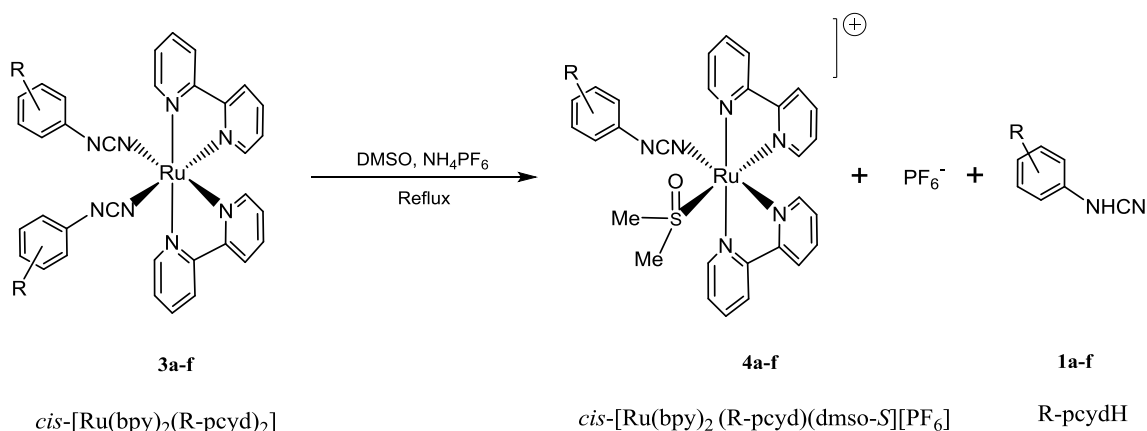
Both linkage isomerism rates of $k_{SO} \approx 50 \text{ s}^{-1}$ and $k_{OS2} \approx 0.2 \text{ s}^{-1}$ are expected to vary only slightly for the other complexes of this study based on the slight variation of k_{OS1} with phenylcyanamide ligand in Table 4.3.4. As seen by the electrochemical data in Table 4.3.6, the R-pcyd = Cl₂pcyd⁻, Cl₃pcyd⁻ and Cl₅pcyd⁻ complexes are described by Scheme 4.3.1 while the other complexes showed poor reversibility of the L⁰/L⁻ or Ru(III/II) couples.

4.4 Discussion

4.4.1 Synthesis

The *cis*-[Ru(bpy)₂(R-pcyd)(dmsO-S)][PF₆] complexes (**4a-4f**) were prepared by refluxing slightly acidic solutions of precursor *cis*-[Ru(bpy)₂(R-pcyd)₂] complexes (**3a-3f**) in anhydrous dimethyl sulfoxide for 10-30 minute under inert atmosphere, according to the Scheme 4.4.1.

Scheme 4.4.1: Synthetic Scheme for *cis*-[Ru(bpy)₂(R-pcyd)(dmsO-S)][PF₆] Complexes (**4a-4f**).



Like similar ruthenium-polypyridyl-phenylcyanamide complexes, the synthesis of complexes **4a-4f** were attempted first via the metathesis reactions between the thallium salts of R-pcyd ligands and *cis*-[Ru(bpy)₂(dmsO)Cl][PF₆], however, the synthetic method proved unsuccessful, even after applying various reaction conditions (solvents, temperature, reaction time).⁴²⁻⁵¹ Another attempt to make these complexes from *cis*-[RuCl₂(dmsO)₄] by sequential replacement of bpy and phenylcyanamide ligand was also unsuccessful.⁸ⁱ⁻¹ Both results indicated that the Ru(II) ion in a coordination sphere of π -acceptor bpy and dmsO ligands is substitutionally inert. Finally, the synthetic route described in the Scheme 4.4.1 was determined, which provided an efficient method for

the syntheses of **4a-4f**. The reaction scheme involves partial solvolysis of *cis*-[Ru(bpy)₂(R-pcyd)₂] complexes (**3a-3f**) in dimethyl sulfoxide and requires slightly acidic conditions (using NH₄PF₆) for facile substitution of the phenylcyanamide ligand in its protonated form. Some care must be taken not to heat the reagent complex too long in dimethyl sulfoxide as both phenylcyanamide ligands can be displaced forming the known complex [Ru(bpy)₂(dmsO-S)₂]²⁺.^{11,52} However, by suitable control of the reaction conditions, complexes **4a-4f** could be obtained in high purity and high yields (30-90%)(Section 4.2.3).

Due to the chirality of the ruthenium centres, the complexes (**4a-4f**) are expected to exhibit optical isomerism (Λ and Δ forms). Indeed, the synthesis of the structurally similar *cis*-[Ru(bpy)₂(dmsO)Cl] Cl complex from *cis*-Ru(bpy)₂Cl₂ gave a racemic mixture of both Λ and Δ isomer, which is consistent with a dissociative mechanism that involved a pentacoordinated intermediate.^{52a,52h} Due to similarity in the synthetic procedure, it is likely that the synthesis of complexes **4a-4f** also involves a dissociative mechanism and the isolated complexes are a racemic mixture of both optical isomers. However, no attempt was made to isolate optically pure Λ or Δ forms of complexes **4a-4f**.

4.4.2 Linkage Isomerism in *cis*-[Ru(bpy)₂(R-pcyd)(dmsO-S)][PF₆] Complexes

MLCT irradiation (450 ± 20 nm) of all *cis*-[Ru(bpy)₂(R-pcyd)(dmsO-S)][PF₆] complexes (**4a-4f**) induced excited state S→O isomerization with large quantum yields ($\Phi_{S\rightarrow O}$ =0.43-0.06, Table 4.3.4) which decreased dramatically with increasing donor properties of phenylcyanamide ligands.

In past studies, the quantum yield of isomerization $\Phi_{S \rightarrow O}$ was shown to vary considerably, depending on the nature of the ancillary ligands. For example, $[\text{Ru}(\text{tpy})(\text{L}_2)(\text{dmsO}-S)]^{n+}$, where L_2 is acetylacetonate, tetramethylethylenediamine, 2,2'-bipyridine, 2-pyridinecarboxylate, and 4-methyl-2-pyridinecarboxylate, has $\Phi_{S \rightarrow O} = <10^{-4}$, 0.007, 0.024, 0.25 and 0.79, respectively.^{14a,b} In these complexes, the electronic properties of L_2 vary considerably and it is difficult to deconvolute a specific property responsible for the change in $\Phi_{S \rightarrow O}$ with bidentate ligand. A DFT study of these complexes,²¹ indicated that the percentage ruthenium character of the HOMO followed the trend in quantum yields of isomerization, being greatest for the largest quantum yield. The authors concluded that as the excited state responsible for linkage isomerism is $^3\text{MLCT}$, the Ru(III) character of the state must be important. This result can't be directly compared to the complexes (**4a-4f**) of this study because the HOMO is mostly phenylcyanamide character (Figure 4.3.2). Nevertheless, in Table 4.3.4, there is a clear trend in the quantum yield of photo-induced linkage isomerism, decreasing as the number of chloro-substituents of the phenylcyanamide ligand decrease ($\Phi_{S \rightarrow O} = 0.43$ to 0.06). This trend is opposite to that of the thermal back reaction rates k_{OS1} ($2.61 - 4.52 \times 10^{-3} \text{ s}^{-1}$) but likely has the same chemical explanation, the relative electron donor properties of phenylcyanamide ligands.

Recent ultrafast transient absorption spectroscopic studies on $[\text{Ru}(\text{tpy})(\text{L})(\text{dmsO})]^{n+}$ complexes where $\text{L} = \text{bpy}$ or pic^- , have shown that after rapid relaxation from the excited singlet MLCT state to the triplet manifold, the excited $^3\text{Ru}-S$ species are branched between the ground $\text{Ru}-S$ and isomerized $^3\text{Ru}-O^*$ species and both processes take place at nanosecond to picosecond time scale.¹⁶

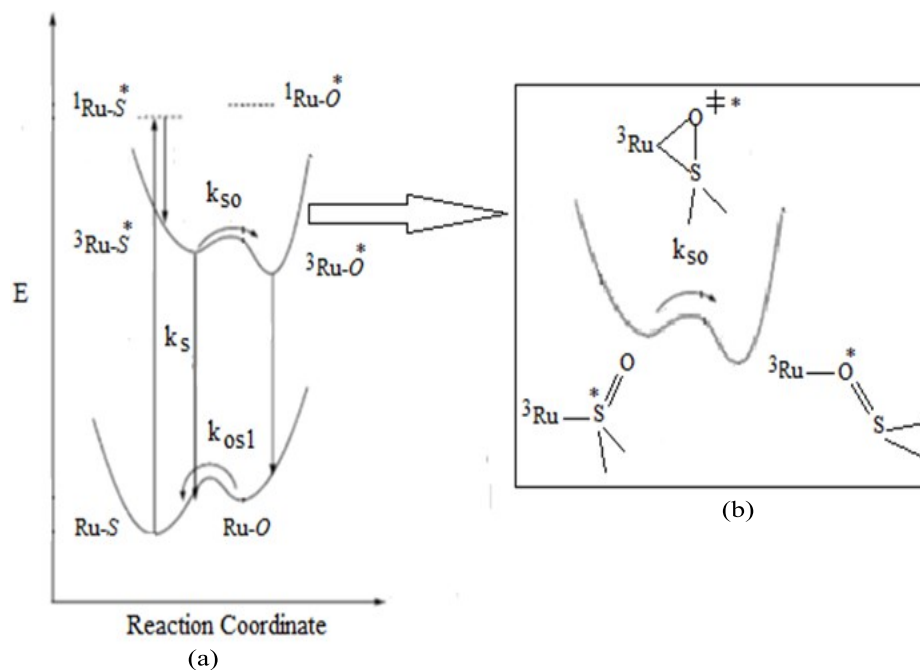


Figure 4.4.2: Qualitative electronic state diagram (a) for photochromic *cis*-[Ru(bpy)₂(R-*pcyd*)(*dmsO*)]⁺[PF₆]⁻ complexes showing excited state. (b) enlarged view of the excited state reaction coordinate.

Assuming analogous photochemistry to that of [Ru(*tpy*)(*pic*)(*dmsO-S*)]⁺, the excited state S→O isomerization in [Ru(bpy)₂(R-*pcyd*)(*dmsO*)]⁺ complexes can be described by a qualitative electronic state diagram, which is shown in the Figure 4.4.3.

The magnitude of $\Phi_{S\rightarrow O}$ is then determined by a linkage isomerism rate (k_{SO}) from the ³MLCT excited state of [Ru(bpy)₂(R-*pcyd*)(*dmsO-S*)]⁺* to [Ru(bpy)₂(R-*pcyd*)(*dmsO-O*)]⁺* that is significantly greater than the rate of ³MLCT decay to the ground state of [Ru(bpy)₂(R-*pcyd*)(*dmsO-S*)] (k_S), according to Eq. 4.4.1

$$\Phi_{S\rightarrow O} = \frac{k_{SO}}{k_{SO} + k_S} \quad (4.4.1)$$

The rate of relaxation to the ground state configuration (k_S) depends on the energy gap between the excited and the ground states. As seen in the Table 4.3.3, there is little

variation in MLCT energies with the number of chloro-substituents on phenylcyanamide ligands in *cis*-[Ru(bpy)₂(R-pcyd)(dmsO-S)]⁺ complexes (**4a-4f**). As the relaxation rates (k_S) are almost constant in this family of complexes, the observed variation in quantum yields must arise from the variation in the rates of S→O isomerization (k_{SO}), with the donor property of R-pcyd⁻ ligands. Gray⁷ and Rack^{9,10,17} suggested that the picosecond excited state S→O isomerization is an activated process for non-chelating dimethylsulfoxide ligands and involves a transition state having side-on (η^2 -S,O) binding mode of dmsO, as shown in the Figure 4.4.1.^{7,16} Thus factors favouring the excited state Ru-O bond formation would lower the activation energy barrier, thereby increasing the excited state S→O isomerization rates (k_{SO}).

For the complexes of this study, the ³Ru-S* species in Figure 4.4.2 can be viewed as a ³MLCT excited state in which Ru(III) is bonded to dmsO-S, a reduced bpy and an anionic R-pcyd⁻ ligand. Poor donor phenylcyanamide ligands destabilize ³Ru-S* and thereby decrease the activation barrier shown in Figure 4.4.2b. Thus with an increase in rate k_{SO} , the quantum yield of isomerization is greatest for poor donor phenylcyanamides. The effect of the donor property of R-pcyd⁻ ligand is also reflected in the observed variation in the rates (k_{OS1}) of the thermal O→S back reaction. However, these rates would have the reverse trend of quantum yields because in the ground state, the Cl₅pcyd⁻ species would have less electron density on Ru(II) (relatively “harder” than pcyd⁻ species) and so stabilize the Ru(II)-O isomer, thereby increasing the activation barrier of the thermal back reaction compared to that of the pcyd⁻ species.

The redox-induced S→O and O→S isomerism that is observed for *cis*-[Ru(bpy)₂(R-pcyd)(dmsO-S)][PF₆] followed a mechanism (Scheme 4.3.1) more

complicated than the simple ECEC mechanism (Scheme 4.1.3), as observed for $[\text{Ru}(\text{NH}_3)_5\text{dmsO}]^{2+}$ and $[\text{Ru}(\text{tpy})(\text{L}2)(\text{dmsO})]^{n+}$.^{8,14,21-22} The complexity in the current system arises from direct involvement of the non-innocent phenylcyanamide ligand in the redox cycles which promoted two O→S linkage isomerism depending on the scan rate: one with the oxidized ligand, $\text{Ru(II)-dmsO}(-\text{O})-\text{L}^0 \rightarrow \text{Ru(II)-dmsO}(-\text{S})-\text{L}^0$ ($k_{\text{OS}2}$), at low to moderate scan rates (0.05-8.0 V/s) and another one with the reduced ligand L^- , $\text{Ru(II)-dmsO}(-\text{O})-\text{L}^- \rightarrow \text{Ru(II)-dmsO}(-\text{S})-\text{L}^-$ ($k_{\text{OS}1}$), at moderate scan rates (0.1-8.0 V/s) (Scheme 4.3.1).

4.5 Conclusion and Future Work

Six new complexes $\text{cis-}[\text{Ru}(\text{bpy})_2(\text{R-pcyd})(\text{dmsO-S})]^+$ (**4a-4f**), where R- pcyd^- is Cl_5pcyd^- , Cl_4pcyd^- , Cl_3pcyd^- , Cl_2pcyd^- , Clpcyd^- and pcyd^- , have been synthesized and characterized by $^1\text{H-NMR}$ and electronic absorption spectroscopy and cyclic voltammetry. These complexes readily undergo photoinduced linkage isomerism to metastable $\text{cis-}[\text{Ru}(\text{bpy})_2(\text{R-pcyd})(\text{dmsO-O})]^+$ followed by a relatively slow thermal rearrangement back to $\text{cis-}[\text{Ru}(\text{bpy})_2(\text{R-pcyd})(\text{dmsO-S})]^+$ in solution and in solid PMMA polymer films. The quantum yields of $^3\text{MLCT}$ excited S→O isomerization ($\Phi_{\text{S} \rightarrow \text{O}} = 0.43 - 0.06$) of $\text{cis-}[\text{Ru}(\text{bpy})_2(\text{R-pcyd})(\text{dmsO-S})][\text{PF}_6]$ (**4a-4f**) increased dramatically as the number of chloro-substituents decreased on the R- pcyd^- ligand. The thermal back reaction rates ($k_{\text{OS}1} = 2.61 - 4.52 \times 10^{-3} \text{ s}^{-1}$) showed a modest increase with increase in the number of chloro-substituent on the R- pcyd^- ligand. DFT calculations of both $\text{cis-}[\text{Ru}(\text{bpy})_2(\text{R-pcyd})(\text{dmsO-S})]^+$ and $\text{cis-}[\text{Ru}(\text{bpy})_2(\text{R-pcyd})(\text{dmsO-O})]^+$ show a mostly phenylcyanamide HOMO and the oxidized complexes show a spin density distribution

mostly localized on the phenylcyanamide ligand. The cyclic voltammetry of *cis*-[Ru(bpy)₂(R-pcyd)(dmsO-S)]⁺ complexes showed two oxidation processes: a phenylcyanamide L⁰/L⁻ couple followed by a Ru(III/II) couple at more positive potential. Upon oxidation to Ru(III), the complexes rearranged to form Ru-O linkage isomers and the scan rate dependent voltammograms permitted estimates of the rates of ground state S→O and O→S linkage isomerism ($k_{SO} \approx 50 \text{ s}^{-1}$ and $k_{OS2} \approx 0.2 \text{ s}^{-1}$). Future studies will use photo-induced linkage isomerism to alter the mixed-valence properties of dinuclear complexes that incorporate phenylcyanamide bridging ligands.

4.6 References

1. Gutlich, P.; Garcia, Y.; Woike, T.; *Coord. Chem. Rev.* **2001**, *219*, 839.
2. Sato, O. *Acc. Chem. Res.* **2003**, *36*, 692.
3. (a) Irie, M. *Chem. Rev.* **2000**, *100*(5), 1685. (b) Raymo, F. M.; Tomasulo, M. *Chem.* **2006**, *12*(12), 3186.
4. Straight, S. D.; Lidelle, P. A.; Tarazono, Y.; Moore, T. A.; Moore, A. L.; Gust, D. *Adv. Funct. Mater.* **2007**, *17*(5), 777.
5. Woike, Th.; Haussuhl, S.; Sugg, B.; Rupp, R. A.; Beckers, J.; Imlau, M.; Schieder, R. *Appl. Phys. B* **1996**, *63*, 243.
6. Imlau, M.; Haussuhl, S.; Woike, Th.; Schieder, R.; Angelov, V.; Rupp, R. A.; Schwarz, K. *Appl. Phys. B* **1999**, *68*(5), 877.
7. Rack, J. J.; Winkler, J. R.; Gray, H. B. *J. Am. Chem. Soc.* **2001**, *123*, 2432.
8. (a) Yeh, A.; Scott, N.; Taube, H. *Inorg. Chem.* **1982**, *21*, 2542. (b) Senoff, C. V.; Maslowsky Jr. E.; Goel, R. G.; *Can. J. Chem.* **1971**, *49*, 3538. (c) Nicholson, R.

- S.; Shain, I.; *Anal. Chem.* **1964**, *36*, 706. (d) Sano, M. *Struct. Bonding* **2001**, *99*, 117. (e) Sano, M.; Taube, H. *Inorg. Chem.* **1994**, *33*, 705. (f) Tomita, A.; Sano, M. *Inorg. Chem.* **1994**, *32*, 5825. (g) Tomita, A.; Sano, M. *Inorg. Chem.* **2000**, *39*, 200. (h) Roecker, L.; Dobson, J. C.; Vining, W. J.; Meyer, T. J. *Inorg. Chem.* **1987**, *26*, 779. (i) Root, M. J.; Deutsch, E. *Inorg. Chem.* **1985**, *24*, 1464. (j) Silva, D. O.; Saika, J. J.; Toma, H. E. *J. Photochem. Photobiol. A* **1998**, *112*, 209. (k) Silva, D. O., Toma, H. E.; *Can. J. Chem.* **1994**, *72*, 1705. (l) Toma, H. E.; De Oliveira, D. *Polyhedron* **1991**, *10*, 1699. (m) Delahay, P.; *J. Am. Chem. Soc.* **1953**, *75*, 1190.
9. Rack, J.J. *Coord. Chem. Rev.* **2009**, *253*, 78.
 10. Rack, J., McClure, B.-A. *Eur. J. Inorg. Chem.* **2010**, 3895.
 11. Smith, M. K.; Gibson, J. A. Young, C. G. *Eur. J. Inorg. Chem.* **2000**, 1365.
 12. Rack, J. J.; Mockus, N. V. *Inorg. Chem.* **2003**, *42*, 5792.
 13. Mockus, N.; Petersen, J. L.; Rack, J. J. *Inorg. Chem.* **2006**, *45*, 8.
 14. (a) Rachford, A. A.; Petersen, J, L. Rack, J. J. *Inorg. Chem.* **2005**, *44*, 8065. (b) Rachford, A. A.; Petersen, J, L. Rack, J. J. *Inorg. Chem.* **2006**, *45*, 5953
 15. Butcher, D. P.; Rachford, A. A.; Rack, J. J. *Inorg. Chem.* **2006**, *45*, 9178.
 16. Rachford, A. A.; Rack, J. J. *J. Am. Chem. Soc.* **2006**, *128*, 14318.
 17. Rachford, A. A. Petersen, J. L.; Rack, J. J. *Dalton Trans.* **2007**, 3245.
 18. Mockus, N.; Marquad, S.; Rack, J. J. *J. Photochem. Photobiol. A.* **2008**, *200*, 39.
 19. McClure, B. A.; Abrams, E. R.; Rack, J. J. *J. Am. Chem. Soc.* **2010**, *132*, 5428.
 20. McClure, B. A.; Mockus, N. V.; Butcher, D. P.; Lutterman, D. A.; Turro, C.; Petersen, J. L.; Rack, J. J. *Inorg. Chem.* **2009**, *48*, 8084.

21. Lutterman, D. A.; Rachford, A. A.; Rack, J. J.; Turro, C. *J. Phys. Chem. A* **2009**, *113*, 11002.
22. Mockus, N. V.; Rabinovich, D.; Petersen, J. L.; Rack, J. J. *Angew. Chem. Int. Ed.* **2008**, *47*, 1458.
23. McClure, B. A.; Rack, J. J. *Angew. Chem. Int. Ed.* **2009**, *48*, 8556.
24. Lutterman, D. A.; Rachford, A. A.; Rack, J. J.; Turro, C. *J. Phys. Chem. Lett.* **2010**, *1*, 3371.
25. Dieckman, V.; Springfield, K.; Eicke, S.; Imlau, M.; Rack, J. J. *Opt. Exp.* **2010**, *18*(22), 23495.
26. Porter, B. L.; McClure, B. A.; Abrams, E. R.; Engle, J. T.; Ziegler, C. J.; Rack, J. J. *J. Photochem. Photobiol. A* **2011**, *217*, 341.
27. King, A. W.; Jin, Y.; Engle, J. T.; Ziegler, C. J.; Rack, J. J. *Inorg. Chem.* **2013**, *52*, 2086
28. Evans, C. E. B.; Naklicki, M.; Rezvani, A.; White, C.; Veniamin, V.; Crutchley, R. J. *J. Am. Chem. Soc.* **1998**, *120*, 13096.
29. Rezvani, A. R.; Crutchley, R. J. *Inorg. Chem.* **1994**, *33*, 170.
30. Reynolds, W. L.; *Prog. Inorg. Chem.* **1970**, *12*, 1.
31. (a) Calligaris, M. *Coord. Chem. Rev.* **2004**, *248*, 351. (b) Cotton, F. A.; Dikarev, E. V.; Petrukhina, M. A. *Inorg. Chem.* **2000**, *39*, 1748. (c) Tanase, T.; Aiko, T.; Yamamoto, Y. *Chem. Commun.* **1996**, 2341. (d) Calligaris, M.; Carugo, O. *Coord. Chem. Rev.* **1996**, *153*, 83. (e) Calligaris, M. *Croat. Chem. Acta.* **1999**, *72*, 147. (f) Mortier, W. J. *Struct. Bond.* **1987**, *66*, 125. (g) Sanderson, R. T.; *J. Chem.*

- Ed.* **1954**, *31*, 2. (h) Alessio, E.; Milani, B.; Bolle, M.; Mestroni, G.; Faleschini, P.; Todone, F.; Geremia, S.; Calligaris, M. *Inorg. Chem.* **1995**, *34*, 4722.
32. Davies, J. A. *Adv. Inorg. Chem. Radiochem.* **1981**, *24*, 115.
33. Balzani, V.; Juris, A.; Barigelletti, F.; Campagna, S.; Belser, P.; Von Zelewsky, A. *Coord. Chem. Rev.* **1988**, *84*, 85.
34. (a) Kirchoff, J. R.; McMillin, D. R.; Marnot, P.A.; Sauvage, J.-P. *J. Am. Chem. Soc.* **1985**, *107*, 1138. (b) Berger, R. M.; McMillin, D. R.; *Inorg. Chem.* **1988**, *27*, 4245. (c) Hecker, C. R.; Fanwick, P. E.; McMillin, D. R.; *Inorg. Chem.* **1991**, *30*, 659. (d) Bonnette, S.; Collin, J.-P. Sauvage, J.-P.; Schofield, E. *Inorg. Chem.* **2004**, *43*, 8346.
35. Grusenmeyer, T. A.; McClure, B.-A.; Ziegler, C.; Rack, J. J. *Inorg. Chem.* **2010**, *49*, 4466.
36. Rezvani, A. R.; Crutchley, R. J. *Inorg. Chem.* **1994**, *33*, 170.
37. Crutchley, R. J. *Coord. Chem. Rev.* **2001**, *219*, 125.
38. Sullivan, B. P.; Salmon, D. J.; Meyer, T. J. *Inorg. Chem.* **1978**, *17*(12), 3334.
39. Gennett, T.; Milner, D. F.; Weaver, M. J. *J. Phys. Chem.* **1985**, *89*, 2787.
40. (a) Hatchard, C. G.; Parker C. G. *Proc. R. Soc. Lond. A* **1956**, *235*, 518. (b) Arnold, G. *The Chemist's Companion: A Handbook of Practical Data, Techniques and References*; Willy: New York, 1972. (c) Kuhn, H. J.; Braslavsky, S. E.; Schmidt, R. *Pure Appl. Chem.* **2004**, *76*(12), 2105. (d) Calvert, J. G.; Pitts, J. N.; *Photochemistry*; Willey: New York, 1966. (e) Il'ichev, Y. V. *Photochemistry: Theoretical Concepts and Reaction Mechanism*; Cordis: Pennsylvania.

41. Aquino, M. A. S.; Crutchley, R. J.; Lee, F. L.; Gabe, E. J.; Bensimon, C. *Acta Cryst.* **1993**, *C49*, 1543. (b)
42. Harb, C.; Kravstov, P.; Choudhuri, M.; Sirianni, E. R.; Yap, G. P. A.; Lever, A. B. P.; Crutchley, R. J. *Inorg. Chem.* **2013**, *52*, 1621.
43. Crutchley, R. J.; McCaw, K.; Lee, F. L.; Gabe, J. E. *Inorg. Chem.* **1990**, *29*, 2576.
44. Mosher, P. J.; Yap, G. P. A.; Crutchley, R. J.; *Inorg. Chem.* **2001**, *40*, 550.
45. Zhang, W.; Bensimon, C.; Crutchley, R. J. *Inorg. Chem.* **1993**, *32*, 5808.
46. Aquino, M. A. S.; Lee, F. L.; Gabe, E. J.; Bensimon, C.; Greedan, J. E.; Crutchley, R. J. *J. Am. Chem. Soc.* **1992**, *114*, 5130.
47. Naklicki, M.; Crutchley, R. J.; *Inorg. Chem.* **1989**, *28*, 1955.
48. Saleh, A. A.; Crutchley, R. J. *Inorg. Chem.* **1990**, *29*, 2123.
49. Evans, C. E. B.; Ducharme, D.; Naklicki, M.; Crutchley, R. J.; *Inorg. Chem.* **1995**, *34*, 1350.
50. (a) Aquino, M. A. S.; Lee, F. L.; Gabe, E. J.; Bensimon, C.; Greedan, J. E.; Crutchley, R. J. *J. Am. Chem. Soc.* **1992**, *114*, 5130. (b) Naklicki, M.; Crutchley, R. J. *Inorg. Chim. Acta* **1994**, *225*, 123.
51. (a) Rezvani, A. R.; Bensimon, C.; Crompton, B.; Reber, C.; Greedan, J. E.; Kondratiev, V.; Crutchley, R. J. *Inorg. Chem.* **1997**, *36*, 3322. (b) Evans, C. E. B.; Naklicki, M. L.; Rezvani, A. R.; White, C. A.; Kondratiev, V. V.; Crutchley, R. J. *J. Am. Chem. Soc.* **1998**, *120*, 13096. (c) De Rosa, M. C.; White, C. A.; Evans, C. E. B.; Crutchley, R. J. *J. Am. Chem. Soc.* **2001**, *123*, 1396. (d) Evans, C. E. B.; Yap, G. P. A.; Crutchley, R. J. *Inorg. Chem.* **1998**, *37*, 6161. (e) Mosher, P. J.; Yap, G. P. A.; Crutchley, R. J. *Inorg. Chem.* **2001**, *40*, 1189.

52. (a) Heseck, D.; Inoue, Y.; Everitte, S. R. L.; Ishida, H.; Kunieda, M.; Drew, M. G. *B. J. Chem. Soc., Dalton Trans.* **1999**, 3701-3709. (b) Wang, Y.; Eichhorn, D. M.; Goswami, Zhao, Q.; Rillema, D.-P. *J. Chem. Cryst.* **1999**, 29(3), 277. (c) Lyttle, F. E.; Petrosky, L. M.; Carlson, L. R. *Anal. Chim. Acta* **1971**, 57, 239. (d) Orellana, G.; Ibarra, C. A.; Santoro, J. *Inorg. Chem.* **1988**, 27, 1025. (e) Heijden, M.; van Vliet, P. M.; Reedijk, J. *J. Chem. Soc. Dalton Trans.* **1993**, 3675. (f) Rutherford, T. J.; Reitsma, D. A.; Keene, F. R. *J. Chem. Soc. Dalton Trans.* **1994**, 3659. (g) Bryant, G. M.; Ferguson, J. *Aust. J. Chem.* **1971**, 24, 441. (h) Heseck, D.; Inoue, Y.; Everitt, S. R. *Chem. Lett.* **1998**, 109.

Chapter 5: Redox Ambiguity of Phenylcyanamide Ligands in Neutral Ruthenium Complexes

5.1 Introduction

5.1.1 Research Scope and Design Criteria

The creation of hybrid polymeric materials that possess useful optical, magnetic, and/or electronic properties requires multi-disciplinary research and is a very active field. New and improved polymeric/macromolecular materials, have shown promising results in generating, processing and storing light signals¹ that may have potential applications in solar energy cells, photonic switching devices, photonic circuits for processing information, optical fiber sensors and imaging devices.^{2,3} Extensive work has focused on the development of donor-acceptor polymeric materials having non-linear optical (NLO) properties because of their potential application in opto-electronic devices.⁴ In this regard, donor-acceptor polymeric materials have found application in a number of devices such as Mach-Zehnder modulators,⁵ solar energy cells⁶ and polymer spintronics.⁷

A greater understanding of conducting polymers and NLO chromophore is important if one is to come up with high performance electro-optical devices.⁴ Electro-optic activity of these devices is determined by the nature of the dipolar moiety, the extent of its noncentrosymmetric order in solid state and change in properties of the NLO material with the application of an electric field.⁵ Materials to be used in such devices must meet several criteria. First, they must be composed of dipolar moieties which under applied potential can be aligned in an ordered fashion (poling) to exhibit desired NLO properties. Charged species are avoided as poling is not effective. Second, the dipolar

units possess significant polarizability so that the poling of dipole moments can be achieved at lower external potentials. Third, they must have sufficient thermal and photochemical stability.

Organic chromophores having a D-spacer-A system, where D is the donor moiety, A is the acceptor moiety and the spacer is a π conjugated molecule that permits coupling between the donor and acceptor moiety, have been well studied as a possible choice of dipolar moiety for NLO materials.^{8,9} The charge transfer transitions of these molecules can give rise to hyperpolarizability¹⁰ and when such donor acceptor molecules are incorporated with a high degree of order into a polymer material, NLO properties can result.^{4,5,9} For neutral organic molecules, the ordering of these molecules in a polymer is achieved by high potential poling in which dipole moments of the molecules are aligned.¹¹ However, organic chromophores present some disadvantages such as having high drive potential and strong $\pi - \pi$ interactions which hinder noncentrosymmetric ordering, resulting in a poor electro-optic activity of the material.¹²

As an approach to overcome these obstacles, a new class of charge-transfer chromophores suitable for electro-optic applications has been introduced.¹³ These are mixed-valence complexes with conjugated bridging ligands. Mixed-valence complexes are donor-acceptor ($M-L-M^+$) systems and possess similar properties to organic donor-acceptor molecules. Specifically, the charge transfer transitions in these molecules can also give rise to hyperpolarizability and complexes can be incorporated into a polymer in an ordered fashion to exhibit NLO properties. In these regard, dinuclear mixed-valence complexes of ruthenium bridged by 1,4-dicyanamidobenzene ($dicyd^{2-}$) ligands have shown potential as building blocks or dipolar units for application in non-linear optical

(NLO) materials.¹⁴⁻¹⁸ The bridging dicyd²⁻ ligand has shown excellent efficiency as a hole-transfer superexchange mediator for metal-metal coupling in dinuclear ruthenium complexes due to its energetically favourable extended π -symmetry HOMO that spans the entire molecule. Extended π -cojugation in the bridging ligand gives rise to high polarizability of the electrons involved in charge transfer transition in the mixed-valence state, which is suitable to achieve “poling” or alignment of dipoles at low drive potentials and compatible with semiconductor electronics (less than 6 V and preferably 1 V).¹² In addition, these complexes have shown well defined spectroscopic and redox properties which can be switched or “turned” by varying the nature of the both inner and outer coordination spheres.¹⁴⁻¹⁸

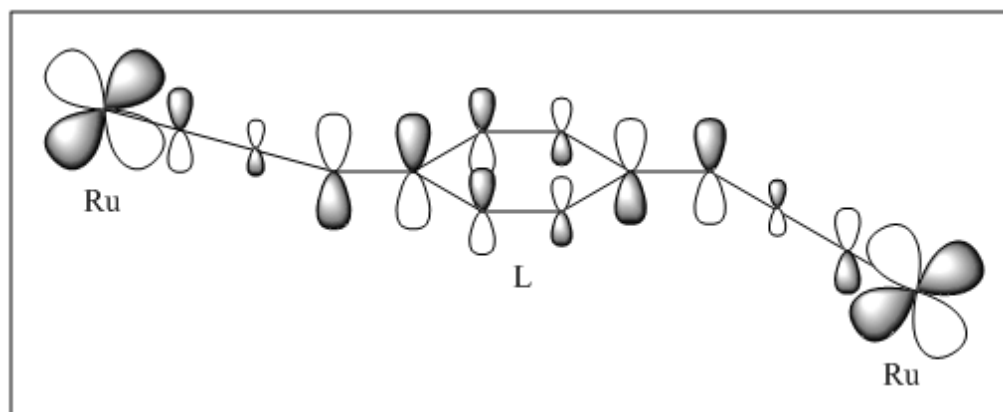


Figure 5.1.1: Ruthenium dinuclear system involving extended π conjugation, where L is a conjugated organic spacer.

In addition to low drive potentials, the stability of these complexes will be an added advantage as NLO materials must show both thermal and photochemical stability. Thermal stability is important when looking at the high temperature (90-140 °C) at which poling is done. This also means that volatile ligands such as NH_3 and CO must be avoided. It is important for the complex chromophore to exhibit appropriate solubility in

spin casting solvents. The solubility of mixed-valence complexes have been shown to be greatly improved by using multidentate ligands with organic substituents, for example, 4'-*p*-tolyl-2,2':6'2''-terpyridine.¹² However, the vast majority of mixed-valence complexes are charged which causes an inherent disadvantage for their application in NLO materials.¹⁹ If charged complexes are incorporated in polymer matrix, poling would cause the complex to migrate to the pole of opposite charge, resulting in an inefficient poling of dipoles and so researchers in this field have largely focused on neutral donor-acceptor mixed-valence complexes. Figure 5.1.2 shows a process of poling in neutral complexes.

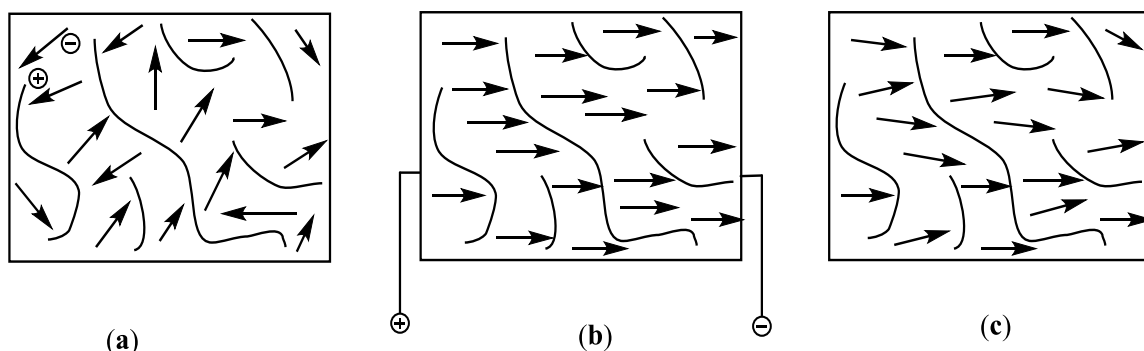


Figure 5.1.2: Poling of a neutral complex (a) random orientation of polar domains prior to poling, (b) introduction of electric field (poling), (c) electric field removed, dipole locked in a non-random manner. Zigzag line represents the polymer matrix.

Before a dinuclear neutral mixed-valence complex can be synthesized, it is first important to develop the synthetic methodology and to understand the electronic properties of the mononuclear Ru(II) and Ru(III) neutral complexes. A family of mononuclear neutral Ru(III) complexes of phenylcyanamide ligands, *trans*-[Ru(tpy)(R-pcyd)Cl₂] where tpy = 4-(*tert*-butylphenyl)-2,2':6',2''-terpyridine and R-pcyd⁻ = chloro-substituted phenylcyanamide ligands was synthesized. These molecules can be thought of as acceptor units of neutral mixed-valence complexes of bridging dicyd²⁻ ligands with the

donor Ru(II) units at the other end, as shown in the Figure 5.1.2. The ttpy ligand was deliberately chosen to meet the solubility requirement.

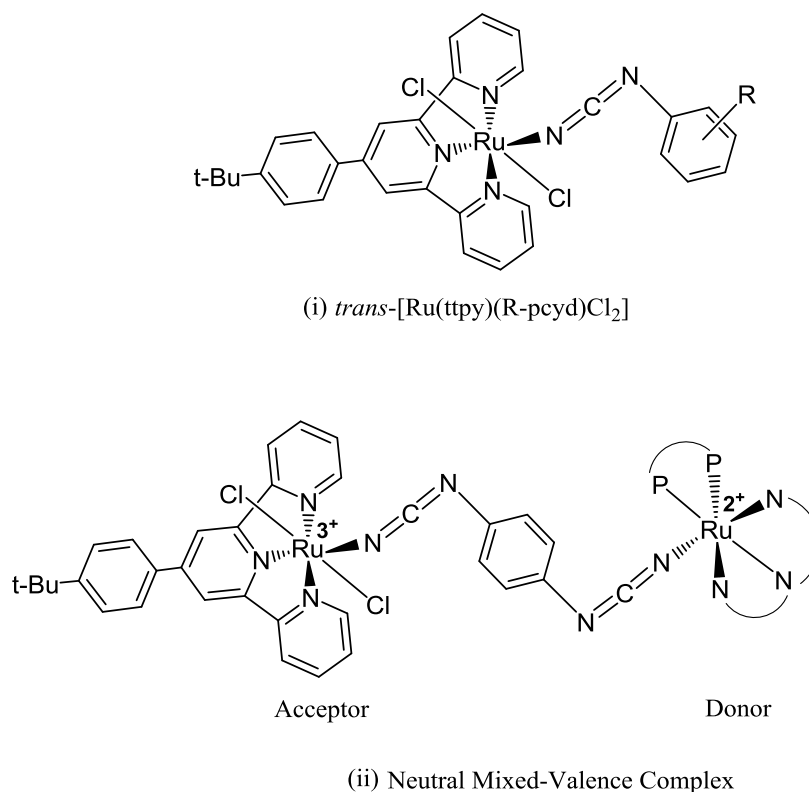


Figure 5.1.3: (i) *trans*-[Ru(tppy)(R-pcyd)Cl₂], (ii) proposed mixed-valence complex [$\{\text{Ru}^{\text{III}}(\text{ttpy})\text{Cl}_2\}(\mu\text{-dicyd}^{2-})\{\text{Ru}^{\text{II}}(\text{N}3)(\text{P}2)\}$] where $[\text{Ru}^{\text{III}}(\text{ttpy})\text{Cl}_2]^+$ is the acceptor Ru(III) and $[\text{Ru}^{\text{II}}(\text{N}3)(\text{P}2)]^+$ is the donor Ru(II) unit. P2 and N3 are P and N based bidentate and tridentate ligands that stabilize Ru(II) state.

5.1.2 Research Objectives

The electronic properties of ruthenium-phenylcyanamide complexes are dominated by the degree of π -interaction between the Ru(III)d π and the π -HOMO of phenylcyanamide ligands. When the Ru(III)d π orbital is significantly above the π -HOMO of the anionic ligand, the bonding can be described as mostly ionic in character with a valence description Ru(III)-R- pcyd^- of the complex. On the other hand, a close energy match between Ru(III) and anionic pcyd^- anion results in strong covalency in Ru(III)-cyanamide bond due to a significant transfer of electron density from the anionic ligand to Ru(III). This situation leads to a delocalized valence description, $\text{Ru(III)-R-}\text{pcyd}^- \leftrightarrow \text{Ru(II)-R-}\text{pcyd}^{\bullet-}$ complexes, in which the degree of electron transfer or non-innocent behavior of phenylcyanamide ligand determines the dominant resonance form describing the complex.

In past studies, the separation between Ru(III)d π and the π -HOMO of the R- pcyd^- ligands could be significantly perturbed by the variation of the electronic nature of (i) ancillary ligands, (ii) π -donor properties of R- pcyd^- ligands and (iii) donor number of solvents.¹⁴⁻²⁴ In this regard, the σ -donor ammine ligands significantly raised the Ru(III)d π orbital relative to the π -HOMO of the R- pcyd^- ligands in $[\text{Ru}(\text{NH}_3)_5(\text{R-}\text{pcyd}^-)]^{2+}$ complexes via specific solvent-solute donor-acceptor interaction between ammine ligands and donor solvent molecules.²⁰⁻²³ The energy gap could be increased further by gradual stabilization of the π -HOMO of the R- pcyd^- ligands by electron withdrawing chloro substituents.²¹ The combination of donor strengths of both solvents and R- pcyd^- ligands resulted in mostly ionic character of the Ru(III)-cyanamide bond. Both EPR and paramagnetic ^1H NMR spectroscopy unambiguously assigned the metal-centred valence

descriptions Ru(III)-R-*pcyd*⁻ of these complexes.²⁵ On the other hand, replacement of ammine ligands by weakly π -acceptor *Tp*⁻ and *dppe* ligands resulted in a significant stabilization of Ru(III) $d\pi$ orbitals in [Ru(*Tp*)(*dppe*)(R-*pcyd*)]⁺ complexes where *dppe* = ethylenebis(diphenylphosphine), *Tp*⁻ = hydrotris(pyrazol-1-yl)borate.²⁶ However, the π -HOMOs of R-*pcyd*⁻ ligands could be gradually stabilized by increasing the number of chloro-substituents on R-*pcyd*⁻ ligands. As shown by DFT calculations,²⁶ the combined effects of π -acceptor ancillary ligands and the donor properties of redox-active R-*pcyd*⁻ ligands resulted in a radical-centred description Ru(II)-R-*pcyd*^{•-} for the Cl*pcyd* complex, while a largely metal-centred Ru(III)-R-*pcyd*⁻ description of the Cl₅*pcyd* complex.

In the current research, the design of neutral *trans*-[Ru(*tppy*)(R-*pcyd*)Cl₂] complexes created an opportunity to examine the degree of non-innocence phenylcyanamide ligands in a coordination sphere of strong π -acceptor *tppy* and σ/π -donor Cl⁻ ligands as a function of the donor properties of chloro-substituted R-*pcyd*⁻ ligands and solvents. To effect this, following research objectives can be stated:

- (i) To synthesize five mononuclear neutral *trans*-[Ru(*tppy*)(R-*pcyd*)Cl₂] complexes (**1-5**) where *tppy* = 4-(*tert*-butylphenyl)-2,2':6',2''-terpyridine and R-*pcyd*⁻ = 4-Cl-, 2,4-dichloro-, 2,4,5-trichloro-, 2,3,4,5-tetra chloro- and pentachloro-phenylcyanamide monoanion, and characterize by elemental analysis, X-ray crystallography, IR and electronic absorption spectroscopy and cyclic voltammetry.
- (ii) To investigate the degree of non-innocence of R-*pcyd*⁻ ligands and assign the most appropriate oxidation state distribution in *trans*-[Ru(*tppy*)(R-*pcyd*)Cl₂]

complexes by paramagnetic ^1H NMR and electronic absorption spectroscopy and DFT calculations.

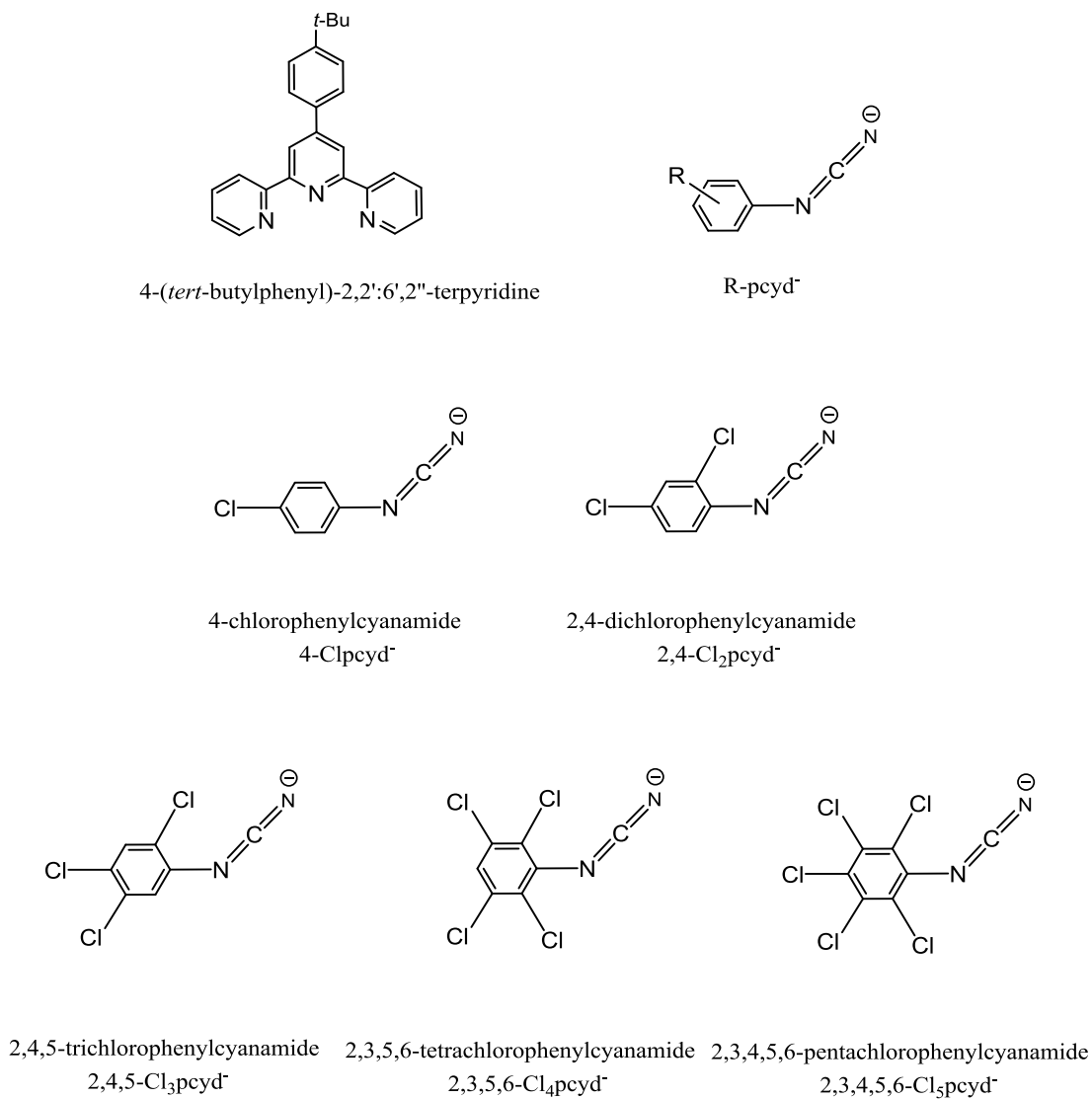


Figure 5.1.3: The R-pcyd⁻ and ancillary ttpy ligands used in the synthesis of *trans*-[Ru(ttpy)(R-pcyd)Cl₂] complexes.

5.2 Experimental

5.2.1 Starting Materials

Reagents for R-pcyd⁻ Ligand Synthesis

Reagents for the synthesis of R-pcyd⁻ ligands and their thallium salts have been described in the Section 4.2 (Chapter 4)

Reagents for Complex Synthesis

Ruthenium (III) chloride hydrate (99.9%, Alfa Aesar) was used as received.

Adsorbent in Column Chromatography and Drying Agents

Aluminum oxide (activated, acidic, Brockman I) for column chromatography was deactivated to grade III by adding water and slowly shaking the mixture for 4h. Phosphorus pentoxide (ACS reagent grade, 98+%, Anachemia) were used as received. Aluminum oxide (neutral, chromatography grade, Woelm) was activated by heating at 300 °C for several hours in a muffle furnace.

Electrochemistry Internal References and Supporting Electrolytes

Tetrabutylammonium hexafluorophosphate (TBAH) was used as supporting electrolyte and the internal reference ferrocene (reagent grade, J. T. Baker) was purified by sublimation. The synthesis of TBAH was achieved the same way as described in the Section 4.2 (Chapter 4)

Solvents for Synthesis

Anhydrous ethyl alcohol (Commercial Alcohols, absolute), acetone (Fisher Scientific, ACS reagent grade), dichloromethane (Caledon Labs, Laboratory Grade) were used as received.

Solvents for NMR Spectroscopy

Dimethyl-*d*₆-sulfoxide (99.9 atom % D, CDN Isotopes) was used as received.

Solvents for Electrochemistry

N,N-Dimethylformamide (Chromosolv®Plus, 99.9%, HPLC grade, Sigma-Aldrich), dichloromethane (anhydrous, 99.8%, Sigma-Aldrich) were used with no further purification or drying. The solvent was stored inside a polyethylene glove bag that was filled with argon when mixtures of TBAH and the solvent needed to be made in 20 mL glass vials.

Solvents for Quantitative Electronic Absorption Spectroscopy

N,N-Dimethylformamide (Chromosolv®Plus, 99.9%, HPLC grade, Sigma-Aldrich), dichloromethane (anhydrous, 99.8%, Sigma-Aldrich) were used as received.

5.2.2: Synthesis

Synthesis of R-pcydH Ligands and Tl[R-pcyd] Salts

Phenylcyanamide (pcydH) and its derivatives 4-chloro- (4-ClpcydH), 2,4-dichloro- (2,4-Cl₂pcydH), 2,4,5-trichloro- (2,4,5-Cl₃pcydH), 2,3,5,6-tetrachloro- (2,3,5,6-Cl₄pcydH), 2,3,4,5,6-pentachloro-phenylcyanamide (2,3,4,5,6-Cl₅pcydH) (**1a-f**) and their corresponding thallium salts (**2a-f**) were prepared by literature methods.^{20,27} Both Cl₄pcydH and Cl₅pcydH possessed a significant impurity of the guanidine dimer as shown by a strong IR $\nu(\text{C}=\text{N})$ band at approximately 1680 cm⁻¹. This dimer impurity reverts to a monomer in basic solutions and does not affect the isolation of the thallium salt of the ligand as discussed previously.²⁸

Synthesis of 4-(*tert*-butylphenyl)-2,2':6',2''-terpyridine (tpty)

This compound has been prepared by following the same procedure as described in the Section 2.2.1 (Chapter 2).^{29,30}

Synthesis of Ru(tpty)Cl₃·2DMSO·H₂O

The reagent complex was prepared by following the same procedure as described elsewhere²⁹ with some modification as described below: A mixture of RuCl₃·3H₂O (1.22 g, 4.66 mmol) and tpty (1.70g, 4.66 mmol) in absolute ethanol (180 mL) has been refluxed for 4hrs during which time the light brown suspension turned dark brown. The suspension was then allowed to cool at -5 °C, filtered and dark brown precipitate containing the desired product washed with absolute ethanol (30 mL), followed by water (3 x 30 mL) and finally with diethyl ether (3 x 30 mL) yielding 2.47 g of the dark brown Ru(tpty)Cl₃(yield: 85 %). The complex was recrystallized from DMSO and the crystalline ample used for elemental analysis incorporated one H₂O molecule in addition to two molecules of DMSO. Anal. Calcd for C₂₇H₃₁N₃Cl₃O₂SRu (M_w = 747.19): C, 46.62; H, 4.99; N, 5.62. Found: C, 46.88; H, 4.64; N, 5.83. ¹H NMR (300 MHz, DMSO-*d*₆): 9.67 (s, 2H); 7.50 (s, 2H); 1.43 (s, 9H); -1.39 (s, 2H); -2.18 (s, 2H); -9.26 (s, 4H); -35.19 (s, 2H).

Synthesis of [Ru(tpty)(R-pcyd)Cl₂] Complexes (1-5)

Preparation of [Ru(tpty)(Cl₅pcyd)Cl₂]·1/2CH₂Cl₂, (5)

A mixture of Ru(tpty)Cl₃·H₂O (1.0 g, 1.34 mmol) and Ti[2,3,4,5,6-Cl₅pcyd] (0.68 g, 1.37 mmol) has been refluxed in acetone (500 mL) for 18 h during which time the deep brown suspension turned dark blue. The reaction mixture was then filtered through Celite to remove fine precipitate of TiCl. Evaporation of the solvent from the

dark blue filtrated using a rotavap gave about 620 mg of the dark crude product. The crude complex was then purified by chromatography using an alumina column (grade III, 490 g) and CH_2Cl_2 as eluent. Elution with CH_2Cl_2 gave a green band which probably contained the *cis*-isomer. The second bright yellow band containing the major *trans*-isomer was collected, which after removal of the solvent (CH_2Cl_2) gave 140 mg of the pure reddish brown complex (**1**). Yield: 12 %. Anal. Calcd for $\text{C}_{32}\text{H}_{23}\text{N}_5\text{Cl}_7\text{Ru}\cdot 1/2\text{CH}_2\text{Cl}_2$ ($M_w = 869.27$): C, 44.91; H, 2.78; N, 8.06. Found: C, 44.75; H, 2.56; N, 7.79. ^1H NMR (300 MHz, $\text{DMSO-}d_6$): 9.52 (s, 2H); 7.28 (s, 2H); 1.34 (s, 9H); -1.50 (s, 2H); -2.09 (s, 2H); -6.49 (s, 2H); -9.03 (s, 2H); -31.18 (s, 2H). IR (KBr): $\nu(\text{NCN})$ 2142 cm^{-1}

Preparation of $[\text{Ru}(\text{ttpy})(\text{Cl}_4\text{pcyd})\text{Cl}_2]$, (**4**)

The complex (**4**) was prepared in the same manner as **5**: A mixture of $\text{Ru}(\text{ttpy})\text{Cl}_3\cdot\text{H}_2\text{O}$ (1.0 g, 1.34 mmol) and $\text{Ti}[2,3,5,6\text{-Cl}_4\text{pcyd}]$ (0.63 g, 1.35 mmol), after refluxing in acetone (500 mL) for 18 h gave a dark crude product, which after purification by chromatography using alumina column (grade III, 315 g) and CH_2Cl_2 as eluent gave 80 mg of the pure reddish brown product (**2**) from the second yellow band. Yield: 8%. Anal. Calcd for $\text{C}_{32}\text{H}_{24}\text{N}_5\text{Cl}_6\text{Ru}$ ($M_w = 792.36$): C, 48.51; H, 3.05; N, 8.84. Found: C, 48.43; H, 2.95; N, 8.61. ^1H NMR (300 MHz, $\text{DMSO-}d_6$): 9.64 (s, 2H); 8.35 (s, 2H); 1.37 (s, 9H); -0.92 (s, 2H); -1.91 (s, 2H); -6.18 (s, 2H); -8.82 (s, 2H); -9.56 (s, 1H); -29.82 (s, 2H). IR (KBr): $\nu(\text{NCN})$ 2136 cm^{-1} .

Preparation of $[\text{Ru}(\text{ttpy})(\text{Cl}_3\text{pcyd})\text{Cl}_2]$, (**3**)

This complex (**3**) was prepared in the same manner as **5**: A mixture of $\text{Ru}(\text{ttpy})\text{Cl}_3\cdot 3\text{H}_2\text{O}$ (1.0 g, 1.34 mmol) and $\text{Ti}[2,4,5\text{-Cl}_3\text{pcyd}]$ (0.40 g, 0.93 mmol), after

refluxing in acetone (300 mL) for 18 h gave 400 mg of the dark crude product. Purification by chromatography using alumina column (grade III, 175 g) and CH_2Cl_2 as eluent gave 76 mg of the pure reddish brown product (3) from the second yellow band. Yield: 11 %. Anal. Calcd for $\text{C}_{32}\text{H}_{25}\text{N}_5\text{Cl}_5\text{Ru}$ ($M_w = 757.92$): C, 50.71; H, 3.32; N, 9.24. Found: C, 50.52; H, 3.20; N, 9.20. ^1H NMR (300 MHz, $\text{DMSO}-d_6$): 14.46 (s, 1H); 9.31 (s, 2H); 8.27 (s, 2H); 1.33 (s, 9H); -0.53 (s, 2H); -1.01 (s, 2H); -1.35 (s, 2H); -7.00 (s, 2H); -16.99 (s, 1H); -24.47 (s, 2H). IR (KBr): $\nu(\text{NCN})$ 2150 cm^{-1}

Preparation of $[\text{Ru}(\text{tpty})(\text{Cl}_2\text{pcyd})\text{Cl}_2] \cdot 1/2\text{CH}_2\text{Cl}_2$, (2)

This complex (2) was prepared in the same manner as 5: A mixture of $\text{Ru}(\text{tpty})\text{Cl}_3 \cdot 2\text{DMSO} \cdot \text{H}_2\text{O}$ (0.23g, 0.32 mmol) and $\text{Ti}[2,4\text{-Cl}_2\text{pcyd}]$ (0.12 g, 0.32 mmol), after refluxing in acetone (300 mL) for 18 h gave 100 mg of the dark crude product, which after purification by chromatography using alumina column (grade III, 150 g) and 10 % acetone in CH_2Cl_2 as eluent gave 30 mg of the pure reddish brown product (4) from the second yellow band. Yield: 12 %. Anal. Calcd for $\text{C}_{32}\text{H}_{26}\text{N}_5\text{Cl}_4\text{Ru} \cdot 1/2\text{CH}_2\text{Cl}_2$ ($M_w = 765.94$): C, 50.96; H, 3.55; N, 9.14. Found: C, 51.11; H, 3.30; N, 9.34. ^1H NMR (300 MHz, $\text{DMSO}-d_6$): 18.94 (s, 1H); 18.03 (s, 1H); 13.39 (s, 2H); 10.04 (s, 2H); 2.14 (s, 2H); 1.58 (s, 9H); -0.74 (s, 2H); -0.87 (s, 2H); -7.13 (s, 2H); -20.09 (s, 2H); -25.00 (s, 2H). IR (KBr): $\nu(\text{NCN})$ 2143 cm^{-1} .

Preparation of $[\text{Ru}(\text{tpty})(\text{Clpcyd})\text{Cl}_2] \cdot 1/3\text{H}_2\text{O}$, (1)

This complex (1) was prepared in the same manner as 5: A mixture of $\text{Ru}(\text{tpty})\text{Cl}_3 \cdot \text{H}_2\text{O}$ (1.0 g, 1.34 mmol) and $\text{Ti}[4\text{-Clpcyd}]$ (0.50 g, 1.40 mmol), after refluxing in acetone (500 mL) for 18 h gave 750 mg of the dark crude product, which

after purification by chromatography using alumina column (grade III, 350 g) and CH_2Cl_2 as eluent gave 60 mg of the pure reddish brown product (**5**) from the second yellow band. Yield: 7%. Anal. Calcd for $\text{C}_{32}\text{H}_{27.66}\text{N}_5\text{Cl}_3\text{O}_{0.33}\text{Ru}$ ($M_w = 695.04$): C, 55.30; H, 4.01; N, 10.08. Found: C, 55.20; H, 3.96; N, 10.21. ^1H NMR (300 MHz, $\text{DMSO}-d_6$): 22.71 (s, 2H); 18.84 (s, 2H); 10.33 (s, 2H); 5.24 (s, 2H); 4.37 (s, 2H); 1.73 (s, 9H); 0.40 (s, 2H); -5.48 (s, 2H); -10.89 (s, 2H); -33.58 (s, 2H). IR (KBr): $\nu(\text{NCN})$ 2104 cm^{-1}

5.2.3 Physical Measurements

Elemental Analyses

All elemental analyses were performed by Canadian Microanalytical Services, Ltd. in Delta, B. C., Canada.

X-ray Crystallography

X-ray quality needle shaped dark brown crystals of $\text{Ru}(\text{tpty})\text{Cl}_3 \cdot 2\text{DMSO}$ were obtained by recrystallization of the complex from its warm solution in dimethyl sulfoxide (2.47 g complex in 150 mL). On the other hand, needle shaped crystals of the *trans*- $[\text{Ru}(\text{tpty})(\text{Cl}_3\text{pcyd})\text{Cl}_2] \cdot 2\text{CH}_3\text{CN}$ complex were obtained from acetonitrile by slow evaporation of the solvent. X-ray crystal structure determinations were conducted by Dr. Glenn P. A. Yap at the University of Delaware. The complex data were collected on a 1K Siemens Smart CCD using Mo- $\text{K}\alpha$ radiation ($\lambda = 0.71073 \text{ \AA}$) at 203(2) K using an ω -scan technique and corrected for absorptions using equivalent reflections.

No symmetry higher than monoclinic ($\text{C}2/\text{c}$) and triclinic ($\text{p}-1$) were observed for $\text{Ru}(\text{tpty})\text{Cl}_3 \cdot 2\text{DMSO}$ and *trans*- $[\text{Ru}(\text{tpty})(\text{Cl}_3\text{pcyd})\text{Cl}_2] \cdot 2\text{CH}_3\text{CN}$ complexes respectively, and solutions in the centric space group option yielded chemically

reasonable and computationally stable results of refinement. Direct methods were used to solve the structures and refinement was done with full-matrix least-squares procedures. Anisotropic refinement was performed on all non-hydrogen atoms. Calculations were performed for all hydrogen atoms. Scattering factors are contained in the SHELXTL version 5.1 program libraries. Tables of complete listing of all bond lengths and angles are listed in the Table E.1 and E2 in the Appendix E.

Infrared Spectroscopy

Infrared spectroscopy was performed on a Bomem Michelson 120 FTIR spectrometer as KBr mulls and data were analyzed using Bomem Grams/386 v3.04 Level II software.

NMR Spectroscopy

All standard paramagnetic 1-D ^1H NMR spectra were recorded using a Bruker AMX-400 NMR or Bruker 300 Ultra Shield spectrometers at room temperature in dimethyl- d_6 sulfoxide and all chemical shifts were referenced with respect to TMS (tetramethylsilane). The sample size consisted of 10-15 mg in 1.00 mL of dimethyl- d_6 sulfoxide and the spectrum was measured in a Norell XR-55 NMR tube. The π -spin density distributions on the phenyl carbons of R-pcyd ligands in complexes (**1-4**) were calculated from the observed isotropic shifts of phenyl ring protons using Eq. 1.13 in Chapter 1 and using the g value for free electron ($g_e = 2.0023$).

Electronic Absorption Spectroscopy and Cyclic Voltammetry

Electronic absorption spectroscopy and cyclic voltammetry of complexes were performed in DMF and CH_2Cl_2 using the same instruments as described in the Section

2.2 in Chapter 2.

5.2.4 Oscillator Strength Calculation

The oscillator strength (f) of the low energy Ru(III)-cyanamide LMCT bands of *trans*-[Ru(tpy)(R-pcyd)Cl₂] complexes were calculated using Jandel Scientific peakfit™ v3.0 software by following the same procedure as described in the Section 3. 3 (Chapter 3). The fitting procedure is illustrated in the Figure 5.2.1 for the low energy LMCT band of *trans*-[Ru(tpy)(Cl₅pcyd)Cl₂] in CH₂Cl₂.

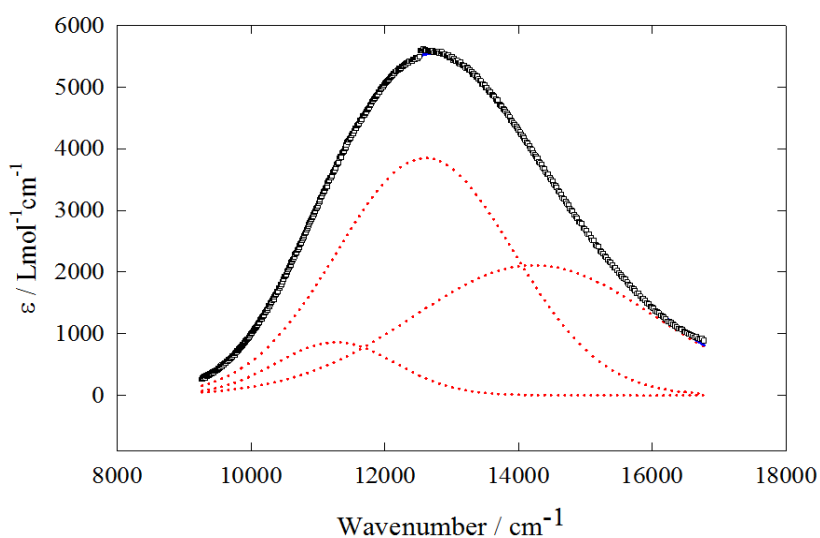


Figure 5.2.1: Electronic spectrum of *trans*-[Ru(tpy)(Cl₅pcyd)Cl₂] (**5**) in CH₂Cl₂ showing the best fit of the three Gaussian curves (dashed lines) used for the calculation of oscillator strength.

5.2.5 Theoretical Calculations

Unrestricted hybrid HF-DFT SCF calculations were performed on *trans*-[Ru(tpy)(R-pcyd)Cl₂] complexes in order to obtain equilibrium geometries, orbital energies, spin density distributions as well as to generate calculated IR and UV-vis spectra of complexes using Wavefunction Inc., Spartan'14 Parallel suite program, with

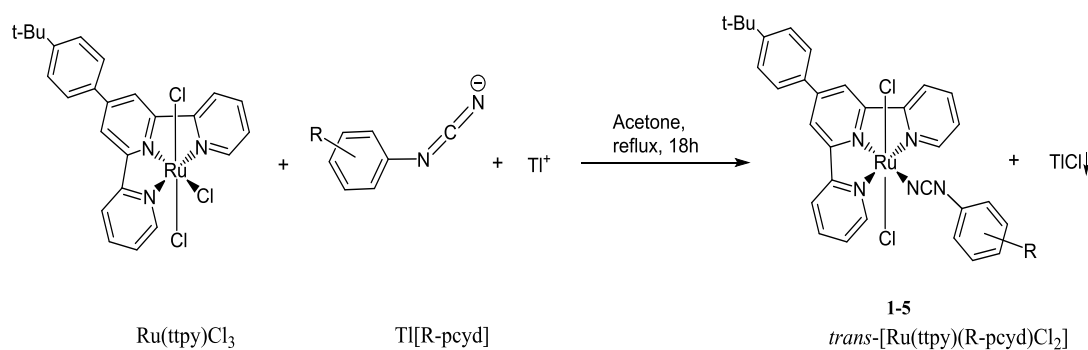
the Beck three parameter hybrid exchange and Lee-Yang-Parr correlation functionals (B3LYP) and the 6-31G* basis set for C, H, N, S and LANL2DZ basis set for Ru atoms.⁴¹⁻⁴² All geometry optimization was performed in C₁ symmetry with subsequent vibrational frequency analysis to confirm that each stationary point was a minimum on the potential energy surface. Wave function stability calculations were performed to confirm that the calculated wave function corresponded to the electronic ground state. Tight SCF convergence criteria (10⁻⁸ a.u.) were used for all calculations. To simplify the calculations, *t*-butylphenyl groups in *trans*-[Ru(tpy)(R-pcyd)Cl₂] (**1-5**) complexes were replaced by H atoms.

5.3 Results and Discussion

5.3.1 Synthesis

The *trans*-[Ru(tpy)(R-pcyd)Cl₂] complexes (**1-5**) have been prepared by the metathesis reaction of Ru(tpy)Cl₃·H₂O with Tl[R-pcyd] in refluxing acetone for 18 h according to the Scheme 5.4.1.

Scheme 5.3.1: Reaction Scheme for the Synthesis of *trans*-[Ru(tpy)(R-pcyd)Cl₂] Complexes. (**1-5**)



The coordination of R-pcyd ligands in **1-5** was established by the presence of the intense $\nu(\text{NCN})$ band at 2104-2150 cm^{-1} in the IR spectra. In addition, **1-5** exhibited a Ru(III)-NCN LMCT band in their electronic absorption spectra (Figure 5.3.11 and 5.3.12), which was absent in the absorption spectrum of Ru(tpy)Cl₃ (Figure 5.3.9). The syntheses of these complexes have been found to be extremely sensitive to the nature of the solvent due to the formation of Ru(II) species in regular organic solvents such as DMF, ethanol, methanol, acetonitrile, DMSO, ethoxy ethanol etc., and only the reaction in acetone gave substantial quantities of the desired Ru(III) complexes. Complexes with a reduced number of chloro-substituents on R-pcyd ligand were found to be difficult to isolate in the Ru(III) state and all attempts to synthesize unsubstituted phenylcyanamide

(pcyd) complex were unsuccessful. Column chromatography using alumina (Brockman, acidic, grade III) as adsorbent and a solvent mixture of CH₂Cl₂ and acetone as eluents enabled isolation of pure **1-5** from Ru(II) impurities. The first green band contained minor quantities of a Ru(III) complex (probably *cis*-isomer, chemistry not pursued), while the second yellow band gave the major product, **1-5**, whose structure was determined by crystallographic analysis of *trans*-[Ru(tpy)(Cl₃pcyd)Cl₂]·2CH₃CN **3**. It is interesting to speculate on the mechanism of this reaction. If the mechanism was dissociative and formed a trigonal bipyramidal intermediate in which the tpy ligand occupies the two axial and one trigonal plane coordination sites, approach by R-pcyd⁻ would experience less steric hinderance if it did so between the chloro ligands and so result in a *trans*-dichloro product.

Complexes **1-5** showed a tendency to get reduced on the column, which also resulted in poor overall yields (7-12%). Elemental analyses were consistent molecular formulae and complex purity was further confirmed by clean cyclic voltammetry, ¹H NMR and IR spectroscopy. The complexes, especially **1** and **2** decomposed in air over a period of months and so should be stored in the refrigerator. In general, all complexes showed less stability in solutions of highly donor solvents such as DMF, DMSO etc. and decompose within several hours.

5.3.2 X-ray Crystallography

Dark-red block crystals of the precursor Ru(tpy)Cl₃·2DMSO complex were grown from a warm solution of the complex in DMSO. Red block crystals of the *trans*-[Ru(tpy)(Cl₃pcyd)Cl₂]·2CH₃CN complex were grown from acetonitrile by slow evaporation of the solvent. Crystal data and selected bond lengths and angles for both

complexes appear in Tables 5.3.1-5.3.2 and 5.3.3-5.3.4, respectively. ORTEP drawing of Ru(tpy)Cl₃·2DMSO and *trans*-[Ru(tpy)(Cl₃pcyd)Cl₂]₂·2CH₃CN complexes are shown in the Figure 5.3.1 and 5.3.2 respectively. The complete X-ray data can be found in the Table E.1 and E2 in the Appendix E.

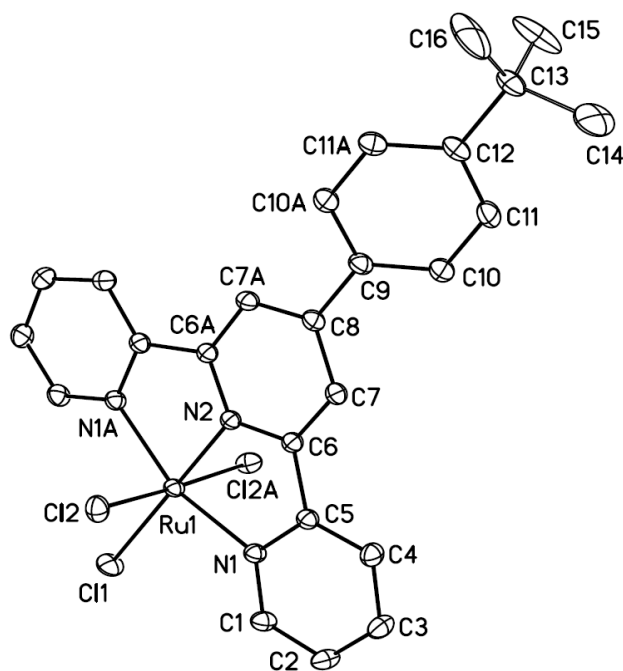


Figure 5.3.1: ORTEP drawing of Ru(tpy)Cl₃·2DMSO complex. The solvent molecules of crystallization have been omitted.

In Ru(tpy)Cl₃·2DMSO, Ru(III) ion occupies a pseudo-octahedral coordination sphere of tridentate 4'-(4-tertbutylphenyl)-2,2':6',2''-terpyridine (ttpy) ligand and three chlorine atoms (Figure 5.3.1). The configuration of the ttpy ligand in the complex closely resembles those in other complexes of 2,2':6',2''-terpyridine (tpy).³³ In a free terpyridine ligand, the three pyridine rings adopt stable *trans* conformation about the interannular C-C bonds, where two terminal pyridine rings are slightly twisted about the interannular

Table 5.3.1: Crystal Data and Structure Refinement of [Ru(ttpy)Cl₃] \cdot 2DMSO Complex.

Empirical Formula	C ₃₃ H ₄₇ Cl ₃ N ₃ O ₄ RuS ₄	
Formula Weight	885.40 g/mol	
Temperature	200(2) K	
Wavelength	0.71073 Å	
Crystal System	Monoclinic	
Space Group	C2/c	
Unit Cell Dimensions	a = 18.309(6) Å	alpha = 90.00°
	b = 17.033(5) Å	beta = 120.897(4)°
	c = 15.163(5) Å	gamma = 90.00°
Volume, Z	4058(2) Å ³ , 4	
Density (calculated)	1.449 Mg/m ³	
Absorption Coefficient	0.828 mm ⁻¹	
F (000)	1828	
Crystal Size	0.39 x 0.14 x 0.11	
Theta range for data collection	2.77 to 28.22°	
Limiting Indices	-24 ≤ h ≤ 24, -22 ≤ k ≤ 22, -20 ≤ l ≤ 20	
Reflections Collected	5039	
Absorption Correction	multi-scan	
Max. And Min. Transmission	0.7389 and 0.9152	
Refinement Method	Full-matrix Least-squares on F ²	
Data/ Restraints/ Parameters	5039 / 8 / 253	
Goodness-of-fit on F ²	1.035	
R1 ^a	0.0306	
wR2 ^b	0.0736	

$${}^a\text{R1} = \sum \left| |F_o| - |F_c| \right| / \sum |F_o|$$

$${}^b\text{wR2} = \left(\sum w (|F_o| - |F_c|)^2 / \sum w |F_o|^2 \right)^{1/2}$$

Table 5.3.2: Selected Crystal Structure Data of [Ru(tpy)Cl₃].2DMSO Complex.**Bond Lengths^a / angstrom**

Ru-N2	1.9723(19)	Ru-Cl1	2.3522(9)
Ru-N1	2.0747(15) 2	Ru-Cl2	2.3555(9) 2
Ru-N1	2.0748(15)	Ru-Cl1	2.0790(18)

Bond Angles^a / deg

N2-Ru-N1	79.97(4) 2	N1-Ru-N1	159.95(7) 2
N2-Ru-N1	79.98(4)	Cl2-Ru-Cl2A	175.57(2) 2
Cl1-Ru-N1	100.03(4) 2	Cl2-Ru-Cl1	92.217(11) 2
Cl1-Ru-N1	100.02(4)	Cl2-Ru-Cl1	92.218(11)
N2-C6-C5	113.46(14)	C11-C12-C11A	116.7(2)

^a Estimated standard deviations are in parenthesis

C-C bonds, making interannular angles of 5-9° with the central pyridine.^{33a,b} However, coordination of the tridentate terpyridine ligand to metal is favoured by the attainment of *cis* configurations of pyridine rings about interannular C-C bonds, which provided a more planar arrangement of three pyridine rings in coordinated terpyridine.^{33a,b} In accordance with this, the terpyridine fragment of the tpy ligand is approximately planar in Ru(tpy)Cl₃·2DMSO complex, with the C4-C5-C6-C7 dihedral angle describing the angle between the terminal and the central pyridine ring being 3.4(3)°. The Ru-N bond lengths show the expected pattern, as seen in other complexes of 2,2':6',2''-terpyridine (tpy), with short contacts to the central ring (Ru-N2 = 1.9723(19) Å) and longer contacts to the terminal rings (Ru-N3, Ru-N4 = 2.0747(15) Å, 2.0748(15) Å). The Ru-N bond lengths very closely resemble those of [Ru(tpy)₂]²⁺ complex (1.97-2.00 Å and 2.06-2.08 Å for the central and terminal bonds respectively).^{33d,e,f} The steric constraints of the tridentate tpy ligand prevent the formation of N1-Ru-N2 and N1A-Ru-N2 angles of 90°, leading to an average bite angles of 79.97(4)-79.98(4)°. These angles are very similar to other transition metal-terpyridine complexes.³³ On the other hand, the *t*-butylphenyl ring is not coplanar with the terpyridine fragment and significantly twisted about the interannular C-C bond, with a C7-C8-C9-C10 dihedral angle of 32.88(13)°. This feature, as observed in other 4'-substituted terpyridine ligands and in their complexes, represents a compromise between a coplanar arrangement in which π -conjugation and steric repulsion between the *ortho* protons of the phenyl ring protons and H3'(5') protons on the central pyridine ring are maximized, and one in which the two rings are perpendicular, in which both π -conjugation and steric repulsion are minimized.^{33b,c,h} The twisted geometry, as also observed in other 4'-substituted terpyridine ligands, causes a decrease in the endocyclic

C11-C12-C11A bond angle ($116.7(2)^\circ$) at the 4' position from that observed in the unsubstituted terpyridine (120°) (ref). The *trans* Ru-Cl2 and Ru-Cl2A bonds are slightly deviated from linearity ($175.57(2)^\circ$), while the other Ru-Cl1 bond is almost colinear with the *trans* Ru-N2 bond (180°). The *trans* disposition of σ -donor chlorine and π acceptor pyridine ligand results in a significantly small Ru-Cl1 bond length ($2.0790(18)$ Å) for this chlorine relative to two *trans* Ru-Cl2 and Ru-Cl2A bonds ($2.3522(9)$ Å and $2.3555(9)$ Å respectively) and is likely to cause shortening of the central Ru-N bond relative to terminal Ru-N bonds.

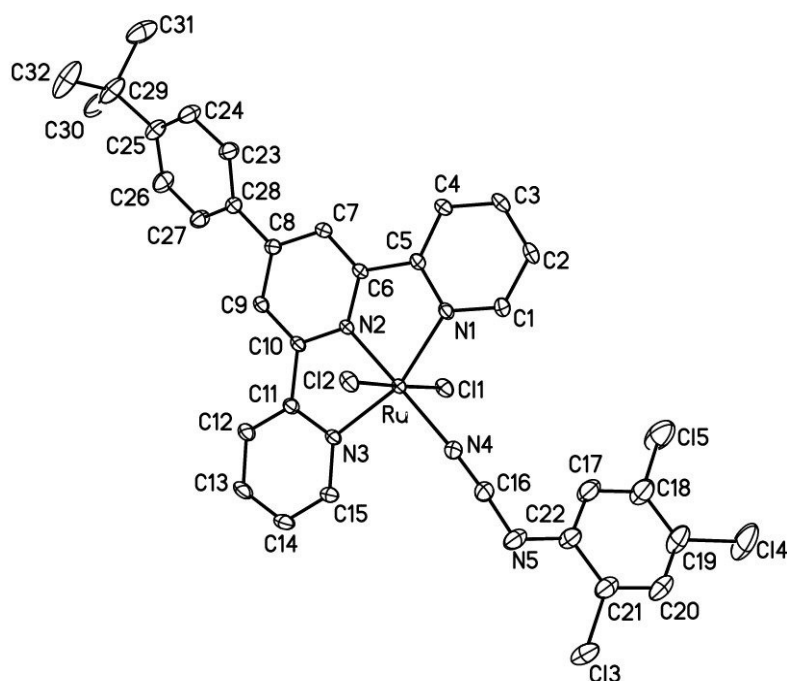


Figure 5.3.2: ORTEP drawing of *trans*-[Ru(tpy)(Cl₃pcyd)Cl₂] \cdot 2CH₃CN complex. The solvent molecules of of crystallization have been omitted.

The ORTEP drawing of *trans*-[Ru(tpy)(Cl₃pcyd)Cl₂] \cdot 2CH₃CN complex indicates that the coordination environment around Ru(III) is that of a distorted octahedron of four nitrogen and two chlorine atoms, with tpy ligand occupying the

equatorial plane and the cyanamide group adopting *trans* disposition with respect to the central pyridine ring of the tpy ligand. The phenyl ring of the phenylcyanamide ligand is twisted about the terpyridine ring by angle of about 60°. The cyanamide group is approximately linear (175.4(3)°), while the angle (162.9(2)°) describing the coordination of its terminal nitrogen to Ru(III) is significantly bent. In contrast, four crystal structures of Ru(III)-cyanamide complexes showed an average Ru(III)-cyanamide bond angle of 174.6°. ³⁴ It has been suggested that the π -bonding between Ru(III) and cyanamide is optimized when this angle is linear, a condition which evidently relaxed when π -bonding is not as important. The ruthenium-cyanamide (Ru-N4) bond length of 2.015 Å is comparable to a value of 1.98 Å in the crystal structure of [Ru(NH₃)₅(2,3-Cl₂pcyd)]²⁺ and to those of other Ru(III)-cyanamide complexes. ²¹ The dihedral C21-C22-N5-C16 angle (170.7(3)°) indicates that both cyanamide and phenyl groups are almost coplanar. This, in addition to the partial double bond character of N5-C22 bond (1.43 Å), is a result of the strong π -interaction between cyanamide and phenyl groups. ^{21,34} The terminal N4-C16 bond (1.169(3) Å) is significantly shorter than the N5-C16 bond (1.279(4)°), indicating significant nitrile character of the terminal CN group. These bond lengths are comparable to those observed in other Ru-cyanamide complexes (ref). ^{21,34} The tpy ligand in *trans*-[Ru(tpy)(Cl₃pcyd)Cl₂] \cdot 2CH₃CN complex exhibits the similar structural feature as in Ru(tpy)Cl₃ \cdot 2DMSO complex. The terpyridine fragment is approximately coplanar with the C4-C5-C6-C7 dihedral angle of 4.0(4)°, which describes the angle between terminal and central pyridine rings. On the other hand, the *t*-butylphenyl group is twisted about the terpyridine plane with the interplanar angle (defined by the C7-C8-C28-C23 dihedral

Table 5.3.3: Crystal Data and Structure Refinement for *trans*-[Ru(ttpy)(Cl₃pcyd)Cl₂] \cdot 2CH₃CN Complex (**3**).

Empirical Formula	C ₃₆ H ₃₁ Cl ₅ N ₇ Ru
Formula Weight	840.00 g/mol
Temperature	200(2) K
Wavelength	0.71073 Å
Crystal System	Triclinic
Space Group	P-1
Unit Cell Dimensions	a = 8.6978(7) Å alpha = 104.0080(10)° b = 11.3678(10) Å beta = 91.3040(10)° c = 21.7117(18) Å gamma = 110.6300(10)°
Volume, Z	1935.5(3) Å ³ , 8
Density (calculated)	1.441 Mg/m ³
Absorption Coefficient	0.785 mm ⁻¹
F (000)	850
Crystal Size	0.33 x 0.20 x 0.14
Theta range for data collection	2.38 to 27.54°
Limiting Indices	-11 ≤ h ≤ 11, -14 ≤ k ≤ 14, -28 ≤ l ≤ 28
Reflections Collected	8906
Absorption Correction	multi-scan
Max. And Min. Transmission	0.8980 and 0.7822
Refinement Method	Full-matrix Least-squares on F ²
Data/ Restraints/ Parameters	8906/ 709 /464
Goodness-of-fit on F ²	1.026
R1 ^a	0.0427
wR2 ^b	0.1019

$${}^a\text{R1} = \frac{\sum \left| |F_o| - |F_c| \right|}{\sum |F_o|}$$

$${}^b\text{wR2} = \left(\frac{\sum w \left(|F_o| - |F_c| \right)^2}{\sum w |F_o|^2} \right)^{1/2}$$

Table 5.3.4: Selected Crystal Structure Data for *trans*-[Ru(tpy)(Cl₃pcyd)Cl₂] \cdot 2CH₃CN Complex.

Bond Lengths^a / angstrom

Ru-N2	1.9636(18)	Ru-Cl2	2.3485(6)
Ru-N1	2.0712(18)	N5-C22	1.431(4)
Ru-N3	2.0790(18)	N4-C16	1.169(3)
Ru-N4	2.015(2)	N5-C16	1.279(4)
Ru-Cl1	2.3470(6)		

Bond Angles^a / deg

N2-Ru-N1	79.36(7)	N4-C16-N5	175.4(3)
N2-Ru-N3	79.72(7)	Cl1-Ru-Cl2	178.57(2)
N4-Ru-N1	101.84(8)	N1-Ru-N3	159.04(8)
N4-Ru-N3	99.07(8)	C16-N4-Ru	162.9(2)
N4-Ru-Cl2	91.97(7)	C16-N5-C22	118.4(5)
N4-Ru-Cl1	88.91(7)	C7-C8-C9	118.0(2)

^a Estimated standard deviations are in parenthesis

angle) of $28.8(4)^\circ$. The Ru-N and two *trans* Ru-Cl bond lengths as well as *bite*-angles are almost similar as those in Ru(tpy)Cl₃·2DMSO complex.

5.3.3 IR Spectroscopy

The infrared spectra of all *trans*-[Ru(tpy)(R-pcyd)Cl₂] complexes (**1-5**) were taken on the KBr discs and the corresponding $\nu(\text{NCN})$ stretches along with those of R-pcydH and Tl[R-pcyd] salts are shown in the Table 5.3.5. Figure 5.3.3 and 5.3.4 show representative experimental and DFT calculated IR spectra of *trans*-[Ru(tpy)(Cl₂pcyd)Cl₂] complex (**2**).

1-5 exhibit strong $\nu(\text{NCN})$ stretches at 2104-2140 cm^{-1} in their IR spectra. Table 5.3.5 shows a slight positive shift in $\nu(\text{NCN})$ with an increase in the number of chloro-substituents on R-pcyd. The intermediate frequency of $\nu(\text{NCN})$ in phenylcyanamide complexes between those in the free neutral ligand and their anionic forms is consistent with coordinated phenylcyanamide ligands.²⁰⁻²³ The $\nu(\text{NCN})$ bands in **1-5** appear at the similar position as those in [Ru(NH₃)₅(R-pcyd)]²⁺ (2110-2140 cm^{-1}), but at slightly lower frequencies than those in [Ru(tpy)(bpy)(R-pcyd)]⁺ (2156-2181 cm^{-1}).²⁰⁻²⁴ The low energy shift of $\nu(\text{NCN})$ in Ru(III)-cyanamide complexes relative to that of Ru(II)-cyanamide complexes has been attributed to an increase contribution from the carbodiimide structure (B) of a cyanamide group attached to a highly electronegative Ru(III) ion.³⁵

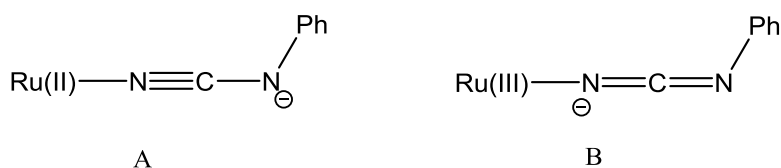


Table 5.3.5: IR Data of $\nu(\text{NCN})$ bands in Free Protonated R-pcydH Ligands, in Thallium Salts and in *trans*-[Ru(tpy)₂(R-pcyd)Cl₂] Complexes (1-5).^a

Ligands	$\nu(\text{NCN})$ in R-pcydH Ligands / cm^{-1}	$\nu(\text{NCN})$ in Thallium Salts / cm^{-1}	$\nu(\text{NCN})$ in Ruthenium Complexes / cm^{-1}
Cl ₅ pcyd	2250	2076	2142
Cl ₄ pcyd	2253	2098	2136
Cl ₃ pcyd	2247	2133	2150
Cl ₂ pcyd	2235	2098	2143
Clpcyd	2235	2058, 2091	2104

^a data recorded on KBr disc.

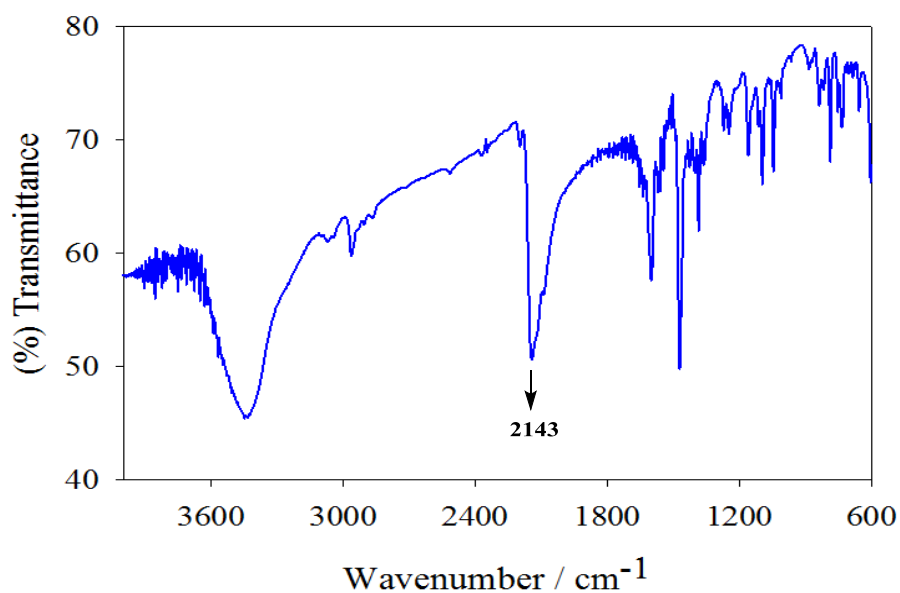


Figure 5.3.3: IR spectrum of *trans*-[Ru(tpy)(Cl₂pcyd)Cl₂] complex on KBr.

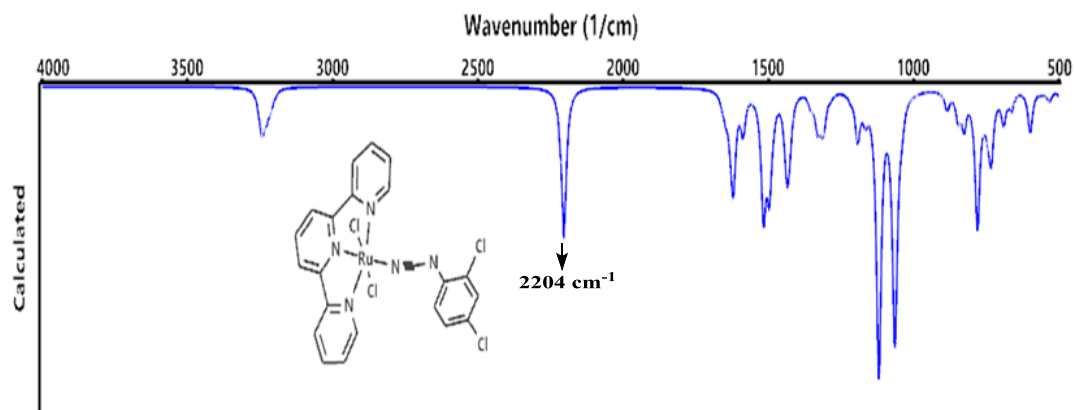


Figure 5.3.4: DFT calculated IR spectrum of *trans*-[Ru(tpy)(Cl₂pcyd)Cl₂] complex in vacuum.

Gas-phase DFT calculations of the IR spectra of all *trans*-[Ru(tpy)(R-pcyd)Cl₂] complexes were performed. Representative experimental and calculated IR spectra of *trans*-[Ru(tpy)(Cl₂pcyd)Cl₂] (Figures 5.3.3 and 5.3.4) show that while there is a good agreement, DFT calculations slightly overestimated the frequency of the $\nu(\text{NCN})$.

5.3.4 Electronic Structure

Unrestricted hybrid HF-SCF DFT calculations were performed on Ru(tpy)Cl₃ and *trans*-[Ru(tpy)(R-pcyd)Cl₂] complexes (**1-4**) in the gas phase using B3LYP/6-31G*-LANL2DZ model. To simplify calculations the tpy ligand was replaced by unsubstituted terpyridine (tpy). A gas-phase DFT calculation of *trans*-[Ru(tpy)(Cl₅pcyd)Cl₂] (**5**) was attempted, however, calculation would not converge. The B3LYP/6-31G*-LANL2DZ model also failed to meet the convergence criteria when solvents are included in calculations. The frontier molecular orbitals and corresponding orbital energies of Ru(tpy)Cl₃, *trans*-[Ru(tpy)(Cl₁pcyd)Cl₂] (**1**) and *trans*-[Ru(tpy)(Cl₄pcyd)Cl₂] (**3**) are shown in Figure 5.3.5, 5.3.6, 5.3.7, respectively. The results for *trans*-[Ru(tpy)(Cl₂pcyd)Cl₂] (**2**) and *trans*-[Ru(tpy)(Cl₃pcyd)Cl₂] (**3**) are shown in the Figures

E.1 and E.2 in Appendix-E. The spin density distributions $\text{Ru}(\text{tpy})\text{Cl}_3$ and *trans*- $[\text{Ru}(\text{tpy})(\text{R-pcyd})\text{Cl}_2]$ complexes (**1-4**) along with that of $[\text{Ru}(\text{tpy})(\text{pcyd})\text{Cl}_2]$ are shown in the Figure 5.3.8 (a-f) for comparison.

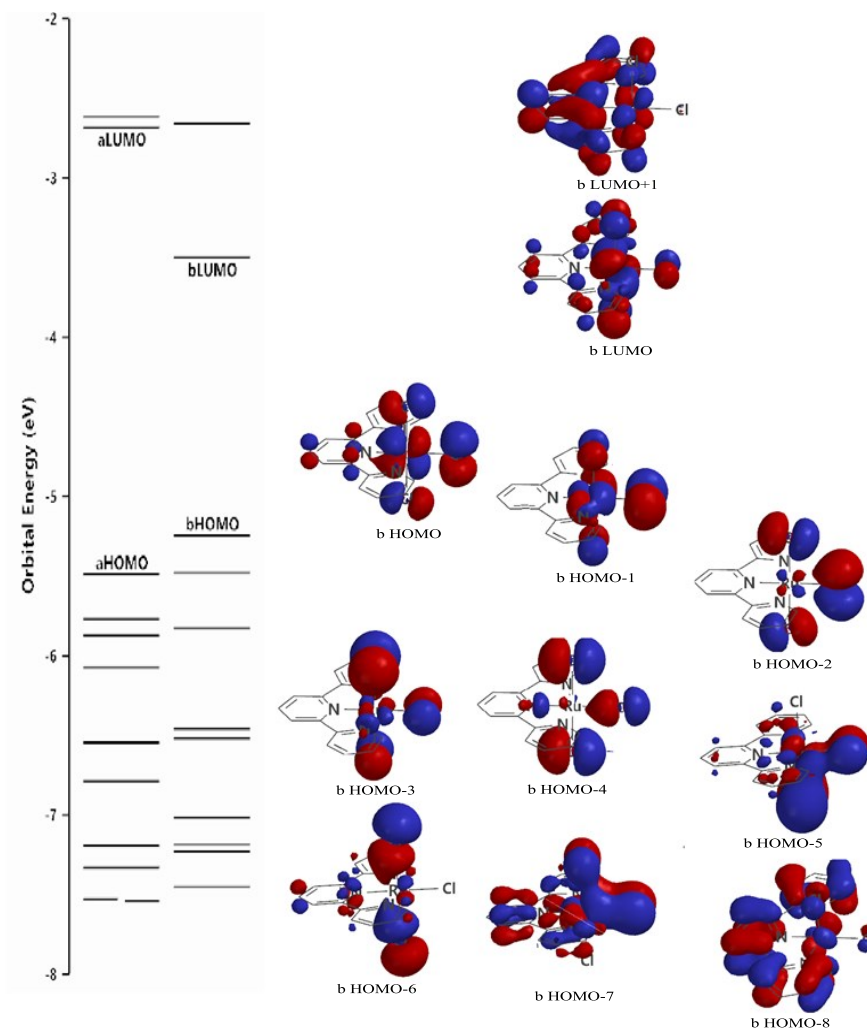


Figure 5.3.5: DFT calculation of orbital energies and selected molecular orbitals of $\text{Ru}(\text{tpy})\text{Cl}_3$ complex.

Gas phase DFT calculations on $\text{Ru}(\text{tpy})\text{Cl}_3$ complex gave both α and β wavefunctions for frontier orbitals. The bonding interactions between Ru and Cl ligands are readily observed in the frontier orbitals described by β wavefunctions as shown in the

Figure 5.3.5. The highest occupied molecular orbitals (β -HOMO, β -HOMO-1) have almost equal contribution from Ru $d\pi$ and $p\pi$ orbitals on three Cl^- ligands (Figure 5.3.3). These HOMOs are comprised of π -antibonding interactions between Ru $d\pi$ and the $p\pi$ orbitals on Cl^- ligands. The β -HOMO-2, β -HOMO-3, β -HOMO-4 show very weak π -bonding interactions between Ru $d\pi$ and Cl^- $p\pi$ orbitals. On the other hand, strong π -bonding interactions are observed in β -HOMO-5, β -HOMO-6 and β -HOMO-7 of this complex. The corresponding antibonding interactions between Ru $d\pi$ β -hole and $p\pi$ orbitals on Cl^- ligands are present in the β -LUMO for β -HOMO-5 and β -HOMO-7 and β -LUMO+1 for β -HOMO-6. This may give rise to multiple electronic transitions from low lying β -HOMOs to β -LUMO, which could be assigned to Cl^- $p\pi$ to Ru(III) $d\pi$ LMCT transitions.

DFT calculations in the gas-phase gave a variation in the optimized geometry as well as frontier orbital features of *trans*-[Ru(tpy)(R-pcyd) Cl_2] complexes. Like Ru(tpy) Cl_3 , the β -wavefunctions, show the bonding interactions between Ru and R-pcyd ligands. As seen in the Figure 5.3.6, the β -HOMO and β -HOMO-1 of *trans*-[Ru(tpy)(Cl-*pcyd*) Cl_2] complex (**1**) are comprised mainly of π -antibonding interactions between Ru $d\pi$ orbitals and Cl^- $p\pi$ orbitals, with some antibonding interaction of the fragment π -MO on the cyanamide group and the Ru $d\pi$ orbital. Of particular importance is the β -HOMO-2, which shows a π -bonding interaction between Ru and the Clpcyd ligand, while corresponding antibonding interaction is present in the β -LUMO. There is significant contribution of Clpcyd π orbital in both bonding β -HOMO-2 and antibonding β -LUMO, indicating significant covalent character of the Ru-Clpcyd bond. On the other hand, β -HOMO-3 and β -HOMO-4 are mainly localized on two *trans* Cl^- ligands, showing very

weak π -bonding interactions between Ru $d\pi$ orbitals and the $p\pi$ orbitals on the Cl ligands. However, like $\text{Ru}(\text{tpy})\text{Cl}_3$, the β -HOMO-5, β -HOMO-6 and β -HOMO-7 in *trans*- $[\text{Ru}(\text{tpy})(\text{Cl-tpcd})\text{Cl}_2]$ are comprised of strong π -bonding interactions between Ru $d\pi$

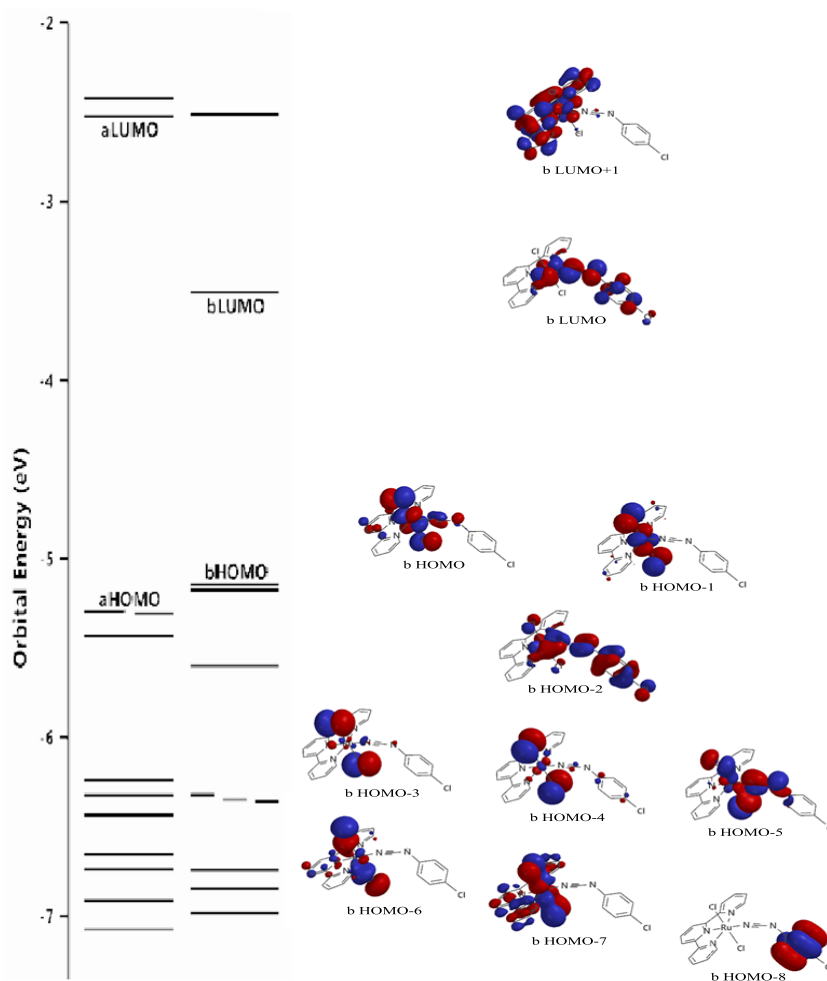


Figure 5.3.6: DFT calculation of orbital energies and selected molecular orbitals of *trans*- $[\text{Ru}(\text{tpy})(\text{Cltpcd})\text{Cl}_2]$ complex.

and Cl $p\pi$ orbitals. While the β -LUMO is mainly localized on Ru and Cltpcd ligand, the β -LUMO+1 is mainly composed of tpy π^* and Ru $d\pi$ orbitals. Interesting thing to be noted here that, there is no contribution from Cl $p\pi$ orbitals on both β -LUMO and β -

LUMO+1, implying more ionic character in the Ru-Cl bonds, as opposed to prominent covalent character in the Ru-Clpcyd bond.

In contrast to Clpcyd⁻ complex (1), the β -HOMOs in the Cl₂-, Cl₃-, Cl₄pcyd complexes (2-4) show π -bonding interactions between Ru d π and π -HOMO of R-pcyd

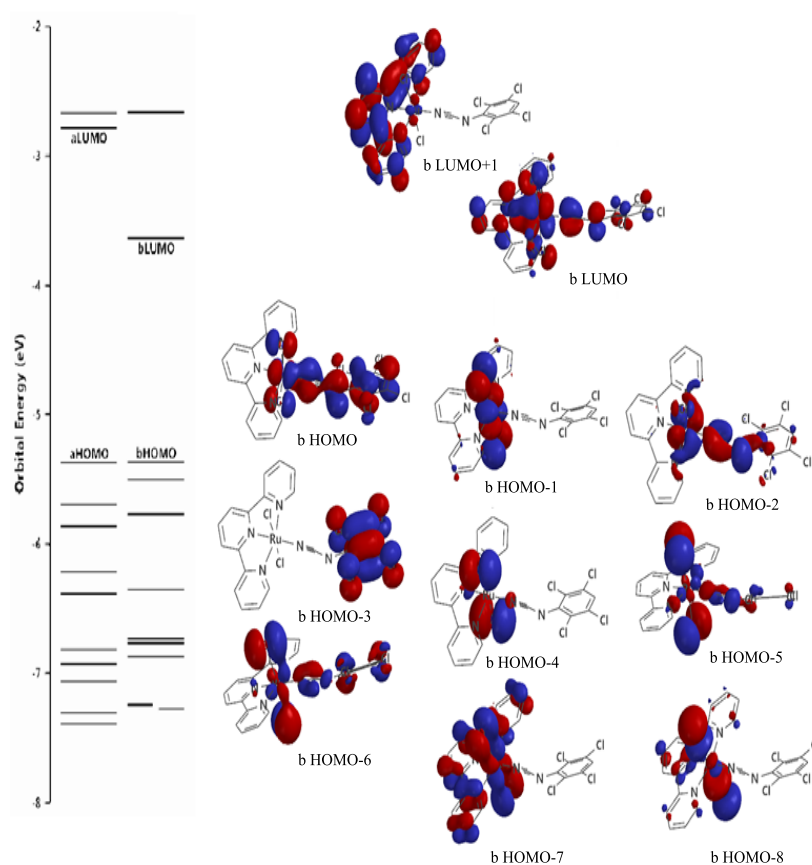


Figure 5.3.7: DFT calculation of orbital energies and selected molecular orbitals of *trans*-[Ru(tpy)(Cl₄pcyd)Cl₂] complex.

ligands, which is shown for Cl₄pcyd complex (4) in the Figure 5.3.7. However, like Clpcyd⁻ complex (1), corresponding antibonding interactions between Ru d π and π orbitals on R-pcyd ligands are present in the β -LUMOs of Cl₄pcyd (4) as well as Cl₂- and Cl₃pcyd⁻ complexes (2-3). The other β -HOMOs and β -LUMOs of Cl₂-, Cl₃-, Cl₄pcyd⁻

complexes (2-4) have similar features as those of Clpcyd complex (1), with β -HOMO-6, β -HOMO-7, and β -HOMO-8 showing π -bonding interactions between Ru $d\pi$ and $p\pi$ orbitals of two *trans* Cl⁻ ligands and the β -LUMO+1 comprising mostly of Ru $d\pi$ and tpy π^* orbitals. From visual inspection of β -LUMO's of complexes 1-4, it is clear that the phenylcyanamide ligand contribution in the β -LUMO is significantly reduced in the Cl₄pcyd⁻ complex (4) relative to that in Clpcyd⁻ complex (1), while contributions from two Cl⁻ ligands are more pronounced in the β -LUMO of the former (4) relative to that of the latter (1). This indicates more ionic character of the Ru-Cl₄pcyd and a greater covalency of the Ru-Cl bonds in the Cl₄pcyd⁻ complex (4) relative to those in the Clpcyd⁻ complex (1), the behavior which is consistent with π -donor properties of R-pcyd ligands. As seen in the Figure 5.3.8, due to lack of charge transfer from the deactivated Cl₄pcyd⁻ ligand, the Ru $d\pi$ -hole tends to adopt a configuration in which it gets some charge density from two *trans* chloride ligands, resulting in almost coplanarity of R-pcyd⁻ ligand with the terpyridine ligand in the Cl₄pcyd⁻ complex (4). On the other hand, in Clpcyd⁻ complex(1), the Ru $d\pi$ -hole receives significant charge density from highly donor Clpcyd⁻ ligand through strong π -bonding interaction, which gives rise to a configuration in which Clpcyd⁻ ligand is almost perpendicular to the plane of the terpyridine ring in Clpcyd⁻ complex (1). Although DFT calculated geometry show coplanarity of R-pcyd⁻ ligand with the terpyridine ring in Cl₂-, Cl₃- and Cl₄pcyd⁻ complexes (2-4) as opposed to their perpendicular orientation in Clpcyd⁻ complex, the crystal structure of Cl₃pcyd⁻ complex (3) shows an intermediate angle ($\sim 60^\circ$) between the Cl₃pcyd⁻ ligand and the terpyridine ring. The variation in donor properties R-pcyd⁻ ligands as well as the resultant geometry of 1-4 is also expressed in their calculated spin density distributions.

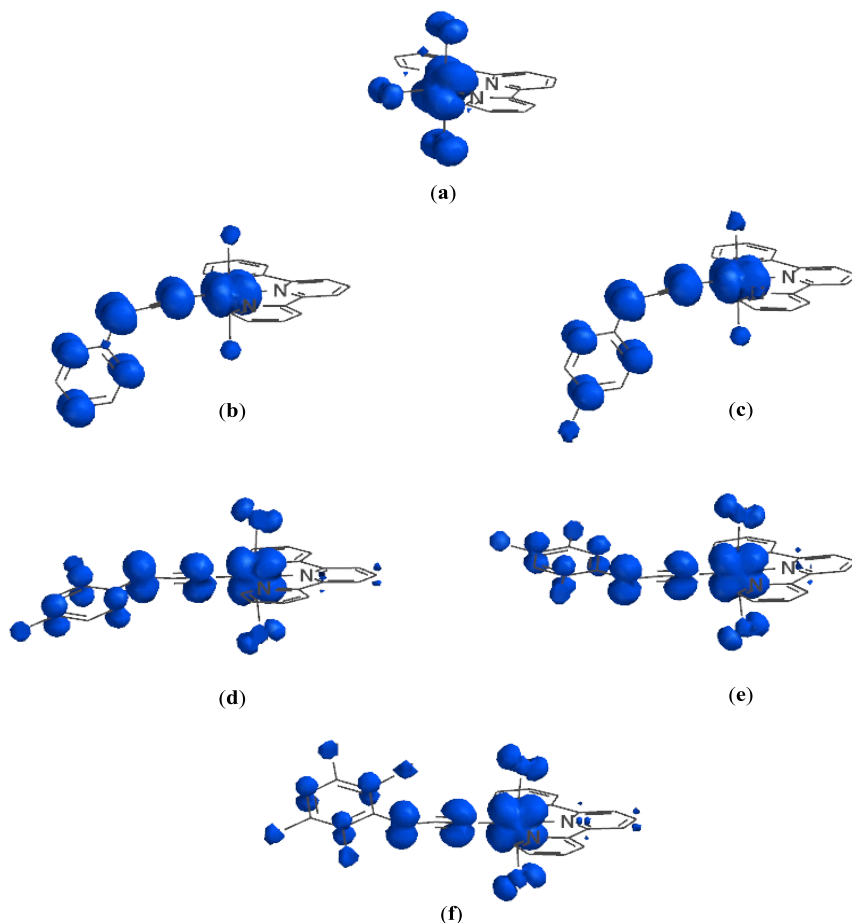


Figure 5.3.8: Calculated spin density distributions of (a) $\text{Ru}(\text{tpy})\text{Cl}_3$ and (b-f) *trans*- $[\text{Ru}(\text{tpy})(\text{R-pcyd})\text{Cl}_2]$ complexes. R = H- (b), Cl- (c), Cl_2^- (d), Cl_3^- (e), Cl_4^- (f).

Gas-phase DFT calculated spin density distributions (Figure 5.3.8 b-f) of *trans*- $[\text{Ru}(\text{tpy})(\text{R-pcyd})\text{Cl}_2]$ complexes are very similar in appearance to the β -HOMO-2 in unsubstituted and Clpcyd^- complexes and β -HOMO in Cl_2^- , Cl_3^- and Cl_4pcyd^- complexes, which are the SOMO's in these complexes. In precursor $\text{Ru}(\text{tpy})\text{Cl}_3$ complex (Figure 5.3.8 a), the spin density is mostly localized on the Ru(III) ion and the three chloro ligands. When a chloro ligand is replaced by the pcyd^- ligand (Figure 5.3.8b), a redistribution of spin density occurs with most of the spin density being localized on pcyd^- ligand, strongly suggesting non-innocent behaviour. However, as the number of

chloro-substituents increases on the R-pcyd⁻ ligands, the spin density becomes more localized on the Ru ion and the two *trans*-Cl⁻ ligands (Figures 5.3.8c-f). The R-pcyd⁻ ligands therefore become more innocent with increasing numbers of chloro-substituents.

Gas phase DFT calculations are often misleading because they do not account for solvent-solute interactions that may stabilize a higher metal ion oxidation state.^{25,34} A more realistic picture of spin density distributions of these paramagnetic complexes (**1-5**) was obtained from their solution ¹H NMR studies, which will be discussed in the section 5.3.8.

5.3.5 Electronic Absorption Spectroscopy

The quantitative electronic absorption spectra of Ru(tpy)Cl₃ in DMF and CH₂Cl₂ and the corresponding Gas-phase DFT calculated spectrum are shown in the Figures 5.3.9-5.3.10. Those of *trans*-[Ru(tpy)(R-pcyd)Cl₂] complexes (**1-5**) in DMF and CH₂Cl₂ are shown in the Figure 5.3.11-5.3.12. DFT calculated spectra for *trans*-[Ru(tpy)(R-pcyd)Cl₂] complexes (**2**, **3** and **4**) are included in the Figure 5.3.13 for comparison. The experimental absorption data for precursor Ru(tpy)Cl₃ and *trans*-[Ru(tpy)(R-pcyd)Cl₂] complexes (**1-5**) in DMF and CH₂Cl₂ are compiled in the Table 5.3.6.

The absorption spectra (Figure 5.3.9) of Ru(tpy)Cl₃ complex in DMF and CH₂Cl₂ show strong absorptions at 288-320 nm, two fairly intense overlapping bands at 412-425 nm and a weak shoulder at 490 nm. The high energy 288-320 nm band in the experimental spectra is typical of π to π^* transitions in tpy ligand,^{24,33,36} while the low energy visible bands (412-425 nm) can be assigned, in the light of DFT frontier orbital

calculations (Figure 5.3.10) to multiple Ru(III)-Cl LMCT transitions. These absorption bands show little variation with the polarity of the solvent.

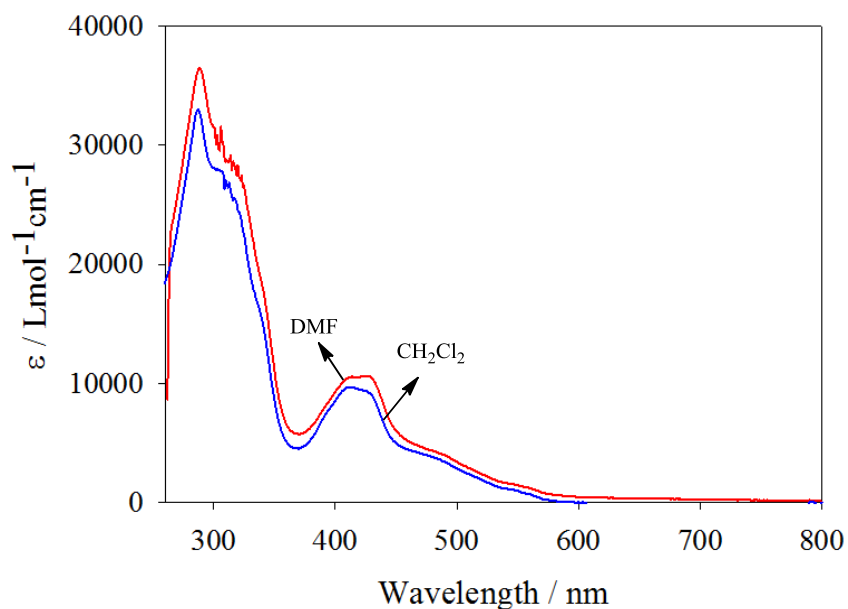


Figure 5.3.9: Quantitative electronic absorption spectra of Ru(tpy)Cl₃ complex in DMF and in CH₂Cl₂.

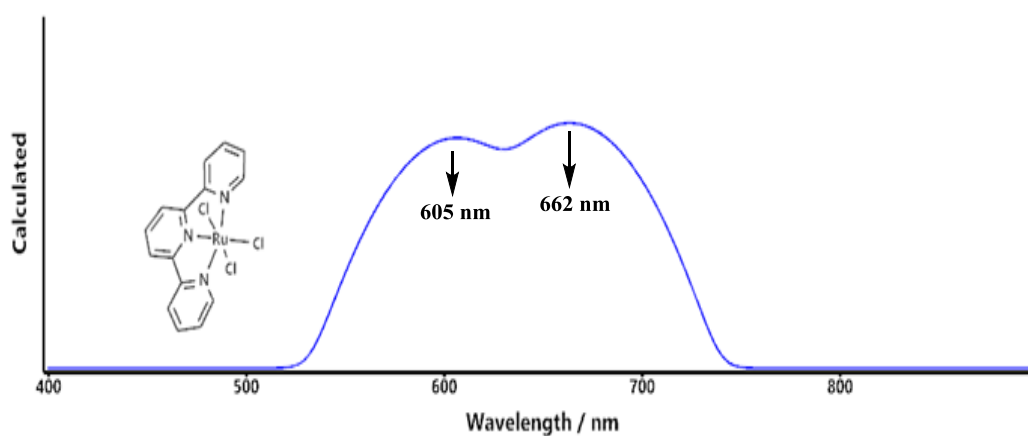


Figure 5.3.10: Calculated electronic absorption spectrum of Ru(tpy)Cl₃ complex in vacuum.

Table 5.3.6: Quantitative Electronic Absorption Data of Ru(tpy)Cl₃ and *trans*-[Ru(tpy)(R-pcyd)Cl₂] Complexes (1-5) in DMF and CH₂Cl₂.^{a,b}

R-pcyd ⁻	Wavelength, λ / nm (Molar Extinction Coefficient, ϵ / mol L ⁻¹ cm ⁻¹)	
	DMF (DN = 26.6) ⁴⁰	CH ₂ Cl ₂ (DN = 1.0) ⁴⁰
Cl ₅ pcyd ⁻	399 (5700), 434 (5500) 721 (2900) [0.062]	286 (44900), 312(sh) (31000), 396 (7600), 449 (7700), 789 (5600) [0.105]
Cl ₄ pcyd ⁻	400 (6000), 436 (5900) 724 (3300) [0.068]	286 (46300), 312(sh) (32500), 394 (8000), 451 (8200), 787 (6000) [0.111]
Cl ₃ pcyd ⁻	398 (6700), 456 (5700) 789 (3900) [0.076]	284 (45700), 312(sh) (28700), 388 (7700), 462 (7000), 860 (6300) [0.124]
Cl ₂ pcyd ⁻	395 (4700), 462 (4000) 828 (3300) [0.073]	284 (43000), 312(s) (28700), 388 (7300), 462 (6400), 908 (7400) [0.151]
Clpcyd ⁻	395 (3400), 460 (3100) 880 (3300) [0.071]	286 (36800), 313(sh) (25100), 382(sh) (6400), 466 (5200) 954 (7800) [0.154]
Ru(tpy)Cl ₃	288 (36481), 314(s) (29171) 412 (10519), 425 (10610), 490(sh) (3968), 556 (sh) (1290)	288 (32900), 312 (26430), 413 (9690), 426 (9340), 486(sh) (3600), 546 (sh) (1050)

^a Data reported as wavelengths in nm and parentheses show the corresponding molar extinction coefficients (ϵ in Lmol⁻¹cm⁻¹), sh = shoulder. ^b data in square brackets show the oscillator strengths of the vis-NIR LMCT bands.

Like the reagent Ru(tpy)Cl₃ complex, all *trans*-[Ru(tpy)(R-pcyd)Cl₂] complexes (**1-5**) exhibited an intense band at 288-320 nm and two fairly intense overlapping bands at 395-462 nm (Figure 5.3.11-5.3.12). However, complexes **1-5** exhibited an additional broad and intense vis-NIR absorption feature at 721-880 nm ($\epsilon = 2900-3870 \text{ Lmol}^{-1}\text{cm}^{-1}$) in DMF and at 787-954 nm ($\epsilon = 5600-7820 \text{ Lmol}^{-1}\text{cm}^{-1}$) in CH₂Cl₂, which undergoes a bathochromic shift as the number of chloro-substituents decreases on R-pcyd ligands. In addition, complexes **1-5** exhibited solvatochromism for their vis-NIR bands, which are blue shifted by about 70 nm in highly donor solvent DMF relative to those in less polar CH₂Cl₂ (Table 5.3.6).

The high energy 288-320 nm bands of **1-5** can be assigned to π to π^* transitions of the tpy ligand.^{36,37} The position and intensities of 395-462 nm bands are similar to those of Ru(tpy)Cl₃ complex (Table 5.3.7), and are assigned to Ru(III)-Cl LMCT transitions accordingly. On the other hand the low energy vis-NIR band is absent in the absorption spectra of precursor Ru(tpy)Cl₃ complex and can be attributed to Ru(III)-cyanamide chromophore. Indeed, these low-energy visible-NIR bands of **1-5** appear at similar positions to those of Ru(III)-NCN LMCT transitions of [Ru(NH₃)₅(R-pcyd)]²⁺ ($\lambda_{\text{max}} = 645-772 \text{ nm}$, $\epsilon = 5754-6456 \text{ Lmol}^{-1}\text{cm}^{-1}$).²⁰⁻²³ The observed bathochromic shift of the low energy vis-NIR band (Figure 5.3.11 and 5.3.12) is therefore attributed to the destabilization of the π -HOMO of the R-pcyd ligand as the number of chloro-substituents decreases. Gas-phase DFT calculations provided further evidence for the assignment of the low energy vis-NIR bands of **1-5**.

As discussed in the Section 5.3.3, the β -HOMOs of **2-4** are comprised of π -bonding interactions between R-pcyd $p\pi$ and Ru $d\pi$ orbitals while the β -LUMOs

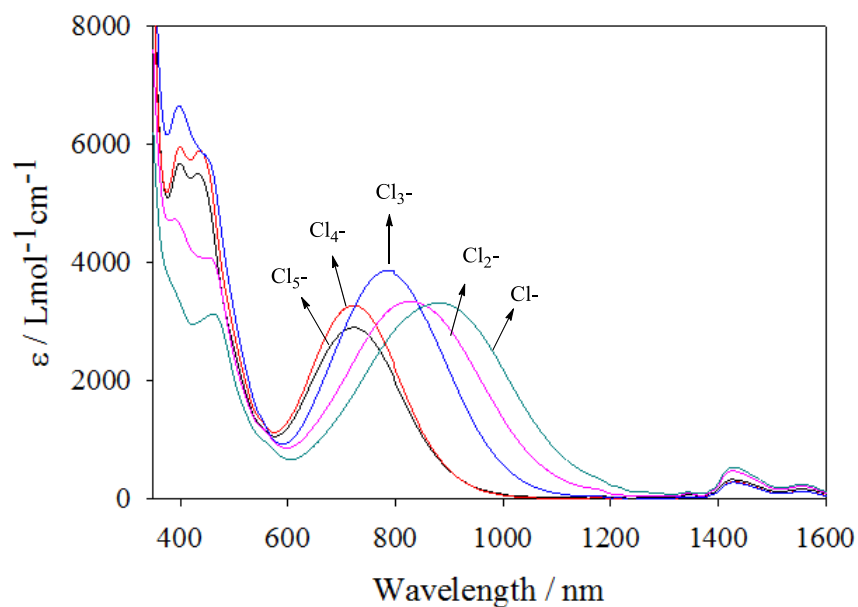


Figure 5.3.11: Quantitative electronic absorption spectra of *trans*-[Ru(ttpy)(R-pcyd)Cl₂] complexes (1-5) in DMF. (R = Cl₅⁻, Cl₄⁻, Cl₃⁻, Cl₂⁻, Cl⁻).

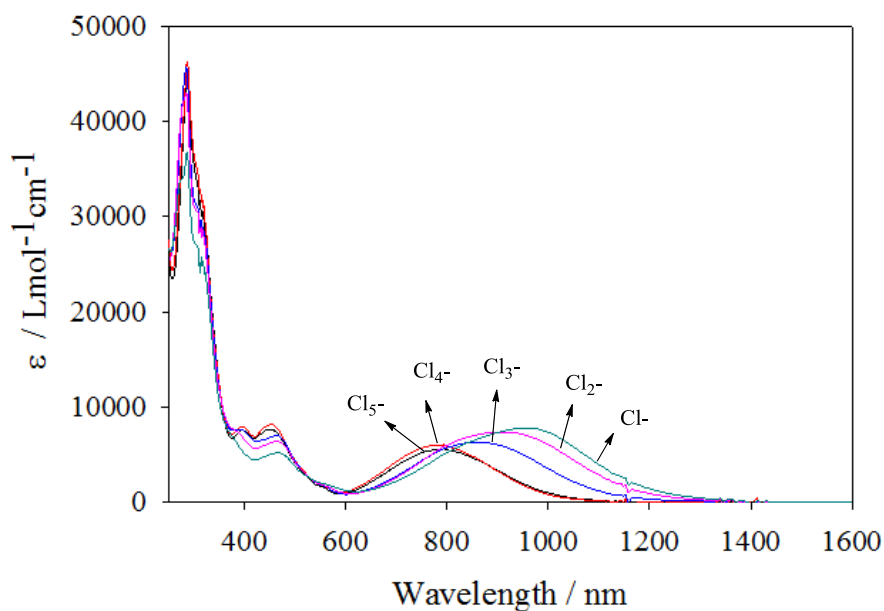


Figure 5.3.12: Quantitative electronic absorption spectra of *trans*-[Ru(ttpy)(R-pcyd)Cl₂] complexes in CH₂Cl₂. (R = Cl₅⁻, Cl₄⁻, Cl₃⁻, Cl₂⁻, Cl⁻).

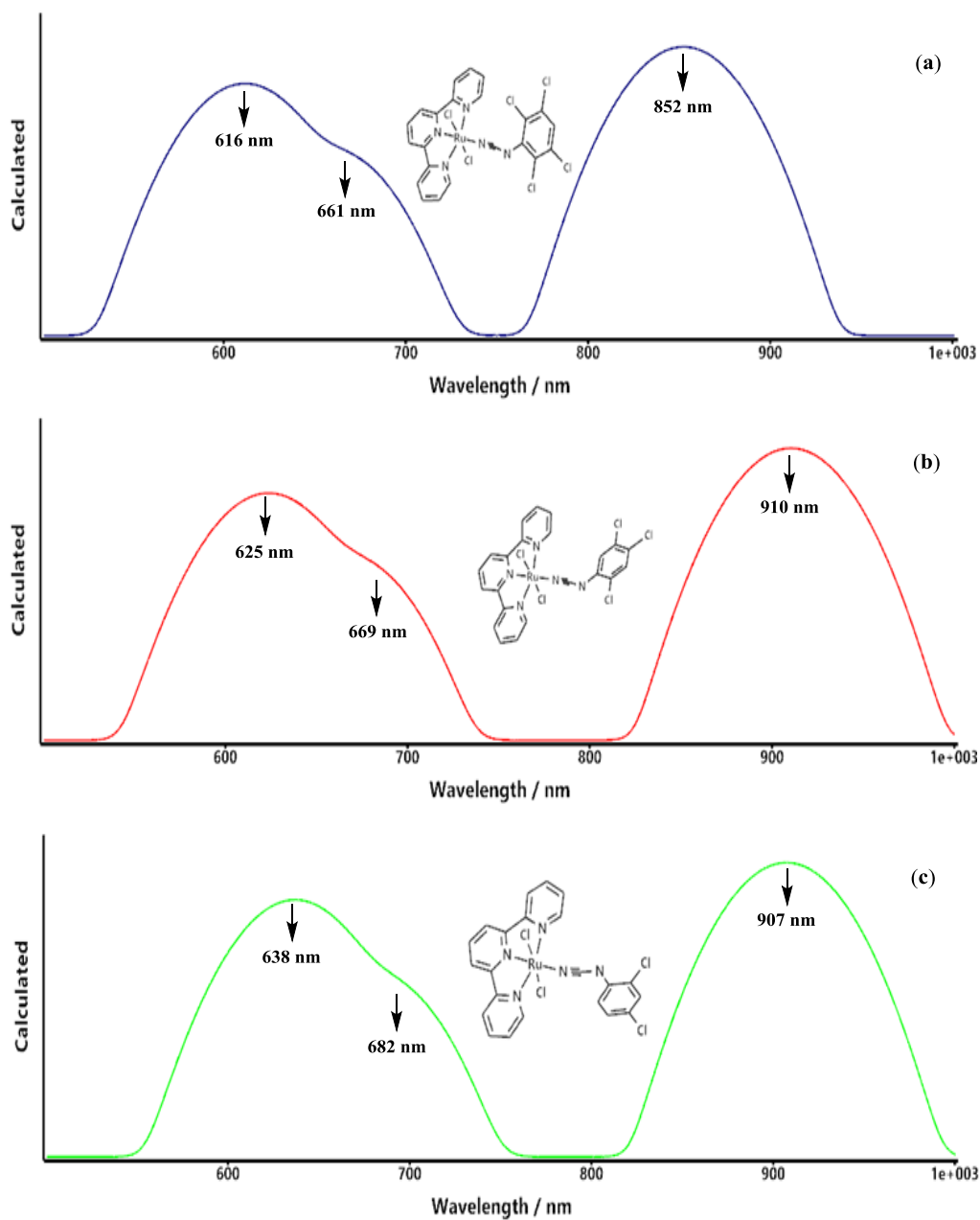


Figure 5.3.13: Calculated electronic absorption spectra (a-c) of *trans*-[Ru(tpy)(R-*pcyd*)Cl₂] complexes in vacuum. R = Cl₄-(a), Cl₃-(b), Cl₂-(c).

represent corresponding antibonding interactions (Figure E.1, E.2 and 5.3.8). The fairly intense vis-NIR bands of **2-4** are therefore assigned to a β -HOMO to β -LUMO transition.

Although both β -HOMO and β -LUMO have significant contributions from R-*pcyd*⁻

ligand and Ru, the ligand contribution is dominant in the β -HOMO while the β -LUMO has greater contribution from Ru ion. The β -HOMO to β -LUMO transition can be therefore assigned to mostly cyanamide-to-Ru(III) LMCT transitions. In the case of **1** for which β -HOMO-2 shows the bonding interaction between Ru $d\pi$ and Clpcyd⁻ ligand (Figure 5.3.6), the cyanamide-to Ru(III) LMCT absorption can be ascribed to β -HOMO-2 to β -LUMO transition. Gas-phase DFT calculated spectra (Figure 5.3.13 a-c) for **2-4** qualitatively reproduced the experimental spectra in the visible and vis-NIR region. There is a good agreement between the DFT-predicted spectra and the experimental spectra of these complexes (**2-4**) in non-interacting solvent CH₂Cl₂, in so far as the band energies of vis-NIR as well as relative intensities of visible and vis-NIR bands are concerned. The predicted spectra also demonstrated the observed bathochromic shift of the vis-NIR band as the number chloro-substituent decreases on the R-pcyd ligand.

The blue shift in low energy LMCT bands of **1-5** in DMF relative to CH₂Cl₂ indicates a strong solvent-solute interaction that destabilizes the Ru(III) $d\pi$ orbital relative to the π -HOMO of the phenylcyanamide ligand. This increase in LMCT energies in the strong donor solvent DMF (relative to CH₂Cl₂) is also accompanied by a decrease in oscillator strengths of the LMCT band (Table 5.3.7).

The oscillator strength of a Ru(III)-NCN LMCT band is a measure of the Ru(III)-cyanamide coupling element (or π -bonding), according to the model developed by Creutz, Newton and Sutin (CNS model).^{32b} As seen in the Figure 5.4.1, there is a clear trend in the oscillator strengths of the LMCT band (or π -bonding) of **1-5** in CH₂Cl₂, decreasing as the number of chloro-substituent increases on the R-pcyd⁻ ligand. This

observation is also supported by the gas-phase DFT calculations of **1-5** (β -HOMO-2, β -HOMOs in Figure 5.3.6, 5.3.7, E.1, E.2).

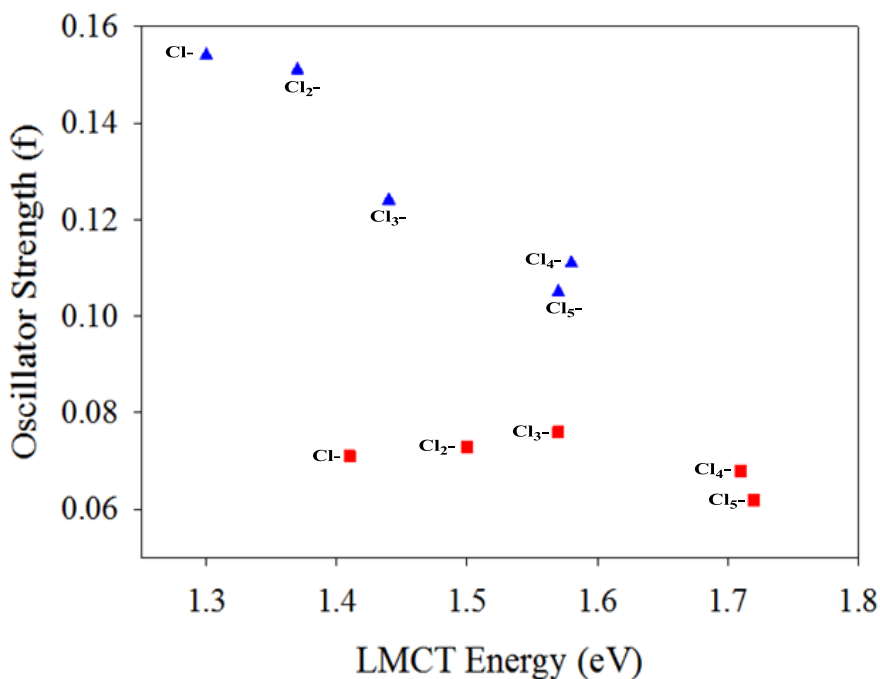


Figure 5.3.14: Distribution of LMCT oscillator strength (f) relative to LMCT energy (eV) for *trans*-[Ru(tpy)(R-*pcyd*)Cl₂] complexes in CH₂Cl₂ (blue triangle) and in DMF (red squares). (R = Cl₅⁻, Cl₄⁻, Cl₃⁻, Cl₂⁻, Cl⁻).

On the other hand, for **1-5** in DMF solution, the LMCT oscillator strengths are smaller and show no trend with R-*pcyd*. Previous studies on [Ru(NH₃)₅(2,3-Cl*pcyd*)]²⁺ have shown that the oscillator strength of the LMCT band decreases as the donor number of the solvent increases and this has been rationalized on the basis of strong solvent-solute donor-acceptor interaction that stabilizes the Ru(III) oxidation state, weakening the Ru(III)-cyanamide π -bonding interaction.²⁰⁻²³ The reduced oscillator strengths of LMCT bands of complexes (**1-5**) in highly donor solvent DMF and their insignificant variation with the number of chloro-substituents on R-*pcyd*⁻ ligands can be therefore attributed to

specific solvent-solute interaction between highly donor DMF molecules and the Ru(III) ion that significantly destabilizes Ru(III) $d\pi$ orbital relative to the π -HOMO of the anionic R-pcyd⁻ ligand, increasing the ionic character in the Ru(III)-cyanamide bond in complexes **1-5**. This effect will be reflected in the ¹H NMR spectra of **1-5** in the strong donor solvent dmsO (discussed below).

5.3.6 Cyclic Voltammetry

Cyclic voltammetry of Ru(tpy)Cl₃·H₂O and **1-5** have been performed in CH₂Cl₂ and in DMF at scan rate of 0.1 V/s. The voltammetric data for all complexes have been placed in the Table 5.3.7 and the corresponding voltammograms in CH₂Cl₂ and in DMF are shown in the Figure 5.3.15-5.3.17 respectively.

The cyclic voltammograms of Ru(tpy)Cl₃ complex show the reversible wave of Ru(III/II) couple at 0.21 V and 0.17 V vs. NHE, in CH₂Cl₂ and DMF, respectively (Figure 5.3.15).

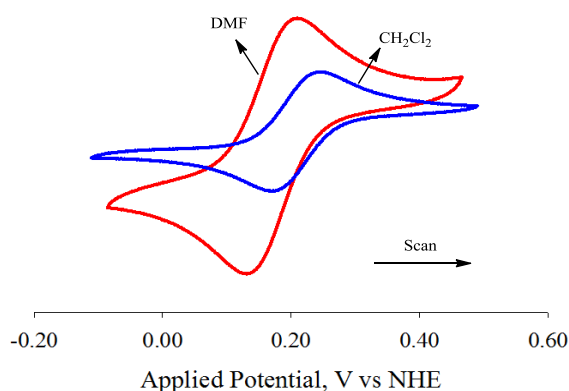


Figure 5.3.15: CV's of Ru(tpy)Cl₃ complex in CH₂Cl₂ (blue) and in DMF (red). Scan rate 0.1 V/s and supporting electrolyte, 0.1 M TBAH.

Table 5.3.7: CV^a and Vis-NIR LMCT Energy^b Data of Ru(tpy)Cl₃ and *trans*-[Ru(tpy)(R-pcyd)Cl₂] Complexes (1-5) in DMF and CH₂Cl₂ at 25 °C.

Complexes	DMF				CH ₂ Cl ₂			
	E ₁ (Ru III/II)	E ₂ (L ⁰ /L ⁻¹) ^c	E ₂ -E ₁	E _{op}	E ₁ (Ru III/II)	E ₂ (L ⁰ /L ⁻¹) ^c	E ₂ -E ₁	E _{op}
Cl ₅ pcyd ⁻	0.33	1.49 (1.46)	1.13	1.72	0.32	1.42 (1.39)	1.07	1.57
Cl ₄ pcyd ⁻	0.32	1.47 (1.44)	1.12	1.71	0.31	1.40 (1.37)	1.06	1.58
Cl ₃ pcyd ⁻	0.34	1.40 (1.37)	1.03	1.57	0.33	1.32 (1.29)	0.96	1.44
Cl ₂ pcyd ⁻	0.34	1.31 (1.28)	0.94	1.50	0.30	1.21 (1.18)	0.88	1.37
Clpcyd ⁻	0.27	1.19 (1.16)	0.89	1.41	0.25	1.11 (1.08)	0.83	1.30
Ru(tpy)Cl ₃	0.17	-	-		0.21	-	-	

^a condition: 0.1 M TBAH as supporting electrolyte, Fc⁺/Fc as internal reference, scan rate 0.1 V / s, data reported in volts (V) vs NHE. ^b E_{op} = Vis-NIR LMCT energy in eV. ^c irreversible wave: anodic wave reported and parentheses show the values obtainable under reversible condition, calculated by subtracting 0.30 V from the values for the anodic waves.

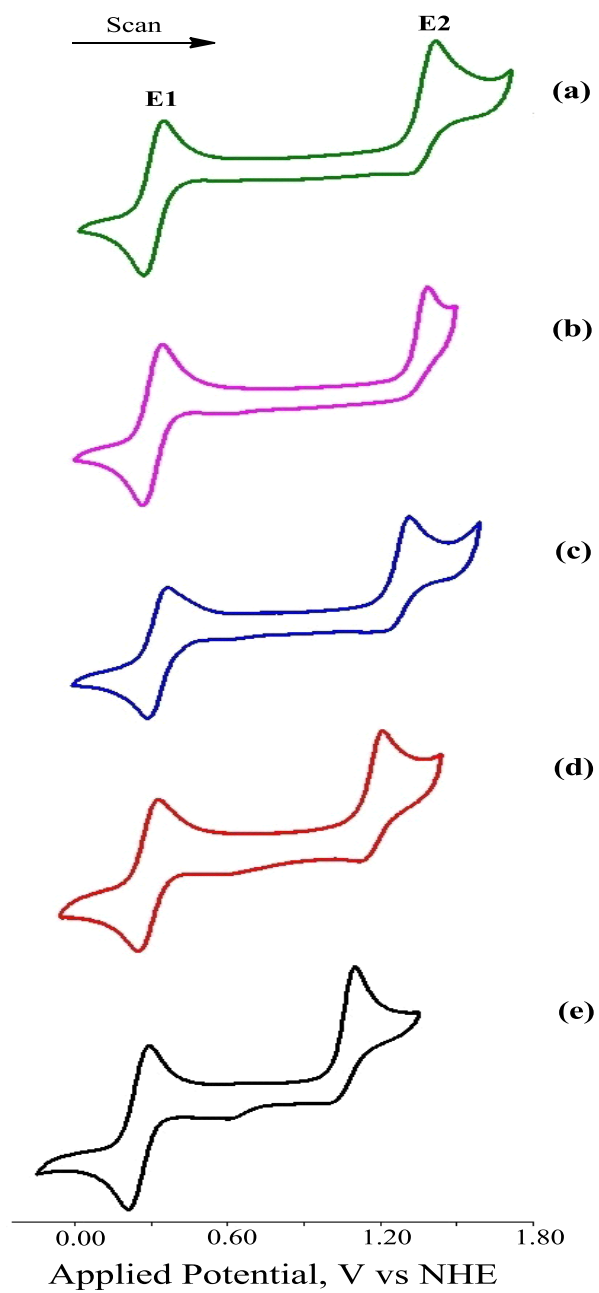


Figure 5.3.16: Cyclic voltammograms of *trans*-[Ru(tpy)(Rpcyd)Cl₂] complexes in 0.1 M TBAH CH₂Cl₂ at scan rate 0.1 V/s. (a) **5**, (b) **4**, (c) **3**, (d) **2**, (e) **1**.

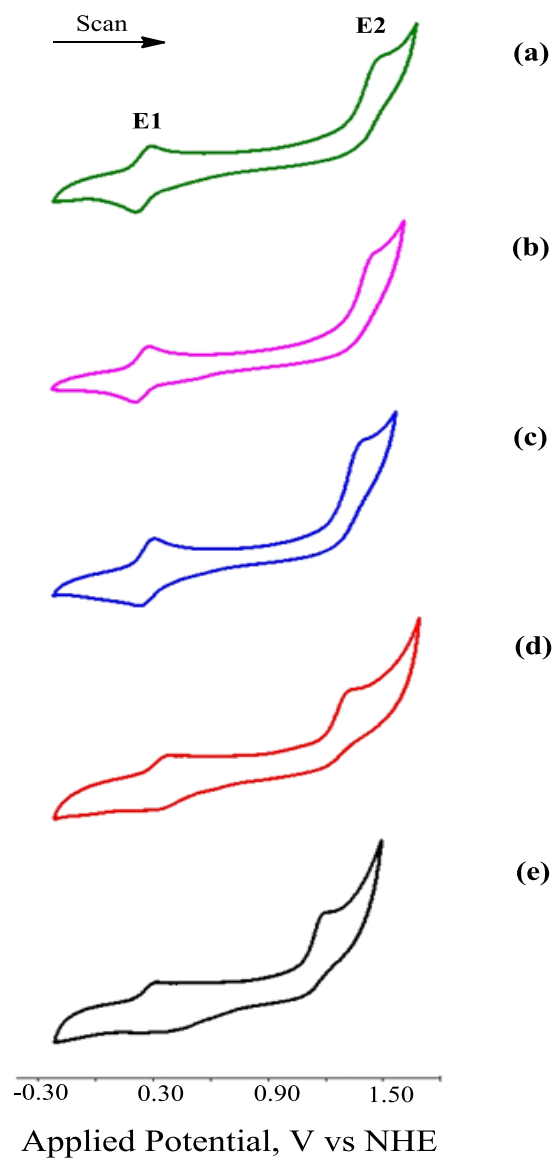


Figure 5.3.17: Cyclic voltammograms of *trans*-[Ru(tpy)(Rpcyd)Cl₂] complexes in 0.1 M TBAH DMF at scan rate 0.1 V/s. (a) **5**, (b) **4**, (c) **3**, (d) **2**, (e) **1**.

The voltammograms of **1-5** in CH₂Cl₂ (Figure 5.3.16) show a reversible wave (E1) at 0.25-0.33 V and an irreversible ($I_a > I_c$) wave (E2) at 1.11-1.42 V vs NHE (Figure 4.3.17). On the other hand, the voltammograms of **1-5** in DMF (Figure 5.3.17) show a quasi-reversible wave (E1) at 0.27-0.34 V and an irreversible ($I_a > I_c$) wave (E2) at 0.89-1.13 V vs NHE. The reversibility of both couples is less in DMF solution and further decreases upon a decrease in the number of chloro-substituents on the R-pcyd⁻ ligands. However, better reversibility of the E1 couple was observed at sweeping potentials lower than the second couple (E2), suggesting some decomposition of complexes at high positive potential. The E1 and E2 couples of **1-5** in CH₂Cl₂ appear at similar potentials as those of [Ru(NH₃)₅(R-pcyd)]⁺ complexes and were assigned accordingly.²¹ Ru(III/II) couples of **1-5** show only a modest variation with the number of chloro-substituents, while ligand couples L⁰/L⁻ are positively shifted by about 0.30 V upon moving from Clpcyd⁻ to Cl₅pcyd⁻ complexes, in agreement with stabilization of the π-HOMO of the anionic R-pcyd ligand by electron withdrawing chloro-substituents.

5.3.7 Paramagnetic ¹H NMR Spectroscopy

The paramagnetic ¹H NMR spectra of Ru(tpy)Cl₃·H₂O and **1-5** were recorded in dms-*d*₆ and the observed chemical shifts were referenced to TMS proton resonances. The ¹H NMR and corresponding ¹H-¹H-COSY spectra of Ru(tpy)Cl₃·H₂O are shown in the Figure 5.3.18-5.3.19, while those of **1-5** are shown in the Figures 5.3.20-5.3.27. The *trans*-[Ru(tpy)(Clpcyd)Cl₂] complex (**1**) is slowly reduced in dms-*d*₆ solution, the process being aided by the high solute concentration and long acquisition time required for gaining sufficient signal intensities from the paramagnetic species. However, a low acquisition time ¹H NMR spectrum of this complex (**1**), showed very weak paramagnetic

signals without significant contribution from diamagnetic impurities, and is included here for comparison (Figure 5.3.27). The ^1H NMR spectral data for complexes, along with those of free R-pcydH ligands, are compiled in the Table 5.3.8.

The ^1H NMR spectra of paramagnetic **1-5** show significantly broad and weak signals in a wide chemical shift range of δ 22.71 to δ -35.19 ppm that were lacking the usual multiplicity and coupling patterns of diamagnetic spectra. The ttpy and R-pcyd protons were assigned on the basis of integration and compared with the spectra of similar paramagnetic complexes. The numbering scheme used to assign ttpy and R-pcyd ligands are shown in the Figure 5.3.28.

In diamagnetic ruthenium complexes, ttpy signals usually appear in the range of 7.00-9.20 ppm. On the other hand, these signals are isotropically shifted for paramagnetic ruthenium complexes in solution due to the interaction of the unpaired electron moment and the magnetic moment of resonating nucleus (Eq 1.7 in Chapter 1). The isotropic chemical shifts may have both contact and pseudocontact contributions as discussed in Chapter 1.

The ^1H NMR spectrum of the precursor $\text{Ru}(\text{ttpy})\text{Cl}_3$ feature two broad signals in the range of δ 9.67 - δ 7.50 ppm and four broad signals in the range of δ -1.39 to δ -35.19 ppm for a total of 14 protons from pyridine and phenyl rings and a singlet at δ 1.43 ppm for *t*-butyl protons (Figure 5.3.17-5.3.18). The spectral pattern of ttpy ligand in complexes (**1-5**) is very similar to that of pbtpy ligand in $\text{Ru}(\text{pbtpy})\text{Cl}_3$ complex, where pbtpy is 4'-(*p*-bromophenyl)-2,2':6',2''-terpyridine, in terms of number of peaks and corresponding peak positions for pyridine and phenyl ring protons.³⁷ With the help of correlation spectroscopy (^1H - ^1H -COSY, ^1H - ^{13}C HMQC and TOCSY), majority of the

peaks of Ru(pbtpy)Cl₃ complex have been assigned, with the most deshielded signal assigned to C3'' protons on the phenyl ring (δ 9.86 ppm) and the most shielded one assigned to A3 protons on the pyridine ring (δ -35.3 ppm). The ¹H-¹H COSY confirmed the assignment of the *ortho* C2'' protons at -1.04 ppm and while TOCSY and HMQC ¹H-¹³C confirmed the assignment of the B3' proton at δ 7.28 ppm. Like Ru(pbtpy)Cl₃ complex, the most downfield signal at δ 9.67 ppm and the signal at δ -1.39 ppm of Ru(tpy)Cl₃·H₂O complex show very weak splitting and correlation with each other (Figure 5.3.18) and accordingly, we assigned these signals to C3'' and C2'' protons, respectively. This small splitting as well as small isotropic shift of C3'' signal with respect to its diamagnetic analogues indicates little influence of unpaired electron density on the phenyl ring of the tpy ligand, where the long range dipolar interaction is presumably very weak due to their remoteness from the paramagnetic center. The small isotropic shift that is observed for C3'' proton is more likely to arise from the contact shift contribution via spin-polarization mechanism. However, the twisted geometry of the phenyl ring about the terpyridine plane (crystal structure) prevents significant π -delocalization of unpaired electron density from the metal ion via the π -system of terpyridine ligand, and thereby restricting accumulation of spin densities on phenyl protons via spin polarization mechanism. Both contact and pseudocontact shifts are likely to contribute to the observed isotropic shifts of pyridine ring protons. The contact shift contributions to the isotropic shifts for protons on pyridine rings arise from both direct π -spin density delocalization and spin polarization of unpaired electron density on the π -system. The most upfield signal at $-\delta$ 35.17 ppm coincides well with that of the abovementioned Ru(pbtpy)Cl₃ complex and accordingly assigned to A6 protons from the pyridine ring. Due to their

Table 5.3.8: ^1H NMR Spectral Data of *trans*-[Ru(tpy)(R-pcyd)Cl₂] Complexes (1-5) and Free R-pcydH Ligands in dms-*d*₆.

Complex	ttpy Ligand Proton Chemical Shifts in Ruthenium Complexes (δ ,ppm)		R-pcyd Ligand Proton Chemical Shifts (δ ,ppm)					
			Ruthenium Complexes			Free R-pcydH Ligands ^c		
	Aromatic Protons	<i>t</i> -Bu	Ho	Hm	Hp	Ho	Hm	Hp
Cl ₅ pcyd ⁻	9.52, 7.28, -1.50, -2.09, -6.49, -9.03, - 31.18	1.34	-	-	-	-	-	-
Cl ₄ pcyd ⁻	9.64, 8.35, -0.92, -1.91, -6.18, -8.82, -29.82	1.37	-	-	-9.56	-	-	8.33
Cl ₃ pcyd ⁻	9.31, 8.27, -0.53, -1.01, -1.35, -7.00, -24.47.	1.33	-16.99	14.46	-	7.29	7.90	-
Cl ₂ pcyd ⁻	10.04, 13.39, 2.14, -0.74, -0.87, -7.13, -20.09	1.58	-25.00	18.94 18.03	-	7.21	7.65 7.45	-
Clpcyd ⁻	10.33, 18.84, 5.24, 4.37, 0.40, -5.48 -10.89	1.73	-33.58	22.71	-	7.10	7.41	-
Ru(tpy)Cl ₃	9.67, 7.50, -1.39, -2.18, -9.26, -9.26, -35.19	1.43	-	-	-	-	-	-

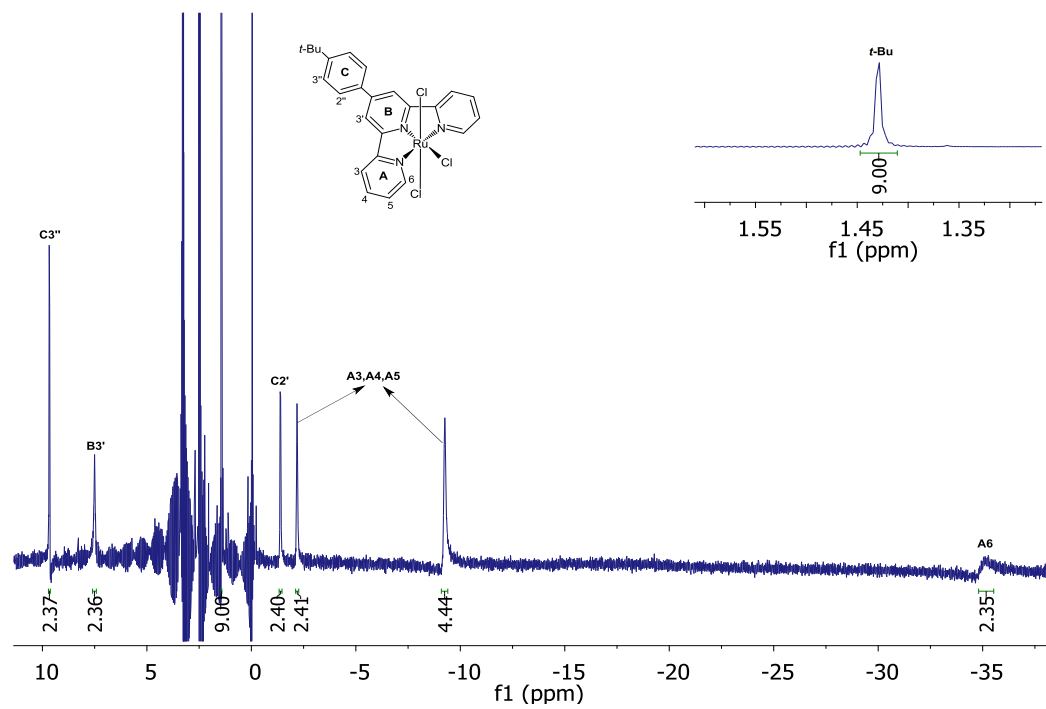


Figure 5.3.18: ^1H NMR spectrum of $\text{Ru}(\text{ttpy})\text{Cl}_3$ complex in $\text{dms-}d_6$.

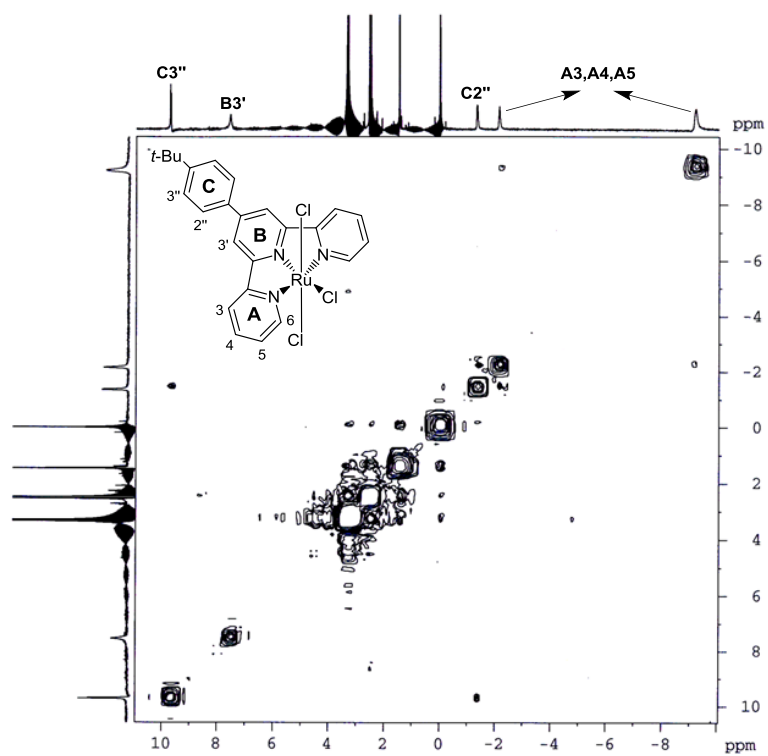


Figure 5.3.19: ^1H - ^1H COSY spectrum of $\text{Ru}(\text{ttpy})\text{Cl}_3$ complex in $\text{dms-}d_6$.

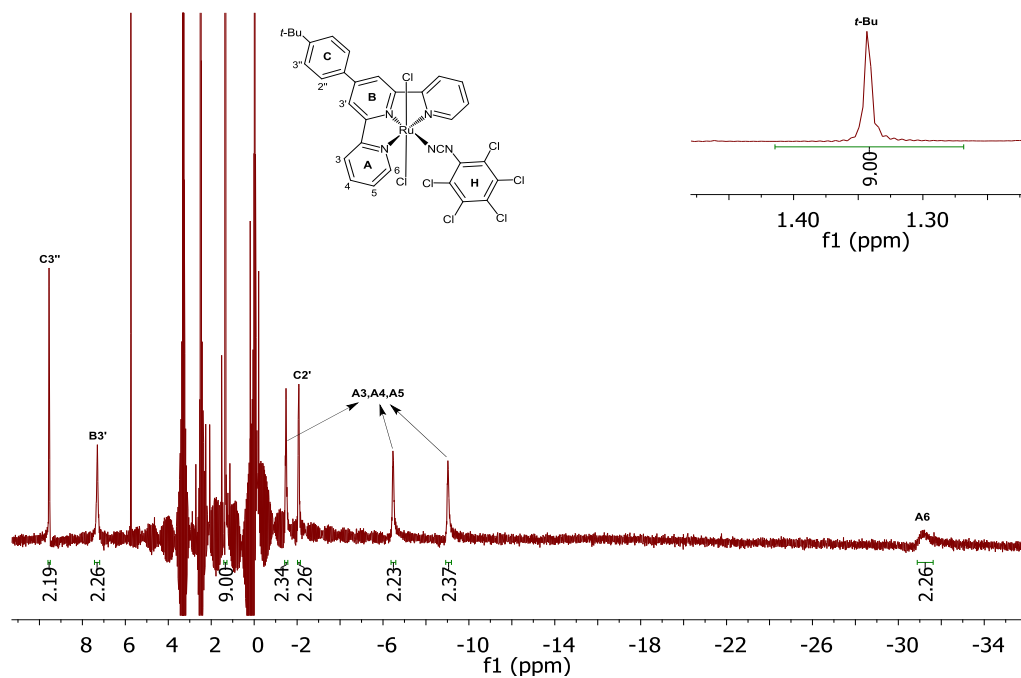


Figure 5.3.20: ^1H NMR spectrum of $\text{trans-}[\text{Ru}(\text{tpy})(\text{Cl}_5\text{pcyd})\text{Cl}_2]$ complex (5) in $\text{dms-}d_6$.

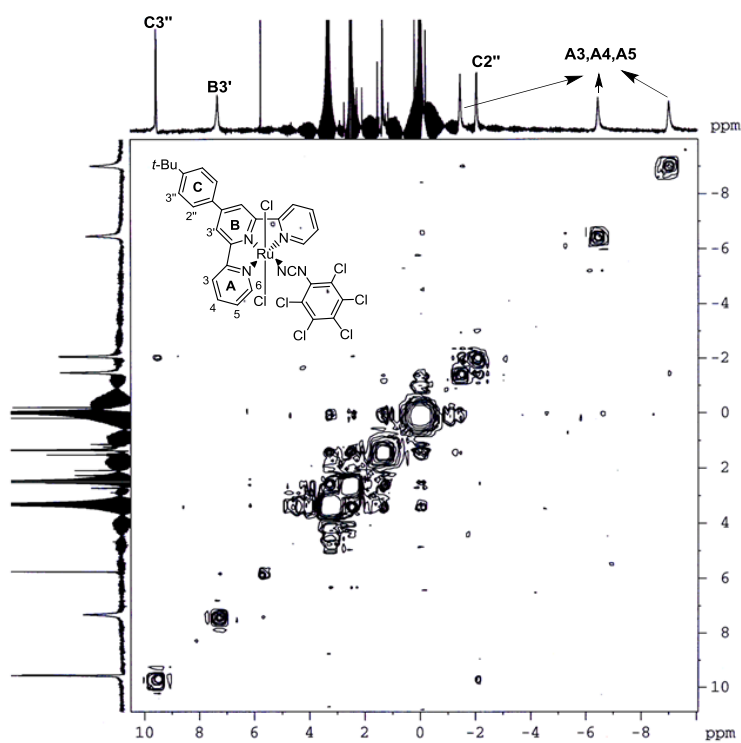


Figure 5.3.21: ^1H - ^1H COSY spectrum of $\text{trans-}[\text{Ru}(\text{tpy})(\text{Cl}_5\text{pcyd})\text{Cl}_2]$ complex (5) in $\text{dms-}d_6$.

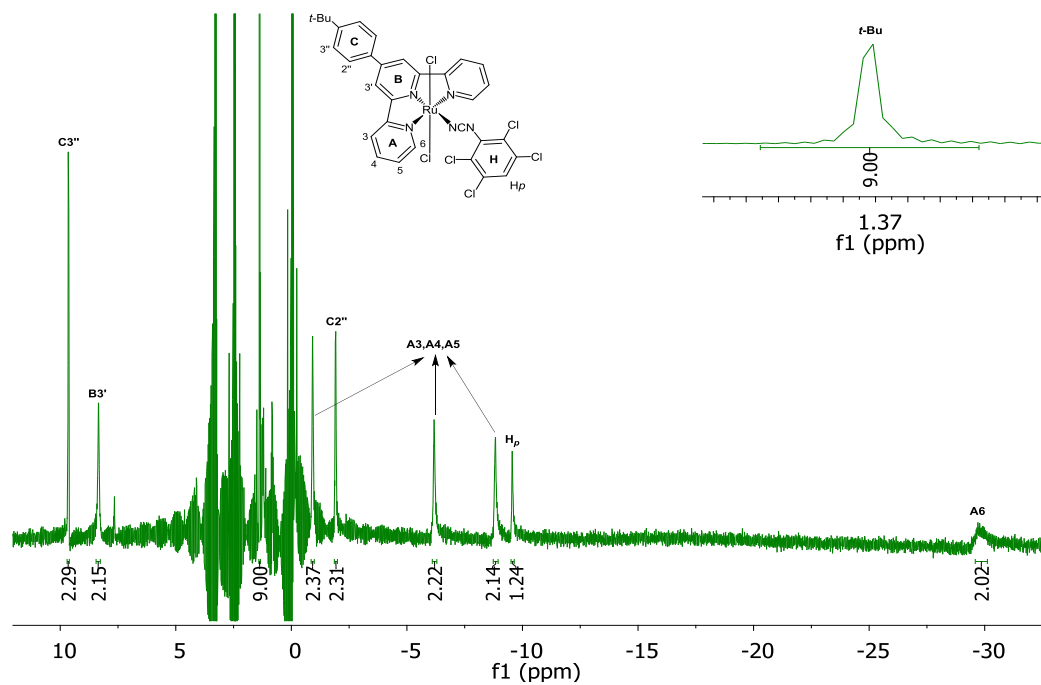


Figure 5.3.22: ^1H NMR spectrum of $\text{trans-}[\text{Ru}(\text{tpy})(\text{Cl}_4\text{pcyd})\text{Cl}_2]$ complex (4) in $\text{dms-}d_6$.

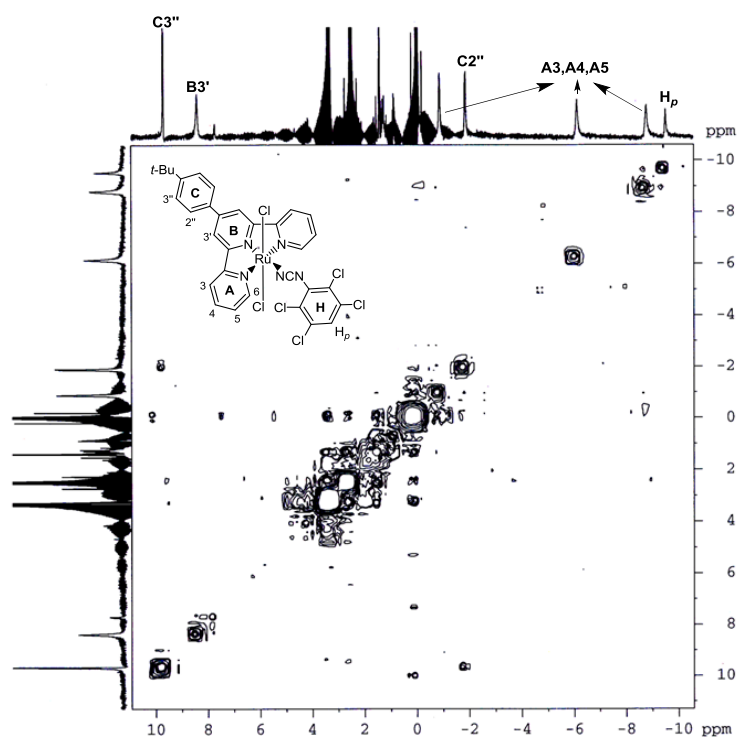


Figure 5.3.23: ^1H - ^1H COSY spectrum of $\text{trans-}[\text{Ru}(\text{tpy})(\text{Cl}_4\text{pcyd})\text{Cl}_2]$ complex (4) in $\text{dms-}d_6$.

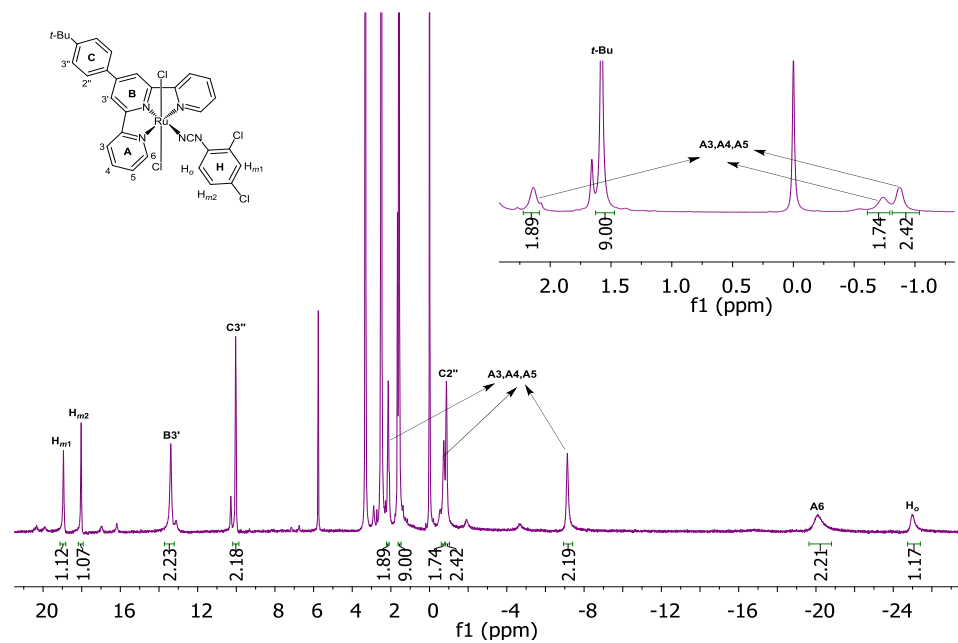


Figure 5.3.26: ^1H NMR spectrum of *trans*-[Ru(tpy)(Cl₂pcyd)Cl₂] complex (**2**) in dms-*d*₆.

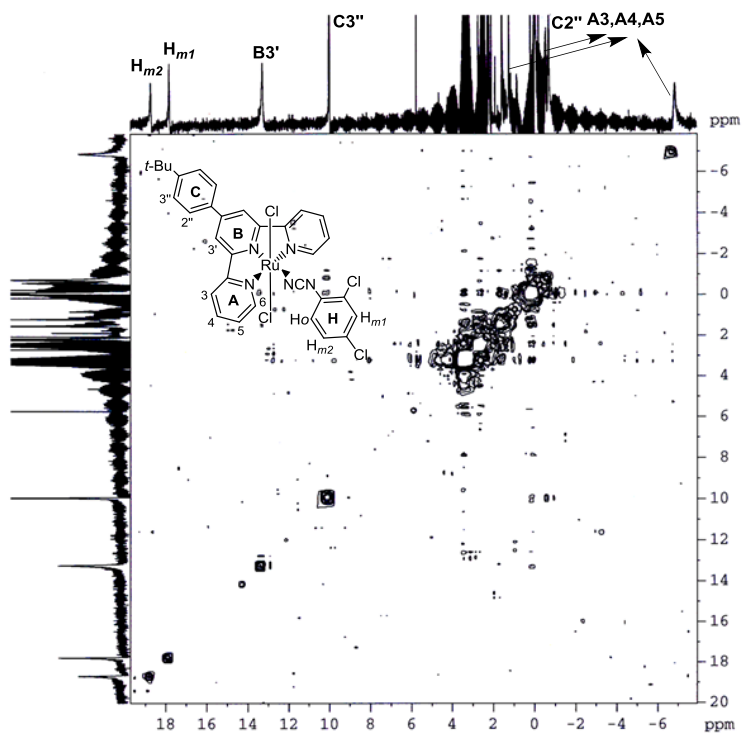


Figure 5.3.27: ^1H - ^1H COSY spectrum of *trans*-[Ru(tpy)(Cl₂pcyd)Cl₂] complex (**2**) in dms-*d*₆.

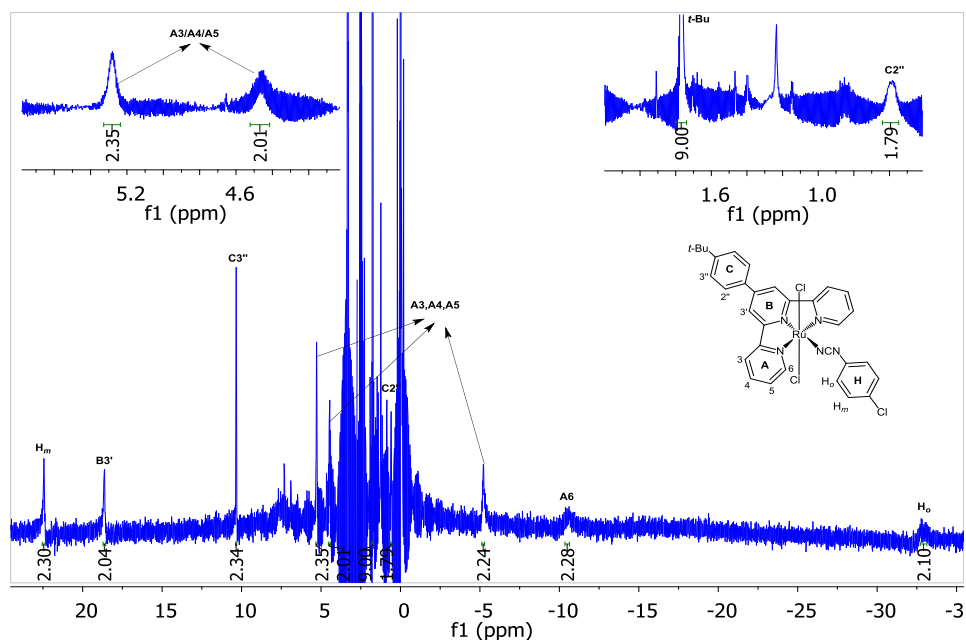


Figure 5.3.28: ^1H NMR spectrum of *trans*-[Ru(tpy)(Clpcyd)Cl₂] complex (**1**) in $\text{dmsO-}d_6$

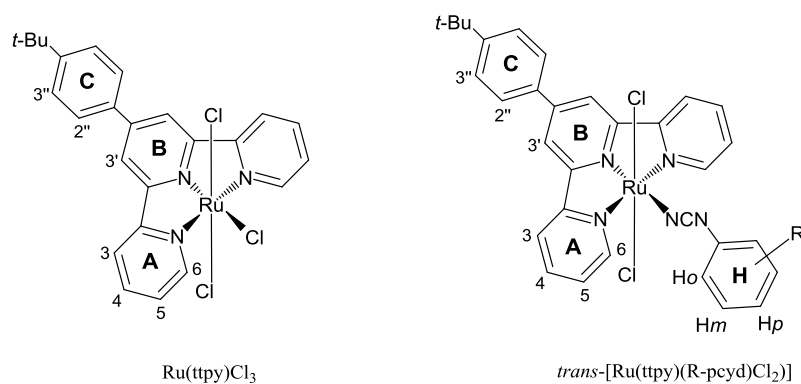


Figure 5.3.29: Numbering scheme used to assign the proton resonances from tpy and R-pcyd ligands in $\text{Ru}(\text{tpy})\text{Cl}_3$ and *trans*-[Ru(tpy)(R-pcyd)Cl₂] complexes (**1-5**).

close proximity to the paramagnetic metal ion, A6 protons are likely to experience the highest isotropic shift. The other upfield signals at δ -2.18 ppm and δ -9.26 ppm are likely to arise from A3, A4, A5 protons, however, absolute assignment of these protons were not possible as A6 protons did not couple with its neighboring protons even at long

acquisition time. In the ^1H NMR spectrum of $\text{Ru}(\text{pbtpy})\text{Cl}_3$ complex, the second deshielded signal at δ 7.28 ppm was assigned to B3' protons on the basis of the absence of signal from structurally similar $\text{Ru}(\text{L})\text{Cl}_3$ complex where $\text{L} = 6-(p\text{-bromophenyl})\text{-2,4-dipyrid-2-yl-1,3,5-triazine}$, which possess all but the B3' proton of the pbtpy ligand. By analogy with the $\text{Ru}(\text{pbtpy})\text{Cl}_3$ complex, we assigned the second downfield signal $\text{Ru}(\text{tpty})\text{Cl}_3$ complex at δ 7.50 ppm to B3' protons from the central pyridine ring of the tpty ligand.

The ^1H NMR spectra of complexes (**1-5**) are characterized by six isotropically shifted signals for tpty protons in the range between δ 13.39 and δ -31.18 ppm and a singlet for *t*-butyl group in the range of δ 1.73-1.33 ppm (Figure 5.3.18-5.3.27 and Table 5.3.8). The spectral pattern for the tpty ligand in **1-5** is very similar to that of $\text{Ru}(\text{tpty})\text{Cl}_3\cdot\text{H}_2\text{O}$, with two most down field signals arising from C3'' (δ 9.31-10.33 ppm) and B3' (δ 7.28-18.84 ppm) protons, the most upfield signal from the A6 protons (δ -10.89 to -31.18 ppm) as well as three signals from A3, A4, and A5 protons (δ 5.24 to -9.03 ppm) (Figure 5.3.19-5.3.27 and Table 5.3.8). The tpty protons were distinguished from those of R-pcyd ligands on the basis of integration ratios of respective protons. As seen in the Table 5.3.8, signals for A3, A4, and A5 protons are gradually shifted more *downfield*, approaching their diamagnetic values as the number of chloro-substituents on R-pcyd $^-$ ligands increases, indicating a decrease in net single spin density on metal by partial charge transfer from highly donor or readily oxidizable R-pcyd $^-$ ligands.

Of particular importance are the observed isotropic shifts of R-pcyd protons in complexes **1-5** (Table 5.3.8), which alternates between *upfield* shifts for *ortho* and *para* protons (δ -16.99 to -33.58 ppm) and *downfield* shifts for the *meta*-protons (δ 14.46-

22.71ppm), in a similar fashion as in $[\text{Ru}(\text{NH}_3)_5(\text{R-pcyd})]^{2+}$ complexes.²⁵ The reason for this difference is the direct delocalization of spin from Ru(III) π d orbital to the π -system of the phenyl ring on R-pcyd⁻ ligand and spin polarization of C-H σ bonding electrons that accumulates net spin density on corresponding nuclei.^{38a,b} The π -delocalization of spin density from Ru(III) to R-pcyd⁻ ligand requires π -coupling of phenyl ring to both cyanamide π and Ru(III) $d\pi$ orbitals. The unpaired electron density on the π orbital of *ortho* carbon induces negative spin density on the *ortho* proton via spin polarization of the C-H σ bonded electrons. The *para* proton experiences similar shift in magnitude and sign while the *meta* protons experience downfield shift due to presence of a node in the π -system leading to spin polarization of *meta* carbon (Figure 5.3.30).^{38a,b} Similar alternate pattern of spin density has been observed for ligands of the type phenyl-X, where X is a donor group $-\text{NR}_2$, $-\text{N} = \text{CHR}$ or O^- .^{38c-e}

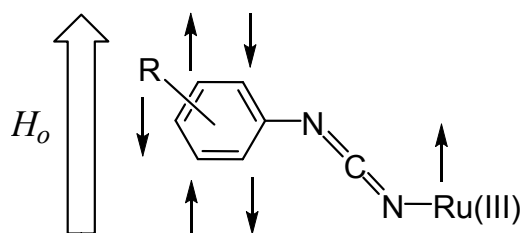


Figure 5.3.30: The alignment of Ru(III) spin with that of an external magnetic field (H_o) and the resultant phenyl hydrogen atom spin moments.

The observed spectral pattern and isotropic chemical shifts values for *ortho*, *meta* and *para*-protons of R-pcyd ligands in *trans*- $[\text{Ru}(\text{tpy})(\text{R-pcyd})\text{Cl}_2]$ complexes (**1-5**) are very similar to those of R-pcyd ligands in $[\text{Ru}(\text{NH}_3)_5(\text{R-pcyd})]^{2+}$ complexes²⁵ for which combined EPR and ^1H NMR spectroscopy as well as DFT calculations in solutions unambiguously established a predominantly Ru(III)-centered spin density distribution.

Table 5.3.9: Isotropic Shifts^a of R-pcyd Protons and R-pcyd Phenyl Carbon π -Spin Densities^b of *trans*-[Ru(tpy)(R-pcyd)Cl₂] Complexes (**1-5**).

R-pcyd ⁻	H _o		H _m		H _p	
	δ_{iso}	$\rho_{\text{c}\pi}$	δ_{iso}	$\rho_{\text{c}\pi}$	δ_{iso}	$\rho_{\text{c}\pi}$
4-Clpcyd ⁻	-40.68	3.00	30.12	-1.10	-	-
2,4-Cl ₂ pcyd ⁻	-32.21	1.19	26.59 25.48	-0.98 -0.94	-	-
2,4,5-Cl ₃ pcyd ⁻	-24.28	0.90	22.36	-0.83	-	-
2,3,5,6-Cl ₄ pcyd ⁻	-	-	-	-	-17.89	0.67
Cl ₅ pcyd ⁻	-	-	-	-	-	-

^a in dms_o-d₆. ^b in percent

This suggested similar Ru(III)-centred spin density distributions for both families of complexes. Assuming dipolar contributions to the isotropic chemical shifts of R-pcyd ligands in *trans*-[Ru(tpy)(R-pcyd)Cl₂] complexes (**1-5**) are negligible as in [Ru(NH₃)₅(R-pcyd)]²⁺ complexes, due to remoteness of R-pcyd ligand from the paramagnetic metal center, the π -spin densities on phenyl ring carbons could be estimated from the observed isotropic shifts (calculated as the difference between the observed shift for a given proton in the complex and that for the protonated ligand in Table 5.3.8) of respective protons by using Eq. 1.13 (Chapter 1) and $g = 2.0023$ (for free electron)^{39a,b} and are included in the Table 5.3.9. It should be noted that, the actual g values for these complexes are larger than that of free electron due to spin-orbit coupling effect of Ru ion that would result in

some g anisotropy.³⁹ As the EPR data are not available for these complexes, the calculated spin densities using g value for free electron in Eq. 1.13 would give slight overestimates of the π -spin densities on the phenyl ring carbons of R-pcyd ligands. However, calculated phenyl carbon π -spin densities (0.7-3.0 %, Table 5.3.9) on R-pcyd ligands in complexes (**1-4**) are very similar in magnitude as those in $[\text{Ru}(\text{NH}_3)_5(\text{R-pcyd})]^{2+}$ (0.83-3.0%)²⁵ and clearly show predominant Ru(III)-centered spin for **1-5** in disagreement with gas-phase DFT calculated spin density distributions (Figure 5.3.8). The data in Table 5.3.9 also show a gradual decrease in π -spin densities on phenyl ring carbons with increase in the number of chloro-substituents on R-pcyd ligands, which is consistent with less transfer of electron density from poorly donor R-pcyd ligand so that net single electron density is increasingly more localized on the Ru(III) ion.

As seen in the Table 5.3.8, the *meta* protons experience gradual downfield shift, while those *ortho* experience gradual upfield shift upon moving from the Cl_3pcyd (**3**) to the Clpcyd (**1**) complex. As the dipolar contribution to phenyl protons remains the same in these complexes due to similarity in their coordination geometry, the observed variation in the isotropic chemical shift must arise from the variation in contact shifts as a function of the donor properties of R-pcyd⁻. The spin density on Ru(III) is transferred through the Ru(III)-cyanamide π -bond into the π -HOMO of the R-pcyd ligand which by the spin polarization mechanism transfers spin density on the phenyl protons. However, the magnitude of the isotropic shifts of *ortho* and *meta* protons of the most donor Clpcyd^- ligand is too small for a ligand-centered radical anion because even 10 % spin densities on *ortho* and *meta* carbons would give isotropic shifts of -135 and 270 ppm (Eq. 1.13),

respectively. This strongly suggests an overall innocent behavior of substituted R-pcyd⁻ ligands in *trans*-[Ru(tpy)(R-pcyd)Cl₂] complexes.

5.4 Conclusion and Future Study

Five mononuclear neutral complexes *trans*-[Ru(tpy)(R-pcyd)Cl₂] complexes (**1-5**) have been synthesized and characterized by X-ray crystallography, IR, UV-vis, ¹H NMR spectroscopy and cyclic voltammetry. Combined electronic and ¹H NMR spectroscopy and gas-phase DFT calculations demonstrated a trend in non-innocent behaviour of R-pcyd⁻ ligands in **1-5** that can be tuned indirectly via inner sphere (through π -donor properties of ancillary Cl⁻ ligands) as well as outer sphere perturbations (through solvent donor number), and directly via number of chloro-substituents on R-pcyd⁻ ligands. Gas-phase DFT calculations on **1-5** showed mostly a R-pcyd ligand-centered spin that gradually decreases with an increase in the number of chloro-substituents on the R-pcyd⁻ ligand and suggested a formal Ru(II) oxidation state in **1-5**. In weakly donor solvent CH₂Cl₂, the LMCT oscillator strengths of complexes are large implying a greater covalency in the Ru(III)-cyanamide bond or a greater degree of non-innocence of the phenylcyanamide ligand which decreases gradually as the donor strength of R-pcyd⁻ ligand decreases. On the other hand, LMCT oscillator strengths of **1-5** are significantly reduced in strong donor solvent DMF, indicating a strong solvent-solute interaction that significantly reduces the Ru(III)-cyanamide π -interaction and stabilizes the Ru(III) oxidation state. The ¹H NMR contact shift derived spin density distributions of **1-5** in deuterated DMSO clearly indicates Ru(III)-centered spin in disagreement with the gas-phase DFT calculation and suggests an oxidation state distribution of Ru(III)-(R-pcyd⁻).

Other theoretical models incorporating specific solvent-solute interactions are being explored and will be the subject of future study. Studies in a range of donor/acceptor solvents would provide more insight into outer-sphere effect on the non-innocent behavior of R-pcyd⁻ ligands. EPR and XANES spectroscopy can be performed to obtain a more quantitative estimate of spin density distribution in *trans*-[Ru(tpy)(R-pcyd)Cl₂] complexes (**1-5**).

The electronic properties of mononuclear complexes (**1-5**) have shown potential for the construction of a neutral mixed-valence complex of polarizable 1,4-dicyanamide benzene (dicyd²⁻) bridging ligand, incorporating [Ru^{III}(tpy)Cl₂]⁺ as an acceptor unit, for possible applications in non-linear optical materials. Unlike other ruthenium-phenylcyanamide complexes with ancillary π -acceptor ligands such as tpy/thd, tpy/bpy, Tp-/dppe that stabilize the Ru(II) oxidation state,^{24,26,27,28} the mononuclear *trans*-[Ru(tpy)(R-pcyd)Cl₂] complexes displayed stable Ru(III) oxidation state even in presence of strong π -acceptor tpy ligand and tunable spectroscopic properties as a function of the donor strengths of the phenylcyanamide ligands and solvents. The redox and spectroscopic properties of complexes **1-5** are very similar to those of [Ru^{III}(NH₃)₅(R-pcyd)]²⁺ complexes^{20,21,22} which being charged species and incorporating volatile ammine ligands are not suitable for applications in non-linear optical (NLO) materials. Besides overall charge neutrality, the presence of tpy ligand in [Ru^{III}(tpy)Cl₂]⁺ would be an added advantage in so far as the solubility of the neutral mixed-valence complexes in the polymer matrix is concerned. Future study will explore the synthesis and characterization of a neutral mixed-valence complex of the type [$\{\text{Ru}^{\text{III}}(\text{tpy})\text{Cl}_2\}(\mu\text{-dicyd}^{2-})\{\text{Ru}^{\text{II}}(\text{N}3)(\text{P}2)\}$] where N3 and P2 are any tridentate and

bidentate ligands, respectively that stabilize the Ru(II) oxidation state in the donor unit. Finally, the neutral mixed-valence complex will be incorporated into a polymer matrix to examine the desired NLO effects.

5.5 References

1. Barber, B.; Giles, C. R.; Asyuk, V.; Ruel, R.; Stulzl, L.; Bishop, D. *IEEE Photonics Technol. Lett.* **1998**, *10*, 1262.
2. Jen, A. K. Y.; Dalton, R. L.; Sassa, T.; Haller, M.; Kang, H. S.; Suresh, S.; Luo, J.; Hong, M. *Adv. Funct. Matter.* **2002**, *12(9)*, September.
3. Heeger, A. J. *Angew. Chem. Int. Ed.* **2001**, *40*, 2591.
4. Prasad, P. N., Williams, D. J. (Eds.), *Introduction to Nonlinear Optical Effects in Molecules and Polymers*; Wiley: New York, **1991**.
5. Marder, S.; R.; Kippelan, B.; Jen, A. K.-Y.; Peyghambarian, N. *Nature* **1997**, 388, 845.
6. Gunes, S.; Neugebauer, H; Sariciftci, N. S.; *Chem. Rev.* **2007**, *107*, 1324.
7. Yan, L.; Wu, Y.; Hu, B. *ACS Symp. Ser.* **2010**, *1061*, 85.
8. Dalton, L.; *Adv. Poly. Sci.* **2002**, *158*, 1.
9. Chemla, D. S., in: J. Zyss (Ed.) *Nonlinear Optical Properties of Organic Materials and Crystals, vols. 1 and 2*; Academic Press: New York, **1987**.
10. (a) Laidlaw, W. M.; Denning, R. G.; Verbiest, T.; Chauchard, Persoons, A. *Nature* **1993**, *363*, 58. (b) Coe, B. J.; Harris, J. A.; Jones, L. A.; Brunshwig, B. S.; Song, K.; Clays, K.; Garin, J.; Orduna, J.; Coles, S. J.; Hursthouse, M. B.; *J. Am. Chem. Soc.* **2005**, *127*, 4845.
11. Kajzar, F.; Lee, K.-S.; Jen, A. K.-Y.; *Adv. Polym. Sci.* **1998**, *120*, 13096.

12. Hunter, C. A.; Sanders, J. K. M. *J. Am. Chem. Soc.* **1990**, *112*, 5525.
13. Mapolo, D. T.; Al-Noaimi, M.; Crutchley, R. J. *Inorg. Chim. Acta*, **2006**, *359*, 1458.
14. (a) Aquino, M. A. S.; Lee, F. L.; Gabe, E. J.; Bensimon, C.; Greedan, J. E.; Crutchley, R. J. *J. Am. Chem. Soc.* **1992**, *114*, 5130. (b) Naklicki, M.; Crutchley, R. J. *Inorg. Chim. Acta* **1994**, *225*, 123. (c) Naklicki, M. L.; Gorelsky, S. I.; Kaim, W.; Sarkar, B.; Crutchley, R. J. *Inorg. Chem.* **2012**, *51* 1400.
15. Rezvani, A. R.; Bensimon, C.; Crompton, B.; Reber, C.; Greedan, J. E.; Kondratiev, V. V.; Crutchley, R. J. *Inorg. Chem.* **1997**, *36*, 3322.
16. Evans, C. E. B.; Naklicki, M. L.; Rezvani, A. R.; White, C. A.; Kondratiev, V. V.; Crutchley, R. J. *J. Am. Chem. Soc.* **1998**, *120*, 13096.
17. De Rosa, M. C.; White, C. A.; Evans, C. E. B.; Crutchley, R. J. *J. Am. Chem. Soc.* **2001**, *123*, 1396.
18. Evans, C. E. B.; Yap, G. P. A.; Crutchley, R. J. *Inorg. Chem.* **1998**, *37*, 6161.
19. (a) Creutz, C.; *Prog. Inorg. Chem.* **1983**, *30*, 1. (b) Crutchley, R. J. *Adv. Inorg. Chem.* **1994**, *41*, 273. (c) Ward, M. D.; *Chem. Soc. Rev.* **1995**, 121.
20. Naklicki, M.; Crutchley, R. J.; *Inorg. Chem.* **1989**, *28*, 1955.
21. Crutchley, R. J.; McCaw, K.; Lee, F. L.; Gabe, J. E. *Inorg. Chem.* **1990**, *29*, 2576.
22. Saleh, A. A.; Crutchley, R. J. *Inorg. Chem.* **1990**, *29*, 2123.
23. Evans, C. E. B.; Ducharme, D.; Naklicki, M.; Crutchley, R. J.; *Inorg. Chem.* **1995**, *34*, 1350.
24. Mosher, P. J.; Yap, G. P. A.; Crutchley, R. J.; *Inorg. Chem.* **2001**, *40*, 550.

25. Mahmoud, L.; Gorelsky, S. I.; Kaim, W.; Sarkar, B.; Crutchley, R. J. *Inorg. Chim. Acta* **2011**, *374*, 147.
26. Harb, C.; Kravstov, P.; Choudhuri, M.; Sirianni, E. R.; Yap, G. P. A.; Lever, A. B. P.; Crutchley, R. J. *Inorg. Chem.* **2013**, *52*, 1621.
27. Rezvani, A. R.; Crutchley, R. J. *Inorg. Chem.* **1994**, *33*, 170.
28. Crutchley, R. J. *Coord. Chem. Rev.* **2001**, *219*, 125.
29. Choudhuri, M. M. R.; Kaim, W.; Sarkar, B.; Crutchley, R. J. *Inorg. Chem.* **2013**, *52(19)*, 11060.
30. Constable, E. C.; Harverson, P.; Smlth, D. F.; Whall, L. A. *Tetrahedron* 1994, *50*, 7799.
31. Gennett, T.; Milner, D. F.; Weaver, M. J. *J. Phys. Chem.* **1985**, *89*, 2787.
32. (a) Hush, N. S. *Prog. Inorg. Chem.*, **1967**, *8*, 391. (b) Creutz, C.; Newton, M. D.; Sutin, N.; *J. Photochem. Photobiol. A: Chem.* **1994**, *82*, 47.
33. (a) Constable, E. C.; Lewis, J.; Liptrot, M. C.; Raithby, P. R. *Inorg. Chim. Acta*, **1990**, *178*, 47. (b) Constable, E. C.; Harverson, P.; Diane, R. S.; Whall, L. *Polyhedron*, **1997**, *16(20)*, 3615. (c) Farlow, B.; Terence, A. Nile; Walsh, J. *Polyhedron*, *12(23)*, 2891, (d) Lashgari, K.; Kritikos, M.; Norrestam, R.; Norrby, T. *Acta Cryst.* **1999**, *C55*, 64. (e) Norrby, T.; Borje, A.; Akermark, B.; Hammarstrom, L.; Alsins, J.; Lashgari, K.; Norrestam, R.; Martensson, J.; Stenhagen, G. *Inorg. Chem.* **1997**, *36*, 5850. (f) Pyo, S.; Perez-Cordaro, E.; Bott, S.; Echegoyen, L. *Inorg. Chem.* **1999**, *38*, 3337. (g) Constable, E. C.; Thompson, A. M. W. C. *Inorg. Chim. Acta*, **1994**, *223*, 177. (h) Fallahpour, R.-A.; Neuburger, Zehnder, M. *Polyhedron*, **1999**, *18*, 2445.

34. Aquino, M. A. S.; Crutchley, R. J.; Lee, F. L.; Gabe, E. J.; Bensimon, C. *Acta Cryst.* **1993**, *C49*, 1543.
35. Kurzar, F.; Douraghi-Zadeh, K. *Chem. Rev.* **1967**, *67*, 107.
36. Balzani, V.; Juris, A.; Barigelletti, F.; Campagna, S.; Belser, P.; Von Zelewsky, A. *Coord. Chem. Rev.* **1988**, *84*, 85.
37. Santoni, M.-P.; Pal, A. K.; Hanan, G. S.; Proust, A.; Hasenknopf, B. *Inorg. Chem. Com.* **2011**, *14*, 399.
38. (a) Drago, R. *Physical Methods for Chemists, Second Ed.*; Surfside Scientific Publishers: Gainesville, **1992**. (b) Bertini, I.; Luchinat, C.; Parigi, G. *Current Methods in Inorganic Chemistry, Solution NMR of Paramagnetic Molecules, Vol.2*; Elsevier, **2001**. (c) Kluiber, R. W.; Horrocks, W. D. *Inorg. Chem.* **1967**, *6*, 430. (d) Bertini, I.; Wilson, L. J. *J. Coord. Chem.* **1971**, *1*, 237. (e) Holm, R. H.; Chakravorty, A.; Dudek, G. O. *J. Am. Chem. Soc.* **1964**, *86*, 379.
39. (a) Kaim, W. *Coord. Chem. Rev.* **1987**, *76*, 187. (b) Weil, J. A.; Bolton, J. T.; Wertz, J. E. *Electron Paramagnetic Resonance*; Willey: New York, **1994**. (c) Kaim, W.; Kasack, V. *Inorg. Chem.* **1990**, *29*, 4696. (d) Roy, S.; Sarkar, B.; Imrich, H.-G.; Fiedler, J.; Zalis, S.; Jimenez-Aparicio, R.; Urbanos, F. A.; Mobin, S. M.; Lahiri, G. K.; Kaim, W. *Inorg. Chem.* **2012**, *51*, 9273. (e) Remenyi, C.; Kaupp, M. *J. Am. Chem. Soc.* **2005**, *127*, 11399.
40. Gutmann, V. *The Donor-Acceptor Approach to Molecular Interactions*; Plenum Press: New York, **1978**.
41. Becke, A. D., *Journal of Chemical Physics* **1993**, *98*, 5648.
42. Lee, C.; Yang, W.; Parr, R. G., *Physical Reviews* **1988**, *B37*, 785.

Chapter 6: Conclusion and Future Work

6.1 Research Summary

In the first study (Chapter 2), four dinuclear complexes $[\{\text{Ru}(\text{tppy})(\text{bpy})\}_2(\mu\text{-R}_2\text{R}_2'\text{dicyd})]^{2+}$ where $\text{R}_2\text{R}_2'\text{dicyd}^{2-} = \text{Me}_2\text{-}, \text{Cl}_2\text{-}, \text{Cl}_4\text{-}$ and unsubstituted 1,4-dicyanamide benzene dianion, were prepared and the singly oxidized complexes $[\{\text{Ru}(\text{tppy})(\text{bpy})\}_2(\mu\text{-R}_2\text{R}_2'\text{dicyd})]^{3+}$ were interrogated by EPR spectroscopy and IR and vis-NIR spectroelectrochemistry and theory to evaluate the non-innocent behaviour of bridging $\text{R}_2\text{R}_2'\text{dicyd}$ ligands as a function of substituent properties. EPR spectra of singly oxidized complexes were characterized by isotropic signals, which unambiguously established the non-innocent behaviour of the bridging $\text{R}_2\text{R}_2'\text{dicyd}^{2-}$ ligand and the valence configuration $\text{Ru}(\text{II})\text{-R}_2\text{R}_2'\text{dicyd}^{\bullet\text{-}}\text{-Ru}(\text{II})$ for all $[\{\text{Ru}(\text{tppy})(\text{bpy})\}_2(\mu\text{-R}_2\text{R}_2'\text{dicyd})]^{3+}$ complexes. The non-innocent behaviour was also supported by the paramagnetic ^1H NMR spectra of complexes in which the observed paramagnetic shifts of phenyl ring protons and the diamagnetic chemical shift of the *t*-butyl group indicate a substantial spin density localized on the bridging $\text{R}_2\text{R}_2'\text{dicyd}^{\bullet\text{-}}$ ligand. However, the mostly ligand-centred SOMO gains increased Ru(III) character as the π -HOMO is gradually stabilized by electron withdrawing chloro-substituents, which is evident from the EPR spectra of complexes which showed a relatively broad and large anisotropic signal ($g = 2.038$, $\Delta g = 0.046$) for the $\text{Cl}_4\text{dicyd}^{2-}$ complex compared to a sharp isotropic signal ($g = 2.012$, $\Delta g = 0.026$) for the unsubstituted dicyd^{2-} complex. This variation in metal character on the SOMO is also reflected in the IR spectroelectrochemical results, which showed a slight high energy shift of the $\nu(\text{NCN})$ band upon generation of the singly oxidized dicyd^{2-} complex, a shift

exemplified by the oxidation of free anionic $\text{Me}_2\text{dicyd}^{2-}$ ligand forming the radical anion $\text{Me}_2\text{dicyd}^{\bullet-}$. In contrast, single electron oxidation of the $\text{Cl}_4\text{dicyd}^{2-}$ complex resulted in a low frequency shift of the $\nu(\text{NCN})$ band, a shift which is observed upon single electron oxidation of the $[\text{Ru}(\text{tpy})(\text{bpy})(2,4\text{-Cl}_2\text{pcyd})]^+$ complex whose redox transformation has been unambiguously assigned by EPR spectroscopy to the oxidation of the Ru(II) to Ru(III). While the second oxidation of $\text{Cl}_4\text{dicyd}^{2-}$ complex is irreversible, the doubly oxidized $\text{Me}_2\text{dicyd}^{2-}$ and $\text{Cl}_4\text{dicyd}^{2-}$ complexes showed a low energy $\nu(\text{NCN})$ band feature for Ru(III)-cyanamide bond, suggesting a greater Ru(III) character in these species. The substituent effect is also reflected in the observed electrochemical and vis-NIR spectral properties of complexes. The cyclic voltammetry data showed that the $\text{Cl}_4\text{dicyd}^{2-}$ complex is about 0.43 V more stabilized towards oxidation relative to the $\text{Me}_2\text{dicyd}^{2-}$ complex, reflecting a large stabilizing effect of electron withdrawing chloro-substituents on the π -HOMO of the $\text{R}_2\text{R}'_2\text{dicyd}^{2-}$ ligands. The second redox-couple of the $\text{Cl}_4\text{dicyd}^{2-}$ complex was also stabilized by about 0.30 V relative to that of $\text{Me}_2\text{dicyd}^{2-}$ complex. The vis-NIR spectroelectrochemical oxidation of Me_2 - and unsubstituted dicyd^{2-} complexes resulted in the growth of a NIR band at 1023-1083 nm which is red shifted to 1265-1376 nm for the Cl_2 - and $\text{Cl}_4\text{dicyd}^{2-}$ complexes, and assigned, on the basis of semi-empirical calculations, to a mostly ligand-centred (ILCT) transition involving π MOs of the radical anion ligand $\text{R}_2\text{R}'_2\text{dicyd}^{\bullet-}$. The second oxidation showed a dramatic substituent effect, the NIR band being shifted to shorter wavelengths (918-959 nm) with an increase in intensity for the Me_2 - and dicyd^{2-} complexes, while shifted to higher energies (855 and 888 nm) with a significant decrease in intensity for the Cl_2 - and $\text{Cl}_4\text{dicyd}^{2-}$ complexes. The vis-NIR spectra of the doubly oxidized Cl_2 -, $\text{Cl}_4\text{dicyd}^{2-}$

complexes showed an additional low energy band feature from 1200-1800 nm. Semi-empirical calculations assuming singlet ground state assigned the 855-959 nm band of complexes to Ru(II) to doubly oxidized dicyd⁰ MLCT transition, however the low energy band feature (1200-1800 nm) of the doubly oxidized Cl₂- and Cl₄dicyd²⁻ complexes also suggested a significant contribution from the valence configuration Ru(III)-R₂R₂'dicyd^{•-}-Ru(II).

In the second study, the non-innocent dicyd²⁻ ligand (L[•]/L²⁻ = -0.47 V vs. NHE) was replaced by the more stable bridging adpc²⁻ dianion (L[•]/L²⁻ = 0.68 V vs. NHE) in dinuclear [$\{\text{Ru}(\text{tpy})(\text{bpy})\}_2(\mu\text{-R}_2\text{R}_2'\text{adpc})\]^{2+} complexes. The energy of the π -HOMO of the bridging adpc²⁻ ligand was “tuned” by a range of electron releasing (Me₄-, Me₂-) and withdrawing (Cl₂-, Cl₄-) substituents. The R₂R₂'adpc²⁻ complexes exhibited greater stability towards oxidation relative to the analogous R₂R₂'dicyd²⁻ complexes, with first and second redox couples of the former being stabilized by about 0.45 V and 0.55 V, respectively, relative to the latter. Gas-phase DFT calculations at B3LYP/6-31G*-LANL2DZ level showed mostly a ligand-centred spin in the singly oxidized [$\{\text{Ru}(\text{tpy})(\text{bpy})\}_2(\mu\text{-R}_2\text{R}_2'\text{adpc})\]^{3+} complexes. However, combined EPR, IR and vis-NIR spectroelectrochemistry have shown a transition in the non-innocent behavior of R₂R₂'adpc²⁻, suggesting ligand-centred Ru(II)-Me₂/Me₄adpc^{•-}-Ru(II) descriptions for the Me₄/Me₂adpc, a delocalized mixed-valence Ru(II^{1/3})-adpc^{1 2/3-}-Ru(II^{1/3}), description of the unsubstituted adpc²⁻, and localized mixed-valence descriptions, Ru(II)-Cl₂/Cl₄adpc²⁻-Ru(III), for the Cl₂/Cl₄adpc²⁻ complexes. This transition is obviously attributable to the gradual stabilization of the π -HOMO of R₂R₂'adpc²⁻ ligands by the electron withdrawing chloro substituents. EPR spectroscopy established the valence configurations of two$$

extreme members, the $\text{Me}_4\text{adpc}^{2-}$ complex being recognized as a radical-centred complex, $\text{Ru(II)-Me}_4\text{adpc}^{\bullet-}\text{-Ru(II)}$, by a sharp isotropic room temperature signal with a small g value ($g = 1.96$), while the $\text{Cl}_2\text{adpc}^{2-}$ complex as a mixed-valence complex, $\text{Ru(II)-Cl}_2\text{adpc}^{2-}\text{-Ru(III)}$, by a broader 110 K EPR signal with a relatively large g value and significantly large g anisotropy ($g_{\text{av}} = 2.075$, $\Delta g = 0.20$) for the Ru(III) ion. The $\text{Me}_2\text{adpc}^{2-}$ and unsubstituted adpc^{2-} complexes remained EPR silent, however, combined IR and vis-NIR spectroelectrochemistry suggested a radical-centred description, $\text{Ru(II)-Me}_2\text{adpc}^{\bullet-}\text{-Ru(II)}$, of the former while a delocalized mixed-valence description, $\text{Ru(II}^{1/3}\text{)-adpc}^{1\frac{1}{2}-}\text{-Ru(II}^{1/3}\text{)}$, of the latter. Single electron oxidation of both Me_4 - and $\text{Me}_2\text{adpc}^{2-}$ complexes resulted in a higher frequency shift of the $\nu(\text{NCN})$ band as observed during oxidation of the free adpc^{2-} dianion forming the radical anion $\text{adpc}^{\bullet-}$. In contrast, single electron oxidation of Cl_2 and $\text{Cl}_4\text{adpc}^{2-}$ complexes resulted in a gradual decrease in intensity of the initial $\nu(\text{NCN})$ band with a gradually developing $\nu(\text{NCN})$ band at a lower frequency, the spectral feature which is associated with the formation of Ru(III)-cyanamide . In addition, the presence of two $\nu(\text{NCN})$ bands suggested a localized mixed-valence description of the singly oxidized Cl_2 and $\text{Cl}_4\text{adpc}^{2-}$ complexes. On the other hand, the unsubstituted adpc^{2-} complex showed an intermediate behaviour upon oxidation, exhibiting a single and a very weak $\nu(\text{NCN})$ band at lower frequency with only a slight decrease in intensity of the $\nu(\text{NCN})$ band, a feature which is consistent with a delocalized state. Vis-NIR spectroelectrochemistry showed that single electron oxidation of the adpc^{2-} complex resulted in a low energy NIR band at 1920 nm, which is significantly red-shifted relative to those of Me_4 - and $\text{Me}_2\text{adpc}^{2-}$ complexes and correlates well with those of Cl_2 - and $\text{Cl}_4\text{adpc}^{2-}$ complexes in so far as the band position and

intensities are concerned. Combined IR and vis-NIR spectroelectrochemical results, therefore, suggested a strongly coupled delocalized mixed-valence description, $\text{Ru}(\text{II}^{1/3})\text{-adpc}^{1/2-}\text{-Ru}(\text{II}^{1/3})$, for the singly oxidized adpc^{2-} complex. The assignments of doubly oxidized $[\{\text{Ru}(\text{tpy})(\text{bpy})\}_2(\mu\text{-R}_2\text{R}_2'\text{adpc})]^{3+}$ complexes are ambiguous because the complexes remained EPR silent. However, combined vis-NIR and higher level DFT calculations using DZVP basis set for Ru and the triple-zeta basis set (TZVP) for other atoms in the gas-phase and in solution (methanol, SMD implicit solvation model) provided some insight into the oxidation state distributions in doubly oxidized complexes. The second oxidation of all dinuclear complexes resulted in similar vis-NIR spectral features, with the NIR bands (1650-1920 nm) of the singly oxidized complexes being shifted to higher energies (900-1000 nm). However, the NIR band of the doubly oxidized Cl_2 and $\text{Cl}_4\text{adpc}^{2-}$ complexes also featured a low energy tail extended from 1200-2000 nm. TD DFT calculated spectra assuming the closed-shell singlet structure, $\text{Ru}(\text{II})\text{-R}_2\text{R}_2'\text{adpc}^0\text{-Ru}(\text{II})$, are in good agreement with the experimental spectra in the region between 400-1200 nm for the doubly oxidized complexes. On the other hand, calculated spectra assuming an open-shell triplet structure, $\text{Ru}(\text{III})\text{-R}_2\text{R}_2'\text{adpc}^{\bullet-}\text{-Ru}(\text{II})$, featured an intense NIR band ca. 1400 nm, suggesting an increased contribution of the triplet structure to the doubly oxidized Cl_2 - and $\text{Cl}_4\text{adpc}^{2-}$ complexes. The *meta*- adpc^{2-} complex showed very different electrochemical and spectroscopic properties than those of its *para* analogues, which is attributable to a discontinuity in the π -conjugation through the bridging ligand, as shown by DFT calculations. Unlike other complexes, the *meta*- adpc complex showed a single reversible wave at 0.98 V on oxidation in its cyclic voltammetry and an associated NIR band at 1100 nm for the oxidized species, which

closely resemble those of the mononuclear $[\text{Ru}(\text{tpy})(\text{bpy})(2,4\text{-Cl}_2\text{pcyd})]^{+2}$ complex and are indicative of Ru(III)-centred spin in the oxidized *meta*-adpc complex.

In the third study, six mononuclear *cis*- $[\text{Ru}(\text{bpy})_2(\text{R-pcyd})(\text{dmsO-S})]^+$ complexes were synthesized and investigated for photo-induced linkage isomerism of dmsO with the specific aim of developing a dinuclear mixed-valence “photo-switch” incorporating this photochromic unit. The mononuclear *cis*- $[\text{Ru}(\text{bpy})_2(\text{R-pcyd})(\text{dmsO-S})]^+$ complexes exhibited fast photo-induced S→O linkage isomerism forming metastable *cis*- $[\text{Ru}(\text{bpy})_2(\text{R-pcyd})(\text{dmsO-O})]^+$ isomers, followed by a relatively slow thermal O→S back reaction in solution and in solid polymer film. The quantum yields ($\Phi_{\text{S}\rightarrow\text{O}}$) of MLCT excited S→O linkage isomerism increased dramatically (0.07-0.43) with a decrease in the donor strength of phenylcyanamide ligands, while the thermal O→S back reaction followed an opposite trend ($k_{\text{OS1}} = 4.52\text{--}2.61 \times 10^{-3} \text{ s}^{-1}$), decreasing as the donor property of phenylcyanamide ligand decreased. The necessity of the formation of a “hard” Ru(III) ion for driving the excited state S→O rearrangement and a “soft” Ru(II) ion to promote ground state O→S rearrangement was revealed. The complexes also exhibited redox-induced S→O and O→S linkage isomerism. Scanning towards positive potentials, the cyclic voltammetry of *cis*- $[\text{Ru}(\text{bpy})_2(\text{R-pcyd})(\text{dmsO-S})]^+$ showed two oxidation processes: a phenylcyanamide L^0/L^- couple (an assignment supported by DFT calculations using B3LYP-6-31G*-LANL2DZ model) followed by a Ru(III/II) couple yielding the Ru(III)-dmsO(-S)- L^0 complex. The latter complex rapidly rearranged (k_{OS}) to form Ru(III)-dmsO(-O)- L^0 . Scanning towards negative potential, reduction forms Ru(II)-dmsO(-O)- L^0 which could then undergo rearrangement (k_{OS2}) to form Ru(II)-dmsO(-S)- L^0 or further reduction to Ru(II)-dmsO(-O)- L^- depending on the potential scan rate. The latter complex

can undergo rearrangement (k_{OS1}) to reform the initial complex Ru(II)-dmsO(-S)-L⁻. The low (0.05V/s) and high (20.0 V/s) scan rate voltammograms provided estimates of $k_{OS2} \approx 0.2 \text{ s}^{-1}$ and $k_{SO} \approx 50 \text{ s}^{-1}$, respectively.

In the fourth study, five mononuclear neutral *trans*-[Ru(ttpy)(R-pcyd)Cl₂] complexes were synthesized with the intention of developing a neutral mixed-valence complex incorporating these acceptor units, for applications in non-linear optical (NLO) materials. As a fundamental study, regarding the electronic nature of Ru(III)-cyanamide bond, these complexes were interrogated by combined paramagnetic ¹H NMR, vis-NIR and gas-phase DFT calculations (B3LYP/6-31G* -LANL2DZ) to examine the degree of non-innocent behavior of phenylcyanamide ligand in the coordination sphere of π -acceptor ttpy and σ/π -donor Cl⁻ ligands. The electronic absorption spectra of these complexes are characterized by a low energy cyanamide to Ru(III) LMCT band at 721-880 nm in strong donor solvents such as DMF, which is bathochromically shifted to 787-954 nm in a weakly donor solvent CH₂Cl₂. The blue shift in strong donor solvent indicates strong solvent-solute donor acceptor interactions between the Ru(III) ion and the donor solvent molecule which destabilize the Ru(III)d π acceptor orbital relative to the donor π -HOMO of the phenylcyanamide ligand. In a given solvent, the LMCT bands also exhibited a large bathochromic shift ($\Delta\lambda \approx 160 \text{ nm}$) with increasing donor strengths of phenylcyanamide ligands, which is attributable to the stabilization of the donor π -HOMO relative to the acceptor Ru(III)d π orbital. The oscillator strengths of the LMCT bands are larger (0.105-0.154) in the weakly donor solvent CH₂Cl₂ relative to those in a strong donor solvent DMF (0.062-0.076), suggesting a greater covalency in the Ru(III)-phenylcyanamide bond and a greater degree of non-innocence of phenylcyanamide

ligands in weakly donor solvents. The LMCT oscillator strengths in CH_2Cl_2 also showed a gradual decrease with increasing number of chloro-substituents on phenylcyanamide ligands in agreement with gradual stabilization of the π -HOMO and weakening of π -coupling between Ru(III) and phenylcyanamide ligand. DFT calculations on complexes in the gas-phase showed spin density mostly located on the phenylcyanamide ligands, decreasing gradually as the number of chloro-substituents increased and shifting to the ancillary Cl^- ligands, without changing much of the spin density on ruthenium ion. However, the spin-density distribution was based on a gas-phase calculation and a more accurate result is expected from calculations that include solvent effects. These will be performed in the near future. A more realistic picture of spin density distributions was obtained from the paramagnetic ^1H NMR spectroscopy of the complexes in $\text{dms-}d_6$, which provided estimates of π -spin densities on the phenyl ring carbons of the phenylcyanamide ligands from the observed isotropic shifts of the phenyl ring protons. Calculated π -spin densities (0.7-3.0 %) on the phenyl ring carbons clearly indicate a Ru(III)-centred spin on *trans*-[Ru(tpy)(R-pcyd) Cl_2] complexes.

6.2 Concluding Remarks

The study of four families of ruthenium phenylcyanamide complexes has shown that the non-innocence of redox-active phenylcyanamide ligands in ruthenium complexes is not a permanent attribute, but rather a function of the electronic nature of ancillary ligands, substituents on the phenyl cyanamide ligands and the solvent medium. The Ru(II) $d\pi$ orbitals are significantly stabilized by π -acceptor ligands in [Ru(tpy)(bpy)(R-pcyd)] $^+$ or [Ru(bpy) $_2$ dms(-S)(R-pcyd)] $^+$ so that upon complex oxidation, the SOMO is either significantly or primarily ligand centred. The replacement of bipyridine in

$[\text{Ru}(\text{ttpy})(\text{bpy})(\text{R-pcyd})]^{2+}$ with chloro ligands to synthesize the *trans*- $[\text{Ru}(\text{ttpy})(\text{R-pcyd})\text{Cl}_2]$ complexes, dramatically raises the energy of $\text{Ru}d\pi$ orbitals above the $p\pi$ orbitals of R-pcyd so that the *trans*- $[\text{Ru}(\text{ttpy})(\text{R-pcyd})\text{Cl}_2]$ complexes have spin density largely localized on ruthenium and have similar ^1H NMR and vis-NIR spectroscopies compared to those of $[\text{Ru}(\text{NH}_3)_5(\text{R-pcyd})]^{2+}$. The degree of redox ambiguity of phenylcyanamide ligand can be directly controlled by electron donating or withdrawing substituents on the phenylcyanamide ligand and this can have important electronic consequences as shown by the quantum yields of linkage isomerism observed for $[\text{Ru}(\text{bpy})_2\text{dms}o(-S)(\text{R-pcyd})]^+$.

For dinuclear $\text{Ru}(\text{ttpy})(\text{bpy})$ complexes, the $\text{Ru}(\text{II})d\pi$ orbitals are significantly below the high energy π -HOMOs of the bridging 1,4-dicyanamide benzene dianion dicyd^{2-} and its substituted derivatives such that the oxidation of $[\{\text{Ru}(\text{ttpy})(\text{bpy})\}_2(\mu\text{-R}_2\text{R}_2'\text{dicyd})]^{2+}$ resulted in the formation of ligand-centred radical species $\text{Ru}(\text{II})\text{-R}_2\text{R}_2'\text{dicyd}^{\bullet}\text{-Ru}(\text{II})$. Chloro-substitution of the dicyd^{2-} ligand stabilized the π -HOMO but it is still above the $\text{Ru}(\text{II})d\pi$ orbital in these complexes. On the other hand, the π -HOMOs of 4,4'-azodi(phenylcyanamide) dianion with energy = 1.4 eV is significantly more stable than that of 1,4-dicyanamidebenzene dianion with energy 3.5 eV. For $[\{\text{Ru}(\text{tpy})(\text{bpy})\}_2(\mu\text{-R}_2\text{R}_2'\text{adpc})]^{2+}$ complexes oxidation to $[\{\text{Ru}(\text{tpy})(\text{bpy})\}_2(\mu\text{-R}_2\text{R}_2'\text{adpc})]^{3+}$ generates ligand centred radicals $\text{Ru}(\text{II})\text{-Me}_4/\text{Me}_2\text{adpc}^{\bullet}\text{-Ru}(\text{II})$ and metal centred radicals $\text{Ru}(\text{III})\text{-Cl}_4/\text{Cl}_2\text{adpc}^{2-}\text{-Ru}(\text{II})$. The unsubstituted adpc^{2-} complex is suggested to be the delocalized case $\text{Ru}(\text{II}^{1/3})\text{-adpc}^{1\frac{2}{3}-}\text{-Ru}(\text{II}^{1/3})$, in which positive charge is shared between ruthenium ions and the bridging ligand. These are formal oxidation state descriptions and greater sharing of positive charge is indicated by EPR spectroscopy. For

example, the EPR spectrum of $[\{\text{Ru}(\text{tpy})(\text{bpy})\}_2(\mu\text{-Cl}_2\text{adpc})]^{2+}$ gives g values which indicate approximately 25% ligand radical character in the SOMO.

The stabilization of the Ru(II) $d\pi$ orbitals appear to be more pronounced in the $[\text{Ru}(\text{bpy})_2\text{dms}o(-S)(\text{R-pcyd})]^+$ coordination sphere. For these complexes, oxidation of the phenylcyanamide ligand occurred at far lower positive potential than the Ru(III/II) couple. Indeed, DFT calculations showed spin density to be almost entirely ligand centred and this must indicate a considerable stabilization of Ru(II) $d\pi$ orbitals because of the Ru-dms $o(-S)$ bond.

Significant solvent effects were observed for the *trans*- $[\text{Ru}(\text{ttpy})(\text{R-pcyd})\text{Cl}_2]$ complexes. In the strong donor solvents DMF or DMSO, the interaction between solvent and complex destabilized the Ru(III) $d\pi$ orbital and this resulted in a shift to higher energy of the Ru(III)-cyanamide LMCT transition. However, in the weak donor solvent CH_2Cl_2 , the reduced energy gap between Ru(III) $d\pi$ and R-pcyd π -HOMO shifted the LMCT band to lower energies. This also resulted in an increase in covalency of the Ru(III)-cyanamide bond and a greater degree of non-innocence, which increased with the donor strength of phenylcyanamide ligands. Metal-ligand coupling elements (bond strength) are directly relatable to charge-transfer oscillator strength and as the LMCT data of the *trans*- $[\text{Ru}(\text{ttpy})(\text{R-pcyd})\text{Cl}_2]$ complexes in CH_2Cl_2 solution showed, oscillator strength increased with the donor properties of the phenylcyanamide ligands.

6.3 Future Studies

Studies on dinuclear $[\{\text{Ru}(\text{tpy})(\text{bpy})\}_2(\mu\text{-R}_2\text{R}'_2\text{adpc})]^{3+}$ complexes showed that the π -HOMOs of the bridging $\text{R}_2\text{R}'_2\text{adpc}^{2-}$ ligands are still close to the Ru(II) $d\pi$ orbital even after incorporation of highly electron withdrawing chloro-substituents. Further

stabilization via incorporation of more electron withdrawing substituents was complicated by synthetic difficulty, which in turn, limited our study on more localized mixed-valence system. One way to achieve further stabilization of the π -HOMO is to incorporate a stronger acceptor unit between two phenylcyanamide groups. Towards this end, a bridging aromatic dicyanamide dianion ligand incorporating a strong acceptor tetrazine unit, 3,6-bis-(4-phenylcyanamide)-1,2,4,5-tetrazine (tadpc^{2-}), has been synthesized in the Crutchley Lab. DFT calculation showed a continuous π -HOMO throughout the molecule as in dicyd^{2-} and adpc^{2-} ligands, which is significantly more stabilized (-4.8 eV) than the π -HOMO of the adpc^{2-} ligand (1.5 eV). Incorporation of the bridging tadpc^{2-} ligand in the dinuclear $[\{\text{Ru}(\text{ttpy})(\text{bpy})\}_2(\mu\text{-tadpc})]^{3+}$ complex would complement the effect of more stabilizing electron withdrawing substituents on the bridging adpc^{2-} ligand and provide an opportunity to study a perturbed, mostly metal-centred SOMO by spectroscopic methods.

The mononuclear *cis*- $[\text{Ru}(\text{bpy})_2(\text{R-pcyd})(\text{dmsO-S})]^+$ complex has met the criteria of the photochromic moiety in a dinuclear mixed-valence “photo-switch”. The next step is to construct a dinuclear complex that incorporates this photochromic moiety and examine the variation of the mixed-valence properties (NIR absorption) of the designed molecule via ultra-fast photo induced linkage isomerism. In this regard, synthesis of a symmetric dinuclear complex of the bridging adpc^{2-} ligand, $[\{\text{Ru}(\text{bpy})_2(\text{dmsO-S})\}_2(\mu\text{-adpc})](\text{PF}_6)_2$, has been attempted in the Crutchley Lab. The purification and characterization of the isolated complex is underway.

The mononuclear neutral *trans*- $[\text{Ru}(\text{ttpy})(\text{R-pcyd})\text{Cl}_2]$ complexes require further characterization by EPR or XANES spectroscopy would complement the paramagnetic

^1H NMR study and provide more quantitative estimates of spin density distributions in these neutral complexes. Two complexes *trans*-[Ru(tpy)(2,4-Cl₂pcyd)Cl₂] and *trans*-[Ru(tpy)(2,3,5,6-Cl₄pcyd)Cl₂] are being investigated by XANES spectroscopy to examine the variation in spin densities in these complexes as a function of the donor properties of the phenylcyanamide ligand. These complexes can be studied in a range of donor/acceptor solvents to further explore the outer-sphere effect on the degree of non-innocence of phenylcyanamide ligand. DFT calculations incorporating specific solvent-solute interactions will be the subject of future study. Finally, the synthesis of a neutral mixed-valence complex of the type [$\{\text{Ru}^{\text{III}}(\text{tpy})\text{Cl}_2\}(\mu\text{-adpc}^{2-}/\text{dicyd}^{2-})\{\text{Ru}^{\text{II}}(\text{L3})(\text{L2})\}$] will be attempted. A possible choice of donor unit is Ru(II)(Tp)(dppe)- where dppe is ethylenebis(diphenylphosphine) and Tp⁻ is hydrotris(pyrazol-1-yl)borate, because a family of mononuclear neutral scorpionate complexes [Ru(Tp)(dppe)(R-pcyd)] have been synthesized and characterized, which showed stable Ru(II) oxidation state and the desired electronic properties. After successful synthesis and characterization of mixed-valence properties, the proposed neutral mixed-valence complex will be incorporated in a polymer matrix and investigated for desired non-linear optical (NLO) effects.

In closing, the design of novel opto-electronic materials based on dinuclear metal systems incorporating non-innocent ligands is a rapidly evolving field. It is hoped that this research work conducted on the redox ambi-valence of phenylcyanamide ligands proves to be an important contribution.

Chapter 7: Appendices

Appendix-A: Supporting Tables and Figures for Chapter 1

Table A.1: Atomic Coordinates of Phenylcyanamide Monoanion (pcyd⁻).

Cartesian Coordinates				
	Atom	X	Y	Z
1	C C1	0.123656	-0.9892245	0
2	H H4	-0.6883716	-1.7129817	0
3	C C2	1.4472012	-1.4167283	0
4	H H6	1.6558454	-2.487623	0
5	C C3	2.510362	-0.5050674	0
6	C C4	2.203314	0.863043	0
7	C C5	0.8863638	1.304322	0
8	H H12	0.65375	2.3670849	0
9	C C6	-0.2113026	0.3968938	0
10	N N1	-1.4782485	0.9089698	0
11	C C7	-2.5084373	0.0980156	0
12	N N3	-3.5047035	-0.5409174	0
13	H H1	3.0095103	1.5978672	0
14	H H5	3.5429879	-0.8482384	0

Table A.2: Atomic Coordinates of 1,4-Dicyanamide Benzene Dianion (dicyd²⁻).

Cartesian Coordinates				
	Atom	X	Y	Z
1	C C1	1.0130312	0.9468551	0
2	H H4	1.7976661	1.7037665	0
3	C C2	-0.3260131	1.3399646	0
4	H H6	-0.5809918	2.4008366	0
5	C C3	-1.3979986	0.4166746	0
6	C C4	-1.0130312	-0.9468551	0
7	C C5	0.3260131	-1.3399646	0
8	H H12	0.5809918	-2.4008366	0
9	C C6	1.3979986	-0.4166746	0
10	N N1	2.7058457	-0.9007289	0
11	N N2	-2.7058457	0.9007289	0
12	C C7	3.7245946	-0.0927928	0

13	C	C8	-3.7245946	0.0927928	0
14	N	N3	4.7361559	0.5377287	0
15	N	N4	-4.7361559	-0.5377287	0
16	H	H1	-1.7976661	-1.7037665	0

Table A.3: Atomic Coordinates of 4,4'-Azodi(phenylcyanamide) (adpc²⁻).

Cartesian Coordinates

	Atom	X	Y	Z
1	C C28	4.5899755	-0.5111505	0.0014705
2	C C29	3.852102	0.7140025	0.0076925
3	H H2	4.4138779	1.646212	0.0139203
4	C C30	2.4692144	0.7362331	0.0061236
5	H H4	1.9288605	1.6787431	0.0110707
6	C C31	1.7140988	-0.46023	-0.0018183
7	N N7	0.317047	-0.5565558	-0.0041304
8	N N8	-0.3161966	0.5551409	0.0013489
9	C C60	-1.7132618	0.4589022	-0.0014543
10	C C61	-2.4684641	-0.7375067	-0.0098355
11	H H3	-1.9281759	-1.6800527	-0.014727
12	C C62	-2.4306052	1.6739145	0.0048584
13	H H8	-1.8521101	2.5961731	0.0114875
14	C C63	-3.8141768	1.7043446	0.002866
15	H H7	-4.3523787	2.6498921	0.0079351
16	C C64	-4.5891361	0.5100292	-0.0057354
17	C C65	-3.8513488	-0.715176	-0.0118529
18	H H5	4.3533642	-2.6510339	-0.0116849
19	C C6	3.815096	-1.7055241	-0.0066237
20	H H6	1.8530889	-2.5974939	-0.0144295
21	C C27	2.4315231	-1.6751949	-0.0081612
22	N N6	5.9515952	-0.6174647	0.0022466
23	C C32	6.7098363	0.4504069	0.0090728
24	N N16	7.4995604	1.3329112	0.0147405
25	H H13	-4.4131938	-1.6473423	-0.0183684
26	N N9	-5.9507473	0.6164259	-0.006849
27	C C59	-6.7090462	-0.451393	-0.013924
28	N N15	-7.4987847	-1.3338852	-0.0198642

Appendix-B: Supporting Tables and Figures for Chapter 2

Table B.1: Atomic Coordinates of [$\{\text{Ru}(\text{tpy})(\text{bpy})\}_2(\mu\text{-dicyd})\}^{2+}$ Complex.

		Cartesian Coordinates		
	Atom	X	Y	Z
1	Ru Ru1	0.0407913	0.006232	-6.6171967
2	N N1	-0.5449257	-1.9653655	-6.6779638
3	N N2	1.9663577	-0.1915237	-5.9574428
4	N N3	1.0272047	-0.103503	-8.4146937
5	N N4	-1.8157702	0.2006611	-7.2886817
6	N N5	-0.1197019	2.0512704	-6.6840744
7	N N6	-0.7027777	0.1151553	-4.7800522
8	C C1	0.5013037	-0.0543593	-9.6846768
9	H H11	-0.5880148	0.0626493	-9.7867496
10	C C2	1.2718095	-0.1442107	-10.8452773
11	H H22	0.7798579	-0.0964883	-11.8247836
12	C C3	2.6461777	-0.2919872	-10.7467016
13	H H20	3.2688041	-0.3645841	-11.6471396
14	C C4	3.2262108	-0.3468434	-9.4817832
15	H H26	4.3138182	-0.4643219	-9.4121273
16	C C5	2.4287242	-0.2534444	-8.3414457
17	C C6	-0.7775306	-0.2578247	-3.6254802
18	C C7	0.7799716	3.0184055	-6.328578
19	H H31	1.7539261	2.6902048	-5.9353823
20	C C8	0.5187457	4.3912917	-6.4237171
21	H H33	1.2911906	5.1054496	-6.1127428
22	C C9	-0.7023897	4.8313455	-6.9018134
23	H H34	-0.9220568	5.9029068	-6.9822026
24	C C10	-1.6598642	3.8868133	-7.276753
25	H H37	-2.6342599	4.2248086	-7.6497876
26	C C11	-1.373258	2.5320417	-7.1684191
27	C C12	-2.3449002	1.4677941	-7.5150389
28	C C13	-3.6537442	1.6129579	-7.979984
29	H H44	-4.082383	2.6066902	-8.1574594
30	C C14	-4.4231487	0.4747027	-8.2126763
31	H H46	-5.4526146	0.582617	-8.5776719
32	C C15	-3.9080419	-0.7992731	-7.9765801
33	H H47	-4.5353752	-1.6817119	-8.1509511
34	C C16	-2.5983388	-0.9291752	-7.5117602
35	C C17	0.1308096	-3.0958585	-6.3125655
36	H H51	1.1515381	-2.9762659	-5.9189407

37	C	C18	-0.4155594	-4.3838689	-6.3945413
38	H	H54	0.1882896	-5.2418515	-6.074131
39	C	C19	-1.7024645	-4.5594886	-6.868931
40	H	H55	-2.1452146	-5.5605948	-6.937287
41	C	C20	-2.4393256	-3.4368916	-7.2539761
42	H	H56	-3.4644235	-3.5647245	-7.622303
43	C	C21	-1.8723487	-2.1731093	-7.158856
44	C	C22	2.4315983	-0.2299928	-4.6656493
45	H	H61	1.6947604	-0.1480664	-3.8428383
46	C	C23	3.7814035	-0.3696779	-4.3314071
47	H	H64	4.0698634	-0.3932997	-3.2727159
48	C	C24	4.7313434	-0.4764832	-5.3330726
49	H	H65	5.7951182	-0.5872029	-5.0903881
50	C	C25	4.3109971	-0.4406173	-6.6607123
51	H	H10	5.0679004	-0.5241145	-7.4487148
52	C	C26	2.9571465	-0.3011261	-6.9612974
53	N	N7	-1.1807907	-0.682464	-2.4670564
54	C	C27	-0.5584666	-0.3113996	-1.2477387
55	C	C28	-1.0257158	-0.9458722	-0.0860811
56	H	H7	-1.8284842	-1.6890303	-0.1516853
57	C	C29	-0.4715731	-0.6366104	1.1467158
58	C	C30	0.5584666	0.3113996	1.2477387
59	C	C31	1.0257158	0.9458722	0.0860811
60	H	H14	1.8284842	1.6890303	0.1516853
61	C	C32	0.4715731	0.6366104	-1.1467158
62	N	N8	1.1807907	0.682464	2.4670564
63	C	C33	0.7775306	0.2578247	3.6254802
64	N	N9	0.7027777	-0.1151553	4.7800522
65	Ru	Ru2	-0.0407913	-0.006232	6.6171967
66	N	N10	-1.9663577	0.1915237	5.9574428
67	N	N11	0.5449257	1.9653655	6.6779638
68	N	N12	-1.0272047	0.103503	8.4146937
69	N	N13	1.8157702	-0.2006611	7.2886817
70	N	N14	0.1197019	-2.0512704	6.6840744
71	C	C34	-0.5013037	0.0543593	9.6846768
72	H	H35	0.5880148	-0.0626493	9.7867496
73	C	C35	-1.2718095	0.1442107	10.8452773
74	H	H38	-0.7798579	0.0964883	11.8247836
75	C	C36	-2.6461777	0.2919872	10.7467016
76	H	H25	-3.2688041	0.3645841	11.6471396
77	C	C37	-3.2262108	0.3468434	9.4817832
78	H	H49	-4.3138182	0.4643219	9.4121273
79	C	C38	-2.4287242	0.2534444	8.3414457

80	C	C39	1.8723487	2.1731093	7.158856
81	C	C40	2.4393256	3.4368916	7.2539761
82	H	H60	3.4644235	3.5647245	7.622303
83	C	C41	1.7024645	4.5594886	6.868931
84	H	H63	2.1452146	5.5605948	6.937287
85	C	C42	0.4155594	4.3838689	6.3945413
86	H	H67	-0.1882896	5.2418515	6.074131
87	C	C43	-0.1308096	3.0958585	6.3125655
88	H	H62	-1.1515381	2.9762659	5.9189407
89	C	C44	2.5983388	0.9291752	7.5117602
90	C	C45	3.9080419	0.7992731	7.9765801
91	H	H28	4.5353752	1.6817119	8.1509511
92	C	C46	4.4231487	-0.4747027	8.2126763
93	H	H75	5.4526146	-0.582617	8.5776719
94	C	C47	3.6537442	-1.6129579	7.979984
95	H	H78	4.082383	-2.6066902	8.1574594
96	C	C48	2.3449002	-1.4677941	7.5150389
97	C	C49	-0.7799716	-3.0184055	6.328578
98	H	H82	-1.7539261	-2.6902048	5.9353823
99	C	C50	-0.5187457	-4.3912917	6.4237171
100	H	H84	-1.2911906	-5.1054496	6.1127428
101	C	C51	0.7023897	-4.8313455	6.9018134
102	C	C52	1.6598642	-3.8868133	7.276753
103	H	H88	2.6342599	-4.2248086	7.6497876
104	C	C53	1.373258	-2.5320417	7.1684191
105	C	C54	-2.4315983	0.2299928	4.6656493
106	H	H91	-1.6947604	0.1480664	3.8428383
107	C	C55	-3.7814035	0.3696779	4.3314071
108	H	H92	-4.0698634	0.3932997	3.2727159
109	C	C56	-4.7313434	0.4764832	5.3330726
110	H	H94	-5.7951182	0.5872029	5.0903881
111	C	C57	-4.3109971	0.4406173	6.6607123
112	H	H98	-5.0679004	0.5241145	7.4487148
113	C	C58	-2.9571465	0.3011261	6.9612974
114	H	H102	0.9220568	-5.9029068	6.9822026
115	H	H1	0.8386949	1.1494538	-2.0427552
116	H	H2	-0.8386949	-1.1494538	2.0427552

Table B.2: Atomic Coordinates of $[\{\text{Ru}(\text{tpy})(\text{bpy})\}_2(\mu\text{-dicyd})]^{3+}$ Complex.

		Cartesian Coordinates		
	Atom	X	Y	Z
1	Ru Ru1	-5.3980658	-1.2054892	3.8804784
2	N N1	-6.7515813	-0.670212	2.4220723
3	N N2	-4.8702687	0.6375398	4.5968752
4	N N3	-6.8061615	-0.9665075	5.3610205
5	N N4	-6.0013046	-3.0005724	3.2648576
6	N N5	-4.2497952	-2.4225734	5.0820653
7	N N6	-3.9704569	-1.2197809	2.5218371
8	C C1	-7.8109015	-1.8316284	5.7361116
9	H H11	-7.9030734	-2.7856259	5.1952745
10	C C2	-8.7195348	-1.5657838	6.7646064
11	H H22	-9.4942618	-2.3054856	7.0058989
12	C C3	-8.6328243	-0.3715137	7.4686437
13	H H20	-9.3379444	-0.1456305	8.2796248
14	C C4	-7.6328606	0.5380493	7.1273133
15	H H26	-7.5708188	1.478736	7.6877979
16	C C5	-6.7388981	0.2432426	6.0932358
17	C C6	-3.1037469	-1.1914671	1.7179256
18	C C7	-3.3157364	-2.1000078	6.029942
19	H H31	-3.1162977	-1.0323079	6.2082152
20	C C8	-2.6063732	-3.0539844	6.7750725
21	H H33	-1.874464	-2.7156842	7.5200505
22	C C9	-2.8346967	-4.4060556	6.5672175
23	H H34	-2.2888739	-5.1635909	7.1446745
24	C C10	-3.7736417	-4.7936078	5.606873
25	H H37	-3.9586378	-5.8612476	5.4323439
26	C C11	-4.4638316	-3.8251008	4.8812492
27	C C12	-5.4629819	-4.1525805	3.8436897
28	C C13	-5.8800825	-5.4182665	3.4110526
29	H H44	-5.464206	-6.332233	3.8535922
30	C C14	-6.8388576	-5.511534	2.3983048
31	H H46	-7.1682889	-6.5020205	2.0555292
32	C C15	-7.383315	-4.3652215	1.8125242
33	H H47	-8.1320273	-4.4631771	1.0162393
34	C C16	-6.9590144	-3.1045997	2.2529593
35	C C17	-7.1259983	0.5695032	1.9773118
36	H H51	-6.6527834	1.4453929	2.4468222
37	C C18	-8.0705751	0.7753147	0.9604408
38	H H54	-8.3195735	1.8015176	0.6603053

39	C	C19	-8.6778613	-0.3106477	0.347874
40	H	H55	-9.4200172	-0.1646581	-0.4478601
41	C	C20	-8.3295454	-1.6007619	0.7583887
42	H	H56	-8.8015508	-2.4666552	0.2767495
43	C	C21	-7.3885588	-1.7761114	1.7706285
44	C	C22	-3.8481909	1.4597842	4.1773747
45	H	H61	-3.2074453	1.113712	3.3490251
46	C	C23	-3.5759364	2.7106183	4.7413235
47	H	H64	-2.742565	3.3073115	4.3491946
48	C	C24	-4.3588032	3.1829069	5.7857507
49	H	H65	-4.1597765	4.1621088	6.2401014
50	C	C25	-5.4068039	2.3887054	6.2495162
51	H	H10	-6.0218825	2.7667678	7.0750675
52	C	C26	-5.6541262	1.143098	5.6649657
53	N	N7	-2.2757583	-1.4275717	0.6789911
54	C	C27	-1.1704812	-0.6971598	0.3885618
55	C	C28	-0.4198185	-1.1082882	-0.7621974
56	H	H7	-0.763955	-1.973369	-1.3433627
57	C	C29	0.7079291	-0.435465	-1.1338176
58	H	H12	1.2714481	-0.7607188	-2.01647
59	C	C30	1.1701001	0.6940985	-0.3896004
60	C	C31	0.4195799	1.1051405	0.7613044
61	H	H14	0.7636538	1.9702502	1.3423939
62	C	C32	-0.7081293	0.4322744	1.1329474
63	H	H19	-1.2716436	0.7575463	2.0155031
64	N	N8	2.2748105	1.4252278	-0.6804417
65	C	C33	3.1028284	1.1895074	-1.7194333
66	N	N9	3.9695956	1.2182703	-2.5232651
67	Ru	Ru2	5.3980951	1.2053845	-3.8810331
68	N	N10	4.8740755	-0.6392464	-4.5960007
69	N	N11	6.7515879	0.6739774	-2.4210979
70	N	N12	6.8079067	0.9674063	-5.3601028
71	N	N13	5.9973268	3.0021775	-3.2664272
72	N	N14	4.2485435	2.4191823	-5.0846638
73	C	C34	7.810948	1.834223	-5.7357642
74	H	H35	7.9002564	2.7894679	-5.1966532
75	C	C35	8.7213159	1.5686124	-6.7628082
76	H	H38	9.4944721	2.3097669	-7.0047368
77	C	C36	8.6383018	0.3727426	-7.464579
78	H	H25	9.3449038	0.1469499	-8.2742788
79	C	C37	7.6400862	-0.5385243	-7.1226549
80	H	H49	7.5809421	-1.4804826	-7.6813165
81	C	C38	6.7441374	-0.2437896	-6.0902715

82	C	C39	7.3857267	1.7817105	-1.7699762
83	C	C40	8.3263086	1.6090698	-0.7568886
84	H	H60	8.796066	2.4763204	-0.2754751
85	C	C41	8.6771202	0.3199715	-0.3452379
86	H	H63	9.4190271	0.1761239	0.4511178
87	C	C42	8.0726249	-0.7677292	-0.957504
88	H	H67	8.3236668	-1.7932035	-0.656526
89	C	C43	7.1283156	-0.5646363	-1.9751917
90	H	H62	6.6572995	-1.4418517	-2.4444366
91	C	C44	6.9537924	3.1089661	-2.253633
92	C	C45	7.3747996	4.3708058	-1.8135064
93	H	H28	8.1224706	4.4709191	-1.0165165
94	C	C46	6.828306	5.5155578	-2.4004499
95	H	H75	7.1551003	6.5070027	-2.0578804
96	C	C47	5.870718	5.4195518	-3.4140929
97	H	H78	5.4531719	6.3323368	-3.8575331
98	C	C48	5.4568978	4.1526525	-3.8464052
99	C	C49	3.3161492	2.0939676	-6.0333104
100	H	H82	3.1192365	1.0257081	-6.2111167
101	C	C50	2.6054499	3.0459207	-6.7797673
102	H	H84	1.8751195	2.7055337	-7.5253383
103	C	C51	2.830461	4.3986273	-6.5724282
104	C	C52	3.7676194	4.7888569	-5.6114049
105	H	H88	3.9499648	5.8570342	-5.4372877
106	C	C53	4.4593397	3.8223207	-4.8845889
107	C	C54	3.8522963	-1.4622655	-4.1773682
108	H	H91	3.209411	-1.1158846	-3.3508183
109	C	C55	3.5828535	-2.7142431	-4.7401085
110	H	H92	2.7494203	-3.311424	-4.3489395
111	C	C56	4.3685179	-3.1870403	-5.7821661
112	H	H94	4.1718485	-4.1672564	-6.2353682
113	C	C57	5.4162303	-2.3920114	-6.2450964
114	H	H98	6.0335128	-2.7705164	-7.0687637
115	C	C58	5.6604835	-1.1450764	-5.6620723
116	H	H102	2.2834332	5.1546056	-7.1507952

Table B.3: Atomic Coordinates of $[\{\text{Ru}(\text{tpy})(\text{bpy})\}_2(\mu\text{-dicyd})]^{4+}$ Complex.

Cartesian Coordinates

	Atom	X	Y	Z
1	Ru Ru1	-5.3938641	-1.2124835	3.9455848

2	N N1	-6.7559831	-0.6652418	2.4909219
3	N N2	-4.9157029	0.6275161	4.7250255
4	N N3	-6.8582054	-1.0094176	5.3896934
5	N N4	-6.0159936	-3.0081329	3.3235711
6	N N5	-4.3229715	-2.4493513	5.2081732
7	N N6	-3.9460825	-1.2071244	2.6513237
8	C C1	-7.8637635	-1.891029	5.7131081
9	H H11	-7.9309898	-2.836836	5.1542429
10	C C2	-8.8092124	-1.6549707	6.7141371
11	H H22	-9.5841778	-2.4079027	6.9154174
12	C C3	-8.7597515	-0.4754714	7.4416734
13	H H20	-9.4945836	-0.2710096	8.2334657
14	C C4	-7.7581947	0.4492811	7.1500623
15	H H26	-7.7266022	1.3800469	7.7308066
16	C C5	-6.8296567	0.1817462	6.1438145
17	C C6	-3.0610187	-1.1772343	1.8774231
18	C C7	-3.4406321	-2.1364035	6.2040613
19	H H31	-3.234401	-1.0712403	6.3905404
20	C C8	-2.7993311	-3.097358	6.9991734
21	H H33	-2.1098641	-2.7670379	7.788336
22	C C9	-3.0437091	-4.4426674	6.7889999
23	H H34	-2.5539755	-5.2083451	7.4069521
24	C C10	-3.9325519	-4.8178479	5.7762123
25	H H37	-4.1323424	-5.8840713	5.6039459
26	C C11	-4.5549631	-3.8435184	5.0069774
27	C C12	-5.5225441	-4.1598794	3.9272145
28	C C13	-5.9593703	-5.4179886	3.5046496
29	H H44	-5.5769712	-6.3371531	3.968848
30	C C14	-6.9011585	-5.5019561	2.4787943
31	H H46	-7.2488429	-6.4896807	2.1416258
32	C C15	-7.4146187	-4.3511208	1.8801562
33	H H47	-8.1636333	-4.4409033	1.081755
34	C C16	-6.9676809	-3.1002611	2.313559
35	C C17	-7.1412401	0.5772301	2.071206
36	H H51	-6.6720726	1.4494161	2.5518985
37	C C18	-8.103685	0.7927011	1.0741571
38	H H54	-8.3682295	1.8226789	0.7976755
39	C C19	-8.7119921	-0.2854318	0.4565675
40	H H55	-9.4720482	-0.1341397	-0.322821
41	C C20	-8.3482509	-1.5794513	0.8435457
42	H H56	-8.8278115	-2.4404289	0.358567
43	C C21	-7.3941606	-1.7614969	1.8360063
44	C C22	-3.88882	1.4661264	4.3583155

45	H H61	-3.2155239	1.1460224	3.5485297
46	C C23	-3.6481445	2.7061171	4.9551543
47	H H64	-2.8073991	3.319524	4.6069779
48	C C24	-4.4704144	3.1499545	5.9784273
49	H H65	-4.2978801	4.1223107	6.460314
50	C C25	-5.5253129	2.3361986	6.3871281
51	H H10	-6.1735373	2.692516	7.1982376
52	C C26	-5.7369091	1.1029925	5.7695785
53	N N7	-2.156878	-1.4436777	0.8756944
54	C C27	-1.1487195	-0.7085544	0.4911776
55	C C28	-0.336845	-1.2408221	-0.6165641
56	H H7	-0.625691	-2.2098176	-1.0501937
57	C C29	0.7248209	-0.566756	-1.0870823
58	H H12	1.3231471	-0.972675	-1.9145291
59	C C30	1.1224126	0.7230116	-0.5214469
60	C C31	0.3075288	1.257561	0.5828726
61	H H14	0.5945133	2.2280698	1.0144232
62	C C32	-0.7541818	0.5835725	1.0533348
63	H H19	-1.354921	0.9916284	1.8781543
64	N N8	2.136108	1.4540381	-0.8995631
65	C C33	3.0451111	1.1847984	-1.8961569
66	N N9	3.9358177	1.2128159	-2.6636582
67	Ru Ru2	5.3933979	1.2130653	-3.9468294
68	N N10	4.9196807	-0.6292268	-4.7235845
69	N N11	6.7435513	0.6700004	-2.4794573
70	N N12	6.8692161	1.0034714	-5.3782396
71	N N13	6.0117657	3.0104755	-3.3260959
72	N N14	4.3335187	2.4460936	-5.2222072
73	C C34	7.8777012	1.8833621	-5.6973098
74	H H35	7.9400287	2.832083	-5.1428393
75	C C35	8.8318627	1.6421596	-6.6887504
76	H H38	9.6085871	2.3940425	-6.8870732
77	C C36	8.7887608	0.4589292	-7.4105315
78	H H25	9.53069	0.2502007	-8.1945133
79	C C37	7.7842983	-0.4641099	-7.1233229
80	H H49	7.7576496	-1.3978182	-7.6995824
81	C C38	6.8467991	-0.1912823	-6.1268853
82	C C39	7.3769413	1.7681338	-1.8230255
83	C C40	8.3225895	1.5888623	-0.8219724
84	H H60	8.7986817	2.4511993	-0.335974
85	C C41	8.6821217	0.2958957	-0.4274603
86	H H63	9.4354744	0.1467926	0.3588249
87	C C42	8.078325	-0.7839554	-1.0464523

88	H H67	8.3397807	-1.8131441	-0.7642108
89	C C43	7.1244795	-0.5712965	-2.0522927
90	H H62	6.6588856	-1.4448096	-2.5340726
91	C C44	6.9552704	3.1054914	-2.308678
92	C C45	7.3995671	4.3575006	-1.8760193
93	H H28	8.1420512	4.4495921	-1.0718195
94	C C46	6.8919592	5.5065612	-2.4830042
95	H H75	7.2378391	6.4952051	-2.1466668
96	C C47	5.9583834	5.4196537	-3.5161334
97	H H78	5.5805612	6.3374342	-3.9867309
98	C C48	5.5239478	4.1604085	-3.9376418
99	C C49	3.4592001	2.1302337	-6.2242349
100	H H82	3.2542761	1.0645257	-6.4091297
101	C C50	2.8245128	3.0887911	-7.0274208
102	H H84	2.1413058	2.7561143	-7.8210432
103	C C51	3.0675177	4.4347301	-6.8194982
104	C C52	3.9486092	4.8128934	-5.8010131
105	H H88	4.1474654	5.8796076	-5.6306496
106	C C53	4.5646382	3.8408568	-5.0238293
107	C C54	3.888023	-1.4648388	-4.3633587
108	H H91	3.2073122	-1.140369	-3.5615579
109	C C55	3.6512915	-2.7069579	-4.9573943
110	H H92	2.8062004	-3.3176385	-4.6150021
111	C C56	4.4828265	-3.1562512	-5.9706945
112	H H94	4.3136314	-4.1304448	-6.4500505
113	C C57	5.5426512	-2.3455846	-6.3727261
114	H H98	6.198134	-2.7062173	-7.1760441
115	C C58	5.74993	-1.110029	-5.758482
116	H H102	2.5826605	5.1986233	-7.4434943

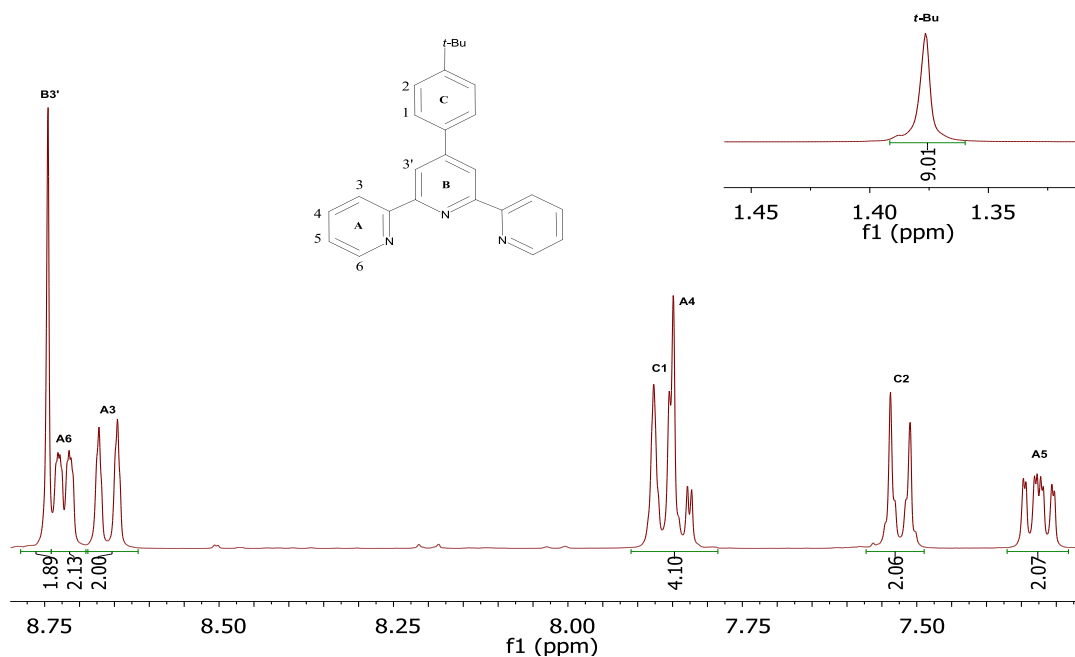


Figure B.1: ^1H NMR spectrum of 4-(*tert*-butylphenyl)-2,2':6',2''-terpyridine (ttpy) ligand in dms0-d_6

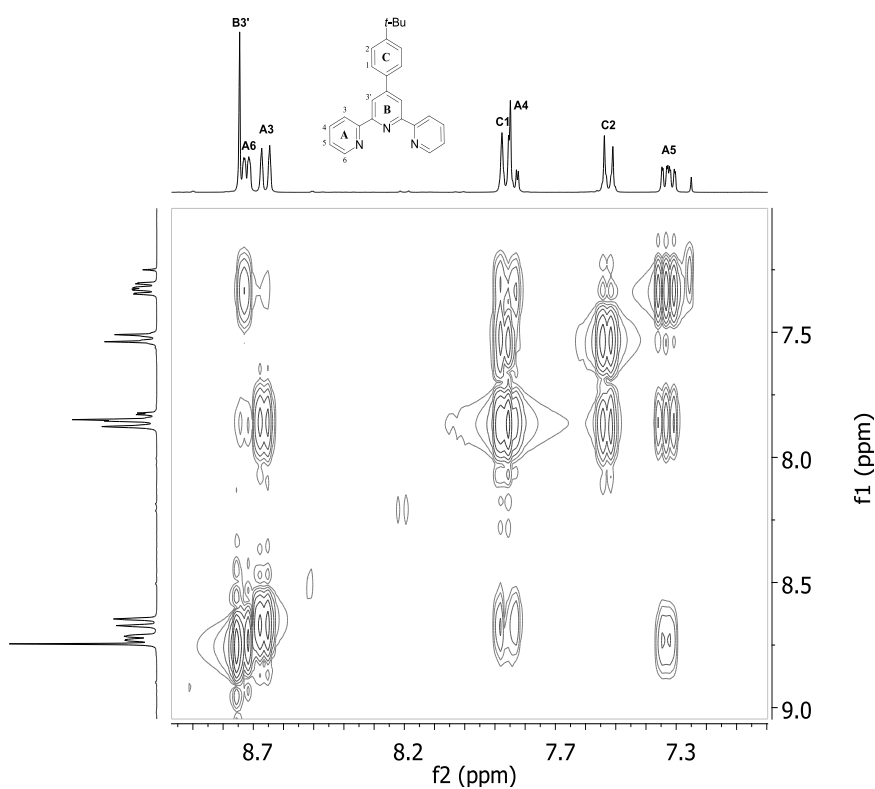


Figure B.2: ^1H - ^1H COSY spectrum of 4-(*tert*-butylphenyl)-2,2':6',2''-terpyridine (ttpy) ligand in dms0-d_6 .

Appendix-C: Supporting Tables and Figures for Chapter 3.**Table C.1: X-ray Crystallography Data of [AsPh]₂[Me₂adpc] (**5g**).****Atomic Coordinates****Cartesian Coordinates**

Atom		X	Y	Z
As	As	0.338089(15)	0.591861(13)	0.337724(5)
N1	N	0.83479(17)	1.10089(11)	0.36071(6)
N2	N	0.78943(15)	0.87745(12)	0.35270(5)
N3	N	0.98869(14)	0.55500(12)	0.50723(5)
C1	C	0.81337(16)	0.99547(14)	0.35918(6)
C2	C	0.82803(15)	0.79972(13)	0.39282(6)
C3	C	0.86996(15)	0.83916(13)	0.44249(5)
H3A	H	0.8619	0.9240	0.4506
C4	C	0.92264(16)	0.75894(13)	0.47999(5)
C5	C	0.92998(16)	0.63241(13)	0.46852(5)
C6	C	0.87853(18)	0.59078(12)	0.42027(6)
H6A	H	0.8773	0.5051	0.4132
C7	C	0.82997(16)	0.67170(14)	0.38312(6)
H7A	H	0.7974	0.6414	0.3506
C8	C	0.9742(2)	0.80703(14)	0.53144(6)
H8A	H	0.9678	0.8969	0.5316
H8B	H	1.0775	0.7819	0.5377
H8C	H	0.9109	0.7736	0.5585
C9	C	0.46133(16)	0.61808(13)	0.27914(5)
C10	C	0.57070(16)	0.70889(13)	0.28119(6)
H10A	H	0.5829	0.7585	0.3110
C11	C	0.66135(17)	0.72530(14)	0.23885(6)
H11A	H	0.7384	0.7850	0.2401
C12	C	0.64030(17)	0.65516(15)	0.19476(6)
H12A	H	0.7010	0.6688	0.1656
C13	C	0.53097(18)	0.56520(16)	0.19303(6)
H13A	H	0.5176	0.5170	0.1629
C14	C	0.44152(16)	0.54583(14)	0.23520(6)
H14A	H	0.3672	0.4838	0.2343
C15	C	0.15303(16)	0.52720(13)	0.31301(6)
C16	C	0.09113(18)	0.57480(14)	0.26770(6)
H16A	H	0.1365	0.6425	0.2510
C17	C	-0.03701(17)	0.52238(16)	0.24742(6)
H17A	H	-0.0800	0.5542	0.2166
C18	C	-0.1029(2)	0.42323(15)	0.27206(7)
H18A	H	-0.1913	0.3882	0.2581
C19	C	-0.04095(18)	0.37508(16)	0.31663(7)
H19A	H	-0.0862	0.3068	0.3330
C20	C	0.08803(18)	0.42699(14)	0.33752(6)
H20A	H	0.1311	0.3944	0.3681

C21	C	0.42668(16)	0.47533(13)	0.38379(6)
C22	C	0.54443(19)	0.40346(13)	0.36764(7)
H22A	H	0.5844	0.4140	0.3342
C23	C	0.60332(19)	0.31576(15)	0.40097(7)
H23A	H	0.6839	0.2657	0.3904
C24	C	0.54461(19)	0.30150(16)	0.44948(7)
H24A	H	0.5855	0.2416	0.4721
C25	C	0.4261(2)	0.37404(18)	0.46560(7)
H25A	H	0.3867	0.3637	0.4991
C26	C	0.36593(18)	0.46121(16)	0.43262(6)
H26A	H	0.2846	0.5106	0.4431
C27	C	0.32065(16)	0.74381(13)	0.37424(5)
C28	C	0.44044(17)	0.77847(14)	0.40577(5)
H28A	H	0.5239	0.7258	0.4100
C29	C	0.43564(19)	0.89115(14)	0.43089(6)
H29A	H	0.5167	0.9165	0.4521
C30	C	0.31181(18)	0.96682(14)	0.42492(6)
H30A	H	0.3084	1.0433	0.4425
C31	C	0.19343(18)	0.93168(15)	0.39362(6)
H31A	H	0.1096	0.9841	0.3898
C32	C	0.19724(16)	0.81960(14)	0.36785(6)
H32A	H	0.1167	0.7952	0.3462

Bond Lengths

As C15	1.9117(16)	As C21	1.9126(16)	As C27	1.9143(17)
As C9	1.9145(16)	N1 C1	1.164(2)	N2 C1	1.313(2)
N2 C2	1.385(2)	N3 N3	1.272(3)	N3 C5	1.411(2)
C2 C3	1.408(2)	C2 C7	1.416(2)	C3 C4	1.389(2)
C4 C5	1.411(2)	C4 C8	1.505(2)	C5 C6	1.407(2)
C6 C7	1.375(2)	C9 C10	1.395(2)	C9 C14	1.397(2)
C10 C11	1.388(2)	C11 C12	1.389(2)	C12 C13	1.388(2)
C13 C14	1.383(2)	C15 C20	1.395(2)	C15 C16	1.397(2)
C16 C17	1.385(2)	C17 C18	1.391(3)	C18 C19	1.383(3)
C19 C20	1.395(2)	C21 C22	1.385(2)	C21 C26	1.396(2)
C22 C23	1.390(2)	C23 C24	1.381(2)	C24 C25	1.395(3)
C25 C26	1.385(2)	C27 C32	1.391(2)	C27 C28	1.399(2)
C28 C29	1.390(2)	C29 C30	1.392(2)	C30 C31	1.387(2)
C31 C32	1.392(2)				

Torsion Angles

C2 N2 C1 N1	156.8(17)	C1 N2 C2 C3	9.9(2)	C1 N2 C2 C7	-168.10(14)
N2 C2 C3 C4	-173.11(14)	C7 C2 C3 C4	4.9(2)	C2 C3 C4 C5	-2.1(2)
C2 C3 C4 C8	176.46(14)	C3 C4 C5 C6	-2.4(2)	C8 C4 C5 C6	179.03(14)
C3 C4 C5 N3	178.02(13)	C8 C4 C5 N3	-0.5(2)	N3 N3 C5 C6	9.3(2)
N3 N3 C5 C4	-171.14(15)	C4 C5 C6 C7	4.0(2)	N3 C5 C6 C7	-176.43(14)
C5 C6 C7 C2	-1.1(2)	N2 C2 C7 C6	174.90(14)	C3 C2 C7 C6	-3.3(2)

C15 As C9 C10 152.59(11)	C21 As C9 C10 -88.80(13)	C27 As C9 C10 28.84(13)
C15 As C9 C14 -27.88(14)	C21 As C9 C14 90.73(13)	C27 As C9 C14 -151.62(12)
C14 C9 C10 C11 -0.8(2)	As C9 C10 C11 178.69(11)	C9 C10 C11 C12 2.0(2)
C10 C11 C12 C13 -1.9(2)	C11 C12 C13 C14 0.6(2)	C12 C13 C14 C9 0.6(2)
C10 C9 C14 C13 -0.4(2)	As C9 C14 C13 -179.97(12)	C21 As C15 C20 14.64(14)
C27 As C15 C20 -105.20(13)	C9 As C15 C20 134.61(12)	C21 As C15 C16 -159.87(12)
C27 As C15 C16 80.30(13)	C9 As C15 C16 -39.89(13)	C20 C15 C16 C17 0.7(2)
As C15 C16 C17 175.19(11)	C15 C16 C17 C18 -0.1(2)	C16 C17 C18 C19 -0.6(3)
C17 C18 C19 C20 0.7(3)	C18 C19 C20 C15 0.0(2)	C16 C15 C20 C19 -0.7(2)
As C15 C20 C19 -175.08(11)	C15 As C21 C22 103.75(13)	C27 As C21 C22 -132.27(12)
C9 As C21 C22 -13.94(14)	C15 As C21 C26 -73.50(14)	C27 As C21 C26 50.49(14)
C9 As C21 C26 168.81(12)	C26 C21 C22 C23 -0.2(2)	As C21 C22 C23 -177.37(12)
C21 C22 C23 C24 -0.2(2)	C22 C23 C24 C25 0.2(3)	C23 C24 C25 C26 0.2(3)
C24 C25 C26 C21 -0.6(3)	C22 C21 C26 C25 0.6(3)	As C21 C26 C25 177.78(14)
C15 As C27 C32 -21.06(14)	C21 As C27 C32 -141.69(12)	C9 As C27 C32 98.44(13)
C15 As C27 C28 161.93(11)	C21 As C27 C28 41.31(13)	C9 As C27 C28 -78.56(13)
C32 C27 C28 C29 -0.3(2)	As C27 C28 C29 176.70(11)	C27 C28 C29 C30 0.8(2)
C28 C29 C30 C31 -0.8(2)	C29 C30 C31 C32 0.2(2)	C28 C27 C32 C31 -0.3(2)
As C27 C32 C31 -177.15(11)	C30 C31 C32 C27 0.3(2)	

Table C.2: Atomic Coordinates of the Geometry Optimized Structure of $[\{\text{Ru}(\text{tpy})(\text{bpy})\}_2(\mu\text{-Me}_4\text{adpc})]^{3+}$ Complex (**7a⁺**).

Cartesian Coordinates

Atom	X	Y	Z
1 Ru Ru1	9.8894838	-0.0479591	0.470025
2 N N1	10.3072565	1.8161983	1.3984849
3 N N2	10.1725552	0.451621	-1.5728505
4 N N3	11.9297448	-0.4602352	0.1831208
5 N N4	9.7438455	-0.5390621	2.4078338
6 N N5	9.4010581	-2.1123611	0.3354381
7 C C1	12.7677784	-0.9276771	1.1283105
8 H H11	12.3344589	-1.0924646	2.1080847
9 C C2	14.1106316	-1.1894292	0.8850375
10 H H22	14.7398375	-1.5653576	1.6845272
11 C C3	14.6162063	-0.9589527	-0.3934719
12 H H20	15.6592765	-1.1508509	-0.6233174
13 C C4	13.7577505	-0.4765068	-1.3760659
14 H H26	14.1342635	-0.2934212	-2.3752333
15 C C5	12.414952	-0.2313858	-1.0715662
16 C C7	9.2583544	-2.8612999	-0.769155
17 H H31	9.4037217	-2.3447363	-1.7114053
18 C C8	8.9428639	-4.2169139	-0.7267124
19 H H33	8.8417133	-4.7762564	-1.6504835

20	C	C9	8.7652052	-4.8228171	0.5150066
21	H	H34	8.5214483	-5.8777106	0.5899837
22	C	C10	8.9080015	-4.0527402	1.6672312
23	H	H37	8.7745135	-4.5074222	2.6422281
24	C	C11	9.2256482	-2.697615	1.5608705
25	C	C12	9.399134	-1.8071941	2.7309178
26	C	C13	9.2370726	-2.1577958	4.0738479
27	H	H44	8.9621894	-3.1667689	4.3579863
28	C	C14	9.4258151	-1.1816441	5.052842
29	H	H46	9.3039687	-1.4362546	6.1004903
30	C	C15	9.7603844	0.1234066	4.6900836
31	H	H47	9.8922958	0.8817485	5.4527126
32	C	C16	9.9114286	0.431794	3.3357164
33	C	C17	10.5833036	2.9902164	0.8108252
34	H	H51	10.6135706	2.9789305	-0.2728676
35	C	C18	10.8128293	4.159082	1.5318253
36	H	H54	11.0324053	5.0822517	1.0065203
37	C	C19	10.7509182	4.1096968	2.9226159
38	H	H55	10.9246363	4.9996357	3.5189855
39	C	C20	10.4596255	2.895862	3.5416727
40	H	H56	10.4036529	2.8387109	4.6227088
41	C	C21	10.2382228	1.7578656	2.7644268
42	C	C22	9.2149427	0.9190792	-2.3969817
43	H	H61	8.2341645	1.0324114	-1.9491509
44	C	C23	9.4644517	1.2369644	-3.7273323
45	H	H64	8.6607094	1.6124708	-4.3515011
46	C	C24	10.7548491	1.0652012	-4.2287089
47	H	H65	10.9867893	1.3035254	-5.2618129
48	C	C25	11.7478616	0.5827093	-3.3813563
49	H	H10	12.7549818	0.4451137	-3.7561467
50	C	C26	11.4366057	0.2813865	-2.0511121
51	Ru	Ru2	-9.8896038	-0.0437479	-0.4654162
52	N	N10	-10.1965986	-1.4404721	1.1059085
53	N	N11	-10.0018185	-1.309302	-2.1679495
54	N	N12	-11.982531	-0.0382424	-0.2542845
55	N	N13	-9.7292448	1.2904883	-1.9516684
56	N	N14	-9.7001854	1.7666999	0.6277548
57	C	C34	-12.8332028	0.7087931	-0.9838695
58	H	H35	-12.3794934	1.3557478	-1.7253522
59	C	C35	-14.2114111	0.6698968	-0.8118022
60	H	H38	-14.849792	1.293598	-1.4281629
61	C	C36	-14.7398118	-0.1785651	0.1601252
62	H	H25	-15.8107366	-0.2375894	0.3255226

63	C	C37	-13.8684974	-0.9525281	0.9199562
64	H	H49	-14.2628377	-1.616404	1.6798475
65	C	C38	-12.4896313	-0.8708205	0.7005278
66	C	C39	-9.8948192	-0.6244555	-3.3485792
67	C	C40	-9.9401287	-1.2949014	-4.5720858
68	H	H60	-9.8587591	-0.7427567	-5.5014069
69	C	C41	-10.0901759	-2.679876	-4.5959174
70	H	H63	-10.1279442	-3.2093622	-5.5424824
71	C	C42	-10.1884554	-3.3679603	-3.3889357
72	H	H67	-10.3017251	-4.4461962	-3.3586649
73	C	C43	-10.1388936	-2.6437021	-2.2007204
74	H	H62	-10.2079457	-3.1355719	-1.2370183
75	C	C44	-9.7273787	0.8414546	-3.2285266
76	C	C45	-9.5701106	1.7504208	-4.2782191
77	H	H28	-9.5662741	1.4164994	-5.309088
78	C	C46	-9.4092086	3.104131	-3.9810262
79	H	H75	-9.2866994	3.8225895	-4.7848169
80	C	C47	-9.3979014	3.5373057	-2.6547312
81	H	H78	-9.2609137	4.5882881	-2.4283089
82	C	C48	-9.5573351	2.5953919	-1.6350194
83	C	C49	-9.6970374	1.9352443	1.9592481
84	H	H82	-9.8055171	1.0316585	2.548529
85	C	C50	-9.5626201	3.1832004	2.5619886
86	H	H84	-9.5694837	3.2631523	3.6436466
87	C	C51	-9.4233167	4.3064662	1.7496447
88	C	C52	-9.4188729	4.1407822	0.3662902
89	H	H88	-9.3109795	5.0021589	-0.2828235
90	C	C53	-9.5565827	2.863318	-0.1792812
91	C	C54	-9.2210102	-2.1089382	1.7511719
92	H	H91	-8.2124707	-1.8908569	1.4193394
93	C	C55	-9.4853929	-3.0169998	2.7700532
94	H	H92	-8.6652908	-3.5322045	3.2585443
95	C	C56	-10.8110078	-3.2445739	3.1397585
96	H	H94	-11.0554286	-3.9467997	3.9303929
97	C	C57	-11.8228279	-2.5549473	2.4783641
98	H	H98	-12.8568866	-2.7204711	2.7558451
99	C	C58	-11.4947146	-1.6528569	1.4605798
100	H	H102	-9.3200723	5.296622	2.1817564
101	C	C28	4.3722873	1.0514346	0.8960441
102	C	C29	3.8909666	0.057948	-0.0363468
103	C	C30	2.5321019	-0.0666061	-0.1999616
104	C	C31	1.5895799	0.7379824	0.50647
105	N	N7	0.2326397	0.6358433	0.3691323

106	N N8	-0.1740888	-0.2566006	-0.4840802
107	C C60	-1.5300492	-0.3744211	-0.6126623
108	C C61	-1.9954791	-1.3460658	-1.5610549
109	C C62	-2.4804015	0.3918532	0.1252469
110	H H8	-2.0878204	1.1160233	0.8303652
111	C C63	-3.8385815	0.24295	-0.0267175
112	C C64	-4.3086675	-0.73687	-0.9787063
113	C C65	-3.3538057	-1.497317	-1.7152157
114	C C6	3.4249247	1.8540899	1.5970737
115	C C27	2.0651255	1.7266535	1.4317175
116	N N6	5.669157	1.3070313	1.177066
117	C C32	6.7635082	0.787914	0.7752333
118	N N16	7.8667818	0.4487987	0.5102029
119	H H13	-3.7501731	-2.2211025	-2.420181
120	N N9	-5.6027202	-1.0169707	-1.2479842
121	C C59	-6.7084774	-0.5590923	-0.8075727
122	N N15	-7.8199556	-0.2796965	-0.5071256
123	H H1	2.1322302	-0.8003589	-0.8908263
124	H H3	3.8282731	2.5895225	2.2858626
125	C C33	-1.0227919	-2.1725456	-2.3602917
126	H H6	-0.3630768	-1.5362179	-2.9594359
127	H H7	-1.5530862	-2.8530786	-3.0324916
128	H H9	-0.3768145	-2.765572	-1.7043182
129	C C66	1.101276	2.5963362	2.1948659
130	H H2	1.6380305	3.2854914	2.8529144
131	H H12	0.4218218	1.9918095	2.8049753
132	H H14	0.4750796	3.1825003	1.5141187
133	C C67	4.8419299	-0.8178234	-0.8107227
134	H H4	5.5151673	-0.2274673	-1.4447628
135	H H15	4.2880123	-1.5011667	-1.4606435
136	H H16	5.4744946	-1.4214139	-0.148697
137	C C68	-4.8015886	1.0789453	0.7761784
138	H H5	-4.2573745	1.75808	1.4385637
139	H H17	-5.4600083	0.4608027	1.3988449
140	H H18	-5.4498345	1.6857631	0.1321266

Table C.3: Atomic Coordinates of the Geometry Optimized structure of $[\{\text{Ru}(\text{tpy})(\text{bpy})\}_2(\mu\text{-adpc})]^{3+}$ Complex (**7c⁺**).

Cartesian Coordinates

	Atom	X	Y	Z
1	Ru Ru1	-9.620271	0.1598121	-0.2352332
2	N N1	-10.1181952	-0.4611816	-2.2058902
3	N N2	-9.4582586	2.2585243	-0.4886825
4	N N3	-11.5862214	0.8137896	0.1362849
5	N N4	-9.8929926	-1.8094344	0.0353727
6	N N5	-9.2296044	-0.0299776	1.847192
7	C C1	-12.6265157	0.0172842	0.4483237
8	H H11	-12.4159167	-1.04458	0.5004975
9	C C2	-13.9045938	0.5039312	0.6941498
10	H H22	-14.7047156	-0.1851374	0.9418337
11	C C3	-14.1242443	1.8781844	0.6135481
12	H H20	-15.108122	2.2971424	0.7981381
13	C C4	-13.0561301	2.7089824	0.2901835
14	H H26	-13.2089867	3.7793188	0.2231783
15	C C5	-11.7915468	2.1604858	0.0530641
16	C C7	-8.9022305	0.9335925	2.7224499
17	H H31	-8.824669	1.9354835	2.315056
18	C C8	-8.6710457	0.6806279	4.0720982
19	H H33	-8.4117085	1.4972149	4.7372179
20	C C9	-8.7806916	-0.6283991	4.5353922
21	H H34	-8.6101426	-0.8647893	5.5807926
22	C C10	-9.1147706	-1.6362618	3.6336376
23	H H37	-9.2049942	-2.6608798	3.9757294
24	C C11	-9.3346133	-1.3207703	2.2917098
25	C C12	-9.690921	-2.3286287	1.267965
26	C C13	-9.8250433	-3.705216	1.4679164
27	H H44	-9.669965	-4.1447108	2.446144
28	C C14	-10.1564264	-4.5150822	0.3810474
29	H H46	-10.2639939	-5.5860488	0.5180035
30	C C15	-10.3420595	-3.9549295	-0.883371
31	H H47	-10.5865437	-4.5889121	-1.7274627
32	C C16	-10.1974592	-2.5738438	-1.0390691
33	C C17	-10.209756	0.2899685	-3.3142511
34	H H51	-10.0205396	1.3496053	-3.1848757
35	C C18	-10.5232707	-0.2414791	-4.5625599
36	H H54	-10.5843546	0.4113236	-5.426512
37	C C19	-10.7507093	-1.6115228	-4.6676687

38	H H55	-10.9984084	-2.062784	-5.6230595
39	C C20	-10.6531834	-2.400508	-3.5234909
40	H H56	-10.8235035	-3.4691288	-3.5869391
41	C C21	-10.3334169	-1.8099823	-2.3000033
42	C C22	-8.3279375	2.9124628	-0.8194135
43	H H61	-7.4552158	2.2848196	-0.9589697
44	C C23	-8.2815173	4.29313	-0.9749396
45	H H64	-7.347292	4.7742411	-1.2437506
46	C C24	-9.4501016	5.0298208	-0.7808745
47	H H65	-9.4529342	6.1092353	-0.893804
48	C C25	-10.6209124	4.3589983	-0.4399694
49	H H10	-11.5357632	4.9187407	-0.286536
50	C C26	-10.6061961	2.9672088	-0.2993909
51	Ru Ru2	9.6200565	-0.1660667	0.2738277
52	N N10	9.487392	-2.13626	1.0454025
53	N N11	10.2382053	0.9169746	1.994702
54	N N12	11.5631403	-0.9040844	-0.0415723
55	N N13	9.8588006	1.6730517	-0.4915069
56	N N14	9.0885547	-0.492536	-1.7603055
57	C C34	12.5766239	-0.2145234	-0.5990253
58	H H35	12.3472167	0.7974687	-0.911485
59	C C35	13.8478304	-0.7479053	-0.77291
60	H H38	14.627128	-0.1458618	-1.2274779
61	C C36	14.0880103	-2.0559171	-0.3542406
62	H H25	15.0675501	-2.5076886	-0.472549
63	C C37	13.0463962	-2.7765063	0.2212974
64	H H49	13.2156393	-3.7936001	0.5534194
65	C C38	11.7876497	-2.1853324	0.3709076
66	C C39	10.4441545	2.2466134	1.7390496
67	C C40	10.8381968	3.1185458	2.7548918
68	H H60	10.9988398	4.1692025	2.542125
69	C C41	11.0230985	2.6348144	4.0483026
70	H H63	11.3294737	3.306155	4.8440745
71	C C42	10.8071401	1.2817981	4.2989062
72	H H67	10.9357671	0.8615341	5.2903992
73	C C43	10.4151615	0.4611221	3.2443237
74	H H62	10.230802	-0.5969645	3.3916827
75	C C44	10.2170815	2.6775206	0.3408943
76	C C45	10.3291448	3.9781525	-0.1572374
77	H H28	10.6157812	4.7998318	0.4883776
78	C C46	10.055242	4.2112826	-1.5054433
79	H H75	10.1368227	5.2159979	-1.9068374
80	C C47	9.6666243	3.1598028	-2.3364404

81	H H78	9.4391798	3.3461182	-3.3793476
82	C C48	9.5678556	1.8743804	-1.7973215
83	C C49	8.7181704	-1.6411984	-2.3474764
84	H H82	8.6777556	-2.5107374	-1.7007332
85	C C50	8.4018987	-1.7292251	-3.7006824
86	H H84	8.1119178	-2.6840651	-4.1256533
87	C C51	8.4699406	-0.5761118	-4.4793333
88	C C52	8.8488181	0.6219603	-3.8776119
89	H H88	8.9072763	1.5293997	-4.4677812
90	C C53	9.1547198	0.6474413	-2.5158623
91	C C54	8.382586	-2.6842511	1.5878551
92	H H91	7.5118627	-2.0390005	1.6158125
93	C C55	8.3579183	-3.9840185	2.0809179
94	H H92	7.4440817	-4.3800149	2.5105821
95	C C56	9.521143	-4.7506087	2.0106081
96	H H94	9.540405	-5.7690557	2.385295
97	C C57	10.6654609	-4.1888511	1.4521483
98	H H98	11.5763499	-4.7725067	1.3933603
99	C C58	10.6298851	-2.8750654	0.9738259
100	H H102	8.2339111	-0.6048316	-5.5382307
101	C C28	-4.2448017	-0.9619568	-1.1733824
102	C C29	-3.8404415	0.0202864	-0.2117027
103	C C30	-2.514617	0.2439535	0.0553136
104	C C31	-1.5040739	-0.5036708	-0.6231231
105	N N7	-0.1533001	-0.3639248	-0.4393444
106	N N8	0.1907119	0.5434719	0.4209268
107	C C60	1.5413071	0.677559	0.6104117
108	C C61	1.9430577	1.6719224	1.5449502
109	C C62	2.5503768	-0.0918896	-0.0455883
110	H H8	2.23805	-0.8464568	-0.7584618
111	C C63	3.8759961	0.1252751	0.2273396
112	C C64	4.2818014	1.1240168	1.1714481
113	C C65	3.2694502	1.8925733	1.8187801
114	C C6	-3.2308459	-1.7082857	-1.8437241
115	C C27	-1.9044432	-1.4831595	-1.5737753
116	N N6	-5.5312182	-1.2314536	-1.4958268
117	C C32	-6.5759966	-0.6699247	-1.0068253
118	N N16	-7.6240725	-0.2392065	-0.6703754
119	H H13	3.58359	2.6481171	2.5310945
120	N N9	5.5683248	1.3891348	1.4977896
121	C C59	6.6078957	0.7982087	1.0314229
122	N N15	7.65193	0.3412054	0.7190667
123	H H1	-2.2034852	0.9866283	0.7811028

124	H H3	-3.5437943	-2.4513122	-2.5696094
125	H H19	-4.6090906	0.58771	0.3076489
126	H H21	-1.1244734	-2.0437917	-2.0791278
127	H H23	1.1642668	2.2485437	2.0338557
128	H H24	4.6437063	-0.4603105	-0.2730419

Table C.4: Atomic Coordinates of the Geometry Optimized Structure of $[\{\text{Ru}(\text{tpy})(\text{bpy})\}_2(\mu\text{-Cl}_4\text{adpc})]^{3+}$ Complex ($7\mathbf{e}^+$).

Cartesian Coordinates

	Atom	X	Y	Z
1	Ru Ru1	9.8450737	-0.270261	0.6785175
2	N N1	9.9365649	1.5757679	1.7309766
3	N N2	9.752188	0.4037216	-1.3301177
4	N N3	11.8777659	-0.1462776	0.1515219
5	N N4	10.0627264	-0.9095609	2.5687076
6	N N5	9.8412931	-2.3788644	0.4036694
7	C C1	12.9129951	-0.4334017	0.9638963
8	H H11	12.6583189	-0.745234	1.9702193
9	C C2	14.2393829	-0.3407514	0.5599097
10	H H22	15.0330007	-0.5851363	1.257634
11	C C3	14.5146569	0.0677394	-0.7441011
12	H H20	15.5370995	0.1517675	-1.0979562
13	C C4	13.4517652	0.369322	-1.5894097
14	H H26	13.6478903	0.6892063	-2.6056095
15	C C5	12.1370713	0.2588785	-1.1254548
16	C C7	9.724629	-3.0673437	-0.7425296
17	H H31	9.6188282	-2.4738107	-1.6434356
18	C C8	9.7314183	-4.4589789	-0.7914089
19	H H33	9.6339541	-4.9650833	-1.7457102
20	C C9	9.8633905	-5.1691813	0.3992364
21	H H34	9.8754477	-6.2543965	0.4015605
22	C C10	9.9791863	-4.4637277	1.5951803
23	H H37	10.0819543	-4.9995402	2.5318727
24	C C11	9.9635347	-3.0682779	1.5808017
25	C C12	10.0721618	-2.2418491	2.8045329
26	C C13	10.1726466	-2.7084089	4.1179005
27	H H44	10.1835976	-3.7701684	4.3342365
28	C C14	10.2508583	-1.7823056	5.1586038
29	H H46	10.3267891	-2.1282146	6.1842527
30	C C15	10.2234332	-0.4138732	4.8875676

31	H H47	10.2723947	0.3013925	5.7002369
32	C C16	10.1231016	0.009599	3.5596717
33	C C17	9.8643386	2.8192459	1.2316999
34	H H51	9.7534225	2.8908575	0.1555923
35	C C18	9.9228436	3.9575581	2.0315325
36	H H54	9.8602903	4.9400283	1.5763754
37	C C19	10.0623234	3.8006749	3.4085564
38	H H55	10.1143981	4.6638453	4.0642997
39	C C20	10.1334748	2.5131683	3.9365838
40	H H56	10.2410549	2.3707134	5.0057002
41	C C21	10.0656308	1.410283	3.083802
42	C C22	8.6185839	0.6677492	-2.0081502
43	H H61	7.6987747	0.5165988	-1.4550425
44	C C23	8.622762	1.1032827	-3.3289827
45	H H64	7.6827723	1.3027608	-3.8320878
46	C C24	9.8462273	1.2737343	-3.9763629
47	H H65	9.8892105	1.6121978	-5.006654
48	C C25	11.0202367	1.0028859	-3.2792641
49	H H10	11.9780025	1.1323793	-3.768783
50	C C26	10.9531332	0.5673752	-1.9519011
51	Ru Ru2	-9.847142	0.2270315	-0.7163057
52	N N10	-9.6761639	-1.1736781	0.8716165
53	N N11	-10.1338603	-1.0495028	-2.3940865
54	N N12	-11.846603	-0.0186528	-0.1125776
55	N N13	-10.1349136	1.5667018	-2.1821812
56	N N14	-9.6628874	2.0543872	0.3556211
57	C C34	-12.9074997	0.6011895	-0.664037
58	H H35	-12.6903919	1.2915481	-1.4703507
59	C C35	-14.2137556	0.3845791	-0.2428905
60	H H38	-15.0296458	0.9120514	-0.7251127
61	C C36	-14.440405	-0.5154533	0.7970881
62	H H25	-15.4460988	-0.7145477	1.1528739
63	C C37	-13.35049	-1.1584139	1.375161
64	H H49	-13.5083564	-1.8612108	2.184133
65	C C38	-12.057637	-0.8972396	0.9100107
66	C C39	-10.3346222	-0.35974	-3.5592151
67	C C40	-10.5271844	-1.0339845	-4.766128
68	H H60	-10.6901542	-0.4786148	-5.682734
69	C C41	-10.5073973	-2.4271283	-4.7900405
70	H H63	-10.6563419	-2.9597069	-5.7238894
71	C C42	-10.2920655	-3.1187843	-3.6004052
72	H H67	-10.2632653	-4.2026359	-3.5721897
73	C C43	-10.1095231	-2.3906182	-2.4275803

74	H H62	-9.9325209	-2.8838452	-1.4783942
75	C C44	-10.3245639	1.1164052	-3.4439181
76	C C45	-10.4804941	2.0335395	-4.4866824
77	H H28	-10.6333946	1.6992723	-5.5059646
78	C C46	-10.4275217	3.3976325	-4.1986895
79	H H75	-10.5462112	4.1229457	-4.9969056
80	C C47	-10.2124675	3.8338103	-2.890868
81	H H78	-10.1588404	4.8943755	-2.6746527
82	C C48	-10.0602055	2.8832436	-1.878025
83	C C49	-9.4161043	2.2281267	1.6631365
84	H H82	-9.3042463	1.3215717	2.2471619
85	C C50	-9.3054796	3.4864217	2.2488566
86	H H84	-9.1052314	3.5709383	3.3114517
87	C C51	-9.4565815	4.6137456	1.4448627
88	C C52	-9.7087565	4.4433147	0.0851974
89	H H88	-9.8278542	5.3085516	-0.556675
90	C C53	-9.8067647	3.1557999	-0.4448653
91	C C54	-8.5202397	-1.698167	1.3237343
92	H H91	-7.6238442	-1.3678533	0.8117984
93	C C55	-8.4723418	-2.5988336	2.3820623
94	H H92	-7.5160851	-2.9917747	2.7101547
95	C C56	-9.6651817	-2.9745276	2.9993831
96	H H94	-9.6668608	-3.6750083	3.828399
97	C C57	-10.8617	-2.4343979	2.5371882
98	H H98	-11.7957089	-2.7146897	3.009099
99	C C58	-10.8472226	-1.5319115	1.4684731
100	H H102	-9.3794274	5.6112462	1.865424
101	C C28	4.2632236	-0.2116319	1.4524344
102	C C29	3.808666	-0.266273	0.0855909
103	C C30	2.4794351	-0.1922272	-0.2310101
104	C C31	1.4793091	-0.0668472	0.7764786
105	N N7	0.1407731	0.0163459	0.523894
106	N N8	-0.1793211	0.0083866	-0.7312949
107	C C60	-1.5188657	0.0746852	-0.9833547
108	C C61	-1.9536366	0.0927912	-2.3460972
109	C C62	-2.5230865	0.124813	0.026821
110	H H8	-2.1952545	0.1151446	1.0598386
111	C C63	-3.8532945	0.1823262	-0.2886236
112	C C64	-4.3040988	0.2004408	-1.6579508
113	C C65	-3.2876067	0.1568125	-2.660163
114	C C6	3.2498507	-0.1029056	2.4530065
115	C C27	1.9164877	-0.0318258	2.1380524
116	N N6	5.5248799	-0.2471309	1.9010024

117	C	C32	6.6611544	-0.2852065	1.3092631
118	N	N16	7.7922519	-0.2942455	0.9717853
119	H	H13	-3.6129009	0.1701332	-3.6935881
120	N	N9	-5.5654548	0.2500459	-2.1073601
121	C	C59	-6.6964048	0.262981	-1.5023077
122	N	N15	-7.823642	0.2563125	-1.1540479
123	Cl	Cl2	-5.0238708	0.2441754	1.0186435
124	Cl	Cl1	-0.7874532	0.0309394	-3.6368845
125	H	H1	2.1496123	-0.2299106	-1.2627108
126	H	H3	3.5771882	-0.0681787	3.4852523
127	Cl	Cl4	4.9712388	-0.4511707	-1.215814
128	Cl	Cl3	0.7541267	0.1147921	3.4256488

Table C.5: Atomic Coordinates of the Geometry Optimized Structure of $[\{\text{Ru}(\text{tpy})(\text{bpy})\}_2(\mu\text{-meta-adpc})]^{3+}$ Complex (**7f⁺**).

Cartesian Coordinates

	Atom	X	Y	Z
1	Ru Ru1	9.697135	-0.252374	0.5471999
2	N N1	9.7295467	1.4394313	-0.7391231
3	N N2	10.0022429	-1.8327408	-0.8436836
4	N N3	11.7973411	-0.4099689	0.4858539
5	N N4	9.5479708	1.2456134	1.8707534
6	N N5	9.5939073	-1.3300193	2.3747155
7	C C1	12.6518237	0.3460572	1.2012349
8	H H11	12.2000104	1.0845643	1.8530074
9	C C2	14.0318994	0.2025269	1.1267548
10	H H22	14.6737192	0.839367	1.7258362
11	C C3	14.5574246	-0.7684579	0.2754798
12	H H20	15.6296296	-0.9122367	0.1891047
13	C C4	13.681821	-1.5560231	-0.4652964
14	H H26	14.0742377	-2.316128	-1.1300163
15	C C5	12.3013101	-1.3646805	-0.3481666
16	C C7	9.6176956	-2.6591334	2.5557183
17	H H31	9.7185916	-3.255747	1.6561787
18	C C8	9.5164639	-3.2514116	3.8120839
19	H H33	9.5419918	-4.3319006	3.9023123
20	C C9	9.3825629	-2.4301992	4.9292112
21	H H34	9.3025375	-2.8538028	5.9251397
22	C C10	9.350528	-1.0486874	4.7500716
23	H H37	9.2435917	-0.3931494	5.6066047

24	C	C11	9.4549448	-0.5144037	3.4651822
25	C	C12	9.4199201	0.9382844	3.1826805
26	C	C13	9.2673769	1.9644753	4.1188203
27	H	H44	9.1640064	1.7461157	5.175259
28	C	C14	9.2415225	3.2862229	3.6730327
29	H	H46	9.1243912	4.0946485	4.3871825
30	C	C15	9.3579043	3.5731732	2.312377
31	H	H47	9.3254399	4.6004987	1.969164
32	C	C16	9.5075763	2.5174014	1.4094618
33	C	C17	9.8354969	1.4614941	-2.0769837
34	H	H51	9.9057813	0.4939113	-2.5612614
35	C	C18	9.8562106	2.6434779	-2.8127217
36	H	H54	9.947246	2.6046499	-3.8928453
37	C	C19	9.7612515	3.855856	-2.1331256
38	H	H55	9.7782392	4.7979451	-2.6716428
39	C	C20	9.6444864	3.8431438	-0.7448021
40	H	H56	9.5692787	4.7768566	-0.199126
41	C	C21	9.6288541	2.6253525	-0.0620209
42	C	C22	9.0235811	-2.5122386	-1.4726998
43	H	H61	8.0132993	-2.2061365	-1.2269557
44	C	C23	9.2861476	-3.5375333	-2.3741987
45	H	H64	8.4631302	-4.0553601	-2.8549125
46	C	C24	10.6131046	-3.8765676	-2.6378406
47	H	H65	10.8563292	-4.671521	-3.3355825
48	C	C25	11.6281963	-3.1797364	-1.9888667
49	H	H10	12.6634362	-3.4339928	-2.1819326
50	C	C26	11.3018537	-2.1579029	-1.0908808
51	Ru	Ru2	-9.6927918	0.3700943	-0.4870643
52	N	N10	-10.0013034	1.954841	0.8978434
53	N	N11	-9.7342671	-1.3167139	0.8056765
54	N	N12	-11.7929412	0.5319408	-0.4365331
55	N	N13	-9.5407506	-1.1332805	-1.804157
56	N	N14	-9.5797879	1.4405365	-2.3182212
57	C	C34	-12.6455633	-0.2238676	-1.1543391
58	H	H35	-12.1923051	-0.9652216	-1.8018301
59	C	C35	-14.0256596	-0.0767301	-1.0874838
60	H	H38	-14.6658945	-0.7136959	-1.6881292
61	C	C36	-14.5532352	0.8979504	-0.2417497
62	H	H25	-15.6255056	1.0447762	-0.1615483
63	C	C37	-13.6795623	1.685376	0.5014516
64	H	H49	-14.0735859	2.4484251	1.1618246
65	C	C38	-12.2989443	1.4901763	0.3922473
66	C	C39	-9.6328212	-2.5053889	0.1335342

67	C	C40	-9.6536702	-3.7205461	0.8208486
68	H	H60	-9.5777882	-4.6564868	0.2790898
69	C	C41	-9.7766099	-3.7277816	2.2086803
70	H	H63	-9.7977352	-4.667795	2.7506777
71	C	C42	-9.8723799	-2.512654	2.8832336
72	H	H67	-9.9681678	-2.4695332	3.962786
73	C	C43	-9.8462087	-1.3334976	2.143098
74	H	H62	-9.9167263	-0.3639373	2.6233822
75	C	C44	-9.504947	-2.4033377	-1.337785
76	C	C45	-9.3535633	-3.4628545	-2.2360183
77	H	H28	-9.3246738	-4.4889184	-1.8887256
78	C	C46	-9.2306902	-3.1813523	-3.5972326
79	H	H75	-9.1120549	-3.9927621	-4.3077449
80	C	C47	-9.25187	-1.8612719	-4.0482353
81	H	H78	-9.1433815	-1.6471748	-5.1050391
82	C	C48	-9.4064773	-0.8312057	-3.1167179
83	C	C49	-9.6005425	2.7689744	-2.5043999
84	H	H82	-9.7039956	3.3690825	-1.6074577
85	C	C50	-9.4931953	3.3562608	-3.762603
86	H	H84	-9.5164881	4.4364391	-3.8570565
87	C	C51	-9.3561532	2.5305157	-4.8760197
88	C	C52	-9.3271733	1.1496346	-4.6914397
89	H	H88	-9.2179639	0.4906276	-5.5450221
90	C	C53	-9.4377148	0.6204597	-3.4049521
91	C	C54	-9.0243962	2.6336777	1.5302697
92	H	H91	-8.0135555	2.3252573	1.2897886
93	C	C55	-9.2893472	3.6610123	2.4287549
94	H	H92	-8.4676622	4.1781373	2.9124958
95	C	C56	-10.6169039	4.0028292	2.6856136
96	H	H94	-10.8619646	4.7993171	3.3809628
97	C	C57	-11.6301957	3.306723	2.0330516
98	H	H98	-12.6658695	3.5629992	2.2210629
99	C	C58	-11.3014951	2.282862	1.1382358
100	H	H102	-9.2713911	2.9501393	-5.8732432
101	C	C28	4.3430264	0.9889319	-0.9055737
102	C	C29	4.174489	0.0110887	0.1096865
103	C	C30	2.8601486	-0.3518378	0.4807143
104	C	C31	1.7608606	0.2360559	-0.1370534
105	N	N7	0.4939741	-0.211294	0.318902
106	N	N8	-0.4899913	0.3272051	-0.2562013
107	C	C60	-1.7567713	-0.120144	0.2000683
108	C	C61	-1.9387709	-1.0924497	1.2090744
109	C	C62	-2.8563015	0.4678487	-0.4172438

110	H H8	-2.7047734	1.2129879	-1.1902395
111	C C63	-4.1704697	0.1050272	-0.0455647
112	C C64	-4.3386167	-0.8728499	0.969693
113	C C65	-3.2330076	-1.4560408	1.5801895
114	C C6	3.2376375	1.5718795	-1.5167068
115	C C27	1.9432516	1.2082071	-1.1461511
116	H H13	-3.3801142	-2.2024135	2.3557233
117	H H1	2.7083695	-1.0969426	1.2536905
118	H H3	3.3850042	2.3181531	-2.2922843
119	H H21	1.0725466	1.6525602	-1.6133846
120	H H23	-1.0678996	-1.5368672	1.6759355
121	H H9	5.3493329	1.2757465	-1.2003301
122	N N6	5.2131412	-0.611114	0.7569352
123	C C32	6.4537432	-0.3998516	0.5426849
124	N N16	7.6323925	-0.3268031	0.4392176
125	H H19	-5.3447961	-1.1595714	1.2649532
126	N N9	-5.209599	0.7274584	-0.6920609
127	C C33	-6.4498798	0.5155745	-0.4767325
128	N N15	-7.628172	0.4409176	-0.3701041

Table C.6: Atomic Coordinates of the Geometry Optimized Structure of *meta*-adpc²⁻ (**5e**).

Cartesian Coordinates

	Atom	X	Y	Z
1	C C28	4.390513	-1.1469215	0.1512876
2	C C29	3.9462276	0.2044129	0.0285095
3	C C30	2.5424533	0.4074492	-0.0013243
4	H H4	2.1597412	1.4180672	-0.0902956
5	C C31	1.6439358	-0.6608731	0.0862581
6	N N7	0.2224405	-0.544043	0.0740988
7	N N8	-0.224044	0.6312301	-0.0327168
8	C C60	-1.6450339	0.7512689	-0.0341881
9	C C61	-2.5468393	-0.3118129	0.0797576
10	H H3	-2.1686018	-1.3237418	0.1742399
11	C C62	-2.1090886	2.0737525	-0.1583708
12	H H8	-1.3818214	2.8756472	-0.241453
13	C C63	-3.4856849	2.302349	-0.16546
14	H H7	-3.863402	3.3212088	-0.2591924
15	C C64	-4.3902543	1.2508252	-0.0517686
16	C C65	-3.9499535	-0.101145	0.0780941

17	H	H5	3.8699634	-3.2220423	0.3292013
18	C	C6	3.4892745	-2.2041679	0.2355981
19	H	H6	1.3866904	-2.788256	0.2708184
20	C	C27	2.1117148	-1.9825278	0.2047001
21	H	H12	-5.4613832	1.4413181	-0.057247
22	H	H15	5.4621389	-1.3321621	0.1804685
23	N	N1	4.7745163	1.2939277	-0.0581228
24	N	N2	-4.7809875	-1.1851761	0.1991342
25	C	C1	6.072492	1.1332457	-0.0240798
26	C	C2	-6.0787513	-1.0192886	0.2008505
27	N	N3	-7.2636558	-0.984509	0.2149989
28	N	N4	7.2574381	1.100857	-0.0034881

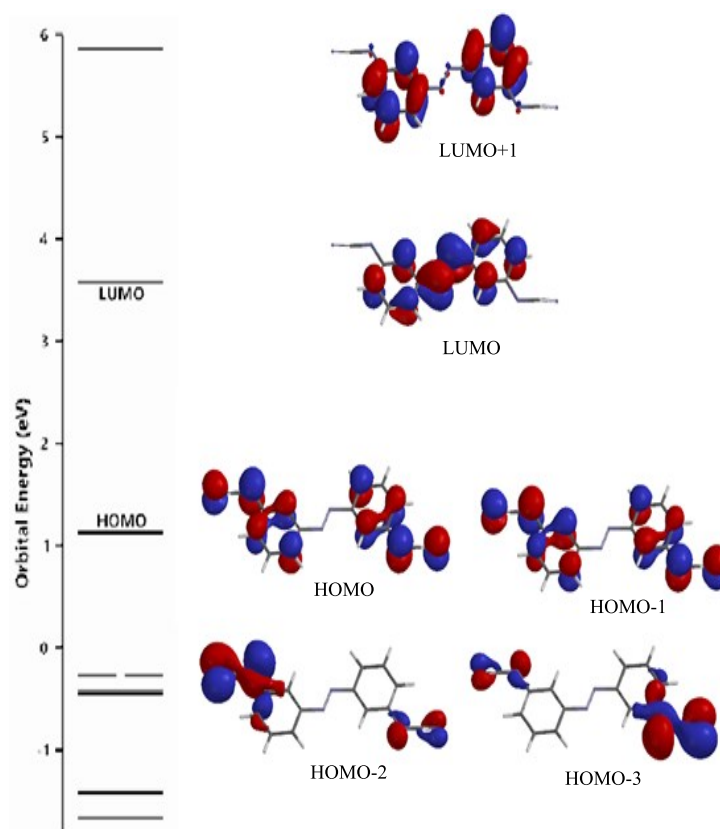


Figure C.1: DFT calculation of orbital energies and selected frontier molecular orbitals of free *meta*-adpc²⁻ dianion.

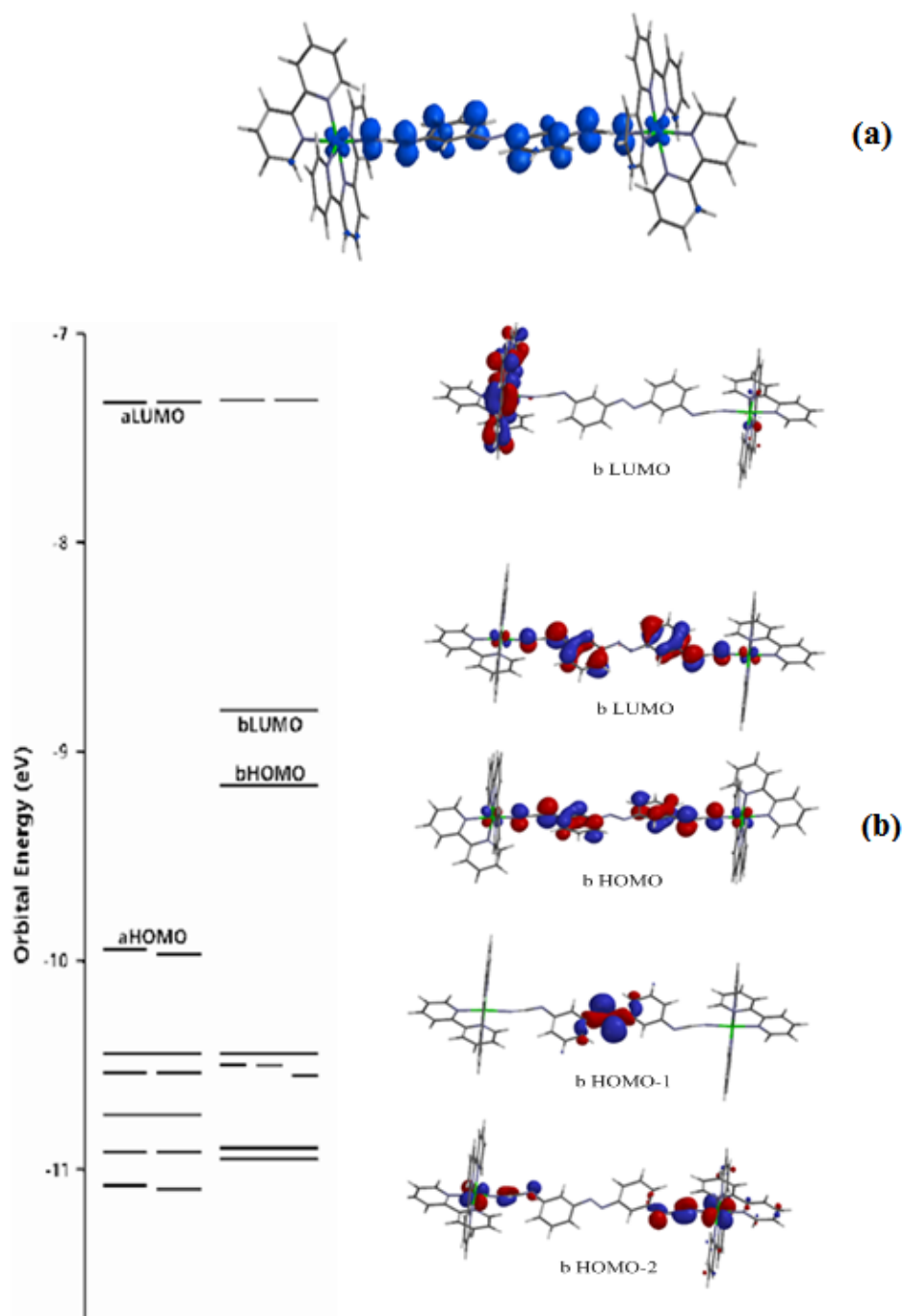


Figure C.2: DFT calculation of (a) spin density distribution and (b) orbital energies and selected β -molecular orbitals of $[\{\text{Ru}(\text{tpy})(\text{bpy})\}_2(\mu\text{-meta-adpc})]^{3+}$ ($7\mathbf{a}^+$).

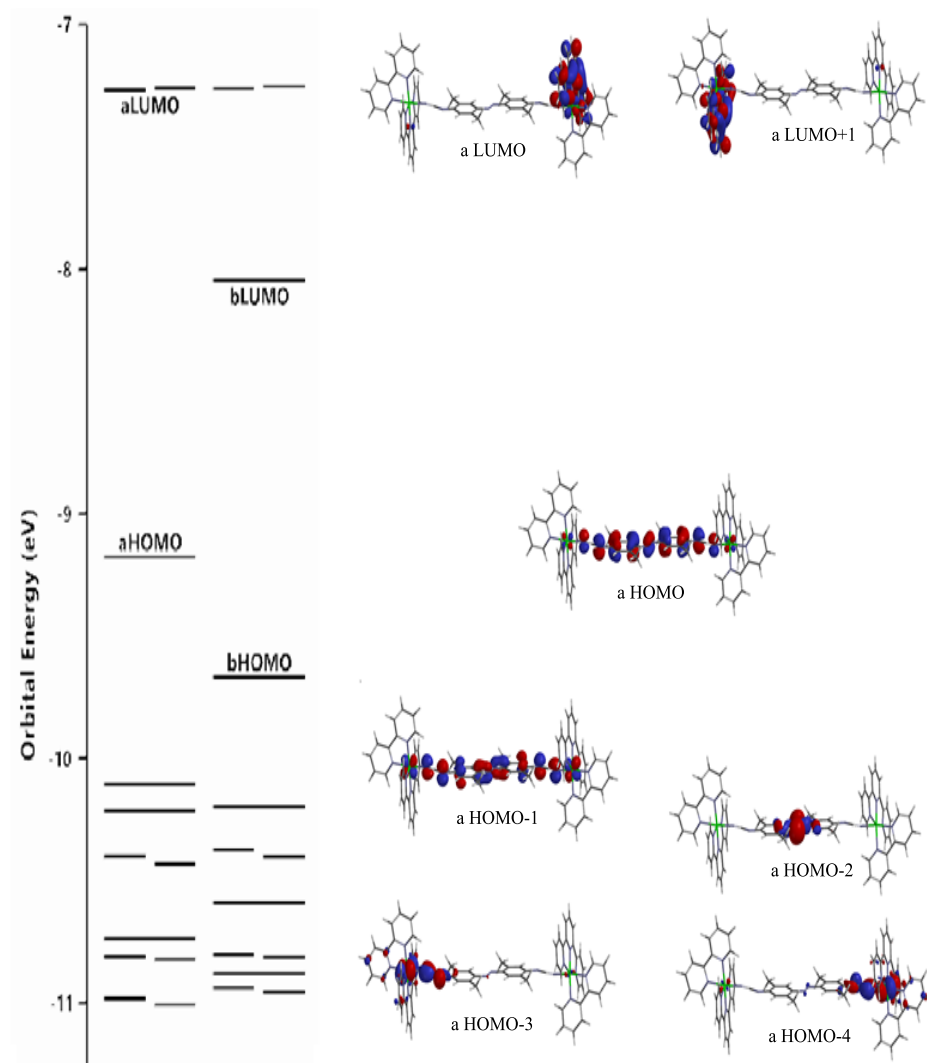


Figure C.3: DFT calculation of orbital energies and selected α -molecular orbitals of $[\text{Ru}(\text{tpy})(\text{bpy})_2(\mu\text{-Me}_4\text{adpc})]^{2+}$ (7a^+).

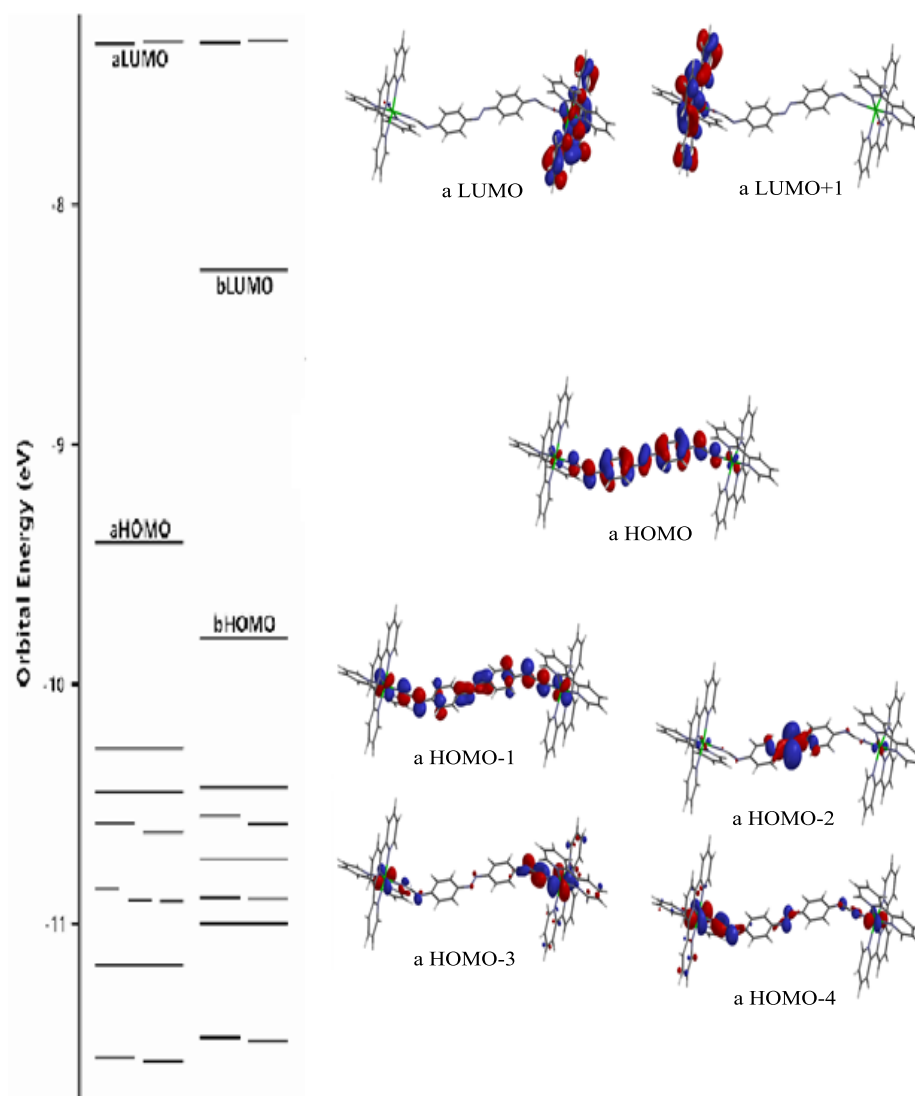


Figure C.4: DFT calculation of orbital energies and selected α -molecular orbitals of $[\text{Ru}(\text{tpy})(\text{bpy})_2(\mu\text{-adpc})]^{2+}$ (7c^+).

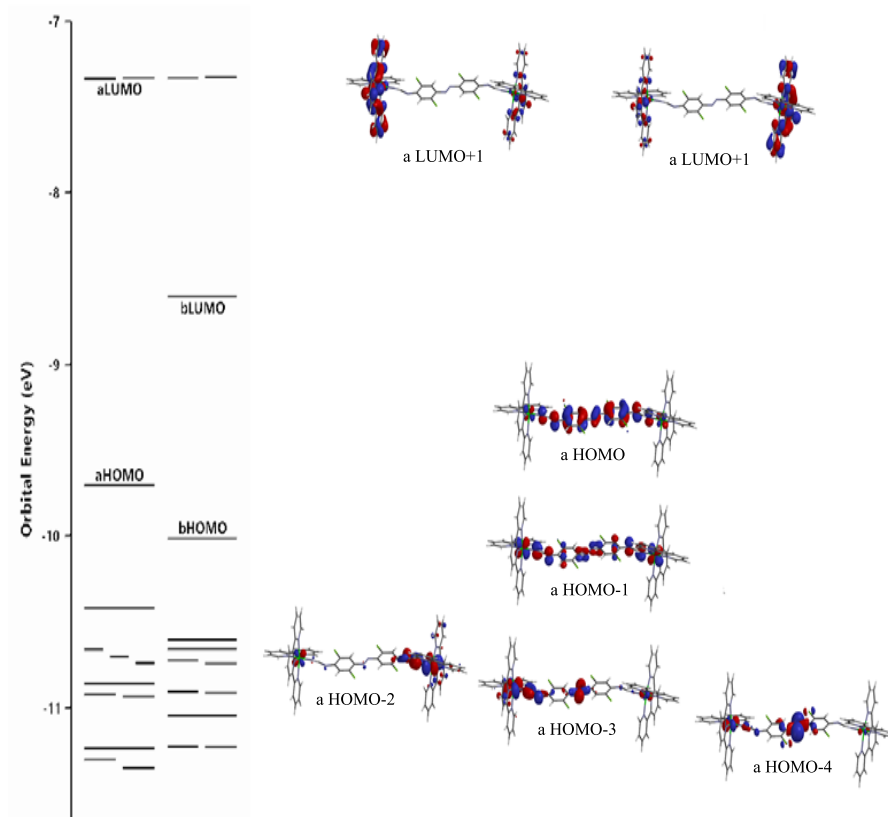


Figure C.5: DFT calculation of orbital energies and selected α -molecular orbitals of $[\text{Ru}(\text{tpy})(\text{bpy})]_2(\mu\text{-Cl}_4\text{adpc})^{2+}$ ($7e^+$).

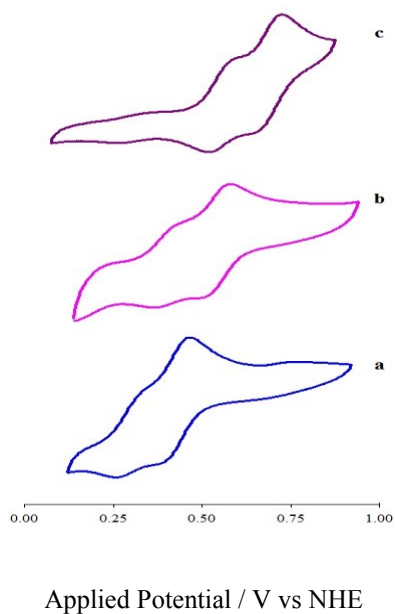


Figure C.6: Cyclic voltammograms of $\text{Tl}_2[\text{R}_2\text{R}'_2\text{adpc}]$ in DMF. 0.1M TBAH, scan rate 0.1 V/s. $\text{R}_2\text{R}'_2\text{adpc}^{2-} = \text{Cl}_2\text{adpc}^{2-}$ (a), adpc^{2-} (b), $\text{Me}_2\text{adpc}^{2-}$ (c).

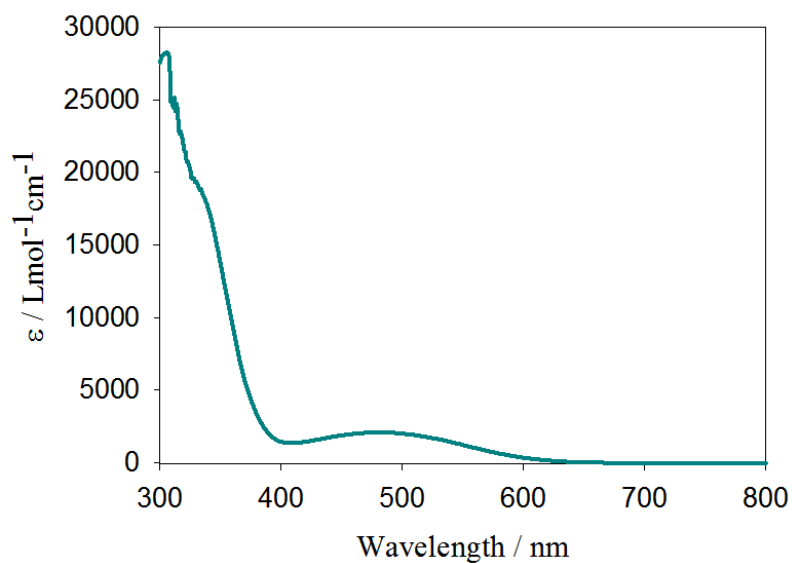


Figure C.7: Quantitative electronic absorption spectrum of $\text{Tl}_2[\text{meta-adpc}]$ (**5e**) in DMF.

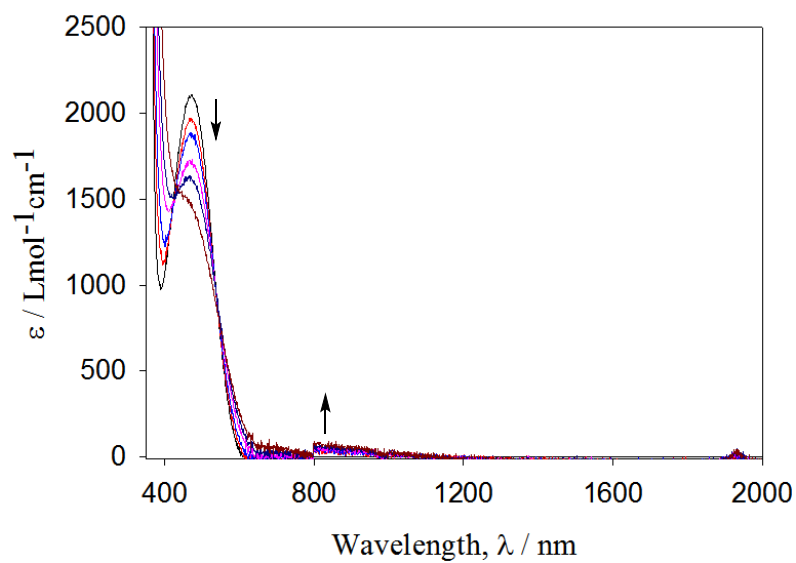


Figure C.8: Vis-NIR spectroelectrochemical oxidation of meta-adpc^{2-} (**5e**) forming $\text{meta-adpc}^{\bullet-}$ radical anion (**5e⁺**)

Appendix-D: Supporting Tables and Figures for Chapter 4

Table D.1: Atomic Coordinates of *cis*-[Ru(bpy)₂(pcyd)(dmsO-S)]⁺ Complex (**4a**).

		Cartesian Coordinates		
	Atom	X	Y	Z
1	Ru Ru1	-0.7565884	0.1936633	-0.2282549
2	N N1	0.7674403	-0.3132182	-1.6020417
3	N N2	-1.7823556	-1.6018714	-0.5965614
4	N N3	0.4596034	-0.6141346	1.2922292
5	N N4	-2.4698507	0.3781018	1.0184386
6	N N5	0.3551553	1.8875002	0.4138004
7	C C1	-1.3452055	-2.5518301	-1.4462317
8	H H17	-0.4300368	-2.2986054	-1.9741644
9	C C2	-2.0173121	-3.7575805	-1.6150076
10	H H4	-1.6318859	-4.496496	-2.3095704
11	C C3	-3.1784633	-3.9882936	-0.8766024
12	H H22	-3.7270574	-4.9191847	-0.981167
13	C C4	-3.6294492	-3.0074873	0.0022402
14	H H21	-4.5287687	-3.1772718	0.5827491
15	C C5	-2.9161109	-1.8105386	0.1295253
16	C C6	0.423323	-1.8853385	1.7285178
17	H H28	-0.3799672	-2.4998686	1.3427408
18	C C7	1.3609877	-2.408292	2.6102682
19	H H29	1.2828221	-3.4423697	2.9280599
20	C C8	2.3943873	-1.5840663	3.0513178
21	H H30	3.1589246	-1.9590127	3.7239213
22	C C9	2.4334235	-0.2661277	2.6116447
23	H H34	3.2325728	0.3866063	2.9391889
24	C C10	1.4476168	0.2068108	1.738934
25	C C11	-2.7800106	1.4475784	1.7715558
26	H H13	-2.086036	2.2779642	1.7206978
27	C C12	-3.3099125	-0.6960485	1.0186036
28	C C13	-4.4706015	-0.7015619	1.7988772
29	H H40	-5.1323075	-1.55947	1.7898948
30	C C14	-4.779297	0.4059974	2.5835637
31	H H41	-5.6783431	0.4126121	3.1914026
32	C C15	-3.9192993	1.5029315	2.5666274
33	H H45	-4.1228165	2.3921971	3.153246
34	C C16	0.1872355	3.163312	0.0111577
35	H H3	-0.6705809	3.3480678	-0.6276231

36	C	C17	1.0411092	4.1918651	0.3963229
37	H	H49	0.8591874	5.1984268	0.035489
38	C	C18	2.1137321	3.8995838	1.234431
39	H	H52	2.8082094	4.6731731	1.546444
40	C	C19	2.275588	2.5918448	1.6778837
41	H	H47	3.0946447	2.3471713	2.3427878
42	C	C20	1.3817445	1.6008597	1.2632733
43	C	C21	1.9489263	-0.0502475	-1.5658532
44	N	N6	3.1409669	0.3208624	-1.6364693
45	C	C22	5.3023984	-2.2814991	-0.0496588
46	H	H12	5.2227436	-3.2781874	0.378326
47	C	C23	6.5448996	-1.6451268	-0.1090528
48	H	H54	7.4328889	-2.1384393	0.2754142
49	C	C24	6.6340192	-0.372683	-0.6790185
50	H	H58	7.5959191	0.1297444	-0.7387695
51	C	C25	5.4982178	0.2591356	-1.1807583
52	H	H43	5.5583153	1.2448522	-1.6322575
53	C	C26	4.2456192	-0.3717323	-1.1184511
54	C	C27	4.1612046	-1.6550696	-0.546772
55	H	H59	3.1982252	-2.1601239	-0.5113845
56	S	S1	-1.895145	1.3201789	-1.979806
57	O	O1	-2.4423976	2.6814638	-1.6169571
58	C	C29	-3.2790668	0.3830804	-2.707916
59	H	H1	-4.0029156	0.1962174	-1.9125701
60	H	H5	-2.9161052	-0.5589024	-3.1249311
61	H	H6	-3.7315729	1.008545	-3.4813757
62	C	C28	-0.8646135	1.5032426	-3.4688256
63	H	H2	-0.0074878	2.119176	-3.1922873
64	H	H7	-1.4661505	1.9992579	-4.2346864
65	H	H8	-0.5082922	0.5211719	-3.7831556

Table D.2: Atomic Coordinates of *cis*-[Ru(bpy)₂(pcyd)(dmsO-*O*)]⁺ Complex.

Cartesian Coordinates				
Atom	X	Y	Z	
1	Ru Ru1	-0.7379035	-0.0389595	0.0519277
2	N N1	0.8214001	0.8923405	-1.0105561
3	N N2	-2.1662817	0.5543251	-1.3622423
4	N N3	-0.2453106	-1.8703517	-0.7673566
5	N N4	-2.5323365	-0.7222385	0.9220379
6	N N5	0.6285657	-0.7666653	1.448961

7	C	C1	-1.8772835	1.1888485	-2.5157885
8	H	H17	-0.8202965	1.3758326	-2.679247
9	C	C2	-2.8636537	1.5780168	-3.415096
10	H	H4	-2.5844048	2.0852834	-4.3324852
11	C	C3	-4.1981737	1.3052253	-3.1108124
12	H	H22	-4.9940044	1.5924715	-3.7908437
13	C	C4	-4.4986318	0.6558184	-1.9170058
14	H	H21	-5.529852	0.4361369	-1.6666608
15	C	C5	-3.4647068	0.287523	-1.0492555
16	C	C6	-0.7490383	-2.3762874	-1.9102526
17	H	H28	-1.512013	-1.779124	-2.3942501
18	C	C7	-0.3188412	-3.5784137	-2.456049
19	H	H29	-0.7598226	-3.9360334	-3.3802678
20	C	C8	0.6822958	-4.2949416	-1.8004133
21	H	H30	1.0479712	-5.2352647	-2.2001355
22	C	C9	1.2085753	-3.780252	-0.6212766
23	H	H34	1.9900809	-4.3187393	-0.0983368
24	C	C10	0.732815	-2.5662888	-0.1161504
25	C	C11	-2.6431447	-1.3760894	2.0933771
26	H	H13	-1.7100146	-1.5904335	2.6014292
27	C	C12	-3.6694108	-0.4164569	0.2323423
28	C	C13	-4.9290132	-0.7670226	0.7297165
29	H	H40	-5.8251982	-0.5143654	0.1752652
30	C	C14	-5.0327935	-1.4414056	1.9414869
31	H	H41	-6.0064199	-1.7167607	2.3340229
32	C	C15	-3.8647171	-1.7537964	2.6369939
33	H	H45	-3.8925928	-2.2784477	3.5860035
34	C	C16	1.0008105	-0.12525	2.5716215
35	H	H3	0.491052	0.8146379	2.7512231
36	C	C17	1.9732311	-0.6264648	3.4284157
37	H	H49	2.2433163	-0.0726416	4.3210882
38	C	C18	2.5921242	-1.8354298	3.1083609
39	H	H52	3.3627598	-2.252128	3.7488887
40	C	C19	2.21149	-2.5006444	1.9475507
41	H	H47	2.6861938	-3.4372339	1.6801663
42	C	C20	1.2228115	-1.9483408	1.1271461
43	C	C21	1.9551167	1.1732094	-0.7058895
44	N	N6	3.0591703	1.6435275	-0.3371615
45	C	C22	5.797597	-0.4643563	-1.7524396
46	H	H12	5.9320227	-1.2897963	-2.4473749
47	C	C23	6.9062221	0.1026107	-1.1187153
48	H	H54	7.9042988	-0.2787528	-1.3137337
49	C	C24	6.7173368	1.1713239	-0.2394461
50	H	H58	7.5717977	1.6259429	0.255184
51	C	C25	5.4388586	1.6669718	0.0075133

52	H	H43	5.2841868	2.5010686	0.6856788
53	C	C26	4.3211028	1.0977652	-0.6218727
54	C	C27	4.5157088	0.0244404	-1.5097955
55	H	H59	3.6574093	-0.4093303	-2.0181755
56	O	O1	-1.0117753	1.8287522	1.1609279
57	S	S1	-0.6919774	3.1920859	0.4562639
58	C	C29	0.8487749	3.8093522	1.2043162
59	H	H5	1.6787962	3.1879239	0.8533752
60	H	H9	0.7596438	3.7707248	2.2937378
61	H	H10	0.9976615	4.8396905	0.8665597
62	C	C28	-1.8547088	4.3203239	1.2857495
63	H	H2	-1.7495795	4.216301	2.3687964
64	H	H1	-2.8613162	4.0307818	0.9769863
65	H	H6	-1.6490549	5.3465812	0.9688758

Table D.3: Atomic Coordinates of *cis*-[Ru(bpy)₂(pcyd)(dms_o-S)]²⁺ Complex(**4a**⁺).

		Cartesian Coordinate		
Atom		X	Y	Z
1	Ru Ru1	-0.6491756	-0.0215556	-0.2210202
2	N N1	1.3042397	-0.6296873	-0.349511
3	N N2	-1.3950749	-1.790403	0.6751472
4	N N3	-0.1961992	0.9241795	1.6146769
5	N N4	-2.6972166	0.4221902	-0.004661
6	N N5	-0.0522205	1.9376475	-0.8475306
7	C C1	-0.6653455	-2.882929	0.9763583
8	H H17	0.3776298	-2.8489607	0.6832365
9	C C2	-1.2022895	-3.9851592	1.6322247
10	H H4	-0.5734272	-4.8413619	1.8511151
11	C C3	-2.5484719	-3.9561525	1.9970339
12	H H22	-3.0027675	-4.7954317	2.5140099
13	C C4	-3.3067911	-2.8302504	1.6879968
14	H H21	-4.3529983	-2.7942348	1.9667964
15	C C5	-2.7139192	-1.7538752	1.0197977
16	C C6	-0.3114446	0.3518965	2.8260333
17	H H28	-0.6991048	-0.6587701	2.8415222
18	C C7	0.0464134	1.0000182	4.0026101
19	H H29	-0.0686067	0.4928183	4.9542988
20	C C8	0.5473894	2.2979489	3.9220763
21	H H30	0.8356587	2.8401249	4.816995
22	C C9	0.6724479	2.8931263	2.6707221

23	H	H34	1.0585251	3.902007	2.5936966
24	C	C10	0.2950744	2.188791	1.5223067
25	C	C11	-3.2959676	1.5465645	-0.4356494
26	H	H13	-2.6604767	2.2570777	-0.9478556
27	C	C12	-3.4430289	-0.5296779	0.626053
28	C	C13	-4.8101673	-0.3391001	0.8425178
29	H	H40	-5.3991107	-1.0979473	1.3433561
30	C	C14	-5.4229311	0.8326273	0.4039197
31	H	H41	-6.4845978	0.9877563	0.5669657
32	C	C15	-4.653076	1.7908151	-0.2510599
33	H	H45	-5.0878278	2.713212	-0.6201395
34	C	C16	-0.0398733	2.4047418	-2.1112659
35	H	H3	-0.4455161	1.739994	-2.8663305
36	C	C17	0.4229307	3.6772761	-2.4366877
37	H	H49	0.4079353	4.0009888	-3.4717833
38	C	C18	0.8897171	4.503861	-1.4190005
39	H	H52	1.2608228	5.5010035	-1.6336165
40	C	C19	0.8620755	4.0322939	-0.1089593
41	H	H47	1.2084749	4.6687531	0.69595
42	C	C20	0.383491	2.747208	0.1588099
43	C	C21	2.4289959	-0.9781436	-0.4619907
44	N	N6	3.557381	-1.5242907	-0.7385259
45	C	C22	6.2879792	0.2069063	1.0472334
46	C	C23	7.3773379	-0.5503019	0.5695139
47	H	H54	8.3833635	-0.3091525	0.8989324
48	C	C24	7.1716491	-1.6121102	-0.327402
49	H	H58	8.0175534	-2.1880362	-0.6883885
50	C	C25	5.891846	-1.9215973	-0.7487018
51	H	H43	5.6989146	-2.7344652	-1.4407449
52	C	C26	4.7814188	-1.1628332	-0.2754798
53	C	C27	5.0042229	-0.0876825	0.6356686
54	H	H59	4.1549497	0.4878074	0.9941848
55	S	S1	-1.1121578	-0.8883032	-2.4249095
56	O	O1	-1.67889	0.1362519	-3.3720692
57	C	C28	0.3419942	-1.6502653	-3.210788
58	H	H2	0.7142982	-2.4644499	-2.5851532
59	H	H7	1.1046619	-0.8764856	-3.3132583
60	H	H8	0.0367536	-2.0103485	-4.1965927
61	C	C29	-2.2323794	-2.3240374	-2.4575704
62	H	H1	-1.8077522	-3.1472445	-1.8787347
63	H	H5	-2.3657861	-2.6064663	-3.5049973
64	H	H6	-3.1889957	-2.0076441	-2.0387931
65	H	H9	6.4646407	1.02353	1.7402312

Table D.4: Atomic Coordinates of *cis*-[Ru(bpy)₂(pcyd)(dmsO-O)]²⁺ Complex.

Cartesian Coordinates			
Atom	X	Y	Z
1 Ru Ru1	-0.5971635	-0.0813363	0.3293087
2 N N1	1.1786919	0.6814127	-0.2985611
3 N N2	-1.77105	0.6480992	-1.272144
4 N N3	-0.1155281	-1.9476379	-0.4641232
5 N N4	-2.5288459	-0.7230009	0.865823
6 N N5	0.4072171	-0.9852423	1.9399508
7 C C1	-1.3035105	1.3386295	-2.3306127
8 H H17	-0.2330496	1.5047121	-2.3473146
9 C C2	-2.1315471	1.8145375	-3.3406743
10 H H4	-1.7059964	2.3644164	-4.1731768
11 C C3	-3.5019017	1.5715846	-3.2519763
12 H H22	-4.1808229	1.9279783	-4.0201528
13 C C4	-3.9913546	0.861018	-2.1596761
14 H H21	-5.0537107	0.6655111	-2.0780117
15 C C5	-3.1082919	0.4047212	-1.1754862
16 C C6	-0.4258344	-2.3680738	-1.7043255
17 H H28	-0.9848005	-1.6704758	-2.3160127
18 C C7	-0.057597	-3.6184854	-2.187377
19 H H29	-0.3329281	-3.9074183	-3.1958036
20 C C8	0.6610881	-4.4736523	-1.3540196
21 H H30	0.9640342	-5.4582225	-1.6955436
22 C C9	0.9848999	-4.0454023	-0.0701706
23 H H34	1.5399253	-4.7002246	0.5908574
24 C C10	0.5903542	-2.7751534	0.3598015
25 C C11	-2.8372276	-1.4158431	1.9770606
26 H H13	-2.0079776	-1.6694714	2.62571
27 C C12	-3.5293521	-0.3612334	0.0143215
28 C C13	-4.8569695	-0.7099861	0.2783811
29 H H40	-5.6468434	-0.4232017	-0.4053802
30 C C14	-5.1677219	-1.431123	1.4277637
31 H H41	-6.1959361	-1.706515	1.6389258
32 C C15	-4.1382922	-1.7888363	2.2957983
33 H H45	-4.3315359	-2.3473083	3.2052565
34 C C16	0.6175283	-0.406366	3.1350036
35 H H3	0.2047991	0.5902454	3.2453956
36 C C17	1.313373	-1.0452351	4.1561344
37 H H49	1.4574303	-0.5444594	5.1073041
38 C C18	1.8121408	-2.327433	3.9263335

39	H	H52	2.3612663	-2.8556568	4.6992318
40	C	C19	1.5950082	-2.9275703	2.6882224
41	H	H47	1.9740076	-3.9245382	2.4978882
42	C	C20	0.8859607	-2.2361607	1.7015769
43	C	C21	2.2268742	1.1375889	-0.6119457
44	N	N6	3.271665	1.8266749	-0.8845713
45	C	C22	5.8958964	-0.4146343	-2.2126112
46	H	H12	6.0700806	-1.4567762	-2.4621969
47	C	C23	6.9208702	0.5305753	-2.4071893
48	H	H54	7.8797857	0.2090316	-2.8012875
49	C	C24	6.7112981	1.8830451	-2.0947603
50	H	H58	7.5068327	2.6045334	-2.2513676
51	C	C25	5.4908907	2.2958495	-1.588709
52	H	H43	5.3006843	3.3346426	-1.3397926
53	C	C26	4.4488291	1.3499753	-1.3833956
54	C	C27	4.6731758	-0.0184489	-1.7067438
55	H	H59	3.8726388	-0.7374448	-1.5555082
56	O	O1	-0.9891574	1.7362707	1.4758494
57	S	S1	-0.7697137	3.160567	0.8558387
58	C	C29	0.6938195	3.8476717	1.6907662
59	H	H5	1.5661184	3.2966648	1.3337281
60	H	H9	0.5852655	3.7438739	2.773525
61	H	H10	0.7868723	4.9007848	1.4092481
62	C	C28	-2.05234	4.1644007	1.6613804
63	H	H2	-2.007157	4.0067495	2.7417183
64	H	H1	-3.017134	3.8353401	1.2705752
65	H	H6	-1.8885214	5.2160965	1.4098569

Table D.5: Atomic Coordinates of *cis*-[Ru(bpy)₂(Cl₅pcyd)(dms_o-S)]⁺ Complex (**4f**).

Cartesian Coordinates

	Atom	X	Y	Z
1	Ru Ru1	-2.0509362	0.1680116	0.0256353
2	N N1	-0.3233007	0.2479566	-1.1686056
3	N N2	-3.3205722	-0.0668637	-1.6298994
4	N N3	-1.6790768	-1.8982253	0.2371713
5	N N4	-3.9560263	0.0683148	0.9395869
6	N N5	-0.835524	0.1014238	1.7727998
7	C C1	-2.8968863	-0.1352214	-2.9071561
8	H H17	-1.8268866	-0.0067099	-3.0390496

9	C C2	-3.7699574	-0.3698383	-3.9641378
10	H H4	-3.3869122	-0.4171493	-4.9779397
11	C C3	-5.1265612	-0.5467847	-3.6888798
12	H H22	-5.8352881	-0.7362695	-4.4888622
13	C C4	-5.563886	-0.4816587	-2.3688722
14	H H21	-6.6133405	-0.6258156	-2.1407239
15	C C5	-4.6421555	-0.2361831	-1.3455051
16	C C6	-2.1575392	-2.859706	-0.5712111
17	H H28	-2.8579587	-2.5398776	-1.332273
18	C C7	-1.7756715	-4.1915941	-0.4689553
19	H H29	-2.1924329	-4.9252447	-1.1503395
20	C C8	-0.849129	-4.5460742	0.5095153
21	H H30	-0.5171229	-5.5736518	0.6174819
22	C C9	-0.348449	-3.5561836	1.3471469
23	H H34	0.3774303	-3.8139197	2.1080375
24	C C10	-0.7764984	-2.2327739	1.1965384
25	C C11	-4.2049113	0.2084213	2.2536045
26	H H13	-3.3388026	0.3837145	2.8803885
27	C C12	-5.0003739	-0.1343216	0.0856602
28	C C13	-6.3125873	-0.2095026	0.5616059
29	H H40	-7.136745	-0.3654666	-0.1243964
30	C C14	-6.5616569	-0.0733652	1.9244892
31	H H41	-7.5773589	-0.1286286	2.3027681
32	C C15	-5.487689	0.1421869	2.7866199
33	H H45	-5.6328063	0.2637369	3.8544803
34	C C16	-0.4928941	1.1438534	2.5557029
35	H H3	-0.9729151	2.0887004	2.3218647
36	C C17	0.4025871	1.0274809	3.6145876
37	H H49	0.6442031	1.9042812	4.2055205
38	C C18	0.9719814	-0.2141487	3.882649
39	H H52	1.6842849	-0.3415489	4.691538
40	C C19	0.603719	-1.2995964	3.0942564
41	H H47	1.0275409	-2.2762217	3.2922665
42	C C20	-0.306908	-1.1242315	2.0485249
43	C C21	0.8387616	0.5180146	-1.0337918
44	N N6	1.978519	1.0412337	-0.9738356
45	C C22	4.9401321	-1.2076904	-0.5135339
46	C C23	5.9315794	-0.2472781	-0.2639542
47	C C24	5.5832936	1.115057	-0.2587419
48	C C25	4.2612056	1.5016299	-0.497343
49	C C26	3.2370832	0.5527913	-0.7480858
50	C C27	3.6187246	-0.8099349	-0.7547991
51	S S1	-2.2313624	2.5397679	-0.0438876

52	O	O1	-2.4318737	3.2015729	1.2995809
53	C	C28	-0.8200145	3.3384145	-0.8685598
54	H	H2	-0.745179	2.9659026	-1.8917834
55	H	H7	0.087942	3.0723675	-0.3246782
56	H	H8	-0.9863854	4.4181526	-0.8372481
57	Cl	Cl1	2.4039159	-2.0219672	-1.0832282
58	Cl	Cl2	3.8269611	3.1883829	-0.4807486
59	Cl	Cl3	6.7996389	2.3146546	0.0503196
60	C	C29	-3.5685834	3.150068	-1.1224238
61	H	H1	-3.3976155	2.829888	-2.1528252
62	H	H5	-3.5812506	4.2397825	-1.0449861
63	H	H6	-4.5059164	2.7400069	-0.7425383
64	Cl	Cl4	5.3563039	-2.8973422	-0.5208589
65	Cl	Cl5	7.5704196	-0.7358029	0.0345558

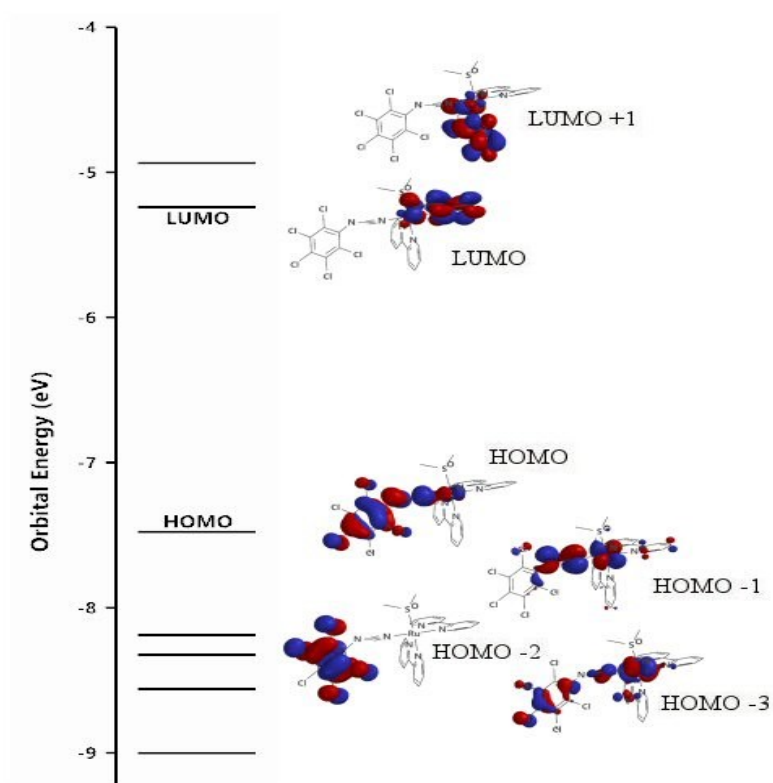


Figure D.1: DFT calculation of orbital energies and selected molecular orbitals of $[\text{Ru}(\text{bpy})_2(\text{Cl}_5\text{pcyd})(\text{dmsO-S})]^+$ (**4f**).

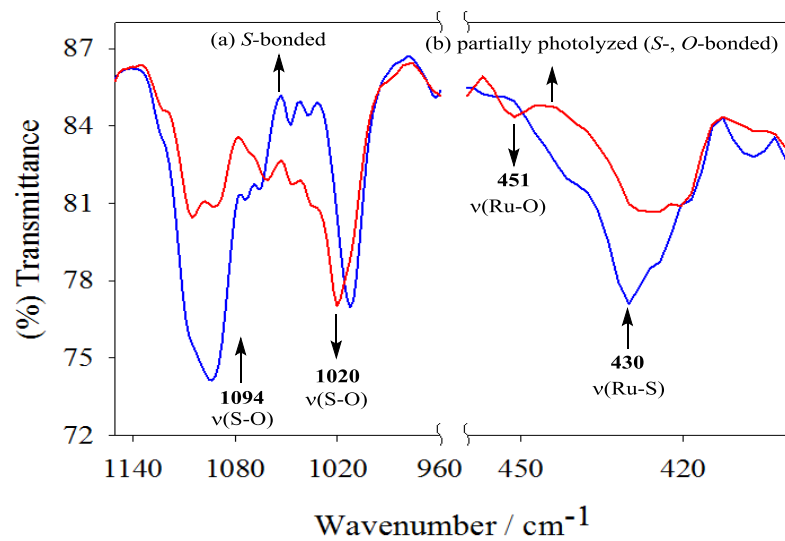


Figure D.2: IR spectra of *cis*-[Ru(bpy)₂(Cl₅-pecy)(dms)]⁺[PF₆]⁻ complex (**4f**) on KBr pellet: (a) S-bonded (blue) and (b) partially photolyzed (red).

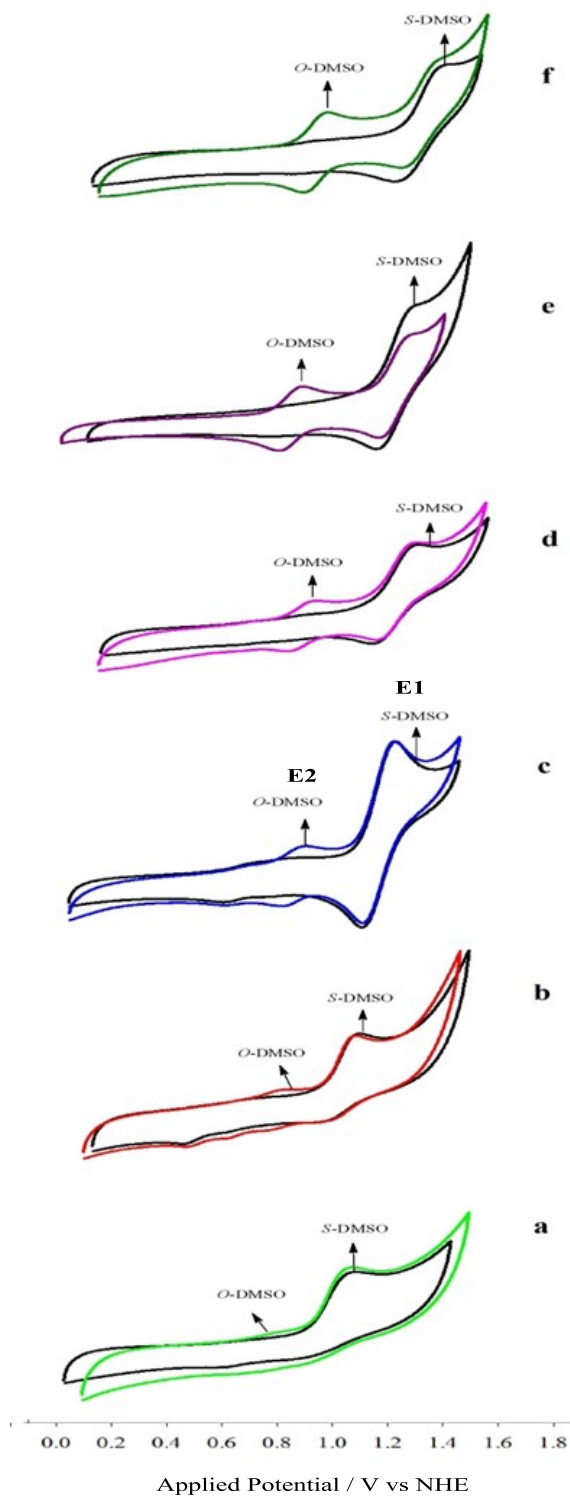


Figure D.3: Cyclic voltammograms of *cis*-[Ru(bpy)(R-pcyd)(dmsO-S)][PF₆] complexes (**4a-4f**) in dmsO. R-pcyd is (a) unsubstituted, (b) Cl⁻, (c) Cl₂⁻, (d) Cl₃⁻, (e) Cl₄⁻, (f) Cl₅-phenylcyanamide Scan rate 1.0 V/s, 0.1 M TBAH.

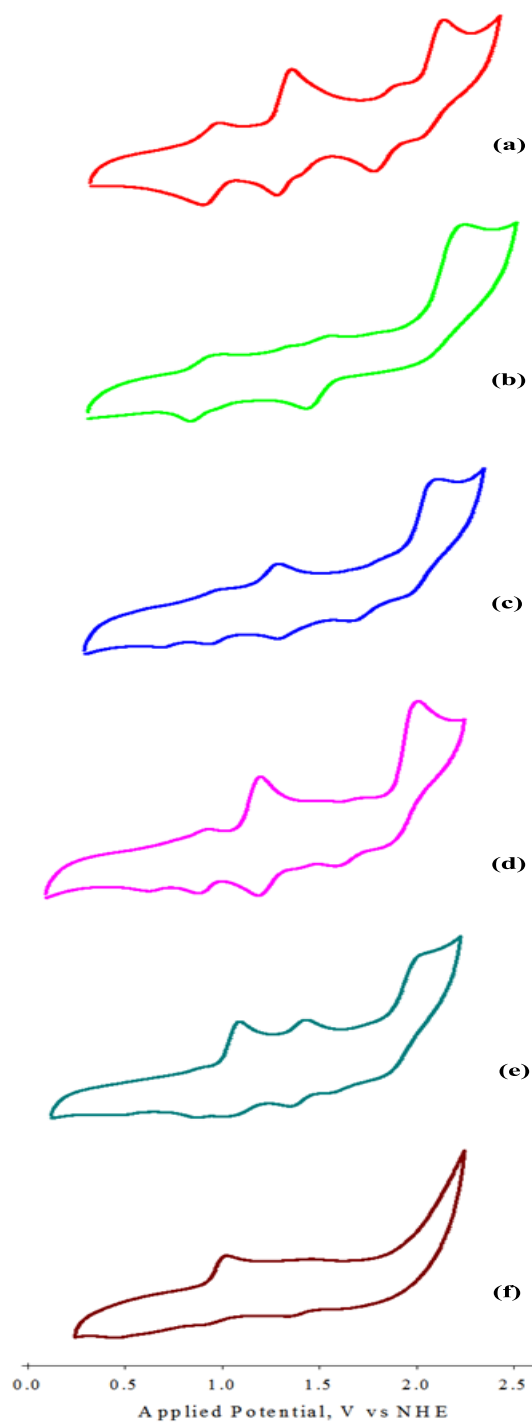


Figure D.4: Cyclic voltammograms of *cis*-[Ru(bpy)(R-*pcyd*)(dmsO-*S*)] $[PF_6]$ complexes (**4a-4f**) in acetonitrile. R-*pcyd* is (a) unsubstituted, (b) Cl-, (c) Cl₂-, (d) Cl₃-, (e) Cl₄-, (f) Cl₅-phenylcyanamide Scan rate 1.0 V/s, 0.1 M TBAH.

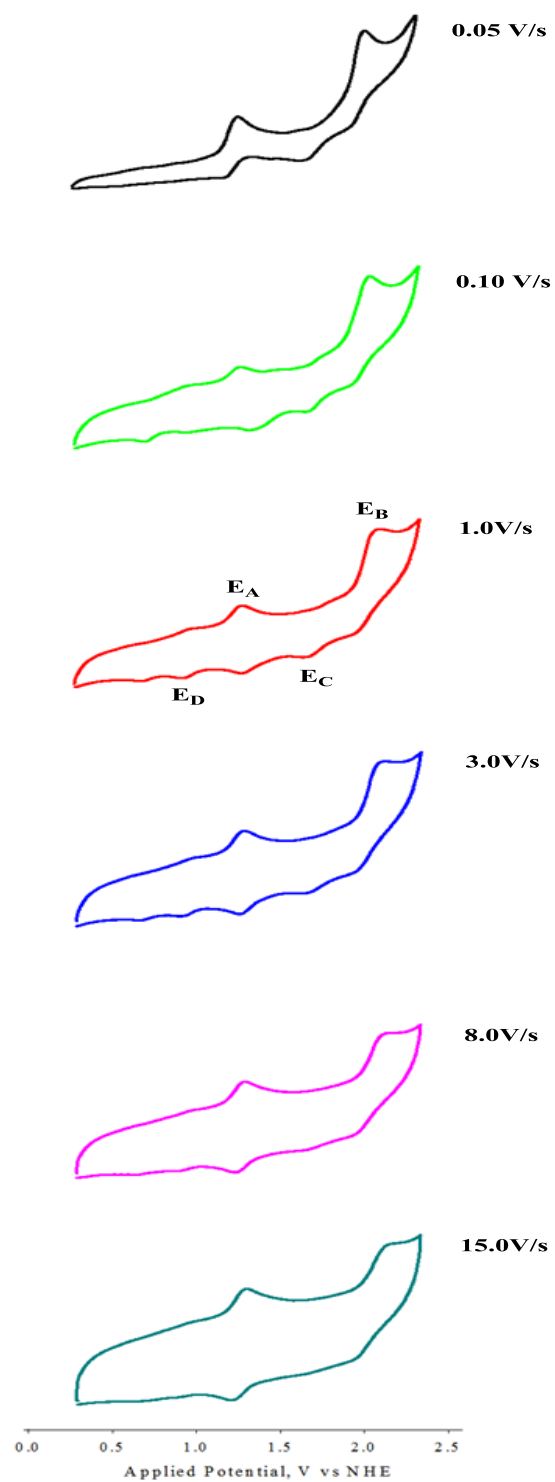


Figure D.5: Cyclic voltammograms of *cis*-[Ru(bpy)₂(Cl₃pcyd)(dmsO-S)][PF₆] complex (4d) in acetonitrile, 0.1 M TBAH, at scan rates from 0.05 to 15 V/s.

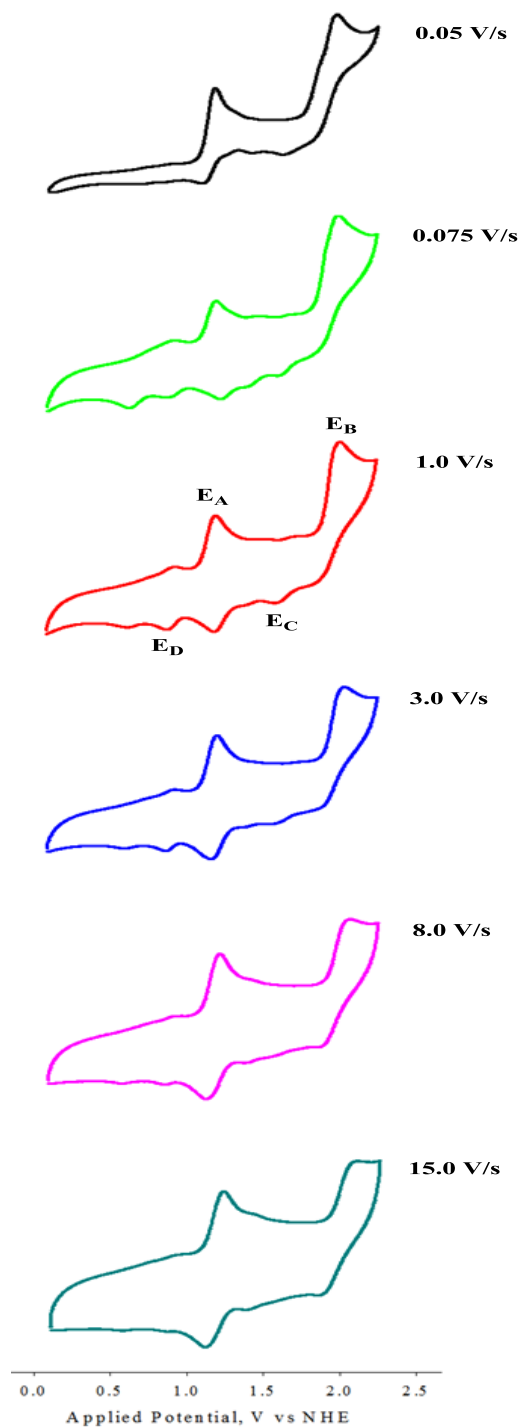


Figure D.6: Cyclic voltammograms of *cis*-[Ru(bpy)₂(Cl₂pcyd)(dmsoS)][PF₆] complex (**4c**) in acetonitrile, 0.1 M TBAH, at scan rates from 0.05 to 15 V/s.

D.1 Measurement of Quantum Yield of S→O Isomerization

Eight solutions of the *cis*-[Ru(bpy)₂(Cl₅-pcyd)(dms_o-S)][PF₆] complex (**4f**) of the same concentration 7.15×10^{-5} M in dms_o were prepared in the dark and transferred to 3 mL cuvettes using a 3 mL graduated pipette. The solutions were degassed using argon bubble for 10 minutes in the dark and irradiated at lowest energy isosbestic point \sim 444 nm for 0.0, 1.2, 2.3, 4.1, 5.1, 6.2, 7.1, 8.0 seconds (upto 50-80% conversion to the *O*-isomer), respectively and absorbances of each solution were measured subsequently at wavelengths 512 nm and 600 nm, respectively. After the data for quantum yield measurement were collected, experimental solution was replaced with ferrioxalate solution and the intensity of the incident light, $I_0 = 6.71 \times 10^{-8}$ Einstein s⁻¹ cm² was measured by ferrioxalate actinometry, as described in the Section 4.2. The concentrations of the product C_p (*O*-isomer) were calculated as a function of irradiation time (t) using simultaneous Eq. 4.2.2 and 4.2.3 (Chapter 4). The data for $\epsilon_{R,\lambda_1(512)}$, $\epsilon_{R,\lambda_2(600)}$, $\epsilon_{P,\lambda_1(512)}$, $\epsilon_{P,\lambda_2(600)}$ were obtained from the quantitative absorption spectra of both *S*- and *O*-bonded isomers. In order to obtain the values for the *O*-bonded isomer, an initial solution of *S*-isomer was irradiated for 120 s to completely form the *O*-bonded isomer, such that $C_p = C_R$ and the molar extinction co-efficients for the *O*-isomer were calculated using Beer's law. The derived data are shown in the Table. Finally, $\Phi = 0.43$, calculated from the slope of the plot of $[\ln(C_T) - \ln(C_T - C_p)]$ vs t , by using Eq.4.2.4.

Table D.6: Raw and Derived Data for the Determination of Quantum Yield of S→O isomerization of *cis*-[Ru(bpy)₂(Cl₅-pcyd)(dmsO-S)][PF₆] Complex (**4f**) in dmsO.

Irradiation Time/ <i>t</i>	Absorbance at 512 nm/ <i>A</i> (λ ₁)	Absorbance at 600 nm/ <i>A</i> (λ ₂)	<i>C_p</i> × 10 ⁵	(<i>C_T</i> - <i>C_p</i>) × 10 ⁵	ln(<i>C_T</i> - <i>C_p</i>)	[ln(<i>C_T</i>) - ln(<i>C_T</i> - <i>C_p</i>)] -
0.0000	0.1556	0.0216	0.0000	7.1490	-9.5460	0.0000
1.2000	0.2741	0.0603	2.0484	5.1006	-9.8836	0.3376
2.3000	0.3373	0.0816	3.2050	3.9440	-10.1407	0.5947
3.0000	0.3725	0.0909	3.6105	3.5385	-10.2492	0.7032
4.1000	0.4287	0.1093	4.5841	2.5649	-10.5710	1.0250
5.1000	0.4608	0.1194	5.1094	2.0396	-10.8002	1.2542
6.2000	0.4859	0.1279	5.5722	1.5768	-11.0575	1.5115
7.1000	0.5024	0.1328	5.8045	1.3445	-11.2169	1.6709
8.0000	0.5111	0.1385	6.2233	0.9257	-11.5901	2.0441

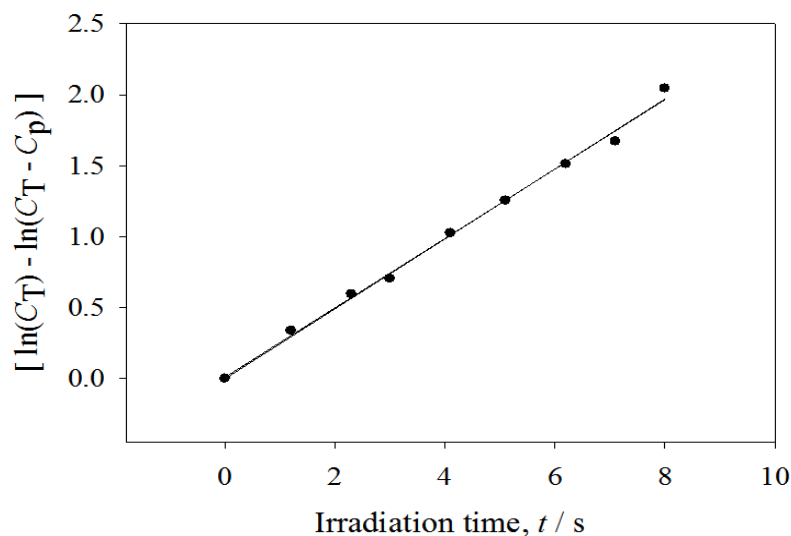


Figure D.7: Plot of [ln(*C_T*) - ln(*C_T* - *C_p*)] versus irradiation time (*t*) to determine the overall quantum yield Φ_{S→O} for *cis*-[Ru(bpy)₂(Cl₅-pcyd)(dmsO-S)][PF₆] complex (**4f**) in dmsO. The equations for the line is $y = 0.24x$, with $R^2 = 0.995$. Data taken from Table D.6.

D.2 Determination of Thermal Back O→S Isomerization Rates

A 3.0 mL 7.12×10^{-5} M solution of the *cis*-[Ru(bpy)₂(Cl₅-pcyd)(dmsO-O)][PF₆] Complex (**4f**) in dmsO was transferred to a 1.0 cm path-length quartz cell and the solution was irradiated for 120 s for complete conversion to the O-bonded isomer. Absorbance of the irradiated solution (A_t) was measured in the dark at $\lambda_{\text{max}} = 512$ nm of the O-bonded isomer as a function of time, t . Data were collected almost 90-95% conversion to the initial S-bonded isomer. $A_\alpha = 0.1549$ was obtained from the absorbance of the initial S-bonded isomer at 512 nm. Absorbance and derived data are shown in the Table D.6 and fitted to the first order rate Eq. 4.2.6. The slope of the plot gave the thermal O→S isomerization rate, $k_{\text{OS1}} = 2.61 \pm 0.03 \text{ s}^{-1}$.

Table D.7: Raw and Derived Data for the Determination of Thermal O→S Isomerization Rate (k_{OS1}) of *cis*-[Ru(bpy)₂(Cl₅-pcyd)(dmsO-O)][PF₆] Complex (**4f**) in dmsO.

Time, t/s	Absorbance at 512 nm	$A_t - A_\alpha$	$\ln(A_t - A_\alpha)$
0.0000	0.5809	0.4260	-0.8533
78.0000	0.4941	0.3392	-1.0811
140.0000	0.4357	0.2808	-1.2700
195.0000	0.3797	0.2248	-1.4927
247.0000	0.3556	0.2007	-1.6059
300.0000	0.3368	0.1819	-1.7044
355.0000	0.3153	0.1604	-1.8302
410.0000	0.2948	0.1399	-1.9671
465.0000	0.2771	0.1222	-2.1019
527.0000	0.2584	0.1035	-2.2681
588.0000	0.2446	0.0897	-2.4112
651.0000	0.2312	0.0763	-2.5726
710.0000	0.2206	0.0657	-2.7227
777.0000	0.2114	0.0565	-2.8740
835.0000	0.2032	0.0483	-3.0301
898.0000	0.1959	0.0410	-3.1939
1017.0000	0.1849	0.0299	-3.5082
1137.0000	0.1770	0.0221	-3.8126
1327.0000	0.1675	0.0126	-4.3741
1498.0000	0.1622	7.3000e-3	-4.9199

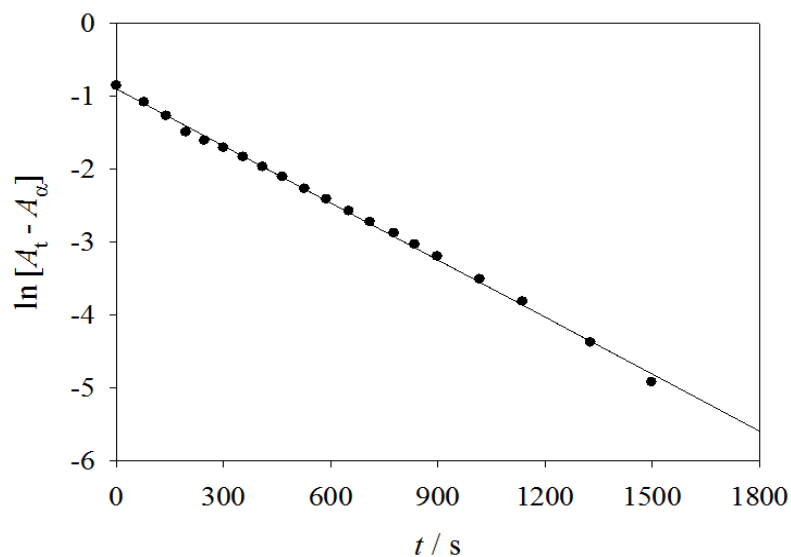


Figure D.8: First order plot for thermal O→S linkage isomerism of dmsO in *cis*-[Ru(bpy)₂(Cl₅-pcyd)(dmsO-O)][PF₆] complex (**4f**) in dmsO. The equation for the line is $y = -0.0026x - 0.894$, with $R^2 = 0.999$.

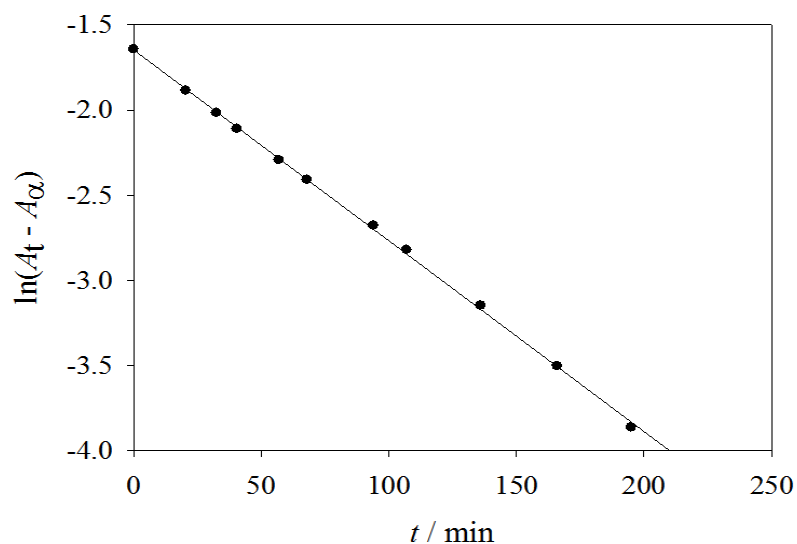


Figure D.9: First order plot for thermal O→S linkage isomerism of dmsO in *cis*-[Ru(bpy)₂(Cl₅-pcyd)(dmsO-O)][PF₆] complex (**4f**) in propylene carbonate. The equation for the line is $y = -0.011x - 1.65$, with $R^2 = 0.999$.

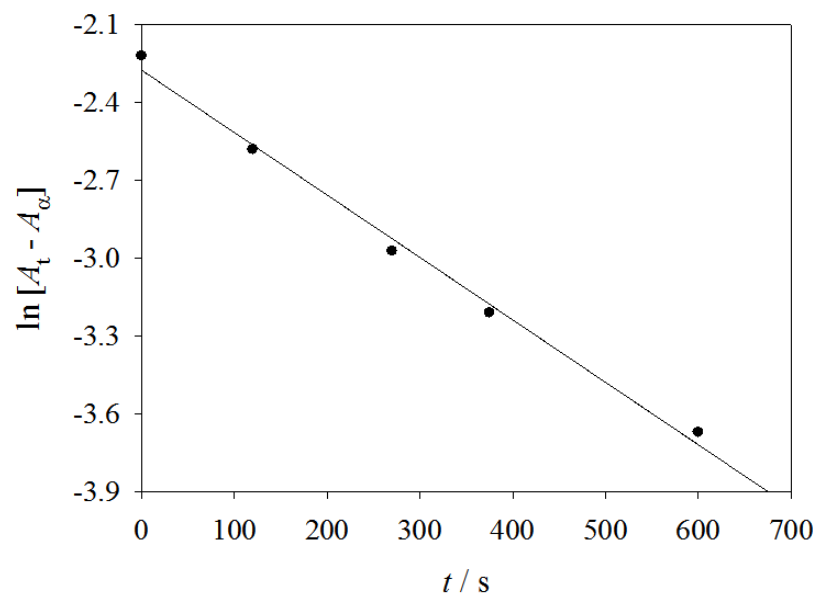


Figure D.10: First order plot for thermal O→S linkage isomerism of dmsO in *cis*-[Ru(bpy)₂(Cl₅-pcyd)(dmsO-O)][PF₆] complex (**4f**) on PMMA polymer film. The equation for the line is $y = -0.0024x - 2.27$, with $R^2 = 0.993$.

Appendix-E: Supporting Tables and Figures for Chapter 5

Table E.1: X-ray Crystallography Data of Ru(tpy)Cl₃·2DMSO Complex.

Atomic Coordinates

Cartesian Coordinates

Atom		X	Y	Z
Ru1	Ru	0.0000	0.168102(9)	0.2500
Cl1	Cl	0.0000	0.03000(3)	0.2500
Cl2	Cl	0.00072(3)	0.17345(3)	0.40568(3)
S1	S	0.33993(3)	0.52745(3)	0.45249(4)
S2	S	0.11932(8)	0.44526(7)	0.04287(9)
S2'	S	0.14920(12)	0.40469(9)	0.11996(13)
N1	N	0.12999(8)	0.18931(8)	0.32669(10)
N2	N	0.0000	0.28390(10)	0.2500
O1	O	0.26667(11)	0.48098(9)	0.44359(13)
O2	O	0.15990(17)	0.48467(14)	0.1396(2)
C1	C	0.19302(11)	0.13640(10)	0.36303(13)
H1A	H	0.1796	0.0822	0.3593
C2	C	0.27754(11)	0.15884(11)	0.40602(15)
H2A	H	0.3212	0.1203	0.4306
C3	C	0.29742(11)	0.23737(11)	0.41267(15)
H3A	H	0.3549	0.2535	0.4412
C4	C	0.23277(11)	0.29300(10)	0.37730(14)
H4A	H	0.2455	0.3475	0.3824
C5	C	0.14938(10)	0.26756(9)	0.33441(12)
C6	C	0.07534(10)	0.32140(9)	0.29339(12)
C7	C	0.07734(10)	0.40289(9)	0.29562(13)
H7A	H	0.1301	0.4302	0.3274
C8	C	0.0000	0.44441(13)	0.2500
C9	C	0.0000	0.53122(13)	0.2500
C10	C	0.06269(12)	0.57328(10)	0.24414(16)
H10A	H	0.1064	0.5460	0.2407
C11	C	0.06173(13)	0.65479(10)	0.24332(17)
H11A	H	0.1045	0.6822	0.2380
C12	C	0.0000	0.69766(13)	0.2500
C13	C	0.0000	0.78781(14)	0.2500
C14	C	0.0958(4)	0.8190(3)	0.3078(8)
H14A	H	0.0961	0.8762	0.3146
H14B	H	0.1225	0.8048	0.2681
H14C	H	0.1278	0.7951	0.3762
C15	C	-0.0415(6)	0.8162(3)	0.1447(4)
H15A	H	-0.1006	0.7978	0.1069
H15B	H	-0.0112	0.7963	0.1116
H15C	H	-0.0407	0.8737	0.1447
C16	C	-0.0368(7)	0.8209(3)	0.3098(8)

H16A	H	-0.0981	0.8105	0.2734
H16B	H	-0.0270	0.8777	0.3174
H16C	H	-0.0095	0.7964	0.3778
C17	C	0.0379(10)	0.3838(16)	0.033(2)
H17A	H	-0.0021	0.4151	0.0437
H17B	H	0.0630	0.3429	0.0862
H17C	H	0.0076	0.3594	-0.0347
C18	C	0.1876(18)	0.3724(19)	0.041(2)
H18A	H	0.2423	0.3962	0.0593
H18B	H	0.1615	0.3496	-0.0280
H18C	H	0.1967	0.3311	0.0907
C17'	C	0.0419(13)	0.375(2)	0.040(3)
H17D	H	0.0113	0.3821	0.0769
H17E	H	0.0400	0.3196	0.0217
H17F	H	0.0149	0.4071	-0.0225
C18'	C	0.187(3)	0.384(3)	0.036(3)
H18D	H	0.2469	0.3995	0.0689
H18E	H	0.1534	0.4136	-0.0279
H18F	H	0.1815	0.3278	0.0210
C19	C	0.29406(15)	0.60813(14)	0.3661(2)
H19A	H	0.2640	0.6422	0.3892
H19B	H	0.2538	0.5884	0.2970
H19C	H	0.3391	0.6381	0.3647
C20	C	0.37667(18)	0.47563(16)	0.3811(3)
H20A	H	0.4027	0.4260	0.4158
H20B	H	0.4190	0.5075	0.3762
H20C	H	0.3286	0.4648	0.3120

Bond Lengths

Ru1 N2 1.9723(19)	Ru1 N1 2.0747(15)	Ru1 N1 2.0748(15)
Ru1 C11 2.3522(9)	Ru1 C12 2.3555(9)	Ru1 C12 2.3556(9)
S1 O1 1.5026(16)	S1 C20 1.775(3)	S1 C19 1.783(2) . ?
S2 O2 1.427(3)	S2 C17 1.766(13)	S2 C18 1.771(17) . ?
S2' O2 1.387(3)	S2' C18' 1.766(18)	S2' C17' 1.772(16) . ?
N1 C1 1.340(2)	N1 C5 1.369(2)	N2 C6 1.3460(18) 2 ?
N2 C6 1.3460(18)	C1 C2 1.389(3)	C2 C3 1.376(3) . ?
C3 C4 1.391(2)	C4 C5 1.386(2)	C5 C6 1.483(2) . ?
C6 C7 1.388(2)	C7 C8 1.406(2)	C8 C7 1.406(2) 2 ?
C8 C9 1.479(3)	C9 C10 1.394(2)	C9 C10 1.394(2) 2 ?
C10 C11 1.388(2)	C11 C12 1.392(2)	C12 C11 1.392(2) 2 ?
C12 C13 1.536(3)	C13 C15 1.454(6)	C13 C15 1.454(6) 2 ?
C13 C16 1.490(6)	C13 C16 1.490(6)	C13 C14 1.597(6) . ?
C13 C14 1.597(6)		

Bond Angles

N2 Ru1 N1 79.97(4)	N2 Ru1 N1 79.98(4)	N1 Ru1 N1 159.95(7)
--------------------	--------------------	---------------------

N2 Ru1 C11 180.0	N1 Ru1 C11 100.03(4)	N1 Ru1 C11 100.02(4)
N2 Ru1 C12 87.783(11)	N1 Ru1 C12 90.97(4)	N1 Ru1 C12 88.25(4)
C11 Ru1 C12 92.217(11)	N2 Ru1 C12 87.782(11)	N1 Ru1 C12 88.25(4)
N1 Ru1 C12 90.98(4)	C11 Ru1 C12 92.218(11)	C12 Ru1 C12 175.57(2)
O1 S1 C20 106.48(12)	O1 S1 C19 106.13(11)	C20 S1 C19 96.81(13)
O2 S2 C17 109.5(10)	O2 S2 C18 110.3(10)	C17 S2 C18 99.0(10)
O2 S2' C18' 106.6(17)	O2 S2' C17' 114.3(14)	C18' S2' C17' 99.1(12)
C1 N1 C5 119.28(14)	C1 N1 Ru1 127.69(12)	C5 N1 Ru1 112.95(10)
C6 N2 C6 123.33(19)	C6 N2 Ru1 118.34(9)	C6 N2 Ru1 118.33(9)
S2' O2 S2 51.34(11)	N1 C1 C2 121.65(16)	C3 C2 C1 119.39(16)
C2 C3 C4 119.54(16)	C5 C4 C3 118.83(16)	N1 C5 C4 121.28(14)
N1 C5 C6 115.17(13)	C4 C5 C6 123.55(15)	N2 C6 C7 119.60(15)
N2 C6 C5 113.46(14)	C7 C6 C5 126.94(14)	C6 C7 C8 118.91(15)
C7 C8 C7 119.6(2)	C7 C8 C9 120.19(10)	C7 C8 C9 120.18(10)
C10 C9 C10 118.2(2)	C10 C9 C8 120.92(11)	C10 C9 C8 120.92(11)
C11 C10 C9 120.49(17)	C10 C11 C12 122.05(18)	C11 C12 C11 116.7(2)
C11 C12 C13 121.63(11)	C11 C12 C13 121.63(11)	C15 C13 C15 141.1(5)
C15 C13 C16 49.5(5)	C15 C13 C16 113.4(5)	C15 C13 C16 113.4(5)
C15 C13 C16 49.5(5)	C16 C13 C16 135.5(4)	C15 C13 C12 109.4(2)
C15 C13 C12 109.4(2)	C16 C13 C12 112.3(2)	C16 C13 C12 112.3(2)
C15 C13 C14 107.4(4)	C15 C13 C14 58.6(5)	C16 C13 C14 59.7(5)
C16 C13 C14 104.6(5)	C12 C13 C14 109.4(2)	C15 C13 C14 58.6(5)
C15 C13 C14 107.4(4)	C16 C13 C14 104.6(5)	C16 C13 C14 59.7(5)
C12 C13 C14 109.4(2)	C14 C13 C14 141.2(4)	

Torsion Angles

N2 Ru1 N1 C1 -179.30(15)	N1 Ru1 N1 C1 -179.31(15)	C11 Ru1 N1 C1 0.70(15)
C12 Ru1 N1 C1 -91.25(14)	C12 Ru1 N1 C1 93.12(14)	N2 Ru1 N1 C5 -2.56(10)
N1 Ru1 N1 C5 -2.56(10)	C11 Ru1 N1 C5 177.44(10)	C12 Ru1 N1 C5 85.49(11)
C12 Ru1 N1 C5 -90.14(11)	N1 Ru1 N2 C6 0.78(9)	N1 Ru1 N2 C6 -179.22(9)
C11 Ru1 N2 C6 -28(84)	C12 Ru1 N2 C6 92.16(8)	C12 Ru1 N2 C6 -87.84(8)
N1 Ru1 N2 C6 -179.22(9)	N1 Ru1 N2 C6 0.78(9)	C11 Ru1 N2 C6 152(70)
C12 Ru1 N2 C6 -87.84(8)	C12 Ru1 N2 C6 92.16(8)	C18' S2' O2 S2 51.5(15)
C17' S2' O2 S2 -56.8(16)	C17 S2 O2 S2' 56.1(10)	C18 S2 O2 S2' -51.9(11)
C5 N1 C1 C2 -1.7(3)	Ru1 N1 C1 C2 174.86(13)	N1 C1 C2 C3 0.7(3)
C1 C2 C3 C4 0.7(3)	C2 C3 C4 C5 -1.1(3)	C1 N1 C5 C4 1.2(2)
Ru1 N1 C5 C4 -175.81(13)	C1 N1 C5 C6 -179.13(14)	Ru1 N1 C5 C6 3.83(17)
C3 C4 C5 N1 0.2(3)	C3 C4 C5 C6 -179.44(16)	C6 N2 C6 C7 0.77(11)
Ru1 N2 C6 C7 -179.23(11)	C6 N2 C6 C5 -178.97(15)	Ru1 N2 C6 C5 1.03(15)
N1 C5 C6 N2 -3.27(19)	C4 C5 C6 N2 176.36(14)	N1 C5 C6 C7 177.01(16)
C4 C5 C6 C7 -3.4(3)	N2 C6 C7 C8 -1.5(2)	C5 C6 C7 C8 178.20(13)
C6 C7 C8 C7 0.75(11)	C6 C7 C8 C9 -179.25(11)	C7 C8 C9 C10 32.88(13)
C7 C8 C9 C10 -147.12(13)	C7 C8 C9 C10 -147.12(13)	C7 C8 C9 C10 32.88(13)
C10 C9 C10 C11 -0.54(14)	C8 C9 C10 C11 179.46(14)	C9 C10 C11 C12 1.1(3)
C10 C11 C12 C11 -0.56(15)	C10 C11 C12 C13 179.44(15)	C11 C12 C13 C15 83.3(5)
C11 C12 C13 C15 -96.7(5)	C11 C12 C13 C15 -96.7(5)	C11 C12 C13 C15 83.3(5)
C11 C12 C13 C16 30.1(5)	C11 C12 C13 C16 -149.9(5)	C11 C12 C13 C16 -149.9(5)
C11 C12 C13 C16 30.1(5)	C11 C12 C13 C14 -34.2(4)	C11 C12 C13 C14 145.8(4)
C11 C12 C13 C14 145.8(4)	C11 C12 C13 C14 -34.2(4)	

Table E.2: X-ray Crystallography Data of *trans*-[Ru(tppy)(Cl₃pcyd)Cl₂] \cdot 2CH₃CN Complex.**Atomic Coordinates****Cartesian Coordinates**

Atom		X	Y	Z
Ru	Ru	-0.03116(2)	0.686103(17)	0.868898(8)
N1	N	0.1462(2)	0.61327(18)	0.88865(9)
N2	N	-0.0063(2)	0.73709(19)	0.96276(9)
N3	N	-0.1953(2)	0.78311(18)	0.88517(9)
N4	N	-0.0586(3)	0.6371(2)	0.77256(10)
N5	N	-0.0773(4)	0.6434(3)	0.66091(12)
Cl1	Cl	0.18971(7)	0.87824(6)	0.86874(3)
Cl2	Cl	-0.24790(7)	0.49269(6)	0.87076(3)
C1	C	0.2302(3)	0.5602(3)	0.84665(12)
H1	H	0.2049	0.5493	0.8023
C2	C	0.3527(4)	0.5210(3)	0.86611(13)
H2	H	0.4113	0.4843	0.8356
C3	C	0.3885(4)	0.5356(3)	0.93009(14)
H3	H	0.4706	0.5075	0.9441
C4	C	0.3041(4)	0.5918(3)	0.97431(13)
H4	H	0.3280	0.6030	1.0187
C5	C	0.1845(3)	0.6312(2)	0.95229(11)
C6	C	0.0948(3)	0.6999(2)	0.99511(11)
C7	C	0.1075(3)	0.7284(2)	1.06100(11)
H7	H	0.1783	0.7017	1.0836
C8	C	0.0148(3)	0.7972(2)	1.09460(11)
C9	C	-0.0882(3)	0.8347(2)	1.05907(11)
H9	H	-0.1517	0.8815	1.0804 0.032
C10	C	-0.0972(3)	0.8035(2)	0.99317(11)
C11	C	-0.2030(3)	0.8309(2)	0.94855(11)
C12	C	-0.3041(3)	0.8999(3)	0.96833(12)
H12	H	-0.3070	0.9338	1.0126
C13	C	-0.4013(3)	0.9192(3)	0.92299(13)
H13	H	-0.4708	0.9668	0.9358
C14	C	-0.3951(4)	0.8680(3)	0.85916(13)
H14	H	-0.4618	0.8790	0.8274
C15	C	-0.2911(3)	0.8005(2)	0.84152(11)
H15	H	-0.2874	0.7656	0.7974
C16	C	-0.0615(3)	0.6423(3)	0.71944(12)
C17	C	0.2277(10)	0.7459(9)	0.6645(2)
H17A	H	0.2421	0.7584	0.7094
C18	C	0.3648(6)	0.7822(6)	0.6318(2)
C19	C	0.3438(6)	0.7639(5)	0.5660(2)
C20	C	0.1855(8)	0.7092(5)	0.5330(2)
H20A	H	0.1711	0.6967	0.4881
C21	C	0.0483(5)	0.6729(8)	0.5657(4)

C22	C	0.0694(7)	0.6913(10)	0.6315(4)
Cl3	Cl	-0.1441(6)	0.6136(4)	0.5219(3)
Cl4	Cl	0.5122(3)	0.8035(4)	0.52246(10)
Cl5	Cl	0.5598(4)	0.8562(4)	0.67591(15)
C17'	C	0.211(3)	0.760(3)	0.6668(7)
H17B	H	0.2235	0.7675	0.7113
C18'	C	0.3461(18)	0.8195(18)	0.6374(8)
C19'	C	0.3275(19)	0.8088(15)	0.5723(8)
C20'	C	0.174(3)	0.7386(18)	0.5365(7)
H20B	H	0.1608	0.7313	0.4920
C21'	C	0.0381(16)	0.679(2)	0.5659(13)
C22'	C	0.057(2)	0.690(3)	0.6310(13)
Cl3'	Cl	-0.150(2)	0.5865(14)	0.5235(8)
Cl4'	Cl	0.4896(10)	0.8718(11)	0.5318(3)
Cl5'	Cl	0.5332(13)	0.9059(13)	0.6793(5)
C23	C	0.0545(4)	0.7447(3)	1.19802(12)
H23	H	0.0804	0.6727	1.1754
C24	C	0.0496(4)	0.7677(3)	1.26352(13)
H24	H	0.0695	0.7095	1.2847 0.053
C25	C	0.0163(4)	0.8739(3)	1.29919(12)
C26	C	-0.0098(4)	0.9568(3)	1.26612(13)
H26	H	-0.0285	1.0319	1.2893
C27	C	-0.0093(4)	0.9338(3)	1.20054(12)
H27	H	-0.0305	0.9917	1.1795
C28	C	0.0219(3)	0.8262(2)	1.16502(11)
C29	C	0.0046(5)	0.8950(3)	1.37135(14)
C30	C	0.0250(10)	1.0288(6)	1.4056(3)
H30A	H	-0.0724	1.0465	1.3937
H30B	H	0.1239	1.0903	1.3941
H30C	H	0.0372	1.0389	1.4517
C31	C	0.1620(10)	0.8730(7)	1.4010(3)
H31A	H	0.2641	0.9307	1.3895
H31B	H	0.1511	0.7820	1.3837
H31C	H	0.1659	0.8928	1.4476
C32	C	-0.1420(10)	0.7880(7)	1.3820(3)
H32A	H	-0.2421	0.7867	1.3597
H32B	H	-0.1515	0.8027	1.4279
H32C	H	-0.1288	0.7044	1.3654
C30'	C	0.052(2)	0.8176(13)	1.4040(5)
H30D	H	-0.0159	0.7254	1.3852
H30E	H	0.0371	0.8426	1.4492
H30F	H	0.1691	0.8311	1.4002
C31'	C	-0.1880(13)	0.8755(15)	1.3793(5)
H31D	H	-0.2133	0.9441	1.3663
H31E	H	-0.2065	0.8806	1.4240
H31F	H	-0.2601	0.7900	1.3522
C32'	C	0.086(2)	1.0443(11)	1.4028(9)
H32D	H	0.0407	1.0907	1.3793
H32E	H	0.2058	1.0729	1.4017
H32F	H	0.0625	1.0635	1.4473
N6	N	-0.4155(9)	0.4693(7)	1.2813(2)

C33	C	-0.4554(7)	0.4793(7)	1.3293(2)
C34	C	-0.5096(7)	0.4874(8)	1.3924(2)
H34A	H	-0.6305	0.4589	1.3886
H34B	H	-0.4606	0.5778	1.4188
H34C	H	-0.4744	0.4311	1.4124
N7	N	-0.4741(5)	0.8154(4)	1.1130(2)
C35	C	-0.4712(5)	0.8163(4)	1.1645(3)
C36	C	-0.4675(8)	0.8120(7)	1.2305(3)
H36A	H	-0.5807	0.7833	1.2419
H36B	H	-0.4031	0.8992	1.2581
H36C	H	-0.4160	0.7508	1.2363

Bond Lengths

Ru N2	1.9636(18)	Ru N4	2.015(2)	Ru N1	2.0712(18)
Ru N3	2.0790(18)	Ru C11	2.3470(6)	Ru C12	2.3485(6)
N1 C1	1.343(3)	N1 C5	1.363(3)	N2 C6	1.350(3)
N2 C10	1.354(3)	N3 C15	1.342(3)	N3 C11	1.364(3)
N4 C16	1.169(3)	N5 C16	1.279(4)	N5 C22'	1.351(10)
N5 C22	1.431(4)	C1 C2	1.386(3)	C1 H1	0.9500
C2 C3	1.373(4)	C2 H2	0.9500	C3 C4	1.390(4)
C3 H3	0.9500	C4 C5	1.386(3)	C4 H4	0.9500
C5 C6	1.482(3)	C6 C7	1.381(3)	C7 C8	1.410(3)
C7 H7	0.9500	C8 C9	1.406(3)	C8 C28	1.479(3)
C9 C10	1.382(3)	C9 H9	0.9500	C10 C11	1.480(3)
C11 C12	1.383(3)	C12 C13	1.389(4)	C12 H12	0.9500
C13 C14	1.378(4)	C13 H13	0.9500	C14 C15	1.384(4)
C14 H14	0.9500	C15 H15	0.9500	C17 C18	1.3900
C17C22	1.3900	C17 H17A	0.9500	C18 C19	1.3900
C18 C15	1.741(4)	C19 C20	1.3900	C19 C14	1.746(3)
C20 C21	1.3900	C20 H20A	0.9500	C21 C22	1.3900
C21 C13	1.726(5)	C17' C18'	1.3900	C17' C22'	1.3900
C17' H17B	0.9500	C18' C19'	1.3900	C18' C15'	1.677(13)
C19' C20'	1.3900	C19' C14'	1.710(11)	C20' C21'	1.3900
C20' H20B	0.9500	C21' C22'	1.3900	C21' C13'	1.700(14)
C23 C24	1.387(4)	C23 C28	1.396(3)	C23 H23	0.9500
C24 C25	1.395(4)	C24 H24	0.9500	C25 C26	1.388(4)
C25 C29	1.538(4)	C26 C27	1.384(4)	C26 H26	0.9500
C27 C28	1.397(3)	C27 H27	0.9500	C29 C30'	1.413(9)
C29 C30	1.467(7)	C29 C32	1.488(7)	C29 C32'	1.555(11)
C29 C31	1.622(7)	C29 C31'	1.630(11)	C30 H30A	0.9800
C30 H30B	0.9800	C30 H30C	0.9800	C31 H31A	0.9800
C31 H31B	0.9800	C31 H31C	0.9800	C32 H32A	0.9800
C32 H32B	0.9800	C32 H32C	0.9800	C30' H30D	0.9800
C30' H30E	0.9800	C30' H30F	0.9800	C31' H31D	0.9800
C31' H31E	0.9800	C31' H31F	0.9800	C32' H32D	0.9800
C32' H32E	0.9800	C32' H32F	0.9800	N6 C33	1.099(6)
C33 C34	1.450(6)	C34 H34A	0.9800	C34 H34B	0.9800
C34 H34C	0.9800	N7 C35	1.114(6)	C35 C36	1.446(7)
C36 H36A	0.9800	C36 H36B	0.9800	C36 H36C	0.9800

Bond Angles

N2 Ru N4 178.69(8)	N2 Ru N1 79.36(7)	N4 Ru N1 101.84(8)
N2 Ru N3 79.72(7)	N4 Ru N3 99.07(8)	N1 Ru N3 159.04(8)
N2 Ru C11 90.63(6)	N4 Ru C11 88.91(7)	N1 Ru C11 86.69(6)
N3 Ru C11 92.16(6)	N2 Ru C12 88.52(6)	N4 Ru C12 91.97(7)
N1 Ru C12 92.02(6)	N3 Ru C12 88.81(6)	C11 Ru C12 178.57(2)
C1 N1 C5 119.09(19)	C1 N1 Ru 127.17(16)	C5 N1 Ru 113.59(14)
C6 N2 C10 121.81(19)	C6 N2 Ru 119.25(15)	C10 N2 Ru 118.87(14)
C15 N3 C11 119.20(19)	C15 N3 Ru 127.73(16)	C11 N3 Ru 113.06(14)
C16 N4 Ru 162.9(2)	C16 N5 C22' 120.9(13)	C16 N5 C22 118.4(5)
C22' N5 C22 2.8(18)	N1 C1 C2 121.9(2)	N1 C1 H1 119.1
C2 C1 H1 119.1	C3 C2 C1 119.1(2)	C3 C2 H2 120.4
C1 C2 H2 120.4	C2 C3 C4 119.8(2)	C2 C3 H3 120.1
C4 C3 H3 120.1	C5 C4 C3 118.7(2)	C5 C4 H4 120.7
C3 C4 H4 120.7	N1 C5 C4 121.4(2)	N1 C5 C6 115.13(19)
C4 C5 C6 123.4(2)	N2 C6 C7 120.3(2)	N2 C6 C5 112.51(19)
C7 C6 C5 127.1(2)	C6 C7 C8 119.7(2)	C6 C7 H7 120.1
C8 C7 H7 120.1	C9 C8 C7 118.0(2)	C9 C8 C28 120.8(2)
C7 C8 C28 121.2(2)	C10 C9 C8 120.1(2)	C10 C9 H9 120.0
C8 C9 H9 120.0	N2 C10 C9 119.96(19)	N2 C10 C11 112.85(19)
C9 C10 C11 127.2(2)	N3 C11 C12 121.0(2)	N3 C11 C10 115.47(19)
C12 C11 C10 123.5(2)	C11 C12 C13 119.5(2)	C11 C12 H12 120.2
C13 C12 H12 120.2	C14 C13 C12 118.9(2)	C14 C13 H13 120.6
C12 C13 H13 120.6	C13 C14 C15 119.7(2)	C13 C14 H14 120.2
C15 C14 H14 120.2	N3 C15 C14 121.7(2)	N3 C15 H15 119.2
C14 C15 H15 119.2	N4 C16 N5 175.4(3)	C18 C17 C22 120.0
C18 C17 H17A 120.0	C22 C17 H17A 120.0	C19 C18 C17 120.0
C19 C18 C15 121.8(4)	C17 C18 C15 118.1(4)	C18 C19 C20 120.0
C18 C19 C14 121.7(4)	C20 C19 C14 118.3(4)	C21 C20 C19 120.0
C21 C20 H20A 120.0	C19 C20 H20A 120.0	C20 C21 C22 120.0
C20 C21 C13 117.2(6)	C22 C21 C13 122.7(6)	C21 C22 C17 120.0
C21 C22 N5 116.5(6)	C17 C22 N5 123.3(6)	C18' C17' C22' 120.0
C18' C17' H17B 120.0	C22' C17' H17B 120.0	C19' C18' C17' 120.0
C19' C18' C15' 118.9(15)	C17' C18' C15' 121.1(15)	C18' C19' C20' 120.0
C18' C19' C14' 122.8(14)	C20' C19' C14' 117.1(14)	C19' C20' C21' 120.0
C19' C20' H20B 120.0	C21' C20' H20B 120.0	C22' C21' C20' 120.0
C22' C21' C13' 118.4(19)	C20' C21' C13' 121.6(19)	N5 C22' C21' 120(2)
N5 C22' C17' 120(2)	C21' C22' C17' 120.0	C24 C23 C28 120.7(2)
C24 C23 H23 119.6	C28 C23 H23 119.6	C23 C24 C25 121.8(3)
C23 C24 H24 119.1	C25 C24 H24 119.1	C26 C25 C24 116.8(2)
C26 C25 C29 122.0(3)	C24 C25 C29 121.2(3)	C27 C26 C25 122.2(3)
C27 C26 H26 118.9	C25 C26 H26 118.9	C26 C27 C28 120.6(2)
C26 C27 H27 119.7	C28 C27 H27 119.7	C23 C28 C27 117.8(2)
C23 C28 C8 121.2(2)	C27 C28 C8 121.0(2)	C30' C29 C30 119.4(7)
C30' C29 C32 68.7(7)	C30 C29 C32 117.0(5)	C30' C29 C25 119.5(5)
C30 C29 C25 114.2(3)	C32 C29 C25 109.3(3)	C30' C29 C32' 114.4(8)
C30 C29 C32' 19.0(8)	C32 C29 C32' 134.4(7)	C25 C29 C32' 107.1(7)
C30' C29 C31 35.8(6)	C30 C29 C31 104.5(4)	C32 C29 C31 104.5(4)

C25 C29 C31 106.2(3)	C32' C29 C31 90.7(8)	C30' C29 C31' 109.4(7)
C30 C29 C31' 80.2(6)	C32 C29 C31' 45.3(6)	C25 C29 C31' 105.1(5)
C32' C29 C31' 99.0(7)	C31 C29 C31' 142.8(5)	C29 C30 H30A 109.5
C29 C30 H30B 109.5	C29 C30 H30C 109.5	C29 C31 H31A 109.5
C29 C31 H31B 109.5	C29 C31 H31C 109.5	C29 C32 H32A 109.5
C29 C32 H32B 109.5	C29 C32 H32C 109.5	C29 C30' H30D 109.5
C29 C30' H30E 109.5	H30D C30' H30E 109.5	C29 C30' H30F 109.5
H30D C30' H30F 109.5	H30E C30' H30F 109.5	C29 C31' H31D 109.5
C29 C31' H31E 109.5	H31D C31' H31E 109.5	C29 C31' H31F 109.5
H31D C31' H31F 109.5	H31E C31' H31F 109.5	C29 C32' H32D 109.5
C29 C32' H32E 109.5	H32D C32' H32E 109.5	C29 C32' H32F 109.5
H32D C32' H32F 109.5	H32E C32' H32F 109.5	N6 C33 C34 177.9(8)
C33 C34 H34A 109.5	C33 C34 H34B 109.5	H34A C34 H34B 109.5
C33 C34 H34C 109.5	H34A C34 H34C 109.5	H34B C34 H34C 109.5
N7 C35 C36 177.7(6)	C35 C36 H36A 109.5	C35 C36 H36B 109.5
H36A C36 H36B 109.5	C35 C36 H36C 109.5	H36A C36 H36C 109.5
H36B C36 H36C 109.5		

Torsion Angles

N2 Ru N1 C1 -173.3(2)	N4 Ru N1 C1 6.2(2)	N3 Ru N1 C1 -169.4(2)
Cl1 Ru N1 C1 -82.0(2)	Cl2 Ru N1 C1 98.6(2)	N2 Ru N1 C5 2.24(16)
N4 Ru N1 C5 -178.31(16)	N3 Ru N1 C5 6.1(3)	Cl1 Ru N1 C5 93.50(16)
Cl2 Ru N1 C5 -85.87(16)	N4 Ru N2 C6 -160(4)	N1 Ru N2 C6 -3.73(17)
N3 Ru N2 C6 177.67(19)	Cl1 Ru N2 C6 -90.25(17)	Cl2 Ru N2 C6 88.60(17)
N4 Ru N2 C10 24(4)	N1 Ru N2 C10 179.32(19)	N3 Ru N2 C10 0.72(17)
Cl1 Ru N2 C10 92.80(17)	Cl2 Ru N2 C10 -88.35(17)	N2 Ru N3 C15 -178.8(2)
N4 Ru N3 C15 1.8(2)	N1 Ru N3 C15 177.4(2)	Cl1 Ru N3 C15 91.0(2)
Cl2 Ru N3 C15 -90.1(2)	N2 Ru N3 C11 0.19(16)	N4 Ru N3 C11 -179.29(16)
N1 Ru N3 C11 -3.6(3)	Cl1 Ru N3 C11 -90.05(15)	Cl2 Ru N3 C11 88.91(15)
N2 Ru N4 C16 36(4)	N1 Ru N4 C16 -119.6(7)	N3 Ru N4 C16 58.8(7)
Cl1 Ru N4 C16 -33.2(7)	Cl2 Ru N4 C16 147.9(7)	C5 N1 C1 C2 1.2(4)
Ru N1 C1 C2 176.5(2)	N1 C1 C2 C3 0.5(5)	C1 C2 C3 C4 -1.3(5)
C2 C3 C4 C5 0.3(5)	C1 N1 C5 C4 -2.2(4)	Ru N1 C5 C4 -178.1(2)
C1 N1 C5 C6 175.2(2)	Ru N1 C5 C6 -0.7(3)	C3 C4 C5 N1 1.4(4)
C3 C4 C5 C6 -175.8(3)	C10 N2 C6 C7 0.4(4)	Ru N2 C6 C7 -176.44(18)
C10 N2 C6 C5 -178.8(2)	Ru N2 C6 C5 4.3(3)	N1 C5 C6 N2 -2.2(3)
C4 C5 C6 N2 175.2(2)	N1 C5 C6 C7 178.6(2)	C4 C5 C6 C7 -4.0(4)
N2 C6 C7 C8 -0.3(4)	C5 C6 C7 C8 178.8(2)	C6 C7 C8 C9 0.0(4)
C6 C7 C8 C28 178.3(2)	C7 C8 C9 C10 0.3(4)	C28 C8 C9 C10 -178.1(2)
C6 N2 C10 C9 -0.1(3)	Ru N2 C10 C9 176.72(17)	C6 N2 C10 C11 -178.3(2)
Ru N2 C10 C11 -1.4(3)	C8 C9 C10 N2 -0.2(4)	C8 C9 C10 C11 177.6(2)
C15 N3 C11 C12 -1.9(4)	Ru N3 C11 C12 179.1(2)	C15 N3 C11 C10 178.1(2)
Ru N3 C11 C10 -1.0(3)	N2 C10 C11 N3 1.5(3)	C9 C10 C11 N3 -176.4(2)
N2 C10 C11 C12 -178.5(2)	C9 C10 C11 C12 3.5(4)	N3 C11 C12 C13 1.0(4)
C10 C11 C12 C13 -178.9(3)	C11 C12 C13 C14 0.4(4)	C12 C13 C14 C15 -0.9(5)
C11 N3 C15 C14 1.3(4)	Ru N3 C15 C14 -179.8(2)	C13 C14 C15 N3 0.1(4)
Ru N4 C16 N5 -114(4)	C22' N5 C16 N4 -177(4)	C22 N5 C16 N4 -175(4)
C22 C17 C18 C19 0.0	C22 C17 C18 C15 177.5(4)	C17 C18 C19 C20 0.0
Cl5 C18 C19 C20 -177.4(4)	C17 C18 C19 C14 -178.1(4)	Cl5 C18 C19 C14 4.5(5)

C18 C19 C20 C21 0.0	C14 C19 C20 C21 178.2(4)	C19 C20 C21 C22 0.0
C19 C20 C21 C13 176.7(5)	C20 C21 C22 C17 0.0	C13 C21 C22 C17 -176.5(6)
C20 C21 C22 N5 -176.0(8)	C13 C21 C22 N5 7.5(5)	C18 C17 C22 C21 0.0
C18 C17 C22 N5 175.7(9)	C16 N5 C22 C21 170.7(3)	C22' N5 C22 C21 -34(37)
C16 N5 C22 C17 -5.1(8)	C22' N5 C22 C17 150(37)	C22' C17' C18' C19' 0.0
C22' C17' C18' C15' 179.5(13)	C17' C18' C19' C20' 0.0	C15' C18' C19' C20' -179.5(12)
C17' C18' C19' C14' -176.6(13)	C15' C18' C19' C14' 3.9(16)	C18' C19' C20' C21' 0.0
C14' C19' C20' C21' 176.8(13)	C19' C20' C21' C22' 0.0	C19' C20' C21' C13' -177.0(16)
C16 N5 C22' C21' 174.0(8)	C22 N5 C22' C21' 148(38)	C16 N5 C22' C17' -12(2)
C22 N5 C22' C17' -38(36)	C20' C21' C22' N5 174(3)	C13' C21' C22' N5 -9.4(19)
C20' C21' C22' C17' 0.0	C13' C21' C22' C17' 177.1(16)	C18' C17' C22' N5 -174(3)
C18' C17' C22' C21' 0.0	C28 C23 C24 C25 -1.6(5)	C23 C24 C25 C26 -0.8(5)
C23 C24 C25 C29 177.6(3)	C24 C25 C26 C27 2.4(5)	C29 C25 C26 C27 -176.0(3)
C25 C26 C27 C28 -1.6(5)	C24 C23 C28 C27 2.4(4)	C24 C23 C28 C8 -175.5(3)
C26 C27 C28 C23 -0.8(4)	C26 C27 C28 C8 177.1(3)	C9 C8 C28 C23 149.6(3)
C7 C8 C28 C23 -28.8(4)	C9 C8 C28 C27 -28.3(4)	C7 C8 C28 C27 153.4(3)
C26 C25 C29 C30' -172.1(9)	C24 C25 C29 C30' 9.5(9)	C26 C25 C29 C30 -21.2(6)
C24 C25 C29 C30 160.4(5)	C26 C25 C29 C32 112.0(5)	C24 C25 C29 C32 -66.3(6)
C26 C25 C29 C32' -40.1(9)	C24 C25 C29 C32' 141.6(9)	C26 C25 C29 C31 -135.9(4)
C24 C25 C29 C31 45.8(5)	C26 C25 C29 C31' 64.6(7)	C24 C25 C29 C31' -113.7(6)

Table E.3: Atomic Coordinates of Ru(tpy)Cl₃ Complex.**Cartesian Coordinates**

	Atom	X	Y	Z
1	Ru Ru1	-0.0001191	-0.7407216	-0.0476185
2	N N1	-2.0600619	-0.3395651	0.0504455
3	C C3	-4.3802423	-0.8834822	0.1142723
4	C C5	-3.6826188	1.4183697	0.0313562
5	C C4	-4.7037088	0.4712408	0.0788704
6	C C6	-2.354808	0.991859	0.017874
7	C C2	-3.037362	-1.2531397	0.0995039
8	H H7	-5.7408393	0.7927249	0.088538
9	H H8	-2.7036182	-2.2853619	0.1219898
10	H H12	-5.1476261	-1.6488821	0.1527693
11	H H13	-3.9185739	2.4763459	0.0036161
12	N N2	2.0598424	-0.340573	0.0512444
13	C C8	4.3795793	-0.8858501	0.115657
14	C C9	3.6835318	1.4164397	0.0306682
15	C C10	4.7040365	0.4686875	0.0788267
16	C C11	2.3554185	0.9905461	0.017675
17	C C12	3.036553	-1.2546685	0.101397
18	H H5	5.1464279	-1.6517553	0.1548158
19	H H17	3.9196531	2.4743161	0.0021727

20	H H18	5.7414255	0.7893373	0.0880381
21	H H20	2.7024152	-2.2867104	0.1252464
22	N N3	0.0003144	1.2549592	-0.0321316
23	C C14	1.211337	3.2939151	-0.0096646
24	C C15	-1.2094492	3.2947169	-0.0094952
25	C C16	0.0011485	3.9882227	-0.0139938
26	C C17	-1.186946	1.8987214	-0.0146319
27	C C18	1.1880403	1.8980175	-0.014957
28	H H3	2.1509002	3.8345262	0.0049862
29	H H27	-2.1488384	3.8356064	0.0049374
30	H H28	0.0015462	5.0734579	-0.0100565
31	Cl Cl2	0.000122	-0.7626171	2.3728821
32	Cl Cl1	0.001943	-0.6701234	-2.4394885
33	Cl Cl3	-0.0035564	-3.152976	-0.1021522

Table E.4: Atomic Coordinates of *trans*-[Ru(tpy)(Clpcyd)Cl₂] Complex.

Cartesian Coordinates

	Atom	X	Y	Z
1	Ru Ru1	1.0235981	0.0028067	0.4424438
2	N N1	1.4146077	2.0524824	0.2541166
3	C C3	0.9797861	4.3884813	0.5291312
4	C C5	2.97365	3.6661745	-0.594882
5	C C4	2.1660203	4.7008435	-0.1323497
6	C C6	2.5806168	2.3426036	-0.3908725
7	C C2	0.6403221	3.0504799	0.7035651
8	H H7	2.4610298	5.7342842	-0.2857616
9	H H8	-0.2667078	2.7479542	1.212331
10	H H12	0.3211447	5.1622631	0.9084198
11	H H13	3.9029166	3.8850094	-1.1089047
12	N N2	1.3916547	-2.0521911	0.2649733
13	C C8	0.9299681	-4.3816618	0.5512901
14	C C9	2.931204	-3.6877875	-0.5775215
15	C C10	2.1119353	-4.7108522	-0.1096353
16	C C11	2.5537783	-2.3588062	-0.3793399
17	C C12	0.6062028	-3.038998	0.7196756
18	H H5	0.2627047	-5.1459568	0.934736
19	H H17	3.8574648	-3.9197236	-1.0911967
20	H H18	2.3947913	-5.7483515	-0.2584934
21	H H20	-0.2969046	-2.7236402	1.2276276
22	N N3	2.7903485	-0.0096882	-0.4999972

23	C	C14	4.5496685	-1.2305248	-1.5314307
24	C	C15	4.5634199	1.1859093	-1.5373302
25	C	C16	5.1577206	-0.0265845	-1.8850544
26	C	C17	3.3580775	1.1708645	-0.8333735
27	C	C18	3.344533	-1.1982308	-0.8276512
28	H	H3	5.0060475	-2.1750477	-1.8040906
29	H	H27	5.0304677	2.1238199	-1.8146901
30	H	H28	6.0935253	-0.0332119	-2.4345447
31	Cl	Cl1	-0.112247	0.0023731	-1.753728
32	Cl	Cl2	2.1150346	0.00344	2.6374537
33	N	N4	-0.769886	0.0142421	1.2976438
34	C	C1	-1.9335505	0.0183573	1.5440844
35	N	N5	-3.1464155	0.0235974	1.9212705
36	C	C7	-4.1944339	0.0167736	1.0105089
37	C	C13	-5.1139088	-0.0020859	-1.2386172
38	C	C19	-6.6050592	0.0160796	0.6867276
39	C	C20	-6.4026381	0.0037142	-0.6958679
40	C	C21	-5.5035073	0.022575	1.5327215
41	C	C22	-4.0138149	0.0044095	-0.392046
42	H	H2	-7.6129665	0.0204528	1.0884129
43	H	H6	-3.007626	0.0000267	-0.8078697
44	H	H9	-4.9776337	-0.0116348	-2.314763
45	H	H1	-5.6291943	0.0321411	2.6107129
46	Cl	Cl3	-7.7921692	-0.004718	-1.7723077

Table E.5: Atomic Coordinates of *trans*-[Ru(tpy)(Cl₂pcyd)Cl₂] Complex.

Cartesian Coordinates

	Atom	X	Y	Z
1	Ru Ru1	1.3429366	0.0001872	-0.076389
2	N N1	1.5119316	2.0979382	-0.2003466
3	C C3	0.7654047	4.3593317	-0.4254492
4	C C5	3.1057134	3.8914007	-0.1652732
5	C C4	2.0762703	4.8172317	-0.3257007
6	C C6	2.8030109	2.5314225	-0.1043168
7	C C2	0.527216	2.9877229	-0.3584954
8	H H7	2.299347	5.8785736	-0.3739842
9	H H8	-0.469207	2.5680839	-0.4353124
10	H H12	-0.065881	5.0441253	-0.5548214
11	H H13	4.1344069	4.2256303	-0.0898158
12	N N2	1.9413095	-2.0041757	0.0902881

13	C	C8	1.6845389	-4.3812333	0.1754098
14	C	C9	3.8714856	-3.407506	0.3481623
15	C	C10	3.0594414	-4.5397753	0.3224928
16	C	C11	3.2932091	-2.1443637	0.2297541
17	C	C12	1.1645954	-3.0930191	0.061973
18	H	H5	1.0144633	-5.2336981	0.1479352
19	H	H17	4.9455336	-3.5089763	0.4573403
20	H	H18	3.4987074	-5.528306	0.4142718
21	H	H20	0.1027915	-2.9096029	-0.0545566
22	N	N3	3.330921	0.2248904	0.0878378
23	C	C14	5.4621568	-0.7544315	0.3684594
24	C	C15	5.2097152	1.6533021	0.1920693
25	C	C16	6.0176311	0.5253404	0.3454664
26	C	C17	3.8304849	1.4738819	0.0624592
27	C	C18	4.0772621	-0.8852366	0.2338761
28	H	H3	6.0974455	-1.6241303	0.4886148
29	H	H27	5.6502023	2.6433514	0.1766617
30	H	H28	7.0915443	0.6452457	0.4493827
31	Cl	Cl2	1.3080934	0.1929878	2.3519207
32	N	N4	-0.6390038	-0.2790306	-0.1903352
33	C	C1	-1.7754398	-0.6298385	-0.1984607
34	N	N5	-2.9318137	-1.1486257	-0.2419872
35	C	C7	-4.1083141	-0.4582971	-0.0627513
36	C	C13	-5.390096	1.5678439	0.4423923
37	C	C19	-6.5598347	-0.5059212	-0.0314741
38	C	C20	-6.5777845	0.8500664	0.2899279
39	C	C21	-5.3373394	-1.1470439	-0.2028824
40	C	C22	-4.1789728	0.9142376	0.2665266
41	Cl	Cl1	1.6916229	-0.1342141	-2.4771159
42	Cl	Cl5	-8.1223906	1.6610554	0.5079259
43	Cl	Cl7	-5.3393181	-2.8503208	-0.6068287
44	H	H1	-7.4835909	-1.0594107	-0.1480575
45	H	H2	-3.2476916	1.4598035	0.3922209
46	H	H4	-5.4189487	2.6217618	0.6977095

Table E.6: Atomic Coordinates of *trans*-[Ru(tpy)(Cl₃pcyd)Cl₂] Complex.

Cartesian Coordinates				
	Atom	X	Y	Z
1	Ru Ru1	1.61837	-0.0997743	-0.0709104
2	N N1	1.396514	1.9964568	-0.1937994

3	C	C3	0.2456337	4.0886978	-0.3581899
4	C	C5	2.6365536	4.0510463	-0.151345
5	C	C4	1.4524871	4.7761309	-0.2726083
6	C	C6	2.5889312	2.658065	-0.1145708
7	C	C2	0.2637882	2.6956692	-0.3159329
8	H	H7	1.4775393	5.8610991	-0.2996957
9	H	H8	-0.6440769	2.1079714	-0.3815835
10	H	H12	-0.700035	4.6110208	-0.4548496
11	H	H13	3.5875114	4.5675051	-0.0834713
12	N	N2	2.5764477	-1.9599696	0.0857194
13	C	C8	2.7550219	-4.3424523	0.1830016
14	C	C9	4.7356613	-2.9883065	0.2765963
15	C	C10	4.1404135	-4.2487705	0.2785318
16	C	C11	3.934911	-1.8511275	0.1782268
17	C	C12	2.007289	-3.1699378	0.0891227
18	H	H5	2.2497971	-5.3022677	0.1805375
19	H	H17	5.813368	-2.8932352	0.3487949
20	H	H18	4.7538908	-5.141328	0.3528697
21	H	H20	0.926053	-3.1781593	0.0144763
22	N	N3	3.5357525	0.4862953	0.0422306
23	C	C14	5.8166443	-0.0887322	0.2563109
24	C	C15	5.1238359	2.2330397	0.1038655
25	C	C16	6.1278661	1.2711667	0.2240899
26	C	C17	3.7967907	1.8056497	0.0135655
27	C	C18	4.4756566	-0.4695604	0.1621844
28	H	H3	6.6037537	-0.8272378	0.353761
29	H	H27	5.3766238	3.2866241	0.0833911
30	H	H28	7.164565	1.5852769	0.2952423
31	Cl	Cl2	1.616778	0.1007026	2.3522473
32	N	N4	-0.287578	-0.7225399	-0.139633
33	C	C1	-1.3947623	-1.1534679	-0.1260277
34	N	N5	-2.5185804	-1.7445814	-0.1279711
35	C	C7	-3.7244957	-1.0876574	-0.0516741
36	C	C13	-5.0830144	0.936792	0.1713041
37	C	C19	-6.1666599	-1.2069349	-0.0561169
38	C	C20	-6.2592965	0.178466	0.0908602
39	C	C21	-4.9271859	-1.8299147	-0.1249586
40	C	C22	-3.8470587	0.3095577	0.1027502
41	Cl	Cl1	1.9374839	-0.194732	-2.4726411
42	Cl	Cl4	-5.1296288	2.6788107	0.3578128
43	Cl	Cl5	-7.8428979	0.9124605	0.1699259
44	Cl	Cl7	-4.8707383	-3.5671585	-0.3114029
45	H	H1	-7.0715422	-1.7992207	-0.1183162

46 H H2 -2.9446315 0.906461 0.1781485

Table E.7: Atomic Coordinates of *trans*-[Ru(tpy)(Cl₄pcyd)Cl₂] Complex.

Cartesian Coordinates

	Atom	X	Y	Z
1	Ru Ru1	1.7951541	-0.1350495	-0.0867806
2	N N1	1.8696613	1.9408942	-0.4335106
3	C C3	1.0198521	4.1317041	-0.873843
4	C C5	3.388026	3.7808883	-0.6858398
5	C C4	2.3137598	4.6435515	-0.8996007
6	C C6	3.145274	2.42772	-0.4537236
7	C C2	0.8406399	2.7694521	-0.6368618
8	H H7	2.4899609	5.6988939	-1.0833456
9	H H8	-0.1412431	2.3117826	-0.6051579
10	H H12	0.1548433	4.7661558	-1.0344054
11	H H13	4.4039948	4.159447	-0.7003628
12	N N2	2.4817452	-2.0879051	0.2758563
13	C C8	2.3212782	-4.4430395	0.656486
14	C C9	4.4720757	-3.375423	0.6455064
15	C C10	3.7045798	-4.5309559	0.7821879
16	C C11	3.8412469	-2.1588617	0.3899246
17	C C12	1.7474504	-3.198209	0.4023539
18	H H5	1.686117	-5.3168327	0.7540302
19	H H17	5.5514489	-3.423106	0.7376728
20	H H18	4.1850461	-5.4835881	0.9828192
21	H H20	0.6768074	-3.0652803	0.2964746
22	N N3	3.7797062	0.1788781	-0.0238843
23	C C14	5.9563012	-0.6835166	0.2761817
24	C C15	5.5976074	1.677472	-0.1667689
25	C C16	6.4559986	0.6047488	0.0798722
26	C C17	4.2226621	1.4344054	-0.2151299
27	C C18	4.5739258	-0.8793847	0.2178155
28	H H3	6.6321372	-1.5087529	0.4676689
29	H H27	5.9966775	2.674223	-0.3135451
30	H H28	7.5273296	0.7751768	0.1209921
31	Cl Cl1	2.0860463	-0.4938402	-2.4652151
32	Cl Cl2	1.8473246	0.2940217	2.301587
33	N N4	-0.1816755	-0.4725673	-0.109956
34	C C1	-1.3520648	-0.6709843	-0.0558881
35	N N5	-2.5382412	-1.110095	-0.0475676

36	C	C7	-3.7421315	-0.4801137	0.0335541
37	C	C13	-6.1702902	-0.6968869	-0.2493635
38	C	C19	-5.2564196	1.3855519	0.5243006
39	C	C20	-6.3611007	0.620099	0.1653074
40	C	C21	-3.9637863	0.856973	0.4679448
41	C	C22	-4.8916869	-1.2495326	-0.3146252
42	Cl	Cl3	-4.6603177	-2.8916429	-0.8368371
43	Cl	Cl6	-2.6064252	1.8252814	0.9790051
44	Cl	Cl7	-5.5424269	3.0304716	1.0514969
45	H	H1	-7.3573018	1.0411026	0.2109497
46	Cl	Cl4	-7.5859751	-1.6246109	-0.6877283

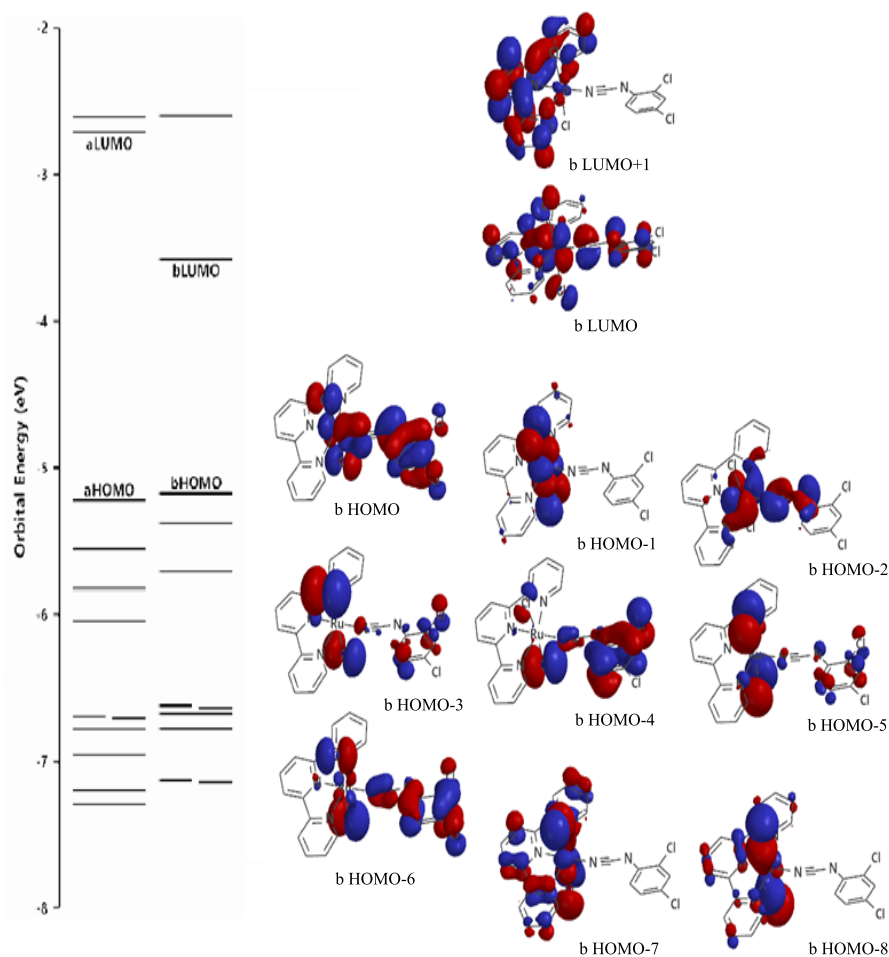


Figure E.1: DFT calculation of orbital energies and selected molecular orbitals of *trans*-[Ru(tpy)(Cl₂pcyd)Cl₂] complex.

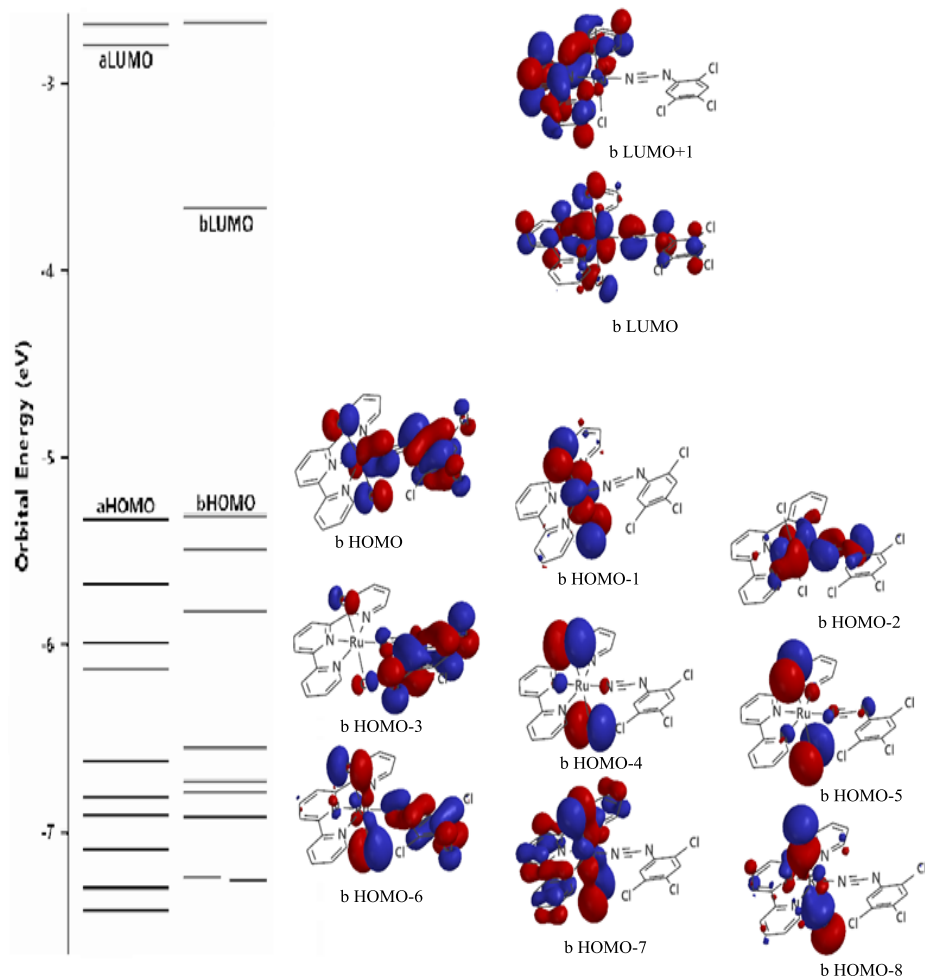


Figure E.2: DFT calculation of orbital energies and selected molecular orbitals of *trans*-[Ru(tpy)(Cl₃pcyd)Cl₂] complex.